Forschungszentrum Karlsruhe
in der Helmholtz-Gemeinschaft

Wissenschaftliche Berichte
FZKA 6966
EUR 21019 EN

Nuclear Fusion Programme Annual Report of the Association Forschungszentrum Karlsruhe/EURATOM

October 2002 - September 2003

Programm Kernfusion

Januar 2004

Forschungszentrum Karlsruhe

in der Helmholtz-Gemeinschaft

Wissenschaftliche Berichte

FZKA 6966
EUR 21019 EN

Nuclear Fusion Programme
Annual Report of the
Association Forschungszentrum Karlsruhe/
EURATOM
October 2002 - September 2003

compiled by W. Bahm
Programm Kernfusion

Forschungszentrum Karlsruhe GmbH, Karlsruhe
2004

Als Manuskript vervielfältigt
Für diesen Bericht behalten wir uns alle Rechte vor

Forschungszentrum Karlsruhe GmbH
Postfach 3640, 76021 Karlsruhe

ISSN 0947-8620

Introduction

Nuclear fusion represents a most promising option for a safe, sustainable energy source which can be made inherently safe and which, even with a substantial contribution to a future global energy supply will not meet resource limits and should not leave burdens for future generations. Fusion research therefore has to fully explore this option as to provide a complete basis of proven information whether energy production by fusion is technically feasible, ecologically tolerable and finally, economically meaningful.

The FZK fusion research programme is fully integrated in the European Fusion Programme which follows a road map towards commercial fusion energy (Fig. 1). Three major elements of research and development are required in order to generate the know-how for the construction of a fusion power station DEMO/PROTO:

A base physics programme targeted to improve capabilities to simulate plasma confinement concepts while making use of existing experimental facilities.

A major facilities programme including ITER as the most important next step, IFMIF for the qualification of materials for DEMO and a component test facility.

A base technology programme comprising plasma support technologies such as superconducting magnets, fuelling systems, high heat flux components, remote maintenance, reactor relevant steady state plasma heating systems etc., and fusion power technologies such as breeding blankets, helium cooled divertor and tritium extraction systems.

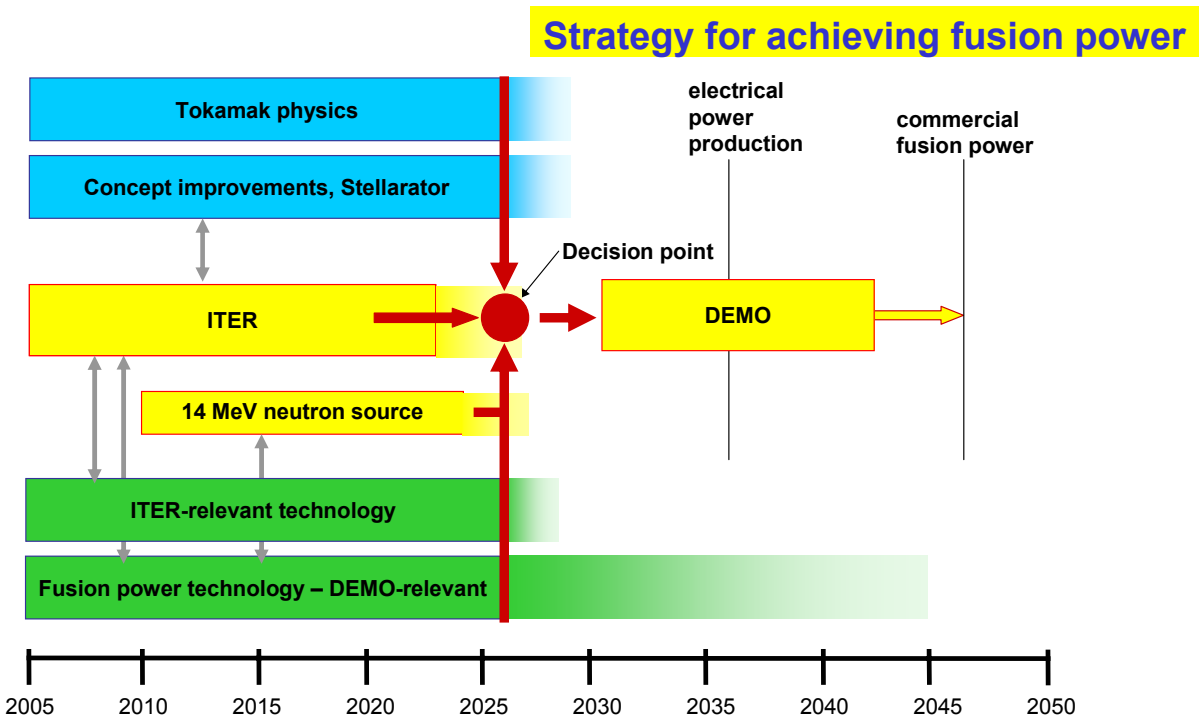

The activities of all the European fusion laboratories (known as EURATOM Associations) and industry are combined into one organisational structure via the European Fusion Development Agreement (EFDA). EFDA has a leader and two associate leaders (one for JET and one for fusion technology). It is guided by a steering committee, consisting of the

heads of association laboratories, which has to approve the major strategy and annual work programmes as well as large contracts with industry or associations.

Within this framework FZK is developing key technologies in the areas of superconducting magnets, microwave heating systems (Electron-Cyclotron-Resonance-Heating, ECRH), the deuterium-tritium fuel cycle, He-cooled breeding blankets, a He-cooled divertor and structural materials as well as refractory metals for high heat flux applications including a major participation in the international IFMIF project. Furthermore investigations on plasma wall interactions and core and divertor modelling are carried out.

The results from experimental activities such as the tests of superconducting model coils in the test facility TOSKA, the quasi-stationary gyrotron operation and the operation of fuel cycle subsystems and components with deuterium-tritium have already been utilised for the design work for ITER. In addition large progress has been made in the development of breeding blankets and in the structural materials development as well as initial progress in the development of a He-cooled divertor for DEMO. All of this work has already been utilised in the European reactor studies.

Substantial efforts are being dedicated towards engineering design demands, which is also true for the DEMO-related work. In order to efficiently manage these tasks a project-oriented approach is required involving a quality assured and quality controlled exploitation of R&D results. The detailed design and construction of ITER components and subsystems needs to be supported by experiments such as prototype testing, validation of scale up factors and additional R&D. This process shall result in the development of complete licensable components and systems. In a later phase support has to be provided to industrial partners who shall produce, assemble and finally install the components or systems into ITER, taking quality control and licensing aspects into account. However, the responsibility for the performance and the overall management of the procurement, installation and commissioning shall remain with the designers.

In order to meet this challenge, a project-oriented organisation structure has been introduced in the FZK fusion programme by establishing task forces in the areas Blanket/Divertor, Microwave Heating, Superconducting Magnets, Fuel Cycle and IFMIF (14 MeV neutron source). A task force which is responsible for a large component or subsystem to be delivered to ITER can be seen as a design and development division with a division head and several groups, each of them having a group leader. A team of design engineers supported by CAD constitutes the nucleus of each group in the task force. Besides the above-mentioned task forces materials research will be also applied for ITER construction and for the DEMO-relevant work.

About 200 professionals and technicians are involved in the fusion programme of the Association FZK-EURATOM with additional support of the technical departments.

Progress from October 2002 to September 2003 is reported. More information is available from the programme management and from the responsible scientists. The website www.fzk.de/fusion offers further access to the fusion activities of FZK.

Contents Page

Introduction

Page

Page

Page

Page

Plasma Edge

T 436/01
Experimental Investigation of Flakes Formation by Redeposition of Carbon eroded by H/D/T

The question whether graphite can be used as target or wall material in ITER is related to two adverse properties of graphite: its high erosion probability in general and the formation of hydrocarbon films or even flakes on cool surfaces. Erosion, and particularly chemical erosion – which is even important for very low plasma temperatures – may lead to intolerably high mass losses. Film formation, on the other hand, can lead to severe problems because of the high amounts of tritium stored in such layers.

These problems were pursued in the plasma generator PSI-2 run by the Berlin division of IPP. It is a stationary high current arc discharge in an axial magnetic field. This facility allows the production of a stationary plasma column of about 2 m in length and 8 cm in diameter. It is used for basic as well as applied research in the field of plasma physics. With respect to the problems arising in connection with nuclear fusion, a number of technical investigations has also been conducted in close contact with the EFDA group in Garching. In particular the problem of chemical erosion of graphite materials being foreseen for ITER has been a joint project. In this context the chemical erosion yield of various CFC materials was studied in hydrogen and deuterium discharges with emphasis on the important question of whether the erosion is dependent on the ion flux density. Starting with moderate or low flux densities around 10^{21} ions /m^2 s each hydrogen ion hitting the target has a chance of nearly 10 % of releasing a methane molecule (or some other carbon-consisting molecule) from the surface. However, extending the measurements up to flux densities of $2 \cdot 10^{23}$ ions /m^2 s a substantial and most favourable reduction in this erosion yield down to values of about 0.5 % was found. In Fig. 1 the results obtained at PSI-2 are shown as part of the total data set that has meanwhile been collected in a world wide effort (see J. Roth, ITPA meeting, St. Petersburg, July 8, 2003).

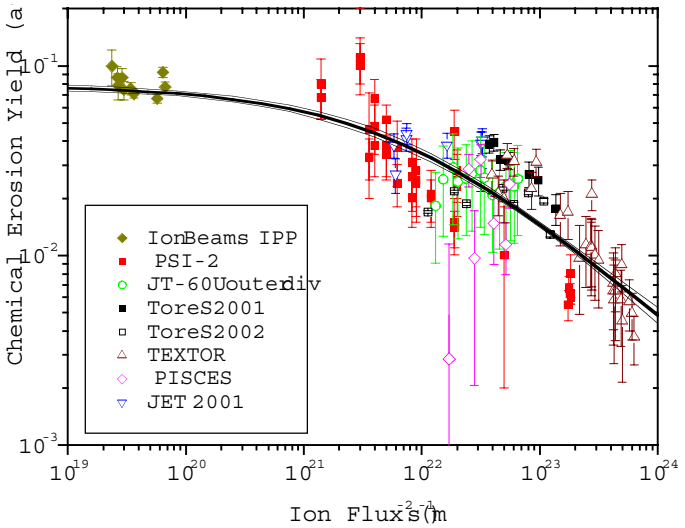

Fig. 1: Chemical erosion yield of graphite as a function of particle flux density.

Already in 2001 a so called “hot liner” arrangement was attached to the plasma generator for studying the erosion and deposition behaviour of hydrocarbons under conditions similar to that of ITER. During the period Sept. 2002 to Oct. 2003 these experiments were continued and extended to discharges using various background gases (H, D, Ar). Furthermore, the plasma density was increased in order to enhance the desintegration processes of hydrocarbon molecules during the first plasma passage. The hydrocarbons were either generated by chemical erosion of a graphite target or were injected as gases into the plasma through a nozzle. The liner duct (1.5 m length, 0.2 m dia.) is mounted opposite to the target and near to the plasma edge. It is equipped with a heated inlet structure and a number of silicon wafers and cavities are distributed along its length for the detection of deposition or erosion of hydrocarbon films. From the experiments we learnt that the net growth of such layers arises from a competition between two processes: deposition of all neutral hydrocarbons which have a high sticking probability and simultaneous erosion of the films by atomic hydrogen. This hypothesis could be verified by comparing methane injection experiments in hydrogen and argon discharges. In Fig. 2 the development of the film thickness is shown for the hydrogen plasma. During the

CH_4 injection phase lasting the first three minutes the layers are seen to grow linearly with time at a rate of 3 nm/min. However, after the methane gas flux has been switched off the layers are eroded at a rate of 0.9 nm/min. A different behaviour is observed when similar experiments are performed in an argon plasma. As shown in Fig. 3 methane is injected this time in a sequence of pulses and pauses during a total period of 130 minutes. Simultaneously the surface temperature of the sample has been varied (rising from 320 to 470 K and then back to 320K). We notice that there is no erosion in this case – during the intermission phases the thickness stays constant. There is, however, a depostion during the injection phases of comparable rate to the hydrogen experiments (3 nm/min) which, most remarkably, is hardly influenced by the change of temperature.

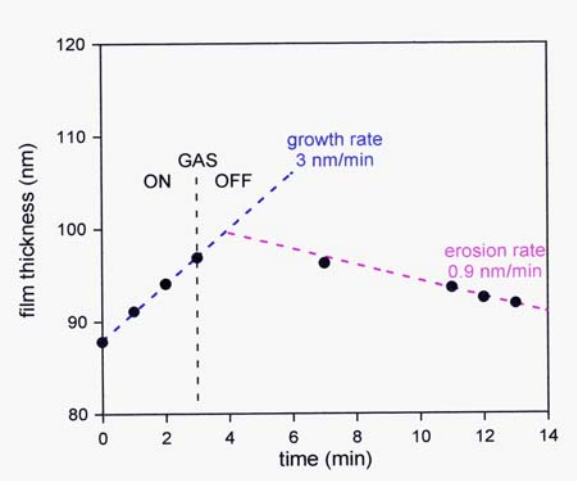

Fig. 2: Methane injection into a hydrogen plasma.

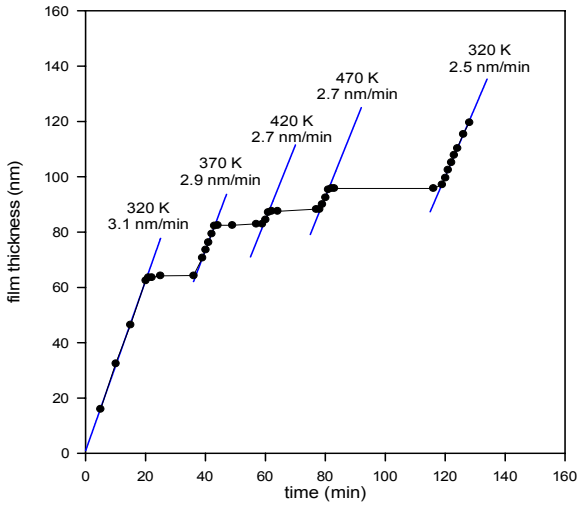

Fig. 3: Intermittend injection of methane into an argon plasma. The surface temperature of the collector was changed as indicated in the figure.

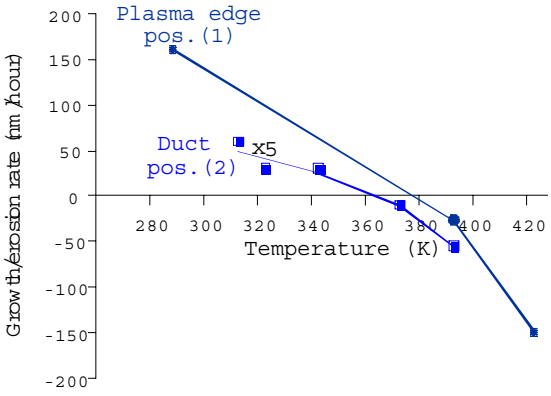

Fig. 4: Growth rate of hydrocarbon films vs. surface temperature.

Whereas deposition can be inferred from the above observations to be nearly independent of the surface temperature, erosion must strongly increase with rising temperature. This is concluded from the data shown in Fig. 4 where a constant flux of methane is injected into a hydrogen discharge. The measured growth– or erosion rate of films is shown for two collectors, one positioned close to the plasma edge, the second at about a distance of 0.4 m. This time we observe a strong dependence of the thickness with the surface temperature. In fact we notice a transition from net deposition to net erosion around T = 370 K. Beyond this transition temperature erosion prevails and films which have been produced previously are dissolved. Of course, the transition temperature is not a universal quantity but increases with the ratio of hydrocarbon to hydrogen fluxes. The equivalent value of about 100° C where the transition takes place in PSI-2 is a moderate wall temperature and will be easily achieved under normal operation conditions in ITER. However, the crucial question of the prevailing flux ratio remains unresolved and the critical temperature could possibly be shifted upwards. Numerical simulations and additional experiments are under way to assess this issue.

Staff:

W. Bohmeyer
G. Fussmann
D. Naujoks
H.-D. Reiner
Max-Planck-Institut für Plasmaphysik, Plasmadiagnostik Division, Berlin

I. Arkhipov
A. Markin
Institute of Physical Chemistry of the Russian Academy of Sciences, Moscow

TW0–T 438/01
Development and Testing of Time Resolved Speckle-Diagnostics

The project aims at the development of a non-contact optical surface measurement device based on the speckle effect, for long range and in situ diagnostics of arc traces, deformation, erosion, surface roughness and surface contour in the divertor region of experimental fusion devices.

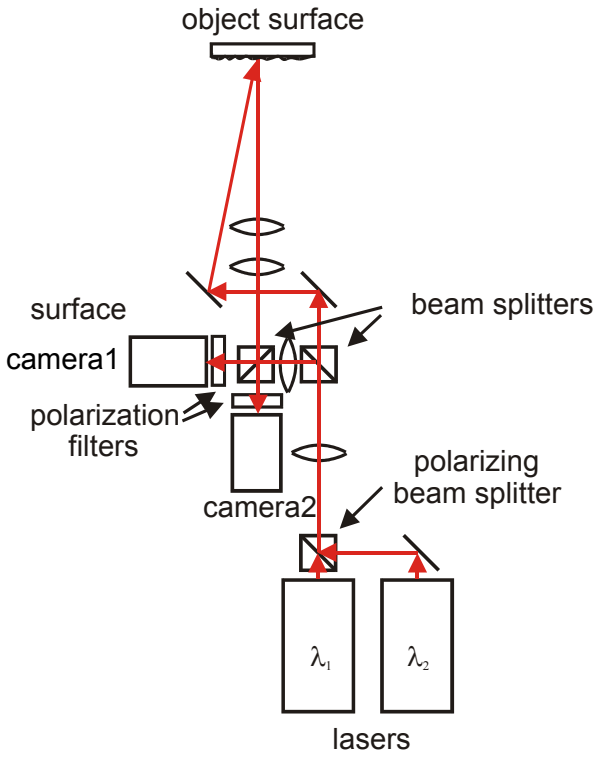

Fig. 1: Two-camera-setup based employing the polarisation effect.

The proposed method of surface contouring via speckle-interferometry requires two interferograms generated at different wavelengths. The concept of a synchronous two-camera-system combined with a spatial phase-shifting technique allows to prevent any decorrelations of two interferograms with respect to each other. Further disturbance of the interferograms caused by movements are suppressed by short exposure times of the cameras.

The first setup was designed using a multiline Ar-ion laser. The wavelengths were separated by interference filters arranged in front of the two cameras. The main disadvantage of this setup was a fixed measurement sensitivity. Moreover this setup was hardly capable of measuring surfaces at non-perpendicular observation angles. Such angles normally cause a high fringe density in the phase image and by that prevent a fringe evaluation.

Thus a new setup was developed, as shown in Fig 1., using two separated, linearly polarised and tunable laser sources. The polarisation direction of the lasers are adjusted perpendicular to each other. The separation of the two wavelengths in this setup is achieved by polarization filters in front of the cameras, adjusted according to like the laser polarization direction. The ability of tuning of the lasers permits a variation of the measurement sensitivity which is determined by the so called synthetic wavelength, determined by:

$$\Lambda = \frac{\lambda_1 \cdot \lambda_2}{2 \cdot |\lambda_1 - \lambda_2|} \qquad (1)$$

Furthermore the use of separated laser sources allows to impose a tilt between the laser beams.

As shown in Fig. 2 this tilt can be used in order to compensate non-perpendicular observation angles. The detected position of the object in the first interferogram generated by laser 1 is expressed by h. The tilt between the two lasers results in a different detection of positions in the second interferogram, expressed by Δh.

The difference of these two interferograms yields:

$$I_1 - I_2 = -2 \cdot I_0 \cdot \lambda \cdot \cdot \sin\left(2\pi \cdot \left(\frac{\lambda_2 - \lambda_1}{|\lambda_1 \cdot \lambda_2|} \cdot h - \frac{1}{\lambda_2} \cdot \Delta h\right)\right) \cdot \sin\left(2\pi \cdot \left(\frac{\lambda_2 + \lambda_1}{|\lambda_1 \cdot \lambda_2|} \cdot h + \frac{1}{\lambda_2} \cdot \Delta h\right)\right) \quad (2)$$

with I1, I2 representing the Intensities of the first, resp. the second Interferogram, referring to eq. (3) and (4).

In the second line of eq. (2) it can be seen, that already very small difference angles between the laser beams cause large changes in the detected phase. This effect can be used in order to compensate high fringe densities in the phase image.

λ_1 :

$$I_1 = I_0 \cdot \left(1 + \gamma \cdot \cos\left(\frac{4\pi}{\lambda_1} \cdot h\right)\right) \quad (3)$$

λ_2 :

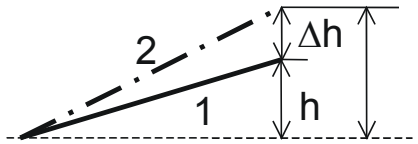

$$I_2 = I_0 \cdot \left(1 + \lambda \cdot \cos\left(\frac{4\pi}{\lambda_2} \cdot (h + \Delta h)\right)\right) \quad (4)$$

Fig. 2: Effect of tilt between two laser beams in the interferometer.

The setup was already tested using moving measurement objects without vibration damping environment. First results show a high stability against movements resulting in a maximum shift of 60 µm during the exposure time of the cameras permitting a velocity of 30 mm/s at an exposure time of 2 ms. Referring to eq. (5) an extrapolation of this result shows clearly that the acceptable velocity of the measurement object could increased significantly by a further reduction of the cameras exposure time.

$$v_{max} = \frac{s_{max}}{T_{exp}}; \quad (5)$$

Therefore intensified cameras could be used combined with increased laser power.

Staff:

Koch, A.W.
Purde, A.
Kirilenko, P.
Meixner, A.

Literature:

[1] Meixner, A.; Purde, A.; Zeh, T.; Koch, A.W.: Konzept zur erschütterungsrobusten Konturerfassung mittels Speckle-Interferometrie. Poster-Session auf der 104. DGaO-Tagung vom 10.-14.06.2003 in Münster

[2] Meixner, A.; Zeh, T.; Riemenschneider, M.; Purde, A.; Koch, A.W.: Formvermesssung an bewegten technischen Oberflächen mittels der Speckle-Interferometrie.In: tm - Technisches Messen 70 (2003) 2, S. 93-98.

[3] Purde, A.; Riemenschneider, M.; Meixner, A.; Zeh, T.: Interferometric methods for contour measurement of technical surfaces in vibrating environments. In: Proceedings of the Sensor 2003, May 13-15, 2003, Nürnberg

EFDA 03/1080
Characterization of Material Damage for EU W and CFC ITER Divertor Materials under Repetitive Plasma Energy Fluxes by Modeling and Experimental Validation

1. Introduction

So far most of the modeling and experiments on material damage to tungsten and graphite targets concerning large transient loads in ITER has concentrated on plasma heat deposition Q ~ 10MJ/m^2 and higher, which may occur in ITER disruptions. The understanding of material damage by repetitive plasma fluxes of a much smaller magnitude (Q = 0.2 – 2 MJ/m^2) as may be expected during Type I ELMs in ITER is less developed.

The task involves carrying out a series of dedicated code runs for the divertor plasma conditions expected during Type I ELMs in the ITER scenario in order to determine the accumulative material damage expected for the EU tungsten and CFC candidate materials under repetitive plasma energy fluxes. The modeling will use the anisotropic thermomechanics code PEGASUS–3D for the simulation of CFC brittle destruction, the surface melt motion code MEMOS–1.5D for tungsten targets, and the radiation-magnetohydrodynamics code FOREV–2D for calculating the plasma impact and simulating the heat loads for the ITER regime. These codes should be verified by benchmarking experiments at the plasma gun facilities MK-200 UG and QSPA in Troitsk, Russia. The accumulated material damage caused by plasma pulses of Q = 0.2 – 3 MJ/m^2 and τ = 0.1 – 1 ms will be numerically predicted.

This two-year task has been issued in July 2003 and therefore only some preliminary activities and results are reported. For modeling Type I ELMs in the ITER regime, the experiments at MK-200UG are set up. Essential simulation results for repetitive ELMs are obtained for the tungsten targets by the analysis of vaporization- and melt motion erosion on the base of MEMOS–1.5D calculations.

2. Experimental activity at MK-200UG

Experimental investigation for the ELM conditions including simulation of heat fluxes, analyses of erosion effects in the armour materials, production of impurities, and transport of impurities in plasma is going to be carried out at the plasma gun facility MK–200 UG which can produce plasma pulses of 0.05 ms with ion impact energies up to 2.5 keV and electron temperature Te up to 3×102 eV. These parameters represent the impact physics in ITER rather well. The target surface can be inclined with angles of 20 to 90 degrees in respect to the guiding magnetic field being up to 3 T. The Thomson laser scattering technique and an optic interferometer allow measurements of Te and the plasma density in front of the target. The following experiments will be performed till the end of 2003:

- A search of the new experimental conditions in order to get the ELM relevant regimes of plasma gun operation.
- Investigation of plasma stream properties at the new regimes in the target chamber at the distance of 10 m from the gun as a function of magnetic field induction in the drift tube and in the target chamber.
- Experimental studies of plasma material interaction at the ELM relevant heat loads by optic- and ultraviolet multi-framing cameras.

The obtained results will be used for validation of the FZK numerical models for divertor loads relevant to ITER.

3. Numerical simulation with MEMOS-1.5D

Tokamak operation in the H-mode is the regime with multiple ELMs. During each ITER discharge more than 10^3 ELMs are expected. In ITER, the ELM energy may also exceed the melting threshold as well as the vapour shield threshold. Melt motion produces surface roughness that usually significantly exceeds the vaporization erosion per one ELM. Despite of small surface roughness as great as one micron produced by a single ELM, due to the ELM repetition the total roughness may accumulate and get rather high. The roughness profiles after many ITER ELMs with the heat loads stochastically distributed over the divertor surface are simulated applying the code MEMOS–1.5D [1].

MEMOS–1.5D is a one-dimensional fluid dynamics code. However, it describes two-dimensional process of surface melting, which is possible due to the 'shallow water' model for the moving melt implemented in the code. The code was validated comparing the simulation results with the e-beam facilities JUDITH (Germany) for beryllium and JEBIS (Japan) for tungsten. The melt motion in MEMOS–1.5D is described taking into account the surface tension, viscosity of molten metal, and the radiative losses from the hot tungsten surface. The plasma pressure gradients along the divertor plate, as well as the gradients of surface tension and the Lorentz force of the currents crossing the melt layer immersed in strong magnetic field, produce the melt acceleration.

The simulation with MEMOS–1.5D allowed prediction of the vapour shield threshold. One single ELM of τ = 0.3 ms with Q = 1 – 2 MJ/m^2 produces melting without evaporation. At Q > 2.5 MJ/m^2 the vapour shield forms significantly and the pressure gradient force becomes essential. In the regimes with the melt motion, the magnitude of surface roughness varies in range of 0.3 – 0.5 μm, the melt velocity is of 0.5 m/s, and the evaporation thickness per single ELM of 0.1 μm.

During ELMs, the tokamak separatrix at the armour surface (the separatrix strike point, SSP) changes the position at the surface. The influence of motion of SSP is modelled assuming motionless but random positions of SSP from ELM to ELM, obeying the Gaussian distribution. In the coordinate frame of the random SSP, the time dependent spatial profiles of heat fluxes and plasma pressure at the target surface are calculated with the code FOREV–2D.

For multiple ELMs, the case with fixed SSP position is compared with that of the random SSP. The Gaussian distribution of SSP with the dispersion δ = 0.1 m results in a significant decrease of the crater depth compared to the case with fixed SSP as demonstrates Fig. 1. Fig. 2 demonstrates the dependence of crater depth on the number of ELMs at δ = 0.1 m. It is concluded that in the case with the stochastic SSP the evaporation mechanism becomes to be the main reason of erosion at the ELM number larger than 10^3, and thus the erosion rate acquires a linear dependence on the number of ELMs. For Q < 1 – 2 MJ/m^2 the number of ELMs to erode 1 cm of tungsten armour is obtained to be about 10^5 – 10^6.

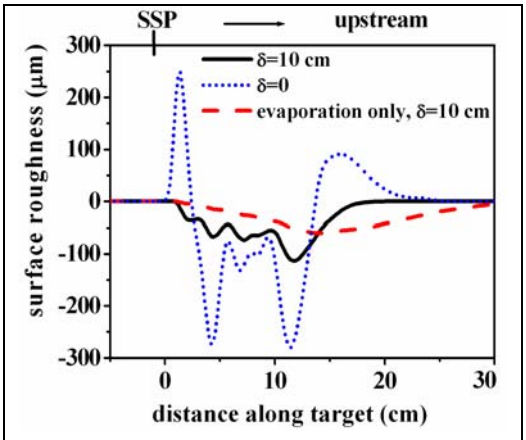

Fig. 1: Comparison of the crater depth after 103 ELMs at fixed and random SSP, Q = 3.5 MJ/m2, τ = 0.5 ms obtained with MEMOS–1.5D.

The stochastic distribution of SSP in MEMOS-1.5D reduces tungsten target erosion because of

smoothing the surface roughness caused by the melt motion at each single ELM. This conclusion will be validated by the experiments as soon as the corresponding results on the multiple ELMs become available.

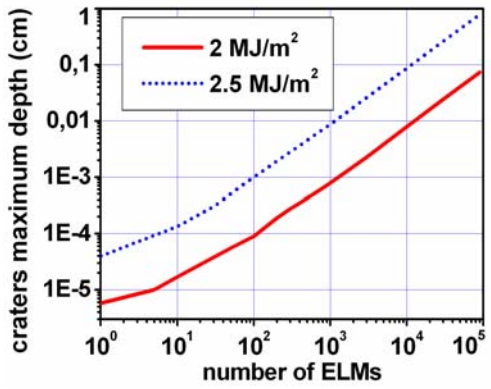

Fig. 2: The dependence of crater depth on the number of ELMs for δ = 0.1 m obtained with MEMOS−1.5D.

Staff:

Bazylev, B.N.
Janeschitz, G.
Landman, I.S.
Pestchanyi, S.E.

Literature:

[1] B.N. Bazylev, G. Janeschitz, I.S. Landman, S.E. Pestchanyi. Erosion of divertor tungsten armor after many ELMs. 30th Conference on Controlled Fusion and Plasma Physics, St.Petersburg, Russia, 7-11 July 2003

TW3-TPP/DISELM
Modeling of ELM-induced Plasma Contamination and Disruption W Macrobrush Damage in ITER Relevant Scenarios

1. Introduction

In this two-year task issued in May 2003, the first part of the work on modeling the contamination of plasma is under way. The investigation on damage to tungsten macrobrush is just started up and the results are not available yet.

Any off-normal event such as ELM or disruption is a complicated physical process of self-consistent plasma wall interaction, because confined plasma and heated surface intensively exchange their contents. In previous years, the important role of the plasma shield generated in front of the armor surface at ITER disruptions and of the radiation processes in this shield was discovered and investigated with the two-dimensional radiation magnetohydrodynamics code FOREV–2D simulating the plasma in one-fluid approximation and in planar geometry. After the off-normal event eroded material propagates along the magnetic field lines in SOL intensively reradiating energy of the pedestal plasma, which is dangerous because it can cause collapse of the confinement. Further development and experimental validation of the code permitted its application for the prediction of the armor erosion and the SOL plasma contamination by the erosion products at ITER disruption conditions.

At the loads relevant to the main ITER regime in ELMy H mode, the vapor shield does not develop or is rather weak compared to the disruptions. Therefore, the structure of DT–plasma flux becomes important and it should be calculated accurately. To meet the requirements of ELMy H-mode, the detailed geometry of the ITER magnetic field and elaborated description of the plasma have recently been implemented in FOREV–2D [1]. The upgraded FOREV-2D can now calculate the ELM consequences in the tokamaks ITER and JET with the graphite divertor for the scenarios that start from some initial DT-plasma state in SOL. Heating of both divertor armour plates and their vaporisation followed by expansion of carbon vapour into SOL was calculated.

2. Implementation of tokamak magnetic flux and divertor geometry in FOREV-2

The numeric scheme of the code was changed to represent the whole SOL, the x–point and inner- and outer divertor plates of ITER and JET, but could be applied for other tokamaks too if necessary. For producing the numerical grids, a standard mesh generator was used. These meshes are non-orthogonal, so the modification of FOREV–2D implies mesh file transformation by means of an additional code to the orthogonal toroidal coordinates already available in a tentative version of FOREV-2D developed so far. For future adjustment of the mesh generator and FOREV-2D, the MHD equations in orthogonal coordinates have been rewritten to the non-orthogonal magnetic flux coordinates however implementation of the non-orthogonal coordinates in FOREV-2D is still to be done.

3. Multi-fluid description of plasma in FOREV-2

For distinguishing the dynamics of plasma components and for better modeling the radiation transport the different involved ions were implemented as a set of interacting fluids. Analytical estimations showed that the characteristic time for establishing the ionisation equilibrium can be of 1 ms for the once ionised atom, and for the multi-charged ions it increases proportionally to the square of the ionisation energy, so that the characteristic time can get of the same order as the duration of the whole process of plasma transport in SOL, which is of a few milliseconds. This means that the concentrations of equilibrium ions species used in the single fluid FOREV-2D version may be drastically different during ELM from real concentrations and thus it is quite important to treat each ions species as a separate fluid.

Therefore the code FOREV-2D is improved to treat the ions species of the vaporized armour material as well as the deuterium- and tritium ions as separate fluids. The plasma in FOREV is now simulated as different ion species D^+, T^+, He^+, He^{++}, C^+, C^{++}, C^{+++} etc.

4. Intermediate results

The following ITER ELM scenario is chosen for initial runs of the upgraded FOREV-2D. The development of ELM is assumed to result in an instantaneous reconnection of the magnetic field lines in the x–point region. After this, a thin layer of DT–plasma of the temperature of 3 keV and of maximum density of $5*10^{19}$ m^{-3} consisting of 50% D^+ and 50% T^+ ions adjacent to the separatrix expands along the reconnected magnetic field lines towards the divertor plates. The plasma density decreases outside separatrix with a half-width corresponding to the half-width of 7 cm along the divertor target. The D-T plasma evolves accelerating towards the divertor armour plates. Heating of both divertor armour plates causes their evaporation, and the vaporised material starts to expand backwards to SOL. The results of the calculation are illustrated in Fig. 1.

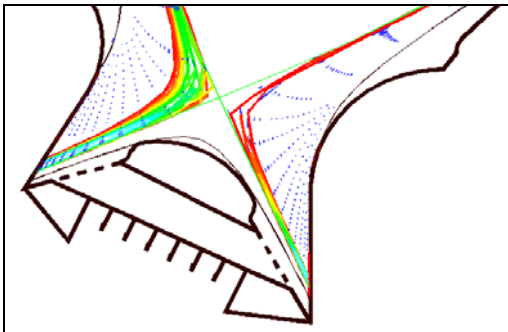

Fig. 1: Backflow of the carbon plasma vaporized from the divertor armor plates to SOL: shown are the density contours and the velocity arrows representing single-charged carbon ions.

Simulation for the ITER graphite divertor armor revealed that due to the fast increase of the electron heat load of 0.5 MJ/m^2 deposited at the armor causes early evaporation, at 0.1 ms after the start. The electric field in the quasineutral DT–plasma also contributes to the fast increase of the load accelerating more effectively the impinging D–ions. The vaporized carbon being ionized by hot electrons expands backwards into SOL as mainly C^+. After ELM, the target plasma remains in SOL during several milliseconds keeping the large density of 10^{20} m^{-3} (see Fig. 2).

The next simulation has been performed for JET geometry of magnetic field and the divertor. Only a rather rough grid could be produced using the standard mesh generator so far. Because generation of the grids with various numbers of meshes is important for systematic simulation of plasmas transport, it is concluded that further improvements of numerical grids generation for different tokamaks remains an urgent problem.

As a conclusion, the work carried out provided first application of FOREV-2D for simulations of the consequences of off-normal events in the realistic tokamak configurations. Further development of FOREV-2D algorithms in the directions of implementation of non-orthogonal magnetic flux coordinates and the mesh generation technique is necessary.

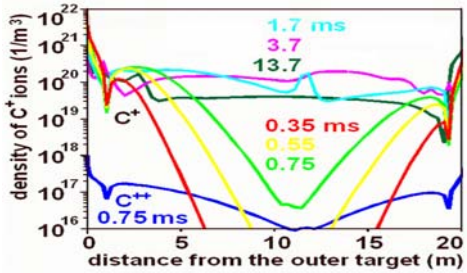

Fig. 2: C^+ density along the separatrix after the start of ELM. Two streams of carbon plasma vaporized from the inner- and outer divertor armour plates mutually interact.

Staff:

Landman, I.S.
Pestchanyi, S.E.

Literature:

[1] S.E. Pestchanyi, I.S. Landman, H. Wuerz. Hot plasma contamination in ELMs by divertor material. 30th Conference on Controlled Fusion and Plasma Physics, St.Petersburg, Russia, 7-11 July 2003

TW4-TPP/CARWMOD
Molecular Dynamics Simulations of Carbon and Tungsten Sputtering

1. Introduction

The objective of this two-year task issued in May 2003 is to carry out molecular dynamics (MD) simulations of carbon and tungsten sputtering taking into account effects that may be important under ITER divertor plasma conditions. The whole task consists of several parts, however FZK is responsible only for one part: chemical erosion of tungsten under simultaneous bombardment of oxygen and deuterium for ITER relevant energy ranges. The first delivery of FZK is scheduled on 31 January 2004. The required MD calculations with the code CADAC need the interatomic potentials to be produced by a task partner from Austria in Autumn 2003. Up to now the information about the potentials is not issued. Therefore, only preliminary development of the theoretical approach is reported.

2. Implementation of many body forces in the code CADAC

Chemical erosion of tungsten by oxygen, through the formation of volatile WO_3 molecules, may be dangerous even if the percentage of oxygen in the hydrogen plasma flux at the divertor surface is at the percent level. MD simulations of W chemical sputtering with simplified pair-interatomic potentials under simultaneous hydrogen and oxygen bombardment with the CADAC code have shown that competition with formation of H_2O can significantly decrease its yield at high temperatures above 10^3 K where the simple approach seems valid. Therefore it is necessary to continue the modelling by including new features that bring the MD calculations closer to the expected situation, in particular including many body forces into the modelling so that the approach is applicable to surface temperatures under 10^3 K, which are relevant for the inner divertor and the baffle region for the ITER reference power loads.

In collections of many atoms the interaction forces are very complicated. The theoretical problem of their rigorous obtaining is hardly solved, and even when they can be approximately calculated with a good accuracy, complicated programming and tremendous number of needed computer operations prevent their practical applications. The main reason of these difficulties is the electron subsystem of the atomic collection. Description of electrons requires solving of a many-body quantum mechanical problem, which cannot generally be tackled with existing mathematical methods. Therefore, prognostic practical methods to be developed should be based on empirical fitting, but they should not necessarily imply explicit analyses for the electrons. One of such not rigorous but realistic methods is the MD simulation based on the classical Newton equations.

Unfortunately, the available empirical and calculation data describe almost exclusively only pair-wise interatomic potentials. However, many important effects of the atomic interactions cannot be analyzed in a such restricted way. One characteristic of atoms is their molecular organization. Here it is discussed how MD simulations can be naturally combined with the known chemical concept of valence. It seems that this approach keeps the advantages of the pair-wise MDS and allows the description of chemical reactions using the data on atomic valences and the pair-wise interactions.

The valence is traditionally treated as a parameter υ prescribed to one atom and characterizing its affinity, i.e. the attraction of the atom by some other ones. The valence is related to a certain extent with the number of the outer shell electrons. For attraction of the others, the atom spends some amount of its valence, and the partners do similarly. The exchanged amount is assumed to depend on the distance *r* between the partners, which is described by a function *p*(*r*) termed the proximity function. The exchanged amount for the partners indexed by *i* and *j* is given by $\upsilon'_{ij} = p(r_{ij})\min(\upsilon_i, \upsilon_j)$. Here r_{ij} are the interatomic

distances. The new theoretical model developed based on this approach gives the following equation for the current valences of the atoms:

$$\upsilon_i = \upsilon_{\max i} - \sum_j p_{ij} \min\left(\upsilon_i, \upsilon_j\right)$$

The valences have the tendency to approach the chemical valence $\upsilon_{\max}$ only at large distance between the atoms, and at the approaching of the atoms the valences substantially decrease.

The problem of simultaneous calculation of the valences for all involved atoms is going to be solved using the fact that in the MD calculations the atomic positions and thus p_{ij} change slowly after each time step. Therefore it is sufficient to update the valence υ_i at each calculation of the pair-wise potentials for the atom *i* assuming that the valences of the neighbors *j* are given.

For modeling of the valence influences, original pair-wise interatomic potentials are supplied with special modification factors ('α-factors'). In the preliminary version the original potential $V(r)$ is constructed as the sum of the Bohr potential $V_B(r)$, which describes the high energy range where the chemical features are not important, and the Morse potential $V_M(r)$, which describes low energies. The α-factors multiply only the Morse potential: $V = V_B + \alpha V_M$. The potential energy of some *N*-atomic assembly takes the form:

$$U\left(\mathbf{r}_1, \mathbf{r}_2, ..., \mathbf{r}_N\right) = \sum_{1 \le i < j \le N} \left(V_{Bij}\left(r_{ij}\right) + \alpha_{ij} V_{Mij}\left(r_{ij}\right)\right)$$

With the accuracy of 10%, the dependence of α_{ij} on the valences is given by

$$\alpha_{ij} = \frac{\upsilon_i \upsilon_j + \upsilon_{ij}'^2 + \upsilon_{ij}' \max\left(\upsilon_{\max i}, \upsilon_{\max j}\right)}{\upsilon_{\max i} \upsilon_{\max j}}$$

This novel approach is now at the stage of implementation in CADAC observing the momentum conservation requirement of the code. The recalculation of the α-factors in the course of calculations will destroy the energy conservation. Due to the fact that in CADAC the calculated assembly of atoms always remains connected to a thermostat, the energy non-conservation seems to be acceptable.

Staff:

I.S. Landman

Divertor and Core Plasma Modelling for ITER

1. Introduction

ITER performance modelling, crucial to establish the expected performance of ITER and to define the operating scenarios to obtain this performance, can be carried out only with an integrated plasma model which describes in a coherent way the entire plasma from the centre via the pedestal and the scrape-off layer to the divertor plate. Such a model has been developed in the framework of a quadripartite collaboration (FZ Karlsruhe, ITER International team, Hydro-Québec, Varennes, Québec, Canada, and INRS-EMT, Varennes, Québec, Canada), as described in the Annual Report 2001- 2002. This model has been further developed and applied to ITER.

The integrated ICPS model presently consists of two parts: the core, from the centre of the plasma to the separatrix and including the pedestal, is modelled with the 1-1/2 D code ASTRA, and the scrapeoff layer and divertor plasma is modelled with the coupled fluid-Monte Carlo code B2-EIRENE for the ITER simulations. A variant of the model, which uses a simpler two-point model for the scrape-off and divertor plasma, is used to fit results from the experiments. Quantitative predictive modelling of ITER is done with the more complete model.

The initial version of the model and the results obtained were described in the Annual report Sept. 2001-2002 and references therein as well as [1], [2], [3], and presented to the meeting of the ITPA Topical Group on Edge and Pedestal Physics [4], [5]. Further results, particularly regarding more realistic modelling of carbon in the edge modelling [6], implementation of the MMM model and carbon in the core modelling [7] and a preliminary study of the H-mode density limit [8] were presented at the 2003 EPS Conference, and a brief presentation was made to the ITPA TG on Divertor and SOL Physics [9]. A summary of the results obtained until July 2003 may be found in [10]. The application of the model to JET and ASDEX Upgrade as well as the determination of an operating window for ITER including an SOL-based density limit was presented at the H-mode workshop [11] and presented to the ITPA TG on Edge and Pedestal Physics [12].

2. Divertor Plasma Modelling

As reported in the previous Annual Report, B2-EIRENE simulations of the edge and divertor plasma in standard ITER FEAT geometry, with carbon targets and metal walls, revealed the existence of two regimes, a regime at normal divertor pressure and a saturated regime at higher divertor pressure. Scaling relations were developed in each regime and these were then used as a boundary condition for the core plasma modelling.

In fact, the various operating parameters can be represented in terms of a normalised divertor neutral pressure $p^* \equiv \left(\Gamma_{\#}/S_{\#}\right)P_{\#}^{-0.87} f_f^{-2}$, which is the ratio of normalised DT throughput to pumping speed times a function of normalised power into the SOL and a weak function f_f of the fuelling conditions (close to 1; core fuelling vs. gas puffing). For ITER, normalisation is relative to 124 Pa-m^3/s, 20 m^3/s, and 100 MW, respectively. Saturation of the separatrix density occurs when p*=1, and is accompanied by almost complete detachment of the inner divertor. This is defined as the SOL-based density limit, in line with the definition of Borrass (see references in [11]).

In the divertor modelling for ITER reported in the previous period (e.g. [1], [2], [3], metallic first wall (Be), baffle (W) and dome (W) surfaces were specified. These absorb completely the carbon sputtered from the divertor targets. In reality, the deposited carbon can be re-eroded and re-deposited elsewhere, yielding an increase of carbon concentration and radiation losses and a decrease of the net eroded flux. A extensive series of simulations

have been carried out in the present period under these conditions. To model realistic surfaces (RS) in ITER, the local erosion or deposition state is determined iteratively during the modelling from the local balance between the carbon erosion and deposition. If erosion dominates, the surface characteristics are set to be those of a metal wall, and the carbon release rate is set equal to the deposition rate; if deposition dominates, the characteristics of the resulting surface layer are those of carbon. The model is described in more detail in [6], [10]. In contrast to previous metal wall calculations and scalings, which used EIRENE in cylindrical mode, the present runs use EIRENE in toroidal mode. The differences are generally minor, except for the SOL-based density limit, which shifts to higher throughputs because the previous calculation underestimated volume recombination. For the realistic carbon surfaces, however, the SOL-based density limit with toroidal EIRENE is similar to that previously obtained for metal walls and cylindrical EIRENE, so that for the present this scaling is used. [6].

Density scans have been carried out to compare the plasma parameters for metal walls, full carbon walls and realistic surfaces (RS). Power law scalings have been developed for the full-carbon wall, analogous to those for metal walls, to relate the separatrix-averaged parameters (temperatures, densities, neutral fluxes) used as boundary conditions for core models to the control parameters (SOL power, divertor neutral pressure, pumping speed, fuelling scheme). These now include scalings for the carbon quantities and the DT density. Similar scalings for the RS will be produced later. The exponents are given in the Tables of [3] and [11].

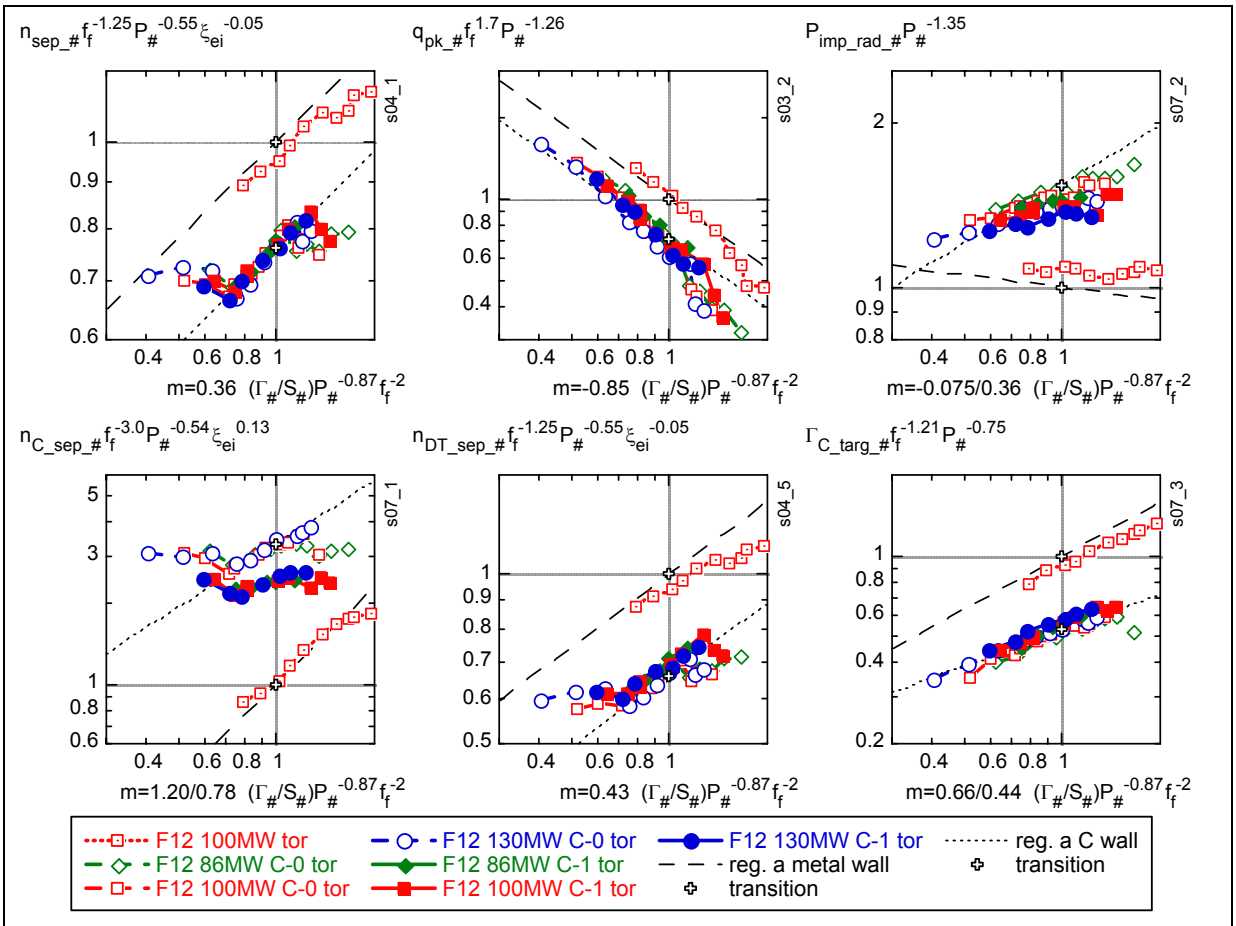

Fig. 1: Normalised separatrix electron density, peak power load, impurity radiation, separatrix carbon and DT ion density, and net eroded flux from the target vs. normalised divertor neutral pressure (throughput over pumping speed) for metal wall (dashed, dotted square), full carbon wall (hollow symbols, C-0) and RS (solid symbols, C–1). Scalings as in[6], [11], hash # denotes normalisation by metal wall values of "scale" of Table 4 of [11], dashed lines for metal walls and cylindrical EIRENE , dotted lines for carbon walls and toroidal EIRENE.

When full carbon walls are compared to metallic walls (Fig. 1), the separatrix density is lower by 20%, the peak power load at the targets decreases by ~ 20%, and the impurity radiation increases by about 50% at the transition point. The separatrix C ion density increases by a factor 3 to 5 to ~ 10^{18} m^{-3}, the DT becomes more diluted, and the net eroded carbon flux at the targets decreases by 50%. Z_{eff} increases from 1.2 to 1.75. The variation of the carbon-related quantities with divertor neutral pressure is also different.

The RS solution lies between the metal and full carbon wall solutions. Compared to full carbon walls, the RS is very similar in density, peak power load, impurity radiation and target erosion. However, Z_{eff} is lower, about 1.55, the separatrix C density is 25% lower, and the DT dilution at the separatrix is only 15% rather than 20%.

In summary, a novel methodology to model plasma-facing metal surfaces with realistic erosion-deposition has been developed in collaboration between ITER International Team and INRS/Hydro-Québec. The inboard wall is found to be erosion-dominated; large areas of the outboard wall are deposition-dominated. The plasma parameters for realistic surfaces for ITER, compared to metal walls, exhibit reduced peak power load and density at given throughput, higher SOL radiation and more realistic Z_{eff}, and reduced target erosion. The RS results with carbon have been applied to core plasma operation as shown in the next section, and found to maintain acceptable performance.

3. Core Plasma Modelling

As reported in the previous Annual Report, a first version of the Integrated Core Pedestal Sol Model (ICPS Model) was developed in the 1.5D Astra code [2]. In the first version of the model, the dominant core ion energy transport is neo-classical plus ITG, (modified IFSPPL model, critical gradient), and core electron energy transport is similar to the RLW model (critical gradient). The plasma is fuelled in DT by the inward neutral flux at the separatrix as well as pellets(approximated by fuelling inside the separatrix with a fall-off length of about 50 cm), and in He by fusion reactions and recycling. The effect of ELM's is represented in a time-averaged sense by limiting the pressure gradient to the ballooning limit.

In the present period, the critical gradient model of energy transport was replaced by a modified multi-mode model (MMM95). The particle transport coefficient is taken as $0.1\,(\chi_e+\chi_i)$ and the Ware pinch is included. Sawteeth are approximated by increasing the transport coefficients by a factor of four inside the q=1 surface. Since the Astra equilibrium solver determines the shear with the correct plasma parameters and geometry, but without an X-point, a correction to the shear in terms of a poloidal flux expansion near the separatrix is applied to account for the effect of the X-point [7], [11].

The non-classical transport is taken to be stabilized by radial electric field shear and magnetic shear, according to $\chi = \chi_{MMM} \Big/ \left\{\left(1+\left(\omega_{E\times B}/\left(G\,\gamma_0\right)\right)^2\right)\cdot \max\left(1,\left(s-t\right)^2\right)\right\}$. The electric field shear term (first term), including the inherent magnetic shear corrected for the X-point, produces a pedestal, which is, however, appreciably lower than experimentally obtained (Fig.2 left, upward triangles). An additional magnetic shear term (second term above) is included, and a threshold formulation is used because the major part of the profile (low shear), is well-represented by MMM transport. (γ_0 is the growth rate in the absence of stabilisation; $\omega_{E\times B}$ the E×B shearing rate, and *s* is the magnetic shear). Smaller numerical values for G and *t* give stronger stabilisation.

The profiles obtained for two combinations of these parameters (*t*=0.5, *G*=0.5 and *t*=0.5, *G*=1.0) are shown on Fig. 2 for JET. The former combination gives an excellent fit to the temperature profile; the density profile is well-fitted for both combinations. This best fit (*t*=0.5, *G*=0.5) also produces good agreement with the ASDEX Upgrade (AUG) database (see [11] and Fig. 3).

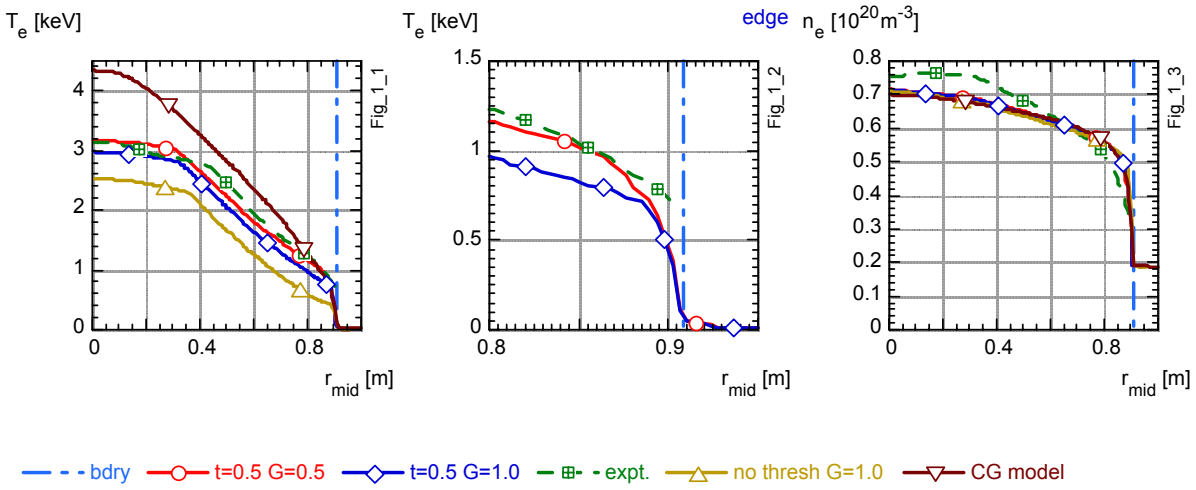

Fig. 2: Profiles for JET - Experiment, MMM for the two parameter set, CG and for MMM without additional shear stabilisation: Electron temperature, Electron temperature at edge, and Density

A further extension of the model in the present period has been the inclusion of carbon impurity, according to the new scalings from B2-EIRENE simulations of the edge and divertor plasma presented in the previous section, for realistic surfaces (RS). The radial carbon profile is determined from a neoclassical impurity accumulation formulation, as further described in [11].

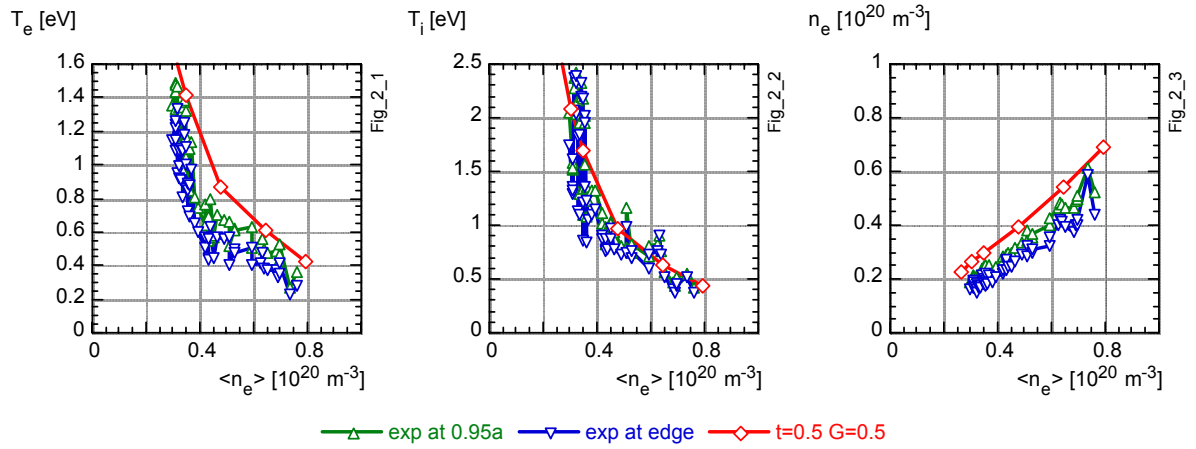

Fig. 3: Edge parameters for a density scan for AUG (t=0.5, G=0.5).

The model described above, with the best fit parameter set (*t*=0.5, *G*=0.5), is applied to ITER. The ITER core plasma must be primarily core-fuelled [11] to establish the pedestal, and gas puffing is used to limit the peak heat load on the divertor plate to 10 MW/m^2. At constant SOL power (~100 MW), high Q-values are obtained without carbon, which become 30 in the presence of carbon at the highest density investigated (Fig. 4_0). Scans at constant density with gradually reduced beam power (Fig. 4_01 to 4_05) map out the operating space, delimited by the density limit (f_{sat_n}=1) and the lowest attainable fraction of this value (70% at the lowest central density calculated to about 85% at the highest) for power balance. A reasonable operating regime exists between these values, i.e with alpha power above ~80 MW and *Q* above 10 (fig. 4_01).

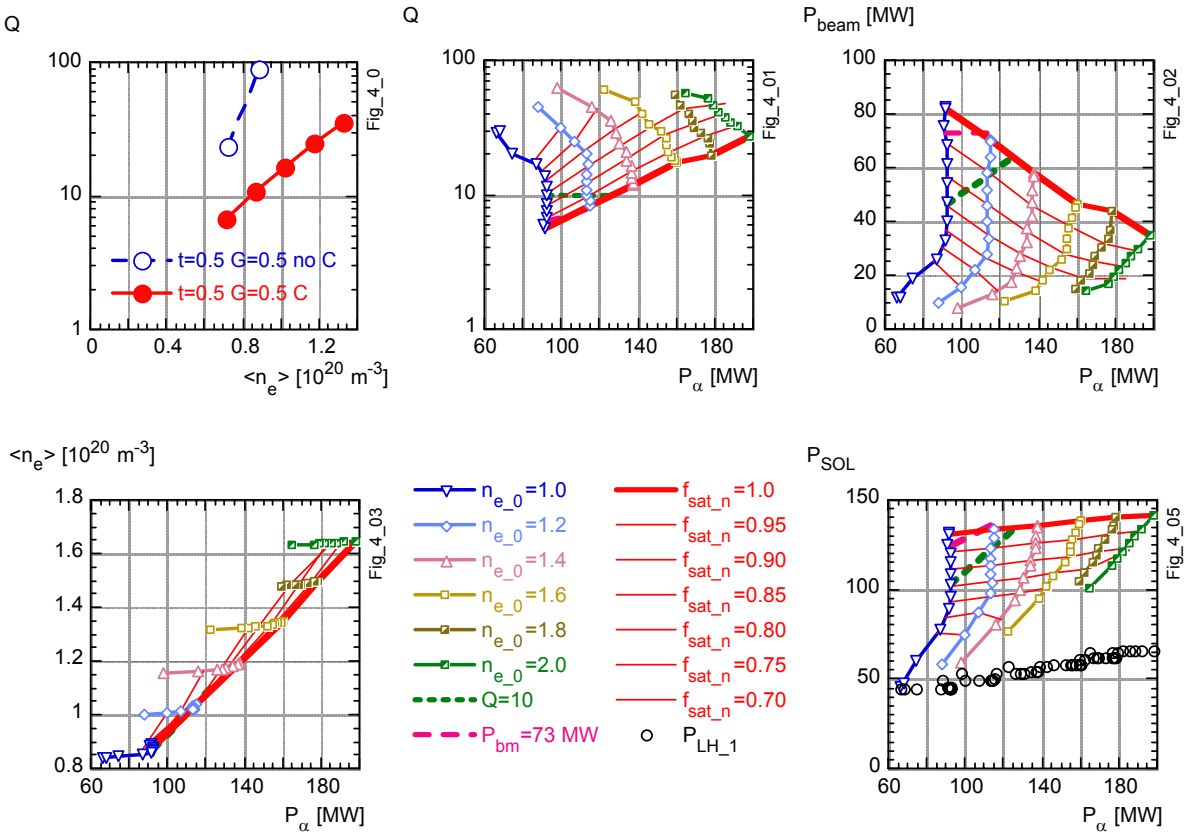

Fig. 4. 4_0 Effect of carbon on fusion performance. 4_1 to 4_05: Operating space of ITER vs. alpha power with MMM model (t=0.5, G=0.5) and intrinsic carbon impurity. Scans are at constant core density. Q=10 maximum heating power and constant fractions of SOL density limit from 2-D SOL modelling also shown.

In summary, the MMM core energy transport model linked with the separatrix parameters from 2-D SOL modelling, calibrated against a JET discharge, fits AUG data well also. Application to ITER in the presence of carbon yields Q between ~8 and ~20 is obtained at the SOL density limit and a reasonable operating regime is found. The fusion performance is sensitive to the stabilisation parameters, so that further validation against experiment (pedestal profiles), is required.

4. Perspectives

Work on divertor and core modelling for ITER is continuing, with particular emphasis on:

- In two-dimensional modelling of the ITER scrape-off and divertor plasma, improvement of the scaling relations for the separatrix and scrape-off layer parameters for walls having realistic carbon erosion-deposition, variations of ITER geometry and plasma position, and examination of existing simulations of ASDEX Upgrade and/or JET to generate scaling relations for these devices

- In one-dimensional modelling of the plasma core, extension of the impurity treatment, particularly carbon from the scaling resulting from the two-dimensional modelling, further development of the implementation of multi-mode transport, and application of the model to density limits, advanced operating modes and continuous operation.

Staff:

G. Janeschitz
A. S. Kukushkin (ITER International Team)
I. Landman
H. D. Pacher (INRS-EMT, Varennes, Québec, Canada)
G. W. Pacher (Hydro-Québec, Varennes, Québec, Canada)
S. Pestchanyi

with the collaboration of
G. Pereverzev (IPP Garching)
Yu. Igitkhanov (IPP Garching)

Literature:

[1] H. D. Pacher, G. W. Pacher , in collaboration with ITER IT , FZ Karlsruhe, MPIPP Garching, EFDA"Divertor and Core Plasma Modelling for ITER - Int. report December 2002", INRS Energie, Matériaux et Télécommunications, Report INRS-EMT-05-1202, Dec. 2002 (2002)

[2] G.W. Pacher, H.D. Pacher, A.S. Kukushkin, G. Janeschitz, G. Pereverzev, Nucl. Fusion **43** (2003) 188-195

[3] A. S. Kukushkin, H. D. Pacher, G. W. Pacher, G. Janeschitz, D. Coster, A. Loarte, D. Reiter, Nucl. Fusion **43** (2003) 716

[4] G.W. Pacher, H.D. Pacher, A.S. Kukushkin, G. Janeschitz, G. Pereverzev, "Core Plasma Operation Consistent with SOL Parameters in ITER", presented to ITPA TG on Edge and Pedestal Physics, Garching, October 2002 (2002)

[5] A. S. Kukushkin, H. D. Pacher, G. W. Pacher, G. Janeschitz, D. Coster, A. Loarte, D. Reiter, "ITER Divertor Plasma Modelling with Consistent Core-Edge Parameters", presented to ITPA TG on Edge and Pedestal Physics, Garching, October 2002 (2002)

[6] A. S. Kukushkin, H. D. Pacher, D. Coster, G. W. Pacher, D. Reiter, "Effect of Carbon Re-deposition on the Divertor Performance in ITER", Proc. 30th EPS Conf.on Contr.Fusion and Plasma Physics, St. Petersburg (2003)

[7] G.W.Pacher, H.D.Pacher, G.Janeschitz, A.S. Kukushkin, G.Pereverzev, "Core Plasma Modelling of ITER with a Consistent Core-Pedestal-SOL Model Including Carbon and MMM Transport", Proc. 30th EPS Conf.on Contr.Fusion and Plasma Physics, St. Petersburg (2003)

[8] G. Janeschitz, Yu. Igitkhanov, L. Giannone, G.W. Pacher, H.D. Pacher, M. Sugihara, "A possible Explanation of the H-mode Density Limit", Proc. 30th EPS Conf.on Contr.Fusion and Plasma Physics, St. Petersburg (2003)

[9] G.W. Pacher, H.D. Pacher, G. Janeschitz, A.S. Kukushkin, G. Pereverzev, "Core Plasma Modelling of ITER with a Consistent Core-Pedestal-SOL Model Including Carbon and MMM Transport", presented to ITPA TG on Divertor and SOL Physics, St. Petersburg, Russia, July 2003 (2003)

[10] H. D. Pacher, G. W. Pacher , in collaboration with ITER IT Garching, FZ Karlsruhe, Max-Planck-Institut für Plasmaphysik Garching, EFDA CSU Garching "Divertor and Core Plasma Modelling for ITER - Final report June 2003", INRS Energie, Matériaux et Télécommunications, Report No. INRS-EMT-06-0703, July, 2003 (2003)

[11] G.W. Pacher, H.D.Pacher, G.Janeschitz, A.S. Kukushkin, G.Pereverzev, "Operating Window of ITER from Consistent Core-Pedestal-SOL Modelling Including Carbon and MMM Transport", presented at 9th IAEA Technical Meeting on H-mode Physics and Transport Barriers, Sept. 2003, San Diego, USA (2003), submitted to Plasma Physics and Controlled Fusion (2003)

[12] G.W. Pacher, H.D.Pacher, G.Janeschitz, A.S. Kukushkin, G.Pereverzev, "Operating Window of ITER from Consistent Core-Pedestal-SOL Modelling Including Carbon and MMM Transport", pres. to ITPA TG on Edge and Pedestal Physics, October 2003 (2002)

Heating and Current Drive

ITER ECRF Advanced Source Development
- Coaxial Cavity Gyrotron -

The goal of the development work is to accomplish the experimental investigations on a $TE_{31,17}$ coaxial cavity gyrotron at 165 GHz and to provide all data necessary for fabrication of an industrial prototype of a 2 MW, CW coaxial cavity gyrotron at 170 GHz as could be used at ITER [1-6]. Based on the obtained results the physics design of a 170 GHz 2 MW, CW coaxial gyrotron, taking into consideration its industrial integration and constraints is in progress. The design work is done in cooperation between the EURATOM Associations - FZK Karlsruhe, CRPP Lausanne and HUT Helsinki - together with the European tube industry - Thales Electron Devices, Velizy, France [7,8]. In order to verify the design of main components as electron gun, cavity and RF output system foreseen to be used in the 2 MW, 170 GHz industrial prototype, the experimental 165 GHz gyrotron at FZK is now under modification for operation at 170 GHz. The work on the modifications is progressing well and experiments are expected to start beginning of 2004.

165 GHz coaxial cavity gyrotron - last results:

As has been observed in previous experiments (reported in the last annual report) the build up of a Penning discharge in the technical (rear) part of the electron gun occurred and caused a limitation of the high voltage performance of the gyrotron. In recently performed experiments a suppression of the Penning discharge has been demonstrated by a suitable shaping of the gun geometry in which trapping of electrons is avoided. No high voltage limitations due to a Penning discharge have been observed. At $I_b \approx 50$ A a maximum pulse length of 22 ms has been achieved with an RF-output power of about 1 MW. At this current the pulse length was limited due to the temperature rise of the collector surface by about 600^0C. At reduced beam currents the pulse length has been extended up to above 100 ms without any indications of Penning discharges.

Further on, the leakage current I_{body} to the wall of the body and insert has been measured in dependence of the retarding collector voltage. It has been found that the part of I_{body} flowing to the outer wall is negligible small and that the leakage current is practically given by the current to the insert, $I_{body} \approx I_{ins}$. In operation with single-stage depressed collector (SDC) the value of I_{ins} was found to increase with the retarding collector potential as shown in Fig. 1. The value of I_{ins} increases approximately linearly from about 2 mA (~ limit of accuracy) in operation without depressed collector (U_{body} = 0 kV) to about 35 mA at U_{body} = 27 kV for a beam current around 50 A. No significant influence of cathode voltage and of RF generation on the value of I_{ins} has been observed. The background pressure p_{bg} has been measured to be between 10^{-8} and few times 10^{-6} mbar rising during a pulse and depending on beam current and pulse length. The influence of p_{bg} on I_{ins} is not known, however. In the conditioning phase it has been observed that I_{ins} may strongly increase just before (~ms) a voltage breakdown. From calorimetric measurements of the power deposited on the insert it

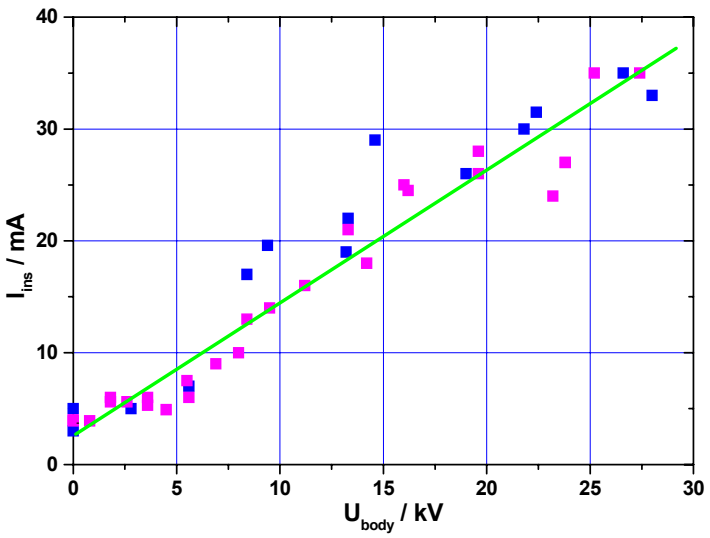

Fig. 1: Iins versus Ubody for Ib ≈ 50 A and cathode voltage varied between Ucath = 40 - 75 kV.

has been estimated that the electron leakage current has in average an energy of only a few keV.

To explain the observations the following mechanism is suggested. In operation with SDC (U_{body} > 0 kV) an electron trap is formed between the negative potentials of the cathode and the collector. Electrons created by ionization of the background gas become trapped and perform oscillation in the trap. Thus a background plasma is created along the beam path. Under stationary conditions the leakage current I_{body}/I_{ins} is determined by the diffusion of the trapped electrons across the magnetic field. It is expected that the parameters of the background plasma depend on the background pressure inside the tube. Further on, the electron diffusion rate and the ion drain current towards the anode and the collector depend on the geometrical conditions. Thus in case of gyrotron operation with depressed collector the conditions of the background plasma determine the degree of compensation of the space charge of the primary electron beam. In case of operation with U_{body} = 0 kV no electron trap exists. Thus the resulting leakage current is low.

Design work on a 2 MW, CW 170 GHz coaxial gyrotron for ITER:

The development of an industrial prototype of a coaxial cavity gyrotron with an RF output power of 2 MW, CW at 170 GHz started recently in cooperation between European Associations (CRPP Lausanne, FZK Karlsruhe and HUT Helsinki) together with European tube industry (TED, Velizy, France). The engineering design is in progress. The basic design of the 2 MW, CW coaxial cavity gyrotron and its components have been performed. Constraints related to an operation at ITER have been taken into account. The main parameter are summarised in Tab. 1. The $TE_{34,19}$ mode has been selected as operating cavity mode. The design of the cavity has been verified by using two different time dependent, multimode and self consistent codes. With those codes the start up behaviour has been simulated considering up to 11 modes as competitors. In order to reduce the diffraction losses at the cut and thus to decrease the amount of microwave stray losses an improved q.o. RF output system is under design. A rippled-wall launcher with reduced field amplitude at the edges of the cut similar as used successfully in the 140 GHz gyrotron for W7-X will be employed. A single-disk CVD-diamond window with a thickness of 1.852 mm = 5λ/2 at 170 GHz can be used for transmission of 2 MW microwave power at 170 GHz. At a loss tangent of 2×10^{-5} (state of the art) 880 W power will be absorbed in the disc. Edge cooling of the CVD diamond disc with water is sufficient for removing the heat load. A single-stage depressed collector with the collector at ground potential will be used. Under nominal operating conditions about 2.4 MW, CW beam power is remained and has to be dissipated in the collector. In operation with modulated microwave power (between about 0.6 MW and 2 MW) the power dissipated at the collector walls increases to about 3 MW, CW.

Table 1: Nominal operating parameters of the gyrotron and some design specifications

Operating mode:	$TE_{34,19}$
Frequency, f	170 GHz
Accelerating voltage, U_{acc}	90 kV
Beam current, I_b	75 A
RF output power, P_{out}	2 MW
RF output efficiency, η_{out}	≥ 45 %
Magnetic field in the cavity, B_{cav}	6.86 T
Ohmic losses (twice the losses of ideal copper at 273 K; P_{RF} = 2.2 MW):	
Peak losses at outer wall p_{cav}	2 kW/cm^2
Peak losses at coaxial insert p_{ins}	0.2 kW/cm^2
Power dissipated in the collector – CW operation:	≤ 2.4 MW
With modulated RF output power (0.6 – 2 MW):	≤ 3.1 MW

Modification of the experimental 165 GHz gyrotron for operation at 170 GHz:

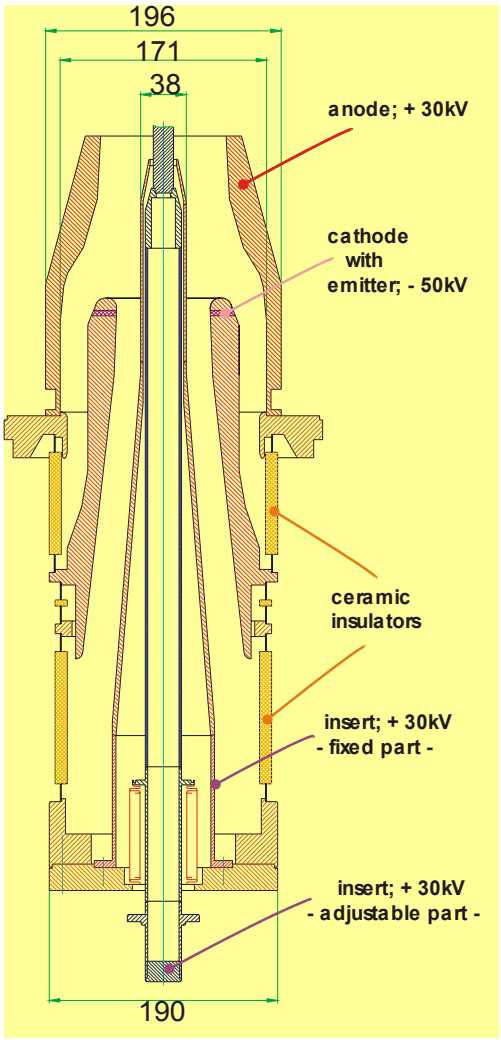

Fig. 2: Schematic arrangement of the coaxial magnetron injection gun for the experimental gyrotron. Dimensions in mm.

In order to verify the design of critical components like electron gun, cavity and q.o. RF output system under realistic conditions, the experimental 165 GHz coaxial gyrotron at FZK is under modification for operation at 170 GHz in the $TE_{34,19}$ mode. The maximum magnetic field of the utilised SC magnet of only 6.667 T requires a reduction of the operating voltage from 90 kV to 80 kV in order to be able to excite the nominal mode ($TE_{34,19}$). The cavity and the quasi-optical RF output system will be identical as designed for the industrial tube. This will allow to prove the RF generation and mode competition as well as the efficiency of the RF output system and to measure the amount of microwave stray radiation lost inside the tube under practically the same conditions. Numerical simulations of the RF interaction have shown that at the reduced beam voltage of about 80 kV an RF output power above 1.5 MW can be expected. A new design of the electron gun (Fig. 2) very similar to the gun of the prototype, has been performed and is now under fabrication [9]. Care has been taken to avoid regions with trapped electrons in order to suppress the build up of a Penning discharge. The modification of all components is in progress. Experimental operation of the experimental short-pulse gyrotron is expected to start beginning of 2004.

Staff:

A. Arnold (Uni Karlsruhe)
H. Baumgärtner
H. Budig
G. Dammertz
O. Drumm (Uni Karlsruhe, until 30.12.2002)
S. Illy
J. Jin (Uni Karlsruhe)
K. Koppenburg
M.V. Kartikeyan (AvH Fellow, until 30.06.03)
W. Leonhardt
H.R. Kunkel
D. Mellein
B. Piosczyk
T. Rzesnicki (Uni Karlsruhe)
W. Spiess
J. Szczesny
M. Thumm
R. Vincon
X. Yang

Literature:

[1] PIOSCZYK, B.; ARNOLD, A.; DAMMERTZ, G.; DUMBRAJS, O.; KUNTZE, M.; THUMM, M.K. "*Coaxial cavity gyrotron - recent experimental results."* IEEE Transactions on Plasma Science, 30(2002) S.819-27

[2] PIOSCZYK, B.; ARNOLD, A.; BUDIG, H.; DAMMERTZ, G.; DRUMM, O.; KUNTZE, M.; THUMM, M , "*ITER ECRF advanced source development - coaxial cavity gyrotron final report*", FZKA 6701, ISSN 0947-8620, Februar 2002, Forschungszentrum Karlsruhe.

[3] PIOSCZYK, B.; DAMMERTZ, G.; DUMBRAJS, O.; KARTIKEYAN, M.V., THUMM, M., YANG, X., "*165 GHz Coaxial Cavity Gyrotron- last results*", accepted for publ. in IEEE Trans. Plasma Sci., June 2004.

[4] AIRILA, M., DUMBRAJS, O., KALL, P., and PIOSCZYK, B., *"Influence of reflections on the operation of the 2 MW, CW 170 GHz Coaxial Cavity Gyrotron for ITER",* accepted for publ. in Nuclear Fusion 2003.

[5] PIOSCZYK, B.; BUDIG, H.; DAMMERTZ, G.; DUMBRAJS, O.; DRUMM, O.; ILLY, S.;LEONHARDT, W.; SCHMID, M.; THUMM, M., " *A 2 MW, 170 GHz coaxial cavity gyrotron",* 30th IEEE Internat. Conf. on Plasma Science, Jeju, Korea, June 2-5.

[6] DUMBRAJS, O.; IDEHARA, T.; IWATA, Y.; MITSUDO, S.; OGAWA, I.; PIOSCZYK, B. *"Hysteresis-like effects in gyrotron oscillators."* Physics of Plasmas, 10(2003) S.1183-86

[7] PIOSCZYK, B.; ALBERTI, S.; ARNOLD, A.; BORIE, E.; BUDIG, H.; DAMMERTZ, G.; DUMBRAJS, O.; DRUMM, O.; ERCKMANN, V.; GIGUET, E.; GOODMAN, T.; HEIDINGER, R.; HOGGE, J.P.; ILLY, S.; KARTIKEYAN, M.V.; KASPAREK, W.; KOPPENBURG, K.; KUNTZE, M.; LECLOAREC, G.; LIEVIN, C.; MAGNE, R.; MICHEL, G.; MÜLLER, G.; THUMM, M.; TRAN, M.Q.; YANG, X., *"A 2 MW, CW, 170 GHz gyrotron for ITER*.", 19th IAEA Fusion Energy Conf., Lyon, F, October 14-19, 2002, ISSN 1562-4153.

[8] PIOSCZYK, B.; ALBERTI, S.; ARNOLD, A.; BARIOU, D.; BEUNAS, A.; BONICELLI, T; BUDIG, H.; DAMMERTZ, G.; DUMBRAJS, O.; DRUMM, O.; GOODMAN, T.; HOGGE, J.P; ILLY, S.; JIN, J.; LIEVIN, C.; MONDINO, P.L.; THUMM, M.; TRAN, M.Q.; YOVCHEV, I.; *"A 2 MW, CW, 170 GHz coaxial cavity gyrotron for ITER"*, IAEA Technical Meeting on ECRH Physics and Technology for ITER, Kloster Seeon, July 14-16, 2003.

[9] PIOSCZYK, B. "*A coaxial magnetron injection gun - recent experimental results and an improved gun design*." Proc.of the 4th IEEE Internat. Vacuum Electronics Conf. (IVEC), Seoul, Korea, May 28-30, 2003 New York N.Y.: IEEE, 2003 S.268-69

TW2-TPHE/ECRWIN
ITER ECRF Window Development

Introduction

This development task is based on the development of large area CVD diamond disks which provide the required microwave transmission characteristics of reliable windows (vacuum and tritium barriers) in high power, long pulse ECH&CD systems. In the previous year, the majority of the deliverables in the subtasks were finalised which were the design, fabrication and test of a CVD diamond window for a 170 GHz gyrotron in collaboration with the Russian Hometeam, pressure tests of a neutron-irradiated 170 GHz torus window in collaboration with the Japanese Hometeam, thermal conductivity measurements of the irradiated window material, dielectric characterisation of bulk and surface losses in brazed CVD diamond windows and identification of methods to reduce surface losses in CVD diamond disks. Two subtasks which depend on new options for window manufacturing processes require longer time scales than anticipated . Thus the enclosure of the torus window disk cooling rim by electroplated copper was continued into the year 2003 as well as the manufacture and test of a double-disk CVD diamond torus window.

Electroplating of copper at the torus window cooling rim

An ongoing issue for Ag-brazed windows is a reliable corrosion protection of the brazed zone arising from its direct contact with the cooling water. The choice of the adequate concentration of the corrosion inhibitor added to the coolant proved to be critical in past. This problem can be solved by covering the braze by copper. The concept of electroplating copper at the window disk cooling rim has the additional advantage that it prevents the ingress of cooling water into the vacuum vessel and of tritium into the cooling water circuit in the case of a window failure by crack formation. After successful application of a Ti/Au bonding layer, the electroplating of the rim of a test disk (outer diameter: 77 mm, aperture diameter: 58 mm, thickness: 1.482 mm) for a high power 170 GHz torus window has been successfully accomplished (cf. Fig. 1).

Fig. 1: High power CVD diamond disk for 170 GHz torus window with electroplated Cu on outer section of Al-braze and cooling rim

Design and manufacturing of a double disk window

The limited space available for the CVD diamond window in the ITER upper port ECH&CD plug calls for a very compact design of double disk window with an evacuated interspace which should be designed to allow a direct replacement for the present ITER reference concept of a single disk window. For this target, a new design has been developed that is based on a double ring structure which provides face cooling only to one side of both diamond disks (cf. Fig. 2a,b)[1]. The thermal properties of the brazing contact were measured using a small model disk and a copper tube. No increase in thermal resistance inside the brazing area was found. By FEM analysis, it could be shown that the proposed

face cooling structure does not introduce higher thermal gradients into the diamond disk than the standard edge cooling approach [2,3].

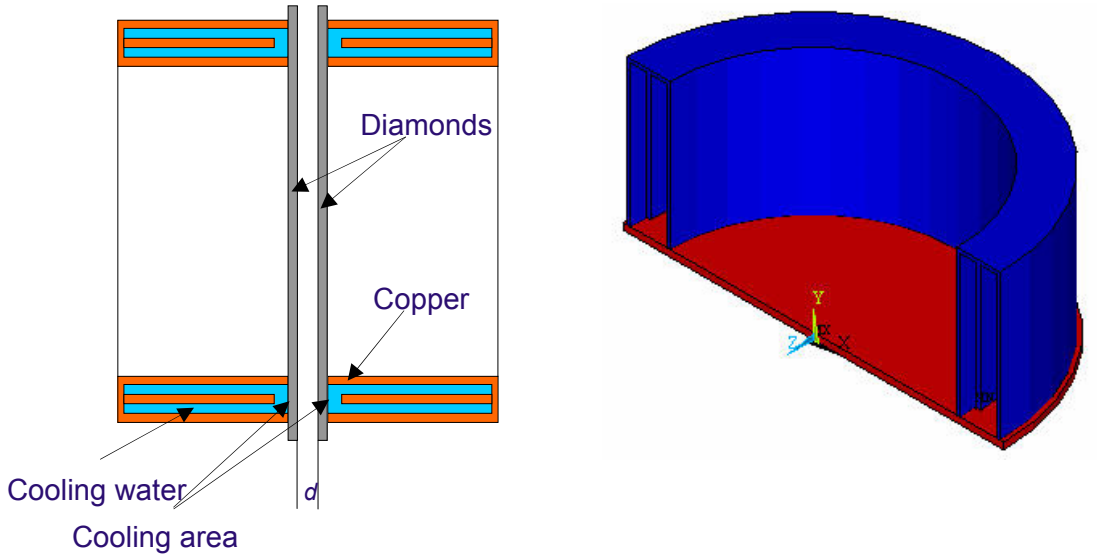

Fig. 2: Two (a) and tree (b) dimensional sketch view of the double ring structure.

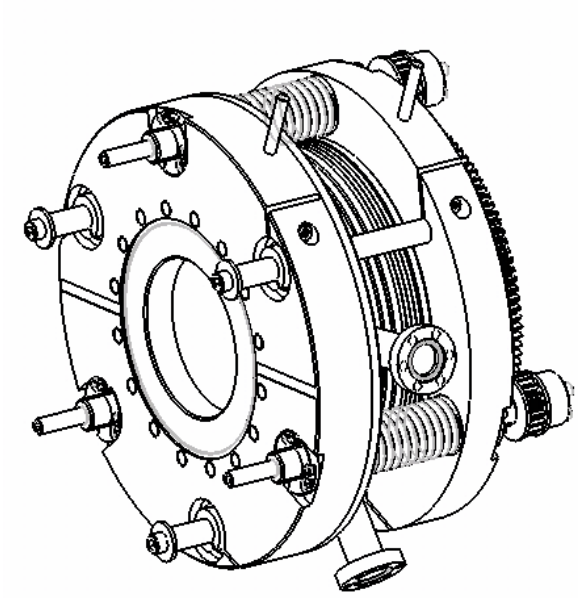

Fig. 3: Engineered design of the double disk window.

Two disks were procured having a thickness identical within 1 µm. The actual thickness was chosen to be resonant at 140 GHz (t=1.803 mm) to allow high power testing with available 140 GHz gyrotrons. The order for the brazing of the double ring structure was placed at Thales Electron Devices (Velizy). With to the new brazing geometry, several brazing runs had to be performed until satisfactory vacuum tightness was achieved for the first disk. This disk was received at FZK and proved to have no bow with the second double ring structure chosen to achieve symmetric brazing conditions. This additional structure is now being removed mechanically at FZK and will then be provided for integration into a cooling and vacuum housing of the entire window structure contracted to Reuter Technologies (Alzenau, Germany) (Fig. 3)

Staff:

M. Blumhofer
J. Burbach
I. Danilov
R. Heidinger
A. Meier
B. Piosczyk
M. Rohde
P. Severloh
M. Thumm

Literature:

[1] Danilov, A. Meier, R. Heidinger, X. Yang, F. Leuterer, D. Wagner. Design of a tuneable double disk window; 15th Joint Russian-German STC Workshop on ECRH and Gyrotrons, Karlsruhe/Stuttgart/Garching, June 25 - July 1, 2003

[2] R. Heidinger, I. Danilov, M. Rohde, J. Burbach, A. Meier, M. Thumm, G. Dammertz, K. Takahashi, K. Sakamoto; Performance and Conceptual Studies of Diamond Windows for High Power Gyrotrons and EC Launchers; IAEA Technical Meeting on ECRH Physics and Technology for ITER, July 14-16, 2003, Kloster Seeon, Germany http://www.ipp.mpg.de/eng/for/veranstaltungen/tmseeon/Talks/Heidinger_window.pdf

[3] R. Heidinger, I. Danilov, G. Dammertz, U. Fischer, G. Hailfinger, K. Kleefeldt, A. Meier, E. Stratmanns, M. Thumm, A.G.A. Verhoeven; Design and analysis of the upper EC launcher for ITER: Windows and main structural components; Proc. Joint US-JA and EU-JA Workshop on RF Heating Technology, Tokai (Japan), 25-26 September 2003

TW3-TPDC-IRRCER
Irradiation Effects in Ceramics for Heating and Current Drive, and Diagnostics Systems:

JW2-EP-ECRH.FZK
Design and Development Studies on CVD-Diamond Window Assemblies for the ITER ECRH System

Introduction

In electron cyclotron wave systems for heating and current drive (ECH&CD) and for plasma diagnostics, special window structures have to fulfil vacuum operation and tritium retention requirements with ideally broadband transmission and low power absorption. It has been established that the reference window materials, which are CVD diamond for high power transmission and fused silica for broadband transmission at low RF energy (short pulse and/or low power), can be used up to fast neutron fluences (E>0.1 MeV) of at least 10^{20} n/m^2 [1,2]. The post-irradiation examination has shown that for CVD diamond the fluence level of 10^{21} n/m^2 is critical as a significant reduction in thermal conductivity sets in to 40-70% of the original value.

Whereas the studies performed on bare model disks have provided a consolidated data base of the relevant material parameters, such as mechanical and dielectric properties, particular aspects of brazed window components are left open. Three different brazing methods are available to integrate CVD diamond disks to the metallic structures. According to the composition of the metallic structure and braze, differences in the levels of tritium permeation, radio activation and the bake-out performance have to be studied. The latter may open a possibility to recover the thermal conductivity in CVD diamond by thermal annealing.

Deuterium permeation studies

Existing brazing techniques for CVD diamond disks are:

1) Al-braze: 600-650°C (ElementSix – UKAEA Culham)

2) Ag-(Cu) braze: 750-850°C (Thales Electron Devices (TED), Velizy)

3) Au-(Cu-) braze 900-1000°C (CPI, Palo Alto)

For permeation studies the first two techniques were available for manufacturing of brazed test structures. The Ag-(Cu) braze is of particular interest because it has been used for the output window of the W7-X ‘Prototype’ 140 GHz gyrotron, which demonstrated practically CW operation (pulse lengths: 15 min). It is the outcome of a collaboration between European Industry (TED), FZK and CRPP Lausanne.

Three test units have been fabricated:

ER4_67: Small test window with aperture 30 mm; Al-braze to Inconel;
Size of CVD diamond disk: 40 mm dia. x 1.7 mm ;

34DB1: Full window size with aperture 88 mm; Al-braze to Inconel;
Size of CVD diamond disk: 106 mm dia. x 1.8 mm ;

36DB1: Full window size with aperture; Ag-braze to Copper
Size of CVD diamond disk: 106 mm dia. x 1.8 mm;

All three window units have been connected to UHV vacuum flanges using adapters made of 1.4031 steel (V2A). The vacuum tight joining of the adapters to the window units was made by brazing to the Copper sleeves or electron beam welding to the Inconel sleeves (cf. Fig. 1).

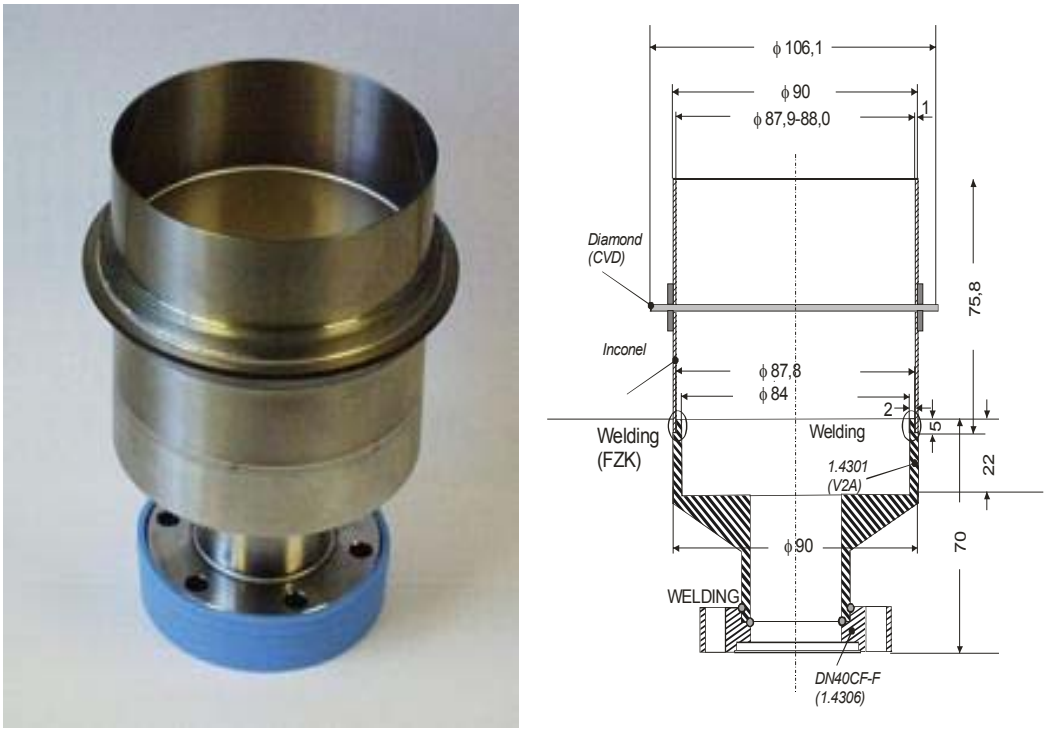

Fig. 1: Sept-up of window unit 34DB1 for permeation tests.

Tritium permeation is modelled by using deuterium as the reference hydrogen isotope. A UHV test stand was set-up, in which the brazed window structures are exposed on their upstream side to deuterium gas up to 0.5 MPa. In the downstream side, the gas composition is analysed by a quadrupole mass spectrometer (cf. Fig. 2).

The mass spectrometer signal yield the D_2 signal in terms of ion currents in pA registered for the atomic mass A=4. The limit of minimum resolved gas flow and the calibration of the mass spectrometer signal to absolute leakage (permeation) rates were determined by a diaphragm formed with a UHV flange which was thinned in the centre and has a central bore hole of 100 µm. It was found that the D_2 signal could be related to the D_2 permeation rate by the constant factor 0.55×10^{-11} (mbar m^3/s)/pA. Given an resolution in the D_2 signal of typically 1 pA, deuterium permeation can be resolved at a rate of $< 10^{-8}$ mbar l/s.

Permeation measurements at room temperature where the applied D_2 pressure was varied in the upstream side between 10^{-2} Pa and 0.4 MPa showed constant signals at the 0.7 – 2 pA D_2 level [3,4]. Typical exposure times were 15 min. Additional experiments were performed with an upstream pressures of 0.4 MPa over periods of 24 h for the large window units 34DB1 and 36DB1. In both cases the D_2 signal remained constant: for 34 DB1 at 0.75 pA and for 36DB1 at 0.67 pA (cf. Fig.3). First measurements were performed at elevated temperatures (upstream pressures of 0.3 MPa) which show increased D_2 signatures. The significance and the origin of the observed effects are still under investigation.

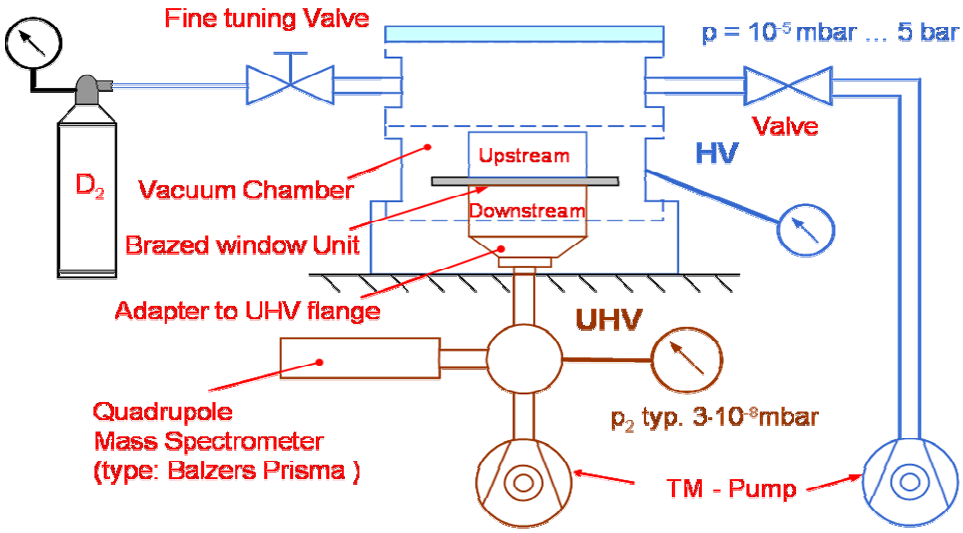

Fig. 2: Sketch for experimental set-up of permeation tests.

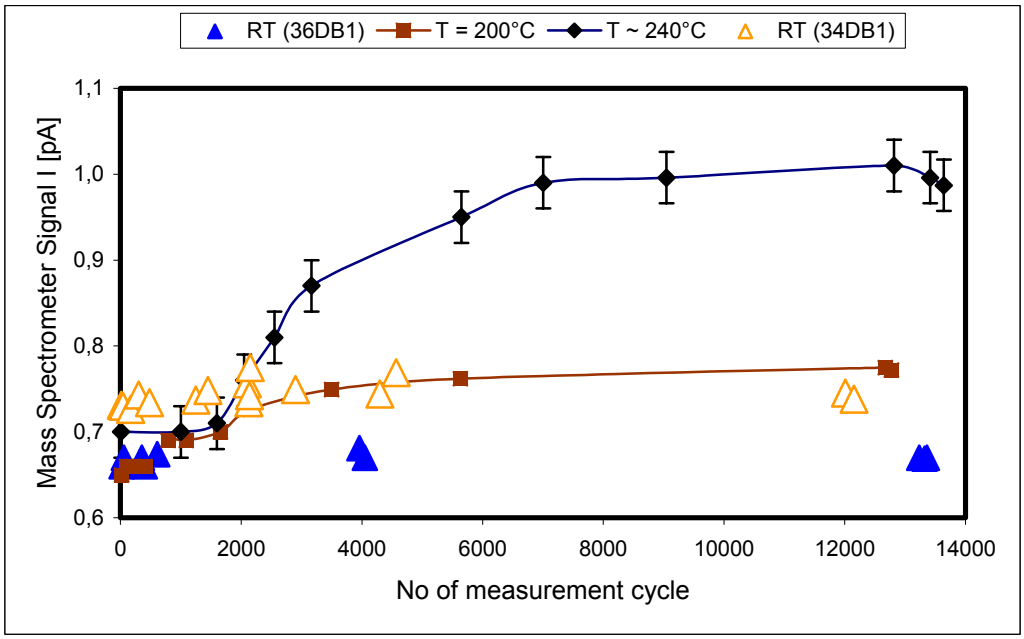

Fig. 3: D_2 signals observed at room temperature for the window unit with the Al braze (34DB1) and the Ag-(Cu) braze (36DB1) at different measurement intervals (500 measurement cycles correspond to 60 min). Results of first tests at elevated temperatures are included.

Assessment of radio activation in the brazing material

At the torus window of an upper ITER ECH launcher without dog-leg structure, the neutron streaming effect can cause a fast neutron flux level of up to 5 x 10^{12} n/m^2·s (cf. work performed at FZK under TW3/4-TPHE-ECHULB).

Chemical analysis of Al braze material recovered from a brazed disk, showed that apart from its majority element the only evidence of trace elements out of more than 30 elements considered was found for Ti (0.1-0.4 mass%) and Fe (0.7-0.8 mass%). The presence of Ti can be related with a layer pre-deposited before Al-brazing to improve the adhesion. The significance of iron is uncertain, as it may be related to the processes of taking the specimens of the brazing material. The estimation of the potential radio activation will use the

data base set-up at FZK for activation of structural materials where the composition of the Ag-(Cu) braze will be taken from technical specifications.

Annealing effects

After successful high power testing of a torus window demonstrator component in cooperation with JAERI Naka, thermal conductivity was measured on the CVD diamond disk taken out of the the Al-brazed structure. The measured value of 1200 W/m·K was much higher than that one of 840 W/m·K in the as-irradiated disk (fast neutron fluence $9 \cdot 10^{20}$ n/m^2)[4]. The difference is attributed to the partial point defect annealing at the typical temperature of the Al-brazing process of 600-650°C. Extended treatments at higher brazing temperatures (f.e. 840°C) are planned.

Conclusions and outlook

The measurement of hydrogen isotope permeation through CVD diamond window units gave no evidence for D_2 permeation at room temperature. The rates fall below the typical resolution limit of $< 10^{-8}$ mbar l/s. Several experiments performed at elevated temperatures (200°C and above) indicate the built-up/presence of increased D_2 signals. The assignment to its origin is not yet conclusive and has to await evidence gained with dummy units which reproduce the window geometry without the presence of the CVD diamond disk. Investigations of possible changes in the dielectric loss of the CVD diamond disks will follow the permeation studies.

For the assessment of the radio activation levels related to the brazing materials, the relevant neutron flux has been fixed together with the chemical composition of the brazing materials. The evaluation based on the data base available at FZK for structural materials will follow.

Staff:

M. Blumhofer
J. Burbach
I. Danilov
R. Heidinger
A. Meier
M. Rohde
P. Severloh
M. Thumm

Literature:

[1] R. Heidinger, Mechanical strength of neutron irradiated window materials, Proc. ICFRM-10, Baden-Baden (D), Journal of Nuclear Materials, 307-311 (2002), 1254-1259

[2] R. Heidinger, Dielectric and mechanical properties of neutron irradiated KU1 and KS-4V glass, Fusion Engineering and Design, 66-68 (2003), 843- 848

[3] R. Heidinger, I. Danilov, M. Rohde, J. Burbach, A. Meier, M. Thumm, G. Dammertz, K. Takahashi, K. Sakamoto; Performance and Conceptual Studies of Diamond Windows for High Power Gyrotrons and EC Launchers; IAEA Technical Meeting on ECRH Physics and Technology for ITER, July 14-16, 2003, Kloster Seeon, Germany http://www.ipp.mpg.de/eng/for/veranstaltungen/tmseeon/Talks/Heidinger_window.pdf

[4] R. Heidinger, I. Danilov, G. Dammertz, U. Fischer, G. Hailfinger, K. Kleefeldt, A. Meier, E. Stratmanns, M. Thumm, A.G.A. Verhoeven; Design and analysis of the upper EC launcher for ITER: Windows and main structural components; Proc. Joint US-JA and EU-JA Workshop on RF Heating Technology, Tokai (Japan), 25-26 September 2003

Magnet Structure and Integration

EFDA 1/605
TFMC Testing with LCT Coil

1. Introduction:

The test of the TFMC is being performed in two phases as it was concluded by the TFMC Coordination Group and the EURATOM Association Forschungszentrum Karlsruhe Steering Committee:

Test Phase I of the TFMC without EURATOM LCT coil (June – October 2001).

Test Phase II of the TFMC in the background of the EURATOM LCT coil (July – December 2002)

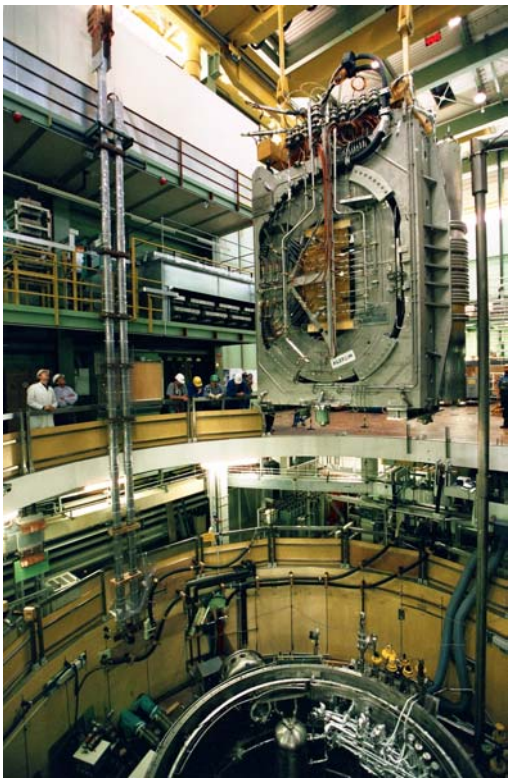

Fig. 1: The 117 t test configuration hanging above the TOSKA vacuum vessel (TFMC in the front, EURATOM LCT coil in the back).

The intention of the testing in two phases was to achieve results of the TFMC as soon as possible in a less sophisticated configuration with a lower risk of occurring faults.

The test phase I ran very successfully from June to October 2001. After that the TFMC was removed from the TOSKA vacuum vessel, assembled with the EURATOM LCT coil and installed again in the TOSKA facility (Fig. 1). The test configuration achieved in the first days of September 2002 the operation temperature. The test phase II where the TFMC was tested in the background field of the EURATOM LCT was performed very successfully [1]. The TFMC achieved by the extended load case (80 kA in the TFMC and 12 kA in the EURATOM LCT coil) the equivalent Lorentz force of the TF conductor (800 kN/m) in the ITER torus. The test was concluded in December 2002. The test configuration was removed in April 2003 from TOSKA facility vacuum vessel.

The evaluation of the test results by the T&A Group is in progress. The results are being published in conference contributions and a joint contribution in a journal.

2. The performance of the test

The test was performed in the following steps:

Cooling down of the test configuration to the operation temperature at 4.5 K and stabilizing of the cryogenic system

Pre-tests at operation temperature (repetition of standard tests: instrumentation continuity tests, leak tests, high voltage tests)

Measurement of the required cooling power, mass flow distribution in winding cooling channels and pressure drop

Low current tests of the single coils and both coils together for checking the interlocks between the cryogenic system and current supply system

Test of the single coils with current

Test of both coils together with current

Fast high voltage discharge of the ITER TFMC

Concluding tests after the current tests (repetition of standard tests)

Warming up to room temperature

Concluding tests at room temperature (repetition of standard tests).

Cool down: The cool down was performed by paying attention to keep maximum allowable temperature differences in order to avoid thermal induced mechanical stresses by different thermal expansion coefficients of the composite materials (windings) and structural materials (steel) [2]. A temperature difference between winding and coil case of < 40 K and across the intercoil structure of < 65 K had to be kept. The temperature gradient in time was about 1 K/h. The control and monitoring was performed computer supported. The test configuration was cooled down within 14 days to the operation temperature. After the end of cool down the helium circulation was switched from the 2 kW Linde refrigerator to the pump circuit. The performance of the pre-tests assured that the test configuration and the facility was ready for testing and no damage happened during cool down.

Current tests: The current tests started as well for the single coils as for the two coil test configuration with low current tests (5% of rated currents) in order to assure the faultless communication between interlocks units of the facility (high current power supplies, switching circuits, cryogenic supply system, quench detectors as well as other protection units) in case of operation disturbances.

The high current tests of the single coils as well as of the two coils were performed in current steps, which increased in 25 % steps of the stored energy respectively of the magnetic forces up to the rated operation data. This procedure allowed a well defined scaling to the next step because effects on magnets, cryogenic and high current system were proportional to the stored energy respectively magnetic forces. Every step consists of two trapezoidal shaped current pulses with a ramp rate (up and down) that was adapted to the needs of the test program. One of the current ramps was terminated by a safety discharge with exponential current decay with a time constant of 4 s for the TFMC and 12 s for EURATOM LCT.

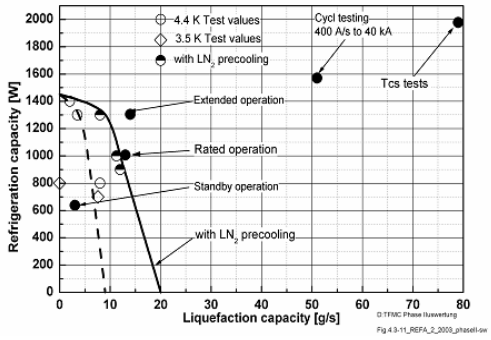

Fig. 2: Cryogenic power available from the 2 kW refrigerator and cryogenic power needed for the T_{CS} measurements

An important measurement was the determination of the operation limits of the superconducting cable of the TFMC. For this, the inlet helium of a double pancake had to be heated up by 2 x 350 W in order to achieve a helium inlet temperature of about 6-11 K. The loading of the refrigerator was in this case far outside its capability (Fig. 2). The requirement was handled by skilful use of stored liquid helium and careful feedback of helium to a warm storage container. Under these conditions the operation with high heat load was possible up to 0.5 h. After such a test 12–24 hours were needed to re-cool the

coils and accumulate sufficient liquid helium.

For EURATOM LCT coil currents above 11.3 kA, the inlet temperature of the winding had to be decreased to about 3.5-3.0 K by use of the 300 W Linde refrigerator in order to get sufficient safety margins for the superconducting cable. Because of the more difficult operation with two refrigerators first all current test at 4.5 K were performed before the tests with need of 3.5-3.0 K were started.

For investigating the behaviour of the special winding construction of the TFMC against transient voltage pulses, fast high voltage discharges with the POLO switching circuit up to 4.4 kV with a discharge time constant of 27 ms were performed.

After the completion of the current tests the standard tests were repeated in order to record the status of test configuration and the facility. A leak rate of 2×10^{-4} mbarl/s was detected in the area of the LCT coil current leads. The high voltage tests showed nearly unchanged results compared with that of test phase I.

Warm up: The warm up was performed under the same boundary conditions as the cool down and was completed in schedule mid of December 2002.

The test configuration was removed from the TOSKA vacuum vessel in April 2003. No damage was found by the visual inspection. The dimensions of the test configuration were checked again by measurements with a laser tracker. No remarkable deviations were found.

The laboratories and working groups of the international ITER collaboration were daily informed about the actual progress of the test by a report via electronic mail.

3. Results of the test

The test program of test phase II was elaborated and agreed in collaboration with the European superconducting laboratories (CEA, CRPP, ENEA incl. POLITO, Univ. Twente), EFDA / CSU Garching and the international ITER team in meetings of the T&A Group. Sixteen guest scientists of the European laboratories and three ones of international ITER teams (JAERI Japan, LLL USA, IT Garching) participated in the performance of the test in changing presents of persons. The detail evaluation and documentation of the test results is being performed by the T&A Group in 2003.

The test of the ITER TFMC in the background field of the EURATOM LCT coil was essentially characterised by increase of the maximum flux density from 7.6 T to about 10 T compared to the single coil test in test phase I. The mechanical stresses were twice as large as in the single coil test and achieved ITER TF coil relevant values.

Load case	ITER TFMC	EURATOM LCT
Rated load	70 kA	16 kA
Maximum load[1)]	80 kA	16 kA

[1)] This was originally the rated load. It was reduced by the coil manufacturer according to FEM calculations, which indicated too high stresses in the outer conductor joint region and in the intercoil structure. On the basis of the analysis of preceding tests by an improved FEM model, it was possible to achieve the maximum load under the continuous monitoring of critical sensors without any risk.

It was confirmed that also under increased forces the TFMC achieved the expected performance.

The most important item of the test was the measurement of the operation limits of the TFMC superconducting cable under the mechanical stresses. The typical test procedure was the current ramping up to a certain current level, at which the experiments were executed. During this procedure about 675 sensors were recorded by a multiplexer every 5 s, changed

into engineering units and stored in a database. For fast changes like a propagating normal conductor zone or a safety discharge, a transient data acquisition system with 164 channels (sampling rate up to 1 MHz) has been available. Also these data were stored in the database.

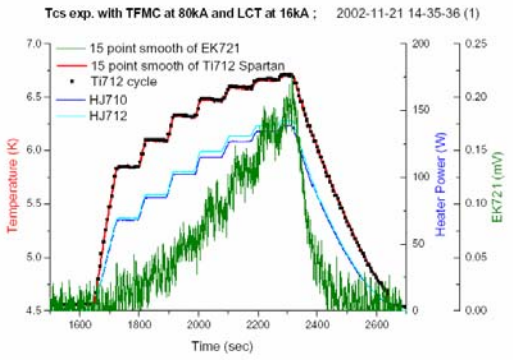

Fig. 3: The inlet temperature, the heating powers and the rising resistive voltage during measurement of the T_{CS}

Electromagnetic measurements: The determination of the operation limits of the TFMC superconducting cable was performed by measuring of the so called “current sharing temperature TCS”. In the range of the TCS (TCS is defined when the electrical field strength achieved 10 µV/m) the current was transferred from the superconductor to copper matrix and a resistive voltage appeared. The stepwise applied heating power for heating up the inlet helium of the double pancake was optimised by the developed thermo hydraulic code called “Multi Conductor MITHRANDIR”. This procedure including the rising of the resistive voltage is shown in Fig. 3. In the first measurements the heating procedure was continued till resistive region started to propagate in a quench. When the adjusted voltage level at the quench detectors was reached a safety discharge was automatically triggered. Because of the heavy impact of the safety discharge at high currents on the cryogenic system and the needed recovery time the procedure was changed in the way that at an achieved resistive voltage level of 200 µV the heaters were switch off and a safety discharge was prevented. The current was then slowly ramped down. That was considerably easier to handle in the experimental operation and saved testing time. A first evaluation is presented in Fig. 4 [3]. It shows very well the equivalence of the CSMC test and the TFMC test phase II where the Lorentz force with about 800 kN/m is at the level of the ITER TF coils, too. The dependence of the TCS difference from the Lorentz forces was unexpected. The reduced temperature margin will be compensated for the ITER coils by using advanced strands with higher current densities [4]. EFDA is issuing a call for tender among the European Industry so that they can be prepared to fulfil the new requirements.

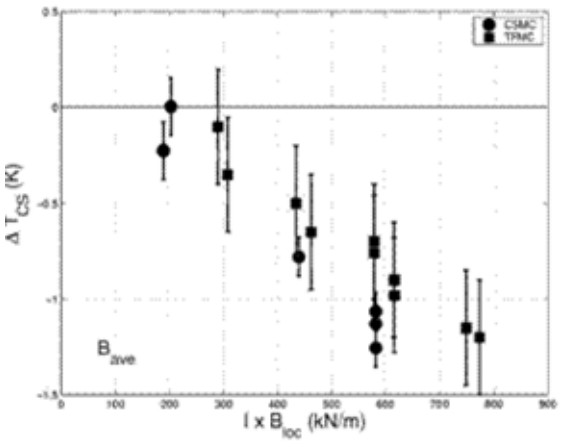

Fig. 4: The measured difference of the T_{CS} of the TFMC including error bars in comparison with central solenoid model coil (CSMC) showing nearly the same behaviour namely a reduction of the T_{CS} with increasing Lorentz force on the conductor [3]

The electric losses during slow ramping and safety discharge were evaluated. A surprising result was the losses caused by the current ripple of the power supply independent of the current level in the range of 40 W [5].

Thermo hydraulic measurements: The results of the thermo hydraulic properties were nearly equivalent to that of test phase I. Pressure drop of the two channel conductor and quench propagation were evaluated more in detail [6].

Mechanical measurements: During the current ramps 140 sensors (single strain gauges, strain gauge rosettes, displacement transducers) measuring mechanical properties were recorded. The measured values were compared with calculations derived from the FEM model and led to improvements in details of the model. The measured and calculated overall deformation across the horizontal mid plane is in fair agreement, which validates the FEM model (Fig. 5). Further results will be presented in [7].

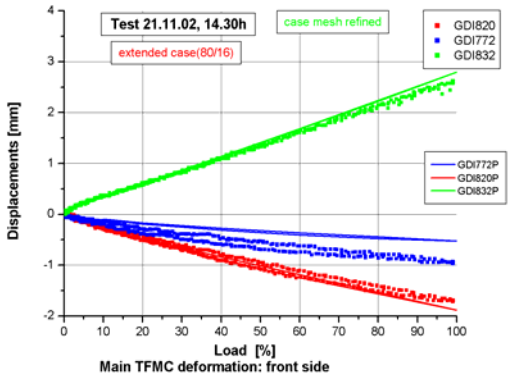

Fig. 5: The measured extension in the horizontal mid plane of the TFMC coil case in comparison with the FEM analysis (symbols measured, lines calculations).

For the maximum load case, the attractive force between the two coils was 82 MN. The EURATOM LCT coil experienced a three times higher out-of-plane load than in the torus test at ORNL, USA, 1986. No effects on the stability of the conductor under this load were observed.

For investigation of setting effects and cycling effects on the superconducting cable, the configuration was operated with triangular periodic current pulses. The LCT coil was ramped up to 16 kA while the TFMC was ramped up and down with 140 A/s. For currents ≥ 75 % rated load, 15 cycles were applied. At 100 % load after the fifth cycle a spontaneous quench occurred in the EURATOM LCT coil. The reason was a too low temperate margin for the temperature increase by the electric losses during cycling. The reduction of the inlet temperature from 3.5 K to 3.1 K solved the problem. No further quench occurred.

As far as evaluated no impact was found by the cycling tests on electrical or mechanical properties.

Dielectric measurements: The degradation of the electrical insulation from the specified value of 10 kV to about 1kV in the Paschen minimum and to about 4.7 kV for pulse voltage found in test phase I was reproduced in test phase II. The 4.7 kV withstand pulse voltage offered sufficient margin for the safety discharge voltage for the current tests. The results of test phase II correspond in principle to the results of test phase I with the following exception:

The loss factor of the TFMC was determined by a Schering bridge to 0.007. The measurements at cryogenic temperatures before and after the current tests gave a difference of about 4 %. Taking into account the boundary conditions it was concluded that the current tests had no impact on the dielectric insulation properties.

During pulse tests at 9.8 kV with feeding the high voltage pulse in the negative terminal two breakdowns were observed at cryogenic temperatures.

The AC voltage test of the TFMC at cryogenic temperatures with 3.5 kVrms (corresponds to 10 kV peak-peak) at the end of test phase II showed sporadic breakdowns.

No further degradation was caused by the breakdowns. Therefore a breakdown in the solid insulation was excluded. Since a 10 minutes DC test showed no abnormalities it was demonstrated that a slide discharge mechanism had to be occurred at weak points of the electrical insulation system. This has been consistent with observed voltage breakdowns for both polarities.

High voltage discharge of the TFMC: The investigations by pulse voltage in phase I resulted in a higher dielectric strength for the minus terminal than for the plus terminal. Therefore it was decided to perform a high voltage with reversed polarity connected by flexible cables to the POLO switching circuit in phase II. According to the pre-tests sufficient margin was available for a discharge voltage of 4.4 kV. The performed 8 high voltage discharges were all successful without a breakdown.

TOSKA facility: The TOSKA facility had an availability of about 98 % over a testing time of 18 weeks. Smaller interruptions caused partly by the high magnetic fringing fields were fixed in

short times with practical no impact on the availability. The static magnetic fringing fields were about 1.5 times higher than during the EURATOM LCT coil test at 1.8 K. The fringing fields achieved in test phase II the outermost level, for which a reliable operation of the grown facility was possible.

The cryogenic system was more difficult to handle than in test phase I because of more components (EURTOM LCT coil with current leads, 300 W Linde refrigerator) and the required cooling power outside the refrigerator capabilities. Nevertheless all requirements of the test program were fulfilled.

Summary

With the results of test phase I and II it was demonstrated that the applied technology is usable for the ITER TF coils. The achieved test results were in the most cases as expected or initiated improvements. The high availability of the TOSKA facility demonstrated suitability of the used components. The test of the ITER TFMC was very successful and concluded in schedule.

Staff:

A. Augenstein
S. Darweschsad
I. Donner
G. Dittrich
P. Duelli
W. Eppler
W. Fietz (for 2. from 01.03.03)
S. Fink
A. Grünhagen
R. Heger
R. Heller
W. Herz
R. Kaufmann (till 28.02.03)
A. Kienzler
O. Langhans
W. Lehmann
V. Leibbrand
V. Marchese
I. Meyer
J. Müller
G. Nöther
U. Padligur (till 28.02.03)
S. Raff
P. Rohr
M. Röhrling (since Mai 2002)
P. Schanz
V. Schulmeister
E. Specht
H.-J. Spiegel
M. Süßer
A. Ulbricht (for 2. till 28.02.03)
D. Weigert
F. Wüchner
G. Zahn (for 1.)
V. Zwecker

Literature:

[1] P. Komarek, Results and conclusions from the ITER TFMC testing, Proc. 20th IEEE/NPSS SOFE, San Diego CA, USA, Oct. 14-17, 2003

[2] G. Zahn et al., Cryogenic test results of the ITER TF model coil test in TOSKA, Proc. CEC/ICMC Anchorage, AL, Sept. 22-26, 2003

[3] R. Zanino et al., Tcs tests and performance assessment of the ITER Toroidal Field Model Coil (phase II), Proc. MT-18, Morioka, Japan, Oct. 20-24, 2003

[4] J.L. Duchateau et al., Exploring the limits of a very large Nb3Sn conductor: the 80 kA conductor of the ITER Toroidal Field Model Coil, Proc. EUCAS, Sorrento, Italy, Sept. 15-18, 2003

[5] M. Ricci et al., Modelling and measurement of electromagnetic losses in the ITER TF Model Coil, Proc. EUCAS, Sorrento, Italy, Sept. 15-18, 2003

[6] R. Zanino et al., Thermal-hydraulic issues in the ITER Toroidal Field Model Coil (TFMC) test and analysis, Proc. CEC/ICMC Anchorage, AL, Sept. 22-26, 2003

[7] P. Libeyre et al., Mechanical tests of the ITER Toroidal, Proc. MT-18, Morioka, Japan, Oct. 20-24, 2003

TW1-TMC/CODES
Installation of the Measurement System on the TFMC at Forschungszentrum Karlsruhe

Installation of Hall Probes on ITER Toroical Field Model Coil

The aim of the task was the re-construction of the profile of the current density in a ITER type NbTi superconducting cable using two sets of magnetic field measurements, radial and tangential, suitably located as near as possible to the conductor. The superconducting cable is made of 1152 strands grouped in six petals. From the field measurements, the determination of the current distribution among the six petals, assuming a flat current distribution in each petal, has been formulated as a linear inverse problem, which can be solved minimising the least mean square error between measured and calculated fields at the probes' locations [1]. The hypothesis of linearity was possible thanks to the absence of ferromagnetic materials nearby.

The experimental data have been collected in October and November 2002 during the Phase II of the Toroidal Field Model Coil (TFMC) test campaign performed at the TOSKA facility of the Forschungszentrum Karlsruhe[1]. The work, co-ordinated by EFDA-CSU, was conducted in co-operation with IEE Bratislava, supplier of the measuring heads, and the consortium ENEA-Create, responsible for the data acquisition system and the interpretation codes.

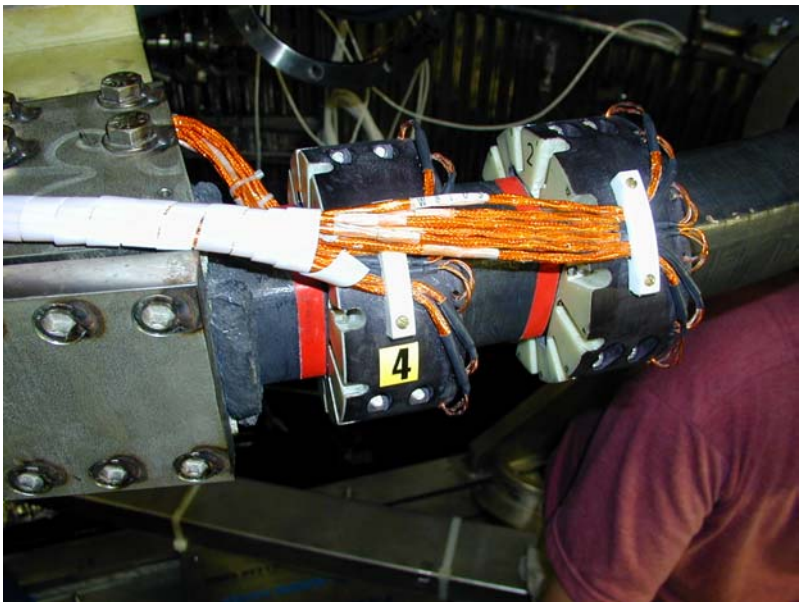

Fig. 1: Location of the two Hall probe measuring heads.

Two measuring heads, each provided with twelve Hall probes, were installed on the TFMC negative type 1 busbar at a distance of a quarter of pitch from each other (Fig. 1). The head on the left (H4) is provided with six tangential and six radial probes, the head on the right (H2) is provided with ten tangential and two radial probes. The sensing current amplitude is selected in such a way that the voltage signal from the Hall probes, in absolute value, does not exceed 100 mV at the maximum field. The data acquisition system (DAQ), from National Instrument, included amplifiers with differential inputs and variable gain, a three-pole antialiasing filters at 200 Hz and a16 bit ADC. The overall sampling frequency was 1 kHz. The DAQ software, running under Windows 2000 on a Pentium PC, was entirely developed with LabVIEW. The accuracy of the DAQ was estimated to be better than 0.1 % with a sensitivity of about 1.2 μV.

The precision of the measurements is affected by the positioning errors of the Hall probes, by the calibration precision, by the uncertainties of the actual position of the conductor axis inside the steel jacket and by the presence of magnetic fields generated by external sources.

---

[1] Subtask EFDA/01-605, **TFMC testing with the EURATOM LCT coil.**

In order to evaluate the effect of positioning inaccuracies, the measuring heads were tested in laboratory, mounted on a resistive busbar in a coaxial arrangement (i.e. the return current was flowing in an external concentric cylindrical conductor) to eliminate the influence of the return current. This provided a good indication of the inaccuracy of the Hall probes positioning and alignment with nominal sensing direction (2° – 3° at the worst). The Hall probes were individually calibrated at room temperature (B from –0.4 T to +0.4 T), at 77 K (B from –0.4 T to +0.4 T) and at 4.2 K (B from –2 T to +2 T). The uncertainty on the initial voltage of the Hall probes is eliminated removing the offset from each field measurement at the beginning of each pulse when the current in the two coils (i.e., LCT and TFMC) is zero. The precision on the magnetic field measurement is expected to be better than 0.5%. The compensation of the external fields is achieved calculating the magnetic field produced by the external currents (i.e., coils and return busbar).

As typical in the case of inverse problems [2], the ill conditioning of the equations system makes the solution extremely sensitive either to the inaccuracies of the geometrical parameters and to the measurement noise. To limit as much as possible the errors in the reconstructed currents instead of considering as unknown variables the total currents in each petal, the system was reformulated in terms of “petal current unbalances” with respect to the “resistive” (i.e. uniformly distributed) current profile. The advantage of such a formulation is that the evenly distributed current contribution can be measured in a situation in which the cable is in the normal state, and then scaled, for each experiment, to the actual total transport current in the cable. An example of current re-construction with TFMC transport current equal to 10 kA and zero current in LCT is shown in Fig. 2 and Fig. 3.

The encouraging results obtained from the measurements indicates that the detection of current unbalances in ITER type conductors is possible using measuring heads based on Hall probes. As a part of a wider activity co-ordinated by EFDA aimed

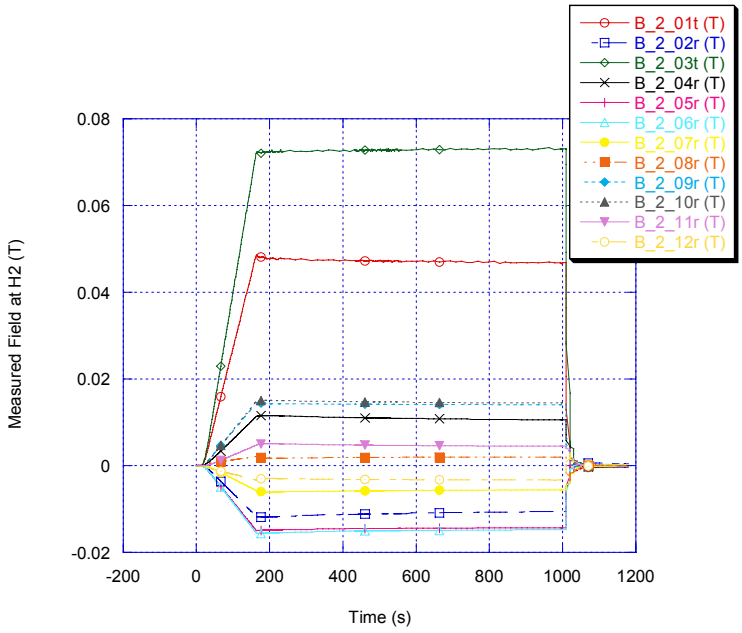

Fig. 2: Field measured by Head 2 with I_{TFMC} = 10 kA and I_{LCT} = 0 kA

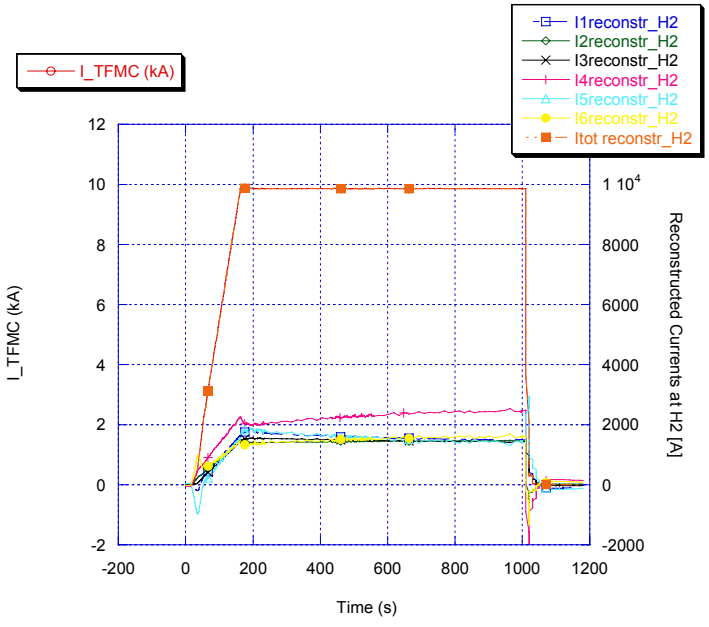

Fig. 3: Current in the six petals reconstructed from measurements at Head 2.

at the study and measurements of current imbalances, a new experiment is planned for 2004[2] in parallel with the tests of the 70 kA High Temperature Superconductor current lead.[3]

Staff:

V. Marchese
F. Wuechner

Literature:

[1] F Bellina, T Bonicelli, M Breschi, M Ciotti, A Della Corte, A Formisano, Yu Ilyin, V Marchese, R Martone, A Nijhuis, M Polak, A Portone, Superconductive Cables Current Distribution Analysis, 22nd SOFT Conference, Helsinki, 9-12 September, 2002.

[2] A. Formisano, R. Martone, Current Profile Estimation from Magnetic Measurements in SC Cables, Proceedings of EUCAS 2003, 15-17 Sept. 2003, Sorrento, Italy

[2] TW3-TMSC-CODES, Validation of theTHELMA Code and its Application to Experimental Results
[3] EFDA 01-598, Design, Development and Constructing of High Temperature Superconductor Current Leads for 70 kA

EFDA 03/1059
Validation of the THELMA Code and its Application to Experimental Results

A non-uniform current distribution affects both the steady state and the transient performance of superconducting magnets. A good understanding of the phenomena leading to non-uniform current distributions in sub-cables1 and the validation of computer codes able to interpret experimental results and to predict the behaviour of complete superconducting systems is therefore essential for a reliable design of those magnets and for an optimisation of their design parameters.

The positive results obtained on the re-construction of the profile of the current density using magnetic field probes, based on the Hall effect, during the Toroidal Field Model Coil (TFMC) test Phase II[4] has encouraged EFDA to launch a new experimental campaign [1] mainly directed to the validation of the Thermo-Hydraulic Electro-Magnetic Analysis - (THELMA) code [2] in conjunction with the test of the High Temperature Superconductor (HTS) current lead on-going at the TOSKA facility of the Forschungszentrum Karlsruhe[5]. The work, co-ordinated by EFDA-CSU, is conducted in co-operation with IEE Bratislava, supplier of the magnetic sensors, ENEA, responsible for the data acquisition system, Create and a pool of Universities (i.e., Bologna, Napoli, Torino, Twente and Udine) responsible of the reconstruction and simulation codes.

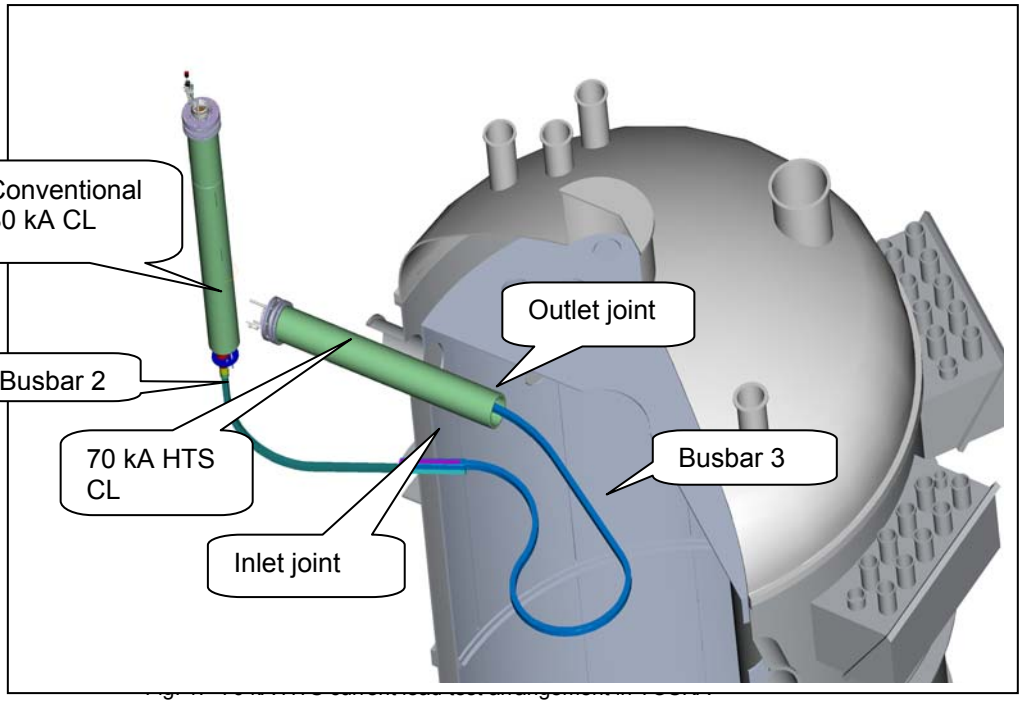

The aim of the subtask is the participation in the design and assembly of the measurement and data acquisition system, the assistance during the tests, some of which will be parasitic (i.e., HTS current lead test at 70 kA), with one week of dedicated tests to investigate the effect of a re-distribution of the current at the current sharing temperature T_{cs} . The test specimen is a NbTi conductor connecting busbar 2 (see Fig 1) to the cold end of the HTS current lead, called busbar 3 (BB3). The conductor is a Cable in Conduit Conductor (CICC) made of 1152 strands grouped in six sub-cables ("petals") and a 51 mmx51 mm steel jacket. Two resistive heaters will be used: the first, up to 1 kW, on the inlet He and the second, up to 500 W, directly to the busbar steel jacket (Fig. 2). The control of the heaters will be

[4] Subtask TW1-TMC-CODES. Installation of Hall probes on the TFMC, Final report 30 Sept. 2003.
[5] Subtask EFDA 02-1013. Testing of the HTS 70 kA Current Lead

performed from the TOSKA control room using an existing application of Diadem 6.1, distributed by National Instruments (NI) and developed by FZK for the tests of ITER TFMC.

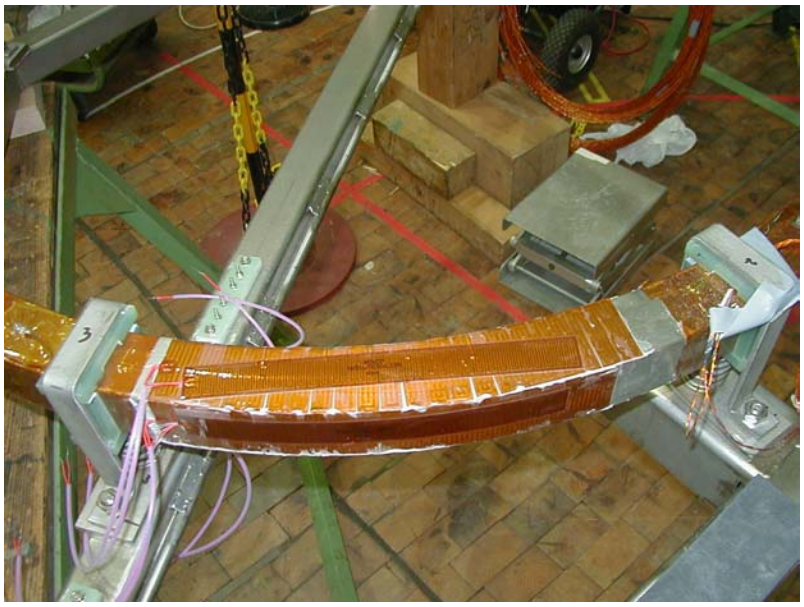

Fig. 2: Busbar 3 jacket resistive heaters (500 W)

The measurement system includes up to 48 Hall probes, 10 temperature sensors, 4 pressure drop measurements, two heating power signals and voltage taps on BB3 and on inlet and outlet joints for a total of 80 channels. Figure 3 shows two circular measuring heads similar to the one used during the last campaign, each fitted with 12 Hall probes, installed one twist pitch apart, and a 2D linear array fitted in between. Two additional Hall probe carriers are fitted at the inlet joint and three carriers at the outer joint to measure the longitudinal and transverse field. The wiring from the sensors to the vacuum feed-through is performed with Kapton insulated twisted pairs with screen. The wiring from the vacuum feed-through to the data acquisition system cabinet, located about 25 meters away, is performed with Teflon insulated twisted pairs also screened. The measurement system shall be able to withstand the insulation test voltage of 1 kV dc for one minute which will be applied daily to the busbar system during the experimental campaign.

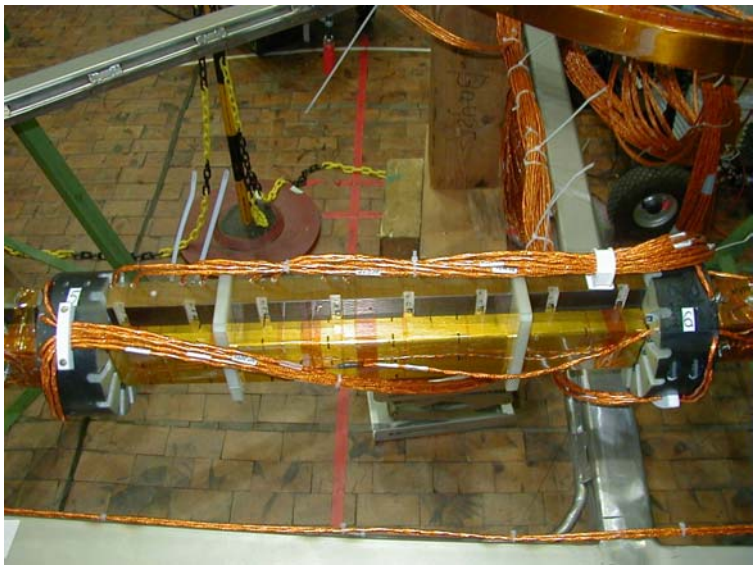

Fig. 3: Hall probe circular and linear arrays

The current sources are housed inside the data acquisition system cabinet. Up to twelve Hall probes have been connected in series in order to reduce the number of current sources. The amplitude of the sensing current is selected in such a way that voltage signal from the Hall probes, in absolute value, does not exceed 100 mV at the maximum field.

The 70 kA current is delivered from two 12 pulse ac-dc thyristor converter, respectively at 30 and 50 kA, connected in parallel. Due to the very low circuit inductance the power supply voltage ripple components superimposed to the dc output, mainly at 300, 600 and 1200 Hz (e.g., estimated voltage across BB3 in steady state 1 V peak), can introduce unwanted aliasing on the measured channels if suitable low pass filters are not used before the analogue to digital converter.

The data acquisition system hardware includes two NI-1102B signal conditioning modules (i.e., 32 differential inputs and 200 Hz anti-aliasing filter), two NI-1120 isolation amplifiers (i.e., 8 differential inputs and 4Hz anti-aliasing filter), the SCXI multiplexer and a 16 bit ADC board (i.e., PCI 6032E) with maximum sampling speed of 100 kS/s. The data acquisition system software, as for the previous campaign, will be developed by ENEA with LabVIEW. The application will include data sampling at 1 KHz, conversion in engineering units, graphical interface, and additional smoothing to reduce even further the effect of the voltage ripple of the power supply and data decimation to reduce data storage.

Calibration tests of Hall probes with BB3 in the resistive state, therefore with a current distribution essentially uniform, are foreseen (e.g. at 77 K) to identify positioning inaccuracies.

Staff:

W. Fietz
S. Fink
R. Heller
V. Marchese
M. Süßer
F. Wüchner
G. Zahn

Literature:

[1] T. Bonicelli, A. Vostner, Instrumentation of Busbar 3 for the Current Distribution Measurements, EFDA Call for Tender, 18.03.2003.

[2] F Bellina, T Bonicelli, M Breschi, M Ciotti, A Della Corte, A Formisano, Yu Ilyin, V Marchese, R Martone, A Nijhuis, M Polak, A Portone, Superconductive Cables Current Distribution Analysis, 22nd SOFT Conference, Helsinki, 9-12 September, 2002.

EFDA 03/1055
Study of the Transient Voltage Behaviour of the Present ITER TF Coil Design for Determination of the Test Voltages and Procedures

Large coils have relative low resonance frequencies as shown by the transient voltage calculations for the full size ITER EDA magnets [1]. During a fast discharge or fault excitation high dielectric stress can occur within the ITER coil system. The goal of the task is the determination of the voltage stress of the ITER TF coils under rated and fault conditions to give a reliable basis for the high voltage test specifications and for the verification of the insulation coordination of the TF coils. The work is performed in collaboration with the "Institut für Elektroenergiesysteme und Hochspannungstechnik" (IEH) of the University of Karlsruhe.

Capacitances and frequency depending resistances, inductances and mutual inductances within one coil were calculated and a detailed network model for a single ITER TF coil was established. With this network model the investigation of the dielectric stress can be performed for ground insulation, radial plate insulation and conductor insulation.

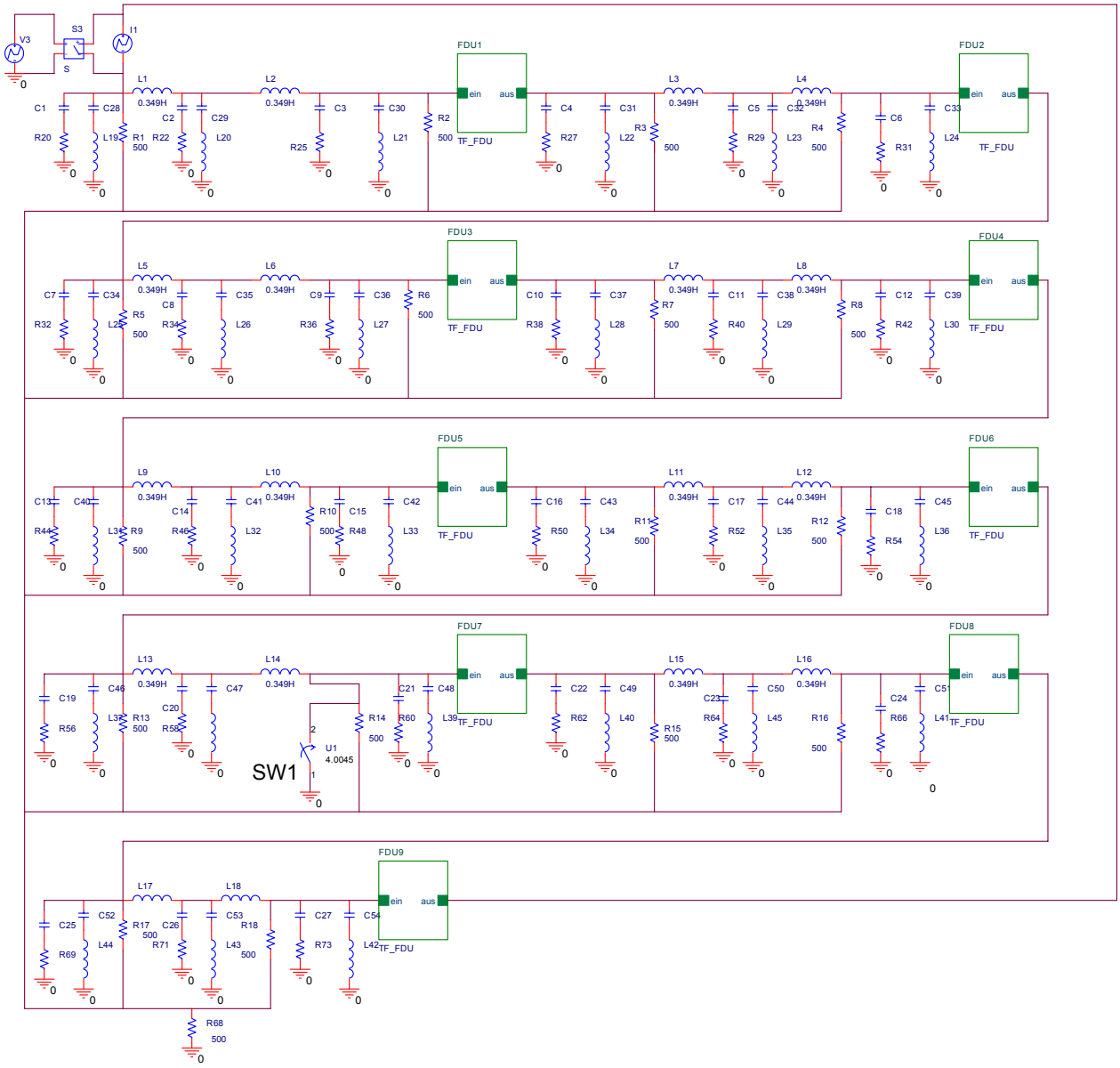

Fig. 1: Network model of the ITER TF coil system. The ITER coils were represented by their inductances and coupling inductances. Every fast discharge unit (FDU) contains a vacuum breaker, a snubber circuit, a capacitor bank and a discharge resistor. The switch SW14 at coil 14 (L14) represents a ground fault.

For the establishing of the ITER TF coil system, 9 fast discharge units, 18 simplified coils including their mutual inductances, the grounding system and the instrumentation cables were combined and excited with a current source of 68 kA (Fig. 1). The simulation of a fast discharge with the commutation in the resistor paths of the fast discharge units allows the calculation of the voltage excitations at the coils.

In addition, two fault scenarios were investigated:

- Scenario 1: Fast discharge with the failure of 2 neighboured fast discharge units.
- Scenario 2: Fast discharge with the failure of 2 neighboured fast discharge units aggravated by an earth fault at the terminal with the highest potential to ground.

Worst case voltages that are calculated to appear at coil terminals (voltages to ground or terminal to terminal voltages) are applied to the detailed single coil network which allows the investigation of the maximum dielectric stress for all 3 types of insulation.

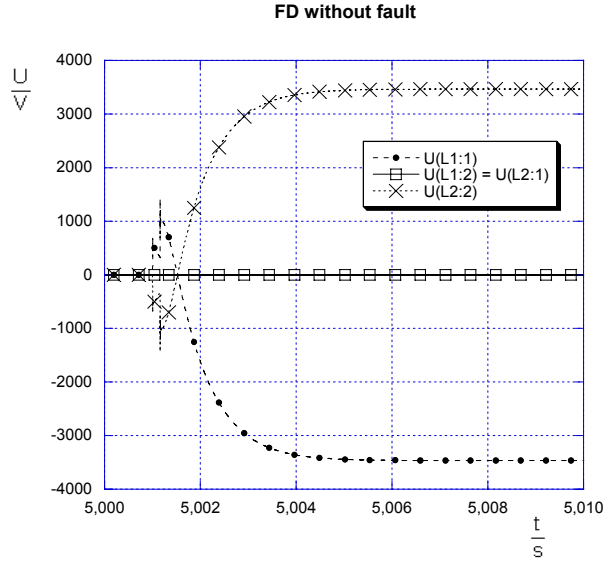

Fig. 2: Terminal voltages to ground during a fast discharge without a fault calculated for the first 2 coils (in Fig. 1). The two terminals, where the coils are connected with each other, are on ground potential. The outer terminals, where the coils are connected with their Fast Discharge Unit, have a maximum voltage of ±3.5 kV to ground.

The grounding system leads to a unipolar stress of the coil for a fast discharge under rated conditions (Fig. 2). An excitation at one terminal and the grounding of the other terminal is therefore sufficient. Under fault conditions a shift of the terminal to ground voltage makes it necessary to inject 2 voltage excitations in both terminals of the detailed single coil network model. In addition different coil excitations have to be examined because it was found that the maximum terminal to terminal voltage and the maximum terminal to ground voltage appear at different coils.

Presently the coil excitations under fault conditions are investigated in detail. After collecting all possible excitations, suitable circuits for impulse tests will be elaborated. From this it will be possible to define representative high voltage tests for single ITER TF coils.

Staff:

W.H. Fietz
S. Fink
A. Ulbricht (till 28.02.2003)

Literature:

[1] A. M. Miri, N. Riegel, C. Sihler, A. Ulbricht, Addendum to the Final Report – Transient voltage effects in the ITER TF coils (Subtask1 of ITER Task MD9), Karlsruhe, 1997

EFDA 02-692
Cryogenic Testing of Materials and Welds for Magnet Structures

The cryogenic material testing and qualification program within the framework of the European fusion technology task consists of investigations on newly developed cryogenic materials with respect to highly stressed parts of the ITER Toroidal Field (TF) coil case and a Type 316LN jacket material for the Central Solenoid (CS) coil. The main activities regarding the ITER coil case are devoted to investigations on tensile, fracture toughness, and fatigue crack growth rate (FCGR) measurements of a modified cryogenic stainless steel foreseen for the use of the TF coil case inner leg. For this task a representative Mock-up designated as Model 3 was forged after casting a manganese enriched Type 316LN block of 40 t. This material along with the two former Models [1], Model 1 (~ 44 t forging) and Model 2 (~ 25 t cast) were investigated with respect to their FCGR behavior at load ratios between 0.1 and 0.7 at 7 K. A data base was established for all these three Models to be used in the design of the ITER TF coils. Furthermore, to improve the cryogenic tensile behavior of the Model 3 a representative batch of the same cast material was forged to achieve smaller grain sizes and obtain higher and uniform yield strengths.

Table 1: Chemical composition of the investigated materials in weight %

Material	C	Si	Mn	P	S	Cr	Ni	Mo	N	Cu	Co	Al	V	Fe
Model 1	0.018	0.370	2.01	0.028	0.002	17.23	13.46	2.52	0.182	-	-	0.009	0.060	Bal.
Model 2	0.016	0.779	6.00	0.022	0.048	17.60	13.97	3.01	0.184	0.182	0.077	0.051	0.057	Bal.
Model 3	0.024	0.690	5.90	0.018	0.001	17.60	13.80	3.20	0.200	0.120	0.030	0.030	-	Bal.
Cefival	0.020	0.400	1.79	0.013	0.0005	17.04	13.28	2.57	0.170	-	-	-	-	Bal.

The cryogenic cyclic performance of the CS conductor's jacket material was investigated recently by FCGR measurements [2]. These FCGR data can be used according to the rules of the damage tolerance versus life expectancy with postulated initial flaw sizes. However, beside the damage tolerance the fail safe philosophy is also important, which can be determined by fatigue life measurements. These fatigue life investigations were carried out with small size specimens of 4 mm diameter at 7 K and with full size jacket structures in liquid helium. The data obtained are very important because few information exist about 4 K fatigue life tests [2-4]. Furthermore, the full size jacket results also validate the reliability of the small size specimen test results for structural applications. The obtained new results also include the effect of the fatigue life testing procedure on the obtained S-N data with the Type 316LN aged jacket materials. A data base could be established and compared to former results with similar type of structural materials.

ITER Mock-up Alloy Results

From the provided 3 sections of the 20 t Model 3 block, tensile measurements in all three spatial orientations were performed. Table 1 shows the chemical composition of all three Models and also the investigated jacket material. These tests were conducted with small 4 mm Ø tensile specimens as well as with 12 mm Ø specimens. The latter ones were tested at 4 K in LHe, whilst the smaller specimens at 7 K in helium gas environment. Between those two test modes there was no significant difference of tensile properties. Table 2 shows all the obtained results of these measurements. The yield strength data of top section in long transverse orientation resulted in lower values compared to the other two sections. This may be related to the forging process. Therefore, a second section from the 20 t batch was forged again in a different plant. The obtained tensile property results with these section show in

Table 3 values of yield strength well above 1000 MPa, a design requirement. Investigations on fracture toughness carried out with JETT procedure [5-7] show fracture toughness values fulfilling the required data of > 200 MPa√m (Table 4).

Table 2: Tensile properties of Model 3 cast & forged manganese enriched Type 316LN alloy in three different spatial orientations (L refers to long, S-T to radial, and L-T to transverse forging orientations) between 7 K and 4 K (LHe) using 12 mm and 4 mm diameter specimens

	Specimen Ø Temperature K	Young's Modulus GPa	Yield Strength MPa	UTS MPa	Uniform Elongation %	Total Elongation %	Reduction of area %
TxBot-1 (L-T)	12 mm Ø, LHe	196	1080	1456	~35	~43	36
TxBot-2 (L-T)	4 mm Ø, 7 K	195	1032	1455	~31	-	43
TxBot-3 (L-T)	4 mm Ø, 7 K	207	1062	1472	~36	-	41
TyBot-1r (S-T)	12 mm Ø, LHe	191	1060	1476	~35	~45	35
TyBot-2 (S-T)	4 mm Ø, 7 K	196	1002	1426	~30	-	43
TzBot-1 (L)	4 mm Ø, 7 K	195	982	1436	~32	-	43
TzBot-2 (L)	4 mm Ø, 7 K	200	1016	1417	~31	~34	42
TxMid-1 (L-T)	4 mm Ø, 7 K	194	1064	1501	~40	~41	51
TxMid-2 (L-T)	12 mm Ø, LHe	206	1069	1455	~34	~37	50
TxMid-3a (L-T)	12 mm Ø, LHe	206	1091	1468	~40	~47	50
TyMid-1 (S-T)	4 mm Ø, 7 K	184	944	1455	~39	~43	43
TyMid-2 (S-T)	4 mm Ø, LHe	192	1056	1497	~37	~43	-
TzMid-1 (L)	4 mm Ø, 7 K	195	1069	1481	~34	-	43
TzMid-2 (L)	4 mm Ø, 7 K	202	1051	1450	~36	~43	40
TxTop-1 (L-T)	4 mm Ø, 7 K	195	921	1454	~33	~40	39
TxTop-2 (L-T)	4 mm Ø, 7 K	200	922	1426	~33	~38	43
TxTop-3 (L-T)	12 mm Ø, LHe	205	942	1451	~37	~43	-
TyTop-1 (S-T)	4 mm Ø, 7 K	195	1054	1445	~37	~43	36
TyTop-2 (S-T)	12 mm Ø, LHe	198	1041	1400	~35	~40	-
TyTop-3 (S-T)	12 mm Ø, LHe	205	1075	1462	~35	~35	-
TzTop-1 (L)	4 mm Ø, 7 K	200	950	1434	~30	~36	39

The FCGR properties of the two Models 1 and 2 have been already tested at 7 K but only at R = 0.1 load ratio [8]. The present work shows the results of all three mock-up Models with respect to load ratios of R = 0.1, 0.5, and 0.7. The determined Paris law constants C and m by regression analysis is given in Table 5. The slightly lower FCGR of two specimens from Model 1 is confirmed to be a reason of the different material property of the core region compared to the outer sections of the heavy forging (first row of the Table 5). The pierced piece from the core of the 44 t block had larger grain sizes owing to higher cool down times after the forging process. As shown in Table 5, the Model 3 material has significant lower FCGR at R = 0.1 compared to higher load ratios. Another important finding is also that this material has superior cyclic characteristics compared to the two other mock-ups.

Fatigue Life of CS-Jacket Materials

The existing cryogenic S-N data with aged jacket materials [2] refer to the former production line of Valinox material [2]. A further check of Valinox by fatigue life tests using the welded reserve specimens confirmed the previous data. These former findings showed that the fatigue failure occurred always inside the weld region starting in most cases from the specimen surface. However, the jacket material Cefival, having almost similar composition as Valinox is shown from tests using same type of specimens a fatigue failure starting in majority of cases from the weld fusion boundary. Especially, all Cefival fatigue life tests carried out above 1100 MPa peak load level showed a crack nucleation from the surface of the fusion boundary. In addition, the weld specimens of aged Cefival material showed to be inferior to Valinox as given in Figure 1. The results of Cefival base metal fatigue life are also

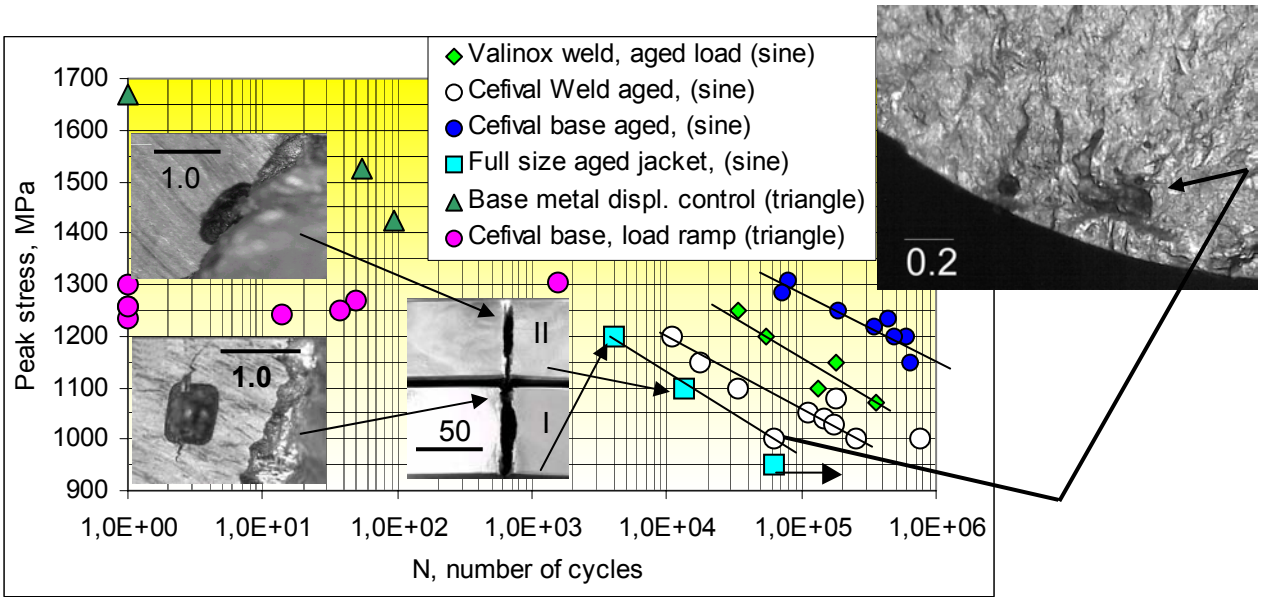

Fig. 1: Fatigue life S-N results (4 - 7 K) with 4 mm Ø hour glass type specimens of Type 316LN material (Cefival and Valinox jackets) in aged condition for both weld and base metals. The three photographs at the left side show the failed full size jackets (samples I and II) under fatigue load. The crack initiation and the failure images are depicted after the failure at 4 K (left upper and bottom). The upper right side photography shows the internal defect inside the weldment and its influence to unusual early cyclic failure of Cefival weld metal. All measurements are carried out at a load ratio of R = 0.1

included in this diagram. During the fatigue life measurements it was detected that the starting frequency and type of machine control determines the cyclic life of the specimen. A triangle mode load control show beyond the general yielding time dependent displacement behavior, which influences extremely the life expectancy of the specimen. Several base metal specimens failed at initial ramp up start period of the test. However, later by programmed load control using the machine microprofiler the base metal specimens could be tested successfully. In addition, as shown in Figure 1, cyclic displacement controlled loading with 5 mm/min stroke rate (here only the plot with failure at 1670 MPa stress (N = 1 cycle) is the result of the stress strain measurement with an usual 0.5 mm/min stroke rate) reveal that the specimen failure stress increases considerably in low cycle mode.

Table 3: Tensile properties of Model 3 cast & forged manganese enriched Type 316LN alloy in three different spatial orientations at 7 K. These results are obtained with the second block forged at Morandini plant, Italy

File & orientation	Young's Modulus GPa	Yield Strength MPa	Ultimate Tensile Strength MPa	Uniform Elongation %	Total Elongation %
CAFOR-T1 (L-T)	202	1121	1504	29	36
CAFOR-T2 (L-T)	186	1132	1434	18	27
CAFOR-T3 (L-T)	204	1129	1559	40	45
CAFOR-T4 (L-T)	182	1099	1539	40	47
CAFOR-L1 (L)	190	1055	1525	35	41
CAFOR-L2 (L)	199	1106	1556	30	42
CAFOR-Q1 (L-S)	184	1166	1578	30	37
CAFOR-Q2 (L-S)	194	1170	1574	32	44

The full size jacket test results at 4 K are also shown in Figure 1. Altogether two full size jackets are tested. Specimen number one (I), an aged Cefival jacket was loaded at 1200 MPa peak stress (R = 0.1, T = 4 K) and its surface had 10 artificial EDM prepared defects equally distributed between weld, heat affected zone, and base metal. The four point bending loading ensured a constant surface stress in this region, where the defects are positioned.

Only one defect at the weld metal surface out of 10 small defects positioned on weld and base metal served as a failure starter.

Table 4: Fracture mechanical tests results of Model 3 material obtained by JETT technique [4-6] at 7 K.

File and orientation	Critical J N/mm	Converted K_{IC}m MPa$\sqrt{m}$
JxBot-1, (L-T)	211	208
JxTop-1, (L-T)	215	210
JxMid-1, (L-T)	216	211
JyBot-1, (S-T)	370	275
JyMid-1, (S-T)	269	234
JyTop-1 (S-T)	205	205
JzTopt-1, (L)	214	209

The second unaged specimen (II) from the former batch Valinox having only two artificial defects at the surface of the weldment was loaded initially at 950 MPa peak stress for 65000 cycles at 4 K. After its survival it was decided to age the specimen and test it at higher loads a second time. The cyclic loading at 1100 MPa (R = 0.1, T = 4 K) resulted in a failure at 13402 cycles. As here the failure occurs also inside the weld metal, it is confirmed that the weld joint is the weakest part of the jacket. Therefore, these full size tests with artificial defects, devoted as worse case, validate the obtained results with the small size specimens.

Table 5: FCGR Paris law constants determined at different load ratios for all three Mock-up Models at 7 K.

Material	Load ratio (P_{min}/P_{max}), R	C, cycle /mm	m	Square of regression coeff., R^2	Comments
Model 1	0.1	1.228 E-10	3.726	0.960	Sample from core region
Model 1	0.1	9.762 E-10	3.182	0.979	Sample from 44 t forging
Model 1	0.5	6.198 E-09	2.711	0.961	Sample from 44 t forging
Model 1	0.7	5.814 E-09	2.713	0.931	Sample from 44 t forging
Model 2	0.1	6.619 E-11	3.856	0.977	Sample from 25 t cast
Model 2	0.5	9.532 E-11	3.867	0.958	Sample from 25 t cast
Model 2	0.7	2.795 E-09	2.794	0.878	Sample from 25 t cast
Model 3	0.1	2.547 E-11	3.805	0.859	Top section of 20 t forging
Model 3	0.5	3.183 E-11	4.048	0.950	Top section of 20 t forging
Model 3	0.7	4.023 E-11	4.020	0.967	Top section of 20 t forging

With respect to the residual stresses due to the weld, the surface of the weld metal has a maximum stress of ~400 MPa, which was measured using neutron diffraction measurements and confirmed using macro-displacement measurements of the weld section. Considering the presence of the tensile residual stresses on jacket surface with the existing defects, the lower fatigue life of the full size jacket is within expectations. In Figure 1 the image taken from the failed full size jacket surface (insert shown at left bottom belonging to Valinox aged jacket) shows the crack initiation under cyclic loading from the small artificial defect. However, the failure of this full size jacket occurred from the second defect positioned symmetrically on the weldment as shown by the image given at left top. The upper right side picture given in Figure 1 belongs to an aged Cefival specimen failed at very early stages of the cyclic test. The reason was found to be due to the weldment having an internal small defect of 0.26 mm length, which facilitated the crack nucleation.

Staff:

A. Nyilas
H. Kiesel

Literature:

[1] Bevilacqua, G., et al., “Manufacturing of full scale models of the ITER TF coil cases“, in Fusion Engineering and Design, 58-59, (2001), pp. 281-287

[2] Nyilas, A., Portone, A., and Sborchia, C., “Cryogenic investigations on cyclic properties of Type 316LN and Incoloy 908 alloys for superconducting magnet applications”, in Fatigue 2002, edited by A. F. Blom, Stockholm 2002, Vol. 4/5, pp. 2581-2586.

[3] Nyilas, A., Zhang, J., Obst, B., and Ulbricht, A. “Fatigue and fatigue crack growth properties of 316LN and Incoloy 908 below 10 K”, in Advances in Cryogenic Engineering (Materials) 38A, edited by F. R. Fickett and R. P. Reed, Plenum, New York, 1992, pp. 133-140.

[4] Grinberg, N. M., Aleksenko, E. N., Yushchenko, K. A., and Kulikova, L. G., “The influence of microstructure on fatigue fracture of austenitic steel at 293 and 11 K”, in Cryogenics, July 1982, pp. 348-353.

[5] Rice, J. R., Paris, P. C., and Merkle, J. G., “Some further results of J-integral analysis and estimates”, in ASTM Special Technical Publications 536, (1973) pp. 231-245.

[6] Shindo, Y., Mano, Y., Horiguchi, K., and Sugo, T., “Cryogenic fracture toughness determination of a structural alloy weldment by notch tensile measurement and finite element analysis”, in Journal of engineering Materials and Technology, Vol. 123, (2001) pp. 45-50.

[7] Nyilas, A., Nishimura, A., and Obst, B., “Further aspects on J-evaluation demonstrated with EDM notched round bars and double-edged plates between 300 and 7 K”, ”, in Advances in Cryogenic Engineering (Materials) 48, edited by U. B. Balachandran et al., Plenum, New York, 2001, pp. 131-138.

[8] Nyilas, A., Portone, A., and Kiesel, H., “European cryogenic material testing program for ITER coils and intercoil structures”, in Advances in Cryogenic Engineering *(Materials)* 48, edited by U. B. Balachandran et al., Plenum, New York, 2001, pp. 123-130.

EFDA 01/598
Design, Development and Constructing of HTS Current Leads for 70 kA

EFDA 02/1013
Testing of the HTS 70 kA Current Lead

Introduction

The Forschungszentrum Karlsruhe and the Centre de Recherches en Physique des Plasmas (CRPP) are responsible for a development program to construct and test a 70 kA current lead using High Temperature Superconductor (HTS) for the TF Coil system of ITER. The current lead (CL) is designed with respect to the requirements given in the ITER-magnet design document. Special attention is given to the safety requirement: The current lead has to withstand a loss of helium mass flow for 3 minutes at nominal current. One further requirement is that the lead will be installed horizontally in the coil-terminal-boxes.

The current lead consists of an HTS part operated in the temperature range 4.5 to 65 K and a conventional copper part operated in the temperature range 65 K to room temperature (RT). The HTS part is cooled by heat conduction from the 4.5 K level and the copper part is actively cooled with 50 K helium. This concept was also successfully applied in the former 20 kA HTS current lead program.

One important requirement is that it must be possible to install the current lead into the TOSKA facility. This means that the interfaces between the current lead and the facility are fixed and can not be changed, i.e. clamp contact to the superconducting bus bar III at 4.5 K level, connection to the water cooled flexible bus bar at RT level, and total length of the current lead. This is a restriction for the designer and does not necessarily lead to a prototype current lead for ITER although the HTS part is constructed in a way that should allow adopting the design for a prototype without problems.

After an invitation of tenders, American Superconductor Corp. (AMSC) received the contract for design and manufacturing of the HTS part of the current lead. The Forschungszentrum Karlsruhe is responsible for design of the HTS CL, the construction of the heat exchanger, the final assembly and the test of the CL. The test of the HTS CL will be performed in the TOSKA facility of FZK using the equipment available from the former TFMC program (80 kA conventional CL, superconducting short circuit bus bar III). Since in the ITER design all CLs are installed in horizontal position, the HTS CL will be tested horizontally, too.

Design and manufacturing of the HTS module

The HTS current lead module (HTSCLM) is designed to be cooled by heat conduction from the bus bar side and will be operated in vacuum. It consists of the HTS part and two copper end caps, one at each end, to provide the current transfer to the other parts of the CL. The connection to the copper bar which will perform the clamp contact to the bus bar is done by soft soldering. The connection to the heat exchanger part is performed by a screw contact via a gold plated conical surface.

To simplify the fabrication and ease the required pretests, a modular design has been chosen for the HTS part: The basic component is the CryoBlock™ wire of AMSC with a cross section of 4.1 x 0.2 mm^2 and a critical current >100 A at 77 K in the self field (s.f.). 13 of these wires are sintered into stacks which are monolithic and easy-to-use building blocks for high current CLs. The stack dimension is 2.6 x 4.1 mm^2 in cross section and about 700 mm in length, the latter one the longest stacks fabricated so far. The stacks are soft soldered onto stainless steel carriers with copper tips (so-called panels). The connection between stainless steel and copper is brazed. The total current carried by each panel is 5.6 kA at 77 K. This current level can be handled by the test facility at AMSC. The panels are soft-

soldered into the end caps to form a 12-fold prism. This monolithic assembly will withstand all forces applied to the CL during installation and operation. The total design current at 77 K, s.f. results in 68 kA.

The HTSCLM is instrumented with temperature sensors, voltage taps and Hall probes to measure the temperature profile, the contact resistances and the current distributions both in steady state as well as during normal transition. The temperature sensors (Cernox and Platinum) and voltage taps were installed by AMSC whereas the Hall probes were attached by the Forschungszentrum Karlsruhe. For all temperature sensors, AMSC provided the calibration files as part of the whole documentation.

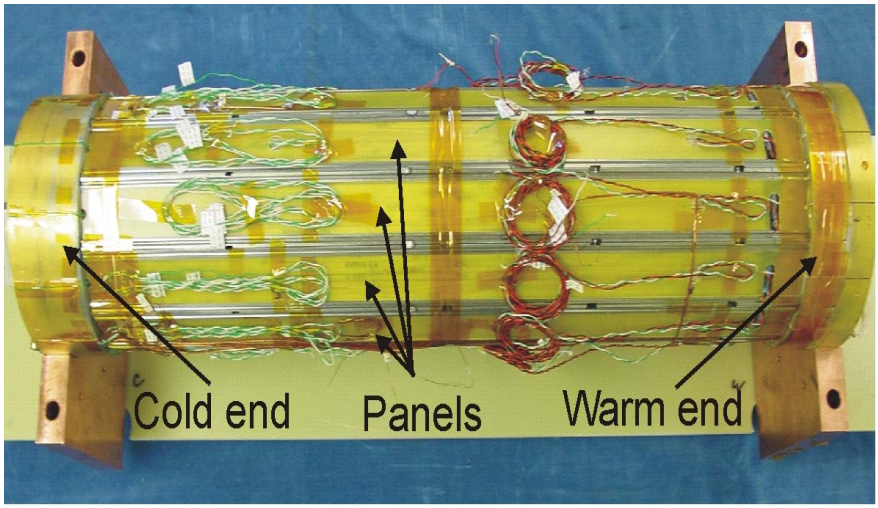

A G10 tube encases the HTS elements which will not only protect the HTS, it will also allow to affix the instrumentation rings that need to hold 52 4-pin connectors.

Fig. 1 shows a picture of the HTSCLM without G10 tube.

Fig. 1: Picture of the 70 kA HTS current lead module (HTSCLM)

Design and manufacturing of the current lead

The heat exchanger is designed to be actively cooled by 50-K helium gas leading to a temperature at the lower end of 65 K. A clamp contact piece is needed for connecting the CL to the superconducting bus bar III which serves as a connection to the conventional 80 kA CL (return terminal). Its dimension is the same as used in the 80 kA CL and is equipped with Nb_3Sn inserts to reduce the resistance in the contact area.

All boundary conditions led to the following layout of the CL:

The copper or resistive part is formed as a heat exchanger unit. The design is as developed at the Forschungszentrum Karlsruhe for the conventional high current CL. The cross sectional dimensions of the heat exchanger are the same as for the conventional 80 kA current leads which were manufactured for the test of the TFMC. This allowed the use of existing perforating plates for the heat exchanger and to reuse the tools for manufacturing various components. The length of the heat exchanger is optimized for 70 kA steady state operation but was adopted to fit in the cryostat port of TOSKA.

For the installation of the CL into the TOSKA facility (Task EFDA 02/1013), a so called cryostat extension is necessary which serves as the support structure and as thermal shield against the room temperature region outside the vacuum vessel.

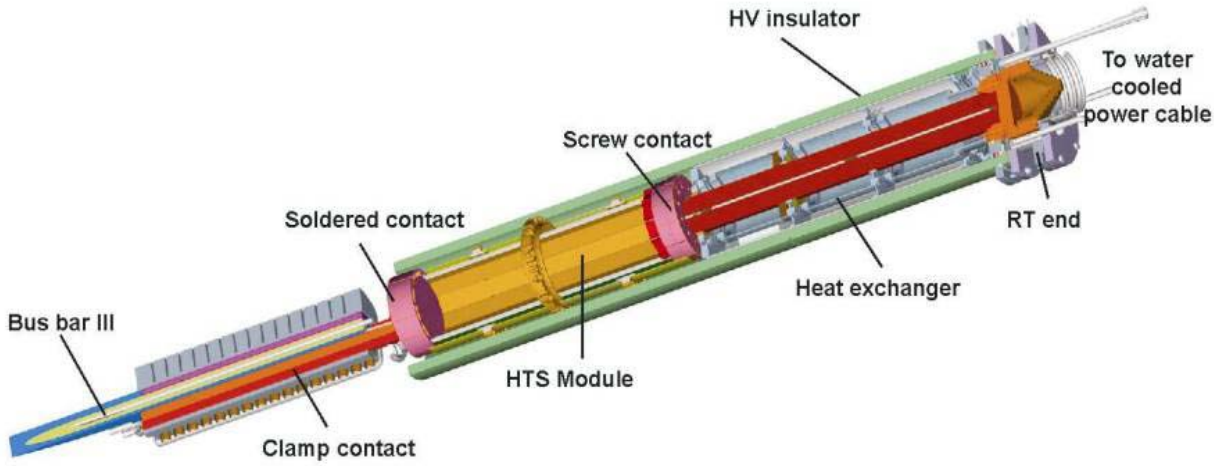

Fig. 2: Artists view of the 70 kA HTS current lead

Figure 2 shows an artists view of the 70 kA HTS CL. On the left hand side, the clamp contact to the bus bar is shown. On the right hand side, the connection to the water-cooled flexible cable is located. In between, the HTSCLM including the copper end caps and the heat exchanger are shown. Figure 3 shows a picture of the heat exchanger during assembly. All parts are fabricated and the final assembly is presently being done. The CL assembly will be completed in end of October. Afterwards it will be installed into the TOSKA facility.

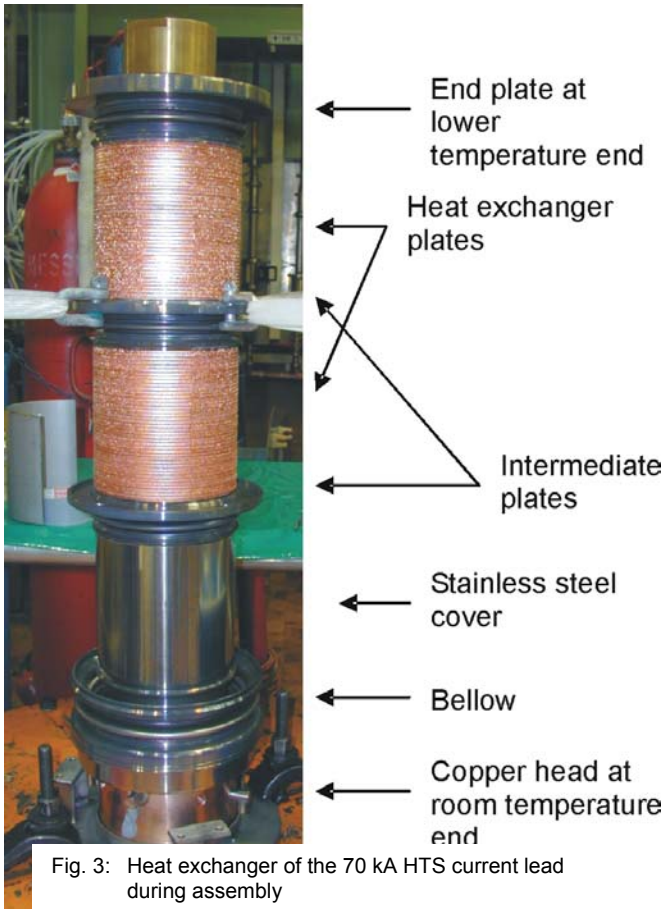

Fig. 3: Heat exchanger of the 70 kA HTS current lead during assembly

Qualification and acceptance tests

During the manufacturing of the HTSCLM, a detailed quality inspection was carried out. Before soldering the different stacks in the panels, their critical currents were measured at 77 K. After soldering, their critical current and contact resistances of each panel were measured again in LN2. The average critical currents measured at 77 K was Ic = (5691±143) A, which results in an estimated total current for the HTSCLM of 68296 A. This number is an underestimation because the magnetic field distribution of each panel has a higher perpendicular component as for the whole HTSCLM. It is interesting that the n-value, i.e., the exponent of the voltage-current-transition curve, is higher for the panels as for the stacks.

After assembly, a final acceptance test at 77 K was performed at AMSC. There, the completed HTSCLM was ramped up to 15 kA to check the instrumentation and to measure the contact resistances between the superconducting stacks and the copper end caps. The resultant resistances were in the range of 2 nΩ. Although a quantitative interpretation of the numbers was not possible because of the different current flow geometry at the end caps during the acceptance test compared to the geometry realized in the HTS CL, it could be concluded that the spread of the contact resistances is acceptable.

Status of the HTS CL construction and outlook

The HTSCLM with the completed instrumentation is ready. The heat exchanger and the cold end contact piece are completed; the final assembly will be performed in October. The cryostat extension is ready. The whole CL including the support structure for the installation in TOSKA will be ready in November. This will be the end of the EFDA Task 01-598.

Modification work for the TOSKA facility for the test of the HTS CL

The 70 kA HTS CL which is being manufactured at the Forschungszentrum Karlsruhe (EFDA Task 01/598) will be tested in the TOSKA facility. For this, the facility is being modified according to the special requirements of this experiment.

Besides the infrastructure equipment of the TOSKA (vacuum vessel, power supplies, switching circuit, refrigerator and control dewar), some equipment fabricated within the frame of the TFMC program can be used, i.e., one 80 kA conventional CL as return terminal and a superconducting short circuit bus bar (BB III). The other 80 kA CL including its cryostat extension and water cooled connection to the bus bars will be replaced by the HTS CL.

Due to the horizontal installation, an extension of one of the water cooled aluminum bus bars that transport the current from the power supply to the CL is necessary. This bus bar has been fabricated in industry and is being installed in TOSKA. Figure 4 shows a scheme of the test arrangement including the 70 kA HTS CL (test object), the superconducting bus bar (BB III) and the conventional 80 kA CL.

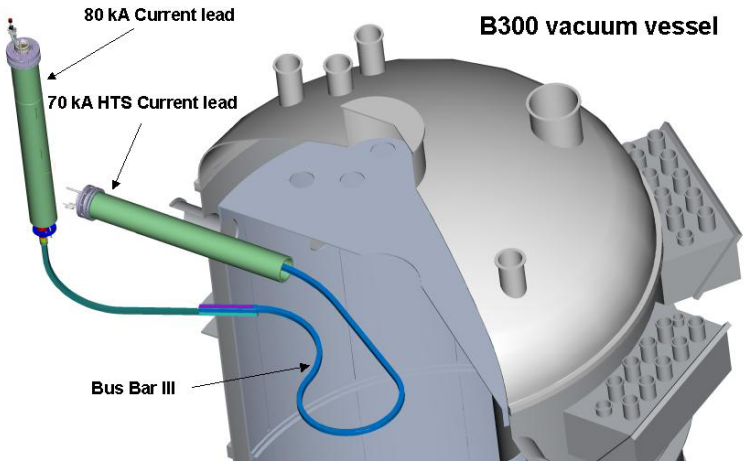

Fig. 4: Schematic of the arrangement of the HTS current lead experiment in TOSKA

The helium gas in the temperature range between 20 and 80 K which is needed for cooling the heat exchanger of the HTS CL will be provided directly from the refrigerator. The coolant gas for the BB III, the conventional CL and for the HTS CL in case of a cooling at 4.5 K will be provided by the secondary cooling loop of the control dewar B250. Figure 5 shows the cooling scheme of the HTS CL experiment in TOSKA.

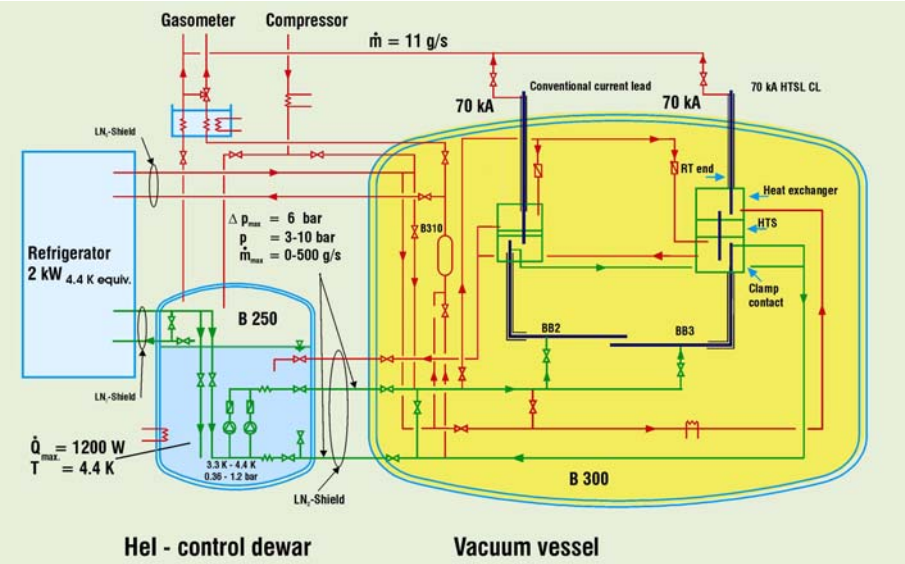

Fig. 5: Flow scheme of the current lead experiment in TOSKA

The test program has been defined which will address and quantify the following points:

1. The real heat load as a function of the He-inlet temperature
2. Specification check of the HTS CL part and the whole CL design
3. Thermal stability
4. Assess the optimum operating parameters to minimize the losses
5. Thermal cycling / Quench degradation
6. Current distribution between the individual HTS stacks
7. Temperature profile of the whole current lead assembly

The estimated total testing time will be 4 weeks.

Additional work for the superconducting bus bar

In addition to the HTS CL experiment, EFDA placed a contract for measuring the current distribution in the NbTi bus bar (BB III) both in normal operation as well as in current sharing conditions (CDM experiment). This experiment requires an additional measurement time of about one week.

This addition is subject of a separate task which is a collaboration between ENEA, ENEA-CREATE, Bratislava and the Forschungszentrum Karlsruhe and requires additional work to perform this experiment because a large number of temperature sensors, voltage taps, Hall probes and also heaters have to be manufactured, installed and connected to a DAS that will be operated separately from the TOSKA DAS.

Status of the installation work and outlook

The BB III is being modified according to the requirements coming from the CDM experiment and will be installed in TOSKA in October 2003. The HTS CL is almost completed (see EFDA Task 01/598) and the installation in TOSKA will start in December. After assembly work, connection to the cooling system and various pretests as well as preparation work for adapting the DAS and the operating and processing systems, the cool down is planned for April 2004 and the experiment will take place in May and June 2004.

Staff:

A. Akhmetov (until April 2003)
M. Darweschsad
G. Dittrich
W.H. Fietz
S. Fink
U. Fuhrmann
R. Heller
W. Herz
A. Kienzler
V. Leibrand
A. Lingor
V. Marchese
I. Meyer
G. Nöther
V. Schulmeister
E. Specht
M. Süsser
D. Weigert
F. Wüchner
G. Zahn
S. Zimmer

Literature:

A. Akhmetov, R. Heller, A. Kienzler, A. Lingor, „ Final Design Report on 70 kA HTS Current Leads - Contract EFDA 01-598, Deliverable 4.2.", Internal Report, March 2003, unpublished

Breeding Blanket
HCPB Blanket Concept

TTBB-001
HCPB: TBM Design, Integration and Analysis

TW3-TTBB-001 D2
Review of HCPB Blanket Design

Introduction

The design review of the current DEMO HCPB blanket concept is motivated by (a) blanket design guidelines, e.g. large module segmentation, that have evolved during the European Power Plant Conceptual Study (PPCS); and, (b) by the decision to use Helium cooling for both European test blanket modules to be tested in ITER. The focus of the design review is the proposal of a blanket concept that

- is compatible with requirements fed back from the European PPCS
- withstands the full coolant pressure of 8 MPa under fault conditions
- achieves a high level of modularity
- is adaptable to solid breeder and lithium lead; and,
- is consistent with functional requirements for a breeding blanket, considering the increased amount of structural steel imposed by the requirements above

The design review of the HCPB blanket started from scratch at the beginning of the reporting period. Work was carried out within a close co-operation with the CEA which is responsible for the design review of the Helium cooled liquid lead blanket concept. At the end of the reporting period, a design has been finalised and reported that fulfils the above requirements.

Design description

Overview

(See Figures 1 to 4) The blanket box is made up from a steel plate with internal cooling channels bent into U-shape, the two remaining sides being closed by cap plates. Welded into the box is a stiffening grid of cooled radial-toroidal and radial-poloidal plates. The space inside the stiffening grid is open to the radial back. Cooled breeder units containing ceramic breeder and Beryllium pebbles are inserted into the blanket much like drawers in a chest while the radial back side is still open. The blanket back plate is built up successively from several steel plates that are welded to the stiffening grid and to coolant pipes from the breeder units. Main coolant headers and collectors are mounted on the back plate.

Main design issues

The key challenges in the design turn out to be (1) making the box strong enough to withstand accidental pressurisation to coolant pressure, and (2) keeping the ceramic breeder and Beryllium content large enough to achieve sufficient Tritium breeding.

(1) The strength of the box is determined by the geometry of the FW/SW and by the distance of stiffening plates. The latter was chosen as 216 mm (which is a fraction of the box of 2m x 2m). In the FW (and partly in the caps) where the stiffening plates welded to the wall are the ones perpendicular to the wall channels, FW geometries from previous design are strong enough to achieve the pressurisation goal. However, in the side wall the orientation of stiffening plates is parallel to the channels, producing a soft side wall

with large local stress. A geometry has been proposed (slightly hexagonal channels; channels next to stiffening plates narrower than the others) that withstands accidental pressurisation. This geometry can be used in both side wall and the First Wall, where large surface heat flux and acceptable structural temperatures are an issue.

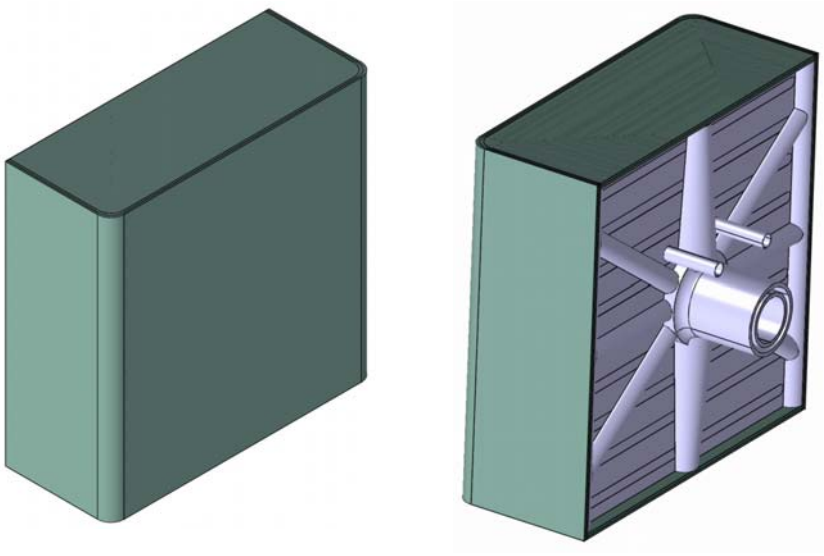

Fig. 1: HCPB blanket box seen from plasma side (left) and from the radial back (right).

(2) Greater strength of the blanket box is achieved by additional cooled structure (stiffening grid) in the blanket. It turned out during the design review that the margin for increasing the steel/Helium fraction at the expense of ceramic breeder/Beryllium is small.

Parts: First Wall/side wall (see Figure 2)

The FW/side wall design is virtually identical to that of the previous HCPB blanket. It is a U-shape with the FW 2m high, 2m wide, and the side walls 0.8m long. The channels are closed at their radial end, but are opened towards FW headers and collectors on the inside of the box.

Parts: Stiffening grid (see Figure 2)

Stiffening plates (SP) are produced by machining channels into half plates and HIPping (hot iso-statically pressing) two halves to produce a full SP. SPs are welded together to produce the stiffening grid, and are joined to the FW, SW, and caps by welding. Coolant enters and leaves the plates at the radial end, where they are connected to the corresponding coolant headers and collectors. Stiffening plates are 11mm high, with 6mm-high channels inside.

Parts: Caps (see Figure 2)

The caps are cooled steel plates like the First Wall/side wall. The channels are U-shape; it is proposed to machine the two halves of the cap and then join them by HIPping. The channels are connected to coolant headers and collectors at the radial end.

Parts: Breeder unit (see Figure 3)

The breeder unit is a rectangular shape of 205 x 205 x 500 mm^3 that is inserted into the grid from the radial back. 81 of these units fit into a module of the poloidal-toroidal size 2m x 2m. Inside the breeder unit are two large double-bed pebble breeder canisters surrounded by Beryllium pebble beds.

All beds are separated by cooling plates containing a dense array of radial cooling channels. At the radial end, these channels are connected to breeder-unit headers and collectors. The units are connected with one inlet and outlet pipe each to the header/collector in the back plate. Depending on the amount of heat to be removed a cooling plate might be needed in the central Be bed.

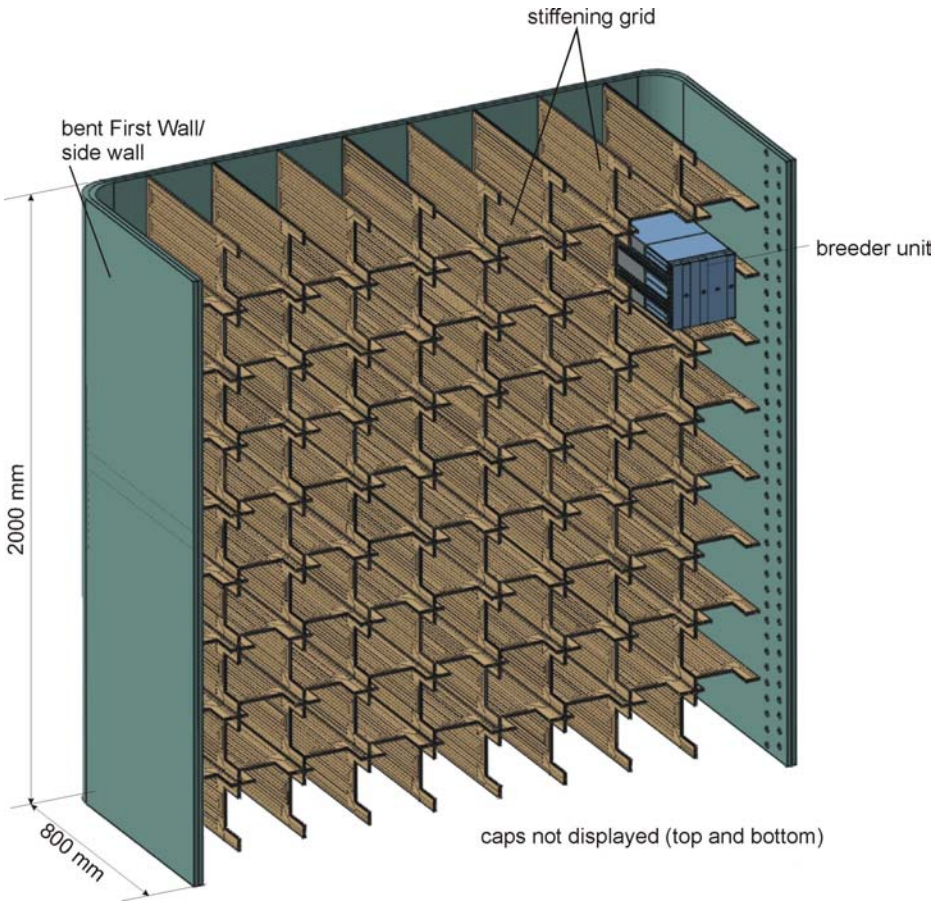

Fig. 2: Open blanket box seen from radial back (caps not shown). Caps and stiffening grid are welded into the box, breeder units are inserted at this stage.

Part of the breeder unit is the Tritium purge system to remove the Tritium bred. Purge supply lines run inside the pebble beds and feed into the region close to the FW. The gas is collected in a void behind the radial end of the breeder units. Inside the back plate of the module, there are two purge inlet manifolds for Be and ceramic, respectively, and a common outlet manifold. The manifolds are connected to the outside with pipes that cut through the module back wall.

Parts: Back wall (see Figure 4)

The back wall is built up successively on the stiffening grid, inside the side walls and caps of the blanket box, see Figure 4. After installing the purge *separator plates A* and *B*, the blanket box is closed with the 40mm-thick *back plate C*, and all coolant pipes and mechanical stiffening grid connections welded to that plate. After that, a pre-fabricated part containing the walls of the *breeder units coolant outlet manifold*s and *separator plate D* is placed over the crosses of the stiffening grid inlet and outlet channels and welded to *back plate C* and to side walls and caps. *Closure plate E* with open slots is put into position and welded to side walls/caps and to the walls of the *breeder units coolant outlet manifold*s.

After that, the slots in the back plate are welded closed with plugs.

Parts: Blanket box headers and collectors

(See Figure 4) The headers and collectors supplying the blanket are proposed to be half shells of cylindrical tubes welded onto the back plate. For the moment it has been assumed that concentric tubes are being used at the inlet, with 500°C Helium in the inner tube.

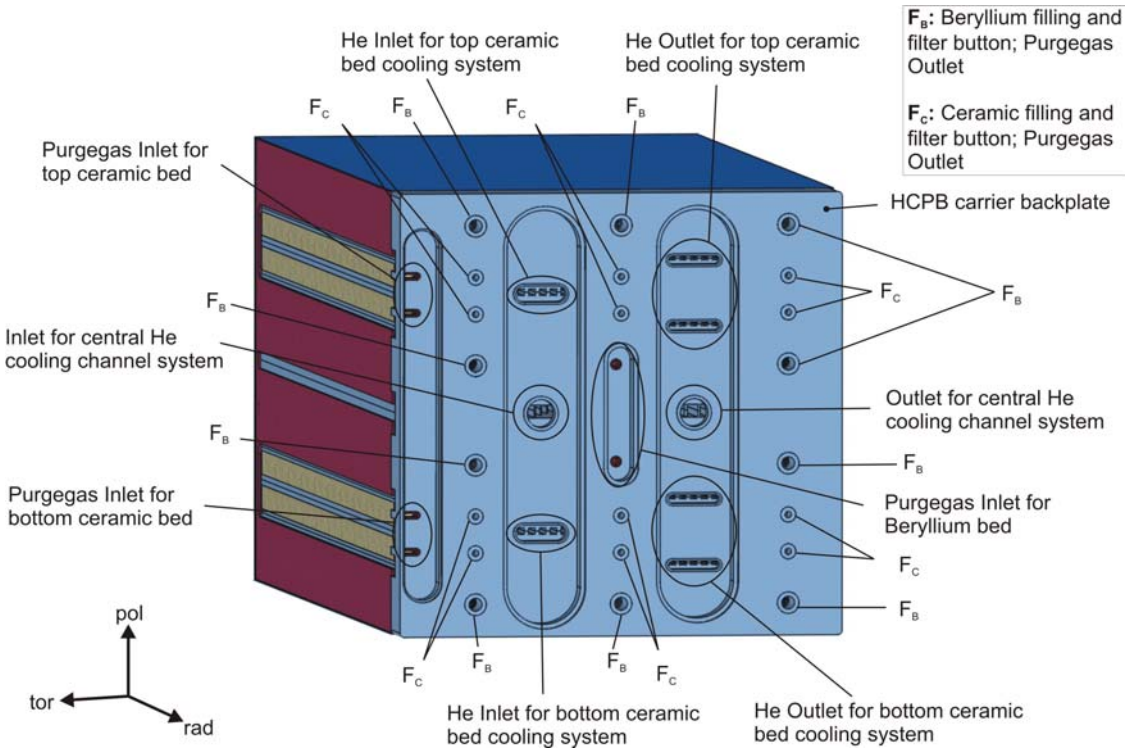

Fig. 3: HCPB breeder unit seen from radial back (manifold covers and coolant pipes not displayed).

Coolant flow

Supplying all structures with sufficient cooling is one of the challenging tasks of designing the blanket. In the present design Helium coolant passes the major blanket parts in series:

- First pass is through the U-shape First Wall/side walls
- Second pass are the stiffening grid plates (75%) and the caps (25%) in parallel
- Third pass are the breeder units

The manifolding in between these passes is contained within the back wall which contains three manifolding spaces between *back plate C* and *closure plate E* (Figure 4):

- The *breeder units coolant outlet manifolds* cover the full height between the two steel plates C and E
- The remaining space is divided by *separator plate C* into two manifolds, *outlet FW, inlet stiffening grid/caps* and *outlet stiffening grid/caps, inlet breeder units*

The headers for the First Wall channels are quarters of a cylindrical tube fitted on both side walls and *closure plate D*, and are supplied from the central Helium inlet of the blanket by three half tubes. Opening only every second FW/SW channel allows alternating flow in neighbouring channels of the FW, which supports an even temperature distribution.

Purge system

All ceramic breeder and Beryllium pebble beds are purged to remove Tritium. As a low pressure system, the purge manifolds are placed next to the low pressure breeding region, implying low weld requirements. Purge manifolds have inlet and outlet tubes placed on the back of the blanket module, see Fig. 4.

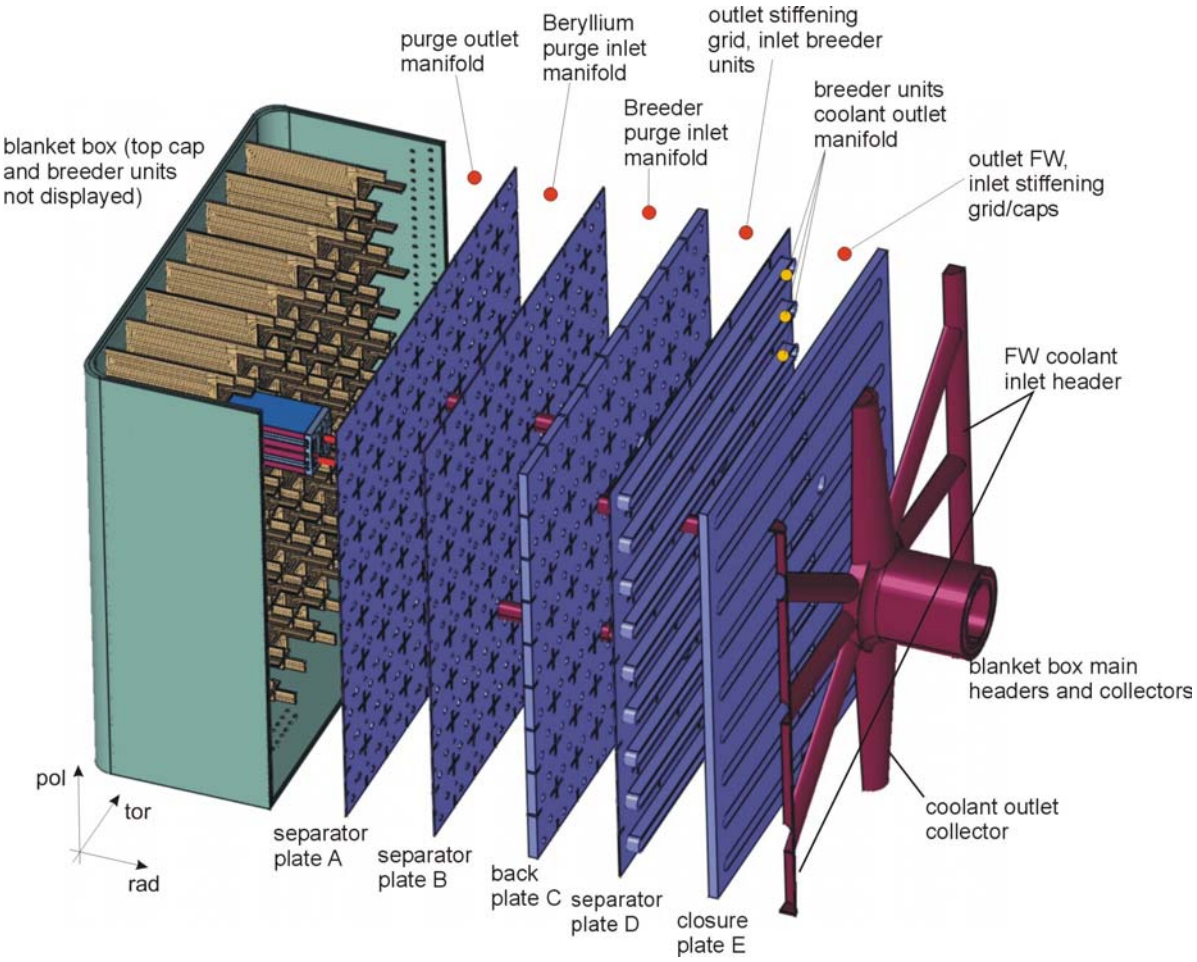

Fig. 4: Successively built-up blanket back wall and manifolds.

Conclusions and further work

The design review has fully achieved the goals set out in the beginning. Analyses on temperature distribution, heat flow, pressure drop and mechanical stress in the box under accidental pressurisation have been part of the work. The new design is a key input for the EU tasks focussing on the design of test blanket modules for ITER. With its complex manufacturing technology it will also be the subject of an industry feasibility in 2004.

Further work is based on the fact that the integration of the blanket into a DEMO reactor concept has not been part of the design review. This integration work will start in the coming year with a study of the impact of curved geometry in a reactor, and a conceptual study of a DEMO in-vessel system including shield, manifolding, attachment. Basic remote handling considerations will be part of the work.

Staff:

S. Hermsmeyer
C. Köhly
J. Rey
Z. Xu

Literature:

[1] S. Hermsmeyer, B. Dolensky, J. Fiek, U. Fischer, C. Köhly, S. Malang, P. Pereslavtsev, J. Rey and Z. Xu, Revision of the EU Helium cooled pebble bed blanket for DEMO, SOFE conference, 14.-17. October 2003, San Diego, USA.

[2] S. Hermsmeyer, B. Dolensky, J. Fiek, U. Fischer, C. Köhly, S. Malang, P. Pereslavtsev, J. Rey and Z. Xu, European DEMO Helium cooled pebble bed (HCPB) blanket designed for large module blanket segmentation, FZKA 6919, to appear

TW2-TTBB-001b D1
Helium Cooled Pebble Bed TBM Design, Integration and Analysis

Objectives: Forschungszentrum Karlsruhe has taken up the engineering designing of the HCPB TBM system to be installed in ITER, comprising the test blanket module, the port plug and external cooling- and tritium extraction loops, taking into account remote handling requirements. An engineering group has been created in order to master this challenging task supported by CAD designers using the CATIA software. Besides the design, analysis by using the computer code ANSYS, plays an important role. Both tools are also used by ITER IT which facilitates the exchange of data and drawings.

The activities in the reporting period were devoted to the TBM design and analysis of temperature profiles and tritium permeation.

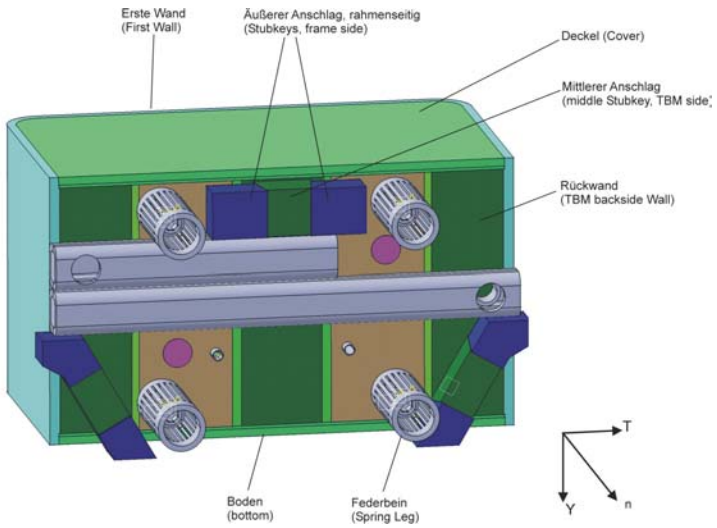

Fig. 1: Back side of TBM2000 with attachment.

TBM system design: For current version of the HCPB TBM, the so-called TBM2000 a detailed design has been made including the fabrication sequence. Small changes were made e.g. regarding the purge gas flow which now flows first through the Beryllium pebble bed and then through the Lithium ceramic pebble bed.

In terms of integration of the TBM into ITER its attachment to the port plug has been designed taking into account the ITER concept based on flexible attachments in order to cope with the temperature differences between TBM and theframe, and stub keys to withstand the forces during disruptions. Several solutions have been considered. The main criteria for selection of the best solution have been a) definite support and b) minimum space requirements. Figure 1 shows the developed solution.

In order to provide a back-up solution in case that the TBM must by removed from the ITER by any reason the conceptual deign of a dummy blanket module has been designed based on the concept of the shield blanket modules.

Another activity was focused on the design of the port plug. The main feature is a break down into four subcomponents which are the so called specs, having the function of the ‘first wall’ for the plug, the front shield accommodating the TBM, the rear shield and the flange. The body of the port plug is water cooled with radial cooling channels and inserts similar as used for the shield blanket. The flange cantilevers the whole port plug, the rear shield is welded to the flange, to the rear shield the front shield is fastened with screws and shear keys, the front shield is electrically isolated against the rear shield. The specs are fixed to the front shield in a way that removal can be done with minimum effort. The TBM Helium cooling tubes run in ‘s’ shape through the front and rear shield. The dimensions of the Helium tubes are such that in bore tools can be used to cut and weld the supply lines of the TBM.

In order to design and locate also the circuit components of the TBM system like Helium cooling system and Tritium extraction system, the reactor building of ITER has been taken from ITER in CATIA V4 and has been converted to CATIA V5 R10. This was an extremely

cumbersome procedure because a lot of elements used in the special V4 environment to design buildings were not understood by CATIA V5 and had to be corrected manually.

Analysis : To transfer the CATIA design data direct to the ANSYS analysis a special tool of ANSYS was used. The selected solution, however, was not optimal. Too much manual corrections and back and forth iterations were necessary to get a satisfying result. Therefore variations for sensitivity analyses should not be made in this way. It seems to be more efficient to make first coarse models in ANSYS and iterate the main parameters until the main parameters can be fixed, then for a detailed design the direct data transfer may be used.

In the blanket design at Forschungszentrum Karlsruhe, so far, for fluid flow analysis and structural analysis different tools have been used. ANSYS offers a 1d fluid pipe element for the analysis, FLUID116. This element was felt to be adequate to describe the channel flows in the TBM. To test the quality of the element in question a comparison with a 3d fluid code, STAR CD, was made. For the test a representative portion of the first wall has been modeled a) with STAR CD using a 3d k-ε model and b) with ANSYS using the element FLUID116. While in STAR CD pressure difference was given, for ANSYS the mass flow was prescribed instead. Looking at the temperatures shown in Fig. 2 we find a good agreement between the solutions and can conclude that for the channel flows the simpler ANSYS analysis is sufficient. As an improvement local heat transfer coefficients between the channel surface element and the fluid element can be applied using a tested customized version of ANSYS. Additionally, for coupled channels the automatic transfer of e.g. the outlet temperature of one channel to the inlet of the subsequent was established, again with a customized subroutine. In this way the coupling between the channels in the first wall and in the cooling plates between the pebble beds can be done during solution of the problem.

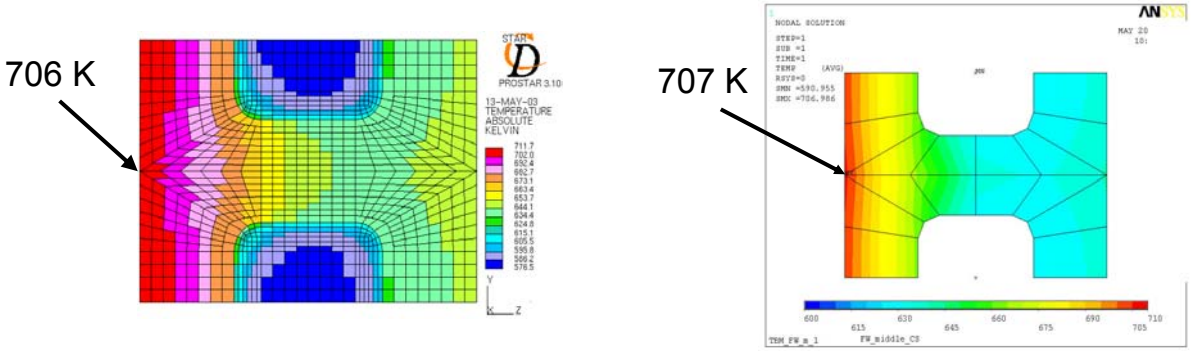

Fig. 2: Comparison of temperatures in first wall, calculated with STAR CD, left, and ANSYS, right.

Another activity was the analysis of the Tritium permeation from the purge gas of the pebble beds through the steel plates, separating the Lithium ceramic and Beryllium pebble beds, to the Helium coolant system. This analysis so far has been done with experimentally validated formulas with the problem of averaged values for big zones. The diffusion coefficients in the steel and the gas surface effects, however, depend exponentially on temperature and the use of local temperatures is necessary to get realistic results. As a thermal analysis of these structures will be done for the purpose of thermal stresses, mesh and local temperatures are already available only the diffusion equation and the special surface effects of the permeation process have to be modeled additionally. This was done by use of a customized version of the heat conduction element in ANSYS. The basic equations for heat conduction and diffusion are similar, only the temperature dependence of the diffusion coefficient was missing. By courtesy of ANSYS we got the source of the heat conduction element SOLID70 and could install the proper dependence. The modeling of the surface effects could be done via the tools available in ANSYS input. A test was made simulating one channel of a cooling plate and the Lithium ceramic bed above and the beryllium bed below. Due to the abilities of

this element also the purge flow in the beds could be simulated. Figure 3 shows the concentrations in the Lithium ceramic and on the steel plate.

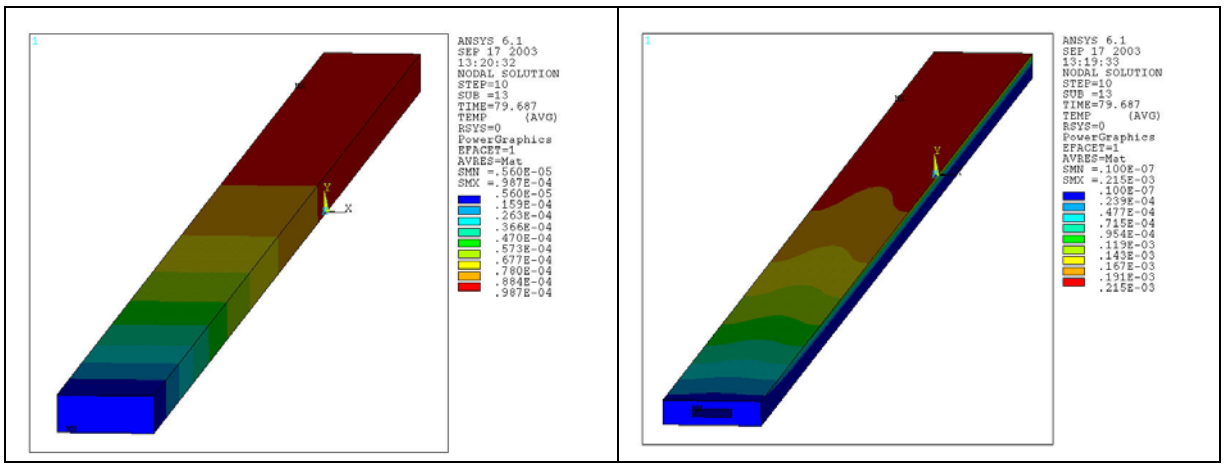

Fig. 3: Tritium concentration in a TBM, left for Lithium ceramics, right in steel. The term 'TEMP' in the plots is misleading. Shown are concentrations in parts per m^3 normalized with Loschmidt number.

In accordance with the requirement of EFDA the initial HCPB concept is being re-designed targeted to develop a new design which should include common elements with the HCLL concept to the most possible extent. The HCPB TBM will be adapted to the new design accordingly.

Staff:

Lux, M.
Meyder, R.
Schanz, P.
Stickel, S.

Literature:

[1] M. Lux et al.: Auslegung der flexiblen Befestigung des Test Blanket Moduls in ITER. Forschungszentrum Karlsruhe, interner Bericht IRS / Fusion

[2] R. Meyder, X. Jin: Method to analyze Tritium permeation in a HCPB blanket of a fusion reactor using ANSYS. ANSYS User meeting 2003 Berlin, to be published

TTBB-002b
Helium Cooled: Blanket Manufacturing Technologies

TW2-TTBB-002b D2
Procurements of Li_4SiO_4 Pebbles and Quality Control

In collaboration with Schott Glaswerke Mainz, FZK is developing and investigating slightly overstoichiometric lithium orthosilicate pebbles (Li_4SiO_4 + 2.5 wt% SiO_2) to be used in the HCPB blanket. The pebbles are fabricated in a semi-industrial scale facility by a melting and spraying method, which allows a production of 200 - 300 kg/year. Since 2002 also LiOH and SiO_2 have been used as raw materials.

The characteristics of the final product are strongly influenced by the fabrication parameters, which are rather difficult to monitor in the small facility and difficult to maintain for different batches. Consequently, the reproducibility from one production run to the other is not very high, and it is therefore required to control the quality of each batch of pebbles received from the industrial producer, in order to use a well-defined standard material in all experimental activities with pebbles or pebble beds.

Characterization of Li_4SiO_4-pebbles produced from LiOH and SiO_2 as raw materials

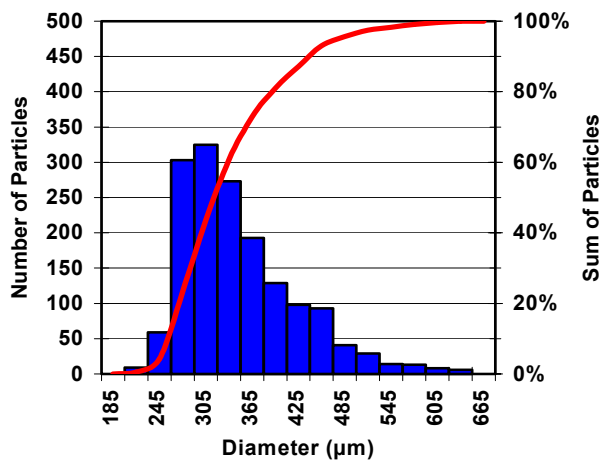

Fig. 1: Diameter distribution of the lithium orthosilicate pebble batch OSi 03/1-3.

Different batches of lithium orthosilicate pebbles were fabricated by the melting and spraying technique. The parameters of the preparation process were optimized to improve the pebble density and the microstructure as well as to minimize the cracks. A mean value of 10 ± 3 N was obtained in crush load experiments of 40 pebbles with a diameter of 500 µm. The delivered pebbles were screened to a diameter range of 250 – 630 µm, resulting in a fraction with a mean diameter (d_{50}) of 310 µm (Fig. 1). Due to the rapid quenching from the melt, the pebbles exhibit the typical dendritic microstructure at the surface as well as in cross sections (Fig. 2). They consist of Li_4SiO_4 as a main constituent and the quenched high-temperature phase $Li_6Si_2O_7$ as a minor constituent. An open porosity of 3.5 % and a closed porosity of 2.7 % were measured by Hg-porosimetry and He-pycnometry, respectively. Using lithium hydroxide and silica as raw materials, the chemical impurities of the pebble batches could be reduced (Table 1). For the OSi 03/1-3 batch a silica excess of 2.41 wt% was determined, which meets the demands on the ceramic breeder material. An amount of 50 g of this material were delivered to HFR Petten for the high fluent irradiation HICU.

New lithium orthosilicate pebble batches will be fabricated and characterized to ensure the material quality and availability of the Li_4SiO_4 pebbles for further experiments. Together with Schott Glaswerke some more basic investigations of the fabrication process are scheduled for October 2003. The aim is to improve the reproducibility and yield of the melting and spraying process.

Long-term annealing

The long term annealing experiment that had been started in 2002 was terminated in January 2003. The characterization of lithium metatitanate (produced by CEA) and two

different lithium orthosilicate pebble batches, that were annealed for up to 96 days at 970°C under helium + 0.1 vol% hydrogen, are partly still ongoing. The pebbles were characterized in the initial state as received from the producer, after a thermal conditioning and after different annealing times.

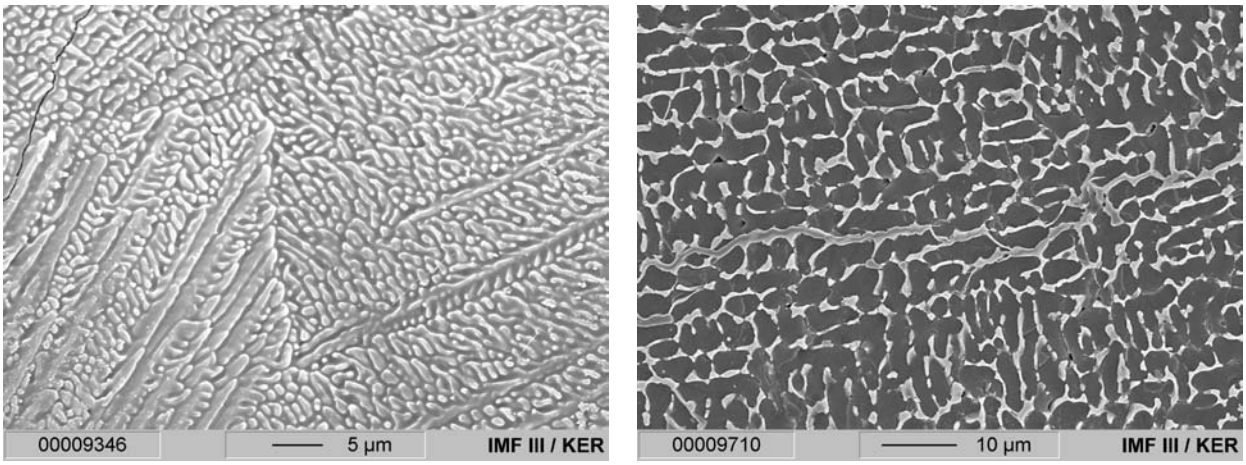

Fig. 2: Li_4SiO_4 pebble as received from the industrial producer (SEM). The dendritic microstructure that is caused by the rapid quenching is revealed at the pebble surface (left) as well as in the cross section (right).

In contrast to the orthosilicate pebble batch fabricated from Li_2CO_3 (OSi 01/3-3) the initial material of the pebble batch fabricated from LiOH (OSi 01/3-4) did not exhibit the typical dendritic microstructure and had a higher specific surface area. After thermal conditioning and during annealing, however, no significant differences could be observed for the two different batches. Microscopic investigations reveal that the initial microstructure of the lithium orthosilicate pebbles is already transformed during the conditioning. The high-temperature phase $Li_6Si_2O_7$ is thereby disintegrated to Li_4SiO_4 and Li_2SiO_3 (Fig. 3). During annealing a coarsening of the microstructure by grain growth was observed (Fig. 4). The initial crush load of about 7 N is reduced to about 5 N during annealing. The decline of the crush load already appears during the conditioning for the OSi 01/3-3 batch, whereas for the OSi 01/3-4 batch the crush load is decreased during the first 3 days of annealing (Fig. 5). During annealing no significant further decline of the crush load was observed.

Table 1: Chemical analysis of the batch OSi 03/1-3

Principal Constituents (wt%)	
Li_2O	48.44
SiO_2	51.12
Impurities (wt%)	
C	0.054 ± 0.002
Al	0.00238 ± 0.00016
Ca	0.00231 ± 0.00014
Co	< 0.0002
Cr	< 0.0001
Cu	< 0.0001
Fe	0.00028 ± 0.00011
K	0.00072 ± 0.00012
Mg	0.00024 ± 0.00007
Mn	< 0.00005
Na	0.00122 ± 0.00031
Ni	< 0.0001
Ti	0.00032 ± 0.00012
Zn	< 0.0002
Zr	< 0.0001

The characterization of the long-term annealing will be finalized in the next months and the results will be given in a more detailed report at the end of 2003.

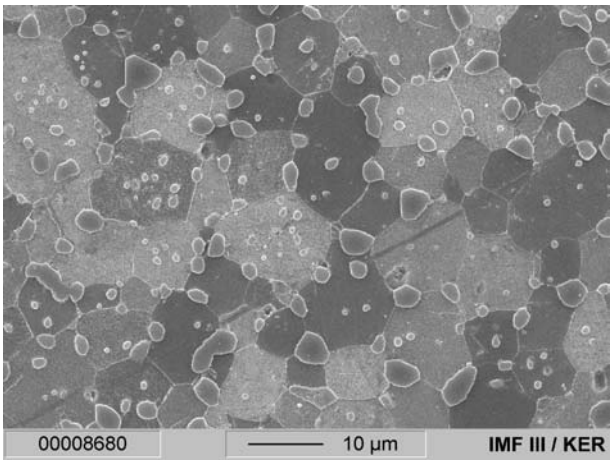

Fig. 3: Cross section of a lithium orthosilicate pebble (OSi 01/ 3-4, ex hydroxide) after a thermal conditioning for 2 weeks at 1000°C under air. Li_2SiO_3 is formed at the grain boundaries.

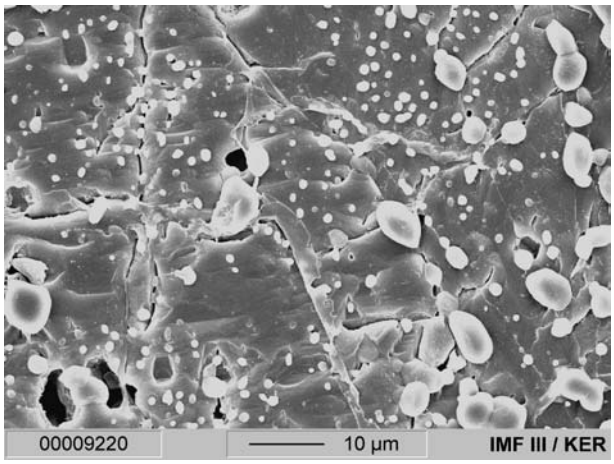

Fig. 4: Grain growth and a coarsening of the microstructure are revealed in the cross section of a lithium orthosilicate pebble (OSi 01/3-4, ex hydroxide) after an annealing time of 96 days.

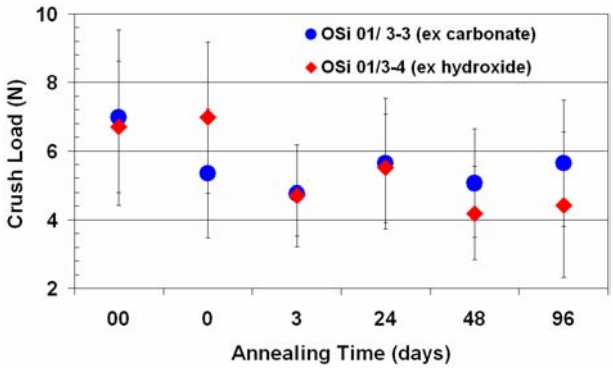

Fig. 5: Crush load versus annealing time for two lithium orthosilicate batches (00: material as received; 0: material thermally conditioned for 2 weeks at 1000°C). Mean values and standard deviation represent measurements of 80 pebbles.

Staff:

C. Adelhelm
R. Bosbach
J. Erbe
R. Knitter
C. Odemer
G. Piazza
P. Risthaus
R. Rolli
O. Romer
B. Wagner

Literature:

[1] Piazza, G.; Reimann, J.; Günther, E.; Knitter, R.; Roux, N.; Lulewicz, J.D.: Characterisation of ceramic breeder materials for the helium cooled pebble bed blanket. J. Nucl. Mater. 307-311 (2002), 811-816.

TW2-TTBB-002b D4
Procurement of Beryllium Pebbles and Quality Control

The main objective of this task is the supply of the HCPB blanket reference beryllium pebbles to be used in experimental activities and their quality control (optical and electron microscopy, helium pycnometry and Hg-porosimetry, micro-hardness tests, mechanical behaviour of single pebbles at high temperatures). As the possibly low tritium release from the beryllium pebbles at operating temperatures in the blanket represents a concern, in parallel to the characterisation and optimisation of the available reference NGK pebbles, also the possibility is being considered to improve the tritium release of the neutron multiplier in the blanket by modifying microstructural characteristics. Specifically, recent parametric calculations with the ANFIBE code have shown that the tritium release properties of the metallic beryllium pebbles can be strongly improved by reducing the grain size under 10 μm, hence the development of beryllium pebbles having smaller grain size is being investigated.

Pebbles from Rotating Electrode Process

In order to qualify further Be-pebbles for the HCPB blanket, a dedicated irradiation programme HIDOBE in the HFR reactor is presently prepared that aims at the accumulation of blanket relevant He concentrations of 3000 and 6000 appm, respectively. Therefore, Be pebbles with different diameters have been procured during the reporting period at NGK insulators Ltd. These reference beryllium pebbles have been produced by rotating electrode process (REP). Three batches with 200 gram each have been procured with pebble diameters of 0.5 mm, 1.0 mm and 2.0 mm.

Fig. 1: Be pebbles with 1mm diameter from NKG produced by REP.

This method consists of arc melting the end of a long cast cylinder, which is rotating about its axis in a chamber filled with helium. Molten droplets of metal are thrown off the end of the rotating cylinder and solidify in flight. The size and quality of the REP beryllium pebbles depends essentially on the material used and on the production process parameters (e.g. electrode impurity content, electrode diameter, electrode angular velocity, cooling velocity, etc.). Usually, this method mostly produces spherical pebbles (diameters approximately in the range 0.2 mm - 2 mm) with a very small surface roughness and a beryllium oxide layer covering the pebbles with thickness estimated to be about 50-150 nm.

The optical microscopy (Figure 2) of the as-fabricated pebbles show an almost fully dense metallographic structure characterized by the presence of large grains. However, a quite large number of pebbles exhibit a big pore (up to 0.1-0.2 mm) at their centre together with a fully dense region near the external surface. This kind of pebble structure is typical for a fabrication process with a rapid cooling in the gas atmosphere. Main features of the coolant process include:

- Rapid condensation of the liquid drop from the outer surface to the center,
- Frequent appearance of a big cavity in the center, and
- Grain boundaries in radial direction and, as a consequence, grain diameters that strongly correlates with the pebble radius.

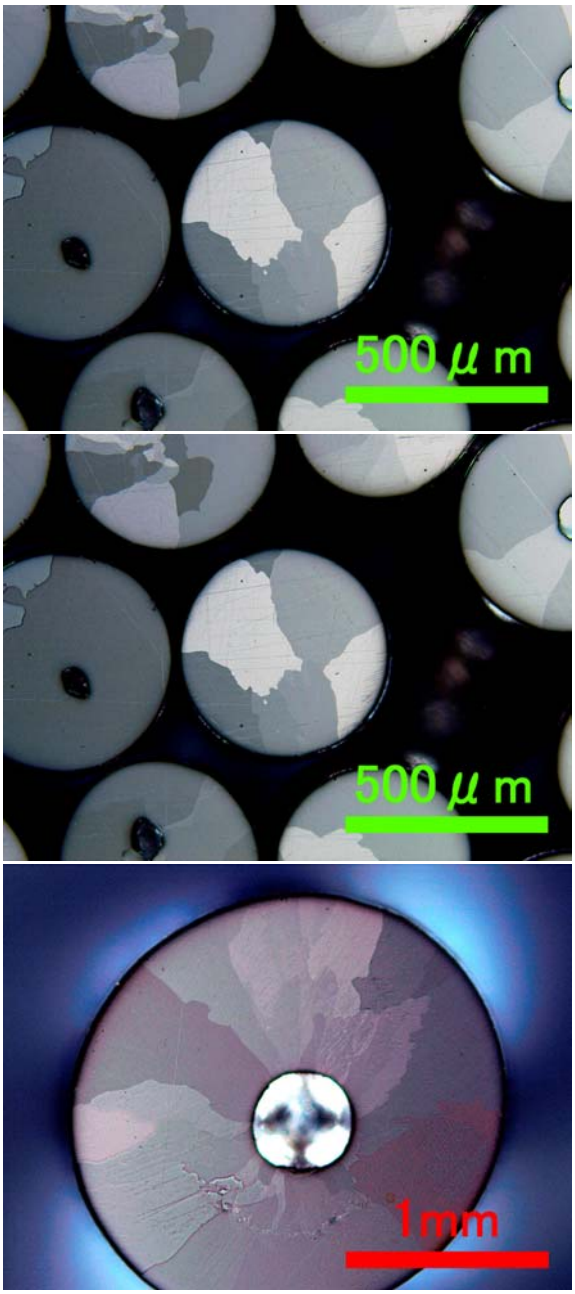

Fig. 2: Pebbles with diameters of 0.5 mm (top), 1.0 mm (middle), and 2mm (bottom).

From the observation that a bisection of pebbles also reduces the grain diameter by a factor of two, it can preliminary concluded, that small pebbles are much more favourable with respect to T-release.

A possibility to decrease the grain size of the pebbles could be by increasing further the cooling rate of the molten beryllium but, according to information from NGK, as the pebbles solidify in a quite short time (~13000 °C/s cooling rate) and the temperature of molten beryllium is relatively low, it seems unrealistic to reduce the grain sizes further from hundreds of µm down to a few µm, only by changing the parameters of the process. An option could be to add certain additives to the beryllium electrodes, which would work as nuclei of grains. In this case, the effects of the additives on the properties of the pebbles, especially during irradiation, should be carefully investigated.

Several other methods of pebble production are presently screened experimentally at FZK. Among them are: (i) pebble produced by sintering of small size beryllium powder (~1µm), and (ii) production of powder by wet chemical processes followed by hot pressing.

A fraction of the NGK pebbles is presently prepared for shipping to Petten for the HIDOBE irradiation. In parallel, further characterisations as mentioned above will be performed.

Staff:

G. Bürkle
P. Kurinskiy
A. Möslang

Literature:

[1] A. Möslang, G. Piazza, L. Boccaccini, A. Cardella, E. Rabablino; “Status of the EU R&D on Berylium as multiplier materials for breeder blankets”; 6th IEA Internat. Workshop on Be technology for Fusion, Miyzaki, Dec 2-5, 2003.

TW2-TTBB-002b D6
Investigation of Beryllium Alloys

A key issue of the helium cooled ceramic breeder blankets is the long term structural integrity and reliability of Beryllium as appropriate neutron multiplier. In order to overcome some of the disadvantages of existing Be pebbles like Tritium release and He embrittlement at blanket operating temperatures, an attempt has been started to systematically investigate relevant properties by producing own beryllium and Be-alloys on laboratory scale and by varying fabrication parameters followed by gas release experiments.

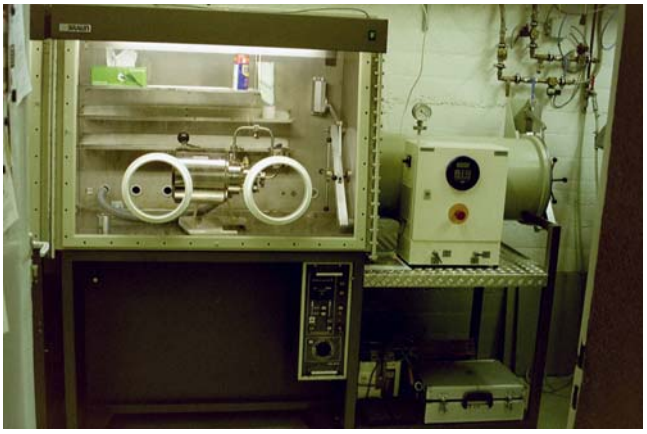

Fig. 1: Ball milling device NETSCH-MINIZETA 03, installed in a sealed glove box.

In the present EU concept, the main strategy for the reduction of the tritium release temperature is either (1) to reduce the grain size of Be pebbles and/or tablets, or (ii) to use a suitable Be-alloy. Since a couple of years JAERI has been investigating Be-Ti, Be-V and Be-Mo intermetallic compounds (beryllides) in view of their use for the Japanese pebble bed blanket concept. Presently, $Be_{12}Ti$ produced by NGK insulators Ltd. seems the most promising beryllide and characterisation work has been being performed in cooperation with several universities in Japan. According the available test results, $Be_{12}Ti$ shows, in comparison with metallic beryllium, faster tritium release, much smaller swelling, smaller reactivity with stainless steel, steam and water, therefore, it is becoming interesting also in view of its use in the EU-HCPB blanket.

Due to a high toxicity of beryllium, R&D works on beryllium and Be alloys has to be performed in a dedicated laboratory which has glove-boxes with controlled inert-gas atmosphere. In the reporting period, the following devices have been assembled and installed in glove boxes within a dedicated beryllium laboratory (Goraieb Versuchstechnik Company) at FZK:

- A ball milling device, NETZSCH MINIZETA 03b, for powder production or mechanical alloying (Figure 1),
- an arc furnace for ingot production of Be-alloys under controlled atmospheres, and
- a 20-ton hydraulic press to produce tablets e.g. from Be-powders (figure 2) at temperatures of several hundred degrees.

All devices have been tested successfully by fabrication of Ti-powders and Ti-tablets. The next steps are (i) Be-powder production and tablet fabrication with different grain sizes by variation of the process parameters, (ii) fabrication of Be-Ti ingots with a high fraction of Be12Ti and related parameter optimization, (iii) broad based characterization including compatibility tests, structural integrity tests and microstructural characterizations.

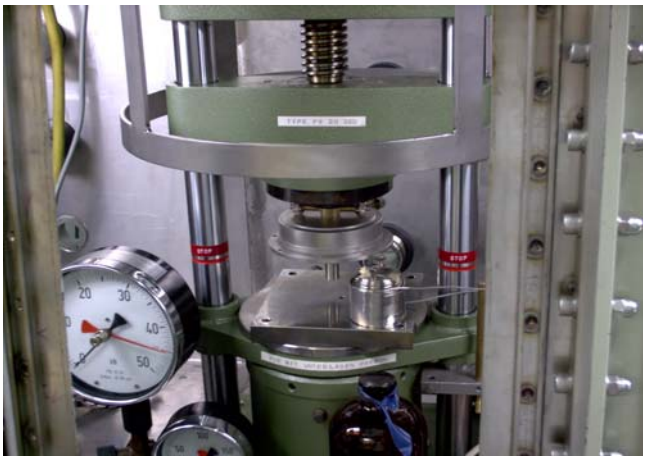

Fig. 2: 20 ton hydraulic press for tablet fabrication in a furnace.

Staff:

G. Bürkle
P. Kurinskiy
A. Möslang

Literature:

[1] A. Möslang, G. Piazza, L. Boccaccini, A. Cardella, E. Rabablino; “Status of the EU R&D on Berylium as multiplier materials for breeder blankets”; 6th IEA Internat. Workshop on Be technology for Fusion, Miyzaki, Dec 2-5, 2003.

TTBB-005a
Helium Cooled: Development of Ceramic Breeder Pebble Beds

TW2-TTBB-005a D7
Thermomechanical Tests of Ceramic Breeder Pebble Beds

Pebble bed experiments were performed in order to characterise the pebble beds in respect to the stress-strain behaviour in different bed geometries, and different temperatures. At high temperatures, the measurement of thermal creep rates is of special importance. During this year, the work concentrated on:

A) Tests with Pebble Bed Assembly (PBA) mock-ups,

B) Further thermal creep experiments with new batches of CEA meta-titanate (MTi) pebbles.

A) PBA Mock-up Pepple Bed Tests

For the investigation of the behaviour of pebble beds under irradiation, experiments [1] are to be performed in the High Flux Reactor in NRG, Petten, Netherlands, with Pebble Bed Assemblies (PBAs) which represent a characteristic section of the HCPB blanket, consisting of two beryllium pebble beds (Bed 1 and 3) with a ceramic breeder pebble bed (Bed 2) in between, compare Fig. 1a which shows a PBA relevant mock-up where 17 cylindrical rods simulate tubes containing thermocouples. In order to obtain equal stresses in all three beds, Bed 2 is enclosed by a “floating” capsule which is not connected with the outer structure. In order to generate an increased thermal conductivity of the beryllium beds, the pebble beds were precompressed uniaxially at NRG prior to irradiation using the top plate as piston. X-ray radiography pictures showed that the measured irreversible deformations were significantly smaller than expected; furthermore, the compression of the lower beryllium bed was distinctively smaller than that of the upper beryllium bed.

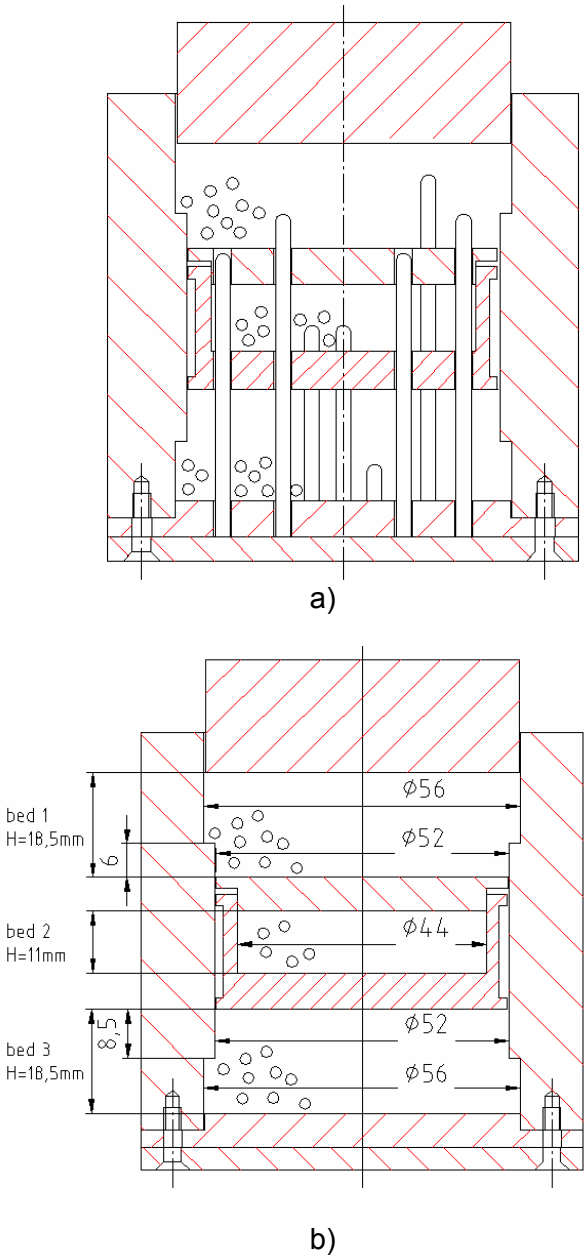

Fig. 1: PBA-mock-ups;
a) with inserts,
b) without inserts.

In order to quantify the influence of the inserts and the cross section changes on the mechanical behaviour of the pebble beds it was decided to carry out appropriate tests in FZK. PBA-mock-ups, Fig.1, were built with the relevant PBA dimensions which allowed tests both with separate individual pebble beds and bed combinations and both without and with internal inserts.

The experiments were performed with either orthosilicate (OSi) pebbles or metatitanate (MTi) pebbles in all beds. The MTi pebbles are closer to the NGK beryllium pebbles in respect to their diameter (about 1mm). The OSi pebbles (diameters between 0.25 and 0.6mm) are more similar to the beryllium pebbles in respect to surface roughness. Previous experiments [2] proved that the mechanical behaviour at ambient temperature does not differ significantly for ceramic and beryllium pebble beds.

The experiments were performed in the uniaxial compression test (UCT) facility already used extensively previously [2,3]. In the following, only some results for MTi pebble beds are presented; similar results were obtained with OSi pebble beds, see [4].

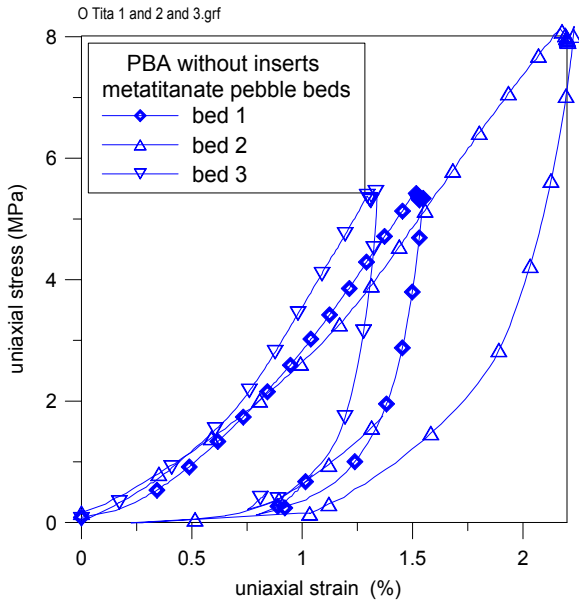

Fig. 2: Stress-strain behaviour of individual MTi pebble beds.

Figure 2 shows results for the individual Beds 1, 2, and 3: Bed 1 and Bed 3 are stiffer (smaller strain for a given stress value) compared to Bed 2 because of the larger influence of wall friction at larger bed heights. Another influence arises from cross section changes in Beds 1 and 3: For Bed 1 one could expect a stiffening effect because the pebbles in the annular zone close to D_1=56mm can not move downwards as easily as the pebbles in the zone with $D_2 \leq 52$mm. Therefore, this outer zone could act like a “stiffening ring”. Correspondingly, the cross section expansion in Bed 2 should then result in a softer bed. The measurements are in agreement with this explanation.

Figure 3 contains results the following pebble bed combinations: Beds 1+3, Beds 2+3, and Beds 1-3 (total cavity filled with pebbles).

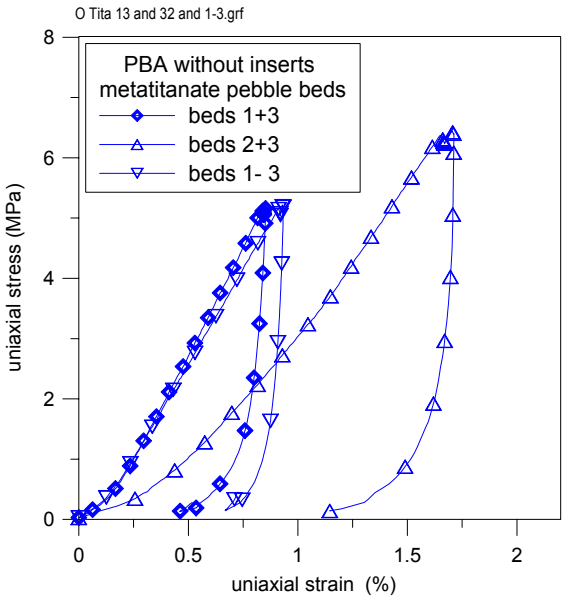

Fig. 3: Stress-strain behaviour of pebble bed combinations.

Due to the increased wall friction effect, the deformation of combined beds is smaller than the sum of the deformations for the corresponding individual beds, compare Fig. 2.

Figure 4 shows measured strains for an uniaxial stress of 4MPa and mock-ups with and without inserts. The data for pebble beds with inserts are generally within the data scatter of the results for the mock-up without inserts which might indicate that the influence of the inserts is negligible. However, the expected increased friction effect might have been compensated by the lower packing factors achieved for these beds.

It can be concluded that the experiments with PBA mock-ups are in agreement with the PBA precompression measurements. The reasons for this are primarily frictional effects at the cylindrical walls and the flow contraction in the upper bed where the outer pebble bed zone might act in a stiffening way. It would be of

significant interest if these effects are adequately described by computational models. The present experiments were not performed with the relevant material combinations (two beryllium pebble beds, one ceramic breeder pebble bed in the middle); therefore, the data cannot be used quantitatively for the analysis of the PBA behaviour. Future irradiation experiments will show if the temperature distribution is significantly affected by the unequal bed precompression. If required, PBA mock-up tests with the correct granular materials composition could be performed in another UCT facility of the FZK.

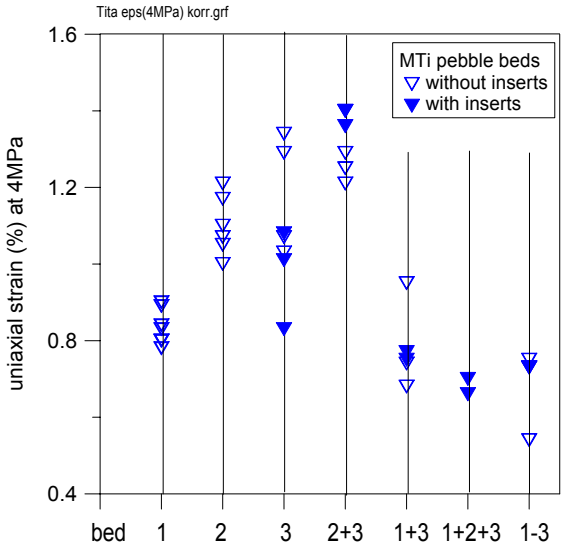

Fig. 4: Strain values at 4 MPa for mock-ups with and without inserts

B) Thermal Creep Tests with CEA Metatitanate Pebble Beds (Ti-M)

Further thermal creep tests with CEA metatitanate pebble beds (charge CTI 942 Ti 1100; FZK designation: Ti-M) were performed in (UCT facility at temperatures of 750 and 800°C. The pebbles are characterised by small pebble sizes (diameter between 0.6 and 0.8mm). Figure 5 shows a summary of measured thermal creep strains at 750°C for a constant pressure of 6.4MPa. It is clearly seen that the Ti-M pebbles belongs to those granular materials characterised by small creep strains. Therefore, creep strain can be described fairly well by the correlation developed previously for this group of materials [2]:

Table 1: Thermal creep correlations (from [2]).

Granular material	$\varepsilon_{cr}(1) = A \exp(-B/T(K)) \sigma(MPa)^p t(s)^n$			
	A	B	p	n
FZK-Li_4SiO_4	12.12	10220	0.65	0.2
CEA-Li_2TiO_3 (lta)	0.67	7576	0.65	0.18
JAERI-Li_2TiO_3	0.37	6947	0.65	0.19

Small creep rates are supposed to be beneficial because stress relaxation processes during the first hours of blanket operation are believed to be sufficiently fast; however, agglomeration of pebbles is less expressed than for MTi pebbles characterised by larger creep rates.

Staff:

J. Reimann
C. Strobl
Fa Goraieb

Literature:

[1] J. G. van der Laan et al, In pile testing of submodules for the HCPB DEMO Blanket concept in the HFR Petten, Proc. of 22th Symp. Fusion Technology, Marseille, Sept.1-11, 1998, 1243-1246.

[2] J. Reimann, L. Boccaccini, M. Enoeda, A. Y. Ying, Thermomechanic of solid breeder and Be pebble bed materials, ISFNT-6, San Diego, USA, April 2002.

[3] J. Reimann, D. Ericher, G. Wörner, Influence of pebble bed dimensions and filling factor on mechanical pebble bed properties, CBBI-10, FZK 6720, June 2002, 161-174.

[4] J. Reimann, C.Strobl, Thermomechanical Tests of Ceramic Breeder Pebble Beds; Annual Report 2002 for TW2-TTBB-005a D7, March 03.

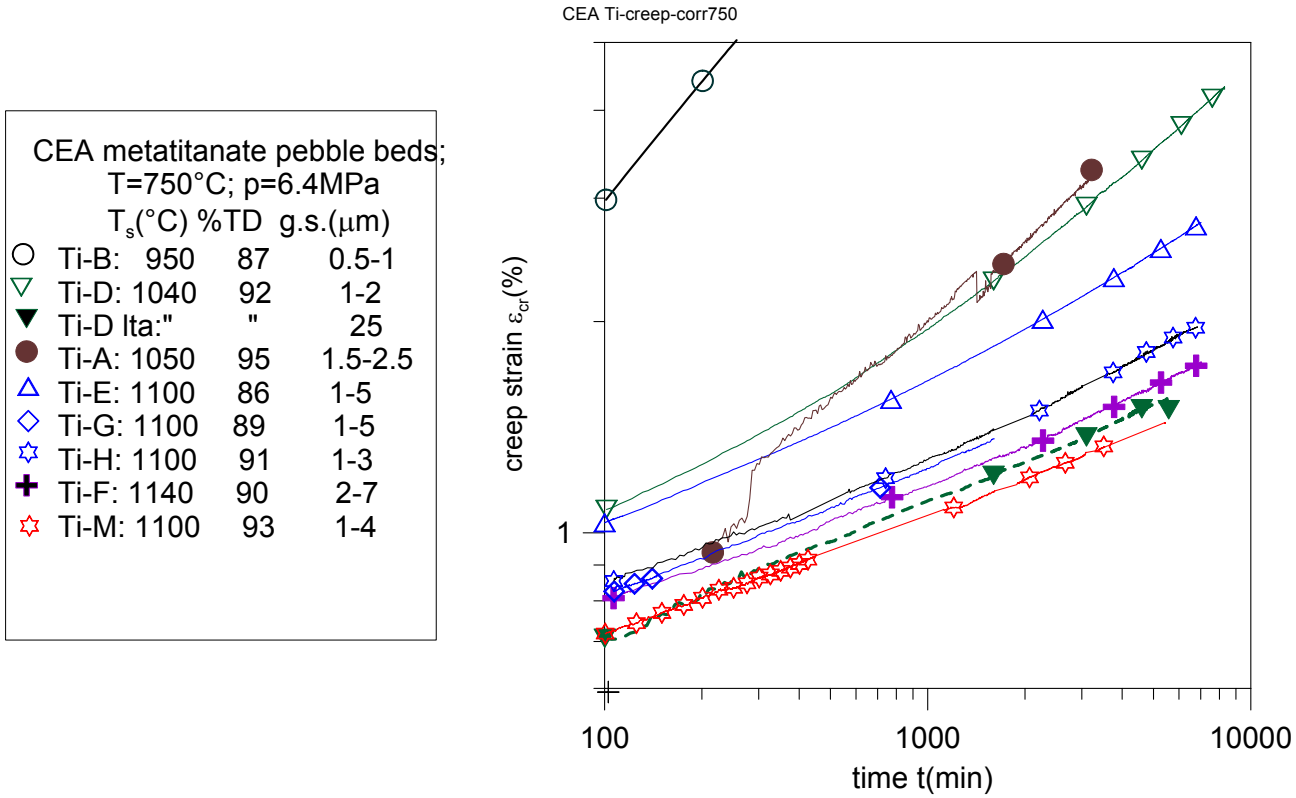

Fig. 5: Thermal creep of metatitanate pebble beds at 750°C and 6.4 MPa.

TW2-TTBB-005a D8
Thermal-mechanical Pebble Bed Modelling of Ceramics

TTBB-007a
Helium Cooled: Development of Beryllium Pebble Bed

TW2-TTBB-007a D5
Thermal-mechanical Pebble Bed Modelling of Beryllium

The thermomechanical interaction of the breeder and beryllium pebble beds with fusion blankets is expected to be critical for blanket design. The key issue is high stress exerted due to the thermal expansion and swelling of pebbles, and stress relaxation through creep.

Based on the experiences from soil mechanics, a modified Drucker-Prager model is used to predict the mechanical behaviour of pebble beds. The goal for this work is to modify and calibrate the model in order to evaluate the temperatures, stresses, deformations and mechanical interactions between pebble beds and blanket material.

The modelling of Beryllium and of the ceramic breeder are based on the same approach.

Starting conditions

The Drucker-Prager Cap model excluding creep combined with a nonlinear elasticity law called porous elasticity, was calibrated with data from uniaxial and biaxial compression tests of pebble beds. The analyses have been performed with the ABAQUS finite element code. The model has been extended to creep by writing a user-defined subroutine (UEXPAN). Uniaxial experiments at 800 °C with isothermal creep were used for the calibration.

Simulations showed that the model is able to predict the following phenomena:

- pebble flow
- bed deformation
- stress and strain distribution of the uniaxial and biaxial experiment without volume heating

Convergent solutions for combinations of creep and volume heating, however, have not been achieved.

Current status of work

The aim of the current work started in April 1st is focused on the modification of the existing approach in order to achieve convergent solutions for combinations of creep and volume heating. Therefore the ABAQUS creep model has been used instead of UEXPAN. It has been verified that the ABAQUS creep model predicts consolidation creep for special combinations of the Drucker-Prager-Cap material parameters.

Unfortunately it is not allowed to combine the ABAQUS creep law with the porous elasticity option.

In order to model the nonlinear elastic behaviour of the pebble bed, several elasticity laws have been implemented in the ABAQUS Finite Element Code using the user defined field option (USDFLD). One approach is given by Di Maio, Oliveri and Vella [1]. Here, the Young's modulus varies as a function of volumetric elastic strains. The adoption of this model induces the necessity of changing the Cap Hardening law.

The results of this approach have been compared with a second elasticity law proposed by Coube [2]. In this approach, the Young's modulus is given as a function of stress invariants.

Conclusions and further work

The work of the upcoming year will be focused on thermo-mechanical modelling of pebble bed behaviour, especially the combination of creep with volume heating, which has caused problems with the current creep model implemented in UEXPAN. Should this approach ultimatively fail, an alternative constitutive model has to be implemented via a user defined material subroutine. Possible models are:

- Model to describe sintering processes (IWM Freiburg) [3]
- Cam Clay model, A. Duchesne, X. Reapsaet [4]

Staff:

Hofer, D.
Kamlah, M.

Literature:

[1] P. A. Di Maio, E. Oliveri, G. Vella, Fusion pebble bed thermomechanical modelling, Parts A-C, Internal reports, Nuclear engineering department, University of Palermo, 2002.

[2] O. Coube, Modelling and numerical simulation of powder die compaction with consideration of cracking, Phd thesis, University Pierre et Marie Curie, Paris IV.

[3] O. Coube, H. Riedel, Numerical simulation of metal powder die compaction with special consideration of cracking, Powder Metallurgy Vol. 43, 2000, pp. 123-131.

[4] A. Duchesne, X. Raepsaet, un modèle élasto-plastique de CASTEM 2000 utilisable pour la modélisation mécanique d'un lit de particules, Rapport DMT 97/237, SERMA/LCA/2054, CEA, France.

TW2-TTBB-007a D4
Thermal-mechanical Pebble Bed Tests of Beryllium

In the helium cooled pebble bed (HCPB) blanket [1] the neutron multiplier and the breeder material are arranged in pebble beds between flat cooling plates. The maximum temperatures in the breeder and beryllium pebble beds are about 900 °C and 650 °C respectively. Temperature differences and different thermal expansion coefficients between pebble beds and structural materials and irradiation effects will result in elastic and plastic pebble deformations which influence the effective thermal conductivity of the beds.

The modelling of the thermal mechanical behaviour the HCPB blanket requires as important input data the thermal conductivity of beryllium pebble beds. First results for strongly deformed beryllium pebble beds with an independent variation of temperature and deformation and maximum temperatures of 480°C were presented in [2,3] using the Hot Wire method. This method is a standard technique for low conductivity materials but the accuracy for materials like beryllium is somewhat questionable. An important result obtained by these measurements was the linear relationship between conductivity and bed strain for the first pressure increase and a small conductivity decrease during depressurisation.

In order to obtain more accurate measurements for temperatures up to 600°C, the test facility HECOP (**HE**at **CO**nductivity in **P**ebble beds) was built. Another important goal was to obtain data on thermal creep of beryllium pebble beds which did not exist at all. In first experiments [4] up to temperatures of 350°C, again, a fairly linear relationship between conductivity and bed strain was observed, however, the measured conductivity values were about 25% higher. Unfortunately, an important component failed. Because

- repair operations in the glove box are complicated,
- several thermocouples were already quite brittle, and
- the displacement measurement system did not operate satisfactorily,

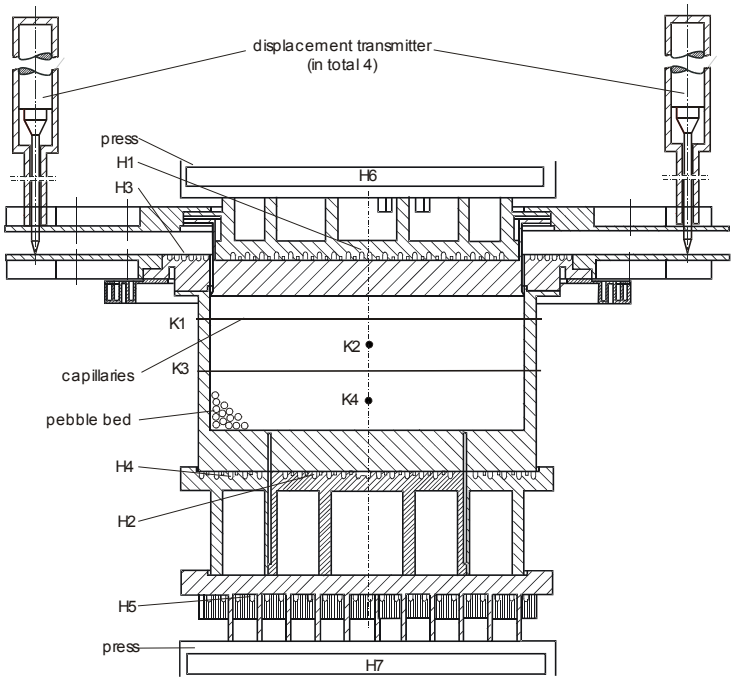

Fig.1: HECOP II test section.

it was decided to redesign completely the facility and to build HECOP II. However, the characteristic features of the old version (HECOP I) in respect thermal control were retained.

Figure 1 shows schematically HECOP II. The test section is positioned between the pistons of a hydraulic press (maximum load: 50 kN). For thermal control, a system of 7 heaters (H1...H7) is used. H1 and H2 generate the temperature gradient in the bed. H3, H4 are used to minimise the radial heat losses by controlling the power of the annular guard heaters H3 and H4 such that the temperature difference between two neighbouring thermocouples becomes zero.

The heat flux Q_2 [W/m^2] produced by H2 is used to calculate the thermal bed conductivity k given by

$$k(W/(mK)) = Q_2 \Delta x / \Delta T \qquad [1],$$

with Δx (m) the axial distance of thermocouples in the bed and ΔT(K) the corresponding temperature difference.

In order to minimise the axial heat flow from H2 to the press bottom plate, the heater H5 is controlled such that the temperature difference of a thermocouple below the heater H2 and above the heater H5 becomes zero. For experiments at the highest temperatures , the heaters H6 and H7 which are part of the press are additionally used.

In order to thermally insulate HECOP II from the helium environment in the glove box, refractory ceramic fibre (Kerlane) was used (not indicated in the figure).

Compared to HECOP I, the main modifications are:

1. pebble bed container with a larger diameter and a larger height with 4 capillaries at different bed heights, each containing 5 thermocouples at different radial directions,

2. larger number of thermocouples (in total 60) in order to measure in more detail the temperature distribution in the total system,

3. larger heating powers of heaters H2, H4, H5 in order to reach maximum temperatures of about 650°C. This is an important improvement for thermal creep measurements,

4. measurement of the bed displacement by measuring the displacement between piston and pebble bed container using two rings which are fixed on the piston and container, respectively. (In HECOP I, the displacements were measured between the two press cooling plates. Therefore, the deformation of the total system in between was measured and not the bed deformation alone).

A detailed modelling was performed using the FLUENT code in order to understand the thermal behaviour of HECOP II. Figures 2 and 3 show the mesh structure in a quarter of HECOP II and the calculated radial temperature profiles for the case where the temperature in the H1-H3 plane was assumed to be constant and equal to that of the H2-H4 plane (isothermal case). It is seen that temperatures in the bed decrease because of heat losses in the cylindrical part to the helium atmosphere. By increasing the temperatures in the heaters H3 and H4 it can be reached that the temperatures in the bed become constant and heat losses are not powered by H2.

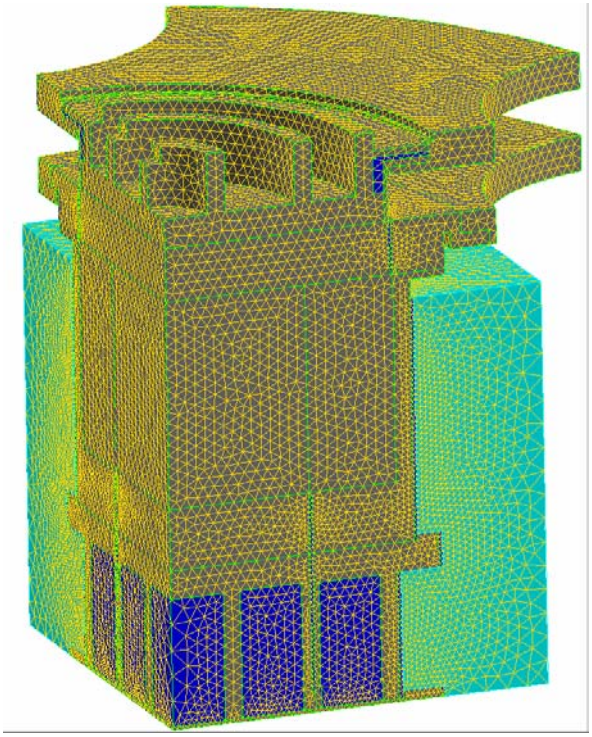

Fig. 2: Meshing of one quarter of HECOP II

Before the transfer of the system into the glove box, the new displacement system was tested in air atmosphere using a similar press as installed in the glove box. Uniaxial Compression Tests (UCTs) with orthosilicate pebbles were performed because the behaviour of this granular material is well

known from other tests, compare e.g. [3]. The measured uniaxial stress-strain dependence, Fig. 4, agrees well with previous results confirming the anticipated accuracy of the new system. Further tests were performed in order to calibrate the thermocouples in an oven before fixing them mechanically on the corresponding components. Then, tests had been carried out in order to prove that the heaters and the corresponding temperature control systems work as anticipated.

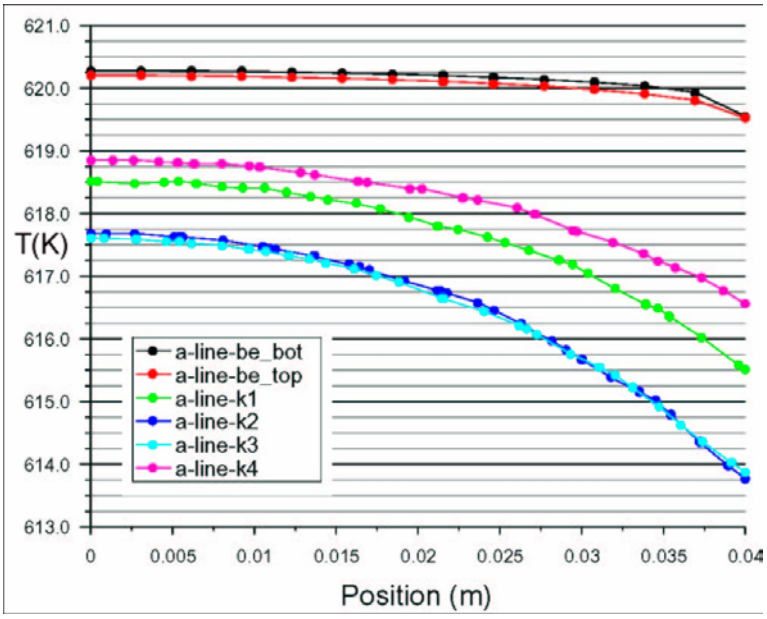

In the glove box, measurements were repeated in the temperature range already covered by HECOP I. The new data agree well with the HECOP I results, confirming that previous Hot Wire results were too low.

Figure 5 shows first thermal creep data for beryllium pebble beds performed at temperatures above 500°C. Concerning the time dependence, an exponent of n ≈ 0.4 is found compared to n ≈ 0.2 for orthosilicate.

Fig. 3: Calculated radial temperature profiles.

Staff:

G. Piazza
J. Reimann
Z. Xu
Fa Goraieb

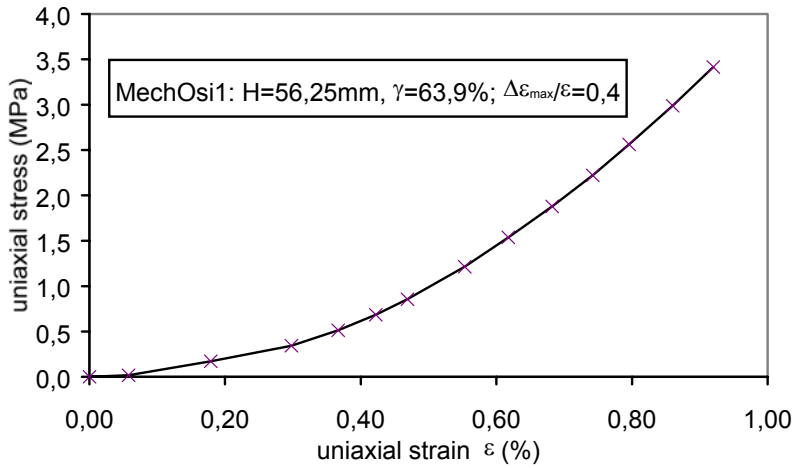

Fig. 4: HECOP II tests with orthosilicate pebble beds.

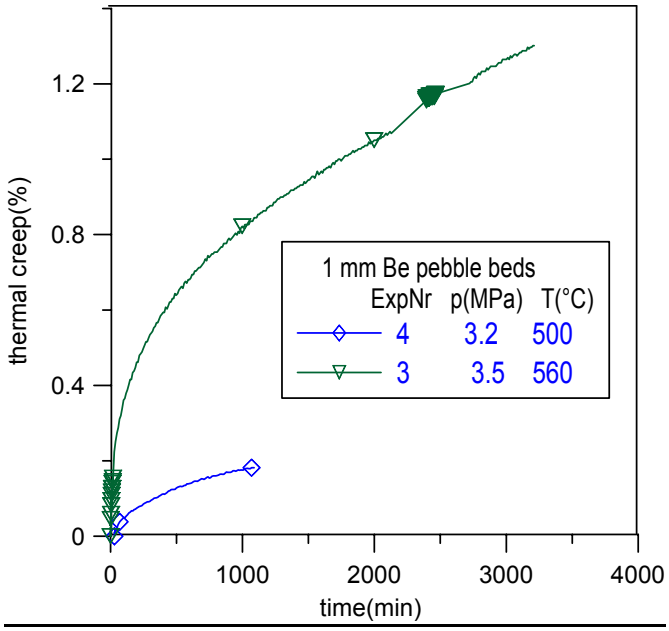

Fig. 5: Thermal creep at 500 and 560°C.

Literature:

[1] S. Hermsmeyer, J.Fiek, U. Fischer, C.Köhly, S.Malang, J.Rey, Z.Xu, Revison of the EU helium cooled pebble bed blanket for DEMO, SOFE, San Diego, USA, Oct. 2003.

[2] J. Reimann, S. Hermsmeyer, G. Piazza, G. Wörner, Thermal conductivity measurements of deformed beryllium pebble beds by hot wire method, proceedings of the CBBI-9, Sept 27-29, Toki, Japan.

[3] J. Reimann, L. Boccaccini, M. Enoeda, A. Ying, Thermomechanics of solid breeder and Be pebble bed materials, proceedings of the 6th Int. Symp. Fusion Nucl. Techn., San Diego, USA, April 7-12, 2002.

[4] G. Piazza,_J. Reimann, G. Hofmann, S. Malang, A.A. Goraieb, H. Harsch, Heat Transfer in Compressed Beryllium Pebble Beds, 22nd Symposium on Fusion Technology, Sept. 9-13, 2002 Helsinki, Finland: Paper J 2.

TTBB-005b
Helium Cooled: Modelling of Swelling and Tritium Release in Beryllium under Irradiation

TW2-TTBB-005b D1
Modelling of the Behaviour of Irradiated Beryllium (Swelling and Tritium Release)

1. Aim and general overview of the activities

In the beryllium pebbles of the Helium Cooled Pebble Bed (HCPB) blanket, large quantities of helium and a non-negligible amount of tritium are produced under fast neutron irradiation. The code ANFIBE (ANalysis of Fusion Irradiated BEryllium) is being developed in order to predict swelling due to helium bubbles and tritium inventory in the range of operating and accidental conditions of a fusion power reactor. Due to the absence of data in this range, ANFIBE has to be extrapolated. Consequently, in comparison to codes which predict gas retention in UO_2, the development of a more sophisticated solid state physics model for the description of gas kinetics and a more careful and detailed validation procedure are required. The programme for the improvement of ANFIBE runs under the European Fusion Development Agreement on a period of five years (2000 – 2004) and is carried out in collaboration with the JRC - ITU (Karlsruhe, Germany), the NRG (Petten, the Netherlands), the SCK-CEN (Mol, Belgium) and the ESRF (Grenoble, France), as far as a part of the experimental studies are concerned. The theoretical evaluation of experimental data and related development of ANFIBE, as well as the definition of open key issues to be solved with further experimental studies, is under the responsibility of FZK. The contribution of FZK to the experimental activities is focused on the following points: (1) study of gas diffusion and release during out-of-pile temperature transients up to the melting point; (2) study of the microstructure of irradiated beryllium in connection with different gas release stages. The final aim of these studies is to improve the gas kinetics model in ANFIBE and to validate it also from the microscopic point of view, i.e. to verify if the different gas diffusion phases (atomic diffusion, precipitation into bubbles, bubble diffusion and growth, gas release pathways) are correctly described.

The R&D activities aimed at improving the ANFIBE code run under EFDA contract TW2-TTBB-007a-2 in 2002 (deliverable 2 of task TW2-TTBB-007a, “Development of beryllium pebble beds”) and continue in 2003 and 2004 under EFDA contract TW2-TTBB-005b-1 (deliverable 1 of task TW2-TTBB-005b, “Modelling of swelling and tritium release in beryllium under irradiation”).

2. Progress in the period October 2002 – September 2003

In 2002, on the basis of extensive experimental and theoretical studies started in 2000 of out-of-pile helium and tritium release and microstructure evolution [1, 2] in weakly irradiated beryllium pebbles from the BERYLLIUM irradiation experiment (480 appm ^{4}He [3]), it was possible to improve the modelling of gas atomic diffusion and gas precipitation inside the grains [4]. Such microscopic phenomena affect macroscopic gas release significantly. Since pebbles from the BERYLLUM experiment share with the reference material to be used in the HCPB blanket (1 mm pebbles, produced by Rotating Electrode Process [5]) a coarse grain microstructure and the grain size is a fundamental material property in regard to gas release, the improvement of the models obtained with the study of pebbles from the BERYLLIUM experiment can be extrapolated with confidence to the HCPB blanket. In particular, helium and tritium atomic diffusion coefficients were assessed and a gas precipitation hindering phenomenon (i.e. a bias from the classical random capture theory of gas atoms by bubbles), similar to that occurring in irradiated UO_2 for fission gases [6], was identified and quantitatively assessed for helium in irradiated beryllium. In 2003 the gas diffusion and

precipitation model was further improved, especially for tritium and also in relationship with in-pile phenomena, with the aim to implement the results into the ANFIBE code. In particular the following milestones were achieved:

- quantitative assessment of ***precipitation hindering for tritium*** on the basis of a re-assessment of out-of-pile tritium release curves;

- improvement of the ***model for helium and tritium precipitation into bubbles*** in the ANFIBE code (two independent models), in-pile and out-of-pile;

- first application of a methodology for the ***integrated microscopic/macroscopic validation*** procedure for the ANFIBE code, defined in 2000

In 2001 also a study on gas percolation was started in the pebbles from the BERYLLIUM irradiation experiment, with the aim to identify 3D interconnected porosities which are formed in correspondence to gas release peaks. The experimental characterisation is carried out by absorption microtomography based on the use of monochromatic and parallel synchrotron radiation at the European Synchrotron Radiation Facility (ESRF) in Grenoble, France. In 2003 the second microtomography experiment was carried out at ESRF and, after a dedicated software development, the first prototypical 3D rendering of percolation structures was made possible.

As a general comment on the above listed achievements, it has to be pointed out that in the field of the modelling and experimental characterisation of the behaviour of gas-in-solid in view to the prediction of release of irradiation-induced gases from a solid matrix, which is a typical problem of fuels for nuclear fission reactors, the results obtained in the frame of the studies on irradiated beryllium for the ANFIBE code enabled to reach a worldwide leadership position in the experimental techniques, in the theoretical development and in the global methodology of model validation.

3. Assessment of precipitation hindering for tritium

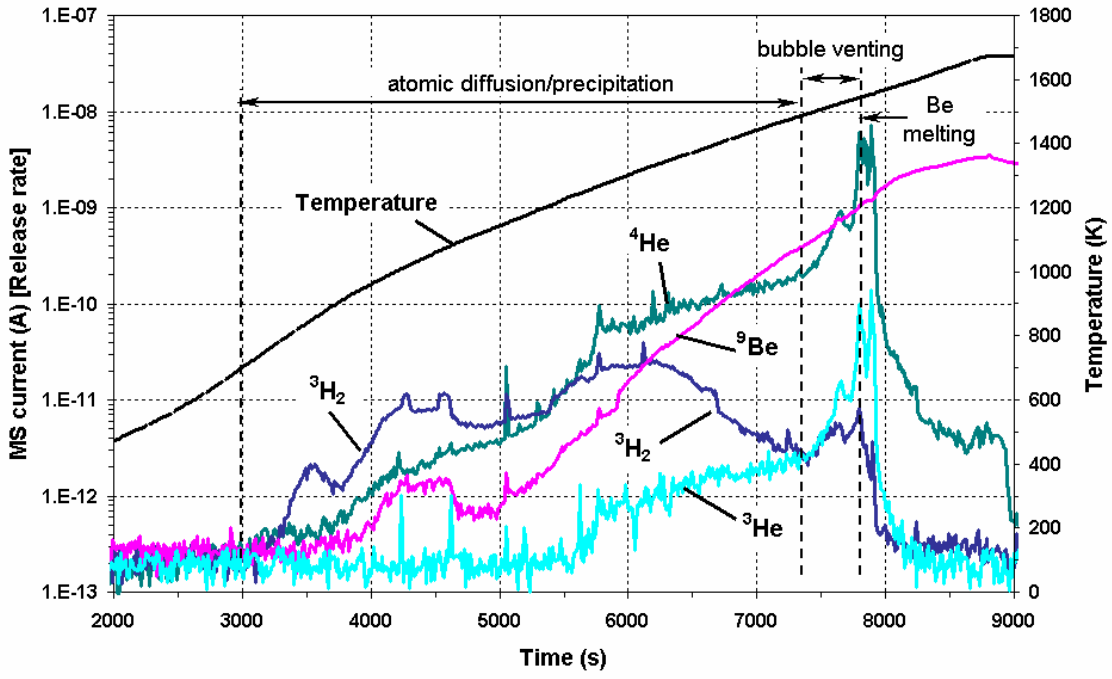

Fig. 1: Helium and tritium release during out-of-pile thermal ramp annealing at about 10 K/min in a vacuum from samples from the BERYLLIUM irradiation experiment (pebbles 2 mm diameter, 40-200 micron grains, 780 K irradiation temperature, 480 appm ^{4}He) [1].

The methodology to quantify gas precipitation hindering has been already described in detail [4, 5]. It is essentially based on an inverse analysis of out-of-pile gas release during thermal ramp annealing, in a range where gas release is due to migration of atoms, initially present in non-equilibrium solution in the lattice, to external grain boundaries (Fig. 1). The model takes into account gas precipitation into intragranular bubbles in competition with gas migration to grain boundaries. Precipitation hindering is described by multiplying the ideal precipitation rate by a *precipitation hindering factor* χ, which is the ratio between the actual reduced capture cross section of bubbles (obtained from the inverse analysis) and the ideal one (which depends on bubble radius and concentration, obtained by Transmission Electron Microscopy studies). The precipitation hindering factor is a function of the concentration of gas atoms in solution, of the atomic diffusion coefficient and of the gas solubility [6,7], therefore *for the same bubble population it is different for different gases*. In particular the applied methodology enabled to assess the following average values of the precipitation hindering factor during the thermal ramp annealing (database of 7 experiments for ^{4}He and 9 experiments for ^{3}H) [5]:

$$\chi = 1.0 \cdot 10^{-3} \qquad \textbf{for 4He}$$

$$\chi = 1.5 \cdot 10^{-6} \qquad \textbf{for 3H}$$

Such values suggest that precipitation hindering is for both ^{4}He and ^{3}H in beryllium relevant, but for ^{3}H the effect is much stronger then for ^{4}He. If helium precipitation into intragranular bubbles is much lower than the classical theory predicts, for tritium it practically does not occur: even in the presence of a bubble population, most tritium atoms are not trapped. This study showed that: (1) tritium atoms precipitate only in a very limited amount into intragranular bubbles and migrate much more easily to grain boundaries as helium atoms; (2) as a consequence, intragranular bubbles are much poorer in tritium than grain boundary bubbles; (3) as a consequence, tritium is practically completely released as interconnected porosities at grain boundary reach the outer surface, while helium remains trapped in bubbles inside the grain.

Such fundamental conclusions are confirmed by all studies of out-of-pile ^{4}He and ^{3}H release performed in FZK from 2000 on, both with weakly irradiated beryllium pebbles of different types (some hundred appm ^{4}He, coarse grains) and with highly irradiated beryllium fragments irradiated at low temperature (about 20000 appm ^{4}He, fine grains) [7].

4. Improvement of in-pile and out-of-pile helium and tritium kinetics model in ANFIBE

After the identification and quantitative assessment of helium and tritium precipitation hindering in beryllium and on the basis of the characterisation of pebbles from the BERYLLIUM experiment (gas release during out-of-pile thermal ramp annealing and related microstructure evolution), the models for helium and tritium kinetics in ANFIBE have been revised, both in-pile and out-of-pile. In the 1995 version of the code ANFIBE 0 [8,9], which was not validated from the microscopic point of view, gas precipitation was dramatically overestimated both in-pile and out-of-pile. In general, ANFIBE 0 predicts for the BERYLLIUM experiment a practically complete gas precipitation in the early stage of the irradiation history, therefore at EOI the whole of the gas inventory is trapped in intragranular bubbles and gas release during the reference out-of-pile thermal ramp annealing is very limited, and it is due not to migration of free gas atoms to grain boundaries but of bubbles. The overestimation of gas precipitation leads to an incorrect assessment of gas balance (gas in solution, gas in intragranular bubbles, gas released). In order to describe gas precipitation hindering, the assumption of a constant precipitation hindering factor, equal to the measured average values during the out-of-pile thermal ramp annealing studies, was made. The two separate analytical models for helium and tritium kinetics in ANFIBE were adapted to this modification. In particular, the output system of ANFIBE was developed in order to enable

the microscopic validation of the tritium model. In addition, in-pile bubble resolution due to fast neutrons was introduced. Such developments enabled a coherent description of tritium behaviour in-pile and out-of-pile with the same analytical model and made it possible to abandon the empirical model implemented in ANFIBE 0 for the out-of-pile case.

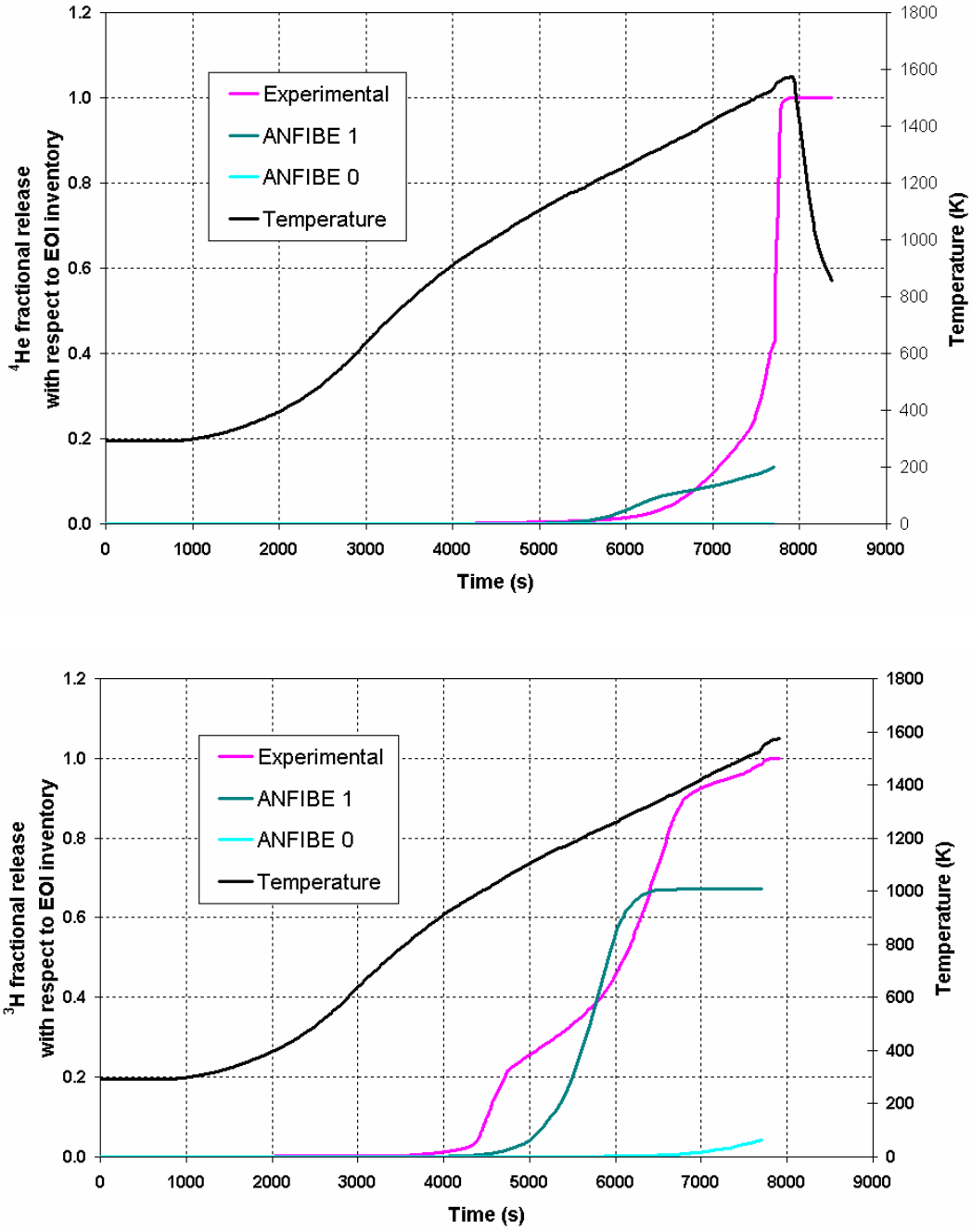

Fig. 2: Comparison of gas release predictions by ANFIBE 0 and ANFIBE 1 during a similar out-of-pile thermal ramp annealing as the one in Fig.1 with the experimental curve. (a) ^{4}He release. (b) ^{3}H release.

Fig. 2 shows a comparison of the prediction of helium and tritium release by the ANFIBE code with the experimental curves during a similar out-of-pile thermal ramp annealing as the one in Fig.1. In Fig. 3 the corresponding theoretical prediction of gas precipitated into intragranular bubbles is shown (the output system of ANFIBE 0 does not include tritium balance quantities, therefore it is not possible to show the prediction of tritium in intragranular bubbles). While ANFIBE 0 predicts that practically 100% of the gas inventory is trapped in intragranular bubbles already at the beginning of the transient, ANFIBE 1 describes correctly the fact that most of gas precipitation occurs during the thermal ramp annealing and,

correspondingly, gas release is significant in spite of the coarse grains, especially for tritium. Nevertheless, also in ANFIBE 1, gas precipitation remains overestimated and the bubble venting stage above 1500 K is not described: these issues will be the object of future developments.

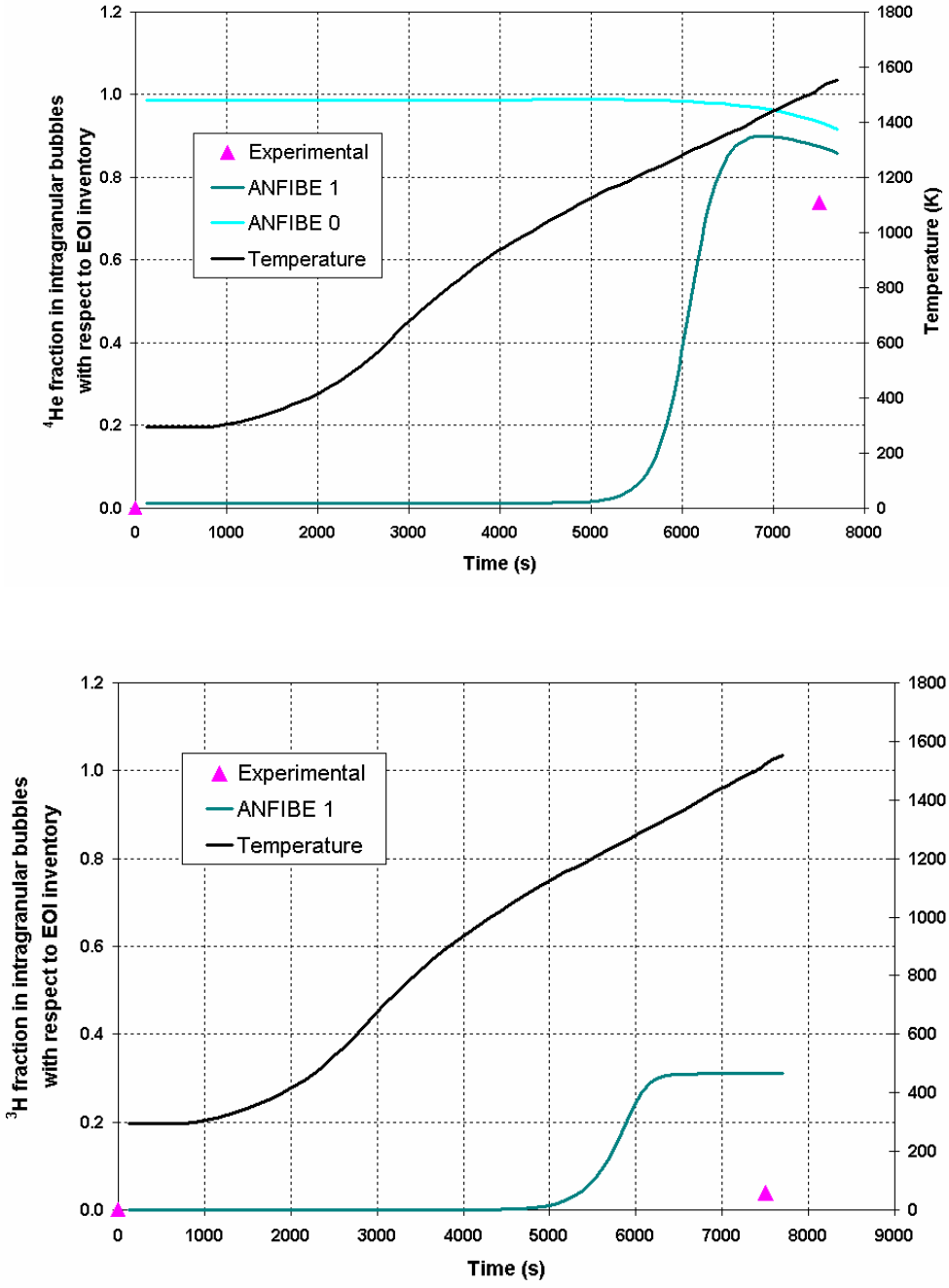

Fig. 3: Prediction of helium and tritium precipitation into intragranular bubbles by ANFIBE 1 and of helium precipitation by ANFIBE 0 during a similar out-of-pile thermal ramp annealing as the one in Fig.1 and comparison with the experimental data. (a) ^{4}He release. (b) ^{3}H release.

The employed validation method, in which a macroscopic phenomenon (gas release) is related to microscopic effects (gas precipitation) is the first example of application of the integrated microscopic/macroscopic validation procedure which was defined for ANFIBE in 2000 in view to enable its extrapolation to End-Of-Life conditions of beryllium in a Fusion Power Reactor, where no experimental data are available. It has been demonstrated that such procedure is extremely effective in identifying key parameters of the models.

5. Characterisation by microtomography of the gas percolation stage.

The gas trapped in bubbles is released only when, at high irradiation dose and/or high temperature, large lenticular bubbles at grain boundaries form open porosity networks. A correct understanding and modelling of the gas percolation stage is extremely important since this phenomenon is responsible of the release of most part of the gas inventory .

In weakly irradiated pebbles from the BERYLLIUM experiment, during a 10 K/min out-of-pile thermal ramp annealing gas percolation starts at 1500 K (Fig. 1). The characterisation by microtomography of the microstructure of the pebbles in such conditions in order to identify 3D percolation structures started in 2001 [9] at the European Synchrotron Radiation facility and was continued in 2003 with an improved experimental set-up. A dedicated software development was carried out in collaboration with ESRF, in order to improve phase segmentation, with the final aim to enable the reconstruction and 3D rendering of porosities, as well as their quantitative analysis, which is at the basis of the validation of the percolation theory.

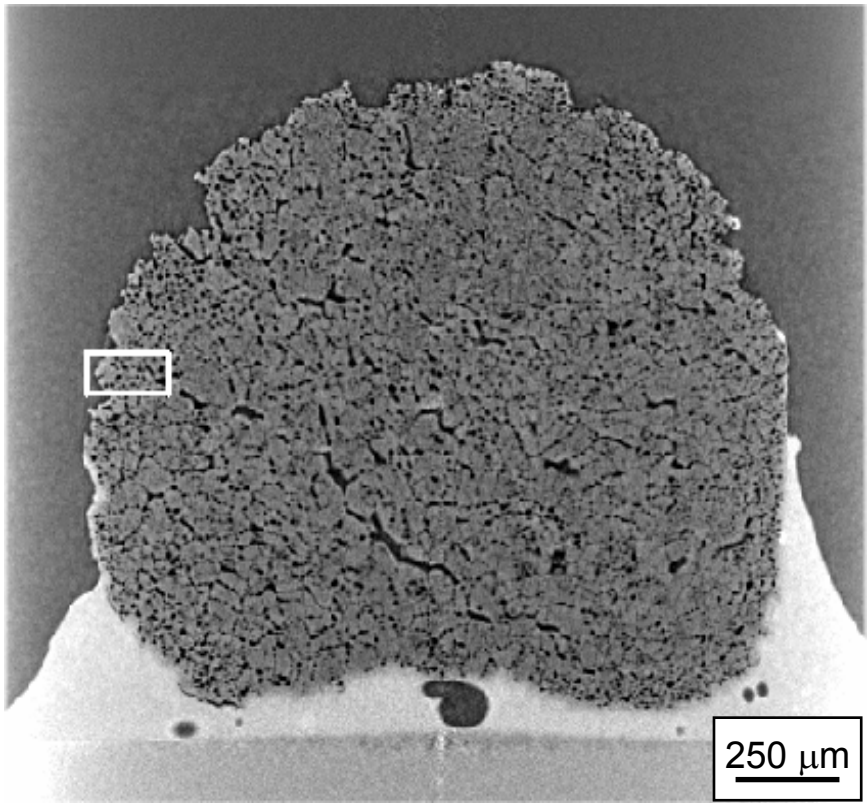

Fig. 4 : Synchrotron radiation microtomography of a beryllium pebble from the BERYLLIUM irradiation experiment, heated at 10 K/min to 1500 K. Cross section at the maximum diameter. A Region Of Interest (ROI) for the extraction of a volume is marked in white.

Fig. 4 shows a central cross section of an irradiated beryllium pebble from a microtomography experiment with 4.9 μm resolution, and Fig. 5 a prototypical 3D reconstruction of porosities in a volume extracted from the sample. The first results of the quantitative analysis suggest that practically the whole of the porosity above the detection limit is open, in agreement with expectations on the basis of gas release experiments [10].

Conclusions and future work

The studies performed in 2003 have allowed remarkable progress in the modelling of helium and tritium diffusion, precipitation and release stages in irradiated beryllium. At the end of 2003 or early 2004 the version 1 of the ANFIBE code will be released, which contains the whole of the R&D performed in FZK since 2000, and in particular, it is validated from the microscopic point of view. In parallel, the experimental characterisation of highly irradiated beryllium from BR2 reactor, started in 2001, will be completed with TEM analyses in order to extend the available database for the microscopic/macroscopic characterisation of ANFIBE with a material very different from pebbles. The quantitative study of the gas percolation stage in the pebbles from the BERYLLIUM experiment will be continued, in order to allow the development and validation of the gas percolation model in ANFIBE. Also the development of an analytical model for a better description of precipitation hindering is foreseen.

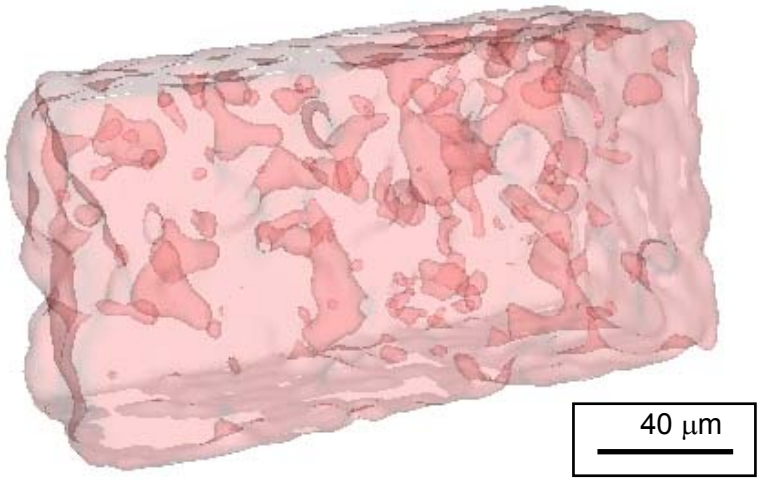

Fig. 5: Prototypical 3D rendering in transparency of porosities in the ROI marked in Fig. 4, extracted from the volume of the pebble. The porosities are the result of growth and coalescence of helium bubbles.

Staff:

E. Rabaglino
C. Ronchi (JRC-ITU)
T. Schulenberg
C. Ferrero (ESRF)
R. A. Pieritz (CNRS)
G. Janeschitz
R. Rolli
M. Holzer

Literature:

[1] E. Rabaglino, J.-P. Hiernaut, C. Ronchi, F. Scaffidi-Argentina, Helium and tritium kinetics in irradiated beryllium pebbles, J. Nucl. Mater. 307(2002) 1424-1429

[2] E. Rabaglino, C. Ferrero, J. Reimann, C. Ronchi, T. Schulenberg, Study of the microstructure of neutron irradiated beryllium for the validation of the ANFIBE code, Fus. Eng. Des. 61-62 (2002) 769-773

[3] R. Conrad, R. May, BERYLLIUM Final irradiation report, EC-JRC-IAM Report P/F1/96/15 (1996), Petten

[4] E. Rabaglino, C. Ronchi, A. Cardella, Recent progress in the modelling of the behaviour of helium and tritium in irradiated beryllium pebbles, Fus. Eng. Des. 69 (2003) 455-461

[5] G. Piazza, in W. Bahm (ed.), Nuclear Fusion Programme Annual Report of the Association Forschungszentrum Karlsruhe / EURATOM, October 2000- September 2001, Report FZKA 6650/EUR 20162 EN, Forschungszentrum Karlsruhe, 2002

[6] C. Ronchi, On the diffusion and precipitation of gas-in-solid, J. Nucl. Mat. 148 (1987) 316-323

[7] E. Rabaglino, Helium and tritium in neutron-irradiated beryllium, Report FZKA 6939, Forschungszentrum Karlsruhe, 2004, to be published

[8] F. Scaffidi-Argentina, M. Dalle Donne, C. Ronchi, C. Ferrero, ANFIBE: a comprehensive model for swelling and tritium release from neutron irradiated beryllium - I: theory and model capabilities, Fus. Tech. 32 (1997) 179-195

[9] F. Scaffidi-Argentina, M. Dalle Donne, C. Ronchi, C. Ferrero, ANFIBE: a comprehensive model for swelling and tritium release from neutron irradiated beryllium - II: comparison of model predictions with experimental results, Fus. Tech. 33 (1998) 146-163

[10] E. Rabaglino, J. Baruchel, E. Boller, E. Elmoutaouakkil, C. Ferrero, C. Ronchi, T. Wiss, Study by microtomography of 3D porosity networks in irradiated beryllium, Nucl. Instrum. Meth. B 200 (2003) 352-357

[11] E. Rabaglino, C. Ronchi, C. Ferrero, G. Janeschitz, R. A. Pieritz, Gas percolation in irradiated beryllium pebbles, 6th IEA International Workshop on Beryllium Technology for Fusion, Miyazaki, Japan, 3 – 5th December 2003

TW2-TTBB-005b D3
TW2-TTBB-007a D12
Tritium Release Enhancement from Beryllium

The tritium accumulation in currently used beryllium pebble materials of ceramic breeder blankets might reach unacceptably high values at the end of blanket life and, therefore, is a critical issue. There are several attempts to develop beryllium-based materials with properties which result in an enhanced tritium release during blanket operation. In the frame of the present subtask, methods are also studied where the tritium release can be enhanced by using other purge gas conditions than presently anticipated (helium at 0.1MPa with 0.1% protium), for details, see [1].

The principal idea is to load the beryllium pebbles with sufficient protium in order to saturate any hydrogen traps with protium instead of tritium and, therefore, to increase the probability that tritium diffuses to the outer surface of the pebbles. Such traps are essentially chemical traps, vacancy/vacancy cluster defect sites, and helium bubbles in which tritium is trapped as gas, compare e.g. [2].

The problem of the investigated method is that the hydrogen solubility in beryllium is very low. Accurate measurements are extremely difficult because hydrogen is readily trapped at BeO surface layers.

The loading of beryllium with protium could be envisaged in the following ways:

1. Continuous loading during blanket operation.

2. Intermittent loading between blanket operation.

To 1): Using a purge flow with a high protium pressure: The question is which maximum value is acceptable for safe blanket operation. Operating the blanket with a purge flow of pure protium at 0.1MPa might be considered as an upper limit.

To 2): Between blanket operational phases the blanket modules could be heated-up with helium to temperatures of about 700°C. First, a portion of the accumulated tritium could be removed by this helium flow; then, the helium would be replaced by protium in order to load the beryllium pebbles.

At present, the efficiency of none of the proposed techniques has been demonstrated. In the future HIDOBE irradiation experiments in the HFR Petten [3], a large variety of beryllium samples enclosed in small capsules will be irradiated for a time period between 2 and 4 years. In these experiments it was discussed to investigate the also influence of protium loading by:

a) the use of small closed capsules with a high initial internal protium pressure,

b) connecting the capsules with an external protium reservoir with a maximum protium pressure of ≈ 0.1MPa.

Method b) would be required if it proves that protium permeation through the capsule walls during the irradiation period is large. An assessment is presented below.

The second part of the work concentrated on the preparation and performance of first experiments in the Fusion Material Laboratory of the Forschungszentrum Karlsruhe on the hydrogen uptake and release kinetics of NGK 1mm beryllium pebbles.

Hydrogen permeation through HIDOBE capsules

In the HIDOBE experiments, beryllium pebbles will be irradiated at temperatures between 400 and 750°C. If capsule materials exist with an acceptably small hydrogen permeation during the irradiation period, then closed capsules could be used with a hydrogen filling prior to irradiation.

Characteristic HFR capsule dimensions were considered and, first, steady-state permeation rates were assessed for different capsule materials as a function of temperature. Figure 1 shows the number of initial hydrogen capsule inventories permeating per year. It is seen that for all materials except tungsten at T≤ 600°C the values are significantly larger than 1 which means that the capsules must be connected to a feeding system.

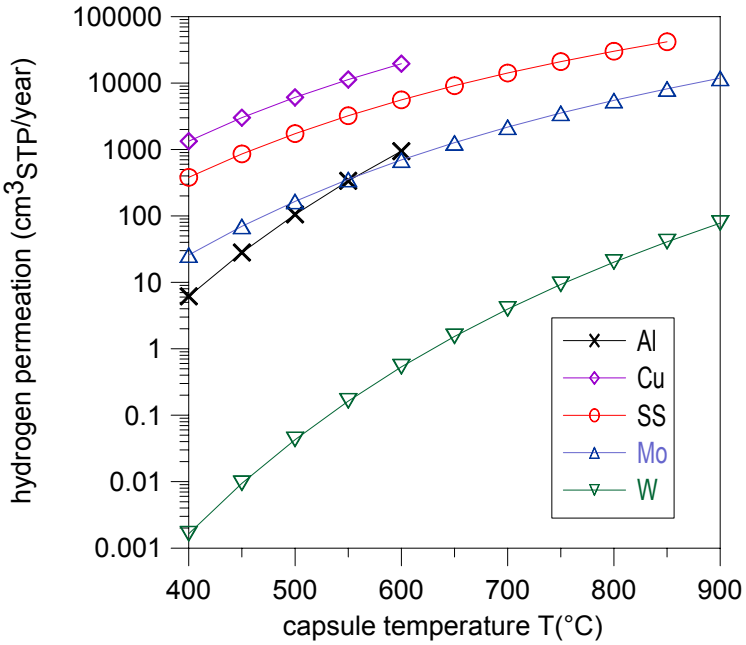

Fig. 1: Hydrogen permeation through HIDOBE capsules.

Considering non steady-state permeation, it proved that even for tungsten the maximum temperature would be limited to ≈ 500°C. Therefore, the conclusion is that protium filled closed capsules are not a reasonable option. Unfortunately, it showed that purged capsules can not be realised in the HFR either, therefore, the influence of protium loading will not be investigated in the HIDOBE experiments.

Protium uptake and release of NGK beryllium pebbles

Experiments to investigate the diffusion of protium into 1mm diameter NGK pebbles and the subsequent release rates have started in the Fusion Material Laboratory of the Forschungszentrum Karlsruhe using a facility where similar experiments were performed in the past [4]. Because protium uptake and release cannot be measured accurately directly, 50ppm tritium is added to the protium and an ionisation chamber downstream is used for analysis of the tritium activity in the gas.

For hydrogen loading, the beryllium pebbles are positioned in an Al_2O_3 tube in a special furnace. After evacuation, the system is filled with the hydrogen mixture, and heated up to the loading temperature T_{load} for a time period t_{load}. Then, the pebbles are transferred to tritium release facility which consists essentially of an inlet gas manifold, a sample furnace chamber connected to a zinc reducer (T≈390°C) which transforms any tritiated water into tritium gas, and the ionisation chamber. The total amount of stored tritium is determined by integrating the measured release rate over time.

The release kinetics are determined by annealing the pebbles with temperature ramps (7°C/min from room temperature to 500°C, then 15°C/min) up to the annealing temperature T_{ann} which is kept constant. A 50cm3/min helium flow with 1 vol%H_2 is used for the tritium removal. Before performing experiments with loaded pebbles, an experiment with unloaded pebbles is performed before in order to measure with the ionisation chamber the background of the system.

Figure 2 shows results of an experiment where loaded NGK beryllium pebbles (m_{Be}=0.8653g, t_{load}=8hs, T_{load}=850°C, p_{H2}=0.2MPa) were heated aup to T_{ann}=1100°C. The figure shows the determined tritium release rates (background signal corrected). A distinct tritium release begins at about 500°C; the maximum release rate occurs still in the heating-up phase; the tritium release is terminated about 30mins after the final annealing temperature of 1100°C has been reached.

The question arises if the main tritium release between t=7500s and 11000s is caused by the tritium release from the bulk material or by release from surface layers.

In future experiments the parameters affecting hydrogen storage and release will be varied in order to separate surface effects from bulk dissolution. In order to increase the measurement accuracy, the ionisation chamber will replaced by a proportional counter. Furthermore, the Al_2O_3 tube in the loading furnace will be replaced by a tube made from a refractory alloy in order to enable hydrogen loading at pressures up to 2MPa.

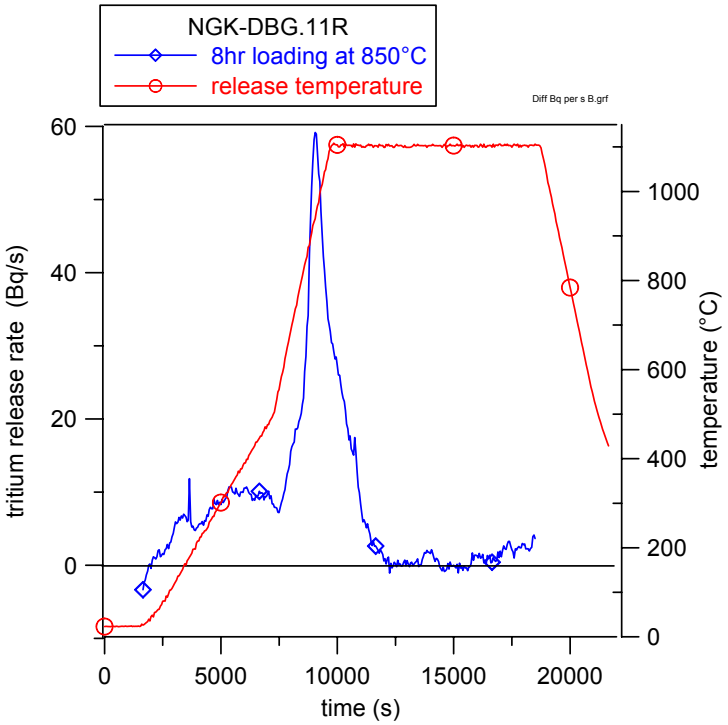

Fig. 2: Tritium release rates from loaded beryllium pebbles.

Staff:

A. Erbe
E. Damm
E. Rabaglino
J. Reimann
J. Rey
R. Rolli

Literature:

[1] J. Reimann, E Rabaglino, R. Rolli, Study on methods to enhance tritium release from beryllium during blanket operation, Internal Report FU-TF 1.1-02/014/00-R, March 03,

[2] E. Rabaglino et al., Helium and tritium kinetics in irradiated beryllium pebbles, J. Nucl. Mat., 307-311 (2003) 582-587,

[3] J. van der Laan, personell communication, 2003,

[4] F. Scaffidi-Argentina, H.Werle, 2nd IEA Int. Workshop on Beryllium Techn. for Fusion, Jackson Lake Lodge, Wyoming, USA, Sept. 1995.

TW3-TTBB-006
Helium Cooled Pebble Bed Blanket: Modelling of Ceramic Breeder Pebble Beds

TW3-TTBB-006 D2
Delivery of Lithium Orthosilicate Pebbles Irradiated in the EXOTIC-8 Experiment to the University of Latvia

Aim and general overview of the activities

Studies performed in the latest years at the Laboratory of Solid State Radiation Chemistry of the University of Latvia (Riga, Latvia) [1,2] have shown that tritium release from Li_4SiO_4 and Li_2TiO_3 pebbles, irradiated by fast electrons, might be influenced by the presence of high magnetic fields (6 to 10 tesla are expected in the HCPB blanket of a fusion power reactor). In particular, in the presence of coarse grains, tritium diffusion and release might be delayed due to the fact that the magnetic field bends the particle trajectory. The characterisation of such phenomenon in neutron-irradiated Li_4SiO_4 is one of the aims of subtask TW3-TTBB006-1, which runs at the University of Latvia in 2003 under the coordination of FZK. An additional milestone in the frame of this subtask is the study of tritium spatial distribution in the neutron-irradiated Li_4SiO_4 pebbles, by an original controlled dissolution technique [3].

The aim of subtask TW3-TTBB006-2 is to deliver to the University of Latvia irradiated Li_4SiO_4 pebbles from the EXOTIC 8 irradiation experiment [4], which are needed for the studies of the effect of magnetic field on tritium release and of tritium distribution foreseen in subtask TW3-TTBB006-1. The samples are stored in the Fusion Material Laboratory of FZK.

In subtask TW3-TTBB006-2 no R&D is foreseen. The main significance of the activity is to provide support to R&D in a new EURATOM-Association (the Association EURATOM-AEUL with the University of Latvia), with the aim of integrating it in the EU Fusion Technology Programme, in the global frame of the enlargement of the European Community. Latvia will be officially a new member state starting from January 2004. The enhancement of the collaboration with the new Member States, in the scientific field in particular, is a fundamental step for the development of new EC member states and their integration in the EU.

Progress in the period January – September 2003

In collaboration with the University of Latvia, the quantity of Li_4SiO_4 pebbles from EXOTIC-8 irradiation to be transported from FZK to Riga has been agreed as 5 grams. Such quantity can be made available by FZK and meets the needs of Riga for studying magnetic field effects on ^3H release from neutron irradiated Li_4SiO_4, as foreseen in subtask TW3-TTBB-006-D1. The procedure to get from the German authorities the authorisation to carry out the international transport of such quantity of material has been successfully completed. A Type A container for the transport of the samples according to the international regulations has been purchased and prepared with the samples and the proper labelling in the Fusion Material Laboratory of FZK. The customs documents have been prepared and the transport by road to Frankfurt airport and then by plane to Riga has been organised with the company FINNAIR. The samples have left the Fusion Material Laboratory of FZK on September 3rd, 2003 and arrived in Riga on September 8th. They were finally delivered to the Laboratory of Solid State Radiation Chemistry of the University of Riga on September 10th. The effect of magnetic field on tritium release from the Li_4SiO_4 pebbles irradiated in EXOTIC-8 experiment (magnetic field up to 2.4 T, annealing temperature up to 900 ºC) and tritium chemical forms and distribution in separate pebbles will be studied by the same method used up to now for electron irradiated pebbles. Upon request from Riga, a certain quantity of the same material, in an unirradiated form, which is necessary to perform comparative studies, was also sent to Riga on September 10th, 2003, by ordinary mail.

Conclusions and future work

The studies on tritium spatial distribution and effect of high magnetic field on tritium release in ceramic breeders will be continued in 2004 on neutron-irradiated beryllium, in the frame of a different task. The collaboration between FZK and the University of Latvia will be continued with the aim to support the integration of the Association EURATOM-AEUL in the EU Fusion Technology Programme.

Staff:

E. Rabaglino
O. Romer
J. Kauffmann
J. Tiliks (University of Latvia)

Literature:

[1] J. Tiliks et al., Influence of high magnetic field on the radiolysis and tritium release from lithium metatitanate and orthosilicate ceramics, Report FU 05-CT-2000-00079, University of Latvia, Riga, Latvia, 2001

[2] J. Tiliks, G. Kizane, A. Vitins, G. Vitins,, J. Meisters, Physicochemical processes in blanket ceramic materials Fus. Eng. Des. 69 (2003), 519-522

[3] A. A. Kaukis, J. Tiliks et al., Preparation and properties of lithium silicates and zirconates ceramic blanket materials, Fus. Eng. Des. 17 (1991) 17-20

[4] J. K. Aaldijk, D.J. Ketema, Irradiation of ceramic breeder material EXOTIC (R212 8/8), Report K5079/01.4662/I, NRG, Petten, The Netherlands, 2002

Breeding Blanket
HCLL Blanket Concept

TTBA-006b
Water Cooled: Magneto-Hydrodynamics

TW2-TTBA-006b D1
Test and Modeling of Forced Convection MHD

The work on pressure driven (forced) magnetohydrodynamic (MHD) flows focused on two main subjects. One was the pressure drop reduction in headers of the previous WCLL blanket and the other was the investigation of flows in expansions and contractions with reference to a HCLL blanket.

Pressure drop reduction by insulating liner technique

The pressure drop in WCLL access pipes is balanced by the Lorentz forces exerting on the moving electrically conducting fluid which is exposed to the effective magnetic field inside the pipe. Perfect electrical insulation at the pipe wall would exclude the additional path for currents through the highly conducting wall and minimize the current in the fluid and the associated MHD pressure drop. Unfortunately, there exists up to now no insulating layer that retains its electrical insulation when being exposed to flowing lead lithium alloys at high temperatures. For that reason a technique is selected were the insulation layer is separated by a thin sheet of steel from a direct contact with the fluid. If the steel sheet is kept thin, its electric resistance is still high so that MHD pressure losses remain small. To demonstrate the feasibility of this approach a test section has been fabricated and tested in the MEKKA laboratory of the Forschungszentrum Karlsruhe.

A sketch of the test section is shown in Fig. 1. In the following we describe briefly how the test section was fabricated: Tubes were cut from raw material and plates from EUROFER were machined; the tubes (upright) and plates annealed; 5 tubes selected for grinding to final diameter, the remaining wall thickness was 0.6mm ; 3 tubes selected for plasma spraying; 8µm molybdenum primer applied; plasma sprayed with 300µm Al_2O_3; grounded to final diameter; thickness of insulating layer tested with ultrasonic device; only one tube met the specification concerning straightness with a layer thickness of 235µm ; ends of tubes enlarged to minimize gap between tube and plates; helium leak test performed; plates machined without oil or coolant; semicircular grooves machined to the tube size; plates and tubes cleaned with ultra pure acetone; all pieces joined and fixed; evacuated in EB welding machine for more than 10h ; outer seams welded; tested; diffusion welded in HIP facility at 980°C and 50MPa ; ultrasonic tests. Finally both ends of the test section were machined until the insulating layer was visible in order to avoid a current path at the ends of the insulating layer into the massive structure. Then the test section was welded to tubes with pressure tabs in the liquid metal circuit.

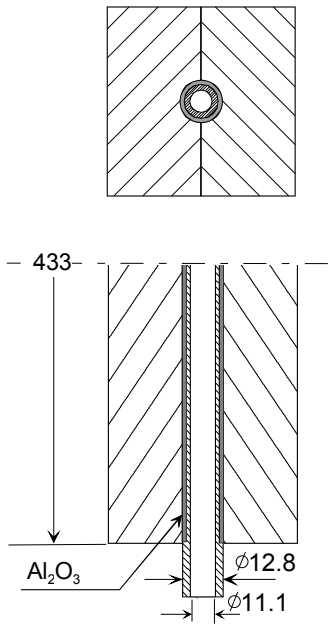

Fig. 1: Geometry of test section.

Measurements of the magnetic field inside the test section yield the result that the relative magnetic permeability of the material after the heat treatment is roughly μ_r=4.5. Such a value could reduce the MHD pressure drop by shielding already by about 5-10% compared with non-ferromagnetic walls. The aim of the experiment was to show the capability of an insulating layer to reduce the pressure drop in massive structures. In fact, calculations show that the pressure drop for a similar test section without insulation (compare Bühler et al. 2002) would be at least higher by a factor of about 5 compared with the experimental results. Therefore the observed reduction of pressure corresponds well to that expected for a perfect

insulation between the liner and the thick wall. Details and further results have been published by Reimann et al. 2003.

MHD flows in expansions and contractions

Magnetohydrodynamic creeping flows in expansions of rectangular ducts are investigated for strong, externally applied magnetic fields, with respect to applications at entrance or exit of the flow to the HCLL breeder units. A non-dimensional measure for the strength of the magnetic field is the Hartmann number

$$Ha = BL\sqrt{\sigma/\eta}\,,$$

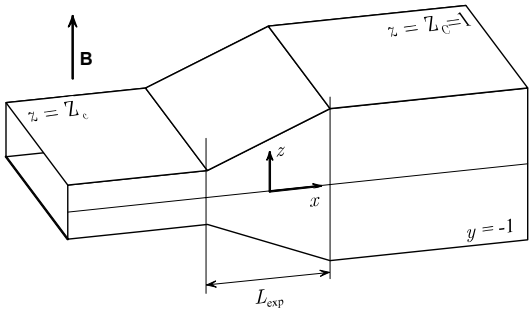

Fig. 2: Geometry of an expansion.

Where $B, L, \sigma,$ and η stand for the magnitude of the magnetic induction, typical length scale, electric conductivity and dynamic viscosity of the fluid. For high Hartmann numbers (10^3 – $3\text{x}10^4$ in fusion applications) the major balance of forces establishes between pressure and Lorentz forces while viscous forces are confined to quite thin boundary layers along the duct walls. Near the expansion an intense exchange of flow establishes between the upstream and downstream cores in which viscous friction is unimportant, with the corresponding side layers at $y = \pm 1$ Calculations are performed for an expansion ratio of 4, for a number of geometries as shown in Fig. 2, where the expansions length *L*exp serves as a parameter. Results for pressure drop are shown in Fig. 3. For the limiting case of a sudden expansion an internal layer develops along magnetic field lines which matches the solutions in both rectangular ducts. This layer is able to carry a significant amount of the total flow in a direction transverse to the duct axis. The three-dimensional flow near the expansion drives additional electric currents which are responsible for higher pressure drop ∆p3D compared with fully developed conditions. It can be shown that the results depend essentially on the aspect ratio of the duct and on the conductivity σ_w and thickness t_w of the walls, i.e. on the wall conductance parameter

$$c = \frac{\sigma_w t_w}{\sigma L}\,.$$

As an example results for *c* = 0.05, *Ha* << 1 is shown in Fig. 3. Some results have been published by Bühler 2003a and further details are described in FZKA 6904.

The results shown so far are based on an inertialess approximation. The importance of inertia for such flows is currently studied by complete numerical simulations.

For the validation of the theoretical results an experiment has been prepared. A test section for a sudden expansion has been fabricated and is ready for being inserted into the MEKKA liquid metal loop. The test module has been pressure tested up to 9.3 bars and is licensed by the authorities. The experimental program had been interrupted because the responsible persons both academic and technical left the IKET

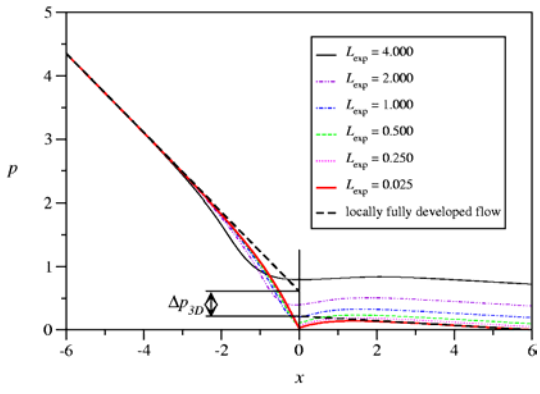

Fig. **3:** Pressure along the axis of expansions, *c* = 0.05, *Ha* >> 1.

institute. The program will be completed in 2004 adequate personal has been hired.

Staff:

L. Bühler
K. Messadek
R. Stieglitz

Literature:

[1] Bühler, L.: 2002, Magnetohydrodynamic flow in ferromagnetic pipes, *Forschungszentrum Karlsruhe,* Technical report, **FZKA 6702**

[2] Bühler, L.: 2003a, Magnetohydrodynamic flows in sudden expansions in strong magnetic fields, 4th International Conference on Electromagnetic Processing of Materials, Proceedings on CD-Rom, Lyon, 14-17 October 2003.

[3] Bühler, L.: 2003b, Inertialess magnetohydrodynamic flows in expansions and contractions, *Forschungszentrum Karlsruhe,* Technical report, **FZKA 6904**

[4] Bühler, L., Messadek, K. Stieglitz, R.: 2002, Magnetohydrodynamic flow in ferromagnetic Pipes, *Fusion Engineering and Design,* **63-64**, 353-359.

[5] Reimann, J., Bühler, L., Messadek, K., Stieglitz, R.: 2003, MHD pressure drop in ferritic pipes of fusion blankets, *Fusion Engineering and Design,* **69**, 309-313.

TTBC-006
Helium-Cooled Lithium Lead: Magneto-Hydrodynamics

TW2-TTBC-006 D1
Natural Convection MHD

In the HCLL blanket the liquid breeder is confined in narrow gaps between parallel cooling plates. The velocities required for tritium removal are typically very small so that the buoyancy induced thermal convection flow may become comparable with the forced, pressure driven flow. As application to the HCLL blanket three-dimensional magneto convection in a strong, horizontal magnetic field in a rectangular box with electrically conducting walls has been considered for high-Hartmann numbers (strong magnetic fields) and negligible convective heat transfer (small Peclet number). Velocity magnitudes in highly conducting ducts are typically of the order $v0=\beta\rho0\alpha gL/\sigma B2$, where β is the coefficient of thermal expansion, $\rho0$ is the reference density, α, g and B are the magnitudes of temperature gradient, gravitational acceleration and magnetic induction, L is a length scale measured in the direction of the magnetic field and σ stands for the electric conductivity of the fluid.

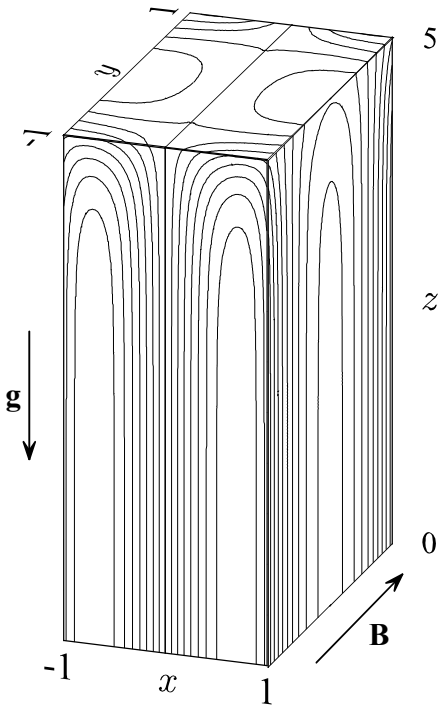

Fig. 1: Isolines of electric potential on the wall of a vertical container

A numerical code based on this model has been developed and described by Molokov & Bühler (2003). The code is valid for an arbitrary temperature distribution resulting from both heating of the first wall and volumetric heating, and for arbitrary and different wall conductivities of all the six walls of the box. For sufficiently long boxes, comparison of the velocity profiles in the middle of a box with fully developed solutions (Bühler 1998) for infinitely long rectangular ducts has been made. The agreement is excellent. Properties of a convective flow have been investigated and examples of flows for various temperature distributions have been presented. It has been shown that the three-dimensional effects are confined to three/four values of the characteristic dimensions of the duct cross-section at the top and the bottom of a blanket. Symmetries of temperature with respect to the magnetic field orientation have been discussed. The flow pattern has been shown to be sensitive to the wall conductivity. This property may be used to optimize the convective flow pattern in applications. The code developed is a flexible, fast tool to analyze and optimize convective flows in various blanket designs. Fig. 1 shows a typical distribution of the electric potential on the wall of a vertical container. The buoyancy driven flow has its origin in internal volumetric heating. The flow goes upwards in the center and down along the cooled lateral walls at x= ± 1 .

At the time when the work has been initiated the liquid metal containers were supposed to have a more-or-less square cross section (WCLL geometry). Now the design concentrates on gaps, i.e. on rectangular cross sections with small transverse aspect ratio. This is taken into account in current calculations. One example is shown in Fig. 2, which shows fully established, buoyancy-driven velocity profiles in a long vertical gap at position y=0. Layers of this type of orientation appear in blanket top modules. In this example there is a uniform lateral heat flux between the side walls which are at $x=\pm d$, i.e. the temperature gradient is

given as DT=α**e**x. The conductivity of the wall is described by the wall conductance ratio $c=\sigma w t/\sigma L$, where the wall has electric conductivity σw and thickness t. We observe that the velocity in the core approaches the relation u/v0=*Ha x* if the walls are insulating (c=0). With increasing conductivity of Hartmann walls (walls at $y \pm 1$, perpendicular to the magnetic field) the magnitude of velocity is reduced. For relatively wide ducts we observe in the core of the duct very small or even reversed velocities while the major mass flux is carried close to the heated wall in the so-called side layers. If the aspect ratio drops below the thickness of the side layers, both side layers merge and the core does no longer exist. This can be seen in Fig. 2 for the case of d=0.1.

The current analysis focuses now on gaps with arbitrary orientation with respect to direction of gravity. This allows the analysis of flows in blankets at any poloidal position. Moreover, the analysis is being extended to account for 3D applications when the liquid metal gap is very thin, when both parallel boundary layers merge. Results for further applications will be published in an upcoming FZK report, in a conference contribution (Molokov et al. 2003) and submitted to international journals.

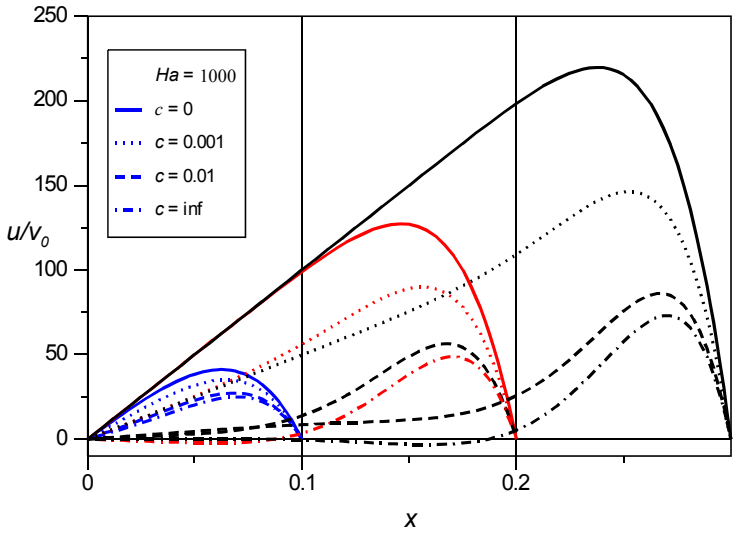

Fig. 2: Velocity profiles in a differentially heated vertical gap for different conductivity of the wall $c(y \pm 1)$=0-B, $c(x \pm d)$=0 and different transverse aspect ratios d=0.1, 0.2, 0.3.

The work has been performed in close collaboration with Prof S. Molokov and his colleagues at the Coventry University, UK.

Further analysis should focus on the nonlinear interaction of velocity and temperature field and most importantly on electrical coupling of neighboring fluid layers.

Staff:

L. Bühler

Literature:

[1] L. Bühler, 1998, Laminar buoyant magnetohydrodynamic flow in vertical rectangular ducts, *Phys. Fluids* **10**, 223-236

[2] S. Molokov, L. Bühler, 2003, Three-dimensional buoyant convection in a rectangular box with thin conducting walls in a strong horizontal magnetic field," Technical report *Forschungszentrum Karlsruhe*, FZKA 6817

[3] S. Molokov, T. Tagawa, S. Aleksandrova, L. Bühler, *2003* Three-dimensional buoyant convection in a rectangular box in a strong horizontal magnetic field, 4th Int.

Materials Development

TTMS-001
Irradiation Performance

TW2-TTMS-001 D5
HFR Irradiation Programme

The HFR Phase IIB programme is abbreviated SPICE (**S**am**p**le Holder for **I**rradiation of Miniaturised Steel Spe**c**im**e**ns Simultaneously at Different Temperatures). It complements the former HFR irradiation programmes MANITU, SIENA, HFR Phase IA, and IB (cf. TTMS-001/14).

The objectives are to evaluate the mechanical properties of material samples after irradiation at doses of 15 dpa and different irradiation temperatures. The material used is the reduced activation alloy EUROFER 97 in different variations: different heat treatments, a HIP powder steel, and various boron contents to investigate the effect of He embrittlement. Heat treatments of the irradiated alloys are given in Tab. 1.

Table 1:Heat treatments of the irradiated alloys

Alloy	Heat treatment
EUROFER 97, as delivered	980°C + 760°C
EUROFER 97	1040 °C + 760°C
EOROF. ODS HIP powder steel	-
EUROFER 97, variations in B and ^{10}B contents	1040°C + 760°C
F82H mod., reference steel	950°C + 750°C
GA3X, reference steel	1000°C + 700°C

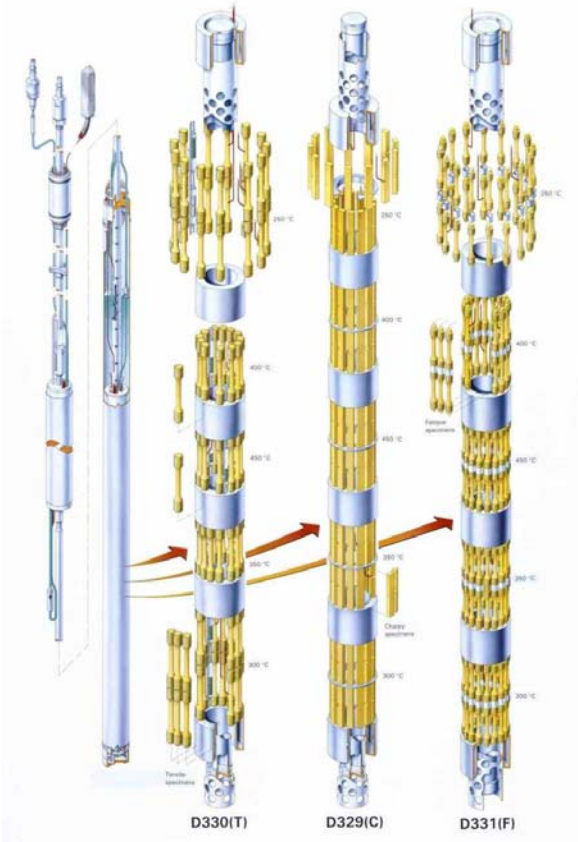

Fig. 1: TRIO irradiation capsule with sample holders. D330: 91 tensile specimens; D329: 130 charpy specimens; D331: 160 fatigue specimens.

The "quasi-saturation" of irradiation-induced embrittlement between 10 and 15 dpa, found for conventional steels in former programmes (SIENA), will be investigated for the EUROFER alloys. The low irradiation temperature ranges of the High Flux Reactor will give a look at embrittlement effects increasing progressively with decreasing temperature in all bcc-alloys irradiated up to now.

The TRIO irradiation capsule (cf. Fig. 1) is fixed in a central core position (C3) of the Petten High Flux Reactor. Surrounded by fuel elements, the neutron flux will be approximately homogeneous and an exactly defined dose rate can be reached in a comparatively short time.

The TRIO capsule offers three parallel separate channels for the different sample holders. Temperature control is effectuated by a controlled sodium flow which facilitates the formation of separate temperature areas of 250, 300, 350, 400, and 450°C in a horizontal arrangement. The neutron flux is relatively homogeneous and varies over the irradiation space between 92 and 107% of the nominal value. A vertical displacement unit allows to follow the centre line of the fluence rate, which is shifted vertically with

the burn-up of the fuel elements. Thermocouples are installed along the irradiation capsule to record the temperature behaviour during the experiment. Activation detectors are installed to ensure the high quality level of HFR irradiations even at higher doses.

This is the first irradiation experiment, in the course of which a damage of 15 dpa will be reached at five different temperature levels simultaneously. Newly applied techniques for these sample holders are the temperature control by sodium and the dosimetry inside the capsule. The liquid sodium cooling provides a highly improved temperature stability in comparison other experiments and to the gas cooling used in former HFR-experiments (cf. Fig. 2).

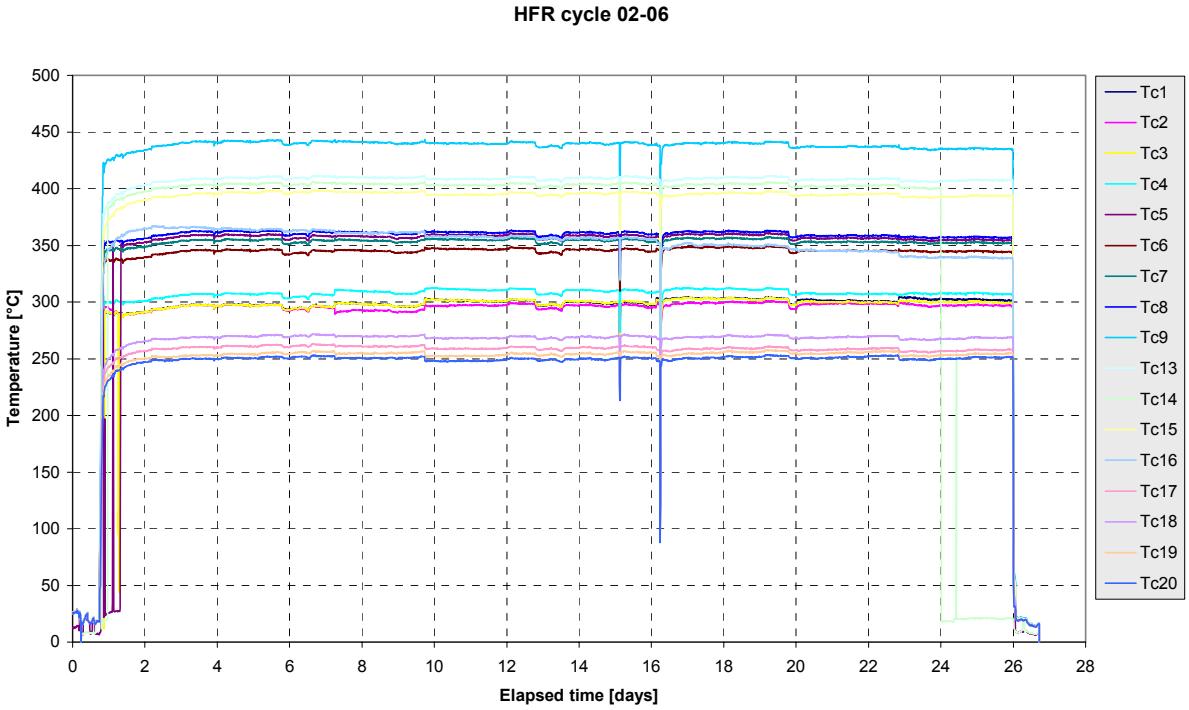

Fig. 2: Active temperature control – recorded signals of the thermocouples in the 329-capsule (KLST-specimens). Cycle 02-06, 25 full power days in July/August 2002.

Post-irradiation examinations (PIE) will be carried out in the Fusion Materials Laboratory of FZK. The design of the capsule provides space for 130 charpy, 91 tensile, and (for the first time simultaneously) 160 fatigue specimens. As result, a full data set of the irradiation effects on Charpy impact, tensile, and fatigue behaviour will be obtained. During the irradiation phase, unirradiated reference samples are investigated. Regarding the EUROFER steel, an embrittlement behaviour comparable to the best alloys investigated in former irradiation programmes is expected, accompanied by good mechanical properties. The higher irradiation dose of 15 dpa will represent a step towards fusion-relevant doses.

Charpy tests of the irradiated specimens: 130 Charpy specimens will be tested by using a fully automatic instrumented pendulum in the Hot cells facilities of FZK. The impact properties as ductile to brittle transition temperature, upper shelf energy, and dynamic yield stress will be determined and compared with the unirradiated properties.

Tensile tests of the irradiated specimens: The 91 tensile specimens will be tested in an universal testing machine in the Hot cells facilities of FZK. These tests will be performed at the irradiation temperatures and at room temperature and will be compared with the unirradiated data, too.

Creep-fatigue tests of the irradiated specimens: The EUROFER97 specimens will be tested in strain controlled creep-fatigue in the facilities of the Hot cells of FZK. 160 tests will be performed at the temperatures of RT, 250, 300, ..., 450°C and with a total strain rate between 0.4 and 1.5 %.

Fractographic and microstructural investigations (FMI): An important part of this program is the FMI of the irradiated and tested materials. The irradiation induced changes in the materials and the reasons of the embrittlement must be detected. These results must be correlated with the mechanical properties and the fracture behaviour of the materials. These investigations will be performed at the Charpy, tensile and fatigue specimens.

Assembly of the sample holders in Petten had started in January 2001. The start of irradiation was delayed by three months because of the intricate fabrication of the sample holders which are more complex than the ones formerly used (increased precision requirements because of the sodium cooling). The start of the irradiation was in cycle 0701, i.e. August 2001. To reach a damage of 15 dpa, 28 cycles will be needed in a central position. The first cycle was irradiated in position A7, all following cycles are irradiated in position C3. In December 2001, 3.0 dpa were reached, 5.4 dpa by end of June 2002. In December 2002, the accumulated irradiation dose was 9.3 dpa, so the subtask TW2-TTMS-001a Deliverable 5 (7-8dpa) was completed in October 2002.

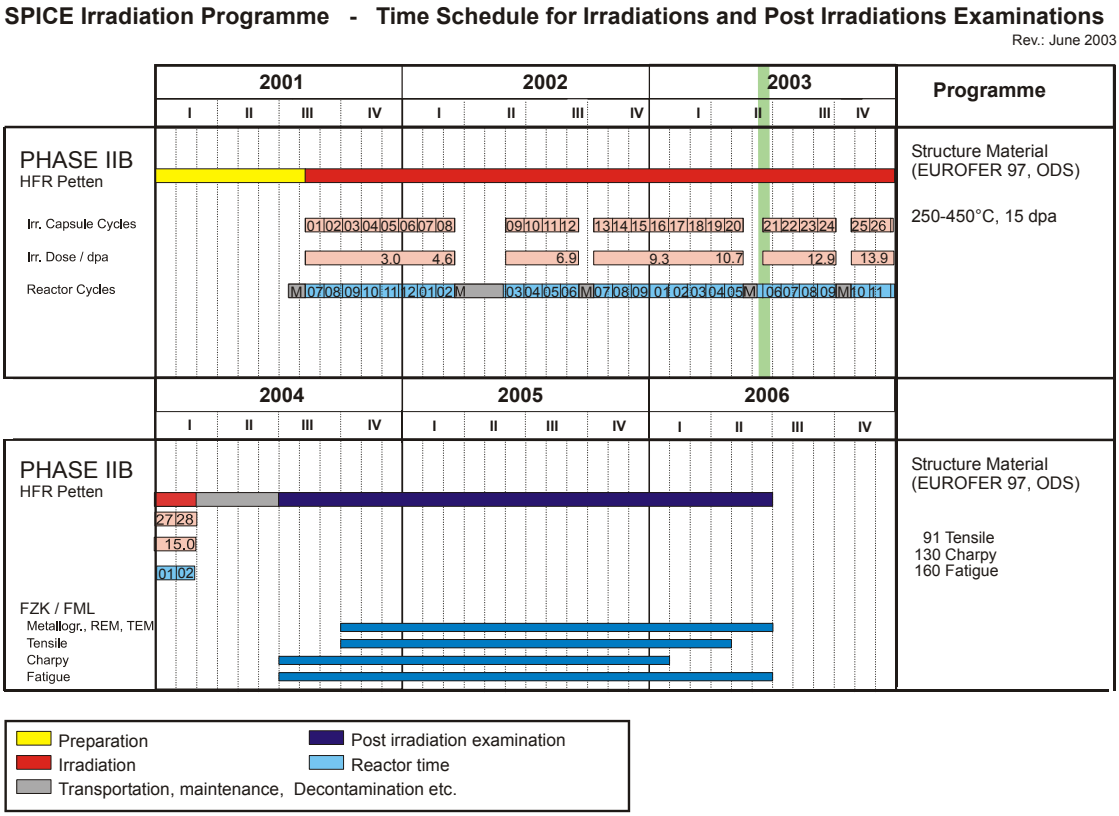

Fig. 3: Time Schedule

At the moment (September 2003), an accumulated dose of 12.5 dpa is reached in irradiation capsule cycle 24, cf. Fig. 3. The irradiation programme is running according to schedule, active temperature control by sodium is providing very constant temperature ranges in the different levels of the sample holders, cf. Fig. 2.

The irradiation phase will be finished by the February 2004. According to the time planning, the post-irradiation experiments can start in mid of 2004 after dismantling (Petten), transportation, and decontamination (Karlsruhe) of the specimens. Difficulties similar to the transportation problems with the specimens from the HFR Phase I b programme are excluded, as a new cask with a long-lasting transport permission is under construction. PIE and FMI are foreseen to be finished by mid of 2006.

Staff:

J. Aktaa
B. Dafferner
H.-C. Schneider

TW2-TTMS-001a D9
TW2-TTMS-001b D9
Fast Reactor Irradiations

1. Objectives

In an energy generating fusion reactor structural materials will be exposed to very high levels of irradiation damage of about 100 dpa. Due to the fact, that fast reactor irradiation facilities in Europe are not available anymore, a cooperation with the Russian institution: State Scientific Centre of Russian Federation Research Institute of Atomic Reactors (SSC RF RIAR) has been implemented.

2. The irradiation project ARBOR 1

In the irradiation project “ARBOR 1“ (for Associated Reactor Irradiation in BOR 60) 150 mini-tensile/low cycle fatigue specimens and 150 mini-charpy (KLST) specimens of different reduced activation ferritic/martensitic (RAFM) steels were under irradiation in a special designed irradiation rig of the BOR 60 at a temperature lower than 340°C since November 22nd, 2000. The irradiation rig is instrumented with neutron monitors in the central tube and on three of ten levels of specimen positions as well as with three temperature detectors also on three of ten levels [1].

The irradiation started in the core position D-23, where temperature measurement is possible and was continued in an identical position G-23 of the 5th row of BOR 60 core. The rig reached at a middle position with 30.9 dpa its scheduled damage dose at October 15th, 2002.

All available data of this irradiation are reported [2], while the analysis of the neutron monitors is still running.

The rig was removed from the core position and 50 % of the specimen have been unloaded, transported to RIAR’s hot cell area and prepared for testing in post irradiation experiments (PIE) in the hot cells of SSC RF RIAR.

Fig. 1: Modernized LCF-testing facility with furnace, strain measurement system and control devices

As it was agreed in the Annex of the ARBOR 1 contract, the mechanical PIE will be performed in the hot cells of SSC RF RIAR. For this reason a used but modernized LCF-testing facility (Fig. 1) and a new charpy testing facility (Fig. 2) had been ordered to be contributed to SSC RF RIAR.

After delivery and functional control at FZK the LCF-testing facility is ready now and the functional control of the charpy tester was finished mid of 2003. The packing and transport to Russia is planned for the end of 2003. To reach custom and tax free transport conditions an ISTC partner contract to perform the PIE is negotiated and ready for signature.

3. The irradiation project ARBOR 2

The other half of the specimens of the ARBOR 1 irradiation had been reloaded into the ARBOR 2 rig where they shall reach an irradiation damage of 70 dpa together with fusion relevant specimens from the ALTAIR 1 rig of CEA, Saclay and new specimens from FZK and CEA to reach 40 dpa. All new samples had been delivered to SSC RF RIAR in December 2002.

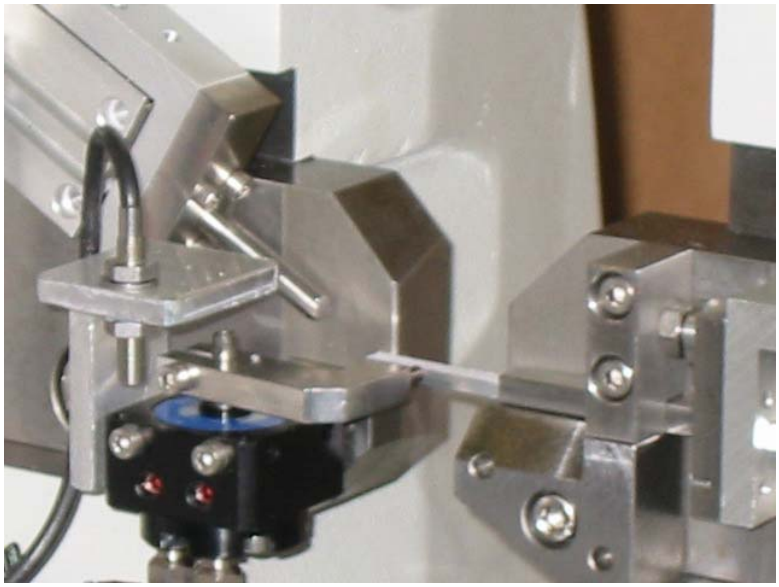

Fig. 2: Charpy testing facility (detail: Automatic specimen positioning system)

The following new materials are included in this irradiation:

From FZK: EUROF 1: EUROFER 97 (as received: 980°C 31 min/air cooled + 760°C 90 min/air cooled) as base material and as diffusion welded specimens, OPTIFER 11 (OPT 11: 1075°C 30 min/air cooled rolled condition) and specimens of mechanically alloyed EUROFER 97 with 0,3% Y_2O_3 as another recent development of higher heat resistant RAFM-steels. The specimen denomination is ODShip3 (as received: 1150°C 2 hrs/furnace cooled).

From CEA: EUROFER 97 HIP joints (HIP 1000 bar, 1100°C 240 min and post-heat treatment: 950°C 180 min + 750°C 180 min), EUROFER 97 TIG welds (980°C 30 min + 760°C 90 min and post-weld treatment: 750°C 120 min), the Japanese JLF-1 (1050°C 60 min + 780°C 60 min), MA957 and EUROFER 0.3 % Yttria (1050°C 15 min/furnace cooled).

The ARBOR 2 irradiation started on February 11th, 2003 and reached at maximum position during two reactor runs 9.2 dpa for the new implemented specimens and 40.1 dpa for FZK's preirradiated specimens.

Staff:

C. Petersen
D. Rodrian

Literature:

[1] C. Petersen, V. Shamardin, A. Fedoseev, G. Shimansky, V. Efimov and J.W. Rensman: "The ARBOR irradiation project", Journal of Nuclear Materials, vol. 307 – 311 (2002) p. 1655 – 1659.

[2] C. Petersen and D. Rodrian: "ARBOR 1: BOR 60 Irradiation Programme Status Report October 2002: End of irradiation", Internal Report, March 2003.

TW1-TTMS-001 D10
Helium in RAFM steels: Comparison between TEM and SANS

Since morphology, distribution and growth mechanisms of helium bubbles can sensitively determine the microstructural reasons for embrittlement effects, their size distribution functions as well as temperature stability must be determined. The important help for the understanding of effects in the irradiated materials is the information about its microstructure. TEM investigations enable direct observation of He-bubbles and deliver the reliable data concerning bubbles morphology and spatial distribution. But a general problem of TEM studies is the resolution limit of ~1 nm of He-bubbles in magnetic Fe-alloys. Therefore, TEM is being combined with small angle neutron scattering (SANS) in order to get full information not only on bubbles below a diameter of about 1-2 nm that are hardly visible in TEM, but also to get sufficiently good statistics on He bubble morphology.

Samples with standard heat treatments have been homogeneously implanted with 400 appm He at 250°C, using the 104 MeV α-particle beam of the cyclotron facility at FZ-Karlsruhe. In order to obtain information on He-bubble growth as a function of the temperature, after irradiation/implantation the samples were submitted to 2 h thermal annealing (at 525°C, 825°C, 975°C) in high vacuum, together with non-irradiated reference samples. For the case of as-implanted samples, the thermal reference was provided by a sample of the same material submitted to thermal annealing at 250°C for a time equivalent to the irradiation time.

The performed TEM investigations show the presence of He-bubbles in all samples (Fig. 1). The respective size distribution histograms evaluated from the TEM micrographs are presented on the Fig. 2. This is an important general result, as the visibility of He bubbles after 250°C implantation/irradiation have been questioned by various international teams over years. In the as-implanted sample the size of the bubbles range from 0.8 to 2.2 nm with an average size of 1.4 nm as shown in the histogram (Fig. 1a,2a). The small bubbles are more easily visible on the image out of defocus. In an underfocus condition the cavity image is bright relative to the background and the image has a dark rim. The reverse is true of an overfocus condition when the bubble is a dark image with a faint bright rim. The rim which decorates the bubbles through its perimeter originates from Fresnel fringes at the boundaries between two phases. The real cavity diameter is that contained inside the rim image. The sizes of the fringes amount usually to 1-2 nm, leading to the certain error in the measurement of the bubbles size. This error is especially significant if the bubble size amount to few nanometer - the case in the as implanted samples and the samples with lower annealing temperature. The detection of the bubbles with sizes down to 1 nm appears not possible.

The results of the TEM investigations of the samples annealed at 525°C during 2 h are shown in the Fig. 1b. Similar to the as implanted sample, the He bubbles have a size of only a few nanometer but seems to be a little bit better visible. They are also homogeneously distributed in the sample. However, a remarkable coarsening has not yet been started. The size of the bubbles ranges from 1.0 to 4.0 nm with an average size of 2 nm as it is shown on the histogram (Fig. 2b). Compared to the as implanted sample, no qualitative differences in the distribution has been observed after annealing at 525°C during 2 h.

The size of the He bubbles significantly increase in the samples annealed at 825°C during 2 h compared to the both first samples. The results of the TEM investigations of the samples are shown in Fig. 1c. The bubbles are not always homogeneously distributed, but are often located along internal interfaces like prior austenite grain boundaries. The size of the bubbles ranges from 1.0 to 10.0 nm with an average size of 3 nm as it is shown on the histogram (Fig. 2c). For sizes lower than about 5 nm, the size distribution has Gaussian form like the both first samples and additionally exhibits a distribution tail which continues up to about 10 nm. The existence of this tail indicates that at this temperature the formation of larger bubbles occurs.

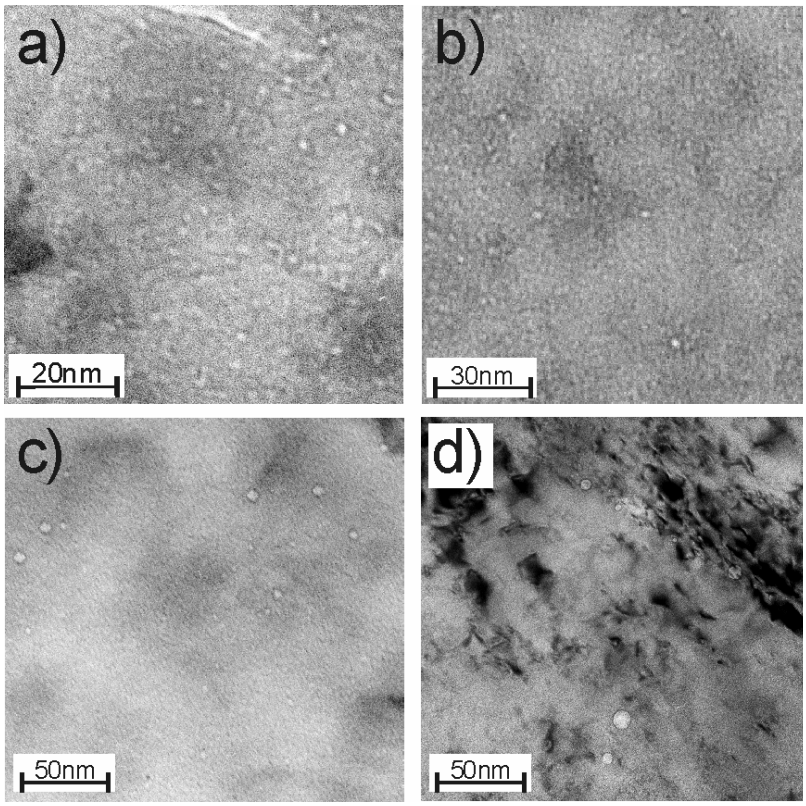

Fig. 1: The TEM micrographs of the He-bubbles in the samples after annealing at different temperatures. The micrograph of the as-implanted sample is presented on the part a) and after annealing at 525°C, 825°C and 975°C on the parts b), c) and d) respectively.

The further growth of the He bubbles was observed after annealing at the 975°C temperature during 2 h. The TEM micrographs of the bubbles are presented in the Fig. 1d. The bubble size distribution is characterised by the broad histogram with non Gaussian character. The bubbles range from less than 3 nm up to 28 nm. The distribution maximum located at 4 nm and then the number of the particles slowly decreasing until 28 nm. The maximum particle size observed after 975°C annealing amounts to 28 nm. It is obvious that this distribution is not only a continuation of the growth process which was observed at the sample with 825°C annealing temperature, but reflects a substantial acceleration of bubble kinetics.

Main conclusions that can be drawn from the TEM analysis of helium implanted RAFM steel and its comparison with SANS measurements:

- The as-implanted F82H samples with 400 appm He implanted at T_{irr} = 250°C show in the TEM analysis an almost homogeneous distribution of very small helium bubbles with typical diameters around 1-2 nm, practically at the TEM resolution limit. This is completely consistent with SANS investigations that revealed a pronounced maximum between 0.6-2 nm for as-implanted samples.

- It is important to note that the SANS investigations suggest with very high confidence this high density of nano-cavities or bubbles below the TEM resolution limit. This observation is basically consistent with the existence of a high density of vacancy clusters that has been born as one of the end-products of subcascades created by higher energy PKAs. If this thesis of vacancy cluster formation and their stability at 250°C irradiation can be confirmed, He atoms would be trapped in this already existing vacancy clusters. As He bubbles are stable at much higher temperatures, the trapped He atoms would very likely stabilize these vacancy clusters which would be visible in the SANS, no matter whether helium and how much helium is trapped. To prove this thesis, careful SANS measurements on neutron irradiated, almost He-free samples should be performed.

- After isochronal annealing at 525 and 825°C, according to TEM investigations, the average bubble diameters are 2-3 nm and 3-5 nm, respectively. This is consistent with the He-bubble volume distribution functions derived from SANS.

- However annealing at 975°C, that is above the $\alpha \rightarrow \gamma$ transition temperature, shows in the TEM analysis a very broad range of large bubbles ranging from less than 3 nm to 25 nm with unusual distribution function. After annealing at 975°C SANS reveals with a very high

confidence a bimodal bubble distribution with a well defined peak below 1 nm and a secondary distribution of bubbles one order of magnitude larger. This fraction of very small He bubbles peaked at a bubble diameter of about 0.4 nm is not visible in the TEM. However from the present analysis it seems that the high intensity of these small He bubbles or clusters might play an important role in the bubble coarsening mechanism above the $\alpha \rightarrow \gamma$ transition temperature. While there was for a long time an uncertainty whether in the fcc lattice above780-820°C the bubbles (i) dissolve and form larger ones or (ii) migrate and coalescence, or (iii) coarsen by an other mechanism, the present TEM investigations after isochronal annealing strongly suggest migration of smaller bubbles and coalescence.

- In any case, as substantial bubble growth in short time does not appear before annealing beyond the $\alpha \rightarrow \gamma$ transition temperature, any temperature excursions beyond 780-820°C of RAFM steels containing helium should be avoided (joining, disruptions). Not only substantial swelling would occur in the fcc phase but also long range migration of helium and substantial bubble formation at grain boundaries which in turn would lead to high temperature helium embrittlement already well known in austenitic steels. Once few but large bubbles have been formed in the fcc phase they remain stable after subsequent cooling down below the $\alpha \rightarrow \gamma$ transition temperature A_{c1e} (780-820°C).

- SANS analysis has shown to be indispensable to quantify density and size of bubbles and voids below the TEM resolution limit of about 1-2 nm. Without SANS a significant fraction of such bubbles/voids would be not visible and therefore comparisons between modeling and experimental validation would likely lead to large systematic discrepancies.

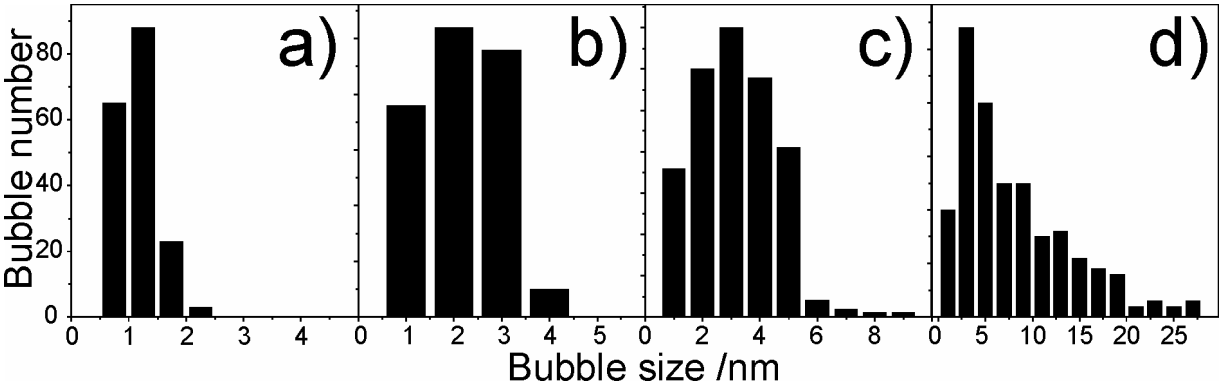

Fig. 2: The size distribution histograms of He-bubbles evaluated from the micrographs presented on the Fig. 1. The size distribution of He-bubbles in the as-implanted sample is presented on the part a) and distribution after annealing at 525°C, 825°C and 975°C on the parts b), c) and d).

Staff:

U. Jäntsch
M. Klimeankou
A. Möslang

Literature:

[1] R. Coppola, M. Klimenkov, E. Materna-Morris, A. Möslang, M.Valli; Helium bubble morphology in RAFM steels – correlation between SANS and TEM; IEA Modelling workshop 30 Sept-4 Oct 2002, Les Diablerets; Switzerland; to appear in Journ Nucl. Mater.

[2] M. Klimiankou, R. Lindau, E. Materna-Morris, A. Möslang, R. Copola, Internal FZK report, July 2003.

[3] R. Coppola, M. KLimiankou, A. Möslöang, M. Vialli; Helium bubble growth in F82H mod – correlation between SANS and TEM; ICFRM-11; 7-12 December 2003, Kyoto; proceedings.

TW2-TTMS-001a D10
TEM of EUROFER-ODS in Support of SANS

The efficiency of future fusion reactors will strongly depend on the operating temperature allowed by selected structural materials. With this regards oxide dispersion strengthened (ODS) steels are attractive candidates since they would allow to increase the operating temperature by approximately 100°C. The reduced activation martensitic steel Eurofer-97 (8.9 Cr, 1.1 W, 0.2 Ta, 0.42 Mn 0.11 C wt%), which is currently considered as a European reference for such fusion related studies, has been selected as a base material and variants with different Y_2O_3 contents are being characterized both concerning their thermo-mechanical and microstructural properties. More specifically the Y_2O_3 particle distribution is being investigated by using both transmission electron microscopy (TEM) and small-angle neutron scattering (SANS).

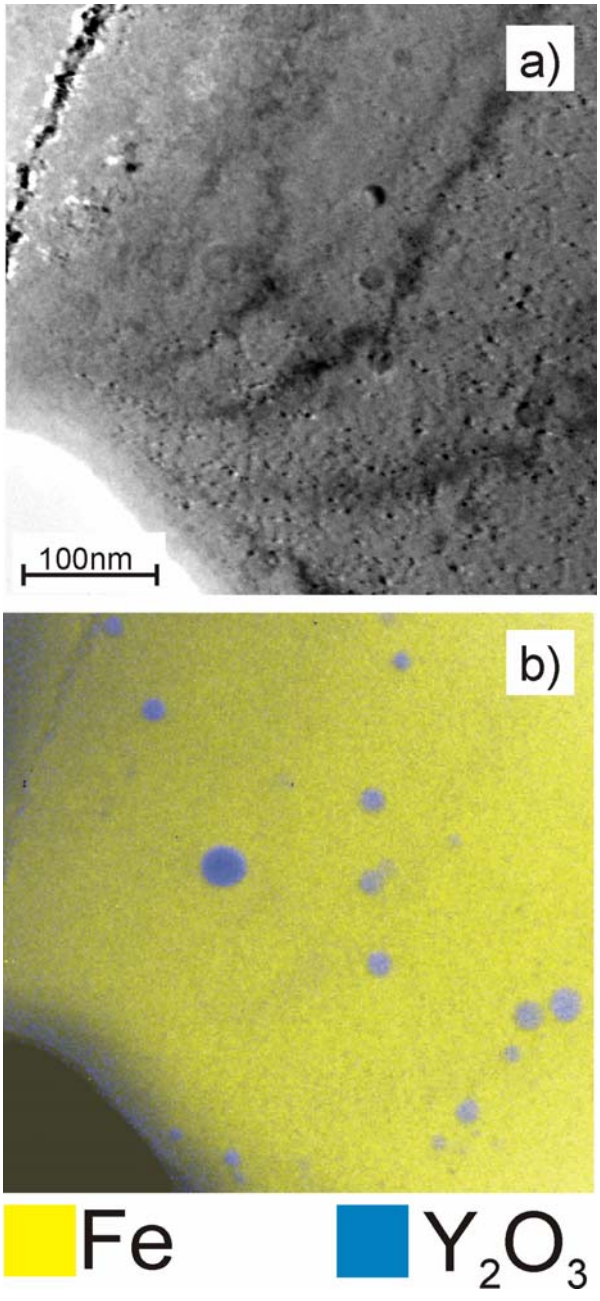

Fig. 1: TEM a) and EFTEM b) micrographs of an EUROFER ODS sample containing 0.5% Y_2O_3. The different phases are presented on the EFTEM image using different colours.

Two variants of EUROFER–97 with Y_2O_3 contents of 0.3 and 0.5 wt% respectively were produced by inert gas atomisation of the base material and subsequent mechanical alloying in the industrial ball mills. Hot isostatic pressing was then chosen as appropriate consolidation process for the production of the final ODS material in the shape of bars 60 mm in diameter and 300 mm in length. The results of electron microscopy examination show a high density of Y_2O_3 particles, varying in average size and distribution following different thermal treatment and Y_2O_3 content.

The ODS particles were found in the matrix using conventional and Energy Filtered Transmission Electron Microscopy (EFTEM) (Fig. 1a,b). The particles have a spherical shape with the sizes ranging from 2 nm to 40 nm. Using EFTEM measurements, it was not only possible to image the ODS particles, which are not visible on the conventional TEM micrograph (compare Fig. 1 parts a and b), but also to determine their chemical composition. The colour image was composed from different energy filtered images where the respective colour reflects the presence of a chemical element or phase. In the presented case the Y_2O_3 phase was coloured blue, whereas the Fe matrix was imaged using yellow colour. The EFTEM investigations performed on the different samples show that all ODS particles consist of Y_2O_3.

TEM investigations show a quite homogeneous distribution of the Y_2O_3 particles in the matrix. Y_2O_3 particles could be found in every investigated grain in TEM specimens prepared from different parts of the bars. A typical micrograph with the

corresponding size distribution histogram of ODS particles is presented in the Fig. 2. The histogram shows a maximum at approximately 12 nm and slight decrease of the particle number with increasing the size to 40 nm (Fig. 2b). Only few ODS particles possess a size above 40 nm. The low particle number at the sizes down to 6 nm can be attributed to the fact that such particles exhibit a low contrast and can be identified on the TEM micrographs only in very thin grains with favourable crystallographic orientation.

The local distribution of the ODS particles appear to be less homogeneous, varying from grain to grain. Close-by grains can show a strongly different ODS particle distribution (Fig. 3a). These differences are clearly visible on the calculated size histograms (Fig. 3b). The black columns show the size distribution of the ODS particles at the lower part of the micrograph whereas the white columns reflect distribution at the upper part. The particle size distribution at the upper part is similar to the average distribution in Fig. 2. The maximum of the particle distribution locates at the size of 9 nm. This value is lower then the one calculated for the 0.3% sample, but taking into account the differences in the local distribution the finding is within the scope of tolerance. The particle density at the lower part of the micrograph is significantly higher and the particle size is much lower than at the upper part of the micrograph. The maximum of the distribution histogram amounts to 3.5 nm. The reliable detection limit of ODS particles in TEM comprises 2-3 nm, what led to the distortion of statistics down to this limit.

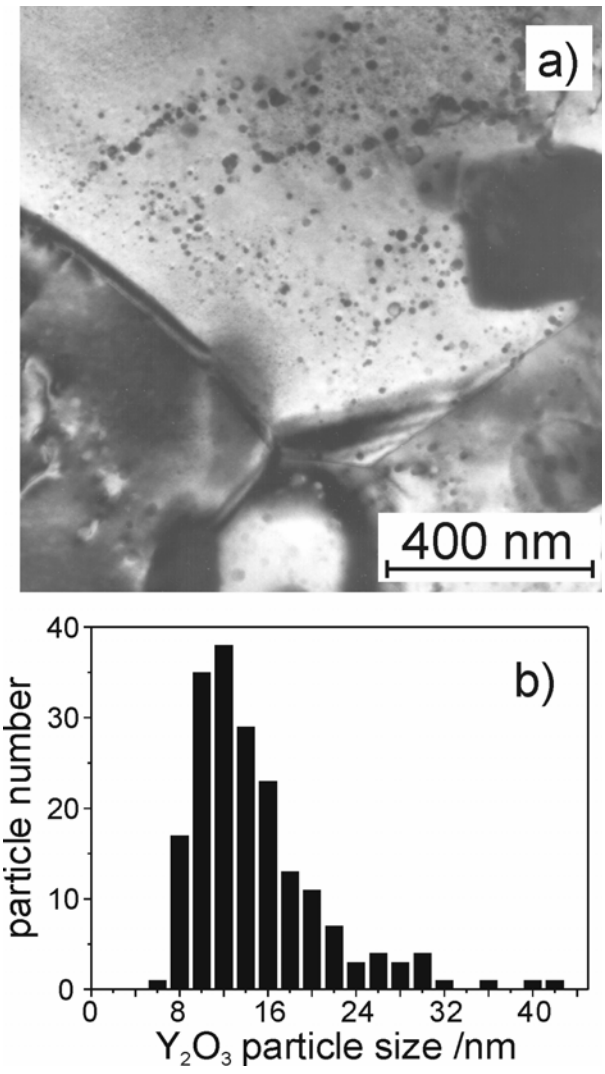

Fig: 2: TEM micrograph showing Y_2O_3 particles in a samples with 0.5% Y_2O_3 a) and the corresponding size distribution histogram b).

The size distribution of the ODS particles obtained from the SANS experiments are shown in the Fig. 3c (solid line). This is in good agreement with the TEM data taking into account the two components of the size distribution [1-3]. Recent results show that the SANS technique is quite sensitive to changes in Y_2O_3 particle distributions in EUROFER-97 ODS material. A good correlation is found with TEM observation carried out on the same material, which are however intrinsically limited in the statistics and in the resolution for particles smaller then 1 nm in diameter.

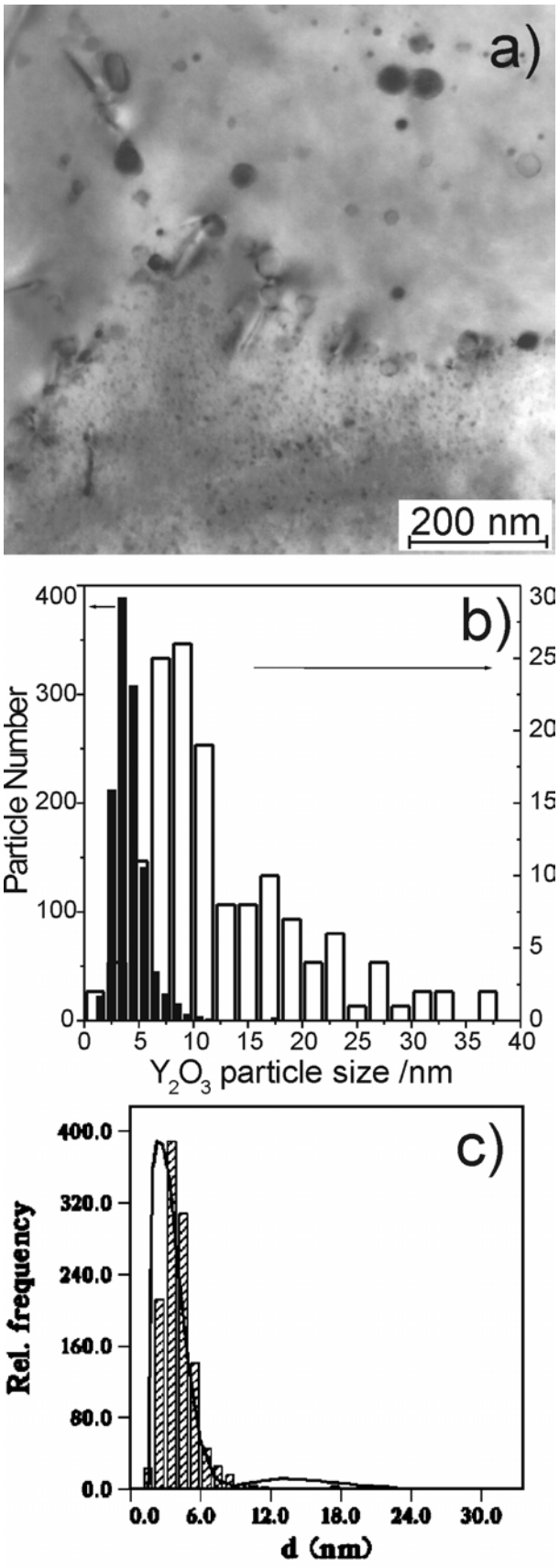

Fig. 3: EM micrograph of two neighbouring grains which have a strongly different distribution of Y2O3 particles a), the histograms evaluated from both grains by TEM b) and the comparison of this results with the SANS measurements. The histogram with the black bars (the right axis of ordinates) shows the size distribution on the lower micrograph part (a), whereas the white bars (the left axis of ordinates) represent the size distribution on the upper part (a), pay attention to the different scale of ordinates!.

Staff:

H. Zimmermann
G. Bürkle
P. Graf
U. Jäntsch
Dr. M. Klimiankou
R. Lindau

Literature:

[4] R. Coppola, M. Klimiankou, R. Lindau, R.P. May and M. Valli, SANS and TEM study of Y_2O_3 particles distribution in oxide dispersion strengthened EUROFER martensitic steels for fusion reactors, submitted to JNM

[5] M. Klimiankou, R. Lindau, A. Moslang "HRTEM Study of yttrium oxide particles in ODS steels for fusion reactor application" **249** (2003) 381-387

[6] M. Klimiankou, R. Lindau, A. Möslang, "TEM Characterization Of Structure And Compound Of Nanosized ODS Particles In Reduced Activation Ferritic-Marthensitic Steels" 11th International Conference on Fusion Reactor Materials, December 7-12, 2003, Kyoto, Japan

TW2-TTMS-001a D14
Post-irradiation Examinations on Microstructure and on Impact and Tensile Properties

The HFR 2.4 dpa irradiation programme complements the former investigations on promising low-activation ferritic/martensitic steels. Post-irradiation examinations (PIE; impact and tensile tests, microstructural investigations) of RAFM steels are performed after irradiation in the HFR Petten at temperatures of 250/300/350/400/450°C. The materials investigated mainly are steels (OPTIFER, F82H mod., JLF1) subjected to different heat treatments and F82H mod. weldings (EB and TIG). To provide early information on generic issues of the effect of the powder HIP process on impact properties after irradiation, samples of F82H mod. HIP powder steel (trial material from the Japanese reference steel) are tested as well.

In spite of the good irradiation behavior of the martensitic 7-10%CrWVTa alloys, a further development was carried out to improve the ductility at lower irradiation temperatures. A critical effect of low-temperature irradiation-induced hardening and embrittlement occurs in the fusion-relevant temperature range of 250 – 400°C. This behavior is shown at moderate neutron doses of only a few dpa up to 15 dpa as observed in former irradiation programs. A remarkable shift of DBTT towards higher temperatures could be observed, together with an increase in the ultimate strength. However, it is shown that this effect can be reduced by chemical modifications, for example, by operating with Cr contents in the range of 9 wt.% and strongly reduced B contents. A further step should be the operation of ODS alloys.

Impact Tests

The aim of the impact test matrix is to define the influence of the alloys' heat treatment, especially lower austenitization temperatures, and the effect of strongly reduced boron contents on the embrittlement behavior, as well as to give ideas of the feasibility of welding and producing processes. Chemical composition of the investigated alloys is given in Tab. 1, heat treatment or temperatures of the technological treatments are listed in Tab. 2.

Tab. 1: Chemical composition of the irradiated alloys.

Alloy	Cr	C	Mn	V	Ta	W	P	S	B	N	Nb	Fe
	In wt.% →						In ppm →					
MANET-I	10.8	0.14	0.76	0.20			50	40	85	200	1600	balance
MANET-II	9.94	0.10	0.79	0.22			<60	<70	70	230	1400	
OPTIFER VII	8.38	0.09	0.37	0.21	0.07	1.03	36	25	4	263		
JLF1	8.70	0.11	0.52	0.18	0.08	1.91	120	30	<5	280		
F82H mod. F82H mod. HIP	7.68	0.09	0.16	0.16	0.02	2.17	20	10-20	4	60-80	100	

Tab. 2: Heat treatments of the irradiated alloys – impact specimens.

Alloy	Heat treatment	Welding/tech. processing
MANET-I	980°C/2h + 1075°C/0.5h + 750°C/2h	
MANET-II	950°C/2h + 1075°C/0.5h + 750°C/2h	1050°C/(1h 18MPa + 1h 7MPa) + 750°C/4h
OPTIFER VII	1040°C/0.5h + 750°C/2h	
OPTIFER VII	950°C/0.5h + 750°C/2h	
JLF1	1050°C/0.5h + 780°C/2h	
F82H mod.	950°C/0.5h + 750°C/2h	EB: 1040°C/0.5h + 750°C/1h (welding) + 720°C/1h TIG: 1040°C/0.5h + 750°C/1h (welding) + 720°C/1h

KLST charpy subsize specimens (3x4x27 mm) are subjected to instrumented impact tests. As a result, force-deflection curves are obtained, the further evaluation of these provides the impact energy, dynamic yield stress, ductile to brittle transition temperature (DBTT), and upper shelf energy (USE). Decontamination and testing of the specimens were finished in the reported period.

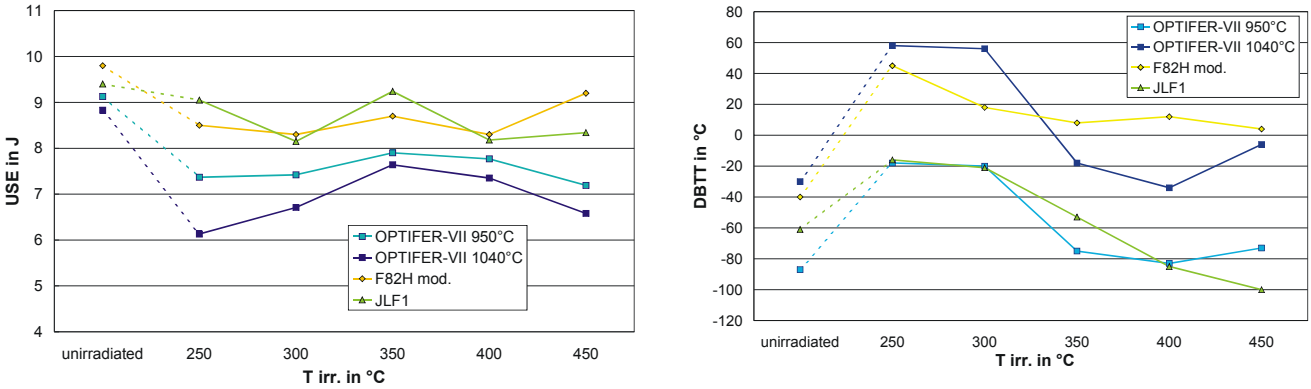

Fig. 1: USE and DBTT of ferritic-martensitic low-activation steels.

High upper shelf energy is found for all low-activation alloys at all temperatures (Fig. 1). Compared to earlier investigations, OPTIFER-VII steel in both heat treatments, JLF1, and F82H mod. are significantly better than the formerly investigated boron-doted steels. At low irradiation temperatures, worsening of the ductile-to-brittle transition temperature is significantly reduced, at irradiation temperatures of 350°C and above, no essential shift in DBTT is found for OPTIFER-VII and JLF1. OPTIFER-VII, JLF1 and F82Hmod. steels are in the range of the best LAAs formerly investigated, while JLF1 provides the best combination of high USE and low DBTT before and after irradiation. The influence of the heat treatment is not affected by irradiation: Both heat treatments of OPTIFER-VII show approximately the same shift in USE and DBTT. As can be seen in Fig. 1, the influence of the shifted austenitization temperature on the DBTT is even higher than the influence of irradiation.

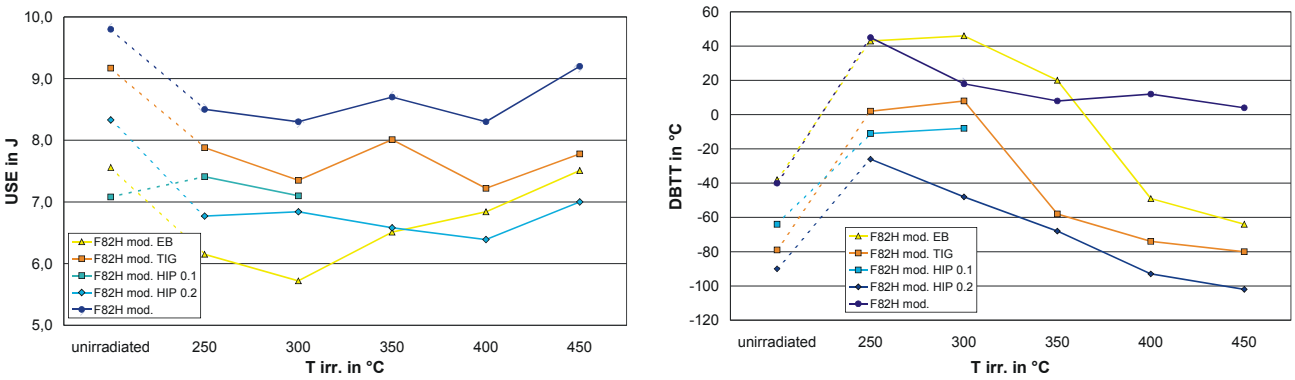

Fig. 2: Technological studies on F82H steels: USE and DBTT

Electron beam (EB) and tungsten-inert gas weldings (TIG) have been done on F82H mod. plate material. Charpy specimens were produced with the notch placed in the heat affected zone, as it was found out that this is the most critical zone for impact tests. Fig. 2 reports the results of the technological studies. The USE is before and after irradiation for about 1 J (TIG) or 2-3 J (EB) lower compared to the base material, but still in an acceptable range – taken into account that the DBTT is clearly better for the welded specimens. TIG welding seems to provide better results than EB welding.

Samples of F82H mod. HIP powder steel with two different notch root radius were subjected to PIE. They also show a for 2 J lower USE than the base material and a clearly better DBTT

(50-100°C lower) before and after irradiation. The increasing notch root radius lowers the DBTT for the HIP material. Both technological studies – weldings and HIP – raise hope for further investigations on these techniques.

Diffusion-welded specimens of MANET-II-Steel were included in the 2.4 dpa irradiation programme as a first investigation on the irradiation damage of diffusion weldings. The welding process was done at 1050°C, for 1 h at 18 MPa and for 1 h at 7 MPa. As it clearly can be seen (Fig. 3), even in unirradiated condition, the USE is far below the basic material's USE – which is found for the irradiated samples in the same range. However, the shift DBTT is not affected by this worsening – the transition temperature of base material and welded specimens is quite similar before and after irradiation. Improved welding processes on EUROFER-steel should give far better results in future, taken into account the better basic properties of newer materials.

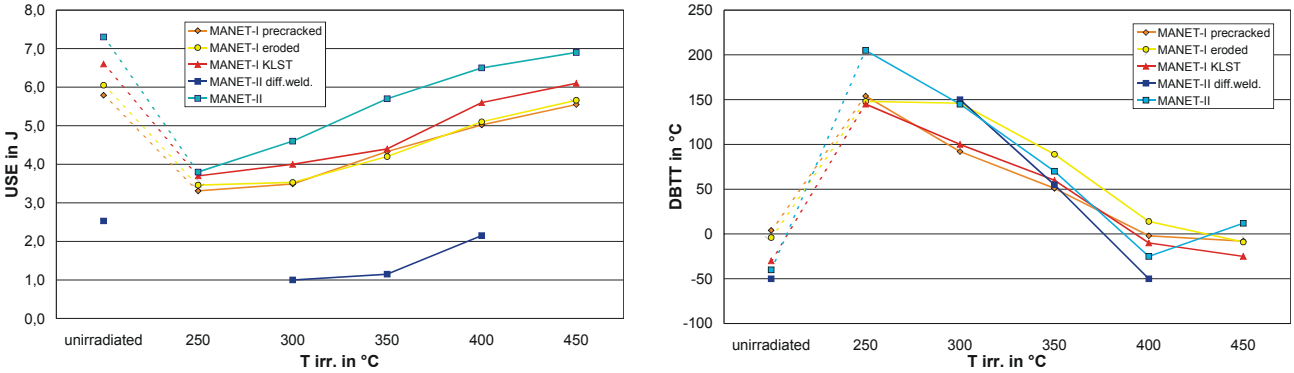

Fig. 3: USE and DBTT of MANET-Steel: diffusion-welded (2.4 dpa) and geometrical modifications (0.8 dpa)

In addition, geometrical modifications of the KLST-specimen (MANET-I) have been irradiated up to 0.8 dpa. Instead of a 1mm V-notch, a fatigue crack or an eroded slot of 1mm depth is manufactured in the specimens. As expected, the USE of the KLST-specimen is slightly higher because of their less critical stress concentration factor. The DBTT of the precracked specimens is after irradiation quite the same as the DBTT of the KLST-specimens – but it was for 40°C worse before irradiation. The DBTT of the eroded specimens is worse for up to 50°C than for the other geometries. Regarding the lower stress concentration factor (in comparison to the precracked specimens), this is astonishing. As a next step, the influence of the irradiation on the crack propagation will be investigated by analysing the surface of fracture and by subjecting the recorded force-deflection curves to fracture mechanics evaluation methods.

Tensile Tests

Series of tempered martensitic 7-10%CrWVTa alloys has been investigated by tensile tests before and after irradiation. The chemical compositions are given in Table 3 and the heat treatment in Table 4. First alloys were melted with B-contents between 40 and 60 ppm (OPTIFER Ia, II, and IV) and a second series as "B-free" alloys with about 2 ppm B (OPTIFER V, VI, and VII). Their carbon content was low and the nitrogen was strongly reduced to achieve a low DBTT. The heat-treatments of the second batches were carried out at higher and lower austenitization temperatures, as can be seen in Table 4. The steel F82H mod. was provided by JAERI/Japan. Circular tensile samples were taken parallel to the rolling direction of the as received material plates. The gauge length was 18 mm with a diameter of 3 mm. The tests were performed with a static mechanical tensile testing machine at a strain rate of 1% min^{-1}. The unirradiated specimens were also tested at RT (Room Temperature) and equivalent irradiation temperatures. The irradiated specimens were tested at their irradiation temperatures.

Tab. 3: Chemical composition of the irradiated alloys.

Elements	OPTIFER						F82H mod.
	Ia	V	II	VI	IV	VII	
Cr wt.% ↓	9.3	9.48	9.5	9.35	8,5	8.38	7.68
C	0.10	0.115	0.125	0.125	0.11	0.09	0.09
Mn	0.50	0.39	0.49	0.61	0.57	0.37	0.16
V	0.26	0.245	0.28	0.275	0.23	0.205	0.16
Ta	0.066	0.061	0.018	0.083	0.15	0.069	0.02
W	0.96	0.985	0.006	0.005	1.16	1.03	2.17
P ppm ↓	46	35	43	43	40	36	20
S	50	25	20	30	40	25	10-20
B	61	2	59	2	40	2	2
N	155	225	159	250	600	263	60-80
O	47	60	90	160	35	170	-
Ce	-	<100	<10	<100	-	<100	-

Tab. 4: Heat treatments of the alloys.

Alloy	Heat Treatment
OPTIFER Ia	950°C 0.5 h + 780°C 2 h
OPTIFER II	950°C 0.5 h + 780°C 2 h
OPTIFER IV	900°C 0.5 h + 750°C 2 h
F82H mod.	1040°C 38 min + 750°C 1 h
OPTIFER V, VI, VII	950°C 0.5 h + 750°C 2 h
OPTIFER V, VI, VII	1040°C 0.5 h + 750°C 2 h

The influence of irradiation is quite obvious by an increase of the tensile strength R_m in all materials at 250 and even more at 300°C, Fig. 4. For higher test- and irradiation temperatures the strength of all alloys decreases. The tensile tests with unirradiated specimens show the thermal effect as a continuous softening due to higher temperatures and the properties are nearly in the same range as for the irradiated samples at 400 and 450°C. The strong increase of strength up to 630 - 750 N/mm^2 between 250 and 300°C must be further discussed, possibly there was a higher irradiation temperature than 250°C as arranged. Total elongation A, a measure of ductility, also confirms the strengthening behaviour with lowest values up to 7 - 10% at 300°C, Fig. 5. The alloys without B (OPTIFER V, VI, and VII) show in the unirradiated state a higher strengthening than the B containing steels, but after irradiation the induced strengthening is lower. The data are concentrated in the lower scatter band. A striking effect by the different heat treatments could not be observed.

In the metallographic cuts the macroscopic structure with prior austenitic grains within the martensitic lath-structure is visible by LM (light microscopy). This structure is characteristic for this kind of steels. In the unirradiated state the materials had a hardness between 200 – 231 HV0.4. The increase of irradiation induced hardness up to 250 – 280 HV0.4 could be determined after irradiation at 250 – 300°C, and after 450°C irradiation within 190 – 220 HV0.4. The martensitic lath-structure could also be observed in the TEM (transmission electron microscopy). The lath boundaries are decorated with Cr-rich $M_{23}C_6$-precipitates. This structure was not changed by irradiation, Fig. 6. But there are some additional irradiation-induced effects: He-bubbles in the diameter of 2 – 10 nm with densities in the range of 10^{21} and 10^{23}. At lower irradiation temperatures, these He-bubbles are homogenously distributed

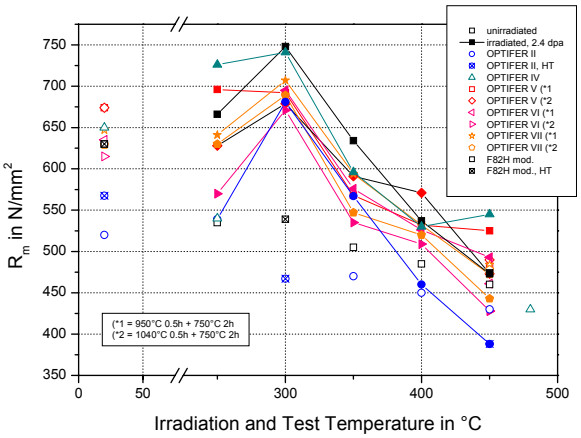

Fig. 4: Ultimate tensile strength R_m as a function of applied irradiation and test temperature.

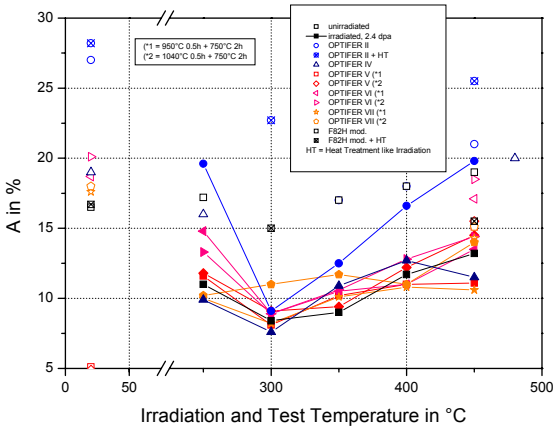

Fig. 5: Total elongation A as a function of applied irradiation and test temperature.

in the matrix, but at higher temperatures, they are mostly fixed in dislocations, Fig. 7. Dislocation loops were found in all materials only at lower irradiation temperatures of 250°C in densities of 10^{21}. The highest density of $5x10^{23}$ could be found in the steel F82H mod., Fig. 8. At these low temperatures, tiny α`-precipitates in a density of 10^{21} are existing in all materials, too. They are no more visible after irradiation temperatures between 350 and 450°C.

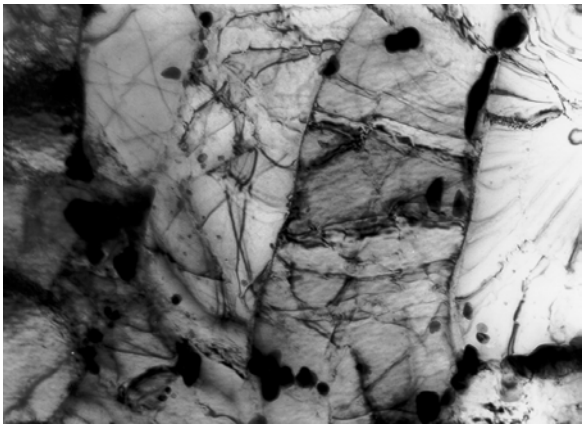

Fig. 6: Lath-structure in OPTIFER IV, 2.4 dpa, $T_{irrad.}$ = 450°C.

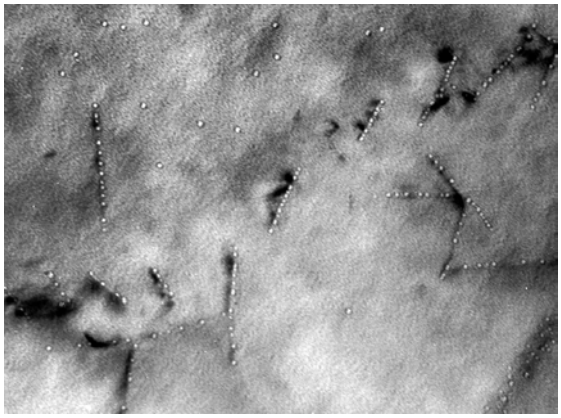

Fig. 7: He-bubbles in OPTIFER II, 2.4 dpa, $T_{irrad.}$ = 450°C.

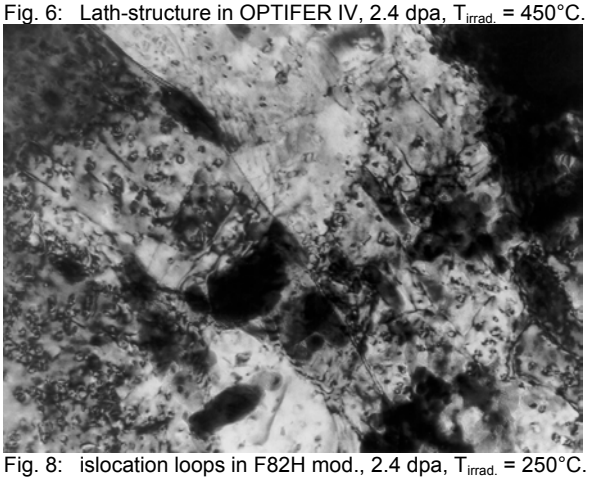

Fig. 8: islocation loops in F82H mod., 2.4 dpa, $T_{irrad.}$ = 250°C.

The correlation between the microstructure and the mechanical properties is quite obvious. The tensile tests of the unirradiated B-containing materials yielded higher strength than the samples without B. However, after irradiation the irradiation induced strength was lower in

comparison to the B-containing steels. This behavior can be related to the lower He-content. The different heat treatments did not show any tendency in the scatter band of the tensile data.

The dynamic tests are much more sensitive to changes in these alloys [2]. The B generates more He-bubbles and with the higher austenitization temperature the grains will be coarser. The tendency to a better DBTT is recognizable in the B-free materials. A further factor for the decrease of DBTT is the finer grain after 950°C austenitization. Regrettably, the USE could not be retained in the same high level. USE decreased due to B-free alloys and the finer grain size due to the lower austenitization temperature, too. Smaller grain sizes have an increase in the hardness. This may be a reason for the loss in ductility at higher impact test temperatures.

The irradiation induced strengthening and hardening of the materials are in clear coherence to the changes in the microstructures. He-bubbles, dislocation loops, and α`-precipitates affects as hardening mechanism. The dislocation movements will be blocked and the strength increases. At higher irradiation temperatures, higher diffusion processes are possible and the He-bubbles are concentrated in few dislocations. The other irradiation induced microstructural changes as dislocation loops and α`-precipitates are dissolved at these high temperatures and do not constrain the movement of the dislocations.

Staff:

J. Aktaa
B. Dafferner
P. Graf
S. Lautensack
E. Materna-Morris
H. Ries
R. Rolli
O. Romer
H.-C. Schneider
H. Zimmermann

Literature:

[1] H.-C. Schneider, B. Dafferner, J. Aktaa: Embrittlement behaviour of low-activation alloys with reduced boron content after neutron irradiation. Journal of Nuclear Materials, Vol. 321/2-3 pp 135-140, October 2003.

[2] E. Materna-Morris, H.-C. Schneider, B. Daffener, R. Rolli, O. Romer, and A. Möslang, Mechanical Properties and Structural Analysis of Martensitic Low-activation Alloys After Neutron Irradiation, 20th IEEE/NPSS SOFE, October 14-17, 2003, San Diego, USA

TW2-TTMS-001a D16
Extrapolation of RAFM Irradiation Behaviour to High Doses and High He-Contents by Modeling

Effect of Irradiation Dose and Particle Morphology on Ductility and Impact Properties of RAFM and ODS-RAFM Steels

The effect of particle morphology and grain refinement to the nano-sized level on strength, ductility as uniform ε_u and fracture strain ε_f as well as Charpy impact behaviour of ODS-RAFM (7-9CrWVTa) steels and additionally ODS-Ta-W alloys have been analysed [1,2] and modelled [3,4]. Particularly, the volume content f_v and mean size d_p of nano-sized (>2 nm) Y_2O_3-oxide particles versus property relations have been considered in dependence of grain refinement to grain sizes of $d_K \geq 10$ nm and a superimposed strengthening by solid solution and irradiation-induced defect formation. For ODS-Ta-W alloys, additional to irradiation strengthening, the tungsten alloying effect has been analysed [1]. As shown from analytical and numerical results, the uniform ductility ε_u of ODS-RAFM steels increases distincly by grain refinement and dispersion hardening (DIGD), particularly in the region of mean volume contents f_v above a critical value f_v^c [4]. For DIGD an optimum particle size $d_p^* \cong 6$ -12 nm and also a lower limiting grain size $d_{K,c} \geq 50$ nm appears corresponding to a critical yield strength σ_L, which both increases with increasing volume content f_v. For nano-sized grains below $d_K \leq d_{K,c}$, unifrom ductility drastically reduces by the combined strong reduction of fracture strain and then finally disappears at a critical nano-grain size $20 \geq d_{K,f} \leq d_{K,c}$, where strength achieves the ductile fracture stress σ_{fd}. Combined with the grain refinement, however, the fracture stress itself might increase. Additionally, the influence of ferritic or martensitic structure of ODS-RAFM together with particle size and area distribution upon ductility have been examined [5]. As shown by this model study such inhomogeneous particle distribution reduces yield strength and distinctly also ductility. Predicted shifts of the ductile-to-brittle transition temperature DBTT and upper shelf energy USE of Charpy-impact tests by dispersion and irradiation strengthening are given in Fig. 1b for stress-induced fracture appearance assuming constant dynamic and ductile fracture stresses.

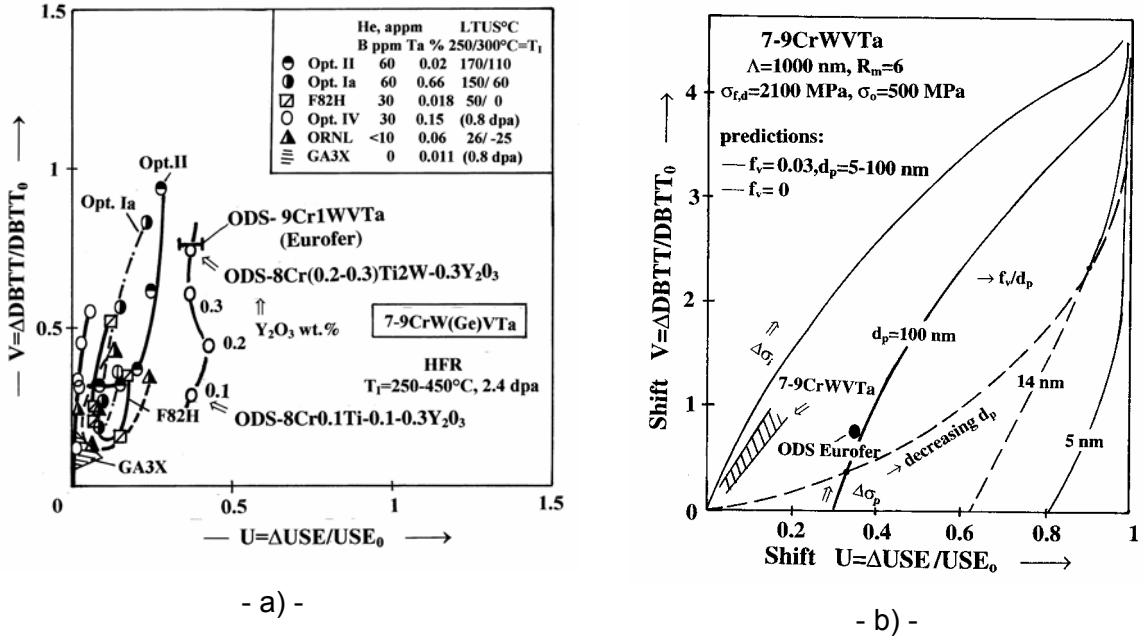

- a) -

- b) -

Fig. 1: Effects of irradiation and particle strengthening on DBTT and USE shifts for rAFM and ODS-RAFM steels. Comparison of predictions b) with results a).

These are compared with experimental results observed on irradiation strengthened RAFM (T_I=250-450 °C, 2.4 dpa) together with various ODS-RAFM steels including ODS-Eurofer in as-received condition (Fig. 1a). The measured dispersion hardening-induced DBTT shifts are indeed comparable to these observed by irradiation defect strengthening $V_i=\Delta DBTT/DBTT_o \leq 0.9$, indicating similar dynamic fracture processes. Contrary, the ductile impact energy USE similar as the fracture strain decreases quite stronger by particle strengthening compared to irradiation defect hardening due to the distinct particle-enhanced work-hardening [3]. Their relative reductions $U_i=\Delta USE/USE_o \leq 0.25$ and $U_p \approx 0.35$-0-4 for 0.1-0.3wt.%Y_2O_3 remains, however, distinctly smaller then those of DBTT. The predictions for constant ductile/dynamic fracture stresses and $f_v/d_p=3\ 10^{-4}\ nm^{-1}$ are only little larger than experimental results of ODS-Eurofer at 0.3wt.% Y_2O_3 and describe the influence of particle morphology. A combined microstructural-induced increase of both dynamic and ductile fracture stresses caused by the heat treatment would decrease both shifts V and U.

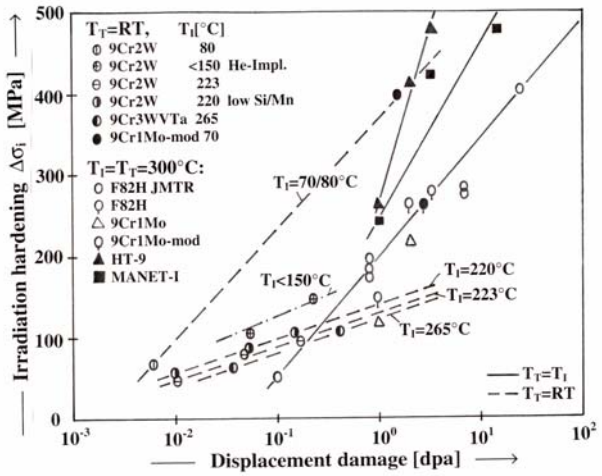

Fig. 2: Irradiation defect strengthening in dependence of logarithmic dose for various RAFM steels at T_I=T_T=300°C.

Moreover, predicted dependence of strength, ductility and Charpy-impact properties on the displacement damage (dpa) have been compared with results obtained from natural boron-doped RAFM and 9-12CrMoVNb steels, irradiated in HFR at T_I=70-475°C to 0.2-2.4(15) dpa. About ≤ 85 appm helium were additionally generated via the $^{10}B(n,\alpha)^7Li$ transmutation reaction. The observed low irradiation dose data have been extrapolated to fusion relevant high doses of up to 100 dpa by models. According to Figs. 2, 3, irradiation strengthening $\Delta\sigma_i$ as well as DBTT increase logarithmically with increasing irradiation damage at lower irradiation and test temperatures $T_{I,T} \leq$ 300°C. That is more pronounced for the conventional, higher chromium 10-12CrMoVNb as for RAFM steels and is clearly related to the chemical composition esp. the Cr, N, C and B content. It directly demonstrates that the DBTT shift is mainly caused by the damage(dpa)-induced irradiation strengthening but might addionally comparably weaker influenced by combined small microstructural-induced changes of the dynamic fracture stress. Such logarithmic dose dependences

$$\Delta\sigma_i = A \ln(dpa) + B \qquad DBTT = R_1 \ln(dpa) + R_2 \qquad (1)$$

are predicted for interstitial-driven defect (loops, clusters) nucleation together with stress-induced fracture, neglecting irradiation-induced precipitate formation. This irradiation strengthening law does not markedly deviate from the frequently reported $\Delta\sigma_i \sim (dpa)^{1/4}$ dependence at lower doses. The constants A, B and R_1, R_2, given in Tab. 1 for various 7-12Cr steels at T_I=T_T=300 °C have clear physical meanings [6]. Slope R_1 decreases with decreasing defect nucleation rate, loading rate and strain rate sensitivity $m=\delta\ln\sigma_y/\delta\ln\varepsilon`$ of strength and increasing dynamic fracture stress. Parameter R_2 otherwise remains independent on defect nucleation. A structural-induced embrittlement as could be result from high helium and hydrogen contents would increase both R_2 and R_1. At T_I=250 °C, the 10-12CrMoVNb steels with R_1=75.2 to 78 °C, R_2= 76 to 131 °C show clearly higher R_1 and R_2 values compared to 7-9CrW(Ge)VTa steels, where R_1=16 to 62 °C and R_2=-38 to 58° C. Within both groups of steels particularly the parameter R_2 is increased with increasing boron/helium content. When a very high critical defect density is achieved, however, as observed in austenitic Cr/Ni steels for $\Delta\sigma_{i,s} \leq 750$ MPa, saturation of the irradiation strengthening is expected too for 10-12CrMoVNb and RAFM steels at $T_{I,T} \leq$ 300 °C due to

strong short-range defect interactions. By fitting experimental results, corresponding DBTT values of 2 to 243°C are predicted for various RAFM steels for 100 dpa at T_I=300 °C as shown in Tab.1, with the lowest value for the ORNL steel. Distinctly higher DBTT≅ 250 to 361 °C values are observed for 10-12CrMoVNb steels with higher B content. Contrary, at higher $T_{I,T}\geq$ 350°C, the irradiation-induced strengthening $\Delta\sigma_{i,s}\leq$ 480 MPa and DBTT-increase clearly saturates above ≈6 dpa in accordance with predictions taking account of a diffusion-induced defect annihilation [6]. The saturation values sensitively decrease with decreasing T_I described by an activation energy of about 0.7 eV. Fig. 4 shows by the plot DBTT vs. $(dpa)^{3/4}$ the comparison of predictions with corresponding results of various 7-12Cr steels at the higher T_I=400 °C (450 °C). It is also compared to the behaviour at lower T_I=250°C for MANET I,II steels. The deduced saturation $DBTT_s$ values vary from -58 to 20 °C and are largest for the Ge-alloyed steel Opt.II. For the 7-9Cr(1-2)WVTa steels ORNL, F82H, Opt.Ia similar low saturation values $DBTT_s \cong$ -10 to -20°C are observed still below RT.

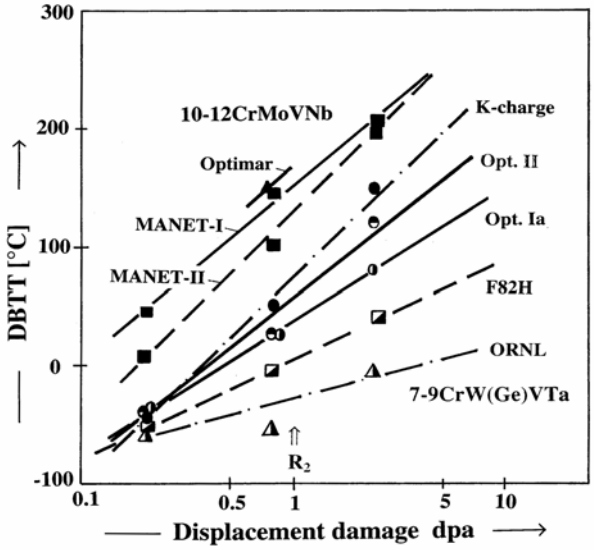

Fig. 3: DBTT vs. ln (dpa) for various RAFM and MANET-I,II steels at T_I=T_T=250°C and ≤ 15dpa.

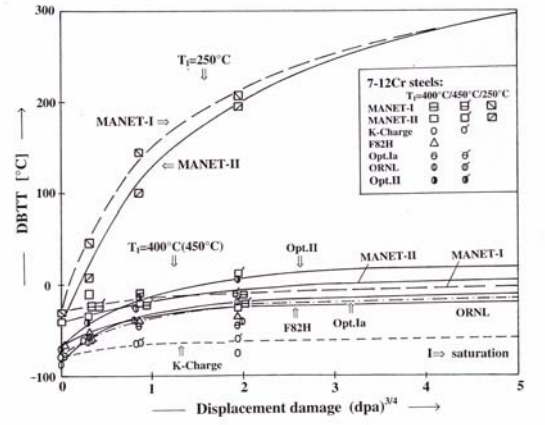

Fig. 4: Comparison of the observed dependence DBTT vs. $(dpa)^{3/4}$ with predictions for various 7-12Cr steels at higher T_I=400 °C (450 °C) and additionally at the low T_I=250°C for MANET-I,II steels.

Generated ≤ 85 appm helium contribute to an additional DBTT shift only weakly via a weak increase of thermal strengthening by enhanced small defect cluster formations at lower irradiation and test temperatures of $T_{I,T}$≈70-250 °C. Helium, however, strongly enhances fracture strain and impact energy USE reductions in addition to damage dpa by a distinct decrease of ductile fracture stress due to enhanced localised flow and microcrack nucleation, especially at higher He(^{10}B) contents and arround of $T_{I,T}$≈300 °C, respectively in steels with higher DBTTs. This is caused by the localised helium and ^{7}Li generation due to preferential enrichment of boron into coarser $M_{23}(B, C)_6$ boroncarbides [3] participating on the ductile fracture process by enhancing micro-crack nucleation.

Taking into account eq. 1, the dose dependence of engineering uniform ductility of RAFM and ODS-RAFM steels can be calculated by the deduced analytic expression

$$\varepsilon_{u,n} = 1 - \{1 - [((1 + 168\ y^2)^{1/2} - 1)/(14\ y)]^2 \}^{-1/12} \qquad (2)$$

$$y^2 = (\Delta\sigma_{\varepsilon,m,o} / \sigma_y)^2 [1 + K \Delta\sigma_p\ f_v^{3/2}],$$

valied for RT with the strength $\sigma_y = \sigma_o + \Delta\sigma_p + A\ \ln(dpa) + B$ and K=0.9554 $(MPa)^{-1}$, whereby $\Delta\sigma_{\varepsilon,m,o}\cong$ 300 MPa is the maximum strain hardening of initial, particle free material. Accordingly, uniform ductility ε_u continuously decreases with increasing dose dpa and disappears if strength $\sigma_y=\sigma_{fd}$ achieves ductile fracture strength. Particle strengthening $\Delta\sigma_p$~

$f_v^{1/2}/d_p$ otherwise due to DIGD additionally shifts the $\varepsilon_{u,n}(\sigma_y)$ dependence to distinctly higher ductilities and strengths, dependent on f_v and d_p. By eq. 2, the uniform ductility of irradiated ODS-RAFM is also defined, assuming particles and heat treatment do not change the ductile fracture stress. For the dose dependence of fracture strain $\varepsilon_f = -\ln(1-Z)$, respectively reduced area of fracture Z of RAFM steels, the dependence

$$Z = 1 - \{1 - [(1- (1 - Z_o)^{12}) [(1 - \sigma_y /\sigma_{fd})^p]^{2L}] \}^{1/12} \quad (3)$$

is observed at RT with $p \approx 1$ and $L \approx 1$. Parameter Z_o describes the extrapolated reduced area of fracture to $\sigma_y=0$, which decreases with increasing particle hardening and additional depends on strain rate sensitivity m. Thus, fracture strain Z decreases more stronger with increasing particle strengthening compared to damage dependent irradiation hardening $\Delta\sigma_i$(dpa) and disappears at $\sigma_y=\sigma_{fd}$.

Table 1: The deduced coefficients $R_{1,2}$ and DBTT values at 50, 100 dpa for various 7-12Cr steels at the low $T_I=T_T=300°C$.

Steel	R_1[°C]	R_2[°C]	for 50 dpa DBTT [°C]	for 100 dpa DBTT [°C]	B [ppm wt]	Type
MANET-I	52	125	327	361	85	10-12CrMoVNb
MANET-II	53	92	300	337	70	"
K-Charge	48	32	218	250	20	"
Opt. II	45	31	212	≈243	60	9Cr1.2GeVTa
Opt. Ia	≈33	≈10	≈140	≈160	60	7-9CrWVTa
F82H	16	-25	-40	≈150	30	"
ORNL	10	-44	-5	2	<10	"

Staff:

D. Preininger

Literature:

[1] D. Preininger, „ Modeling and analysis of grain refinement effects on strength, ductility and impact behaviour of ODS-(7-13)Cr and ODS-Ta-W alloys". European Congress of Advanced Materials and Processes, EUROMAT 2003, 1-5. Sept., 2003, Lausanne, Switzerland; abstract in: http://www.euromat2003.fems.org .

[2] D. Preininger, J. Nucl. Mater. 307-311(2002) 514.

[3] D. Preininger, „Modeling of Strength, Ductility and Impact Behaviour of ODS Ferritic-Martensitic 7- 13Cr steels". Proceedings of the Materials Week, March 2003, CD-ROM, see also http://www.materials week.org .

[4] D. Preininger, „Ultragrain refinement effects on strength, work-hardening and plasticity of dispersion strengthened bcc and fcc alloys". 14. Symposium Verbundwerkstoffe und Werkstoffverbunde, 31.6.-4. 7.2003, Wien, Tagungsband: 1.Metall-Matrixverbundwerkstoffe (Grundlagen), Wiley-VCH Verlag Gmbh/DGM, Weinheim, p.248/256 , Eds. H. P. Degischer.

[5] D. Preininger, „Effect of particle morphology and microstructure on strength, ductility and impact behaviour of ODS (7-13)Cr steels"; presented at ICFRM-11.

[6] D. Preininger, Irradiation dose and helium effects upon strength, tensile ductility and Impact behaviour of boron-doped martensitic 7-12Cr steels, Internal report, will be published.

TTMS-002
Metallurgical and Mechanical Characterisation

TW1-TTMS-002 D19
TW2-TTMS-002a D19
Creep Fatigue Testing on EUROFER

1. Objectives

A structural component like a Test Blanket Module (TBM) is subjected during service to alternating thermal and mechanical stresses as a consequence of the pulsed reactor operation. Since the operating temperatures of a future DEMO reactor increase due to economic considerations, the knowledge of the reasons of the creep fatigue endurance of Reduced Activation Ferrite/Martensite (RAF/M) steels like F82H mod. and EUROFER 97 becomes more important.

2. Microstructural evaluation

Structural materials, like the above mentioned RAF/M steels, subjected to cyclic strain situations mostly soften. These phenomena illustrate the inadequacy of using tensile properties in fatigue based design. The initial high strength of hardened steels can be seriously compromised even after a low number of loading cycles, reducing their original strength and load carrying capabilities. Normalized and tempered ferritic/martensitic steels exhibit attractive tensile strength properties up to approximately 600°C. These properties, in addition to their ability to resist the effects of high doses of irradiation, focused the interest on these alloys for first-wall and blanket structure components of fusion reactors.

Fig. 1:Tempered matensite structure.

The 9 – 12 % Cr alloys subjected to the standard normalizing and tempering treatment are micro structurally stable during subsequent ageing at temperatures up to 600°C for periods up to 1000 hours. The high dislocation density and carbide distribution characteristic of tempered martensite remain essentially unchanged.

Carbides, presumably $M_{23}C_6$ ranging from 0.05 to 0.5 μm in size, were distributed preferentially along lath and prior austenitic grain boundaries. It should be noted that a high density of dislocations produced during quenching of the steel remains after tempering.

However, under cyclic loading conditions, dislocation annihilation and rearrangement occur thereby leading to break the martensite laths and to develop an equiaxed substructure.

TEM micrographs have shown that a well-defined dislocation cell structure is formed during cyclic deformation, gradually replacing the lath martensite structure. This process is already well established at the beginning of the test.

The most striking result during the reporting period was observed by comparing the cyclic softening rate of the RAF/M steels with that of commercial steels. It is proposed that the cyclic softening rate observed in the RAF/M steels depends on the M_s (Martensite start) temperature. A lath martensite structure with a high density of tangled dislocations within their laths is characteristic of steels with higher M_s temperatures. Chemical composition is the main factor affecting the M_s temperature of the steel. RAF/M steels such as EUROFER 97 and F82H mod. with a lower amount of C, Ni, Mo and Nb are steels with a higher M_s temperature. The high dislocation density structure of the lath martensite is stable against thermal treatment but not against cyclic loading. On cycling, martensite laths quickly become untidy loosing and releasing a significant amount of free dislocations per cycle causing a faster cyclic softening.

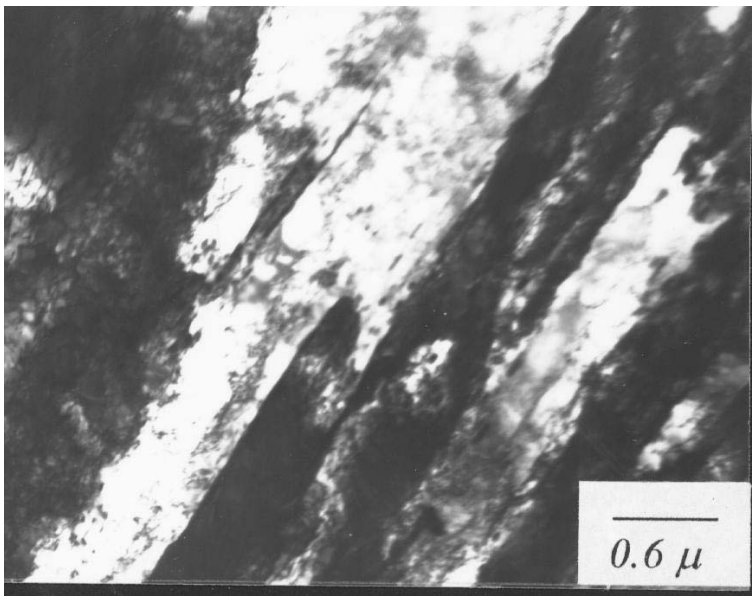

Fig. 2: Martensite lath strcture prior to cyclic deformation.

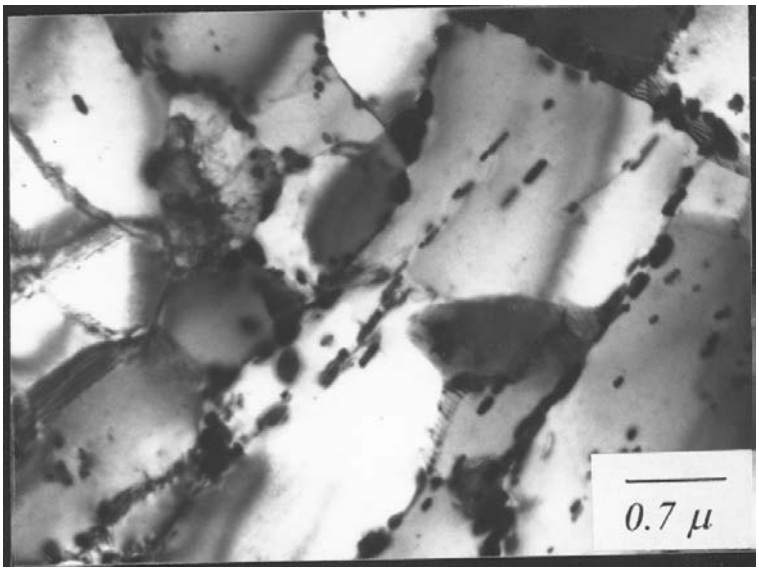

Fig. 3: Dislocation cell structure after cyclic deformation.

Staff:

J. Aktaa
M. Klotz
C. Petersen
M. Pfeifenroth
R. Schmitt

Literature:

A.F. Armas, C. Petersen, R. Schmitt, M. Avalos, I. Alvarez-Armas: „Mechanical and microstructural behavior of isothermally and thermally fatigued ferritic-martensitic stainless steels", Journal of Nuclear Materials, vol. 307-311 (2002) p. 509-513.

C. Petersen, D. Rodrian: "Thermo-mechanical fatigue behavior of reduced activation ferrite/martensite stainless steels", Journal of Nuclear Materials, vol. 307-311 (2002) p. 500-504.

TTMS-003
Compatibility with Hydrogen and Liquids

TW1-TTMS-003
Corrosion Testing in Picolo Loop
Corrosion Behaviour of EUROFER 97 in Flowing Pb-17Li

1. Introduction:

In a future fusion system of the water cooled liquid lead (WCLL) type reduced activation ferritic-martensitic (RAFM) steels are considered as structural materials. The new alloy EUROFER 97, a 9 Cr W V Ta alloy, was developed on base of the experience with RAFM alloys e.g. Optifer type. Meanwhile the thermal and mechanical behaviour was examined [1]. The compatibility with the eutectic lead-lithium cooling and breeding medium of the composition Pb 87 at.% and Li 17at.% is outstanding. In the PICOLO loop [2] cylindrical samples (diameter 8 mm, length 31 mm) made from EUROFER 97 were exposed to the corrosive liquid metal Pb-17Li. The aim of this corrosion tests was to provide a data base on EUROFER 97 corrosion in fusion relevant liquid metal Pb-17Li and to compare these results with the previously examined FM alloys MANET I, Optifer IVa and F82H-mod. [3].

2. Experimental:

The samples for the corrosion tests were fabricated by turning from plate material – alloy produced by Böhler Edelstahl GmbH, Austria (thickness 14 mm, charge No. E 83698, plate No. 14, lot No. 249). The shaping process was followed by fine grinding. All samples showed a bright metallic surface. The average roughness was measured to be about Ra = 0.5 µm, maximal peak values in roughness exceeded, determined by DIN-instructions, R_z = 2.4 µm. The austenitization conditions of the bar materials were 980°C, 27 min and cooling in air. Tempering was done at 760°C for 90 min with subsequent air cooling. The fabricated samples were cleaned in an ultrasonic bath (acetone) and dried before mounting into PICOLO loop. Loading and unloading of the test samples, which were screwed together to a stack of 12 pieces, was carried out in an Ar-glove box connected on top of the loop. The atmosphere of the glove box is purified to guarantee an O_2 level of 1 vpm. The inner diameter of the test section is 16 mm, thus the concentrically mounted samples are surrounded by a Pb-17Li flow of 4 mm in thickness. The chemical composition of the used EUROFER 97 samples together with the above mentioned other FM steels is given in Tab. 1. Specimens were taken out of the loop about every 1500 hours and replaced by fresh ones. The test temperature in the hot leg was about 480 ± 5°C and the lowest one in the loop 350°C. The EUROFER 97 samples were analysed by standard metallographic techniques and by applying SEM and EDX methods. Additionally diameter measurements on fresh and corroded samples were carried out to determine corrosion rates.

Table 1: Analyses of FM steels used in PICOLO loop corrosion tests.

Steel	Cr	Mn	V	W	Ta	Mo	C	Ni
MANET I	10.6	0.82	0.22	--	--	0.77	0.13	0.87
Optifer IVa	8.5	0.57	0.23	1.16	0.16	--	0.11	--
F82H-mod.	7.7	0.16	0.16	1.95	0.02	--	0.09	--
EUROFER 97	8.82	0.47	0.20	1.09	0.13	--	0.11	0.02

3. Results of EUROFER 97 attack:

3. 1 Optical microscopy:

The metallographic pictures didn't show remaining unaffected surface fractions at any sample. All test pieces were covered by a Pb-17Li skin which were in good contact with the base alloy. It is concluded from these analyses that wetting of the complete sample was finished at least at test duration of 1516 h, the time of removing the first sample. In Fig. 1 the micrographs of the first extracted test sample is shown. Two changes in surface structure are evident. First an increase in surface roughness is visible. The dimensions are in the 1 µm range for depth and periodicity. Second, at some positions a concave feature of the surface with depth up to about 10 µm can be detected with long periodicity (some 100 µm). The different erosion depths may be correlated to start of corrosion at a different timescale due to delayed wetting or corrosion attack. The microstructure found in etched status give hints that

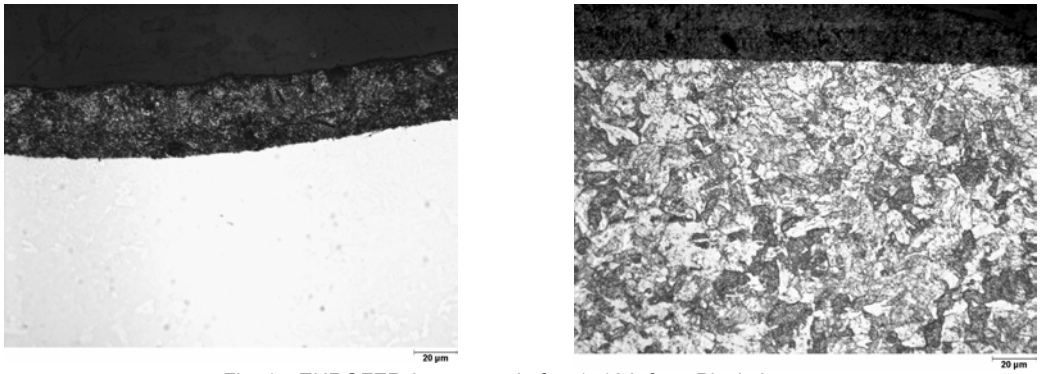

Fig. 1: EUROFER 97 removed after 1516 h from Picolo loop

Left:	unetched	Right:	etched
Black:	Resin	Black:	Pb-17Li scale
Structured black:	Pb-17Li scale	Structured:	EUROFER 97
Gray:	EUROFER 97		

corrosion attack seems to be stronger at formerly austenitic grain boundaries and at positions with high grain boundary amounts. However this fact has to be proven in additional test series and was not a goal of this corrosion campaign. In general the surface structure of all analysed samples did not change much in roughness and global appearance. However, at some local positions (sometimes only one time on the hole analysed surface) reduced corrosion attack was visible.

3.2 SEM EDX analyses:

The SEM/EDX analyses were performed with the samples prepared for optical microscopy. However, the surfaces were freshly polished with diamond additives down to the size of 1 µm under flowing water for short time. This procedure was chosen to minimize Pb contaminations on the steel surfaces coming from the adherent Pb-17Li scale and to achieve mostly flat surfaces due to the fact that edge rounding can affect EDX counting rates by shadowing. Fig. 2 shows the EDX measurements together with the corresponding SEM picture of a sample exposed for 3011 h to the flowing liquid metal. This sample exhibits a nearly perfect cylindrical shape. The surface roughness is of the order 1 µm. The adherent Pb-17Li scale shows a not uniform brightness in the SEM picture. The dark positions can be correlated to low emissive positions e.g. coming from voids or embedded particles with low Z (steel additives). The boundary steel to Pb-17Li is similarly shaped as the boundary Pb-17Li to embedding material in contrast. This may be a hint, that diffusion of Pb into steel is not present. Also by SEM analyses no diffusion of lead into the steel was detected.

The path for performing the element analyses is marked by crosses ranging from the embedding resin to steel. Under investigations were the elements Fe, Cr, Mn, W (the main

steel components) and Pb together with O. The measurements were analysed on wt.% base. Inside of the EUROFER alloy concentrations were constant. Small concentrations of the steel components Fe, Cr, Mn and W were detected in the adherent scale. The measured values were about 2 % for Fe and Cr, 1 % for W and 0.1 % for Mn. However, the signal was not constant in the Pb-17Li scale. This result indicates that particles are embedded due to the fact that the values are above the solubility limits for these elements. Furthermore, it can be concluded, that an adherent not moving scale covers the samples during the tests. Corrosion mechanism has to be attributed to leaching out of these elements under formation of a porous corrosion zone.

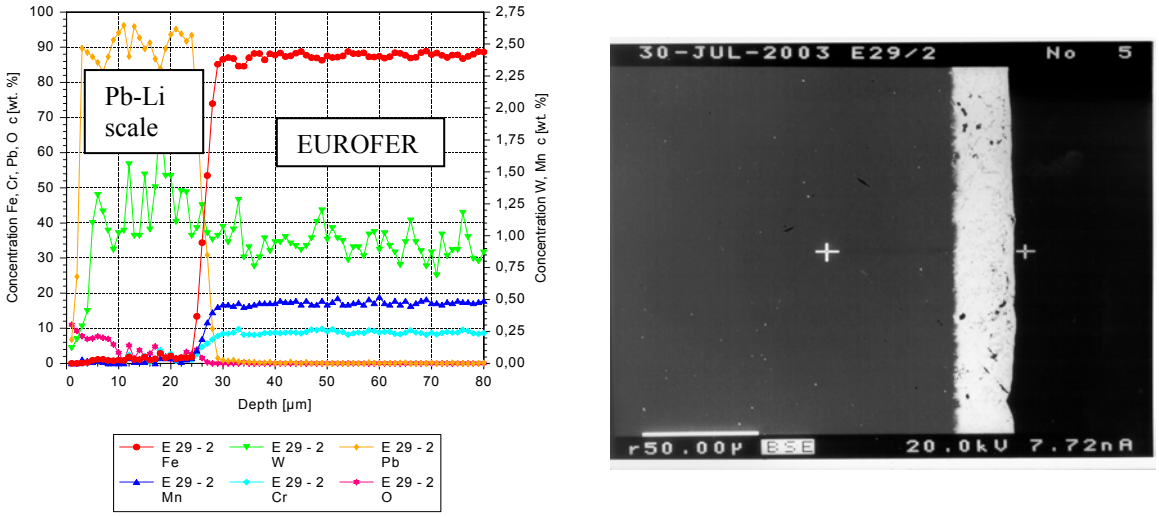

Fig. 2: SEM and EDX analyses of EUROFER 97 exposed for 3011 h to Pb-17Li at 480°C.

3.3 Corrosion rate determined from diameter reduction:

Corrosion rate in dependence of exposure time was determined by evaluation of diameter changes. For this analysis all samples were mechanically measured before inserting into PICOLO loop with accuracy of +/- 2 µm. The diameters of removed samples were determined from the metallurgical cuts by a microscopic method with errors in the same range. In general, no characteristic deviations from the cylindrical shape could be found by diameter determinations performed rectangular to each other. The obtained maxima of radii reductions by corrosion are given in Fig. 3.

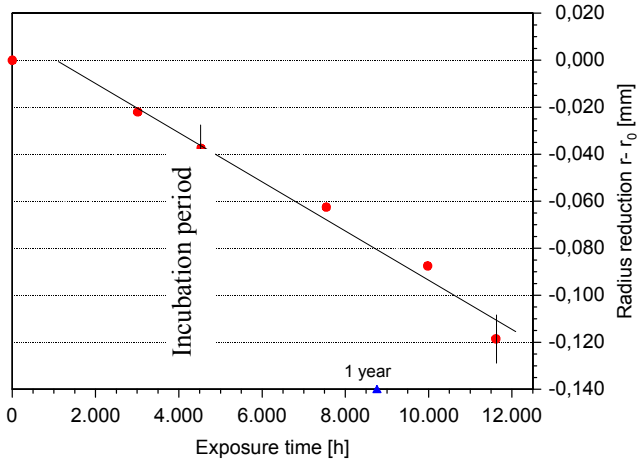

Fig. 3: Exposure of EUROFER 97 rods to flowing Pb-17Li.

The graph shows a linear correlation of corrosion rate and time. The obtained dependency underlines the expected corrosion mechanism of corrosion by dissolution – a linear phenomena – and the existence of effects responsible for delayed corrosion attack in the short term behaviour triggered by delayed wetting or slow dissolution of passivating oxide scales. The performed tests with durations of up to about 1.5 years - about twice the time of tests performed with the previously examined FM-alloys – improve the reliability of describing the corrosion of FM-steels as linear phenomena. The duration for delayed corrosion attack, the so called incubation time, can be estimated to be about 1000 h.

4. Comparison to other RAFM alloys:

Ferritic-martensitic steels (MANET I, Optifer IVa, F82H-mod. and EUROFER 97) were investigated In the PICOLO loop under similar conditions for durations up to about 12000 h. All the steel tests is common, that corrosion performs at long exposure times by dissolution of alloying elements. The steel components (not completely dissolved particles coming from the corrosion zone) could be detected in a Pb-17Li stabilized surface scale of about 20 µm at a flow rate of 0.3 m/s. In none of the tests Pb-diffusion into the matrix was found.

The microstructural analyses showed that corrosion attack is of uniform nature for EUROFER 97 as well as for the other FM steels. Effects, which can cause strong inhomogeneous attack due to passivating scales during short term exposure, as mentioned in results of MANET I tests [3], were not detected. Areas with visible corrosion attack exhibit for all FM-steels similar looking and structure. EUROFER 97 has of all tested alloys the smallest grain size of previously formed austenite. The results of maximal corrosion attack (surface erosion depth vs. time) are given in Fig. 4. The lines for each alloy type were inserted by optical fitting and shall help to illustrate the time dependency. Corrosion of the four alloys can be described by a linear time correlation and the fitted lines are nearly parallel. The EUROFER 97 line give hints on an existing incubation period.

The corrosion line for EUROFER 97 is clearly positioned below the curves for the earlier examined alloys. The advantage of EUROFER 97 in corrosion rate may be valued to be in the range 10 to 20 %. The reduced corrosion rate of EUROFER 97 compared to the other FM-steels can not be explained by chemical composition of the main alloy elements. It is proposed at the moment that minor elements e.g. Ta, N or lower impurity levels and thus grain boundary effects may be responsible for the differences. However this topic lies far a head of the planned work program for this campaign and will need additional tests.

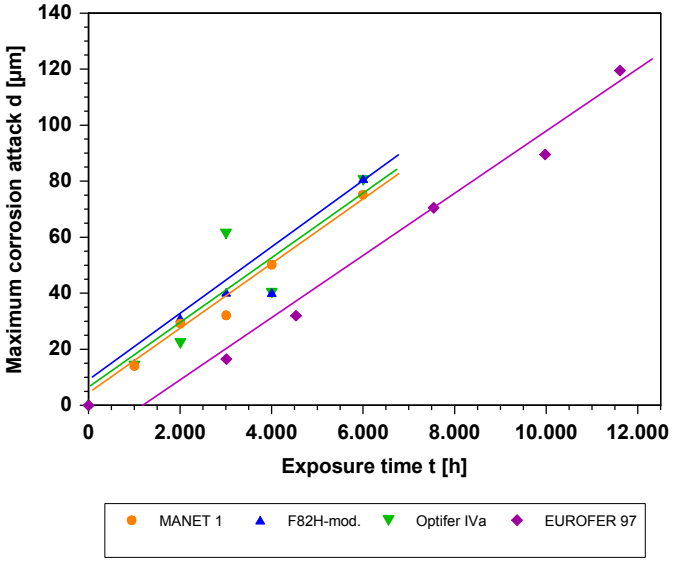

Fig. 4: Comparison of corrosion rates of FM-steels.

5. Conclusions:

The corrosion behaviour of EUROFER 97 was examined in flowing Pb-17Li using PICOLO loop. The detected corrosion rate per year is of the order of about 90 µm at 480°C. The time dependency can be said to be linear neglecting possible incubation effects during beginning of the tests. The corrosion attack seems to be a little bit more pronounced at positions with high density of martensitic grain boundaries and also at locations of former austenitic ones, however these features as well as the presence of ferritic grains and incubation effects need more detailed experiments and evaluation as it is possible by the present tests. Overall EUROFER 97 shows compared to the other FM steels uniform corrosion behaviour and smaller corrosion rates. The corrosion tests with EUROFER 97 run to about 12000 h that is twice the durations of earlier tests. The reliability in time dependence of corrosion rates and their extrapolations could be increased due to this fact for all FM-steels. The reduced corrosion attack of EUROFER 97 compared to the other FM-steels may be due to the finer grain size and microstructure or the higher Ta content similar to the arguments given for its better ageing resistance. Additional effects – topics in future tests - may come from the lower

impurity levels and thus from smaller amounts of precipitations in the grain boundaries or higher N concentrations which are known to reduce diffusion.

Staff:

J. Konys
W: Krauss
J. Novotny
Z. Voss

Literature:

[1] R. Lindau, A. Möslang, M. Schirra; Thermal and mechanical behaviour of the reduced-activation-ferritic-martensitic steel EUROFER, Fusion Eng. Design., 61-62, 2002, 659

[2] H. U. Borgstedt, G. Drechsler, G. Frees, Z. Perić; Corrosion testing of steel X 18 CrMoVNb 12 1 (1.4914) in a pumped loop, J. Nucl. Mat., 155 – 157, (1988), 728

[3] H. Glasbrenner, J. Konys, H. D. Röhrig, K. Stein-Fechner, Z. Voss; Corrosion of ferritic-martensitic steels in the eutectic Pb-17Li, J. Nucl. Mat., 283-287, (2000), 1332

[4] R. Schneider et al., Metallurgie an den Grenzen höchster Reinheitsgraden und niedrigster Spurenelementgehalte, BHM 145, (Jg 2000), Heft 5, 199

Publications:

EFDA final report Deliverable D 14:
TW1-TTMS-003, Corrosion behaviour of EUROFER 97 in flowing Pb-17Li

ICFRM 2003, Kyoto:
Corrosion testing of EUROFER 97 in Picolo loop

TTMS-004a
Qualification Fabrication Processes

TW2-TTMS-004a D6
Optimisation of HIP Joining

The goal of this task consists of the development of a HIP (hot isostatic pressing) joining method. Nearly all components (first wall, stiffening plates) of the HCPB blanket will be manufactured by plates of EUROFER with cooling channels. The plates and their junctions together are loaded by a thermal gradient inside the blanket and the coolant pressure. This demands for optimal welds. One promising method is the HIP-joining technique: It features the advantage of ideal welds and does not need outside resources. But the coolant channels could be damaged by use of a high uniaxial force (perpendicular to the weld surface) or otherwise the performance of the weld would be decreased in the case of a lower temperature, force, bonding time combination. An optimisation of such a method has to answer the question for bonding time, pressure and temperature dependent on the design of the blanket. Moreover, this procedure has to be repeated with different temperature time pressure combinations (two step process).

A numerical model of the HIP-process has been developed and a test facility has been assembled this year. Most experiments related to the model parameters have been performed. A first experimental series of HIP welding samples has been finished.

Numerical model of the HIP process: A computer model is necessary for an optimisation of such a process, because experiments are expensive. Fig. 1 shows the principle of the model. It is based on periodically ellipsoidally shaped surfaces (enclosing voids) of the sample cubes. This precondition has been attested by SEM pictures. The model considers three “driving mechanisms:”

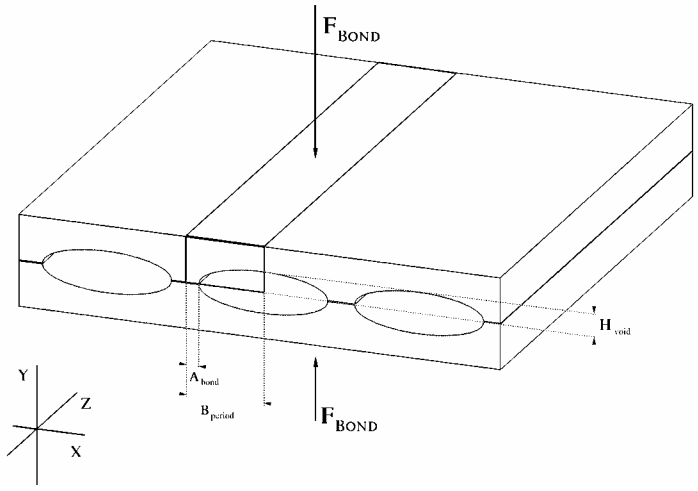

Fig. 1: Principle sketch of a dry milled weld surface

1) Plastic deformation of the voids, 2) surface diffusion and volume diffusion, 3) visco plastic creep. It is possible to find implicit semi analytical expressions for A_{void} and H_{void} for the plastic part. The other “driving mechanisms” are qualified by differential equations. The model needs as input data diffusion constants, yield stress and visco plastic creep law.

A new differential equations based model has been developed for the visco plastic creep behaviour of EUROFER under compression. It consists of a time constant creep velocity part ε_1, a non linear hardening part ε_2, and a “plastic” part ε_3. These last two parts are considering the history of the sample, see Fig 2. All c_i and $\varepsilon_{i,\,j}$ depend on pressure and temperature.

Test facility: It consists of a computer controlled testing machine (Fig. 3), which enables for usual samples a bonding pressure of up to 83 MPa and a bonding temperature of up to 1600°C. A sample consists of two cubes (20x30x25 mm), each with a dry milled surface (roughness approx. 1 µm). The samples have not to be boxed, because a water cooled vacuum oven ($<10^{-5}$ mbar) inhibits chemical reactions. A spot welded thermocouple on the

sample measures the sample temperature. The computer generates a time dependent target temperature, which is compared with the sample temperature. The difference of the temperatures yields two electrical signals by use of different characteristics for the two radiant heaters. This lowers thermal differences inside the sample volume. The bonding pressure is controlled by a force control circuit. The target force will be calculated by the computer. A force adjustment using the results of the sample elongation or deformation enables experiments with first order constant bonding pressure. This is caused by the large deformation of the EUROFER, e. g. see later Fig. 5.

Experiments: Plastic deformation depends on the yield stress. Fig. 4 shows the results for tensile and compression experiments. A pre-series of visco plastic creep experiments has been performed with the aim to find an optimal sample geometry (cube 10 mm). A series of 21 visco plastic creep experiments with different temperatures (range from 900°C to 1050°C) and pressures (range from 18 MPa to 60 MPa) followed. The former shortly described creep model is able to predict the results of 18 of these experiments with a relative error of less than 20 %. The following Fig 5 gives an overview of the temperature and pressure range of this series.

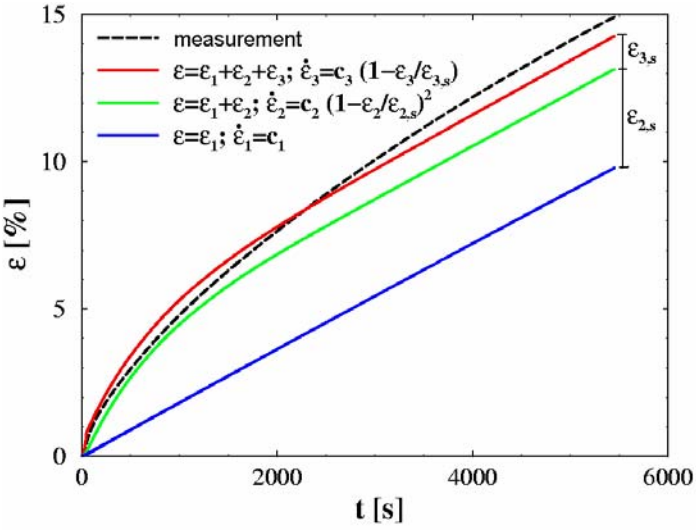

Fig. 2: Principle of the creep model for EUROFER

Fig. 3: Testing machine

A series of 9 HIP-welding experiments has been started in the middle of the year. The samples are dry milled and except sample 1 and sample 2 four times washed in an ultrasonic bath (acetone 40°C). In the next step the samples are welded, e.g. see sample 9, Fig. 6: First a force of 12 kN (according to 20 MPa) has been applied to the sample. Than it has been warmed up to 1010°C, which expands the sample. Note, the green graph in Fig. 6 displays the negative relative elongation of the sample! Therefore the length of the sample is first lowered (green graph steps up) and in the next 3000 s when the sample is warmed up, the green graph steps down. The increasing sample temperature decreases the yield stress till the applied pressure is larger than the yield stress. The sample has been compressed into the grooves of the sample holder. The visco plastic creep starts. The deformation of the sample enlarges the welding area perpendicular to the applied force. This fact would lower the bonding pressure, but this effect is compensated by the computer with increasing the force. This causes the time constant pressure. The sample temperature has been increased in a second step up to 1050°C, use of the former described creep model and the yield stress diagram Fig. 5 yields a maximum possible pressure of 7.5 MPa under condition of stopping

visco plastic creep. The quality of the welding can than be increased by diffusion mechanisms.

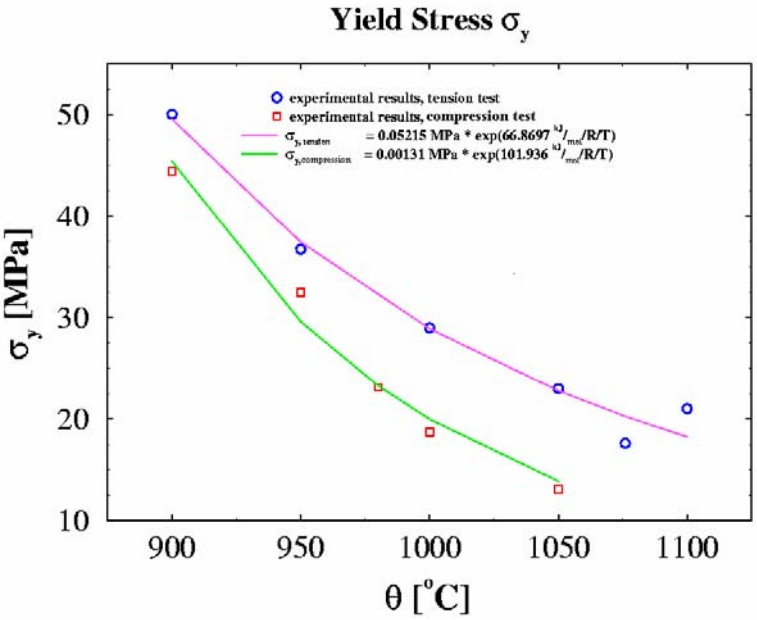

Fig. 4: Experimental results (tensile and compression) for the yield stress of EUROFER. The yield stress differs for tensile and compression load as observed for other materials

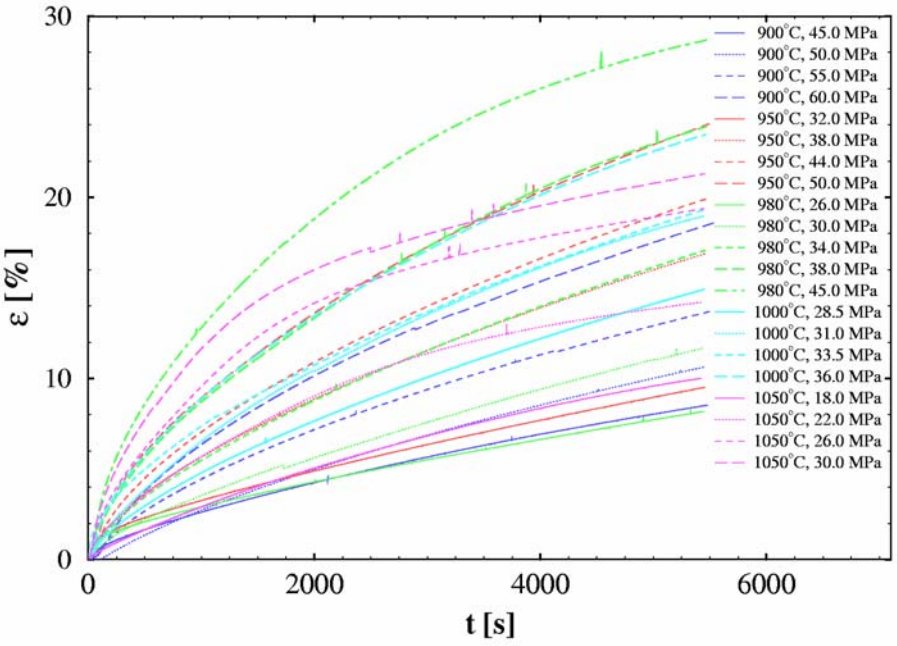

Fig. 5: Overview of visco plastic creep experiments, note only the amount of ε is displayed.

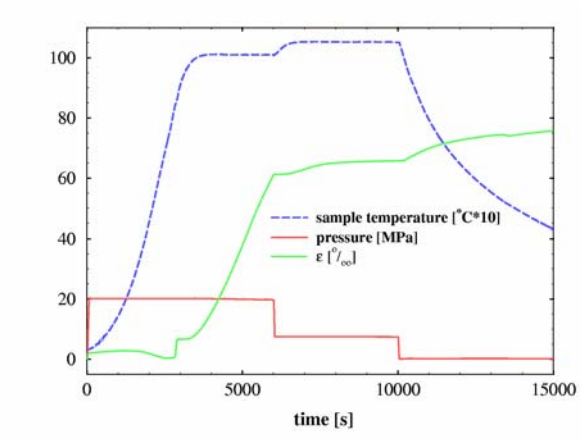

Fig. 6: Time variation of HIP-parameters by a two step method, sample 9, note the negative pressure and negative relative elongation of the sample is displayed.

Two of the welded samples have been tested up to now: sample 1 (one step method, bonding time 12600 s including warm up, bonding temperature 1010°C, bonding pressure 20 MPa) and sample 2 (two step method, 50 MPa, 900°C, 9000 s, 5 MPa, 1010°C, 3600 s) show in tensile tests the same R_{P02} values (30-700°C sample temperature) as the bulk material. The results of the charpy impact tests differ completely, see Fig. 7. Sample 1 reaches the same transition temperature θ_T as the bulk material in contrast to sample 2. A SEM-EDX analysis detects Vanadium and a higher carbon part (oil) in the spectra of the welding surface of sample 2. This suggests a non fitting cleaning procedure (only two times acetone ultrasonic bath).

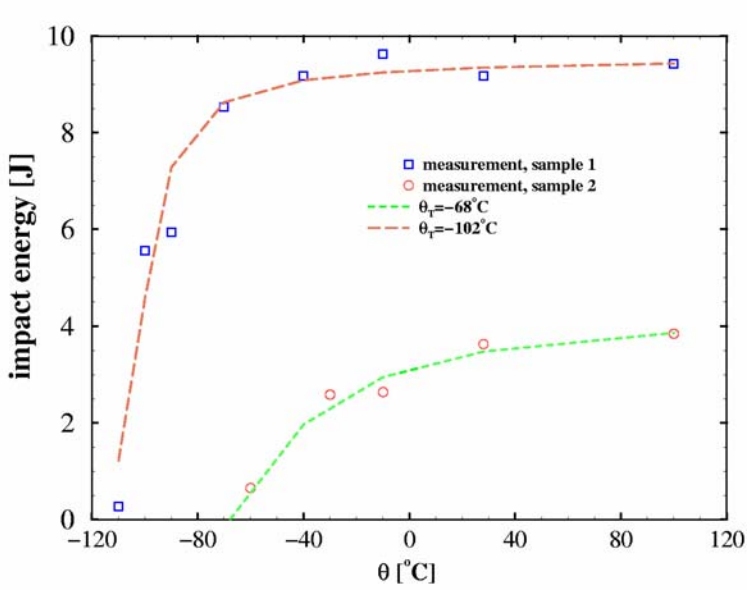

Fig. 7: Results from charpy impact tests

Conclusion: The task "optimisation of HIP joining" can offer some progress: A theoretical model for the HIP process has been developed. A test facility for HIP-joining samples has been assembled, including sample production, preparation and tests. The model results of the visco plastic creep behaviour agree approximately to the experimental results. One of the samples shows a weld with ideal properties. The possibility to govern visco plastic creep by varying temperature and pressure could be shown experimentally. But the advantage of a two step HIP method has to be proven still.

Staff:

J. Aktaa
B. Dafferner
H. Kempe
E. Materna Moris
H. C. Schneider
A. von der Weth

TTMS-005
Rules for Design Fabrication and Inspection

TW2-TTMS-005b D1
TBM Design Rules

The objective of this task is the development of design rules for ITER test blanket modules (TBM) built from RAFM steels. The TBM has to be dimensioned against different kinds of failure: ductile, creep and fatigue failure taking into account the influence of irradiation. The design rules will be build up on existing codes for nuclear applications considering the life time prediction approaches developed within TTMS-005 for RAFM steels and their specific mechanical behaviour. The assessment of the design rules formulated is also a part of this task. Therefore the performance and evaluation of suitable verification experiments among others isothermal multi-axial fatigue tests at room temperature as well as at elevated temperature, close to the operating temperature, on the reduced activation alloy EUROFER 97 are foreseen.

The isothermal multi-axial fatigue tests will be performed using tubular specimens which can be subjected to proportional and non-proportional bi-axial cyclic loadings by varying both the load path and the phase shift. In the reporting period the multi-axial test facility needed for these tests was refurbished. With this test facility, it is possible to generate independent loadings for two different directions. For the measuring of the applied strains an extensometer was developed which is able to detect axial and shear strain simultaneously.

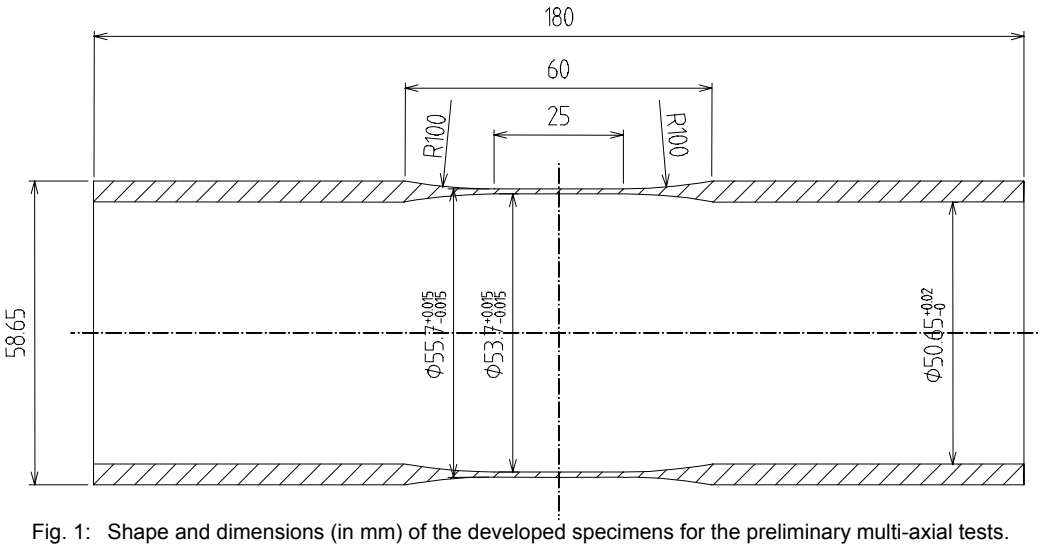

Fig. 1: Shape and dimensions (in mm) of the developed specimens for the preliminary multi-axial tests.

This sensor was fabricated by modifying two norm sensors of the company WAZAU, Berlin, type WAE. Thus we are able to perform fully strain-controlled experiments. Since we have only a few amount left from the first heat of EUROFER 97 and the second heat of EUROFER 97, called EUROFER 97-2 will be at the earliest available in the spring of 2004 we decided to perform preliminary experiments with the alloy 1.4914 which has similar mechanical properties. These preliminary tests are necessary, because for this special case of loading the development of an optimised specimen geometry is not trivial. It is necessary to find a geometry having a sufficient resistance to instability, but not too high stiffness, so that we could achieve sufficient strains. Furthermore, we have to ensure that the distribution of forces in the measurement area is homogeneous. So we decided in favour of a waisted form for the specimens. The actual measurement area is a small part in the middle of the whole specimen only. In this area, the smallest wall thickness constant over a gauge length of 25 mm is located (s. Figure 1). For the preliminary experiments six 1.4914 specimens were fabricated and prepared for testing.

When the preliminary tests are successful, i.e. the specimens show only a minor affinity to instability, EUROFER specimens with the same geometry will be fabricated. Then tests in the following sequence will be performed :

- ❖ Tests at room temperature
  - Proportional tests (0° and 180° phase shift)
  - Non-proportional tests (45°, 90° and 135° phase shift)
- ❖ Tests at elevated temperature (operating temperature)
  - Proportional tests (0° and 180° phase shift)
  - Non-proportional tests (45°, 90° and 135° phase shift)

The experimental results will be used to verify the lifetime prediction models developed so far as well as their implementation in the design code.

Staff:

J. Aktaa
M. Weick
S. Knaak

TW1-TTMS-005 D3
Local Fracture Criteria in the Ductile-to-Brittle Transition Regime

Objective

The objective of this subtask is the development and application of methods that enable the generation of design-relevant fracture mechanics material parameters on the basis of micro-mechanical failure models.

A characteristic feature of these models is the utilisation of an integrated (i.e. combined experimental and continuum mechanics) approach, which means extraction of material parameters for brittle or ductile fracture from (fracture) mechanics experiments by accompanying Finite Element stress analyses.

The main advantage of this so-called 'Local Approach' with respect to global failure criteria is the fact that a mechanism-based fracture description is combined with a numerical stress analysis. Geometrical size effects are thus already accounted for within this approach. Limitations of the local approach originate from different fracture mechanisms. Knowledge of fracture mechanisms is therefore essential, so that fractography invariably is an essential part of the evaluation of the experiments.

Local fracture criteria establish a link between metallurgy and mechanical engineering and they are currently being incorporated into design codes such as the R6 code of British Energy, where guidance on Local Approach methodology is included in the latest issue [1].

Experimental data base

The necessary materials data for F82Hmod and EUROFER97, respectively, were obtained from tensile tests with axisymmetrically notched specimens of different notch radii at selected temperature levels within the lower shelf of the ductile-to-brittle transition regime. Force and diametral contraction at the notch root were continuously recorded and served as input for the subsequent numerical evaluation of the Weibull stress as fracture parameter.

Additionally, a limited number of circumferentially precracked axisymmetrical specimens were tested for transferability reasons.

Extended fractographic examinations of the fracture surfaces were performed to obtain fracture appearance as well as type and distribution of fracture origin sites. These data were used to set up validation limits for the underlying concepts.

Numerical evaluation of experiments

A numerical post-processing routine WEISTRABA [2] to the general-purpose Finite Element code ABAQUS was written and performed well compared to similar approaches that were investigated within a round robin under the auspices of the European Structural Integrity Society (ESIS) [3]. Using WEISTRABA, statistical inference of the Weibull stress parameters was performed as well as prediction of fracture origin location distributions with the help of the calculated local risk of rupture [4, 5, 6]. Predicted and observed fracture origin location were compared and used for transferability considerations of fracture mechanisms in different specimen geometries.

Fracture mechanics concept and validation/limits

The procedure was tested and verified within an ESIS Round Robin on Numerical Modelling [7]. While correct implementation of the cleavage fracture model was verified, stress analysis and subsequent numerical analysis lead to large deviations in the resulting cleavage fracture

parameters, possibly due to the sensitivity with respect to choice of appropriate boundary conditions.

Fractographic analysis of F82Hmod as well as EUROFER97 specimens revealed a limited domain of applicability of the pure cleavage fracture model related to the presence of different fracture mechanisms [8, 9]. Specifically, the presence of carbide decorated grain boundaries and martensite laths leads to the strain induced formation of microcracks in axial direction and a mixed trans-/intergranular fracture appearance at large fracture strains, where large fracture strains can be caused by elevated temperature and/or lower degrees of triaxiality. Transferability in therefore only possible if presence of identical fracture mechanisms can be justified by fractographic investigations.

Summary of results

Results of the subtask have been compiled in two final reports, one containing the procedural steps for a fracture mechanics description of the material behaviour in the ductile-to-brittle transition regime [5], one containing the results applied to the two reference RAFM steels F82Hmod and EUROFER97, respectively [6].

Staff:

E. Diegele
H. Riesch-Oppermann
G. Rizzi

Literature:

[1] British Energy Generation Ltd, Assessment of the integrity of structures containing defects R/H/R6, Rev. 4, 2001.

[2] H. Riesch-Oppermann, A. Brückner-Foit, WEISTRABA - A code for the numerical analysis of Weibull stress parameters from ABAQUS finite element stress analyses – Procedural background and code description -, FZKA Report 6155, Forschungszentrum Karlsruhe, August 1998.

[3] C. Poussard, C. Sainte Catherine, ESIS TC (- Numerical Round Robin on Micro-Mechanical Models, Results of Phase II - Task B2, Cleavage Toughness Prediction on CT Specimen, Rapport DMN, SEMI/LEMO/RT/01-035/A, CEA , 2002.

[4] H. Riesch-Oppermann, E. Diegele, Towards a micro-mechanical description of the fracture behaviour for RAFM steels in the ductile-to-brittle transition regime, J. Nucl. Materials **307-311** (2002), 1021-1025.

[5] H. Riesch-Oppermann, E. Diegele, Elements of a fracture mechanics concept for the cleavage fracture behaviour for RAFM steels using local fracture criteria (Final Report for Task TW1-TTMS-005/D3), Report FZKA 6668, Forschungszentrum Karlsruhe, 2002.

[6] H. Riesch-Oppermann, Verification of a fracture mechanics concept for the cleavage fracture behaviour for RAFM steels using local fracture criteria (Final Report for Task TW2-TTMS-005/D3), Report FZKA 6794, Forschungszentrum Karlsruhe, 2003.

[7] H. Riesch-Oppermann, FZK contribution to the ESIS TC 8 Numerical Round Robin on Micromechanical Models (Phase II, Task B1), FZKA Report 6338, Forschungszentrum Karlsruhe, 1999.

[8] H. Riesch-Oppermann, M. Walter, Status report on experiments and modelling of the cleavage fracture behaviour of F82Hmod using local fracture criteria (Task TTMS-005), Report FZKA 6388, Forschungszentrum Karlsruhe, 2001.

[9] M. Walter, Mechanische und fraktographische Charakterisierung des niedrigaktivierbaren Chromstahls F82H-mod im spröd-duktilen Übergangsbereich, Dissertation, Report FZKA 6657, Forschungszentrum Karlsruhe, 2002.

TW2-TTMS-005a D4
Creep Fatigue Lifetime Prediction Rules

Reduced activation ferritic martensitic (RAFM) steels developed recently inter alia in the framework of EURATOM Fusion Technology programme are potential candidates for structural materials of future fusion reactors. During planed operation of a fusion reactor structural materials of the plasma facing components, blanket and divertor, are subjected to complex thermo-mechanical loading and high irradiation doses which induce different kinds of damage: creep, fatigue as well as irradiation damage. The objectives of this task are in a first step the development of lifetime prediction model for RAFM steels under creep fatigue conditions which can be easily modified to take into account the irradiation influence.

The model developed consists of a damage model coupled with a deformation model. The coupling allows on the one hand the consideration of mutual influence between deformation and damage and on the other hand the lifetime prediction for an arbitrary loading without the need of additional strain or stress measurements. Both, the deformation and the damage model were developed within the framework of the continuum mechanics using the phenomenological concept of state variables to describe complex irreversible processes like inelastic deformation and damage. In addition the models were formulated in a way that they can be implemented in commercial Finite Element codes and thus be used for the assessment of arbitrary shaped components. The development of the deformation and damage models has been based on deep analyses of the experimental observations and identification of important mechanisms influencing damage evolution and thus the lifetime.

The resulting coupled model is a powerful prediction tool, which can be applied to arbitrary creep-fatigue loading provided that the material, temperature and possibly irradiation dose dependent parameters of the model have been determined. Therefore a fitting procedure has been developed for the parameters identification on the base of deformation and lifetime data from standard low cycle fatigue (LCF) tests without and with hold time as well as creep tests.

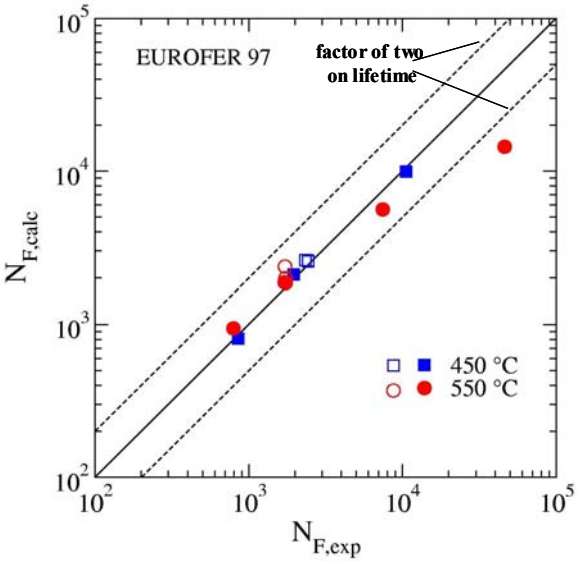

Fig. 1: Comparison between numbers of cycles to failure calculated by the coupled deformation damage model with those determined experimentally for EUROFER97 in LCF tests without (solid symbols) and with hold time (open symbols)

The coupled deformation-damage model has been meanwhile successfully applied to F82H mod. and in the reporting period to EUROFER 97 under isothermal cyclic loading at 450 and 550°C. The comparisons between model and experiment show that the observed lifetimes in the LCF-tests could be fairly well calculated even for the tests with hold time, which were not considered for the identification of the damage model parameters (s. Fig. 1). However before releasing the model further verifications has to be done by applying the model to isothermal two-steps LCF-tests (low-to-high and high-to-low), to thermo-mechanical LCF-tests, to isothermal multiaxial LCF-tests as well as to a suitable mock-up test. To take into account the influence of irradiation applications of the model are in long term foreseen to several irradiated states with sufficient data base.

<u>Staff:</u>

J. Aktaa

TW2-TTMS-005b D4
Creep-fatigue Lifetime Prediction Rules for Irradiated EUROFER

The objectives of this task are the modification of the lifetime prediction model developed in TTMS-005a D4 for RAFM steels under creep fatigue conditions taking into account the irradiation influence and the verification of the modified model by applying it to EUROFER 97 in the post-irradiated state.

The lifetime prediction model developed for RAFM steels under creep fatigue conditions allows the consideration of irradiation influence:

by assuming a dependence of its parameters on the irradiation dose implying that the irradiation influence is limited to the change of the kinetic of already known deformation and damage phenomena

and/or by adding terms driven by irradiation dose in the evolution equations of hardening and damage by which the irradiation induced phenomena can be described.

However the need of one of these possibilities or of both of them for an appropriate modification of the lifetime prediction model can only be determined by analysing deeply the experimental observations in creep and fatigue tests performed on EUROFER 97 in the irradiated state.

Since the post irradiation investigations of EUROFER 97 are in preparation or partly already started the model modification will be done preliminary on the base of literature data of irradiated materials similar to EUROFER 97. The literature study required has been launched and is still in progress. The results of the literature study show so far that deformation as well as lifetime data from creep and fatigue tests on materials in the post-irradiated state are very rare. Most of the data published are those from tensile tests on materials irradiated with doses much lower than those structure materials of a fusion reactor will be subjected to. When analysing the tensile data significant irradiation induced hardening can be recognised for different types of materials already at low doses (< 1 dpa). This hardening results in a shift of the tensile true stress true strain curves to higher stresses, in a remarkable reduction of the failure strain, but not in a significant change of the slope and the hardening exponent, respectively. A saturation of the irradiation induced hardening toward higher doses will be often quoted but due to the lack of data no verification up to a dose of 100 dpa can be found. As far as creep was investigated, irradiation induced creep and creep damage could be observed in particular for materials showing strong swelling due to irradiation. In fact RAFM steels do not belong to these materials as far as the low irradiation dose regime is considered but this could be changed in the high dose regime. In conclusion both modification possibilities mentioned above for the lifetime prediction model might be necessary for RAFM steels, in particular for EUROFER 97, whereas the dependence of the model parameters on the irradiation dose is expected to be limited to a part of them.

Staff:

J. Aktaa

TTMS-006
High Performance Steels

TW2-TTMS-006 D2
Chemical, Physical and Metallurgical Properties of the Two Improved ODS Batches

In the frame of the 2002 activities on high performance steels, CEA and CRPP had to produce independently 5 kg batches of “improved” ODS in two different production routes.

The results of these investigations should help to define a European RAFM ODS steel, which should be produced as a 50 kg batch according to the selected manufacturing route (TW3-TTMS-006 D1).

Microstructural examinations and optimisation of heat treatments were performed at FZK. Due to the different production routes both materials behave different with respect to heat treatment and microstructure and are discussed separately.

CEA-ODS

CEA produced 2 plates of 155x62x10 mm and 4 plates of 164x62x6 mm.

The production route consisted of ball milling of EUROFER 97 powder (particle size < 45 µm) and 0.3% Yttria. The powder was consolidated by Hot Isostatic Pressing in 2 steps, a 1st HIP (1100°C/2 h, 120 MPa), Post HIP Heat Treatment (950°C 1 h/W + 750°C 2 h), a 2nd HIP (1250°C/2h, 120 MPa) and a final heat treatment (950°C 1 h/W + 750°C 2 h) [1].

Samples were cut from different parts of the ODS plates in order to assess the microstructure by means of TEM and metallography and to optimise the post-HIP heat treatment.

Two heat treatments were compared. A high austenitisation temperature (1100°C) was chosen in order to promote the martensitic transformation and a lower one (950°C) according to the standard CEA heat treatment, which should prevent excessive grain growth. The austenitisation was followed by a tempering treatment at 750°C for 2 hours to adjust the mechanical properties.

The CEA-ODS is fully dense and reacts on different heat treatments. A martensitic transformation can be observed after water quenching. From the hardness measurements no preference for low (950°C) or high (1100°C) austenitising temperature can be given, both heat treatments seem to be equivalent. Mechanical tests are needed to make a decision. Table 1 gives the results of hardness measurements after different heat treatments.

Table 1: Vickers Hardness HV30 of CEA-ODS after different heat treatments

Specimen-No.	Aust. Treatment	Ann. Treatment	HV30	HV30	HV30	HV30 (Mean)
1	1100°C 30’ Ar/W	0	492	487	487	489
2	1100°C 60’ Ar/W	0	484	490	482	485
3	1100°C 30’ Ar/W	750°C 2h V/V	319	326	322	322
4	1100°C 60’ Ar/W	750°C 2h V/V	310	306	313	310
CEA-Treatment	950°C 30’ Air/W	750°C 2h	320	321	322	321

Microstructural investigations by TEM using a High Angle Annular Dark Field Detector (HAADF) give no indication of an excessive grain growth in the case of the higher

austenitisation temperature (Fig. 1). The particle size distribution of the strengthening Yttria particles is similar to that of FZK-EUROFER-ODS.

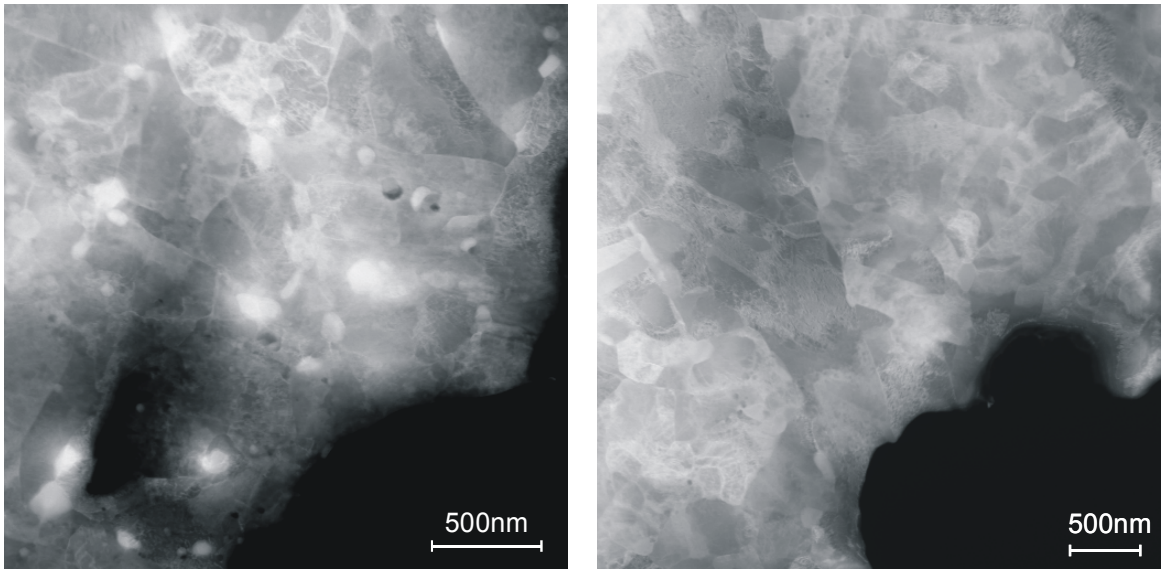

Fig. 1: HAADF images of CEA-ODS with different heat treatments, 950°C 60' Air/W + 750°C 2 h (left) and 1100°C 60' Air/W + 750°C 2 h (right)

CRPP-ODS

CRPP produced 33 discs of about 53 mm in diameter and 7 mm thickness. The production route consisted of mechanical alloying at University Carlos III, Madrid, Spain, by ball milling of EUROFER 97 powder (< 45 µm) and 0.3% Yttria for 24 hours in an attritor mill. The compaction was performed at Haute Ecole Valaisanne, Sion, Switzerland and consisted of a prepressing (1200°C, 35 MPa, 10 min) and a subsequent HIP (1000°C, 180 MPa, 1 h) [2].

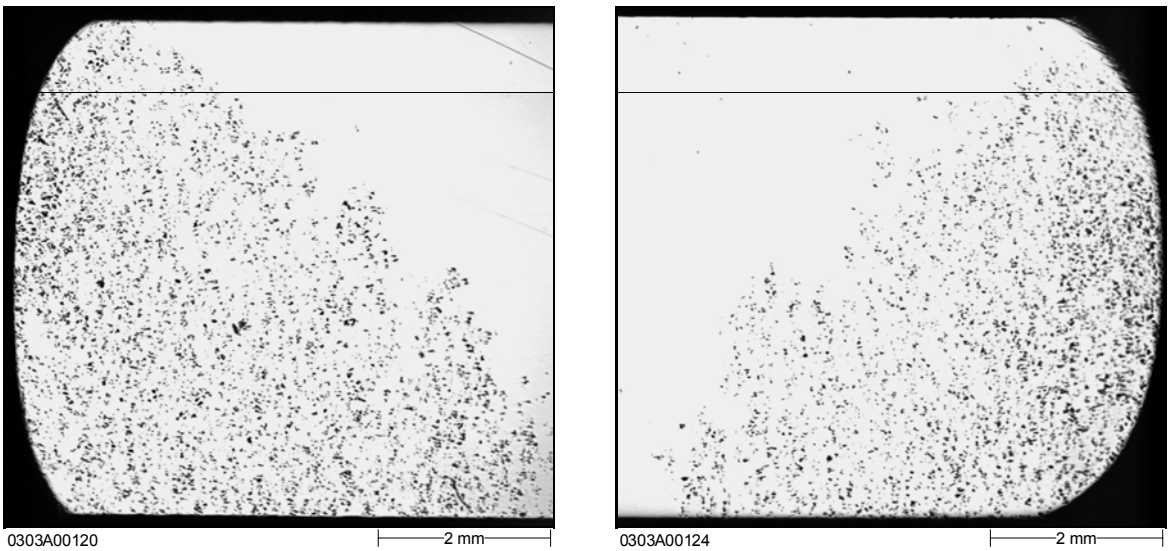

Fig. 2: Central cross section of CRPP-ODS, Disc 11, D/D_{th} 97%, heat treatment as-received.

Three discs were examined in the same manner as the CEA-ODS. The metallographic examinations showed partly a high porosity of the material. Figure 2 gives a metallographic cut through the centre of a disc with a nominal density of 97% of the theoretical density. It can be seen, that this disc is totally porous in the outer region with a fully dense core of about 30 mm in diameter. Other samples with lower nominal densities showed a much higher porosity, making further investigations impossible.

Samples from the dense core of disc 11 were subjected to different heat treatments. The relatively high austenitisation temperature (1100°C) was the chosen in accordance with the results of the heat treatment trials with CEA-ODS. The heat treatments were performed in a three-zone vacuum furnace with a quartz tube. The cooling was carried out by withdrawal of this tube from the vacuum furnace. This procedure leads to cooling rates in the small samples close to those of normal air cooling conditions.

In contrast to the CEA material, CRPP-ODS is air hardening. One reason for this different behaviour is the higher carbon content which builds up during the mechanical alloying process. Table 2 gives the results of hardness measurements after different heat treatments.

Table 2: Vickers Hardness HV30 of CRPP-ODS after different heat treatments

Specimen-No.	Aust. Treatment	Ann. Treatment	HV30	HV30	HV30	HV30 (Mean)
11-1	1100°C 30' V/V	0	496	492	487	492
11-2	1100°C 30' V/V	750°C 2h V/V	362	362	367	364
11-3	as-receved		473	486	486	482

The hardness after the austenitising treatment is comparable to that of CEA-ODS in the same condition but the hardness after the additional annealing at 750°C for 2 h is higher. Therefore it can be assumed that the tensile strength of CRPP-ODS will be higher.

Microstructural investigation show, that the microstructure is more uniform and homogeneous than that of CEA-ODS what gives hope that also the ductility is improved compared to earlier EUROFER-ODS alloys.

Staff:

S. Baumgärtner
A. Falkenstein
P. Graf
M. Klimiankou
R. Lindau
U. Jäntsch
H. Zimmermann

Literature:

[1] C. Cayron, I. Chu, E. Rath, J.M. Heenequin, S. Launois, P. Bucci, J.M. Leibold, "ODS processing and qualification, screening of various parameters, basic characterisation, production of 5 kg improved batch", Note Technique DTEN No. 129/2002, Final report task TW2-TTMS006-D1, CEA Grenoble, December 2002.

[2] R. Schäublin, T. Leguy, C. Bonjour, N. Baluc, "ODS processing and qualification (2nd route), screening of various parameters (powder alloying, consolidation, PHT) basic characterisation, production of 5 kg batch improved batch." Final report on task TW2-TTMS006-D10, CRPP Switzerland, December 2002.

[3] M. Klimiankou, R. Lindau, A. Falkenstein, U.Jäntsch, H. Zimmermann, "Chemical, physical and metallurgical properties of the 2 improved ODS batches". (Final report TW2-TTMS-006-D2) FZK internal report FUSION, in preparation.

[4] R. Lindau, A. Möslang, M. Schirra, P. Schlossmacher, M. Klimenkov, “Mechanical and Microstructural Properties of a Hipped RAFM ODS-Steel”, Journal of Nuclear Materials, 307-311 (2002) 769-772

[5] M. Klimiankou, R. Lindau, A. Moslang “HRTEM Study of yttrium oxide particles in ODS steels for fusion reactor application” Journal of Crystal Growth 249 (2003) 381-387

[6] R. Lindau, A. Möslang, M. Klimiankou, “Results on EUROFER-ODS: Manufacturing and Characterisation” IEA Workshop on Ferritic Martensitic Steels, 14 November, 2002, Garching bei München. Proceedings on CD, 20027/03.54508/I, Editor B. van der Schaaf, NRG Petten

TTMS-006 D13
ODS/EUROFER Joining

Assessment of diffusion bonding process feasibility

This subtask has been completed. The results are summarized and discussed in detail in [1].

Summary and Conclusion

The objective of this work is to investigate the appropriate hot isostatic pressing (HIP) technique including the boundary conditions and parameters in order to achieve good mechanical properties of the diffusion welded joints of ODS EUROFER with other structure materials such as EUROFER. For the first attempt on HIP joining of ODS EUROFER with EUROFER altogether six pairs of semicircular specimens from both materials with a size of each diam. 55 mm and 16.5 mm of thickness (Fig. 1) were manufactured, which are suitable for later production of the standard specimens for tensile and impact tests for the HIP welding joint and the base material zone. The sample preparation is accomplished using the same procedure which was successfully applied to the earlier experiments on HIP diffusion welding of EUROFER specimens. The HIP joining surfaces are dry milled to a surface roughness of Rt ≤ 2 μm. Cleaning was performed in an ultrasonic bath with acetone. Immediately after cleaning, the specimen halves of ODS EUROFER and EUROFER each were seal welded together at the edge of the joining surfaces by means of electron beam welding under vacuum. The HIP diffusion welding was performed in each case at a temperature of 980 °C, 1050 °C as well as 1100 °C and a pressure of 100 MPa, with a following heat treatment with and without austenitizing (austenitizing at: 980°C or 1040°C, 30 min; tempering at 750°C, 2h). Afterwards the production of the specimens for tensile and notched bar impact took place followed by the actual strength tests.

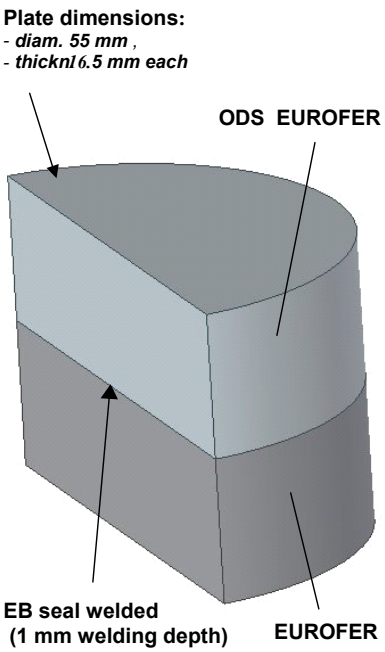

Fig. 1: Specimens for HIP joining of OS EUROFER with EUROFER.

The results of the preceding HIP experiments [2, 3] on MANET and EUROFER specimens had already shown that the quality of the welding joint is the better, the less the separating line in the welding zone of the specimen plates is recognisable. Furthermore, test specimens with fine-grained structure were characterised by a higher impact strength.

If the HIP experimental results are judged by the criteria above by means of the cross cuts, the best results of the HIP joining of the ODS EUROFER/EUROFER specimens seem to be achieved at the HIP conditions with a HIP temperature of approx.1050 °C and a following heat treatment with austenitising at 1040 °C, 30min and tempering at 750 °C, 2h. As exemplarily shown in Fig. 2, the separating lines for the disk pairs 3 and 4, welded at a temperature of 1030-1070 °C are nearly no more recognisable in the un-etched metallographic section.

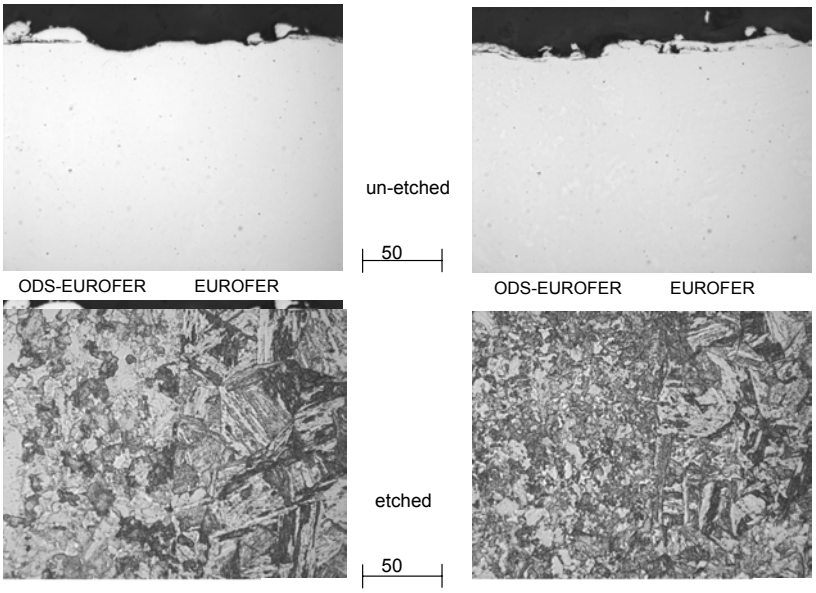

Plate 3, heat treatment: 750 °C 2h

Plate 4, heat treatm.: 1040 °C 30 min.+750 °C 2h

Fig. 2: Micrographs of the disk pairs 3 and 4, HIP temperature 1030-1070 °C.

This finding is confirmed by the results of the mechanical tests (Fig. 3). Regarding only the strength of the welded joints, a complete PHHT would not be necessary. On the other hand, ductility of the base materials, EUROFER and ODS-EUROFER is markedly improved by a two step heat treatment. Therefore a PHHT of 1040°C 30 min + 750°C 2h after hipping at 1050°C 3h at 100 MPa is strongly recommended in order to achieve optimum strength and ductility of the diffusion welded joints.

The results of 114 tensile tests can be summarized as follows:

a) With the selected procedure at first attempt very good welding results were obtained.

b) The tensile strength of all welded samples is equal or lies above the value of the basic material EUROFER with the same hipping and PWHT. Fracture always occurs outside the welding zone.

c) The values of the KLST impact tests at room temperature for samples taken from the welding zone are approx. 80% of the value of basic material EUROFER, and seem to be still in the ductile range.

d) Individual results can be still improved by an austenitizing before tempering.

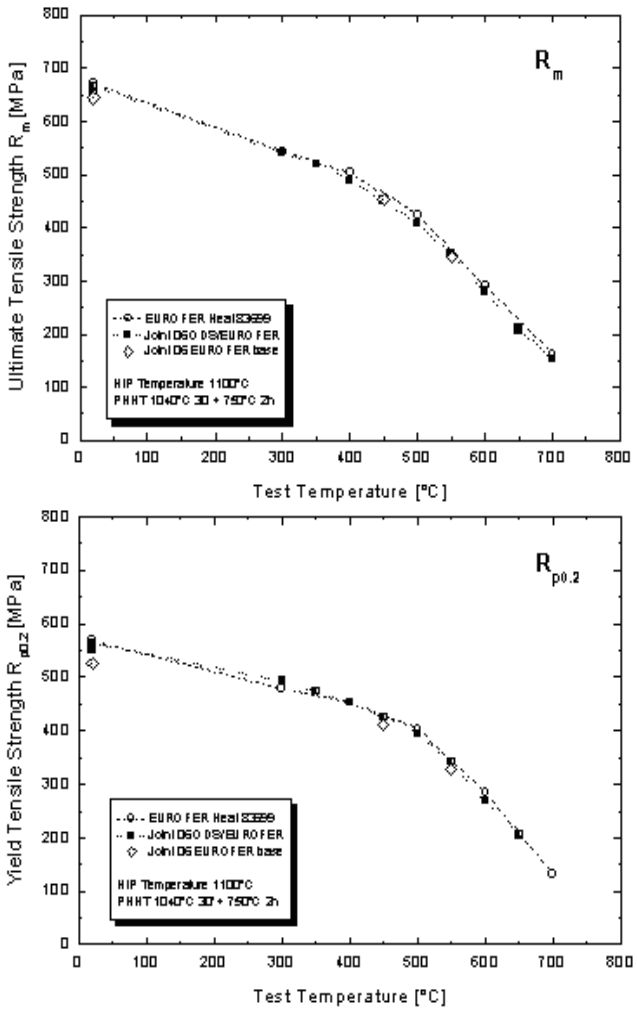

Fig. 3: Ultimate tensile and yield strength of disk pair 6 vs. test temperature.

Staff:

S. Baumgärtner
B. Dafferner
A. Falkenstein
P. Graf
R. Lindau
P. Norajitra
G. Reimann
R. Ruprecht
H. Zimmermann

Literature:

[1] P. Norajitra, G. Reimann, S. Baumgärtner, B. Dafferner, P. Graf, R. Lindau, R. Ruprecht, H. Zimmermann: First experimental results of the HIP joining of ODS EUROFER with EUROFER using small specimens (Subtask TW2-TTMS-006-D11), Internal report, 2003.

[2] P. Norajitra, G. Reimann, R. Ruprecht, L. Schäfer: HIP experiments on the first wall and cooling plate specimens for the EU HCPB blanket, Journal of Nuclear Materials 307-311 (2002), 1558-1562.

[3] G. Reimann, H. Kempe, P. Norajitra, R. Ruprecht, R. Vouriot: Diffusion Welding Tests in Hot Isostatic Presses for Manufacturing Plate Components with Internal Cooling Channels for Fusion Blankets (TTBB-002-D1) - Eighth Test Series -, Final Report, March 2002.

TTMS-007
Modelisation of Irradiation Effect

TW3-TTMS-007 D3
Analysis of Recoil Spectra

Background and Objectives:

Modelisation of irradiation effect in fusion relevant materials is a key issue. Both analytical and computer simulation of different physical processes have extensively evolved during the last 10-12 years to cover several orders of magnitude of both spatial and time scales. Furthermore, by coupling sequentially methods applicable to each scale, it has been shown that the evolution of very complex physical phenomena can be described in a predictive way.

The main objective of this task is to model the radiation effects in the EUROFER reduced activation ferritic-martensitic steel under fusion relevant conditions in the range of temperatures from RT to 550 C in the presence of high concentrations of irradiation induced impurities (e.g. H, He).

For such purpose, the tools and database needed to correlate results from fission reactor – IFMIF - spallation source – fusion neutron source should be developed as well as for the extrapolation to high fluence. Experimental validation of the models is also included.

Recoil spectra of Fe-Cr steels:

The assessment of the primary damage evolution, i.e. the production of point defects, defect clusters and there mutual interaction as well as with other microstructural features, is based on a detailed description of the irradiation source. This effectively includes the production rate of all kinds of neutron induced primary knock-on atoms (PKA) and in particular their energy distribution. In multicomponent materials, like Fe-Cr steels, one has to take into account a variety of atomic species and nuclear interactions to obtain a reliable result of the emerging PKA spectra.

The present work makes use of state-of-the-art nuclear data libraries as well as nuclear processing codes to calculate PKA spectra at different locations from the blanket front section to the manifolds behind the low temperature shield in a fusion power plant study (PPCS model B). Also an assessment of the damage contribution of PKA has been performed in terms of the W(T)-function.

To calculate PKA spectra in Fe-Cr alloys we have selected a rather complete set of nuclear cross section data of all natural isotopes. Due to transmutation channels the PKA spectrum comprises isotopes not only of Chromium and Iron, but also of Titanium, Vanadium, and Manganese. The calculations have been performed using the nuclear processing code NJOY connected to a dedicated utility code for various transformations of the original raw data.

The resulting PKA spectra extend up to roughly 1 MeV for Fe and Mn, but event 2.7 MeV for Cr. Above 0.5 MeV the total PKA spectra are larger than in the case of pure Fe, due to the presence of Cr, V, and Ti. In the hard first wall neutron flux only about 10% of PKA are below 1 eV whereas in the back region of the blanket this share is roughly 33%.

Although the effect of the neutron energy distribution on the corresponding PKA energy distribution is quite pronounced, the expected damage contribution is even more affected. This can be estimated by the W(T)-function which gives the percentage of damage (in terms of NRT-dpa) up to a particular PKA energy. It is obvious, that high energy PKA play a dominating role despite their rather low abundance. Up to 87% of dpa are produced by PKA

above 20 keV, 64% above 100 keV, which should be compared to their share in the total PKA spectrum of 10% and 2%, respectively.

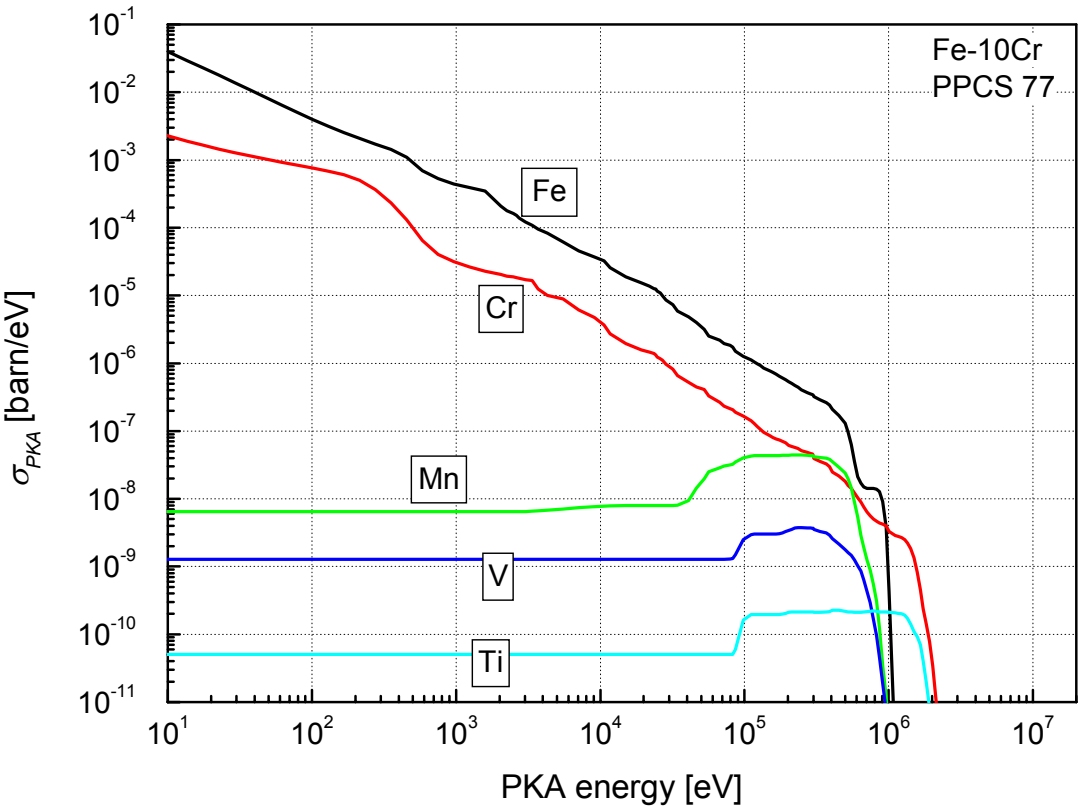

Fig. 1: PKA spectrum in Fe-10Cr in front section of blanket (PPCS 77).

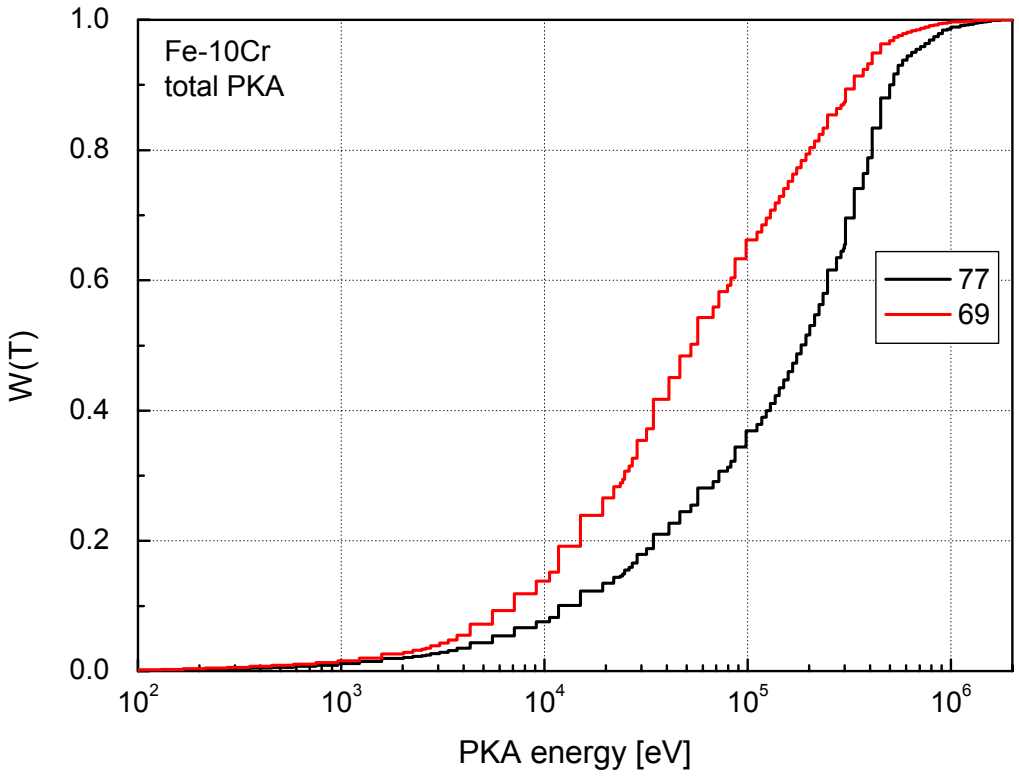

Fig. 2: W(T)-functions in Fe-10Cr for high neutron load (PPCS 77) and low neutron load (PPCS 69).

Conclusions and Outlook:

The present work has established a source to create a database of PKA spectra in Fe-Cr steels which different Cr content. All relevant interactions of all isotopes have been taken into account. The addition of Cr to Fe changes the PKA spectra mainly in the region above 0.5 MeV, which has a significant impact on the expected dpa damage. This is because PKA above 20 keV are most important for primary damage production, which is valid even in the rather soft neutron flux in the back of the blanket.

Since subcascade splitting similar to pure Fe is expected above roughly 20 keV, there is still some work to be done on how this may occur in Fe-Cr alloys and how the effect on damage production may be assessed. These issues are subject of a proposed combined Binary Collision Approximation and Molecular Dynamics study.

The results of the present work are used in Molecular Dynamics as well Kinetic Monte Carlo simulations performed in the frame of the same EFDA task TTMS-007.

Staff:

D. Leichtle

Literature:

[1] D. Leichtle, Primary Knock-On Atom Spectra in Fe-Cr Steels in a Fusion Power Plant, Final report on the EFDA task TW3-TTMS-007, D3, Internal Report FUSION, August 2003

EFDA 01/622
Order of EUROFER Heats

The European programme related to fusion reactor relevant structural materials aims at developing a low activation material, which can withstand high neutron loads under temperature and coolant conditions required in a fusion reactor based on magnetic confinement plasma.

For that purpose the 8-12 Cr reduced activation ferritic/martensitic (RAFM) steel was selected as reference structural material and the present R&D aims at:

- development, characterisation and implementation of a RAFM steel to be used for the fabrication of the Test Blanket Modules (TBMs) to be installed in ITER,

- optimisation of such a RAFM steel for the utilisation in a fusion reactor (DEMO and Power Plant).

Based on the substantial experience gained from various RAFM alloys developed in JA and EU and in order to reduce the long-term activation and improve the mechanical properties of such a steel prior and after irradiation, an industrial 3.5 tons batch of 9 CrWVTa RAFM steel, named EUROFER 97 was specified, ordered, and produced.

Additional EUROFER 97 material is needed for further fabrication trials, particularly to build TBM mock-ups. This new procurement has also as major objective to check the reproducibility of properties compared to batches available from the previous fabrication, to assess the achievable limits of reduction of detrimental impurities like Nb, Mo, Ni, Cu, Al, Co and others and to improve the quality of the tubing production.

Under operation the material will be exposed to temperatures up to 550°C, cyclic loading and neutron irradiation. The limitation of the undesired elements like Nb, Mo, Ni, Cu, Al, Co and others, that produce long-lived radio-active isotopes under neutron irradiation, makes this steel a so-called reduced activation steel. Components made of such a steel can be handled and stored within a manageable period of time after reactor shut down. This steel will be used for components with high reliability requirements.

The scope of this task is to provide a normalised and tempered martensitic steel type 9 CrWTaV designated EUROFER 97-2, under different product forms.

Therefore a technical specification has been elaborated considering all the experiences with the procurement of the first heats of EUROFER 97.

Since reproducibility of the good properties of EUROFER 97 is one important goal of the procurement, the technical specification leans close to that of the first heats produced by Böhler in Austria.

After evaluation of the offers, SaarSchmiede, an experienced German manufacturer of special and super clean steels and producer of the OPTIFER RAFM steels, was selected for the production of about 8 tons of different product forms (forgings, plates and tubes). The use of carefully selected raw materials is essential to achieve high cleanliness and low contents of undesired elements. The required chemical analysis as specified in the technical specification is given in Table 1.

Table 1: Required chemical analysis

Element	MIN Value (wt%)	MAX Value (wt%)	Remarks
Carbon	0.090	0.120	Target 0.11
Manganese	0.20	0.60	Target 0.4
Phosphorus		0.005	
Sulphur		0.005	
Silicon		0.050	
Nickel		0.01	ALAP
Chromium	8.50	9.50	Target 9
Molybdenum		0.005	ALAP
Vanadium	0.15	0.25	
Tantalum	0.10	0.14	Target 0.12
Tungsten	1.0	1.2	Target 1.1
Titanium		0.02	
Copper		0.01	ALAP
Niobium		0.005	ALAP
Aluminium		0.01	ALAP
Nitrogen	0.015	0.045	Target 0.030
Boron		0.002	ALAP
Cobalt		0.01	ALAP
As+Sn+Sb+Zr		0.05	Target
Oxygen		0.01	

The production of EUROFER 97-2 is in progress. The production process includes melting in a 16-ton vacuum induction furnace, remelting in a vacuum arc device and forging to billets, necessary for the production of round bars, plates and tubes. Fig 1 gives a schematic draw of the manufacturing route for EUROFER 97-2. The delivery of the different products is scheduled for end of 2003 and beginning 2004.

Staff:

R. Lindau

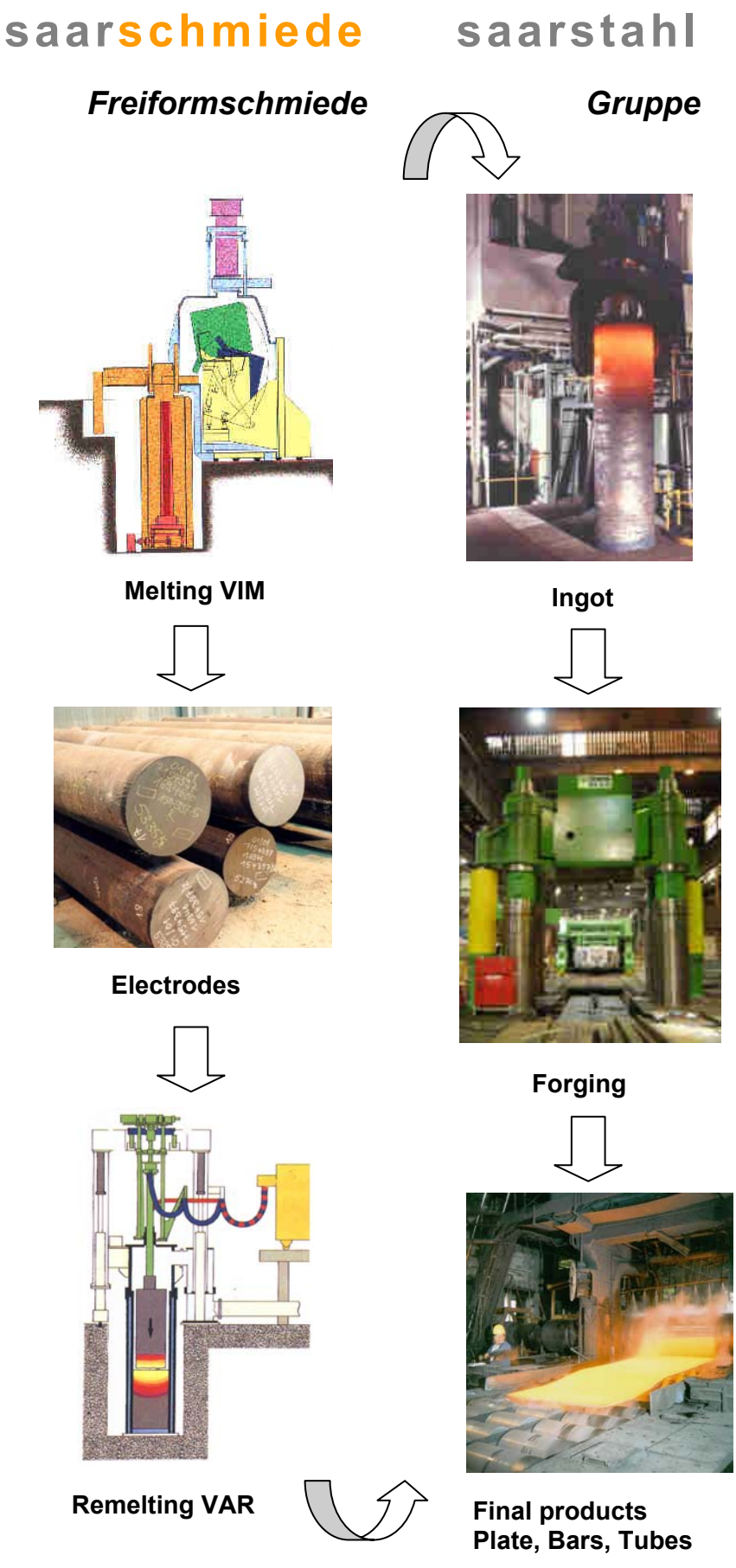

Fig. 1: Manufacturing route EUROFER 97-2

Nuclear Data

TTMN-001
Nuclear Data: EFF/EAF Data File Upgrade, Processing and Benchmark Analyses

The European Fusion File (EFF) and Activation File (EAF) projects aim at developing a qualified nuclear data base and validated computational tools for nuclear calculations of fusion reactors. The related Task TTMN-001 of the EFDA technology work programme is devoted to the evaluation, processing, application, and benchmarking of required nuclear cross section and uncertainty data as well as the development of computational tools for uncertainty calculations. The FZK contribution to Task TTMN-001 is on the evaluation of EFF-3 data, the qualification of new and updated EFF data evaluations through computational benchmark analyses including sensitivity/uncertainty analyses and the development of advanced computational schemes for sensitivity calculations based on the Monte Carlo technique.

TW3-TTMN-001-01
Review of EFF-3 Data Files Required for TBM Design Analyses

A comprehensive review of existing EFF-3 data evaluations was performed with the objective to determine missing data required for the neutronics and sensitivity/uncertainty analysis of the test blanket module (TBM) in ITER [1]. In addition to the European EFF-3/JEFF-3.0 data files, the current state-of-the-art nuclear data libraries ENDF/B-VI (USA), JENDL-3.2 (Japan) and FENDL-2 (IAEA) were included in the review. Based on the data needs for TBM design calculations, the available data evaluations and their quality as revealed in benchmark analyses, a priority list was elaborated for the evaluations to be conducted as part of TTMN-001 in Framework Programme 6 (FP6), see Table 1. At the EFF/EAF monitoring meeting at the NEA data bank, Paris, April 28, 2003, it was agreed to start the evaluation effort on the W isotopes.

Table 1: Priority list of evaluations and co-variance data required for TBM neutronics analyses.

Priority	Co-variance data		Evaluated data files	
High		available sources		available sources
	^{6}Li	ENDF/B-V		
	^{206,207,208}Pb	ENDF/B-VI	^{204,206,207,208}Pb	ENDF/B-VI
	^{16}O	ENDF/B-VI		
	^{182,183,184,186}W	No	^{182,183,184,186}W	ENDF/B-VI
Medium				
	^{29,30}Si	ENDF/B-VI	^{181}Ta	No
	^{54,57,58}Fe	ENDF/B-VI	^{29,30}Si	ENDF/B-VI
	^{50,53,54}Cr	ENDF/B-VI	^{54,57,58}Fe	ENDF/B-VI
	^{63,65}Cu	ENDF/B-VI	^{50,53,54}Cr	ENDF/B-VI
Low				
	^{7}Li	ENDF/B-VI	^{63,65}Cu	ENDF/B-VI
	^{181}Ta	No	^{46,47,49}Ti	JENDL-3.3
	^{46,47,49}Ti	JENDL-3.3		

TW3-TTMN-001-02
Evaluation of High-energy (150 MeV) Cross-section Data for EFF-3

During FP6 a general-purpose nuclear data library is to be developed up to 150 MeV neutron energy by adopting existing high-energy evaluations, up-grading and adapting them to the EFF/JEFF data evaluations and performing new evaluations according to the requirements for neutronics calculations of the IFMIF neutron source. A first survey of available 150 MeV data evaluations was performed in conjunction with the review of the EFF-3 data for TBM design analyses [1]. Highest priority was assigned to the W cross-section data. Accordingly, an evaluation effort was started for the most abundant W isotope 184 to complement the corresponding EFF-3 data evaluation below 20 MeV in the high-energy range relevant to IFMIF.

In the evaluation procedure, use is made of the SCAT2 code for spherical optical calculations, ECIS95 for elastic scattering and coupled channel calculations and the GNASH code for calculations of reaction cross sections using the Hauser-Feshbach theory for equilibrium decay and the exciton model for pre-equilibrium decay. A set of optical potentials has been identified that could be used for the calculations of nucleon and light ion interactions with the highly deformed W nuclides in the intermediate and high energy region. Comparison to experimental cross-section data are required to verify the selected optical potential and the associated set of parameters.

The experimental data basis for W isotopes is, however, very poor. Above 20 MeV only a few experimental results are available. Recently, the total cross-section has been measured up to 600 MeV by Abfalterer et al. Fig. 1 shows a comparison of coupled channel calculations and available experimental data for total cross section of natural tungsten. It is revealed that all optical potentials poorly reproduce the experimental data at higher energies. Therefore a more detailed analysis has to be performed for an optimal optical potential. Results of ECIS95 coupled channel calculations for the differential elastic scattering cross sections of $^{nat.}$W and ^{184}W are shown in Fig. 2. It is noted that both the Young deformed potential and the Koning global spherical potential can reproduce the experimental data rather well.

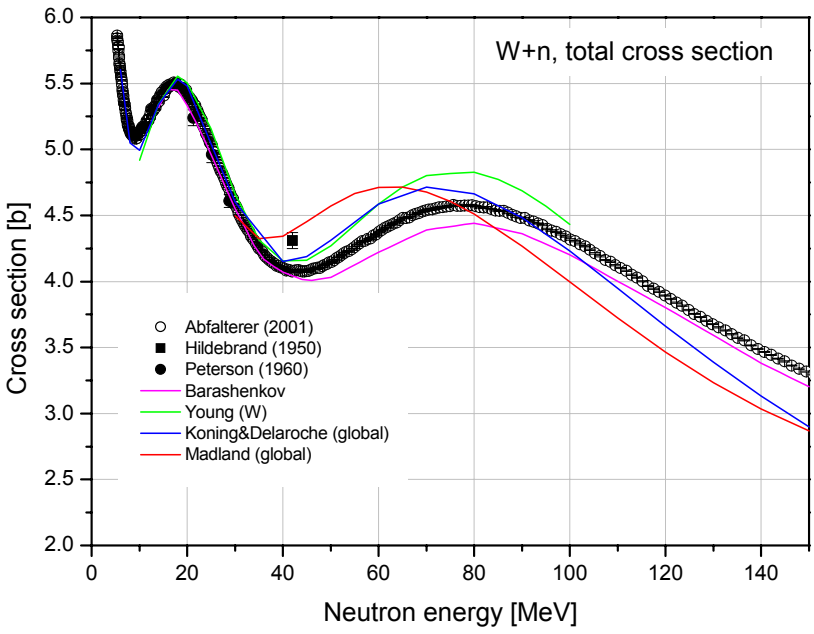

Fig. 1: Total neutron cross section of $^{nat.}$W as function of incident neutron energy: Comparison of experimental data and calculations using different optical model potentials (Barashenkov, Young, Koning & Delaroche, Madland)

The deformation parameters for the optical model were chosen by comparing the results of coupled channel calculations with the ECIS95 code to experimental cross section data for the first excitation levels of ^{184}W. Only the most suitable potentials of Young and Koning were taken into account in this comparison. The results obtained demonstrate the importance of including direct processes in the evaluation of the n + ^{184}W reactions.

As a result of the performed analysis it was concluded that the ongoing evaluation for ^{184}W

should take into account new experimental data not considered in the available ENDF/B-VI data evaluation. The ENDF/B-VI data need to be checked and improved below 20 MeV. The choice of the optical potentials for high energy calculations will be further checked by comparing calculated and experimental data for p + W interactions.

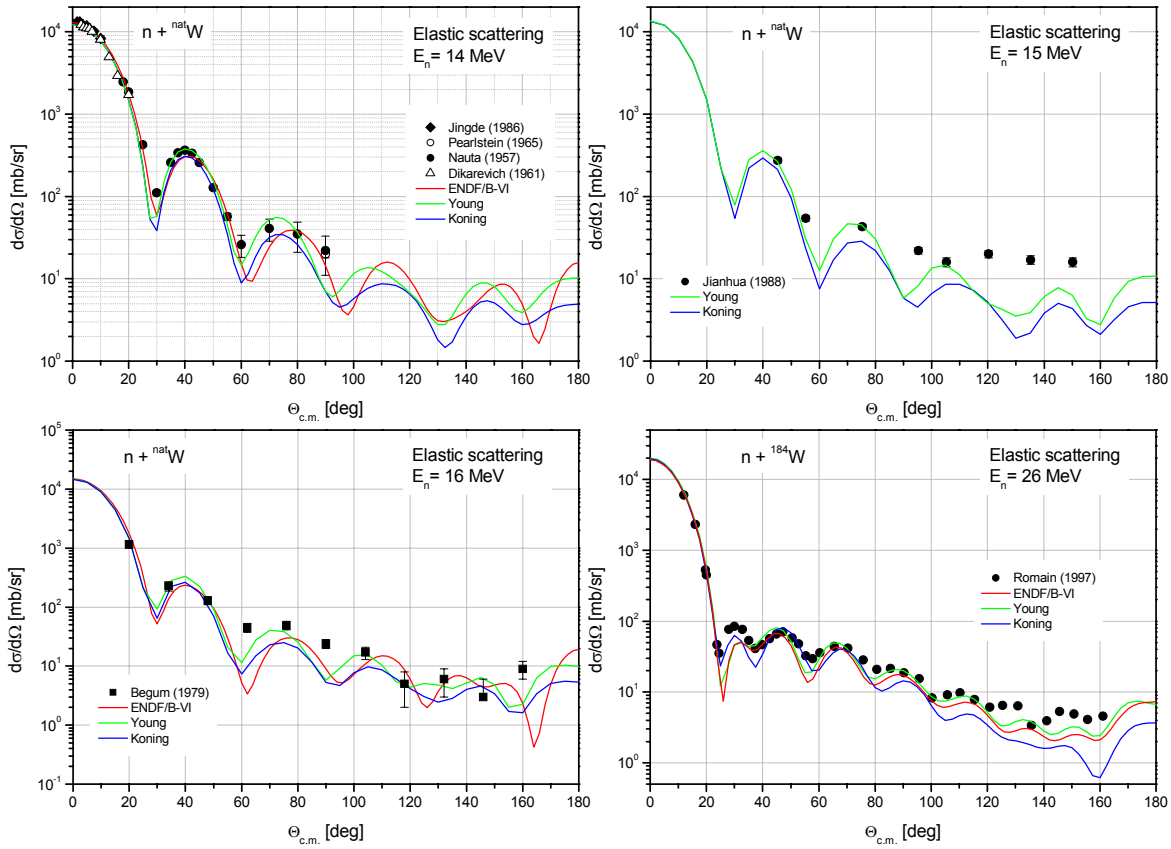

Fig. 2: Differential elastic scattering cross section of ^{nat}W and ^{184}W as function of scattering angle: Comparison of experimental data and calculations using different optical model potentials (Young, Koning & Delaroche, ENDF/B-VI)

TW2/3-TTMN-001-06
Benchmark Analyses on Tungsten

Comprehensive benchmark analyses have been performed using the spectrum measurements provided by the TU Dresden group for the transmission experiment on tungsten as part of Task TTMN-002 [2]. A detailed Monte Carlo based computational analysis of the experiment was performed using W data from EFF-2.4, and, for comparison and cross-checking, FENDL-1 and –2 data [3]. Neutron and photon flux spectra were calculated at the four locations of the spectrum measurements (5, 15, 25 and 35 cm) in the 49 cm thick tungsten assembly. Monte Carlo based sensitivity calculations with the MCSEN code were performed to trace down the observed discrepancies to specific cross-sections and energy ranges.

A detailed three-dimensional model of the experimental set-up was employed in the Monte Carlo transport calculations including an accurate representation of the neutron source, the W assembly with integrated scintillation detector, assembly support structure and experimental hall. Four separate Monte Carlo calculations were run to obtain the spectra at

the four different positions taking into account the fact that the NE-213 spectrometer was inserted in one of the detector holes during the measurement while the other three detector holes were filled with W.

Figs. 3 and 4 show C/E (calculation/experiment) ratios for the neutron fluxes in the energy range above 1 MeV and 12.5 MeV, respectively. Good agreement is obtained for the fast (E> 1 MeV) neutron flux at the first detector position. There is, however, a trend for underestimating the fast neutron flux with increasing penetration depth. At the deepest detector position P4, this underestimation amounts to 20% for EFF-2.4 and FENDL-1 data. FENDL-2 gives the best overall agreement of the fast neutron flux across the assembly with the lowest underestimation at the deep position P4. This is due to a better agreement of the neutron fluence below 5 MeV while the transmitted neutron source peak (E > 12.5 MeV) is systematically underestimated by up to 30% at position P4 (Fig. 4).

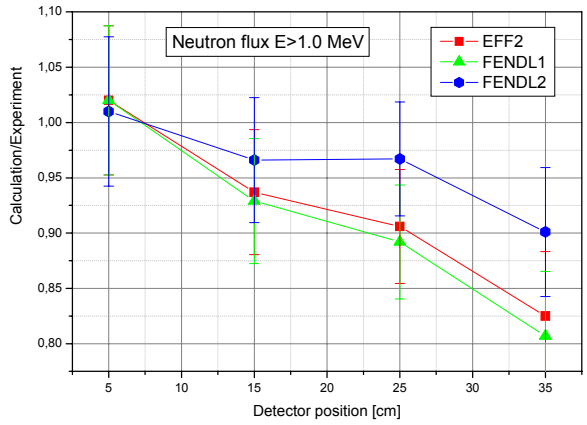

Fig. 3: Comparison of calculated and measured neutron flux integrals (E> 1.0 MeV).

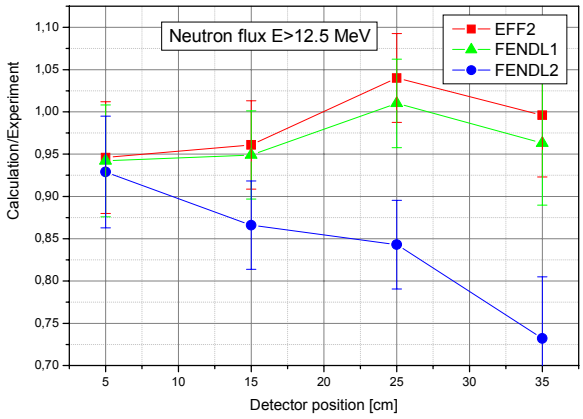

Fig. 4. Comparison of calculated and measured neutron flux integrals (E> 12.5 MeV)..

Table 2: Integrated sensitivities [%/%] of specified neutron flux integrals to specific reaction cross-sections (MT denote reaction numbers according to ENDF format rules; MT=16 is for the (n,2n) reaction).

MT	1-2.5 MeV	2.5-5 MeV	5-7.5 MeV	7.5-10 MeV	10-12.5	>12.5 MeV
2	-0.572	-0.426	-0.207	-0.527	-0.217	-0.431
16	-1.724	-2.307	-3.583	-3.419	-3.845	-3.881
51-52	-0.049	-0.036	-0.034	-0.023	-0.019	-0.017
53	-0.144	-0.071	-0.053	-0.029	-0.036	-0.027
54	-0.129	-0.065	-0.065	-0.054	-0.039	-0.041
55	-0.117	-0.059	-0.065	-0.044	-0.040	-0.032
56-63	-0.201	-0.055	-0.029	-0.020	-0.013	-0.022
64-73	-0.228	-0.032	-0.005	-0.003	-0.001	-0.002
91	-0.770	-2.018	-1.841	-0.931	-0.318	-0.522
102+103+107	-0.051	-0.017	-0.008	-0.006	-0.007	-0.008

The Monte Carlo sensitivity calculations revealed a dominant effect of the W(n,2n) reaction on the neutron flux spectra, see e. g. Table 2 for the integrated sensitivities at detector position P4. In particular, the neutron flux above 12.5 MeV shows a strong negative correlation to the (n,2n) cross-section. At the same time, the (n,2n) reaction is the main

contributor to the neutron population of the low energy range which is overestimated by FENDL-2 (Fig. 5). This indicates a too high (n,2n) cross-section in the FENDL-2 W evaluation. This is supported when comparing the evaluated (n,2n) cross-sections to experimental data available from the EXFOR data base (Fig. 6).

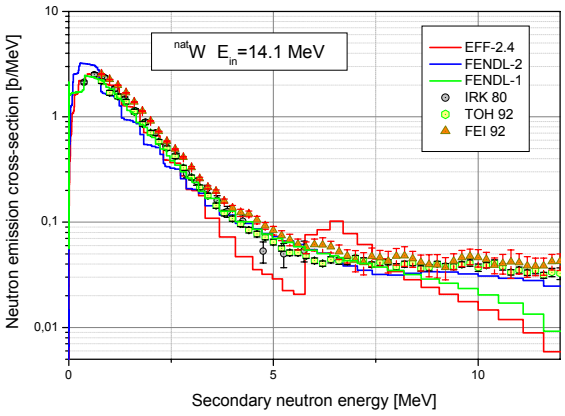

Fig. 5: Neutron emission cross section of ^{nat}W at 14.1 MeV incident neutron energy.

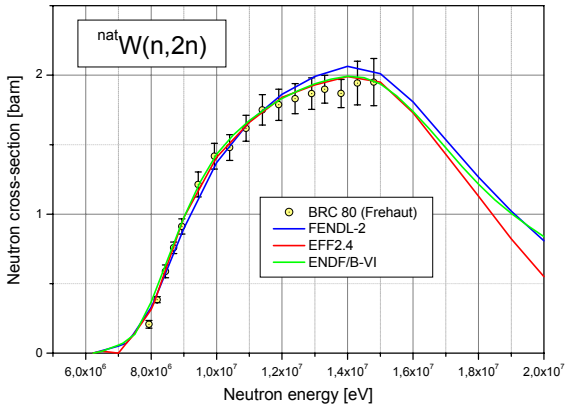

Fig. 6: ^{nat}W (n,2n) cross-section as function of incident neutron energy.

Although the fast neutron flux is predicted with sufficient accuracy across the W assembly, severe deficiencies do exist in the EFF-2.4 W data evaluation. The neutron emission spectrum e. g. shows a non-physical behaviour with a characteristic structure around 7 MeV (Fig. 5) which also becomes apparent in the calculated neutron flux spectra (Fig. 7). The gamma flux, on the other hand, is grossly overestimated by a factor 2-3 [1]. It was thus concluded that a major up-date of the EFF-2.4 data evaluation, which originates from the obsolete JENDL-3.0 data library, is required.

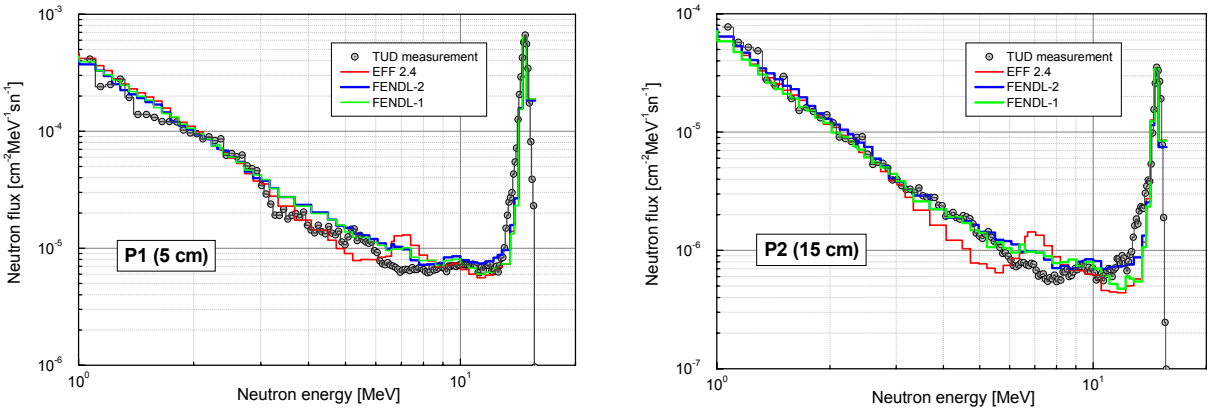

Fig. 7: Neutron flux spectra in tungsten assembly for detector positions P1 and P2 .

TW2-TTMN-001-6
Benchmark Analyses on Graphite

The results of the benchmark analyses performed for the SiC experiment [4] suggested to re-analyse the current EFF data evaluation for carbon (EFF-2.4 C-nat). A 14 MeV neutron transmission experiment on cylindrical graphite slabs with thicknesses of 5.5, 20.2 and 40.5

cm, conducted previously at JAERI/FNS, was considered to this end. In this experiment, time-of-flight (TOF) neutron leakage spectra were measured at angles between 0 and 66.8 degree. The experiment was analysed by means of MCNP-calculations using the EFF-2.4 C-nat and the FENDL-2 C-12 data [5]. The MCNP model and the experimental spectra were taken from the IAEA fusion neutronics benchmark collection. A good reproduction of the neutron spectra was obtained for the high energy range including the peaks formed by elastic and inelastic neutron scattering processes. Therefore, the overestimation of the neutron spectra observed in the SiC experiment for the 5-10 MeV energy range could not be addressed to the C data. No major revision of the EFF-2.4 carbon was thus required. A minor revision of the neutron emission spectrum was indicated for the energy range below 1-2 MeV. The analysis of the FNS-experiment revealed that the measured TOF spectra were transformed into energy spectra without taking into account multiple scattering events. This resulted in shifted peaks for the thick carbon slabs. In principle, this problem can be solved by directly calculating the time-of-arrival spectra and then converting them to energy spectra.

TW2-TTMN-001-4
Multigroup Covariance Data Files

New co-variance data files were processed for the Fe-56 EFF-3.1 and Si-28 EFF-3.0 cross section evaluations using the updated version of the NJOY 97.115 code. The Si-28 covariance matrices, only available above 1.75 MeV, were completed by adding the ENDF/B-VI data below this energy. A full covariance matrix library VITAMIN-J/COVA/EFF3 was prepared to facilitate the use of the EFF-3 data in uncertainty calculations [6]. The library includes the EFF-3 covariance matrices for Be-9, Si-28, Fe-56, Ni-58, and Ni-60 in highly compressed format, as well as the ANGELO-2 code for the extra-/inter-polation of the covariance data to an arbitrary energy structure, and the LAMBDA code for the verification of the mathematical properties of the matrices.

TW2-TTMN-001-5
Monte Carlo Calculation of Point Detector Sensitivities to Secondary Angular Distributions

Algorithms for the Monte Carlo based calculation of point detector sensitivities to secondary angular distributions (SAD) have been previously developed and implemented into MCSEN, a local update to the MCNP Monte Carlo code [7]. Verification was achieved through a computational iron benchmark by means of numerical tests and MCNP comparison calculations with perturbed cross-section data. Over the reporting period application tests were performed for the FNS/JAERI time-of-flight experiment on cylindrical beryllium slabs and the KANT transmission experiment on spherical beryllium shells using the latest Be EFF-3.05/NMOD=5 Be data evaluation [8]. Significant sensitivities were obtained for the elastic scattering and the (n,2n) reaction via the excitation of the 2.49 MeV level (MT=875). The sensitivities for the SAD of the (n,2n) reactions, however, showed large statistical errors even when taking into account more than 100 million source neutron histories. The uncertainties calculated for the neutron flux integrals are in the range of a few percent only. A major contribution to the uncertainty comes from the(n,2n) reaction. The calculated uncertainties, however, are only due to cross-section uncertainties as no SAD co-variance data exists in EFF-3 or any other available Be data evaluation.

TW3-TTMN-001-4
Development of Algorithms for Track Length Estimator Sensitivity Calculations with Local Version of MCNP

A method to calculate sensitivities of Monte Carlo point detector responses has been previously developed and implemented in a local version of the MCNP4C Monte Carlo code called MCSEN. This code has been used for sensitivity- and uncertainty analyses of various

fusion relevant benchmarks in the frame of Task TTMN-001. For such a typical analysis, one had to calculate for a given 14-MeV neutron source the response at a few detectors (around 5), in a fine (175 group) and in a coarse (about 10 groups) group structure. For the coarse group structure responses, sensitivities were then calculated, to many reactions (tens) of a few isotopes (one or two) in a fine group structure (175 groups).

The Monte Carlo based calculation for uncertainties of nuclear responses in the ITER Test Blanket Module (TBM), however, requires the capability to calculate sensitivities for responses by the track length estimator. Basically, the original MCNP4C code has such sensitivity capabilities. However, these capabilities were planned mainly for sensitivities to density, changes in material and isotopic compositions, and not for the systematic calculation of the sensitivity to various cross-sections in a fine group structure. Calculation of sensitivities to “175” groups would be very time intensive, if not prohibitive, since many common quantities would be calculated “175” times. On the other hand, the MCSEN code version is designed specifically with the intention of calculating efficiently the sensitivity to many reactions and to many energy groups. Therefore the capabilities of the MCSEN code are to be extended to calculating efficiently sensitivities for track-length estimators. In the current time-period, the algorithms for the calculation of sensitivities of track-length estimators with the differential operator method were formulated in detail, with special regard for future implementation in the MCSEN code.

Staff:

Y. Chen
U. Fischer
D. Leichtle
I. Kodeli (Josef-Stefan Institut, Ljubljana)
R. Perel (Hebrew University of Jerusalem)
P. Pereslavtsev
S. P. Simakov
I. Schmuck

Literature:

[1] U. Fischer, Nuclear Data for Design Analyses of the Test Blanket Modules in ITER:Review and Recommendations for EFF/JEFF Evaluations, EFF-DOC-852, NEA Data Bank, Paris, April 2003

[2] H. Freiesleben, C. Negoita, K. Seidel, S. Unholzer, U. Fischer, D. Leichtle, M. Angelone, P. Batistoni and M. Pillon: Measurement and analysis of neutron and gamma-ray flux spectra in tungsten; Report TUD-IKTP/01-03, TU Dresden, March 2003 and EFF-DOC-857, NEA Data Bank, Paris, April 2003, see also this status report on Nuclear Data, Task TTMN-002.

[3] U. Fischer, D. Leichtle, R. Perel, Monte Carlo transport and sensitivity analyses for the TUD neutron transport benchmark experiment on tungsten, EFF-DOC-860, NEA Data Bank, Paris, April 2003.

[4] U. Fischer, R. Perel, Y. Chen, Monte Carlo Transport, Sensitivity and Uncertainty Analysis for the TUD Benchmark Experiment on SiC, EFF-DOC-815, NEA Data Bank, Paris, April 2002.

[5] D. Leichtle, U. Fischer, Benchmark analysis of EFF and FENDL carbon cross-section data, EFF-DOC-844, NEA Data Bank, Paris, December 2002.

[6] I. Kodeli, VITAMIN-J/COVA/EFF-3 Cross-Section Covariance Matrix Library, EFF-DOC-837, and ZZ-VITAMIN-J/COVA/EFF-3, Programme Library Package NEA-1264/05 NEA Data Bank, Paris, December 2002.

[7] R. L. Perel: Algorithm for Monte Carlo Calculation of Sensitivities to Angular Segments, EFF-DOC-791, NEA Data Bank, Paris, November 2001.

[8] R. Perel, Monte-Carlo Sensitivity Analysis of FNS-and KANT-Be Experiments using the Be-9 EFF3.0/NMOD=5 Evaluation, EFF-DOC-845, NEA Data Bank, Paris, December 2002.

TTMN-002
Nuclear Data: Benchmark Experiments to Validate EFF/EAF Data

The objective of Task TTMN-002 is to provide the experimental data base required for the validation of the nuclear data libraries EFF (European Fusion File) and EAF (European Activation File) developed in the frame of Task TTMN-001 of the EU Fusion Technology Programme. According to the FP6 programme orientation on ITER (TBM) and IFMIF, the focus is on the experimental validation of TBM design calculations by means of a neutronics mock-up experiment and cross-section validation experiments relevant for IFMIF.

TW2-TTMN-002-2,-3
Measurement and Analysis of Neutron and Gamma-Ray Spectra in Tungsten

An experiment for benchmarking the neutron transport data of tungsten was carried out by a collaboration of ENEA Frascati, TU Dresden, FZ Karlsruhe and JSI Ljubljana. A thick block of W (16 mean free path for 14 MeV neutrons) was irradiated at the Frascati Neutron Generator (FNG) and several responses were measured inside the assembly.

Sub-tasks TW2-TTMN-002-2 and –3 comprised the measurement of neutron and γ-ray flux spectra by TUD, and their analysis with data of the European Fusion File (EFF-2.4) and of the Fusion Evaluated Nuclear Data Libraries FENDL-1 and FENDL-2 by FZK. Details are presented in Ref. [1].

Experiment

The experimental set-up is shown in Fig. 1. The dimensions of the W block were 47 cm x 47 cm x 49 cm of length (z-axis). The FNG tritium target was located at z = -5.3 cm. Flux spectra were measured in four positions (P 1,....P 4) at z = 5, 15, 25 and 35 cm.

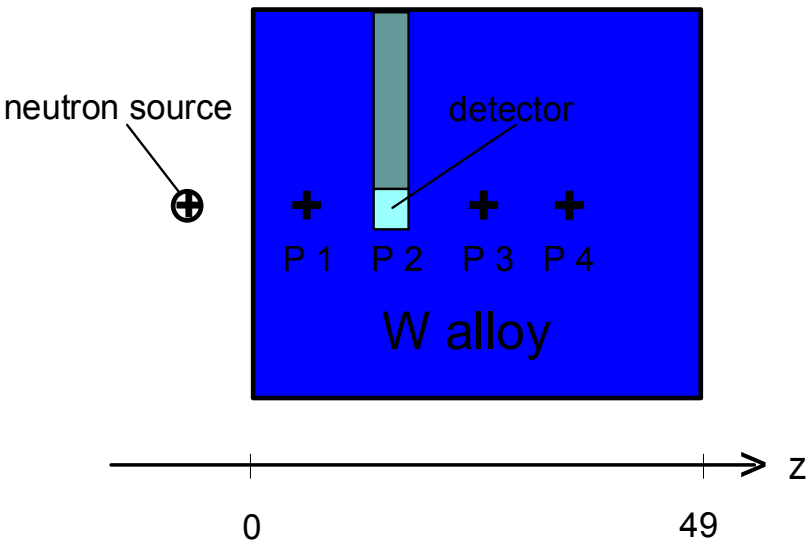

Fig. 1: Horizontal cut through the benchmark assembly with the detector in position 2.

Neutron and γ-ray flux spectra were measured simultaneously, using an NE 213 liquid-scintillation spectrometer. The scintillator was coupled to a photomultiplier by means of a 50 cm long light guide. When the detector was located at one of the positions (P 2 in Fig. 1), the other ones were filled with rods of W.

The pulse-height response matrix of the detector was determined on the basis of detailed simulations of experimental distributions from mono-energetic neu-tron and γ-sources with the MCNP-4A code. The DIFBAS code [2] was employed for unfolding the measured pulse-height distributions of the present experiment in order to generate the neutron and the γ-flux spectra. They were obtained as absolute fluxes, as the response matrices have been determined on an absolute scale.

Analysis

The computational analysis was performed with the Monte Carlo code MCNP-4C [3] using a full 3D geometry model of the assembly, the neutron generator and the experimental hall. Nuclear data were taken from the FENDL/MC-2.0 [4], FENDL-1 [5] and the EFF-2.4 [6] data libraries.

The **neutron flux** spectra are compared with the measured distributions in Fig. 2. The measured spectra show in the low energy part an exponential slope, a flat region between about 5 and 12.5 MeV and a broad peak structure at 14 MeV. In general, such distributions are predicted in the same way by the calculations, except for the EFF-2.4 calculations where a peak structure is obtained in the energy range between 6 and 8 MeV. Differential neutron emission data also do not support this peak [1]. The measured and calculated fluences integrated over energy intervals [1] show, that at the first detector position, the total neutron fluence (E > 1.0 MeV) is well reproduced by all of the calculations. With increasing penetration depth, there is a trend for underestimating the total fluence. For EFF-2.4 and FENDL-2 data, this underestimation amounts to 20% at the deepest detector position. FENDL-2 data give the lowest underestimation due to a better agreement of the neutron fluence below 5 MeV. The transmitted neutron source peak (E > 12.5 MeV), however, is underestimated systematically by FENDL-2 data. Again the underestimation increases with increasing penetration depth. The ratios of experimental-to-calculated value (C/E) obtained with EFF-2.4 and FENDL-1 for the neutron fluence above 12.5 MeV, on the other hand, are close to 1.0. The neutron flux above 12.5 MeV is most sensitive to the (n,2n) cross-section by a negative correlation [7]. At the same time, the (n,2n) reaction is the main contributor to the neutron population of the low energy range. Thus a too high (n,2n) cross-section is indicated for FENDL-2. This is supported by comparing [1] the evaluated (n,2n) cross-section to experimental data.

The **γ-ray flux** spectra are compared with the measured distributions in Fig. 3. The bulk of the γ-rays is emitted with energies of the order of 100 keV (rotational bands of the W isotopes). Then, a relatively smooth part is followed by peaks at energies that correspond to the neutron binding energies of the W isotopes. γ-ray fluxes integrated over these energy intervals [1] show that the total γ-ray fluence measured for the energy range 0.4 – 9.0 MeV is described with deviations of ≤ 20% by FENDL-2 data. A gross overestimation of the total γ-ray fluence with C/E ratios of 1.7 – 2.9 is found for EFF-2.4 data originating from the range E = 0.4 – 5.0 MeV. The fluence in the capture peak region, E = 5.0 – 9.0 MeV, is underestimated by EFF-2.4 and FENDL-1 data, but overestimated by the FENDL-2 calculations up to a factor of 3 at deep detector positions.

Conclusion

The fast (E > 1 MeV) neutron flux in a W benchmark assembly of a thickness corresponding to about 16 mean free path for 14 MeV neutrons can be reproduced by MCNP calculations within 20% using EFF-2.4, FENDL-1 or FENDL-2 data. FENDL-2 shows the best overall agreement with the measured spectra although a too high (n,2n) cross-section is indicated resulting in an underestimated high energy (E> 12.5 MeV) neutron flux of up to 30% at the deepest detector position. The γ-ray flux for E > 0.4 MeV is reproduced within 20% by FENDL-2 data. Overestimations by a factor of 2 or more are found for EFF-2.4 data indicating a gross error of the γ-production cross-section.

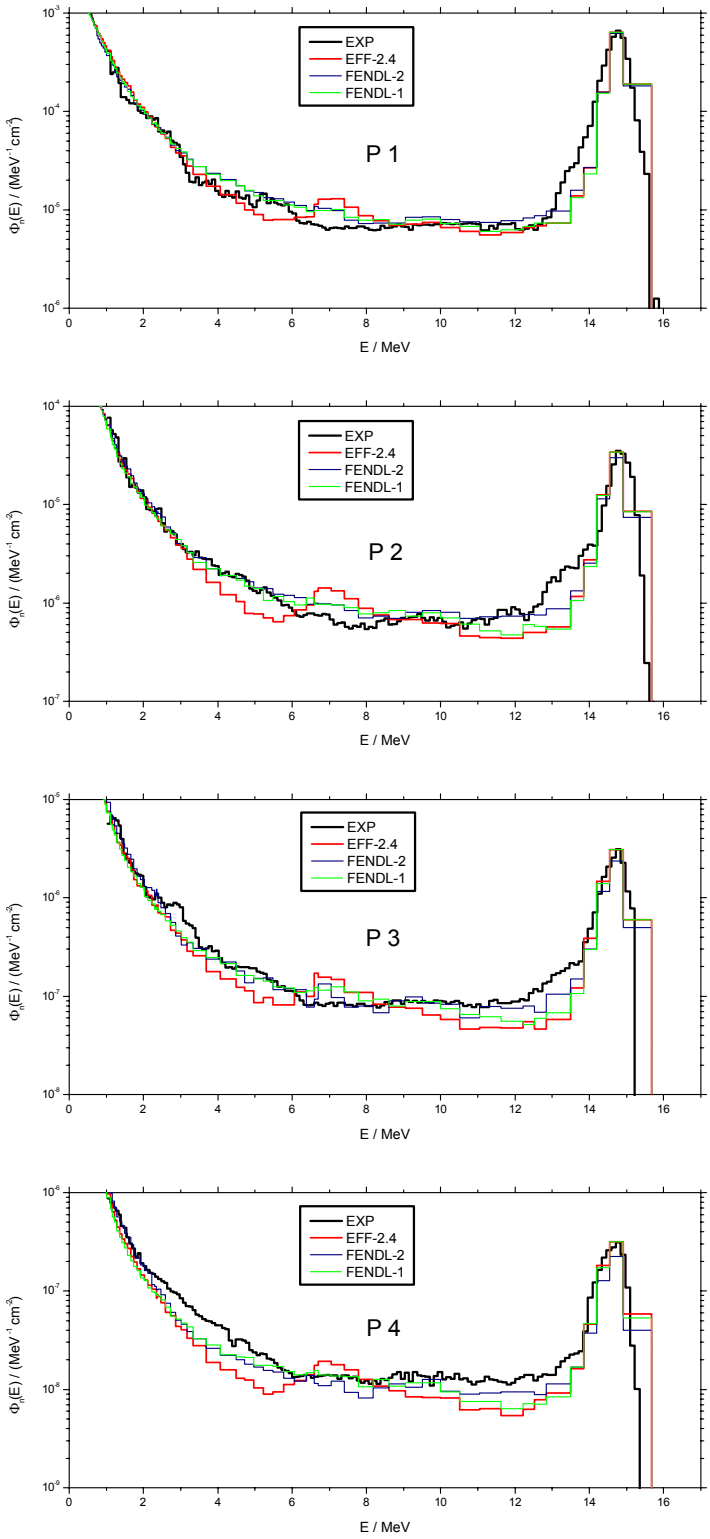

Fig. 2: Measured and calculated neutron flux spectra (normalised to one source neutron) at the four detector positions.

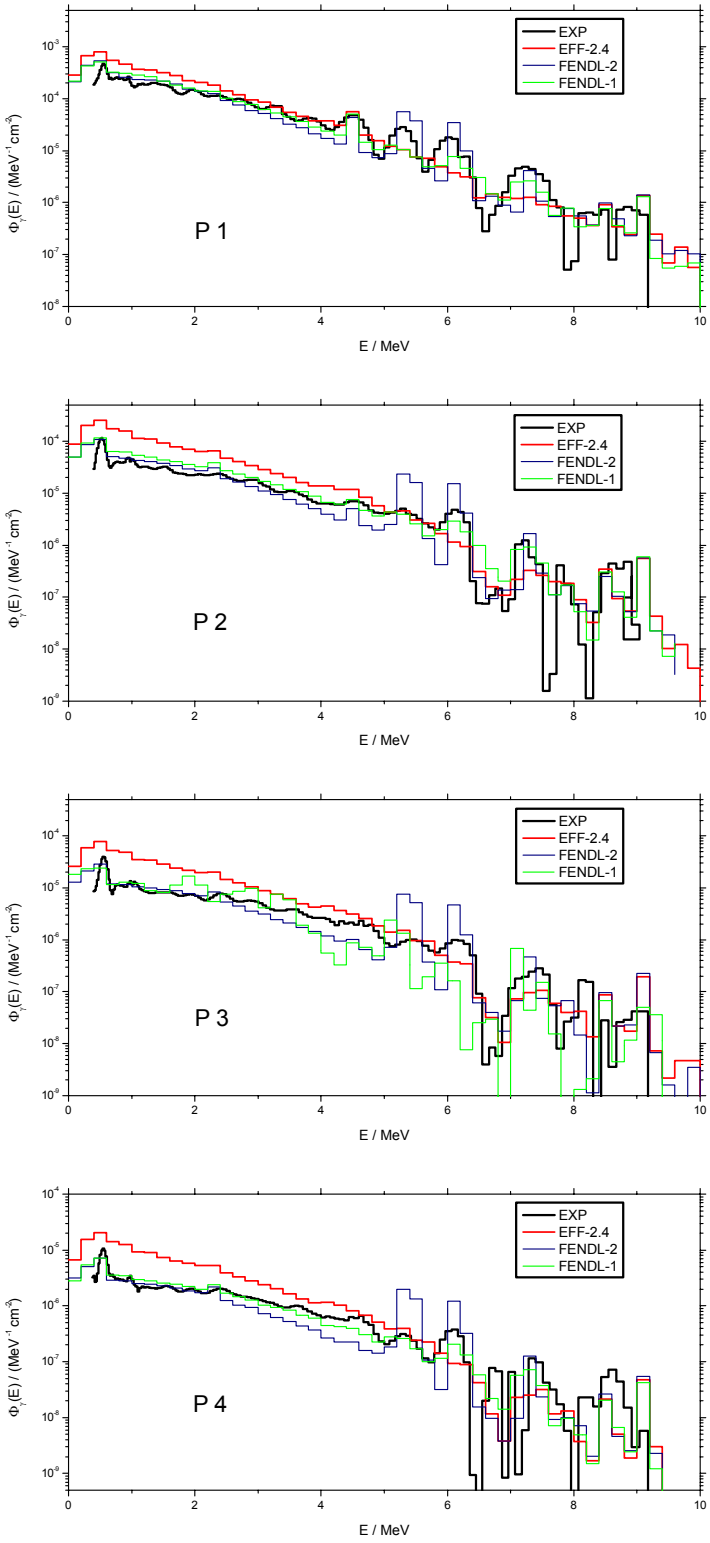

Fig. 3: Measured and calculated γ-ray flux spectra (normalised to one source neutron) at the four detector positions.

Staff:

U. Fischer
H. Freiesleben
D. Leichtle
C. Negoita
R. Perel (Hebrew University of Jerusalem)
K. Seidel
S. Unholzer

Literature:

[1] H. Freiesleben, C. Negoita, K. Seidel, S. Unholzer, U. Fischer, D. Leichtle, M. Angelone, P. Batistoni and M. Pillon, „Measurement and analysis of neutron and γ-ray flux spectra in tungsten", Report TUD-IKTP/01-03, TU Dresden, March 2003.

[2] M. Tichy, „The DIFBAS Program", Report PTB-7.2-193-1, Physikalisch-Technische Bundesanstalt, Braunschweig 1993.

[3] J. F. Briesmeister (Ed.), „MCNP – A General Monte Carlo N-Particle Transport Code", Version 4C, Report LA-13709, Los Alamos National Laboratory, 2000.

[4] H. Wienke and M. Herman, "FENDL/MG-2.0 and FENDL/MC-2.0 – The processed cross section libraries for neutron and photon transport calculations", Report IAEA-NDS-176, Vienna 1998.

[5] S. Ganesan and P. K. Mc Laughlin, "FENDL/E – Evaluated nuclear data library for neutron interaction cross-sections and photon production cross-sections and photon-atom interaction cross-sections for fusion applications", version 1, Report IAEA-NDS-128, Vienna 1994.

[6] J. Kopecky et al., "European Fusion File EFF-2.4 : Final report on basic data file", ECN Petten, Report ECN-C--94-016, July 1994.

[7] U. Fischer, D. Leichtle and R. Perel, "Monte Carlo transport and sensitivity analyses for theTUD neutron transport benchmark experiment on tungsten", EFF-DOC-860, April 2003.

TW2-TTMN-002-10
Activation Experiment in Fusion Peak Neutron Field on CuCrZr

The radioactivity induced by neutrons in the materials of fusion devices represents a central topic of safety-related investigations. The irradiated materials produce radio nuclides with a broad range of half-lives. The short-term radioactivity in the range of minutes to weeks is of interest for the heat production and the shut-down dose rate, whereas the long-term radioactivity in the range up to several hundreds of years is interesting for the waste management.

The spectrum of the neutron flux in a fusion device consists of two parts, the 14 MeV D-T fusion peak and a continuum reaching down to thermal energies. The radioactivity is mainly produced by 14 MeV neutrons, where the number of reaction channels is a maximum, and by thermal neutrons because for some reactions the cross section is large in this region.

CuCrZr is a candidate material for a heat sink in the first wall of the reactor. This plasma facing component will mainly be activated by 14 MeV fusion peak neutrons. CuCrZr material from EFDA Garching (Dr. A. Peacock) was used for the irradiation. The elemental composition was determined at FZ Karlsruhe (Dr. C. Adelhelm), including 42 impurities [1].

In a calculation with the European Activation System (EASY) [2], this material was taken to be irradiated at reactor conditions, this means with a flux density of the 14 MeV neutrons corresponding to a power density of 1.0 MW/m^2, for a period of one year. The results

obtained for the contact dose rate as a function of the decay time after irradiation, are shown in Fig. 4. For the short-term radioactivity the copper isotopes ^{62}Cu and ^{64}Cu are most important. ^{60}Co determines the recycling limit and the hands-on-limit of the material. The dose rate of ^{26}Al is well below the hands-on-limit, i. e. the Al impurities (dominant reaction ^{27}Al(n,2n) ^{26}Al) are sufficiently small. Measurements of the γ-activities and of the dose rate in the range of decay time labeled by t_m, permit the testing of the dominant radioactivity induced up to the recycling limit.

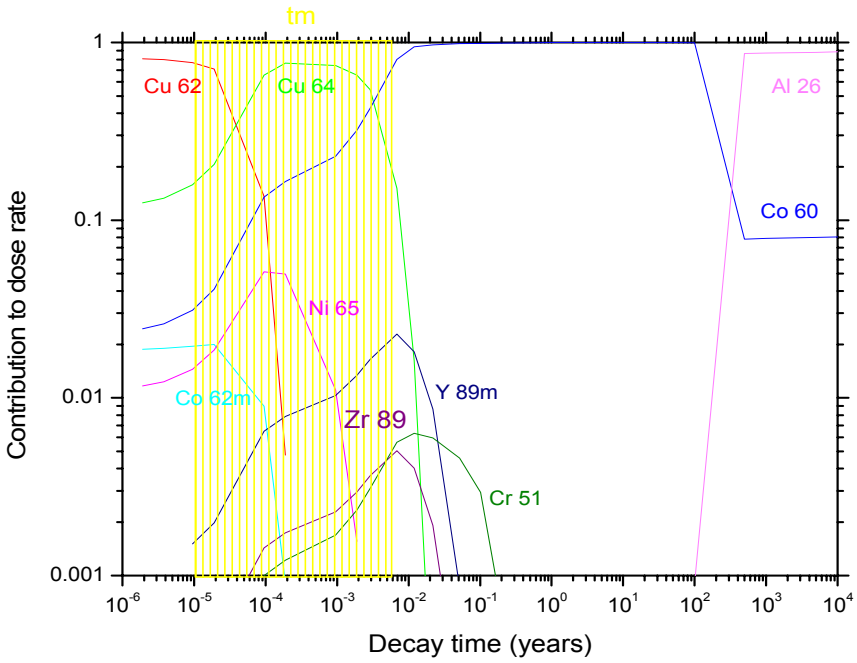

Fig. 4: Calculated contact dose rate (upper part) and contribution of the different radio nuclides to the total dose rate (lower part) after irradiation of CuCrZr with fusion peak neutrons of 1.0 MW/m^2 power density for one year as a function of the decay time.

Experiment

Irradiations of samples were performed at a D-T neutron generator of TU Dresden. The spectral distribution of the neutron flux at the sample position is presented in Fig. 5. The mean neutron energy of the fusion peak is 14.76 MeV; the full width of the peak at half maximum is 0.40 MeV.

The neutron fluence applied, was determined by simultaneous activation of niobium foils and evaluating the activity induced by the ^{93}Nb(n,2n)^{92m}Nb reaction.

The sample had a thickness of 1.02 mm, an area of 98.47 mm^2 and a mass of 0.8334 g.

Gamma-ray spectra were taken with a HPGe-spectrometer at several decay times in the range labeled with tm in Fig.1. The γ-activities identified by energy and half-life were used to determine the nuclide activities using γ-yield data from JEF2.2 [3] as in previous activation experiments [4].

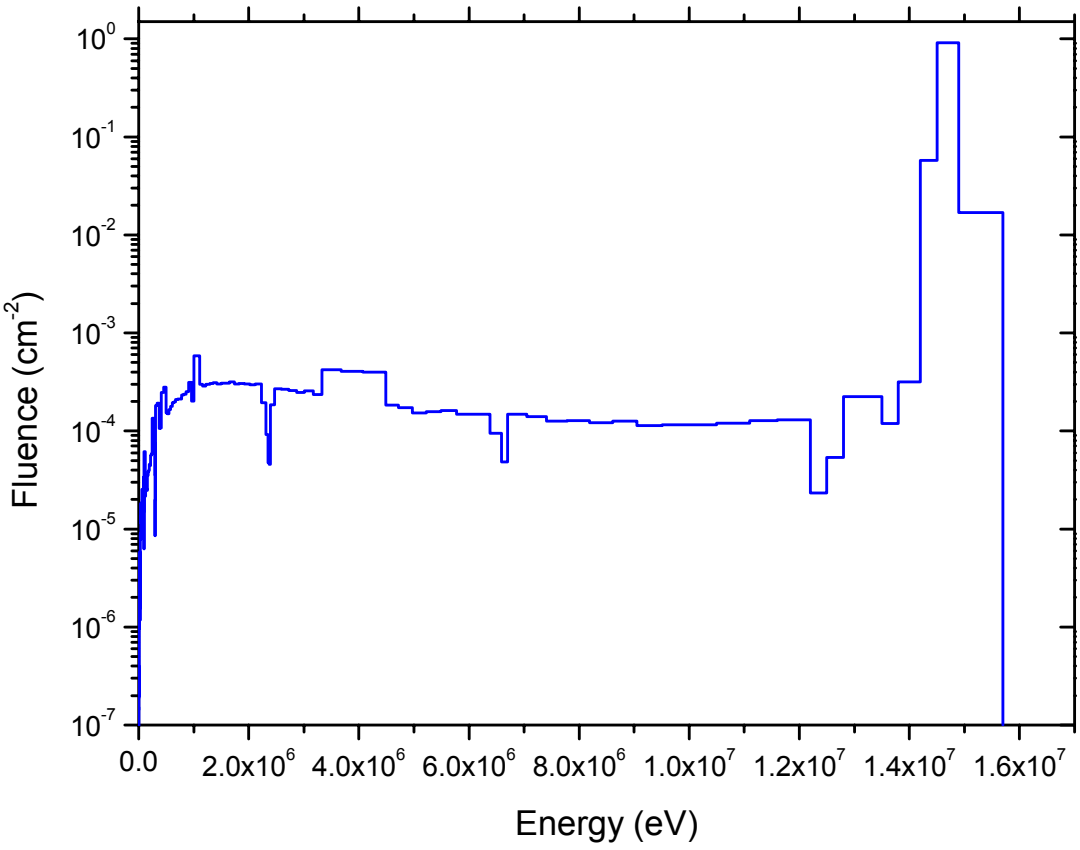

Fig. 5: Spectral distribution of the neutron flux at the sample position normalized to one source neutron and plotted as group fluence in Vitamin-J structure.

Analysis

The measured activities were analysed with the version EASY-99 and the subsequent, improved version EASY-2001 of the European Activation System [2]. The results are presented in Table 1. The uncertainty of the calculated activities ($\Delta C/C$) includes both cross section and half-life errors as estimated by EASY. The uncertainty of the experimental values ($\Delta E/E$) takes into account possible errors of the γ-activity measurements (statistical uncertainty of the γ-counting, the uncertainty of the efficiency calibration of the spectrometer including the geometry factor), of the sample mass, of the γ-yield data and of the neutron flux monitoring.

Ratios of calculated-to-experimental activity (C/E) that deviate from unity more than 50% and are outside the experimental error bars were obtained for ^{61}Co and ^{62m}Co. For ^{60}Co, ^{62m}Co and ^{65}Ni the calculation with EASY-2001 results in better agreement with the experimental data than the EASY-99 calculation.

Conclusion

The activation performance of technological CuCrZr in fusion peak neutron fields was investigated. Calculations with the European Activation System (EASY-99 and EASY-2002) let expect the recycling limit of the material after irradiation under fusion power plant

conditions (power density of 1 MW/m^2, exposition of 1 year) to be reached after about 100 years.

Table 1: Results obtained for the activity of radionuclides; radionuclides identified, their half-life and the γ-rays used to determine the activity, the neutron reactions producing these radionuclides, the ratios of calculated-to-experimental activity (C/E), obtained with EASY-99 and EASY-2001, and the uncertainties of both the calculated (EASY-2001) and the experimental activities.

Radio-nuclide	Half-life	E_γ (keV)	Reaction	Contr. (%)	C/E EASY-99	C/E EASY-2001	ΔC/C (%)	ΔE/E (%)
^{51}Cr	27.7 d	320.2	^{52}Cr(n,2n)	100	1.16	1.16	5.	10.8
^{60}Co	5.27 y	1332.5 1173.2	^{63}Cu(n,α)	100	1.21	1.14	48.6	9.7
^{61}Co	1.65 h	320.2	^{65}Cu(n,n´α)	100	1.73	1.73	20.	9.1
^{62m}Co	13.9 min	1163 2004	^{65}Cu(n,α)	100	0.26	1.53	62.	11.4
^{65}Ni	2.5 h	1481.8 1116.1 366.5	^{65}Cu(n,p)	100	1.24	1.19	10.	7.4
^{62}Cu	9.74 min	1163 875.7	^{63}Cu(n,2n)	100	1.09	1.09	5.	11.3
^{64}Cu	12.71 h	1345.9	^{65}Cu(n,2n) ^{63}Cu(n,γ)	99.4 0.6	1.13	1.13	5.	34.8
^{89}Zr	3.27 d	909.2	^{90}Zr(n,2n)	100	1.12	1.12	51.	10.3

All activities that are important up to the recycling limit were experimentally determined and compared with the calculated values. From the ratios of calculated-to-experimental activities (C/E) can be concluded that the expected activation performance is validated within 15% for EASY-2001 (about 20% for ESAY-99).

The eight C/E values obtained for the individual activities can contribute together with the results of other integral experiments and differential cross section measurements to the validation process of EASY [5] and lead to further improvements of the data base, as shown by detailed discussion [1] of the relevant cross section and decay data.

Staff:

R. Eichin
H. Freiesleben
K. Seidel
S. Unholzer

Literature:

[1] R. Eichin, R. A. Forrest, H. Freiesleben, S. A. Goncharov, D. V. Kovalchuk, D. V. Markovskij, D. V. Maximov, K. Seidel and S. Unholzer, “Measurement and analysis of induced activation in CuCrZr irradiated in fusion peak neutron field”, Report TUD-IKTP/03-02, TU Dresden, December 2002.

[2] R. A. Forrest and J-Ch. Sublet, “FISPACT-2001: User manual” and “The European Activation File: EAF-2001 cross section library”, Reports UKAEA FUS 450 and 451, Culham Science Centre, Abingdon (UK).

[3] The JEF-2.2 nuclear data library, JEFF Report 17, OECD Nuclear Energy Agency, Paris (France), April 2000.

[4] K. Seidel, R. A. Forrest, H. Freiesleben, S. A. Goncharov, V. D. Kovalchuk, D. V. Markovskij, D. V. Maximov, S. Unholzer and R. Weigel, “Activation experiment with Tungsten in fusion peak neutron field”, Report TUD-IKTP/02-01, Technische Universität Dresden, April 2002.

[5] R. A. Forrest, M. Pillon, U. Von Möllendorf and K. Seidel, “Validation of EASY-2001 using integral measurements”, Report UKAEA FUS 467, Culham Science Centre, Abingdon (UK), December 2001.

TW3-TTMN-002-6
Design of TBM Neutronics Experiment

The objective of this sub-task is to provide the data required for designing the experimental set-up and the measurements (neutron and gamma flux spectra, tritium production) in the TBM neutronics mock-up. The mock-up will be of the HCPB blanket type and should replicate the essential nuclear features of the corresponding TBM in ITER. As a preparatory step for designing the mock-up assembly, a TBM based on the latest design of the HCPB blanket was integrated into the test blanket port of the 3D MCNP model of ITER (Fig. 6). First calculations were performed for the radial distribution of the neutron spectra in the beryllium and the breeder ceramics beds in the HCPB TBM. The spectra were submitted to ENEA Frascati to enable a comparison to the flux spectrum profiles in the TBM neutronics mock-up.

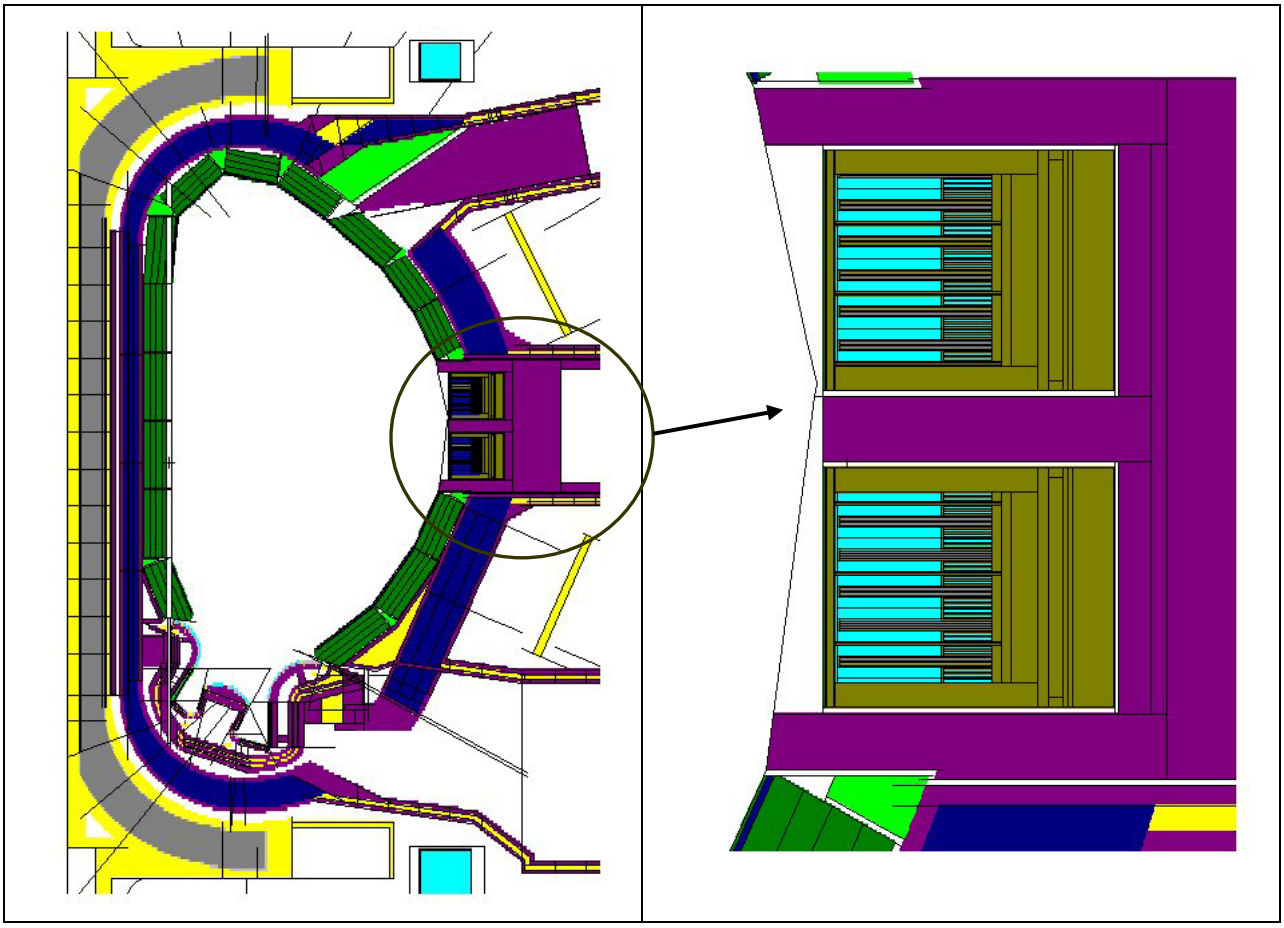

Fig. 6: MCNP model (radial-poloidal cut) of ITER with integrated TBM of the latest HCPB blanket type.

Staff:

U. Fischer
P. Pereslavtsev

TW3-TTMN-002-9
Pre-and Post Analysis of the Validation Experiments for Cross-sections up to 55 MeV in an IFMIF-like neutron spectrum

A thick D_2O target, bombarded by 24 or 36 MeV protons and a beryllium target, bombarded by 18 MeV deuterons, will be used to generate an IFMIF-like neutron spectrum (with energies up to 55 MeV) in the neutron activation experiment to be performed at the Nuclear Physics Institute (Rez) as part of Task TTMN-002. A computational pre-analysis including a numerical prediction of the angular-energy differential yields of these neutron sources is required for the design optimisation of the experiment.

The latest version of the MCNPX high energy particle Monte Carlo code was used for the pre-analysis with evaluated cross section data for protons (LA-150h) and neutrons (LA-150n) as well as built-in analytical models for the neutron generation. The calculation results were compared to experimental data obtained at the NPI Rez cyclotron and other laboratories for p-D_2O and d-Be thick target neutron sources. Detailed geometry models were developed so as to accurately represent in the Monte Carlo calculations the experimental set-up including the target, the ion spatial distribution, the ion beam energy distribution and the neutron detector.

For the p-D_2O neutron source it was found that MCNPX with the built-in Intranuclear Cascade Models INC models (Isabel and Bertini) underestimate the measured yields by one order of magnitude, see Fig. 7. The calculations with LA-150h data, on the other hand, underestimate the neutron spectra by a factor 2 at zero degree but reasonably agree at larger angles. The analyses of the status of the dominating D(p,xn) reaction has indicated that a pure phase-space distribution as used in the LA-150h data file does not represent the p-d differential cross-sections correctly. This explains the disagreement found for the thick D_2O target.

For the d-Be neutron source, no evaluated cross sections are available to describe the deuteron interaction with beryllium, while the ISABEL reaction model built in MCNPX fails to reproduce the experimental data, see Fig. 8. Since Be and Li are neighboring nuclei, the McDeLicious code was used with d-Li evaluated cross section data to simulate the generation of d-Be neutrons. The comparison with available experimental data shows that McDeLicious reasonably reproduces the energy distribution but provides a less anisotropic angular distribution.

The pre-analysis has shown that the presently available models and nuclear data (MCNPX, LA-150) cannot reproduce sufficiently well the thick target neutron yields of p-D_2O and d-Be neutron sources over the whole range of angles and energies. Measured spectra are required for adjusting the calculated neutron source spectra and thus enable a reliable computational analysis of the activation experiments.

Staff:

U. Fischer
S. P. Simakov

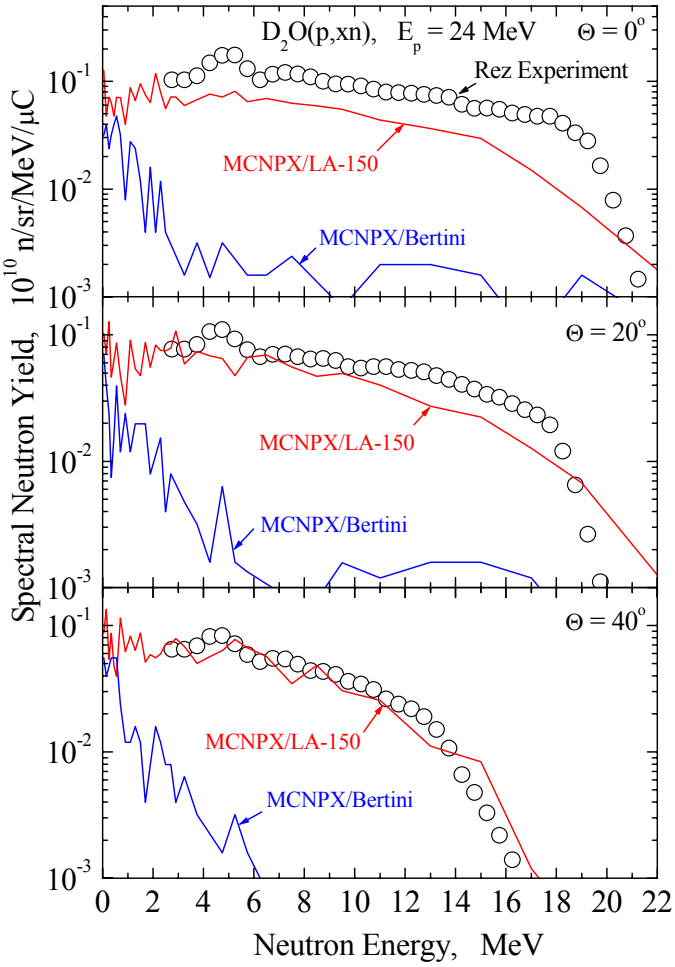

Fig. 7: Double differential neutron yields from thick D_2O target bombarded by 24 MeV protons: NPI (Rez) experiment and MCNPX predictions with LA-150 proton library and Bertini INC model.

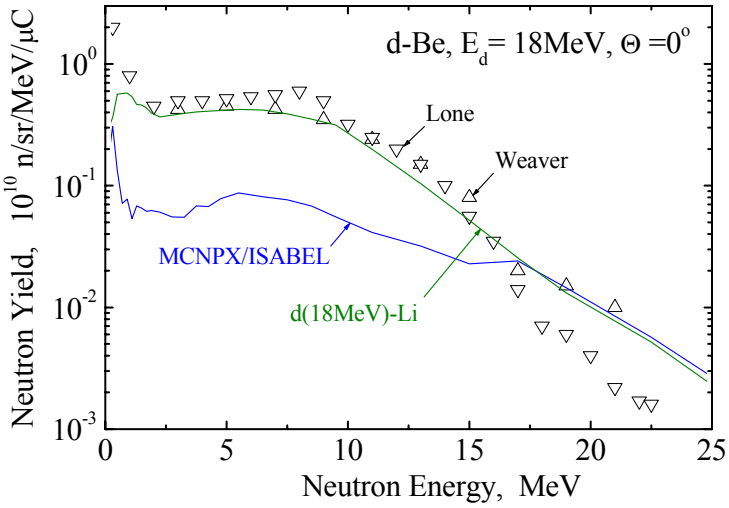

Fig. 8: Forward neutron spectral yield from Be thick target impinged by 18 MeV deuterons. Experiment: Weaver et al. and Lone et al.; calculations: MCNPX/ISABEL. For comparison the neutron spectra from Li thick target bombarded by 18 MeV deuterons is shown as calculated by McDeLicious code.

I F M I F

TTMI-001
IFMIF - Accelerator Facilities

I. Ion Source, LEBT, Diagnostic and RFQ Development

I.1 Ion source

At the University of Frankfurt, a high current H^+/D^+ source was developed and tested. The ion source is an arc discharge driven volume source. It is equipped with a solenoid for the plasma confinement and a variable filter magnet to control the electron energies in the plasma. In operation with an arc power of 10 kW a beam current of 200 mA was extracted [1] using an emission opening radius of 4 mm. This corresponds to the required D^+ current of 140 mA.

Because of problems with the safety in our ion source lab, source operations with hydrogen are not allowed. Before a reconnection of the lab the installation of an exhaust system above the ion source is required. Moreover, different safety lights have to be installed and an operation manual for the use of the test facility has to be written. The installation of the exhaust system will be performed in October 2003.

In the meantime a small hydrogen source has been used to test a CCD camera for a two-dimensional ion beam diagnostic. For the next stage of development it is planed to increase the ion source lifetime. In operation with one tungsten filament (1.8 mm thickness), an arc power of 10 kW dc and a beam current of 200 mA, the ion source lifetime is about 100 h. In order to increase this value the ion source will be equipped with four filaments. After commissioning and optimisation of the source it is planned to measure the beam emittance at full beam current. For this reason a new high power slit grid emittance measurement device was bought and has been tested. This device is ready for operation. Parallel to the emittance measurements a beam investigation using the CCD camera will be performed. This delay is not essential for the IFMIF project, since the source has always achieved the IFMIF - requirements. It is a back up solution for the chosen ECR – source anyway.

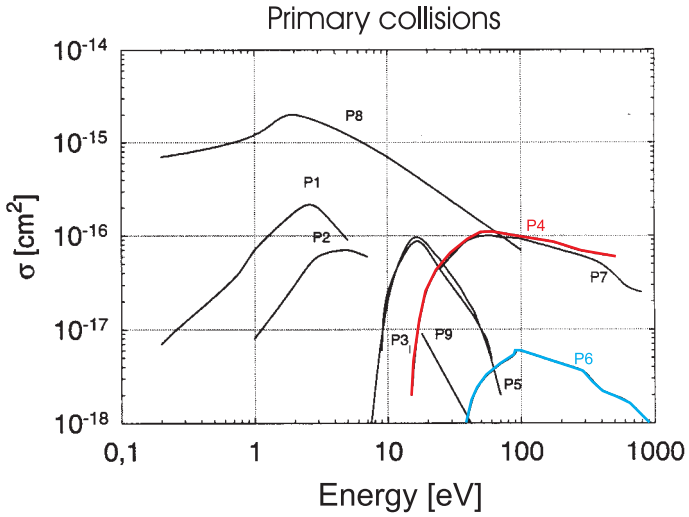

primary collision	reaction	energy [eV]	reference
P1	$e + H_2 \rightarrow H_2^*(rot) + e$	< 0.1	[Iti, Hun, Iti 2]
P2	$e + H_2 \rightarrow H_2^*(vib) + e$	< 0.1	[Iti, Hun, Kie, Iti 2]
P3	$e + H_2 \rightarrow H_2^*(elec) + e$	< 5	[Iti, Hun, Ha, Iti 2]
P4	$e + H_2 \rightarrow H_2^+ + 2e$	15.4	[Kie, Taw 2, Chan]
P5	$e + H_2 \rightarrow 2H + e$	< 5	[Kie, Chan, Taw]
P6	$e + H_2 \rightarrow H^+ + H + 2e$	< 20	[Taw 2]

Fig. 1: Cross sections for primary collisions as a function of electron energy. For H_2^+ production the reactions P4 and P6 are relevant.

From great importance is the development of a high current H_2^+ ion source, which is inevitable for the run in of the accelerator. The use of the D^+ ion source for this action is impossible, the particle losses, which are unavoidable in this phase, would lead to a intolerable activation by the neutrons. This H_2^+ ion source turned out to be more difficult as expected. Our intensive studies showed, that the use of the D^+ ion source for the production of high current H_2^+ ion beams is not possible. Therefore a new source has to be designed. Detailed studies lead us to following design parameters: The cross sections show (see fig. 1 and 2, P_3, P_4, P_6, S_7, S_9), that the integral cross section for the H_2^+ production are very small and the electron energies must lie in a small energy bandwidth (~10 – 30 eV). The plasma density has to be small, the volume large (to achieve the high current), the distance between the filaments and the extraction opening shall be short, the number of filaments 2 – 4. The use of a solenoid is not appropriate, the source has to have a multicusp field. An important question concerns the necessary H_2^+ beam current. So far, an emission current density of 50 mA/cm^2 has been achieved in Berkeley with an H_2^+ fraction of 80 %. But the diameter of the extraction hole was only 1 mm. This best result (0.4 mA) is far away from the required current of about 100 mA. Therefore also a multiaperture extraction system will be considered. But the much larger emittance of such a system may be unacceptable. As a result we can state, that we have got a good overview of the necessary basis parameters of this source, but much more work has to be invested to come to a detailed layout and realisation.

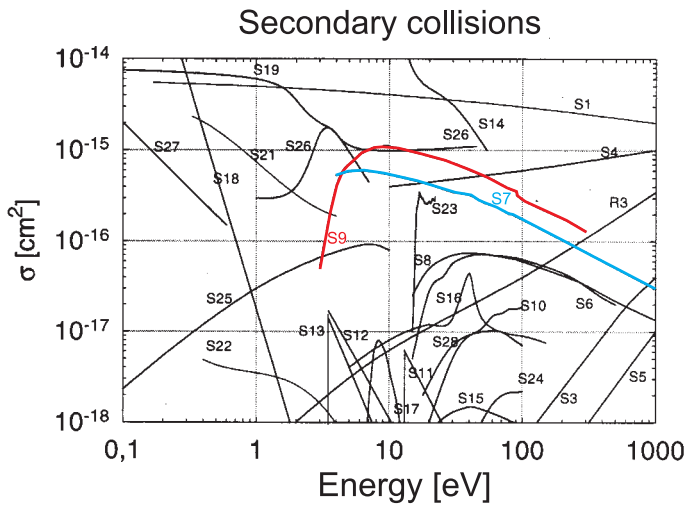

secondary collision	reaction	energy [eV]	reference
S1	$H^* + H \rightarrow H + H^+$	< 0,2	[Taw, Sa]
S2	$e + H_3^+ \rightarrow H_2 + H^+ + e$		[Chan 2]
S3	$H_2 + H \rightarrow H^+$	< 100	[Nak]
S4	$H^- + H_2 \rightarrow H + ...$	< 10	[Nak]
S5	$H^- + H_2 \rightarrow H^+ + ...$	< 300	[Nak]
S6	$e + H \rightarrow H^+ + 2e$	13,6	[Kie, Ch, Taw 2]
S7	$e + H_2^+ \rightarrow H^+ + H + e$	< 1	[Step, Chan]
S8	$e + H(1s) \rightarrow H(2p) + e$	< 13,6	[Cou, Cal]
S9	$e + H(2s) \rightarrow H^+ + 2e$	< 2	[Taw 2]
S10	$e + H_2^+ \rightarrow 2H^+ + 2e$		[Kie, Step]
S11	$h\nu + H(1s) \rightarrow H^+ + e$	13,6	[Cro]
S12	$h\nu + H(2p) \rightarrow H^+ + e$	3,5	[Cro]
S13	$h\nu + H(2s) \rightarrow H^+ + e$	3,5	[Cro]
S14	$e + H(1s) \rightarrow H(1s) + e$		[Cal, Kie 2]
S15	$e + H(1s) \rightarrow H(3s) + e$	< 15	[Cal, Kie 2]

Fig. 2: Cross sections for secondary collisions as a function of electron energy. For H_2^+ production the reactions S7 and S9 are relevant.

I.2 Determination of compensation degree within fringe fields in the LEBT.

The beam transport of high perveance ion beams is mainly influenced by space charge forces. For compensated transport as proposed for IFMIF the detailed knowledge of the degree of compensation along the beam axis is essential to determine the beam transport properties of the LEBT including losses and emittance growth. The processes defining the compensation degree in drift sections are well known and the compensation degree within the solenoids where the magnetic fields are dominant, can be estimated with adequate precision. The transition between these two states in the fringe fields of the solenoids are still under investigation. To measure the degree of compensation within fringe fields, a residual gas ion energy analyser will be installed in the LEBT system between the two solenoids. Three experiments on space charge compensation in fringe fields are planned:

1) both magnetic fields of the solenoids have the same polarity (B_z (z=0)~$5*10^{-3}$ T), only heavy and energetic particles can escape between the solenoids.

2) solenoids have opposite polarity to reduce fringe fields between them (B_z (z=0)=0 !)), a loss channel for all particles between the solenoids is open.

3) drift between both solenoids with magnetic shielding

In a first step the magnetic field strength in transversal and longitudinal direction was determined. The results of the measurements are shown in fig. 3. They show that the magnetic field between the solenoids is small enough to extract compensation particles form the beam in transversal direction. Now a residual gas ion energy analyser will be installed between the solenoids to determine the degree of compensation and the influence on beam transport for the different field configurations.

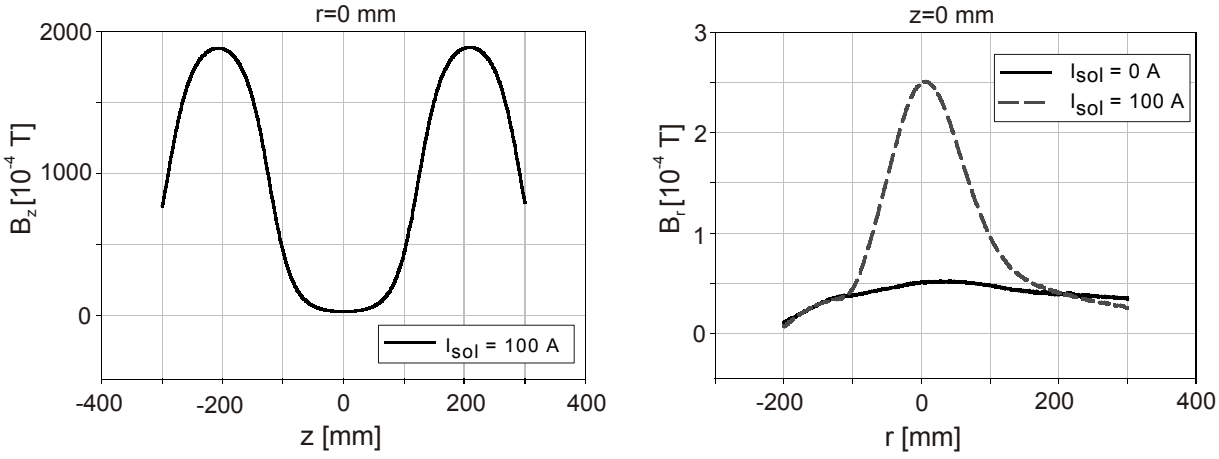

Fig. 3: Result of a magnetic field measurements (field polarity equal) for determination of the compensation degree within the fringe fields. The solid line in the right picture shows the residual magnetism of the solenoids (B_z (I=0)<$5*10^{-5}$ T).

I.3 Non interceptive diagnostics development

To improve the spatial resolution available by optical profile measurements a new intensified slow scan CCD camera will be used. The advantages of the new system compared with the one already in use are:

1) Doubling of the number of pixels in both transversal planes improving the total pixel number by a factor of 4.

2) Identical Pixel size of CCD chip and residual light amplifier (6 μm) to reduce Moire effects.

3) Coupling between intensifier and CCD chip by glass interconnects instead of lens coupling to reduce vignetation.

4) Peltier cooling instead of liquid nitrogen cooling for flexible use within the experiment.

The two systems together allow simultaneously the determination of the beam profiles in both transversal planes. This is necessary due to the different starting conditions for the ions in both transversal planes caused by the magnetic dipole filter field needed to improve the source plasma performance. The new diagnostic system has been set up and successfully tested using a printed target. Fig. 4 shows the images of the target gained from both cameras under identical conditions. For the given experimental set up the transversal resolution is 136 μm/pixel for the old camera (pixel structure on the lower right picture visible) compared with 68 μm/pixel. The new optics allows a smaller minimum distance between camera and the target (ion beam) and therefore the resolution limit for the new camera is 20 □m/pixel. The angular resolution improved from 2°mrad to 1°mrad simultaneously.

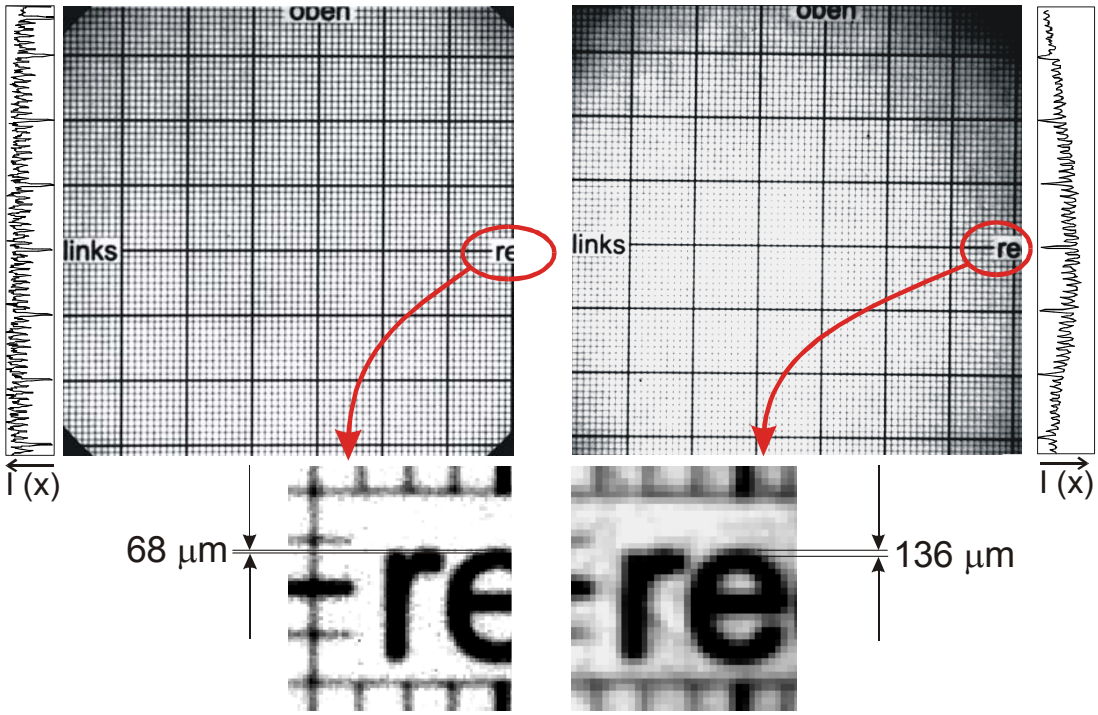

Fig. 4: Comparison between the results gained from the new (left) and the old (right) CCD camera. The overall pictures (above) demonstrated the reduction of the vignetation error. The detailed view (below) demonstrates impressively the resolution enhancement.

The suppression of vignetation effects (upper left picture has a more homogeneous light distribution than the right one) are clearly visible. This new technique will improve the results of the transversal beam diagnostic and simplifies data interpretation and reduces errorbars.

I.4 Diagnostic chamber and vacuum system for the LEBT

The residual gas pressure in the LEBT is dominated by the gas flow from the ion source. On the other hand a residual gas pressure above $5*10^{-5}$ hPa has only a small improvement of the degree of space charge compensation for DC beams. Therefore to reduce particle losses due to interactions between residual gas and the beam ions, the residual gas pressure in the LEBT has to be reduced to be below $5*10^{-5}$ hPa. An effective way to reduce the gas pressure is the use of a differential pumping system. Therefore the first vacuum chamber is divided in two independently pumped chambers connected only by an aperture slightly bigger than the beam diameter. To study experimentally the different aspects of the first LEBT chamber after beam extraction (beam dynamics, vacuum aspects, beam diagnostics, etc.) the chamber with included differential pumping system has been constructed, built in the workshop and

successfully vacuum tested. Figure 5 shows the new device on the vacuum test bench. Flanges for three pumps, a replaceable aperture between both vacuum stages, a Faradaycup, optical beam analyses and residual gas spectroscopy are available. In a next step the device will be installed in the LEBT system between the ion source and the first solenoid and experiments on pumping efficiency and pressure separation in both stages for different apertures will be performed.

Fig. 5: First diagnostic and pumping chamber for LEBT measurements.

I.5 Investigation of beam injection into a RFQ by a Gabor lens LEBT

To investigate the injection of an high perveance ion beam into a RFQ and the Gabor lens option for IFMIF as well, an low power experiment is under construction. The actual status of the experimental set up is shown in fig. 6. The ion source of volume type and the LEBT system are operational, and the beam at the injection point into the RFQ is characterised. The RFQ has been installed and vacuum tested. Low power tests for surface conditioning have been performed successfully as well as measurements of the resonance frequency of the RFQ-cavity and the reflected power (-25 dB). The tuner is installed, successfully tested and operational. The beam diagnostic behind the RFQ is tested and will be installed at the beam line in the near future. High power tests and beam injection into the RFQ is scheduled for autumn 2003.

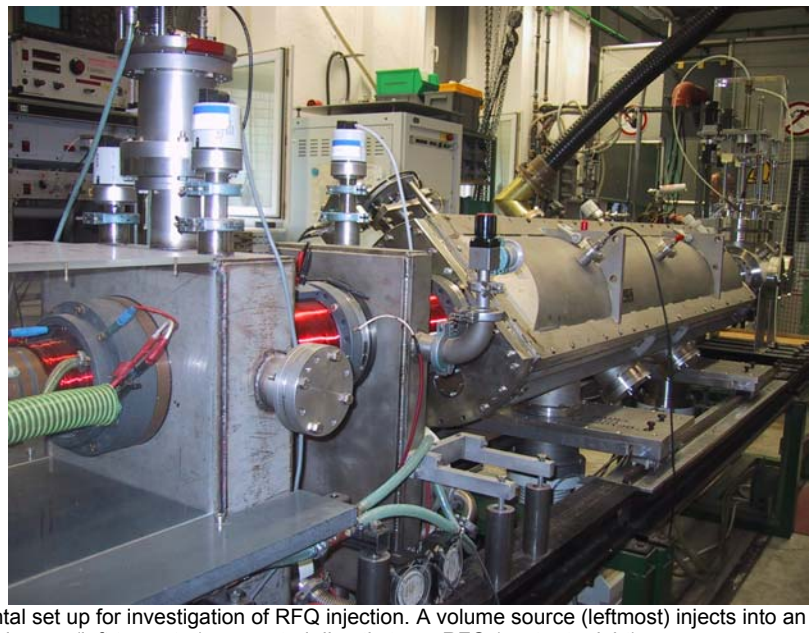

Fig. 6: Experimental set up for investigation of RFQ injection. A volume source (leftmost) injects into an LEBT consisting of two Gabor lenses (left to center) connected directly to an RFQ (center to right).

I.6. Investigation of the 4-Rod RFQ

The 4-Rod RFQ is an alternative solution to the complex 4-Vane structure. The fields are concentrated on the resonating stem structure and with roughly the same power consumption the power density is higher by a factor 2-3.

The RFQ design for the IFMIF accelerator requires a RFQ at 175 MHz and cw-operation. Extrapolating from our experience from existing pulsed machines at 200 MHz and cw RFQs at 108 MHz we have concentrated in rf-modelling of a suitable 175 RFQ resonator. MAFIA and MWS simulations have been done to optimize the design. Shunt impedances of up to 90kOm have been achieved.

The electrode voltage in the design is as high as 120kV, which results in a power consumption of 160 kW/m. Our rf-structure has 10 stems per m. The rf-simulation gave a 65% part of the power losses on the stems, which corresponds to a power density of 36 W/cm^2 , with peak values at the transition from stems to eletrode supports of up to 120 W/cm^2 . We have started simulations of the thermal distribution, possible cooling schemes and and the resulting mechanical deformations.

To test solutions we preparing a short high power test tank to test the critical peak power density effect at the frequency of 175 MHz

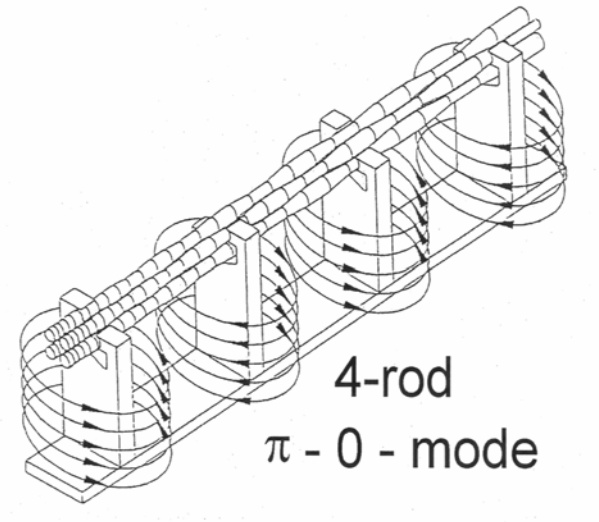

Fig. 7: Scheme of the 4-Rod RFQ insert.

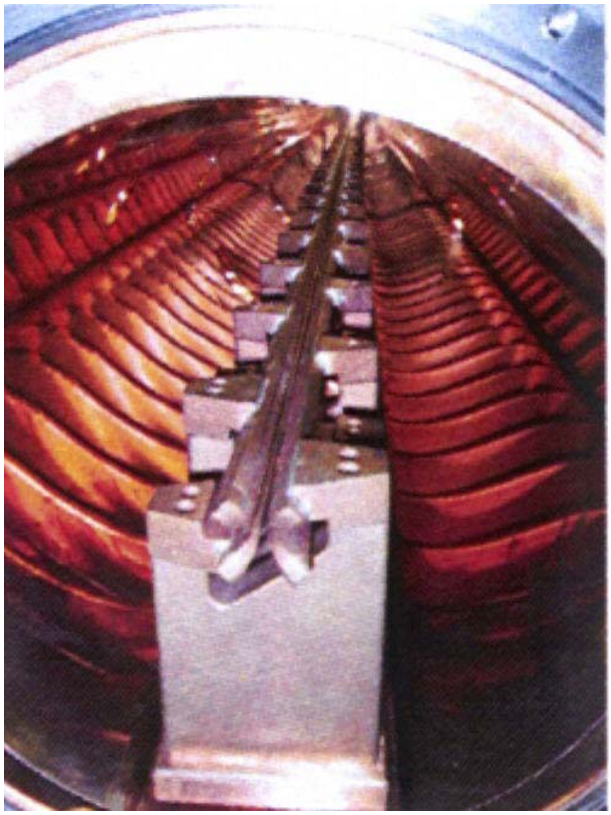

Fig. 8: View of the 4-Rod-RFQ.

-

II. IFMIF Linac Development

The IFMIF project (**I**nternational **F**usion **M**aterials **I**rradiation **F**acility) requests two cw linacs operated in parallel. Each one is designed to provide a 5 MW 125 mA deuteron beam at 40 MeV for the production of an intense neutron flux with an energy around 14 MeV. This paper presents a drift tube linac design for this project, which is completely based on H-type cavities. The room temperature (rt) RFQ and a short IH-DTL (**I**nterdigital-**H**-DTL) are followed

by 4 superconducting (sc) CH-DTL (**C**rossbar-**H**) cavities. The operating frequency is 175 MHz, the designed section lengths are 13 m for the RFQ (**R**adio-**F**requency-**Q**uadrupole) (5 MeV), 1 m for a compact MEBT (**M**iddle **E**nergy **B**eam **T**ransport), 2 m for the IH-cavity (10 MeV) and 9 m for the sc CH-DTL (40 MeV). The structure parameters and end-to-end multiparticle beam dynamics calculations with and without DTL errors for the whole linac will be presented and the results will be discussed.

Extended particle dynamics investigations of the reference IFMIF DTL layout (RFQ+Alvarez-DTL) showed a very robust beam behaviour for the Alvarez-type DTL. Even with the reduction of the input energy – to reduce the length of the RFQ - and with a favourable lower input power per tank the calculations gave in all cases stable solutions, good emittance conservation, strong transverse and longitudinal focusing, no particle losses and sufficient large aperture factors also, when standard quadrupole and rf errors and mismatched input beams were included [1]. This layout has an overall length of 46 m. The rf power consumption per linac is estimated to around 7.5 MW. Technical challenges in case of the Alvarez-DTL are the high thermic load per meter in combination with a quadrupole singlet channel where each magnet is housed in a drift tube on a slim stem. Beam dynamics studies for a corresponding rt IH-type DTL showed its capability for high intensity acceleration with good power efficiency. Investigations on beam stability against matching, field and quadrupole errors showed however, that the IH-DTL is due to the KONUS-dynamics (**Ko**mbinierte – **Nu**llgrad - **S**truktur) more sensitive to errors than the Alvarez [3, 4]. Both rt structures showed in combination with a special compact MEBT no particle loss and smooth beam behaviour, but the RFQ+Alvarez-DTL combination gave higher aperture factors and lower emittance growth [2].

Due to the mandatory cw operation mode of the IFMIF facility the combination of a short rt IH structure and a chain of sc CH resonators with inter tank focusing has been proposed in addition, which fulfills the requirements for a high current IFMIF DTL. The sc CH DTL part provides very high rf and acceleration efficiency and due to its special cell geometry high mechanical robustness. The sc drift tube linac has a total length of ≈ 11 m only, the cryostat length is ≈ 8 m. The estimated total plug power (including all cryostat losses) per meter of this design study is ≈ 1.5 kW/m (for comparison the rt linacs need ≈ 50 kW/m assuming 50 % amplifier efficiency), which demonstrates the high rf efficiency of the sc CH modules. In connection with large drift tube apertures the risk of particle losses in the sc part is reduced. Detailed simulations showed also a low sensitivity of the beam behaviour and beam quality against all combinations of statistic and mechanical errors, i.e. transverse quadrupole triplet displacement errors ± 0.1 mm and a rotation of ±1 °, rf phase errors ± 1 °, rf amplitude errors ± 1 % and quadrupole gradient errors ± 1 % [2].

Table 1: Structure parameters of the RFQ for IFMIF.

RFQ-Parameters	Values
A/q	2 (D^+)
Rf-frequency f [MHz]	175
In / Out energy W [MeV]	0.1 / 5.0
P_{tot} [MW]	1.506
Peak field E_{peak} [MV/m]	23.77
Cells / length [m]	659 / 12.31
In / Out current [mA]	140 / 132.7
In / Out $\varepsilon^{N,rms}$trans [cm×mrad]	0.020 / 0.023
In / Out $\varepsilon^{N,rms}$long [cm×mrad]	0 / 0.043

For all DTL studies the same reference design of an RFQ has been used to be comparable between all design versions for the IFMIF linac. Table 1 gives a summary of the RFQ structure and beam parameters. The main goal was a lowered Kilpatrik factor of 1.7 to reduce the sparking probability due to the required cw operation. Nevertheless the transmission should be high as well as the beam quality at the RFQ output to allow good matching to the following DTL. In the design the recipe of equipartitioning has been applied leading to a parameter set, which fulfills the IFMIF requirements [5].

In Fig 9 the output beam distribution in phase space at 5.0 MeV of the RFQ is plotted, calculated with PARMTEQM® (multipole effects and image charges included) and 50,000 macro particle were used. The transmission is about 94 % with good beam quality. The transverse rms emittance growth is less than 10 % and the beam is well confined with a few halo particles only.

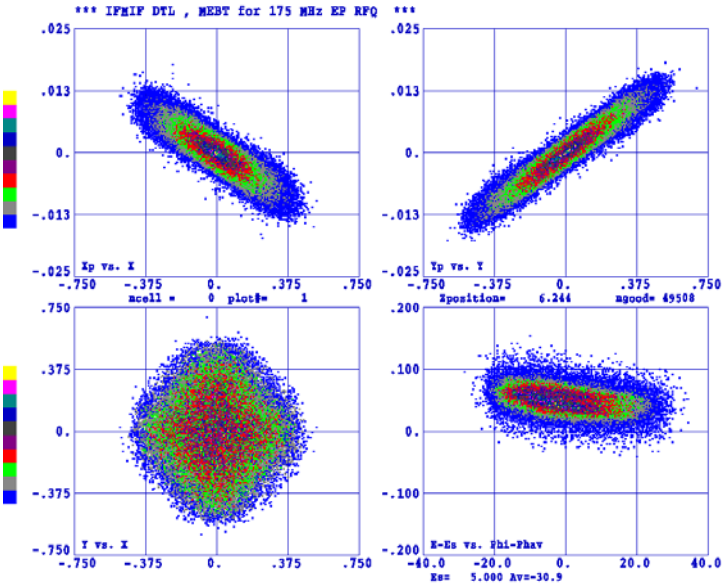

Fig. 9: Output beam distribution in phase space at 5.0 MeV of the Four-Vane-RFQ from table 1 calculated with PARMTEQM® and 50,000 macroparicles were used.

The calculations were repeated with the new full 3D RFQ program called TOUTATIS® to validate the agreement of the used RFQ codes [5]. Fig. 10 compares the transmission efficiency of the IFMIF RFQ from table 1 calculated with PARMTEQM® and TOUTATIS®. The differences are significant and the reasons for the remarkable reduction in transmission efficiency in TOUTATIS® are up to now under detailed discussion [7].

In addition preliminary electromagnetic rf design studies of a 175 MHz 1.7 Kilpatrick Four-Vane resonator were performed with the rf field solver SUPERFISH®. Fig. 11 shows the simulation results of the first quadrant in TE_{210} mode of the resonator with the cell parameters of table 1 and a Kilpatrick factor of 1.7.

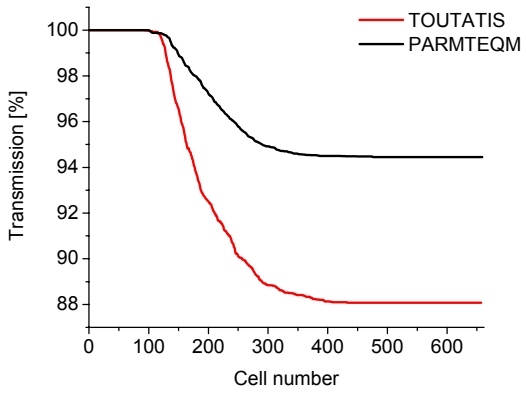

Fig. 10: Transmission efficiency along the RFQ calculated with PARMTEQM® (black line) and TOUTATIS® (red line).

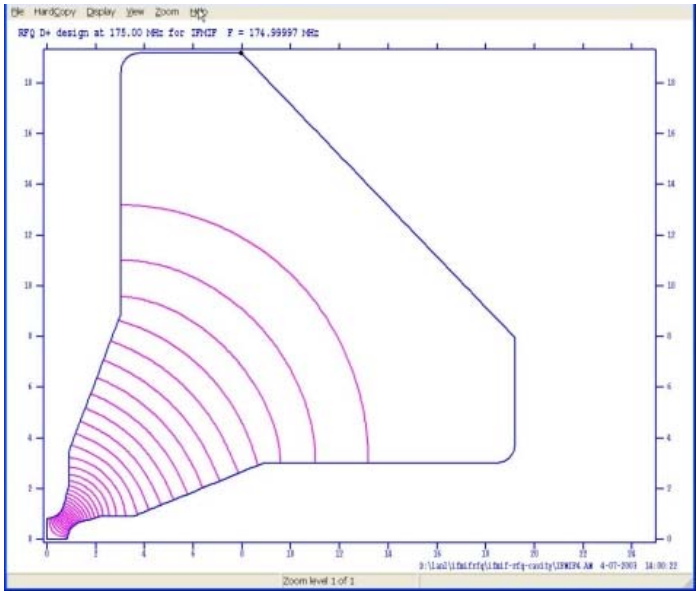

Fig. 11: First quadrant in TE_{210} mode with the electric field lines of an 1.7 Kilpatrick 175 MHz IFMIF Four-Vane RFQ resonator calculated with SUPERFISH®.

The matching to the RFQ can be accomplished by a partly space charge compensated magnetic LEBT (**L**ow **E**nergy **B**eam **T**ransport) with low influence on transmission and beam quality. Therefore the output emittances of Fig. 9 have been taken for the beam dynamics simulations through the DTL, aiming for preliminary results for the beam behaviour from

source to 40 MeV to ensure stable and loss free operation in the whole IFMIF accelerator facility.

The superconducting CH-version (design and structure parameters of table 2 and Fig. 12 made with LORASR©) turned out to be superior to the rt IH-design with respect to the following critical issues: a) no cooling problems in cw operation b) reduced linac length and less tanks, i.e. higher efficiency and lower structure periods c) larger drift tube diameters up to 8 cm. The beam behaviour is smooth, no losses along the linac occurred and a good safety margin could be reached in the sc linac against losses due to mismatch and standard DTL errors. Extended electromagnetic simulations have been performed with Microwave Studio® to optimize the parameters of the first and last superconducting CH cavity for IFMIF. It was possible to further reduce the electric and magnetic peak fields to modest values which is important for reliable routine operation. Fig. 13 gives a realistic 3D sketch of the optimized 175 MHz sc CH tanks 1 in the critical low energy part and 4 at the high energy end of the DTL, calculated with Microwave Studio®.

Table 2: Design parameter of a 175 MHz sc IH/CH-DTL for IFMIF + Cavity parameters of sc CH tank 1 and 4.

Design parameters	SC CH-DTL		Units
A/q	2 (D^+)		
In-/out current	125.0 / 125.0		MA
Frequency	175.0		MHz
Number of tanks	5 (1NC+4SC)		
P_{tot}	4.44		MW
W_{in} / W_{out}	5.0 / 40.1		MeV
Cells / Length	73 / 10.8		M
A_0 of DT	NC:1.5 SC:2.4 - 4.0		Cm
In- / Out rms ε^n_{trans}	0.035 / 0.091		cm×mrad
In- / Out rms ε^n_{long}	0.070 / 0.097		cm×mrad
Cavity parameters	CH 1	CH 4	Units
Beta	0.1	0.2	
Frequency	175.00	175.00	MHz
E_{acc} (=E_0)	5.00	4.3	MV/m
Tank length	1.20	2.30	M
Tank diameter	52.9	67.3	Cm
Gaps	12	12	
E_{peak}/E_{acc}	4.01	3.75	
B_{peak}/E_{acc}	7.73	8.46	mT/MV/m

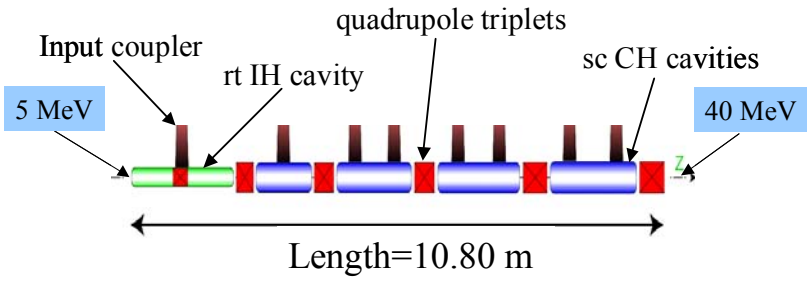

Fig. 12: Scheme of a 175 MHz sc IH/CH-DTL.

For testing the overall stability of the complete injector facility against particle losses integrated multi particle simulation studies through the whole 25 m long sc linac (RFQ +MEBT+sc IH/CH-DTL) were performed with the programs PARMTEQ® and LORASR©. Fig. 14 shows the 100 % transverse beam envelopes along the whole linac in the nominal case without assuming mechanical and rf tolerances. The beam behaviour is smooth, no losses after the RFQ occurred, a good safety margin could be reached throughout the sc part of the H-DTL against losses. The output distribution is well confined with a quasi elliptic dense core.

The overall simulations were repeated with applied combined, statistically distributed standard mechanical, rf and quadrupole triplet gradient errors for the MEBT and the following H-DTL, i.e. transverse quadrupole triplet displacement errors ± 0.1 mm and a rotation of ±1 °, rf phase errors ± 1 °, rf amplitude errors ± 1 % and quadrupole gradient errors ± 1 %. Figs. 15 and 16 show the results of the simulations for the IFMIF linac in this case. The 100 % beam envelopes are still smooth. No further losses occur after the RFQ and the phase space at the exit of the H-DTL at 40.1 MeV is still quasi elliptic and well confined.

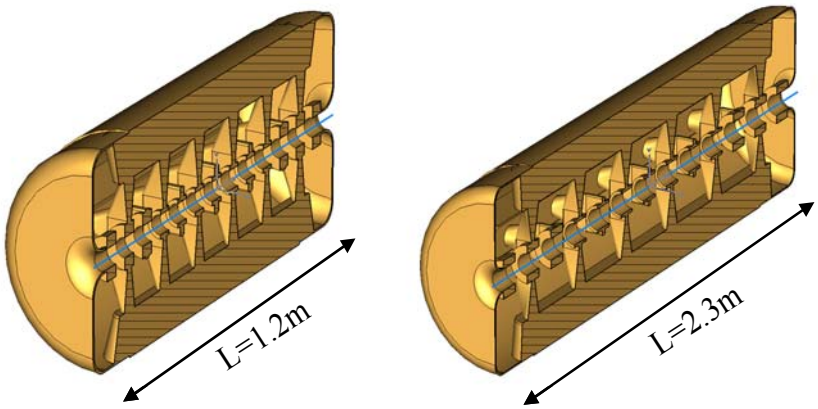

Fig. 13: 3D view of the first and last 175 MHz sc CH-cavities (tank 1 and 4) calculated with MicroWave Studio®.

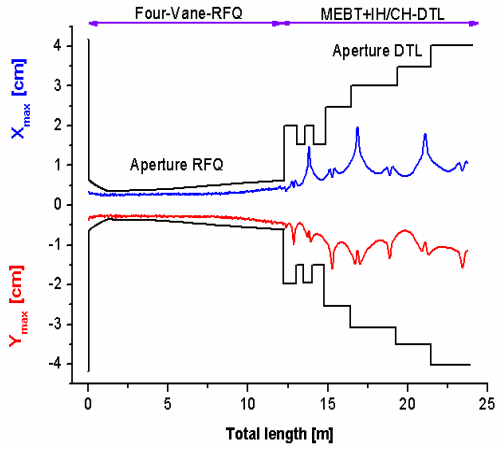

Fig. 14: 100 % transverse beam envelopes along the whole linac (RFQ+MEBT+H-DTL) in the nominal case.

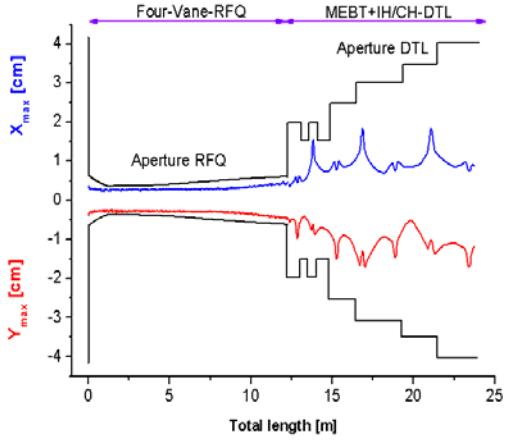

Fig. 15: 100 % transverse beam envelopes along the whole linac with combined errors for the MEBT and H-DTL.

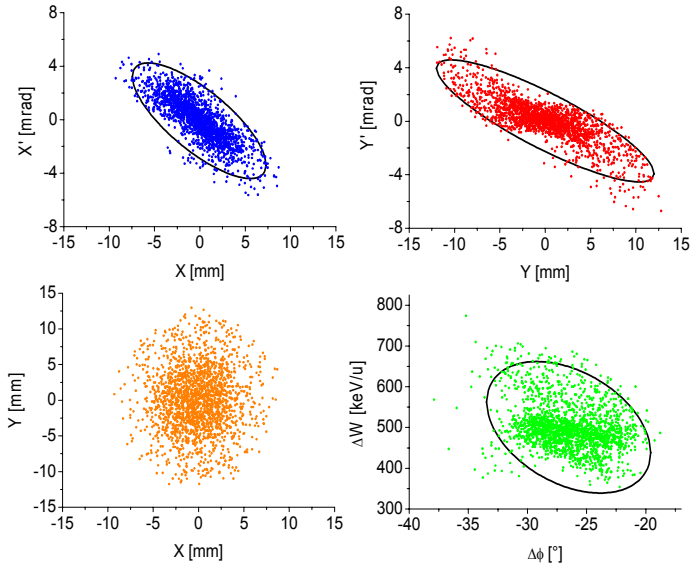

Fig. 16: Output distribution of the linac at 40.1 MeV with combined errors of the MEBT and H-DTL, 2,000 macro particles used.

A down scaled copper model (1:2) has been built to study the basic rf properties of a CH-structure. The model has been modified and new drift tubes have been fabricated. The corresponding particle-beta is now 0.08. By changing the length of the drift tubes and therefore the local capacitance it was possible to obtain a flat field distribution [8]. In addition, a preliminary Higher Order Mode analysis has been performed. The first 15 modes could be identified experimentally and the R/Q-values have been measured. The agreement between the electro-dynamic simulations and the measurement are excellent [8]. Figure 17 shows the field distribution of the first 12 modes. The black curves represent the measurements and the colored curves the simulations.

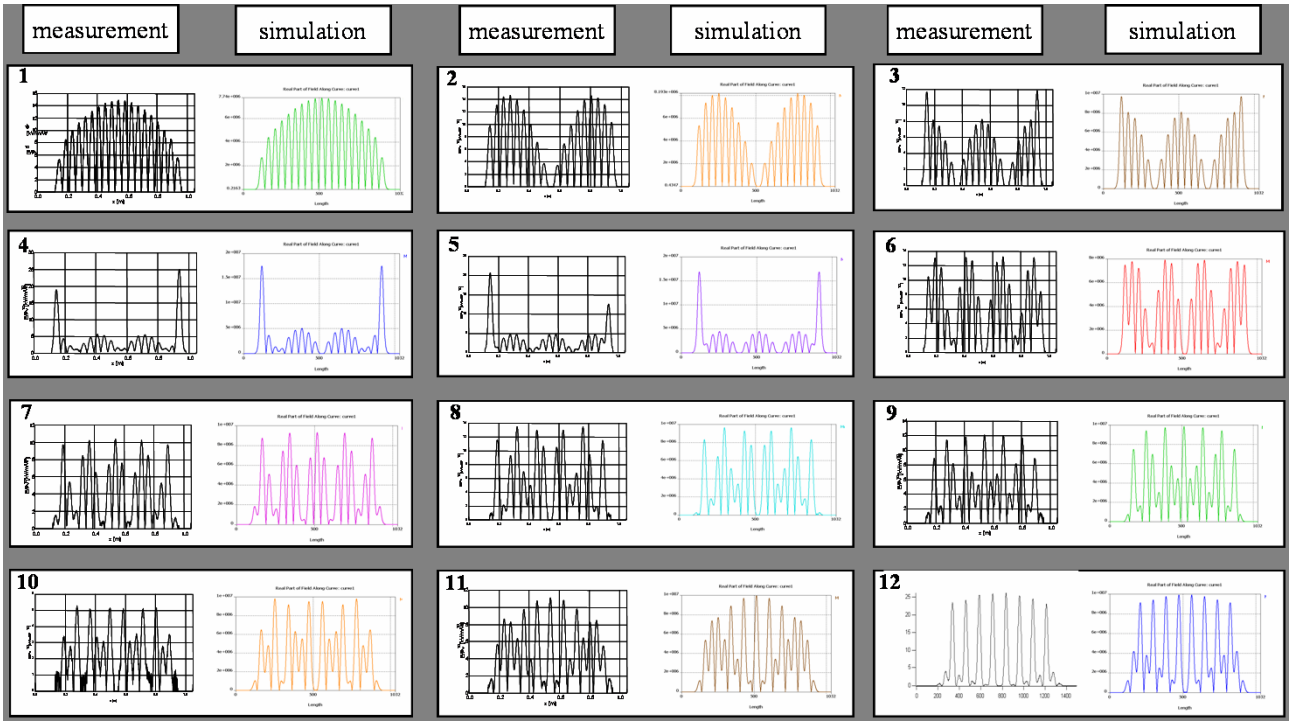

Fig. 17: Comparison of the field distribution of the first 12 modes. The black curves are measurements and the colored curves are simulations.

In a next step we introduced a beta profile in the model cavity. Due to the large number of gaps and the corresponding high energy gain per cavity it is necessary to increase the cell length from cell to cell. Figure 18 shows this modified model with beta profile. The distance between the stems which is correlated to the cell length increases from left to right. By changing the length of the drift tubes keeping the right cell length it was also possible to obtain a flat field distribution. Figure 19 shows the comparison between the simulated (blue) and the measured field distribution. Again, the agreement between simulation and measurement is excellent [9]. The input beta is 0.085 and the output beta 0.12. Additionally, first studies of tuning methods have been performed with very promising results [9].

A superconducting CH-cavity (1:2) has been optimized. This niobium cavity has been ordered and is already under fabrication. The cavity with a beta of 0.1 is expected to be delivered in 2004. To test this superconducting cavity, a cryo-lab has been equipped with a 3m vertical cryostat, a class 100 laminar flow box, transport dewars and a magnetic shielding. First tests will be performed in 2004.

The superconducting CH-structure in combination with the KONUS beam dynamics layout is well suited for the efficient acceleration of intense light ion beams. Extended beam dynamics simulations gave high transmission, also in case of statistically distributed mechanical, rf, quadrupole gradient and matching errors due to a low number of rf and structure periods of the H-DTL with KONUS dynamics. Also integrated overall simulations of the whole linac

(RFQ+H-DTL) with and without mechanical and optical tolerances showed a smooth beam behaviour, moderate emittance growth and a non-chaotic beam behaviour without particle loss. A downscaled 1:2 room temperature copper model has been built and tested in order to investigate basic rf properties, tuning methods and to validate the simulations. There was an excellent agreement between the simulations and the measurements [8][9][10]. The order for a 350 MHz superconducting prototype of bulk niobium has been placed and the delivery is scheduled at the beginning of the year 2004. In addition, further electromagnetic design optimization procedures with MicroWave Studio® of the Four-Vane-Cavity and the CH-Resonators will be made to optimize the rf properties in the view of rf power supply, field flatness, peak fields and thermal distribution of the resonators due the cw operation mode and high beam intensity.

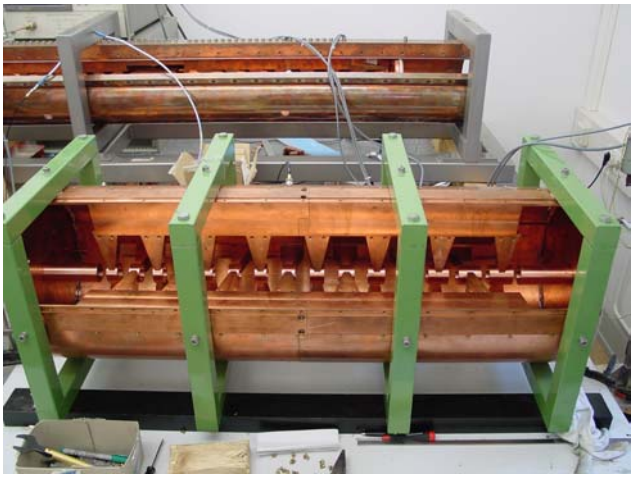

Fig. 18: Copper model with beta profile.

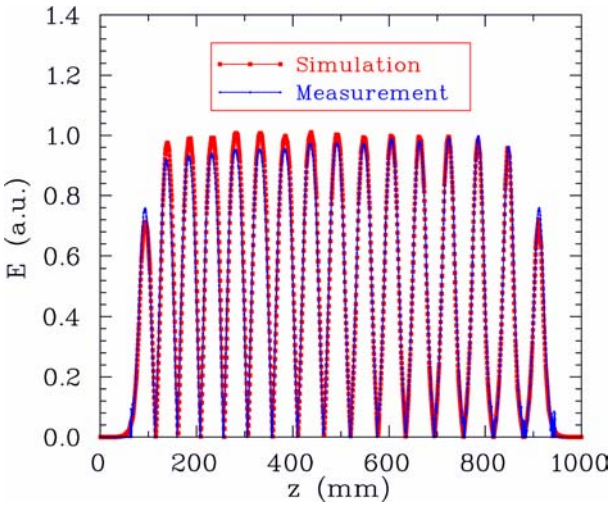

Fig. 19: Measured (blue) and simulated (red) field distribution of the copper model with beta profile.

Staff:

H. Deitinghoff
R. Hollinger
A. Jakob
H. Klein
H. Liebermann
O. Meusel
H. Podlech
J. Pozimski
U. Ratzinger
A. Sauer
A. Schempp
R. Tiede
K. Volk

Johann Wolfgang Goethe-Universität
Institut für Angewandte Physik (IAP)
Robert-Mayer-Strasse 2-4
60486 Frankfurt am Main

Literature:

[1] R. Hollinger, P. Beller, K. Volk, M. Weber, H. Klein, The Frankfurt 200 mA Proton Source, Rev. Sci. Instrum., 71, Volume II, 836-838, 2000

[2] A. Sauer, Ph.D. Thesis, J. W. Goethe-Universität Frankfurt a. M., Germany, March 2003.

[3] A. Sauer et al., "Investigation of a normal conducting 175 MHz Linac design for IFMIF", EPAC 2002, Paris, France, June 2002.

[4] U. Ratzinger, "Effiziente HF-Linacs für leichte und schwere Ionen", J. W. Goethe-Universität Frankfurt a. M., July 1998.

[5] R. A. Jameson, "Some Characteristics of the IFMIF RFQ KP1.7 Designs", Int.-Rep. Institut für Angewandte Physik, Frankfurt a. M., Germany, May 2000.

[6] R. Duperrier, Ph. D. Thesis nr. 6194, University of Orsay, France, June 2000.

[7] R. A. Jameson, A. Sauer, R. Ferdinand, R. Duperrier, private communication.

[8] H. Podlech et al., "Higher Order Mode Investigation of Superconducting CH Structures and Status of the CH Prototype Cavity, PAC 2003, Portland, USA, May 2003.

[9] H. Podlech et. al, “Status of the Development of a Super Conducting 352 MHz CH-Prototype Cavity ”, Proceedings of the SRF2003, Travemünde, Germany, September 2003

[10] H. Liebermann et al., "Design of a Superconducting CH-Cavity for Low and Medium Beta Ion and Proton Acceleration", PAC 2003, Portland, USA, May 2003.

TTMI-003
Test Facility

TW3-TTMI-003 D1
Helium Cooled High-Flux-Test-Module

1. Introduction

In the last annual report on the High-Flux-Test-Module design work showed the first temperature analyses for rigs with capsules equipped with an electric triple heater system. The electric heaters have to adjust the temperature of the specimen in the capsules at beam on and beam off periods within limited tolerances. They have to cope with the helium temperature increase and heat transfer changes along the helium channels and the axial nuclear power distribution. According to the analyses with the CFD-code STAR-CD the temperature within the specimen stack at beam-on periods can be kept at about 450 °C with a tolerance of 15 °C over a stack height of 66 mm. The over all stack height of 81 mm followed investigations on several specimen arrangements with the aim to maximize the specimen number. The temperature in the stack beyond the afore mentioned 66 mm deviates more than 15 °C. The differences are well defined, so that the specimen can be used too. During beam-of periods the temperatures can be adjusted within the same range.

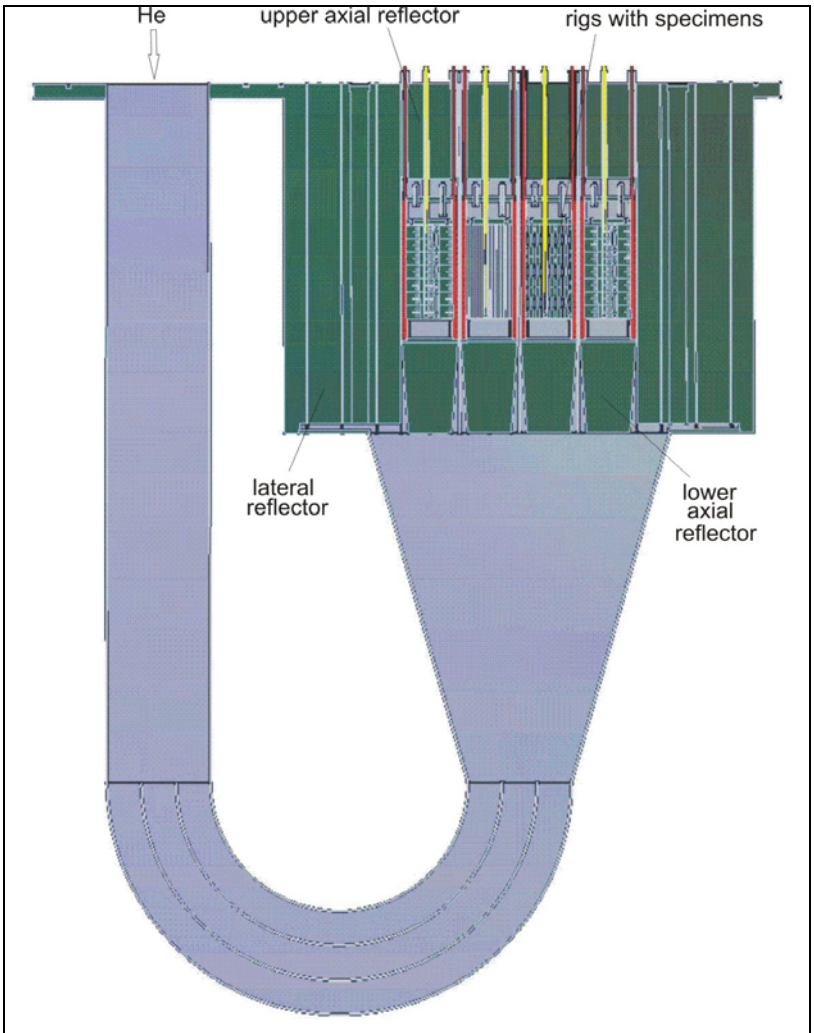

Fig. 1: IFMIF Helium cooled High Flux Test Module (HFTM)

The work of this year on the one hand was dedicated to arrange comparable temperature tolerances at different temperature levels for the same position in the container i. e. at highest nuclear power load [1]. On the other hand the turbulence model used with STAR-CD was validated with an experiment from the literature. Own experiment were started too. The HTM as well the test cell were drawn with the CAD-System CATIA.

2. Description of the design with the triple heater capsules

The optimised design of the HFTM test section with chocolate plate rigs with triple heater systems is shown in Fig. 1. Based on preliminary hydraulic calculations a single rectangular duct with a cross section of 52 x 88 mm has been chosen for the helium flow to the test section. It is positioned asymmetrically at one side of the test section. The uniform feeding of helium to the rigs is improved by two baffles inserted in the 180^0 bend joining the ducts with downward and upward flow. The lateral reflectors are integral parts of the container housing the test rigs. Helium cooling of the

reflectors is provided by a bypass to the main flow. The lower axial reflector is a single bloc with appropriate channels to lead the helium flow to the rigs. The upper axial reflector is split into 12 single parts according to the number of rigs. The outer shape is selected such that cooling channels of the necessary dimensions are generated. Holes in the blocs allow the insertion of thermocouples and heater wires.

Fig. 2 shows a horizontal cross section of the test section (x,z-plane) in the region of the irradiation zone. It consists of a container with an inner cross section of 203 x52 mm and the two lateral reflectors. In the y-z plane the container is divided into four compartments by stiffening plates serving to stabilise the container walls. Each compartment is filled with 3 rigs. The rigs have an outer cross section of 49x16 mm. Cooling channels are provided at all sides of the rigs with a width of 1.0 mm at the large sides and of 0.5 mm at the small sides. The dimensions of the cooling channels are assured by small vertical ribs at the corners and the side walls of the rigs. The attachment of the rigs inside the container is not yet included in the design.

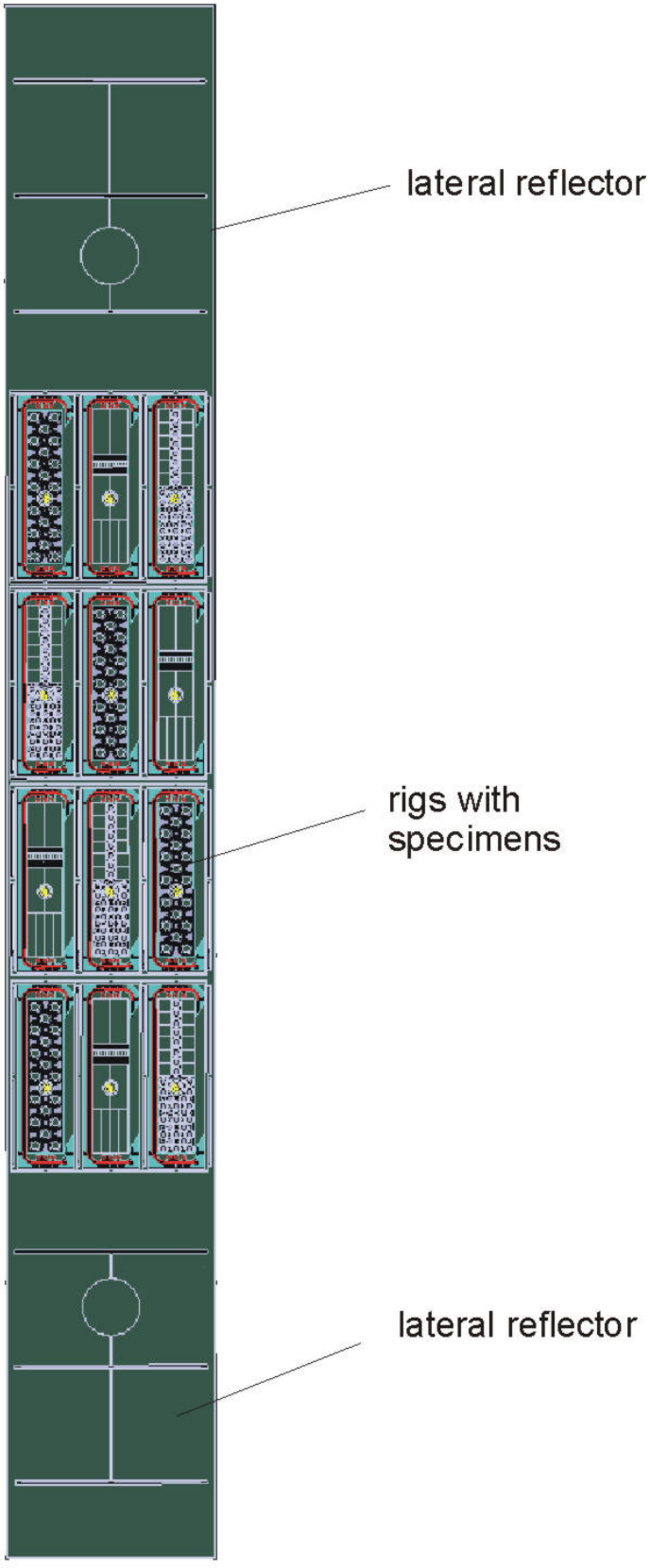

Fig. 2: High Flux Test Module cross section.

Details of the rig design are shown in Fig. 3. They consist of the outer housing (rig wall) and the inner capsule containing the specimens separated by a thermal insulation with a thickness of 1.35 mm at the large side and 1 mm at the small side. The capsule has an inner cross section of 40x9.3 mm. This allows a rather dense arrangement of most of the envisaged test specimens (see Fig. 1). Electrical heaters are wrapped around the capsule in horizontal windings. This concept will lead to temperatures of the capsule close to the irradiation temperature of the specimens, whereas the rig wall is at about the level of the helium temperature.

The length of the rig without the upper reflector is 144 mm. The capsules have a length of 125 mm and are closed by two cup-shaped caps giving the testing zone a length of 81.5 mm.

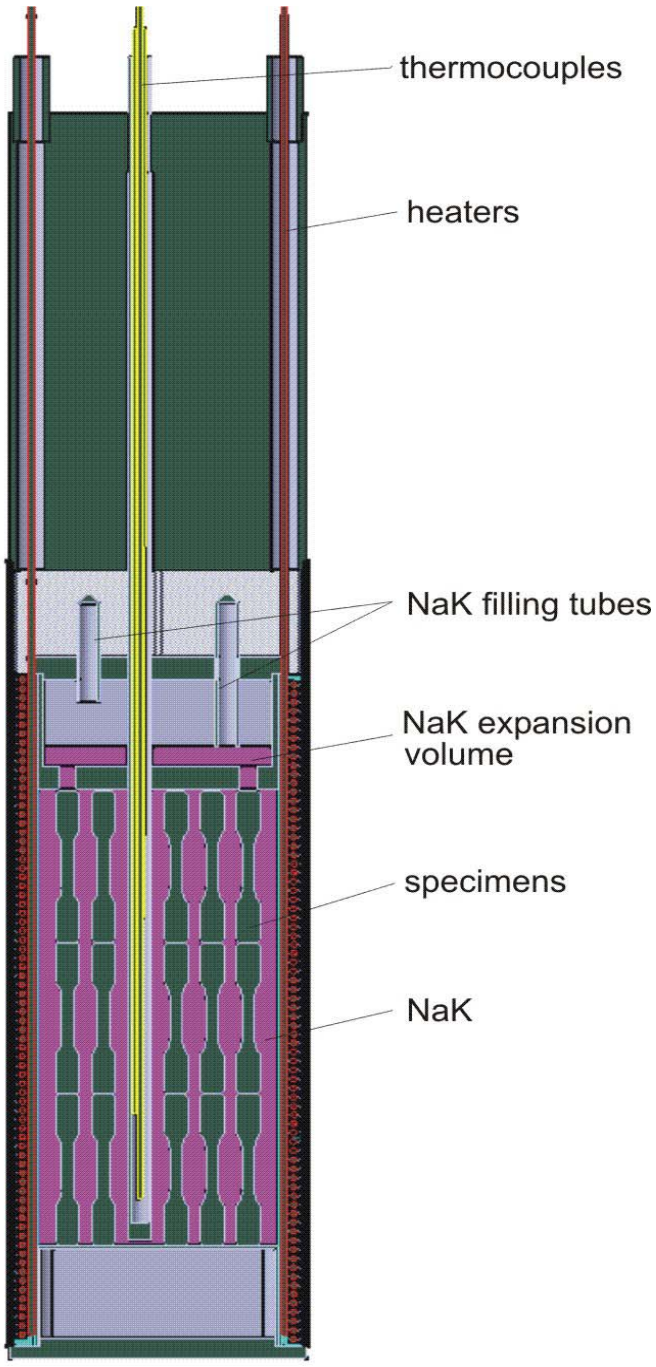

Fig. 3 Test rig with specimens.

This includes 0.5 mm for the accommodation of thermal expansion differences. The capsules are filled with a liquid metal (Na or, if possible NaK) to increase the thermal contact between the specimens and the capsule walls. The upper cap has two holes connecting the test zone with the NaK expansion volume of about 20 mm length located at the top end of the rig. To facilitate filling of the capsule with NaK to a defined level, two tubes are provided at the top side of the expansion tank. One of these tubes dips into the tank to the envisaged filling level, the other one ends at the top plate. The filling level is established by at first filling the tank completely, and then blowing out the surplus NaK via the dip tube by applying a gas pressure to the other one. Finally, both tubes have to be cut and sealed. The volume of the expansion tank and the filling level have been determined taking into account the NaK volume, the filling temperature and the operating temperature.

The main design problem of the rigs is to realise the specified level and constancy of the irradiation temperatures. The maximum thickness of the capsule (in z-direction) is given by the power density and the thermal conductivity of the specimens/NaK mixture in connection with the allowable maximum temperature difference across the specimens. This consideration leads to a maximum thickness of about 10 mm for the first row of rigs. At the rear side of the HFTM the capsule thickness can be larger according to the decrease in power density, but in order to minimise the design and manufacturing effort it was decided to use identical dimensions for all rigs. Taking into account the dimensions and possible arrangements of the specimens (see Fig. 2), 9.3 mm has been chosen as internal capsule widths.

3. Temperature distribution calculations at different temperature levels and design variations – calculations with STAR-CD

In total a number of 9 cases has been analysed with STAR-CD using the Low-Reynolds-Number turbulence model to calculate the heat transfer and pressure loss in the channels between the rigs. The main parameters and results are compiled in Table 1. The parameters changed against the previous case have been marked by bold printing. The cases 1a and 1b represent situations with nuclear heating only. Temperature differences of 121 °C elucidate, that electric heaters are mandatory. Cases 2 through 5b correspond to situations with nuclear and electric heating and electric heating only representing beam-on and beam-off periods respectively. The power levels of the tree heaters are given in lines 7, 8 and 9.

Table 1: STAR-CD Thermal-hydraulic Calculations and Main Results

Case	1a	1b	2	3a	3b	4a	4b	5a	5b
Parameters									
Eff. He gap size (mm)	0.5	0.5	0.5	0.5	0.5	**0.8**	0.8	**0.25**	**0.25**
Lower cap	thin	**thick**	thick	thick	thick	thick	thick	thick	thick
Heating	nucl.	nucl.	**nucl./el**.	nucl./el.	**el.**	el.	**nucl./el.**	nucl./el.	**el.**
El. power in section									
upper (W/cm^3)	-	-	71	**149**	194	147	108	65	111
middle (W/cm^3)	-	-	-	**90**	199	148	39	-	118
lower (W/cm^3)	-	-	74	**158**	206	154	110	70	124
Results									
Fig. No.	23	24	25 to 30	31	32	33	34	35	36
Max. spec. temp.(^{0}C)	403	404	465	650	655	650	650	337	339
Max. temp. diff. in specimens (K)	121	121	30	31	35	13	22	33	33
Max. Helium velocity (m/s)	478	479	504	550	547	514	518	501	499
Stat. press. drop (MPa)									
-modelled section	0.086	0.086	0.089	0.095	0.095	0.091	0.092	.089	0.089
-rig only	0.053	0.053	0.056	0.06	0.06	0.057	0.058	0.055	0.055

In case 2 the upper and lower heater were used to balance the nuclear power distribution. The temperature distribution in the central plane of the specimen stack ranges from 452 to 465 ^{0}C, i.e. the difference amounts to 13 K which is in agreement with the specification. Temperatures below 450 ^{0}C appear only at the upper and lower end of the specimen column. Limitation of the temperature difference to 15 K would reduce the usable length of the specimen column to 66 mm as described already. This is still about 30 % larger than the height of the beam footprint, i.e. the gain against the previous test volume is significant.

Case 3a shows that the maximum irradiation temperature of 650 ^{0}C can be reached with the same geometry as in Case 2 by increasing the power of the electrical heaters. It is evident,

that in this case heating of the middle section is necessary, too. The best temperature distribution was obtained with an electrical power of 158, 90 and 149 W/cm^3 in the lower, middle and upper section, respectively. The calculated temperature distribution in the specimens shows 650 ^{0}C at maximum which is reached along the central y-axis (x = z = 0), but a significant fraction of the test volume is below 630 ^{0}C. The maximum temperature difference amounts to about 31 K. Furthermore, rather large temperature differences (97 K) appear in the rig wall. This may cause high thermal stresses still to be analysed.

In Case 3b the power level and power distribution was determined which is necessary to hold by electrical heating only the same temperature as in Case 3a with nuclear/electric heating. An electrical power density of 209,199 and 194 W/cm^3 was obtained in the lower, middle and upper section, respectively. The calculated temperature in the specimens amounts to 655 ^{0}C at maximum and the temperature difference in the specimens to 36 K. Both values are similar to those obtained in Case 3a.

In case 4a the helium gap between the rig wall and the capsule was increased from 0.5 to 0.8 mm in order to reduce the large temperature difference in the specimens – in particular in Case 3b –. The related increase in thermal insulation should reduce the electrical power, and likewise the differences of the heat flux from the capsule to the rig wall. This expectation is confirmed. To reach a temperature of 650 ^{0}C with electrical heating only a power level between 147 and 154 W/cm^3 is necessary. The temperature difference in the specimens has dropped to 13 K, and in the rig wall to 60 K.

Case 4b corresponds to Case 4a but with nuclear and electrical heating. The temperature level of 650 ^{0}C and the optimum temperature distribution in the specimens is obtained with electrical power densities of 110, 39, and 108 W/cm^3, respectively, in the top, middle and bottom section (see Fig. 3). The temperature difference in the specimens amounts to 22 K.

Case 5a is related to the lower range of irradiation temperatures. Low temperatures can be reached by reducing the thermal resistance between the rig wall and the capsule as far as possible, e. g. by conserving all ribs between the heaters at the capsule surface, and by applying the concept with the lower pressure inside the capsule. It was estimated that in this case a thermal resistance can be achieved equivalent to a helium layer of 0.25 mm thickness. The electrical power in this case is 65 and 70 W/cm^3 in the top and bottom section, respectively. The specimen temperature is between 305 and 337 ^{0}C; this means that the average specimen temperature is about 70 K higher than the specified minimum temperature. The temperature difference in the specimens can be reduced by a further adjustment of the electrical power including the middle heating section, but this would simultaneously rise the average temperature.

Case 5b is complementary to Case 5a – i.e. the isolating gap between the rig and the capsule corresponds to a helium layer with an effective thickness of 0.25 mm – but with electrical heating only.

Table 1 demonstrates, that the temperature levels in the specimen stack can be achieved within acceptable tolerances with mainly the same design from about 320 °C up to about 650 °C.

4. Code validation

STAR-CD provides several turbulence models. For the simulation calculations described above, the Linear-Low-Reynolds-Model (LLRM) was applied. The situation in the narrow channels between the rigs ($\delta \leq 1$mm) is characterized by incompletely developed hydraulic and thermal boundary layers. Furthermore the high heat fluxes at the rig walls create laminarization of the boundary layers, which impairs the heat transfer coefficient. Simulation calculations of an experiment taken from the literature [2] show, that the LLRM reproduces

the experimental data in good agreement (see Fig. 4) [3]. Furthermore, the results reveal the influence of the heat flux on the heat transfer coefficient. They also uncover, that the heat transfer coefficients calculated with the Nusselt-number are too high. Though the Nusselt-numbers used, were given as valid for this application, do not regard sufficiently the gas properties in the boundary layers.

For the measurement from Shehata and McEligot were carried on with a tube with a hydraulic diameter of d_{hr} = 27.4 mm whereas the HFTM channels has d_{hr} = 2 mm. Therewith, in case of the HFTM the surface roughness is larger compared to the diameter so that addition experimental data are needed for validation. This is aimed at with the ITHEX experimental test section. It is installed in a loop which allows in a first step to reach Reynolds numbers up to 10000 with air only. Pressure loss measurements under adiabatic conditions show that experimental data, which separate clearly inlet effects and the pressure loss gradient downstream the channel, are needed for detailed comparisons with the simulation calculations.

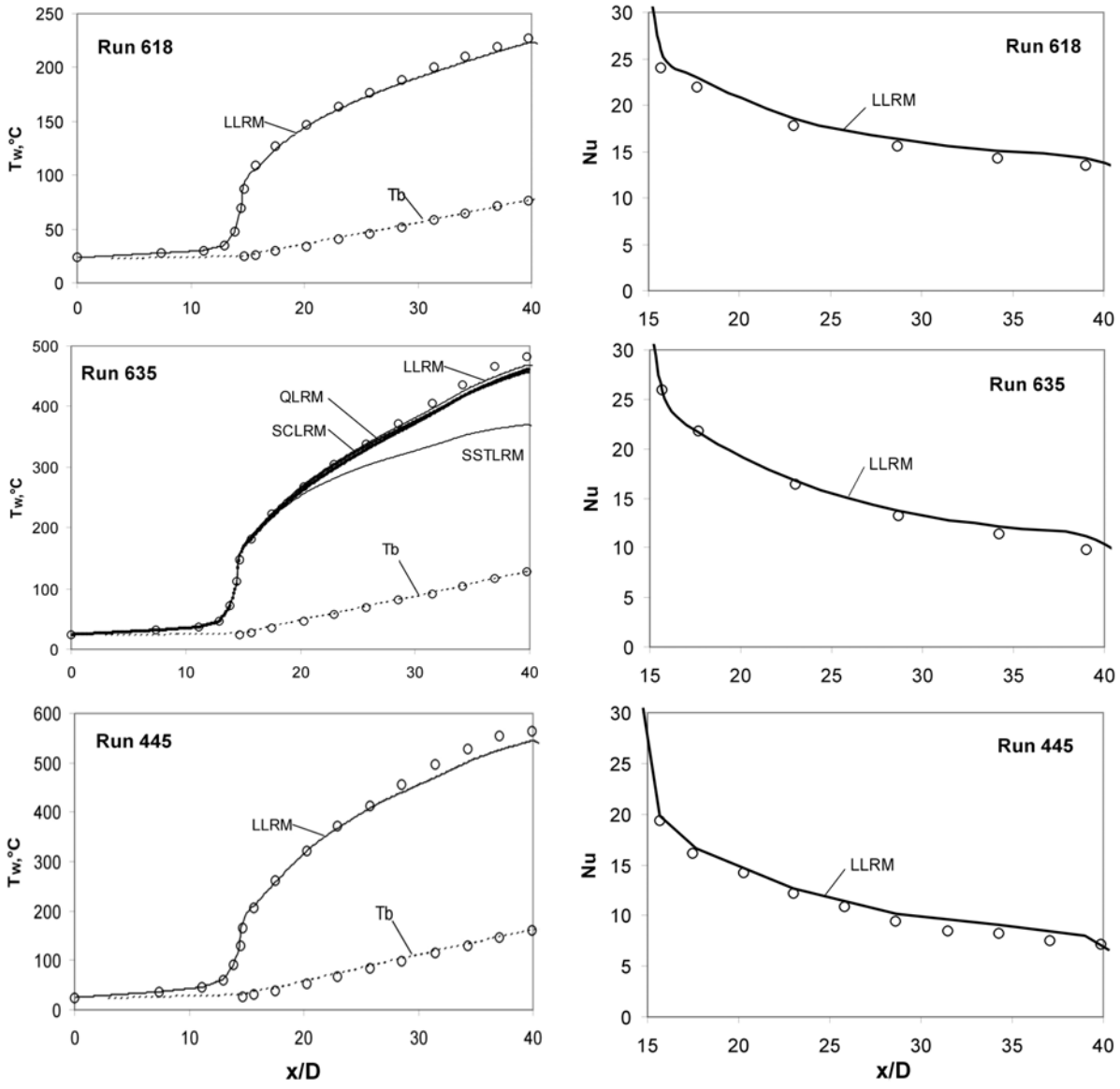

Fig. 4: Calculated local wall temperature and Nusselt number (lines) compared to measurements from Shehata and McEligot (circles) LLRM = Linear-Low-Reynolds-Model, QLRM = Quadratic-Low-Reynolds-Model, SSTLRM = Shear-Stress-Transport-Low-Reynolds-Model, SCKRM = Suga's Cubic Low-Reynolds-Model; T_b = bulk temperature

5. CATIA drawings of the test cell

For preparing a design integration existing drawings of the IFMIF test cell and its internals were put together in a design drawn with the CAD-system CATIA (see Fig. 5).

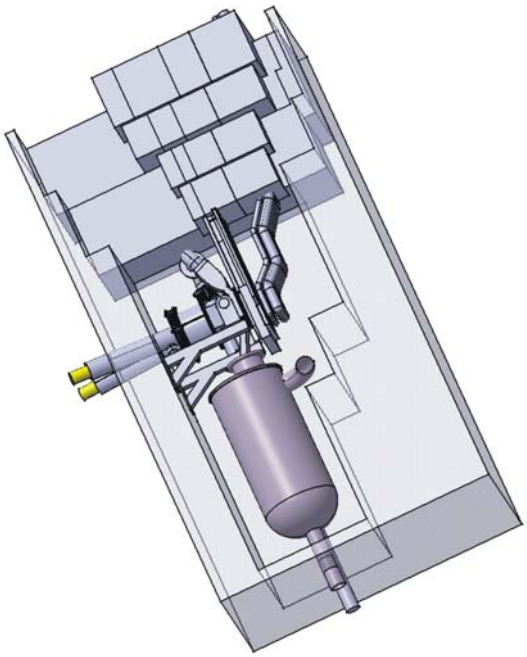

Fig. 5: CATIA drawing of the test cell

Staff:

U. Fischer
S. Gordeev
V. Heinzel
T. Kuhn
S. Simakov
V. Slobodtchouk
E. Stratmanns

Literature:

[1] Sordeev, V. Heinzel, K.H. Lang, A. Möslang, K. Schleisiek, V. Slobodtchouk, E. Stratmanns, Optimised Design and Thermal-Hydrdaulic Analysis of the IFMIF/HFTM Test Section, FZKA 6895, Oct. 2003

[2] A. Mohsen Shehata, Donald M. McEligot, Turbulence structure in the viscous layer of strongly heated gas flows, INEL-95/0223, Tech. Report, Idaho National Engineering Laboratory, November 1995

[3] S. Gordeev, V. Heinzel, V. Slobodtchouk, Features of convective heat transfer in the heated helium channel flow (to be published in an int. journal)

TW0-TTMI-003 D5, D6
TW3-TTMI-003 D5, D7
IFMIF Neutron Source: D-Li Reaction Source Term and Neutron Data

In the framework of Task TTMI-003 of the EFDA technology work programme extensive development work is being conducted to provide the computational tools and nuclear data required for neutronic calculations of the IFMIF neutron source.

D-Li Reaction Source Term

In the IFMIF lithium target, neutrons are generated through the d-Li stripping reaction and various other nuclear Li(d,xn) reactions. The objective of Task TW0-TTMI-003, Deliverable 5, was to provide the computational tools and data required for the simulation of d-Li source neutrons in the transport calculation. Deliverables 5 and 7 of the running Task TW3-TTMI-003 aim at contributing to the improvement of the D-Li neutron source term by updating the d + ^{6,7}Li cross-section data evaluation and validating the neutron source term simulation.

The McDeLicious Monte Carlo code was developed in the frame of Task TW0-TTMI-003 with the objective to simulate in the transport calculation the neutron generation on the basis of evaluated d + ^{6,7}Li cross-section data [1,2]. McDeLicious is an extension to the MCNP-4C Monte Carlo code with additional routines for simulating the deuteron beams, their profiles, the slowing down of the deuterons in the lithium target and the neutron and photon generation due to the deuteron-lithium nuclear reactions. A complete set of evaluated cross-section data for the reaction system d + ^{6,7}Li was prepared and processed for use with McDeLicious calculations [2,3]. The evaluated data include cross-sections for all reaction channels up to 50 MeV deuteron energy as well as energy-angle distributions for the neutrons emitted through the various ^{6,7}Li(d,xn)-reactions.

The McDeLicious approach was extensively tested against available experimental thick lithium target neutron yield at 25, 32 and 40 MeV deuteron energy showing that the total neutron yield as well as the neutron angle-energy spectra can be predicted with considerably better accuracy than with previous semi-empirical approaches [4,5].

New experimental thick lithium target yield data became available early 2003 for 25 and 40 MeV deuteron energy. Baba et al. of the Tohoku University, Japan, have measured the neutron yield spectra at various angles between 0 and 110°at the AVF cyclotron applying the time-of-flight-technique [6]. The analysis of the Baba et al. thick target yield data with McDeLicious using the existing d+6,7Li data evaluations shows in general good agreement between the calculations and the experimental neutron spectra (Figs. 1,2). It was indicated, however, that McDeLicious overestimates the production of neutrons with energies less than 2 MeV due to the fact that the experimental Lone et al. data have been used in evaluating the d + 6,7Li cross-section data. Baba et al. provided also measurements of double-differential d+6,7Li cross-sections at 40 MeV deuteron energy. The analysis of these data showed the need to improve the angular distribution of the neutrons in the current d + 6,7Li cross-section data evaluation. This is being revised with the ongoing re-evaluation as part of TW3-TTMI-003, Deliverable 5.

Neutron Cross Section Data

The neutron cross-section data above 20 MeV, where experimental data are scarce, need to be validated to ensure reliable neutron transport calculations for IFMIF. Validation is achieved through integral experiments with a white IFMIF-like neutron source and their computational analyses using the computational tools and data applied for IFMIF design calculations. A suitable benchmark experiment on iron, the major constituent of the IFMIF high flux test module, has been performed by Bem et al at the U-120M cyclotron of the Nuclear Physics Institute at Rez as part of Task TW3-TTMI-003. This experiment has been

analysed previously using iron cross-section data from the FZK/INPE 50 MeV and the LANL 150 MeV evaluations [7].

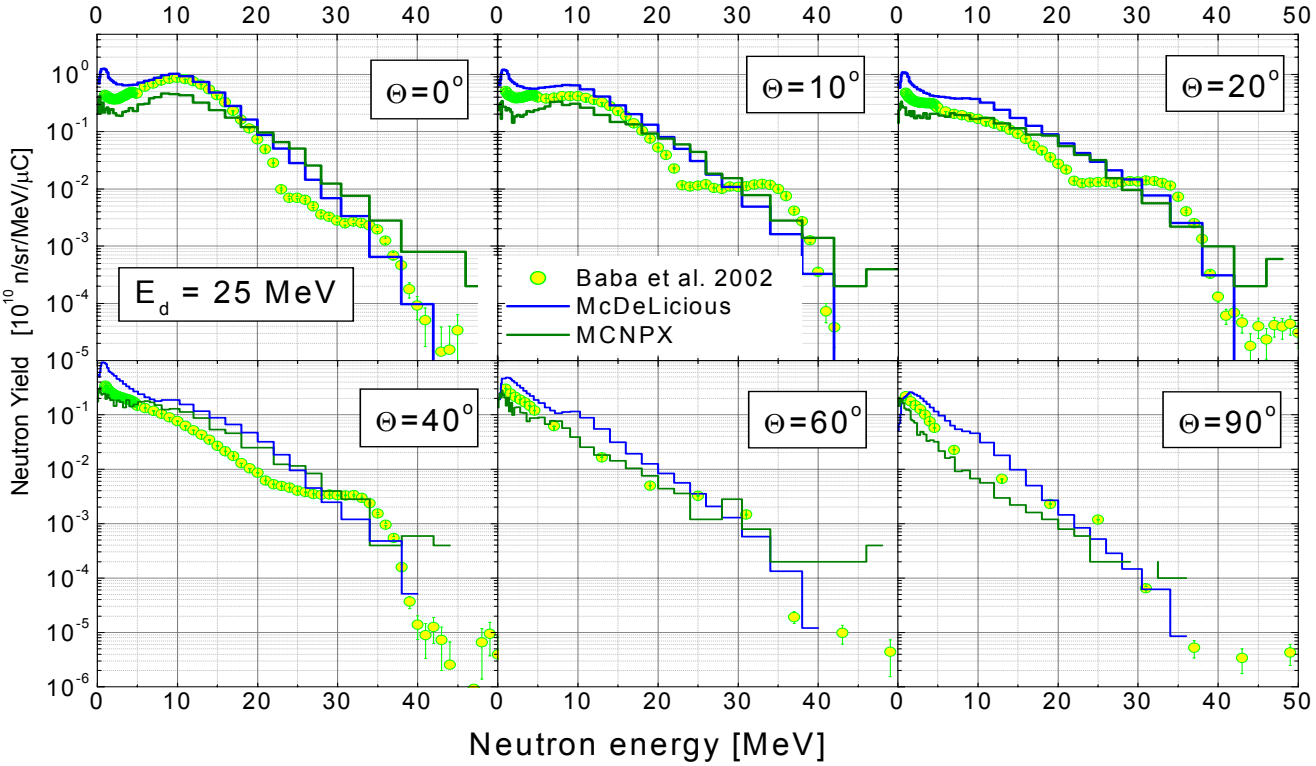

Fig. 1: Measured and calculated thick target neutron yield angular spectra at 25 MeV deuteron incidence energy.

Neutron transmission spectra for iron slabs with 20 to 50 cm thickness have been also measured by Shin et al. using a white neutron source spectrum produced by bombarding a copper target assembly with 65-MeV protons [8]. The neutron spectra were measured with a NE213 scintillation detector applying the pulse height technique. The source neutron spectrum was measured for the bare copper target and was used to represent the neutron source distribution in the MCNP calculations. Fig. 3 compares measured and calculated transmission spectra obtained by MCNP calculations using the LANL-150 MeV and FZK/INPE iron cross-section data. Good agreement is achieved with the LANL-150 MeV iron data in particular for the 20 and 40 cm thick iron slab whereas the FZK/INPE iron data show a significant underestimation. This behaviour is due to a higher total cross-section of the FZK/INPE evaluation above 20 MeV which actually is not supported by the recent measurements of Abfalterer et al., see Fig. 4. A revision of the total cross-section above 20 MeV is thus indicated for the FZK/INPE iron data evaluation. This will result in significantly higher neutron transmission spectra above 15 MeV.

The Intermediate Energy Activation File IEAF-2001 has been developed as part of Task TWO-TTMI-003, Deliberable 6 to enable activation and transmutation calculations for the IFMIF D-Li neutron source [9,10]. The IEAF-2001 data library contains neutron-induced activation cross sections for 679 target nuclides from Z=1 (hydrogen) to 84 (polonium) in the energy range 10^{-5} eV to 150 MeV. Their use in application calculations with activation codes requires the availability of group data stored in a suitable way in working libraries.

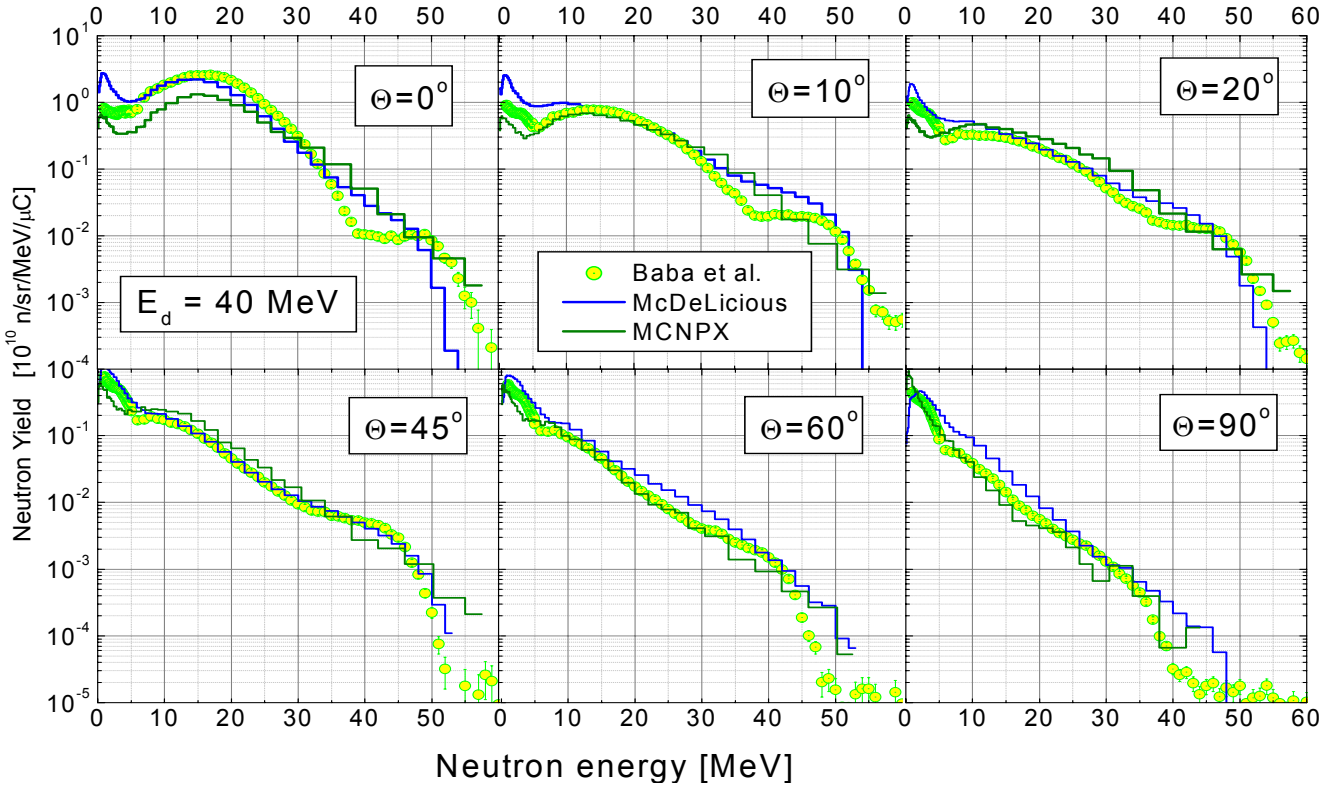

Fig. 2: Measured and calculated thick target neutron yield angular spectra at 40 MeV deuteron incidence energy.

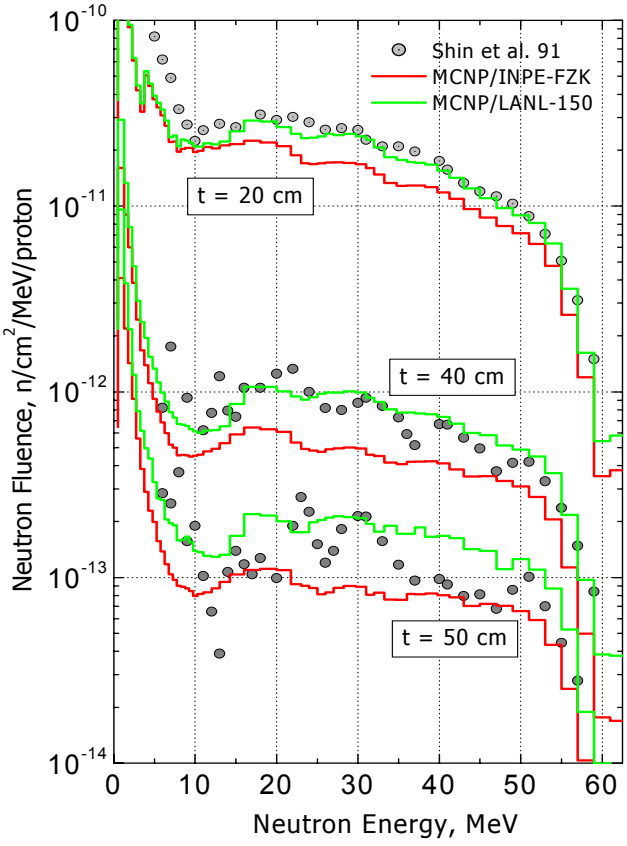

Fig. 3: Energy distribution of neutrons transmitted through 20 to 50 cm thick iron slabs using a Cu(p,xn) source with 65 MeV protons.

Two such working libraries, G-IEAF-2001/XS-256 and G-IEAF-2001/PY-256, with 256 group data stored in different formats have been derived for application calculations [11]. The G-IEAF-2001/XS-256 library, developed in the frame of Sub-Task TWO-TTMI-003, D6, can be used by any activation code capable of handling an arbitrary number of reaction channels such as the ALARA-code of the University of Madison-Wisconsin [12]. The G-IEAF-2001/PY-256 library, developed only recently for use with the FISPACT activation code of UKAEA Culham [13], is based on the use of pseudo fission product yields to describe the generation of transmutation products under irradiation [11].

A series of benchmark calculations has been performed to validate the computational approaches of ALARA/G-IEAF-2001/XS-256 and FISPACT/G-IEAF-2001/PY-256 for IFMIF activation and transmutation calculations. Testing of IEAF-2001 cross-section data was

performed through computational analyses of an activation experiment conducted previously at Forschungszentrum Karlsruhe by irradiating SS-316 samples in a white neutron field produced by a 40 MeV deuteron beam on a thick lithium target [14]. The results of the activation analyses are shown in Fig. 5 in terms of C/E (calculation/experiment) ratios averaged over the measured decay times. It is noted that the ALARA/IEAF-2001 calculations agree with the measurements within the experimental uncertainty of typically 10-30% for half of the measured radio-nuclides. This includes the main contributors to the total activity and the contact dose rate such as ^{56}Mn, ^{57}Ni, ^{58}Co, ^{54}Mn and ^{60}Co. For other radio-isotopes of minor importance, C/E ratios between 0.03 and 5 were obtained. In particular this applies for activation reactions with reaction thresholds above 20 MeV such as ^{92}Mo(n,3na)^{86}Zr.

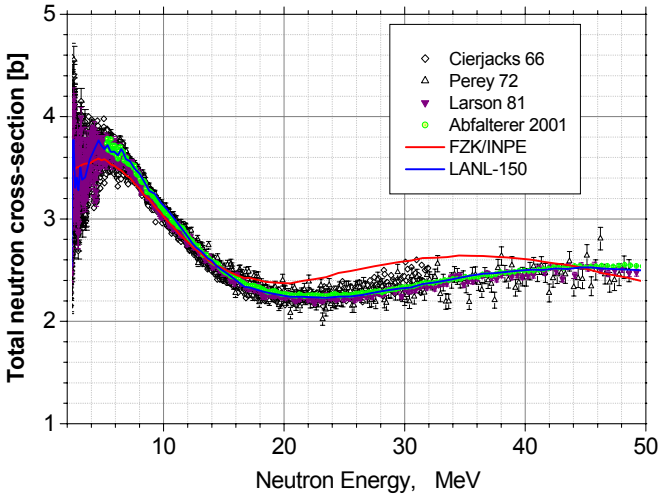

Fig.4: Comparison of evaluated and measured total iron cross-sections up to 50 MeV neutron energy.

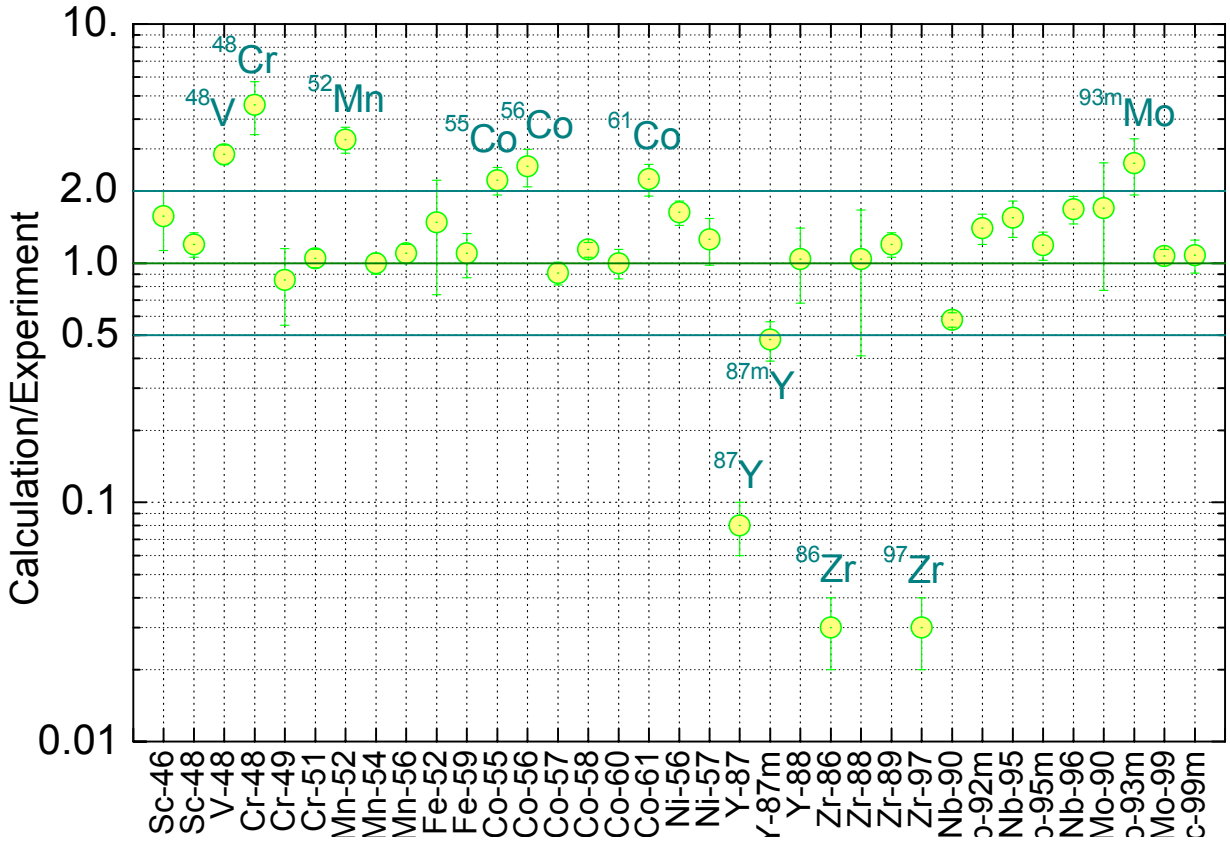

Fig. 5: Comparison of calculated (ALARA/IEAF-2001) and measured radio-activities induced by irradiating SS-316 samples in an IFMIF-like white neutron field. The data shown are average values over all decay times at which activity measurements were performed.

The validation procedure for the FISPACT-calculations using the newly developed G-IEAF-2001/PY-256 group data library comprised two steps. First, FISPACT/G-IEAF-2001/PY-256 calculations were benchmarked against FISPACT/EAF-99 calculations using 175 group data. In this case, the G-IEAF-2001/PY-256 data were cut off at 20 MeV to enable the direct

comparison of the two types of FISPACT calculations which are based on different computational approaches and different group data but on the same underlying ENDF-type cross-section data. The consistency of the two approaches is a pre-requisite to make sure the changes applied to the FISPACT code work properly and can be applied to the energy range above 20 MeV. Next, the FISPACT/G-IEAF-2001/XS-256 calculations were benchmarked against ALARA-calculations using G-IEAF-2001/XS-256 data. Since FISPACT, in its regular version, cannot handle the IEAF-2001 data, this step is required to provide validation of the FISPACT computational approach using G-IEAF-2001/PY-256 pseudo fission product yields over the whole energy range up to 150 MeV.

The benchmark calculations were performed for the intermediate energy activation experiment on SS-316 used above for the IEAF-2001 data validation by means of ALARA/G-IEAF-2001/XS-256 calculations. Detailed comparisons of the nuclide and activity inventories were performed to check the consistency of FISPACT/G-IEAF-2001/PY-256 and FISPACT/EAF-99 calculations using 175 group data. After few iterations including the correction of some bugs in FISPACT, perfect agreement was obtained for the calculated nuclide inventories.

Perfect agreement was also obtained when comparing FISPACT/G-IEAF-2001/PY-256 calculations with the ALARA/G-IEAF-2001/XS-256 calculations using the entire 256 group data set. Table 1 compares the calculated activity inventories for all radio-nuclides which have been measured in the SS-316 activation experiment. Thus it can be concluded that the FISPACT/G-IEAF-2001/PY-256 approach using pseudo fission product yield data can be applied with confidence for IFMIF activation and transmutation calculations.

Table 1: Comparison of activity inventories calculated by ALARA/G-IEAF-2001/XS-256 and FISPACT/G-IEAF-2001/PY-256 for the IFMIF activation simulation experiment on SS-316.

Nuclide	Decay time, h	Activity, Bq/kg (ALARA-calc.)	ALARA/ Experi-ment	FISPACT/ ALARA	Nuclide	Decay time, h	Activity, Bq/kg (ALARA-calc.)	ALARA/ Esperi-ment	FISPACT/ ALARA
Sc-46	49.68	1.0199E+05	**1.91**	**1.002**	**Ni-56**	49.68	1.9961E+06	**1.65**	**1.000**
Sc-48	49.68	2.2868E+06	**1.46**	**1.001**	**Ni-57**	49.68	1.2975E+08	**1.37**	**1.000**
V-48	49.68	2.9916E+06	**2.77**	**1.000**	**Y-87m**	49.68	9.6815E+03	**0.08**	**1.006**
Cr-48	49.68	4.8320E+05	**4.60**	**1.000**	**Y-87**	49.68	8.5569E+04	**0.48**	**1.003**
Cr-49	1.66	1.9296E+08	**0.87**	**0.999**	**Y-88**	3600	1.0968E+04	**1.04**	**1.007**
Cr-51	49.68	2.9580E+08	**1.06**	**1.000**	**Zr-86**	49.68	3.4279E+03	**0.03**	**1.000**
Mn-52	49.68	2.7105E+07	**3.51**	**0.984**	**Zr-88**	700	2.3774E+04	**1.04**	**1.004**
Mn-54	49.68	1.8375E+07	**1.06**	**0.993**	**Zr-97**	49.68	1.3954E+05	**0.03**	**1.000**
Mn-56	25.93	4.1844E+07	**1.09**	**1.002**	**Nb-90**	25.93	3.4776E+06	**0.46**	**1.003**
Fe-52	25.93	5.0635E+05	**1.48**	**0.985**	**Nb-92m**	49.68	2.4108E+06	**1.32**	**1.039**
Fe-59	49.68	3.7147E+05	**1.17**	**1.001**	**Nb-95**	49.68	7.8172E+05	**1.60**	**1.001**
Co-55	49.68	1.5870E+06	**2.70**	**1.001**	**Nb-95m**	49.68	1.1203E+06	**1.19**	**1.001**
Co-56	49.68	8.2991E+06	**2.94**	**1.001**	**Nb-96**	49.68	4.2577E+06	**1.87**	**1.000**
Co-57	49.68	2.0675E+07	**1.02**	**1.001**	**Mo-90**	49.68	2.4587E+04	**1.70**	**1.001**
Co-58	49.68	8.3836E+07	**1.14**	**1.001**	**Mo-93m**	49.68	2.6532E+05	**3.65**	**1.000**
Co-60	49.68	2.5289E+05	**1.08**	**1.000**	**Mo-99**	49.68	3.6165E+07	**1.14**	**1.000**
Co-61	1.66	2.3424E+08	**2.25**	**1.000**	**Tc-99m**	49.68	3.4883E+07	**1.14**	**1.000**

Staff:

U. Fischer
D. Leichtle
U. von Möllendorff
P. Pereslavtsev
I. Schmuck
S. Simakov
H. Tsige-Tamirat
P. Wilson, University of Wisconsin-Madison

Literature:

[1] S.P. Simakov, U. Fischer, U. von Möllendorff, I. Schmuck, A.Yu. Konobeev, Yu. A. Korovin, P. Pereslavtsev, Advanced Monte Carlo procedure for the d-Li neutron source term based on evaluated cross sections files, J. Nucl. Mat. 307-311 (2002), 1710-1714

[2] U. Fischer, S. P. Simakov, Yu. A. Korovin, A. Yu. Konobeyev, P. E. Pereslavtsev, U. von Möllendorff, D-Li Reaction Source Term – Data Evaluation and Code Development, Final Report on the EFDA Task Two-TTMI-003, D5, Forschungszentrum Karlsruhe, Internal Report, May 2003

[3] A. Yu. Konobeyev, Yu. A. Korovin, P. E. Pereslavtsev, U. Fischer and U. von Möllendorff, Developments of methods for calculation of deuteron-lithium and neutron-lithium cross sections for energies up to 50 MeV, Nucl. Sci. Eng. 139 (2001) 1-23

[4] U. Fischer, S. P. Simakov, A. Konobeyev, P. Pereslavtsev, P. Wilson , Neutronics and Nuclear Data for the IFMIF Neutron Source, Fus. Eng. Des. 63-64 (2002), 493-500

[5] U. Fischer, S. P. Simakov, U. von Möllendorff, P. E. Pereslavtsev , P. Bem, P.P.H. Wilson, Validated Computational Tools and Data for IFMIF Neutronic Calculations, ANS 2003 Annual Meeting, Embedded Topical Meeting on Accelerator Applications in a Nuclear Renaissance (AccApp'03), San Diego, CA, June 1-5, 2003

[6] M. Hagiwara, M. Baba, N. Kawata, N. Hirabayashi, T. Itoga., Measurements of Neutron Emission Spectra and the ^{7}Be Production in Li(d,n) and Be(d,n) for 25 and 40 MeV deuterons", JAERI Nuclear Data Symposium, December 2002

[7] P. Bem, U. Fischer, S. Simakov , U. v. Möllendorff, Neutron Transport Benchmark on Iron using a White High-Energy Neutron Field, 22nd Symposium Fusion Technology (SOFT-22), Helsinki, September 9-13, 2002

[8] K. Shin, Y. Ishii, K. Miyahara, Y. Uwamino, H. Sakai and S. Numata, Transmission of Intermediate-Energy Neutrons and Associated Gamma Rays Through Iron, Lead, Graphite, and Concrete Shields, Nucl. Sci. Eng., 109, 380-390 (1991)

[9] U. Fischer, D. Leichtle, U. v. Möllendorff , I. Schmuck, A. Yu. Konobeyev, Yu. A. Korovin, P.E. Pereslavtsev, Intermediate Energy Activation File IEAF-2001, NEA data bank programme library, package NEA-1656/01 (2001), RSICC Oak Ridge, DLC-217/IEAF-2001 (2002).

[10] U. Fischer, Yu. A. Korovin, A. Yu. Konobeyev, P. E. Pereslavtsev, , S. P. Simakov, U. von Möllendorff, P.P.H. Wilson, Evaluation of Neutron Cross Section Data above 20 MeV, Final Report on the EFDA Task Two-TTMI-003, D6, Forschungszentrum Karlsruhe, Internal Report, May 2003

[11] U. Fischer, A. Konobeyev, Yu. Korovin, D. Leichtle, U. v. Möllendorff, P. Pereslavtsev, I. Schmuck, S.P. Simakov, H. Tsige-Tamirat, P. P. H. Wilson, IEAF-2001 Cross Section Data Libraries for Activation and Transmutation Analyses of Intermediate Energy Systems, Workshop on Nuclear Data for the Transmutation of Nuclear Waste, GSI-Darmstadt, Germany, September 1-5, 2003

[12] P. P. H. Wilson and D. L. Henderson, ALARA: Analytical and Laplacian Adaptive Radioactivity Analysis, Volume I, Technical Manual, University of Wisconsin, Report UWFDM 1080, January 1998

[13] R. A. Forrest, J.-Ch Sublet, "FISPACT 99: User Manual", UKAEA Fusion, Report UKAEA FUS 407, December 1998

[14] U. von Möllendorff, F. Maekawa, H. Giese, H. Feuerstein, A Nuclear Simulation Experiment for the International Fusion Materials Irradiation Facility (IFMIF), Forschungszentrum Karlsruhe, Report FZKA 6764, October 2002

TW0-TTMI-003 D8 and D11

Test Facility Neutronics: 3D Calculation of the Complete Nuclear Response in HFTM, MFTMs, L- and VLFTMs

Re-evaluation of Irradiation Parameters for Reduced Cost IFMIF

The International Fusion Material Irradiation Facility (IFMIF) is proposed as an intense neutron source to test fusion reactor materials under relevant irradiation conditions. It should provide a proper neutron spectrum with sufficiently high damage production rates to allow also accelerated tests within an appropriate volume. The primary goal of the present study was calculate on the basis of the cost reduced IFMIF design for various combinations of deuteron beam energy and beam footprint the 3D nuclear responses. This is especially important for the start-up phase of IFMIF and the "Phase 1" which presently foresees irradiation with only one beam on target.

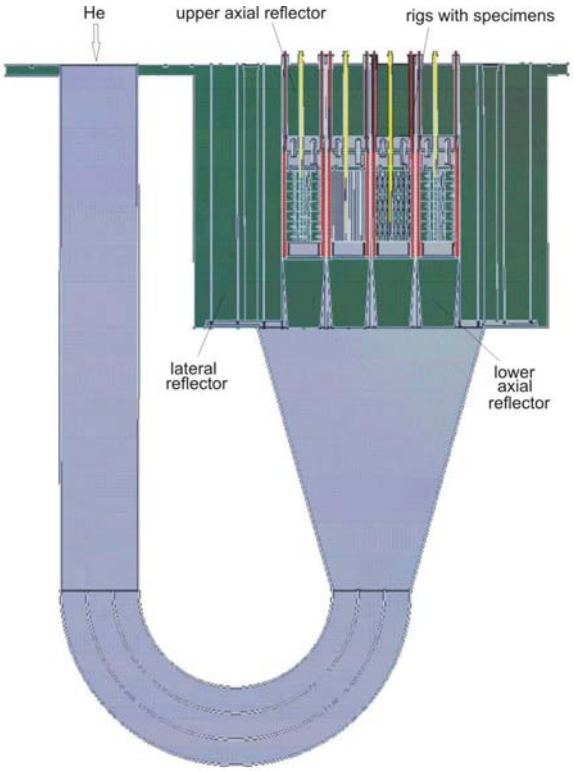

Fig. 1: Design configuration of the High Flux Test Module with He gas coolant (grey), 12 instrumented rigs (centre part), and EUROFER steel (green) serving as neutron reflector.

Previous extensive Monte Carlo simulations [1-5] have clearly shown that the IFMIF irradiation conditions for iron-based structural materials fit quite well to those of a DEMO power reactor, both in the high flux and in the medium flux position. However, it was still desirable to reduce the neutron flux gradients not only to get a flatter damage profile but also to achieve a more homogeneous temperature profile inside the specimen capsules. In order to meet that need, additional material was packed around the high flux test module.

Neutronics calculations have shown that reduced activation steel like EUROFER meets the requirements.

Figure 1 shows therefore a significantly improved high flux test module (HFTM) arrangement with rigs and specimen capsules "wrapped" with EUROFER that acts as efficient neutron reflector. The design development of the HFTM is subject of another task (TW3-TTMI-003-1,2; V. Heinzel et.al.). The High Flux Test Module (HFTM) of the IFMIF neutron source is being designed to provide an irradiation volume of about 500 cm^3 for the testing of fusion reactor materials at a radiation damage level of up to 20 dpa in iron per full power year. Nuclear design calculations must provide the data required for the technical and thermal-hydraulic layout of the HFTM including irradiation rigs, capsules and material specimens. Here the results of 3-D neutronics calculations using the updated computational tools and evaluated nuclear data are presented. In the calculations the full performance operation phase two 40 MeV@125 mA beams horizontally declined by 10 degrees from the symmetry axis are foreseen in accordance with the cost reduced option of the IFMIF project. The beam footprints are considered to be 20×5 cm^2.

Neutron-photon transport calculations and nuclear responses evaluations have been performed with the Monte Carlo code McDeLicious [6]. This is a further enhancement to the McDeLi code with the new ability to sample the neutron and photons generation of the d-Li source from tabulated ^{6,7}Li(d,xn) and (d,xγ) double-differential cross section data. The

McDeLicious approach was validated against measured energy-angular yields from the thick lithium target bombarded by deuterons with energies up to 40 MeV [7]. Two sources of evaluated neutron cross-section data were used for the neutron-photon transport calculations and the nuclear responses: the LANL-150 (14 elements, up to 150 MeV) and the INPE/FZK data evaluations (cross sections for 10 elements up to 50 MeV neutron energy). The calculations have shown differences of no more than 10% in the average nuclear responses due to the different cross-section data evaluations.

The computational model used for neutronics analyses takes into account the essential features of the IFMIF source and the test modules, i.e., geometry configuration and material specifications. It comprises the lithium target (a $26\times2.5\times20$ cm^3 box filled with Li at the density of 0.512 g/cm^3), the EUROFER target back plate ($26\times0.18\times20$ cm^3), the high flux test module ($20\times5\times5$ cm^3 box, filled with EUROFER at 80% of nominal density) and reflector slabs around the HFTM (10 cm thick EUROFER plates at reduced density to account for cooling channels). To get three-dimensional distributions of nuclear responses, the space of the HFTM and the surrounding reflector was divided into a regular lattice with small cubic segments of size $0.5\times0.5\times0.5$ cm^3. The neutron and photon fluxes, nuclear heating, dpa, gas production rates were calculated as 3-d arrays, each quantity being averaged over the volume of the small cubic segment.

The results of the calculations are summarised in Table 1. They show the main irradiation parameters and the nuclear responses calculated for EUROFER steel and Vanadium. There are given maximum and minimum values, which correspond to the centre points at the front and the back surface of the High Flux Test Module, respectively, and the space available for displacement damages exceeding specified levels. The results generally show that the irradiation parameters meet IFMIF requirements. The highest irradiation loadings, which the lithium target back plate made of EUROFER must withstand, are also included in Table 1. For the better understanding the 3-D distributions were visualised in the form of 2-d contour plots on three planes of the Cartesian coordinate system (X-axis: horizontal direction, Y – axis: vertical direction, Z – axis: deuteron downstream beam direction).

Table 1: Main neutronics parameters (given the accelerated deuteron energy of 40 MeV).

Beam/Accelerator Options	
Number of Beams/Accelerators	2
Beam Orientation	Horizontal
Each beam current, mA	125
Beam power, MW	10
Beam footprint (width × height), cm^2	20 × 5
Beam density, mA/cm^2	2.5
Li target backplate: n-flux, dpa and heat generation in the center	
n-flux, 10^{14}/cm^2/s	14.5
Displacement rate, dpa/fpy	63
Nuclear heating, W/cm^3	31
HFTM: Radiation induced effects in Eurofer(*)	
Displacement rate, dpa/fpy	55 – 21
Volume (dpa > 20/fpy), cm^3	52
Volume (dpa > 40/fpy), cm^3	102
H production, appm/fpy	255– 1000
He production, appm/fpy	56 – 210
HFTM: Radiation induced effects in Vanadium(*)	
Displacement rate, dpa/fpy	62 – 23
Volume (dpa > 20/fpy), cm^3	645
Volume (dpa > 40/fpy), cm^3	145
H production, appm/fpy	115 – 470
He production, appm/fpy	200 - 80

(*) The given maximum and minimum values correspond to the centre points at the front and the back surface of the HFTM, respectively.

Figs. 2 and 3 display the contour maps for the displacement damage (dpa) rates induced in EUROFER and heat generation for the IFMIF full performance stage. The contour maps enable to assess the size and shape of the 3-d irradiation volume, which is available for a specified damage displacement level.

In addition to the absolute values of the nuclear responses in the test module, their spatial gradients are of great importance. It was shown that the relative gradient near the test module edges amounts to 25% cm along the beam and vertical directions and is around 50% cm along the horizontal direction. A very important spin-off of the neutron reflector

integration is the significantly higher neutron density inside the high flux test module and the related substantial increase of irradiation volume of about 20% at constant deuteron beam current. The results of the task are also reported in refs [8-11].

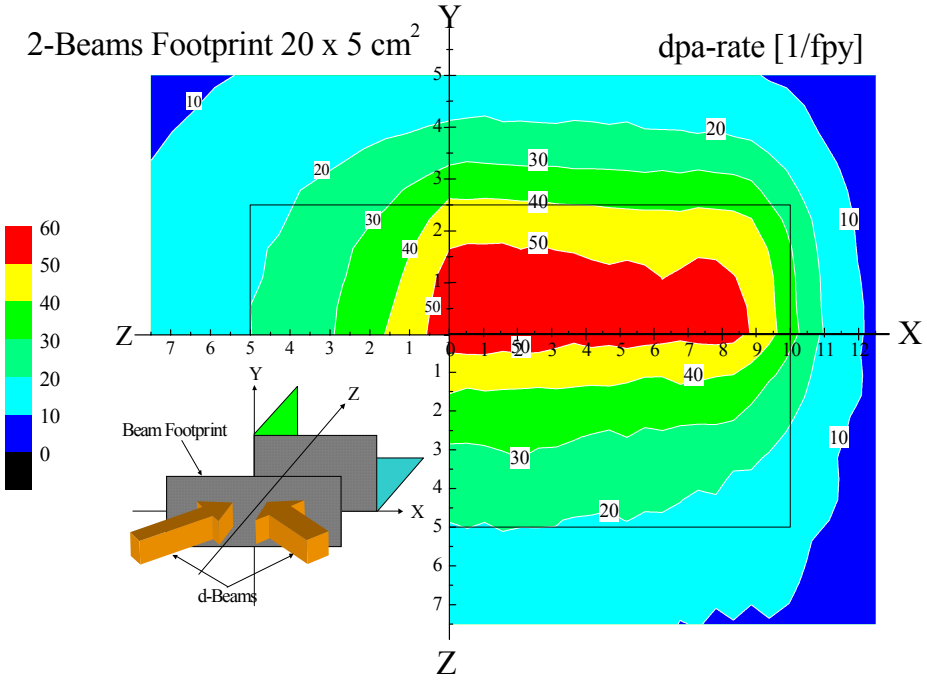

Fig. 2: Spatial distribution of the displacement damage rate induced in EUROFER for the case of a two 125 mA d-beams (horizontal declination) with a footprint 20 × 5 cm2 (full performance stage). The black lines show the HFTM edges.

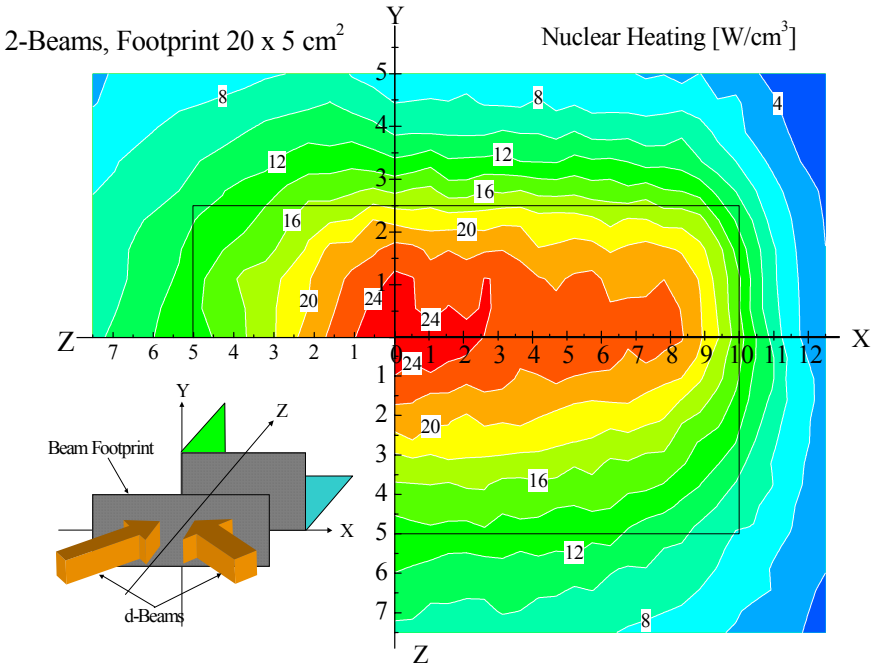

Fig. 3: Spatial distribution of the nuclear heat generation inside HFTM (its edges shown by solid lines) and surrounding neutron EUROFER reflector for the case of a two 125 mA d-beams (horizontal declination) with a footprint 20 × 5 cm^2

Heat deposition in W moderator plates

The tungsten moderator plates (30x20x3 cm3) which serve as neutron spectra shifter and reflector in MFTM are subjected to substantial heat deposition. In this work the results for a model containing a big carbon moderator block surrounding the whole test module are presented (see Figure 4). The W-plates were split by planes parallel to x-axis with separation of 1 cm in between in order to obtain spatial heat distribution.

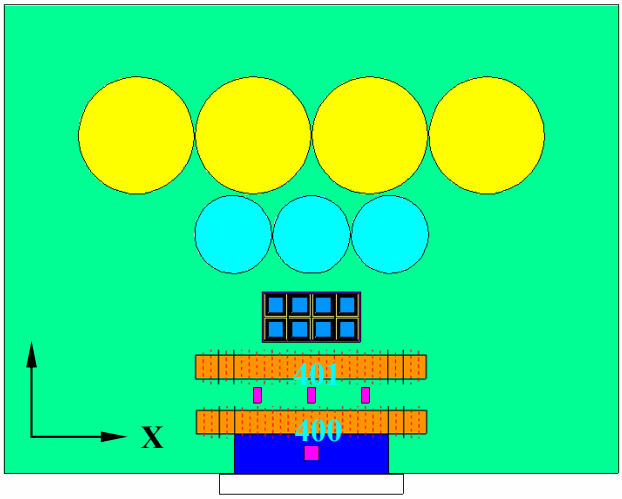

Fig. 4: IFMIF Test Cell Module surrounded with carbon moderator block and with two tungsten reflector/moderator plates (cell # 400, 401).

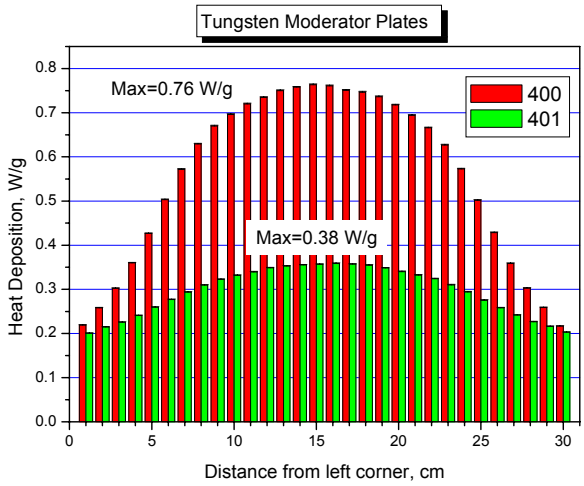

Fig. 5: Heat deposition in W-plates (cell # 400, 401) as a function of distance along X axis.

The spatial distributions of the heat deposition in the tungsten plates are shown in Figure 5. The maximum deposition is about 0.76 W/g for the forward plate (cell #400) and 0.38 W/g for the backward plate (cell #401). The results will be used for MFTM cooling system design. Damage and gas production rates for the tungsten plates were calculated as well though are not shown here.

Staff:

U. Fischer
A. Möslang
S.P. Simakov
P. Vladimirov

Literature:

[1] M. Martone (Ed.), IFMIF International Fusion Materials Irradiation Facility Conceptual Design Activity Final Report, ENEA Report RT/ERG//FUS/96/11 (1996)

[2] Yu. Lizunov, A. Möslang, A. Ryazanov, P. Vladimirov, New Evaluation of Displacement Damage And Gas Production For Breeder Ceramics under IFMIF, Fusion and Fission Neutron Irradiation, J. Nucl. Mater. 307-311 (2002) 1680-1685

[3] A. Möslang, P. Vladimirov, Neutronics calculation and design for medium flux test module of IFMIF, Fusion Eng. and Design 63-64 (2002) 121-126

[4] A. Möslang, P. Vladimirov, Performance improvement of the Medium Flux Test Module by Neutronics Calculations and Revised Design, IFMIF-KEP: International Fusion Materials Irradiation Facility Key Element Technology Phase Report, Report JAERI-Tech-2003-05, March 2003, p. 307.

[5] S.P. Simakov, U. Fischer, V. Heinzel et al., International Fusion Materials Irradiation Facility (IFMIF): Neutron Source Term and Neutronics Analyses of the High Flux Test Module, Report FZKA 6743, Karlsruhe, 2002 (http://bibliothek.fzk.de/zb/berichte/FZKA6743.pdf)

[6] S. P. Simakov, U. Fischer, U. von Möllendorff et al., Advanced Monte Carlo procedure for the IFMIF d-Li neutron source term based on evaluated cross section data, J. Nucl. Mater. 307-311 (2002) 1710

[7] U. Fischer, S.P. Simakov, U. von Möllendorff et al., Valiadated Computational Tools and Data for IFMIF Neutronic Calculations, ANS Meeting AccApp'03 (San Diego, 1-5 June 2003)

[8] A. Möslang et al, Recent advances at the International Fusion Materials Irradiation Facility IFMIF; 19th IAEA Fusion Energy Conference, 14-19 October 2002, Lyon, France, Proceedings.

[9] U. Fischer, S. P. Simakov, A. Möslang, Recalculation of nuclear responses in the HFTM of IFMIF for different beam footprints, Final report on the EFDA task TWO-TTMI-003, D11, IRS/FZK Interner Bericht, May 2003;

[10] U. Fischer, S. P. Simakov, A. Möslang, Recalculation of nuclear response for different beam footprints, IFMIF-KEP: International Fusion Materials Irradiation Facility Key Element Technology Phase Report, Report JAERI-Tech-2003-05, March 2003, p. 419.

[11] S.P. Simakov, U. Fischer, V. Heinzel, A. Möslang, Neutronic Characterisation of the High Flux Test Module of the IFMIF, ANS Meeting AccApp'03 (San Diego, 1-5 June 2003)

TTMI-003 D10
Neutron Moderator/Reflector and Irradiation Conditions

The International Fusion Material Irradiation Facility (IFMIF) is proposed as an intense neutron source to test fusion reactor materials under relevant irradiation conditions. It should provide a proper neutron spectrum with sufficiently high damage production rates to allow also accelerated tests within an appropriate volume. The primary goal of the present study was to select on the basis of neutron transport calculations a suitable design of the IFMIF medium flux test module (MFTM) for a proper irradiation response of ceramic breeder materials. On the basis of systematic screening studies of different material combinations and test module shapes, it was shown that the IFMIF neutron spectrum could be largely adjusted to DEMO reactor conditions by combining tungsten plates serving as spectral shifter and carbon coating of the test modules acting as neutron reflector. In addition, damage code calculations confirmed that IFMIF provides over the entire energy range DEMO reactor specific primary knocked on atom (PKA) spectra, which governs the damage morphology and, hence, mechanical properties of many irradiated materials.

The Vertical Test Assembly 2 (VTA2), which houses the medium-flux modules, is located directly behind the high-flux module and has a specimen volume of ~6 L (1-20 dpa/fpy). For the present reference design concept, two specific types of irradiation experiments have been developed: (1) *in situ creep-fatigue experiments* on structural materials and (ii) *in-situ tritium release experiments* on ceramic breeders and Beryllium. In the present design the helium-cooled VTA2 will be equipped simultaneously with the creep-fatigue and the ceramic breeder test module. In order to significantly improve the neutronics performance for functional materials like Be-alloys or ceramic breeders, (iii) 2 Tungsten plates (2x30 mm thickness) acting as *neutron spectral shifter* and (iv) a carbon envelope (250-300 mm) serving as *neutron reflector* have been included during the reporting periode.

Neutron spectral shifter development

While the existing design outline for the in-situ creep fatigue test module and the in-situ T-release test module is presently being significantly improved both with respect to drawings and Neutronics and therefore will be described in more detail in the forthcoming report, in the following the neutron spectral shifter will be described together with the nuclear heating.

Figure 1 shows a CATIA outline of the spectral shifter. The tungsten moderator plates (30x20x3 cm^3) which serve as neutron spectra shifter and reflector are subjected to substantial heat deposition. In this work the results for a model containing a big carbon moderator block surrounding the whole test module are presented. The W-plates were split by planes parallel to x-axis with separation of 1 cm in between in order to obtain spatial heat distribution.

After the design outline for the W spectral shifter has been done, the spatial heat deposition in the tungsten moderator plates have been calculated with MCNPX code. The

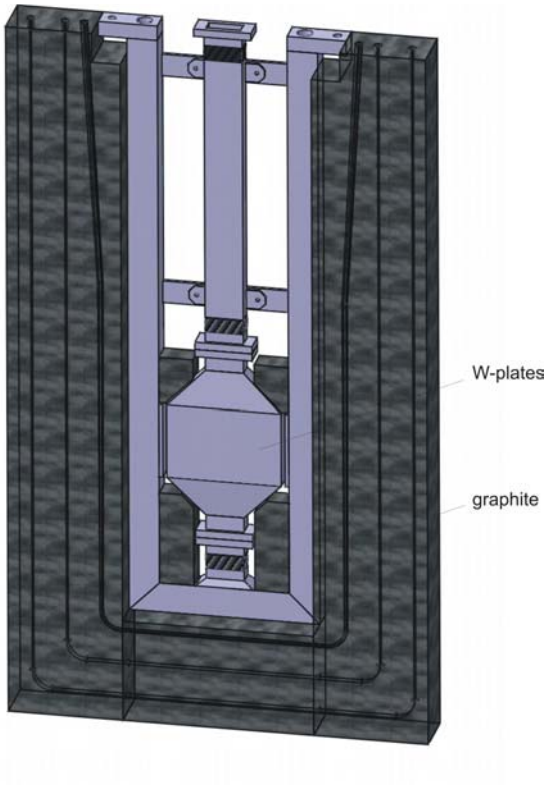

Fig. 1: Between the 2 in situ test modules a neutron spectral shifter (2x30 mm Tungsten) and a neutron reflector (graphite envelope) have been included during the reporting period.

spatial distributions of the heat deposition in the tungsten plates are shown in Figure 2. The maximum deposition is about 0.76 W/g for the forward plate (cell #400) and 0.38 W/g for the backward plate (cell #401). The total heat deposition is 0.5566±0.0004 and 0.2956±0.0001 W/g for the forward and backward plates respectively.

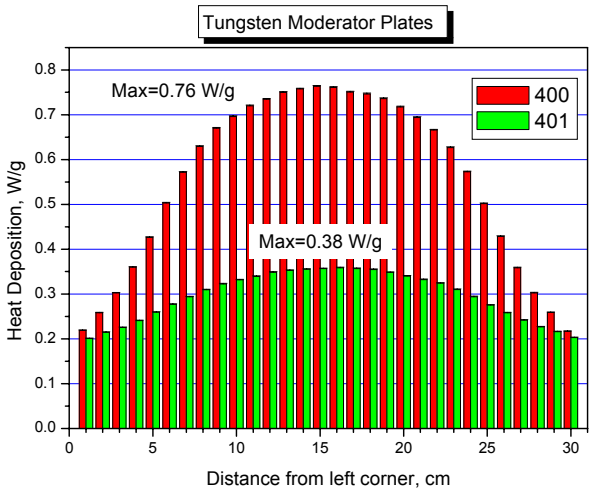

Fig. 2: Heat deposition in W-plates (cell # 400, 401) as a function of distance along X axis

Neutron spectrum

A further task was to improve further the neutron spectrum and the irradiation conditions in the medium flux volume of the test cell. Although the irradiation conditions for structural materials were already quite close to the DEMO conditions (gas and damage production, PKA spectrum) and the significant progress was achieved last year in the improvement of irradiation conditions for Beryllium materials to be used as neutron multipliers. Tritium can be produced in beryllium under irradiation by the direct (n,t) as well as by the multi step reaction (see equation below).

$$^{9}Be + n \rightarrow \alpha + {}^{6}He$$

$$^{6}He \rightarrow {}^{6}Li + e^{-} + \bar{\nu}_{e}$$

$$^{6}Li + n \rightarrow t + \alpha$$

Due to the specific feature of the multistep reaction it is effective only if the neutron spectrum has high population of high and low energy neutrons simultaneously. The Neutron spectrum can be modified by additional neutron moderator/reflector modules that usually improve the irradiation conditions for in-situ tritium release experiments on breeder ceramics in the medium flux region. Therefore three variants have been considered:

1. initial model with tungsten moderator and carbon reflector

2. the model where tungsten moderator was removed in order to increase the total flux and the population of the high energy neutrons

3. the model also without tungsten moderator and with additional carbon reflector placed behind TRIM

Fig. 3 shows the neutron spectra in the Beryllium of the HCPB blanket (PPCS reactor) , the fission reactors HFR and BOR-60 and the IFMIF medium flux test module. When comparing the spectra and Beryllium cross-sections, it is revealed that the irradiation simulations in the fission reactors will result in high displacement damage rates. Due to the high reaction threshold, it will be difficult to achieve sufficiently high Helium production rates in the fission reactor irradiation. Tritium cannot be generated by the ^{9}Be(n,t) ^{7}Li reaction in the fission reactors but through the two-step reaction ^{9}Be(n,□) ^{6}He → ^{6}Li(n,□)t. Because of the large cross-section of the latter reaction in the thermal energy range, the Tritium production will be rather high in a well thermalised fission reactor spectrum such as the HFR. A more detailed evaluation of the irradiation conditions for Beryllium in the medium flux region of IFMIF has been done in cooperation with the IRS, FZK and is published elsewhere [1].

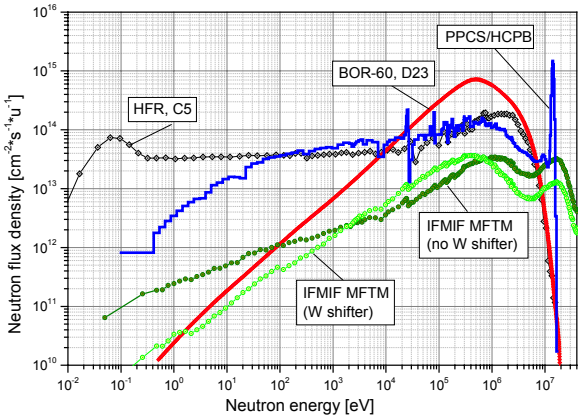

Fig. 3: Neutron spectra in the Beryllium of the HCPB blanket (PPCS reactor), the HFR and BOR-60 fission reactors and the IFMIF MFTM with and without tungsten spectral shifter [1].

Previous extensive Monte Carlo simulations have clearly shown that the IFMIF irradiation conditions for iron-based structural materials fit quite well to those of a DEMO power reactor. In particular it was shown that a proper selection of spectral shifter material and design configuration, IFMIF meets DEMO reactor relevant H, He and dpa production rates as well as H/dpa and He/dpa ratios perfectly in structural materials. A major result of the screening study is that the integration of two 30 mm thick tungsten plates at the front and back side of the IFMIF creep-fatigue test module levels very effectively the high energy neutrons peaked around 12-16 MeV and, at the same time, notedly increase the neutron population in the range $5 \cdot 10^{-3} \div 5 \cdot 10^{-1}$ MeV.

Staff:

G. Bürkle
S. Baumgärtner
A. Möslang
P. Vladimirov

Literature:

[1] U. Fischer, D. Leichtle , A. Möslang, P. Vladimirov, *Nuclear Irradiation Parameters of Beryllium under Fusion, and Fission and IFMIF Irradiation Conditions Sources*, will be presented at ICFRM11, Kyoto, Japan, December 6-12, 2003

[2] Yu. Lizunov, A. Möslang, A. Ryazanov, P. Vladimirov, New Evaluation of Displacement Damage And Gas Production For Breeder Ceramics under IFMIF, Fusion and Fission Neutron Irradiation, J. Nucl. Mater. 307-311 (2002) 1680-1685

[3] A. Möslang, P. Vladimirov, *Neutronics calculation and design for medium flux test module of IFMIF*, Fusion Eng. and Design 63-64 (2002) 121-126

[4] A. Möslang, P. Vladimirov, *Performance improvement of the Medium Flux Test Module by Neutronics Calculations and Revised Design*, IFMIF-KEP: International Fusion Materials Irradiation Facility Key Element Technology Phase Report, Report JAERI-Tech-2003-05, March 2003, p. 307.

[5] A. Möslang et al, *Recent advances at the International Fusion Materials Irradiation Facility IFMIF*; 19th IAEA Fusion Energy Conference, 14-19 October 2002, Lyon, France, Proceedings.

[6] P. Vladimirov, A. Möslang, Comparison of Material Irradiation Conditions for Fusion, Spallation, Stripping and Fission Neutron Sources, will be presented at ICFRM11, Kyoto, Japan, December 6-12, 2003.

Fuel Cycle

GB8-VP 1
Cryopump Development and Testing

The **T**est facility for **I**TER **mo**del pump (TIMO) is used to demonstrate the qualification of the ITER-torus cryopump which is recommended as the reference design for ITER. The test programme with the 1:2 model cryopump covered the simulated ITER conditions with respect to gas flow, gas composition, gas pressure, time periods for heating up and cooling down, temperature of the panels during pumping, partial regeneration and total regeneration [1, 2].

One of the key points is the long term reliability of the cryopump and its peripheral units. In ITER the pump will be operated under radioactive tritium. Replacement of the components requires remote cutting and welding of pipe connections. Maintenance work has to be executed in hot cells. That means long shut down periods in case of failures. Therefore, one of the objectives of the TIMO test programme is the definition of weak design points which would have been the cause of failures found during the tests. The analysis of the failures and operation experiences of the test campaigns which cover more than 1000 pumping cycles is the basis for improvements in design and manufacturing of the 1:1 ITER prototype pump.

The experiences and failures during three test campaigns with the ITER model cryopump in TIMO have been described [3]. It has become obvious that the cryopump itself has a robust design and no critical element has failed during the tests. This technical solution can be recommended for the design of the 1:1 prototype for ITER. The leaks in the metal bellow arrangement of the valve actuator was a failure during commissioning. The main valve, with actuator and sealing have shown no failure during the tests.

The reason for the reduction of the He pumping speed must be confirmed by further tests with 450 K regeneration tests. It must be emphasized, however, that the required pumping speed for the ITER relevant gas mixtures of 1 l/(s·cm²) was achieved throughout the tests.

Most of the failures concern the periphery which is needed for the supply of the cryopump with 80 K gaseous helium and 4.5 K supercritical helium.

The reasons of all failures have been understood and recommendations to avoid them by improved acceptance tests are given in the “Lesson to be learnt” sections in the final report [3].

Staff:

A. Antipenkov
Chr. Day
A. Edinger
H. Haas
V. Hauer
H. Jensen
A. Mack
R. Simon
J. Weinhold
D. Zimmerlin

Literature:

[1] H. Haas, Chr. Day, A. Mack, D.K. Murdoch; Performance tests of the ITER model pump; Proceedings 22nd SOFT, Helsinki, Sept. 2002

[2] H. Haas, Chr. Day, A. Mack, Report on experimental plan and the tests for pumping at panel temperatures between 5 and 40 K, 100 K regeneration tests with matrix of different gas mixtures and gas loads; Internal Report FE.5130.0046.0012/I, Forschungszentrum Karlsruhe, August 2003.

[3] A. Mack, Chr. Day, H. Haas, Report on endurance test results of critical components, Internal Report FE.5130.0046.0012/H, Forschungszentrum Karlsruhe, August 2003.

TW1-TTF/VP 11
Torus Exhaust Cryopump Development and Testing

1. Objectives

After the basic parametric testing of the torus cryosorption model pump in the test facility TIMO performed over the last years, the experimental work in this reporting period was focussed on specific issues which were found to need detailed investigation. The TIMO test bed was employed to assess the minimum temperature which is needed to achieve complete release of hydrogen during partial regeneration. A second emphasis was put on the investigation of heat loads and how they vary with the pressures inside the pump. These results were directly used for the design of the ITER cryoplant.

Underlying experiments to assess the effect of microwave heating on the cryosorption panels and to check their potential to be used for the fast heating step during partial regeneration were finished. The physical feasibility could be demonstrated but the integration of the transmission line system in a real pump is still considered to be quite challenging.

Finally, separate measurements in the COOLSORP facility were performed complementary to the TIMO tests to continue the characterisation of the ITER reference sorbent material. Emphasis was laid on gases with some poisoning potential, such as hydrocarbons and ammonia.

2. Modifications of TIMO

For the tests in 2003 some new devices were installed to upgrade the hardware and experimental capabilities of the TIMO test bed [1].

To be able to perform the multi-cycle tests in ITER relevant time scale, it was necessary to write new programs for the TIMO control system “Siemens S5” as well as for the visualisation system “COROS”. With these modifications in the PLC system the typical test sequences during a pump cycle, namely “cool down of the sorption panel from 80 K to 5 K”, “pump test” and “regeneration of the sorption panels” can be performed automatically.

Fig. 1: 450 K heater.

The high temperature test campaign with the model pump asked for the provision of a 450 K temperature level to perform reactivation tests. So it was necessary to install a new supply line for the helium flow at higher temperatures. The additional heating line was installed in parallel to the already available 300 K helium supply line. An electrical continuous-flow heater with a maximum electrical power of 10 kW was assembled into the 300 K line. To heat up the helium flow of 10 g/s to the set point temperature, a controller for the electrical heater was installed. The pipes and the electrical heater of the new 450 K helium supply line are shown in Fig. 1. With the two supply valves of the 5 K panel circuit and the 80 K circuit it is possible to heat up these circuits to different temperature levels. Also variations of the operating temperatures of the two cooling circuits in the model pump are possible.

Further modifications were carried through to enable online analysis of the composition changes of the processed or regenerated gas. For the analysis of the gas compositions during the different steps of a pumping test a quadrupole mass spectrometer was installed. This high resolution mass spectrometer (type “GAM 400”)

was especially developed by the company BALZERS to resolve between He and D_2, but can also be operated in unit resolution up to 128 amu. Moreover, by using a built-in pressure reduction system it is not only able to analyse gases at low pressures but as well in the high pressure regime. Several years experience for this device was gained in the TITAN test campaign [2]. With these operation options, the mass spectrometer is connected to the TIMO test vessel (representative of the incoming gas), the model pump (representative of the pumped gas) and to a buffer tank (representative of the regenerated gas). The latter buffer vessel was especially installed in the exhaust line of TIMO to provide for this gas sampling possibility. As shown in Fig. 2, it is a cylindrical tube with a diameter of 273 mm and a total length of 1800 mm. It is connected downstream of the model pump and can be filled with the desorbed gases after the regeneration via the regeneration pump station.

These modifications make it possible to observe the changes in the gas composition during the complete pump process, comprising the metering of the gases into the test vessel, the pumping phases and the end of the tests after the regeneration to 80 K or reactivation of the pump to 300 K / 450 K. At the beginning of the new test campaign at TIMO all new installed devices were intensively tested and approved [3].

Fig. 2: New buffer tank in the exhaust line.

3. Tests performed with the ITER model pump

100 K Regeneration tests

To determine the regeneration temperatures required for complete release of protium, deuterium and a D_2 Base/(10 %) helium mixture from the cryosorbed state, regeneration tests were carried out in TIMO. During the tests the temperature rise of the sorption panels was realised by convective heating via the 80 K shield circuit, which was heated to temperatures higher than 200 K. At the beginning of the procedure the supply with 5 K helium gas coolant was stopped. After heating of the 80 K shields with warm helium gas, the temperatures of the cryosorption panel system followed and the pumped gases were released leading to a pressure rise inside the connected volume of model pump and test vessel. In parallel, this volume was pumped by the regeneration pump station, which consists of a large roots pump and rotary vane pump. Thus, the measured pressure evolution is obtained by the mass balance of released and pumped gas, leading to sharp peaks in the temperature region where desorption is the most pronounced (Temperature Programmed Desorption Method TPD), see Fig. 3. Based on the pressure evolution curves measured for each tested gas mixture during the regeneration tests, the respective integral gas release curves were calculated as a function of panel temperature under quasi-stationary conditions. The pumping speed characteristics of the regeneration pump system connected to TIMO had to be determined prior to the regeneration tests so as to achieve quantitative results. Fig. 3 shows the results obtained for deuterium. Depending on the positions of the temperature measurement points (TIR 613, 615, and 620) in the panel cooling circuit, various release rates were calculated. However, T620 is considered to be most representative for the ITER operation. For all gases studied, a 100% release rate was reached at temperature of ~110 K the latest. For practical purposes, it is sufficient to achieve 90 K at the panel surface.

Heat load tests

Tests were performed to check the heat loads inside the ITER model cryopump. During these tests both cooling circuits of the model pump (panel system and shield system) were operated in a steady state mode at constant temperature. The maximum operational pressure inside the ITER torus cryopump is 10^{-1} mbar, which is the pressure for cross-over from mechanical to cryogenic pumping. To measure the heat loads on the cooling circuits at

varied pressure levels between 10^{-4} mbar and 10 mbar the test volume was filled with helium gas. With the collected data for the inlet/outlet temperatures and the flows through the 5 K panel system and the 80 K shield system the heat loads were calculated, see Figs. 4 and 5.

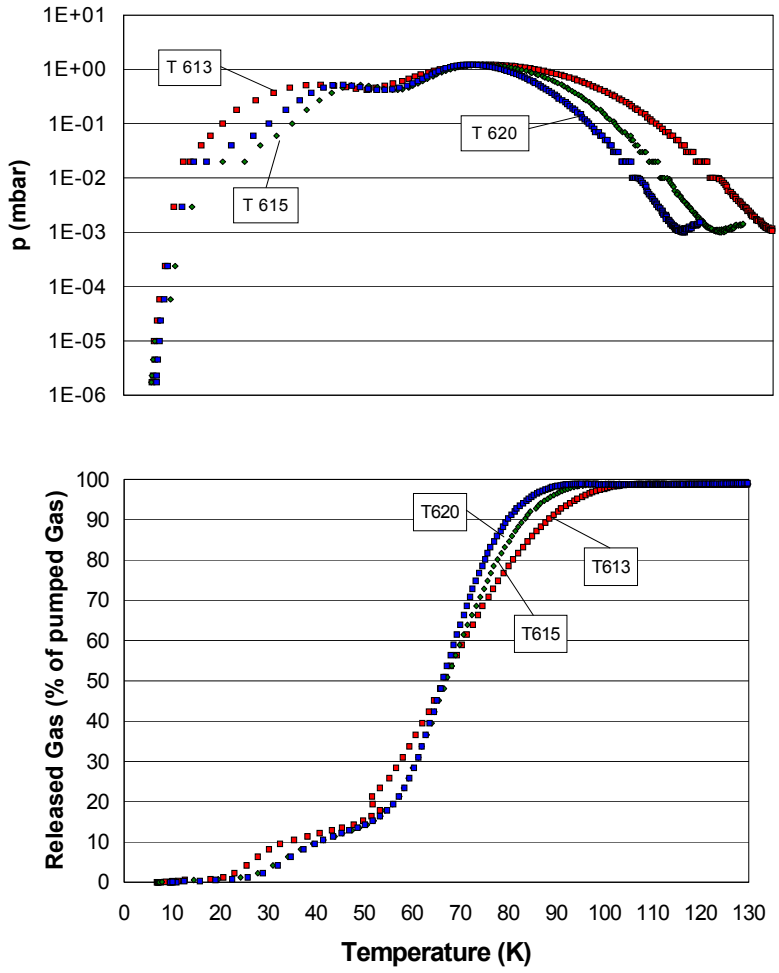

Fig. 3: Measured TPD spectra at 3 typical temperature sensor positions for a D2-Base/(10 %) helium mixture, showing the helium release peak and the deuterium release peak (top) and the obtained deuterium release curve (bottom).

Depending on the pressure in the model pump and the coolant flows the heat loads into the 80 K circuit may rise up to max. values of the order of 4 kW, with about 3 kW at the upper end of the ITER torus cryopump operational pressure range, at 10^{-1} mbar. For the 5 K panel system under these conditions, a max. heat load of ~480 W was measured. At higher pressures, up to 10 mbar, the results rise up to 950 W. Nevertheless such high heat load values are only expected during disturbances in the regular operational process.

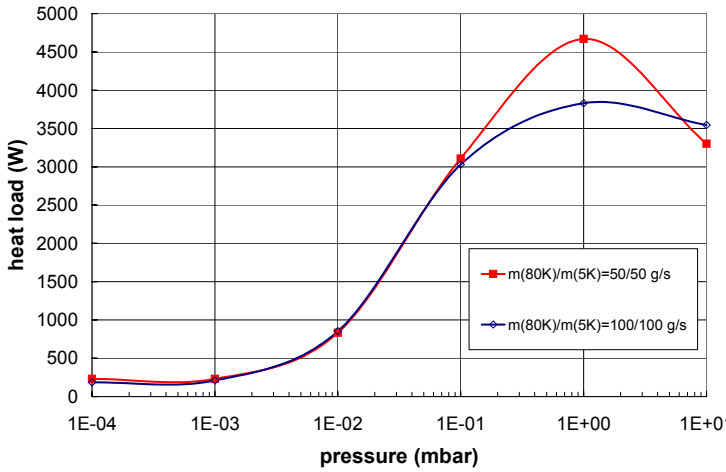

Fig. 4: Heat loads to the 80 K shield system.

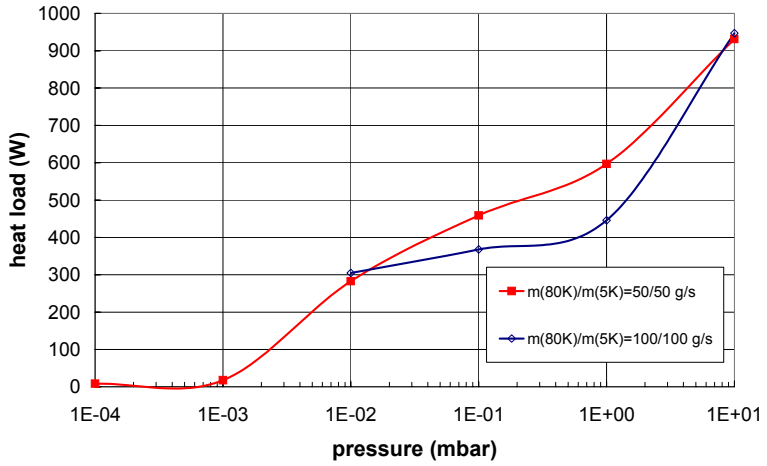

Fig. 5: Heat loads to the 5 K panel system.

4. Microwave heating

It had been demonstrated that the layer of activated charcoal with its typical thickness of about 1 mm shows a good absorption for microwave radiation at the ITER-type high frequencies. Experimental validation of this was performed, however, only at ambient conditions, see Fig. 6 [4].

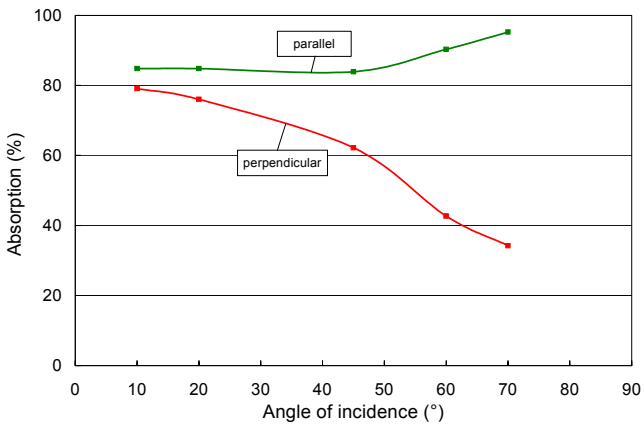

Fig. 6: Measured absorption of the charcoal coated panel when exposed to microwaves @ 140 GHz, for two polarisations.

To estimate the suitability of such an approach also for cryogenic temperatures, a heat flux and electrodynamic energy transfer model was developed. It could be shown that, under cryogenic temperatures, it is very well possible to perform regeneration of the charcoal side of the panels, while keeping the steel side of the panels cooled at 5 K, see Fig. 7. Thus, it is not needed to perform a cool-down of the whole panel system mass. This reduction in the cryosupply requirements is the biggest benefit achieved by this technique. The cryorefrigeration needs for cryopump regeneration could thus be reduced down to 15 to 20%.

The absorption results were promising enough to start a design study for the microwave system and transmission line. It was revealed that there are no principle obstacles which could not be overcome. Nevertheless, it became obvious that a lot of installations (mirrors, antennas) would be necessary. This makes the realisation for the ITER cryopumps questionable from the maintenance point of view, as the design has to fulfil stringent remote handling requirements. Consequently, these activities are no longer continued. A final report has been released, which gives all the details of the work performed in this field [5].

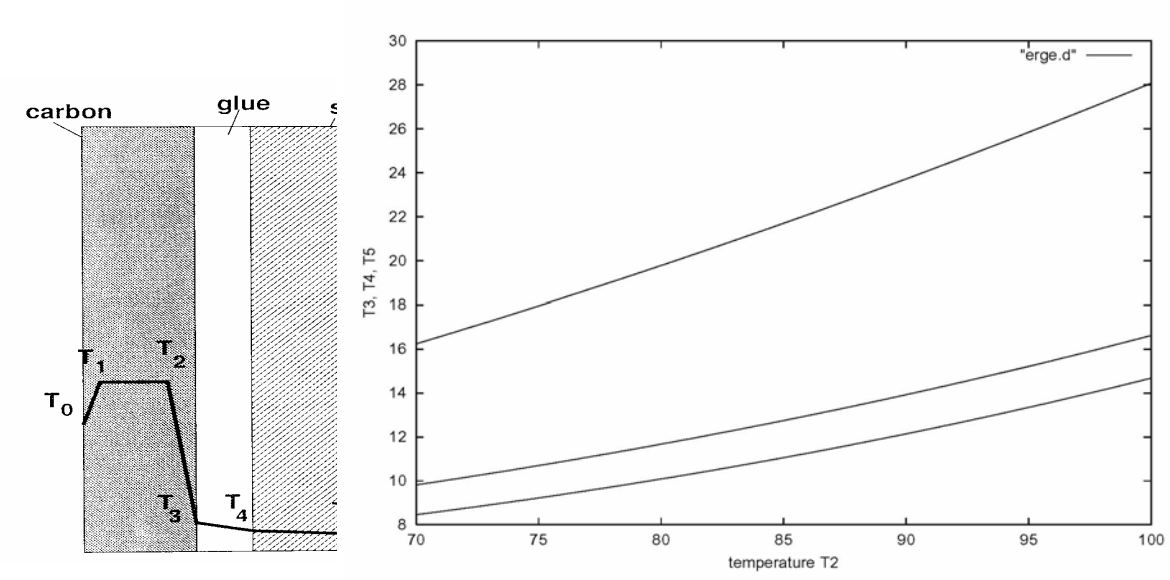

Fig. 7: Layer model indicating the various temperatures and calculated results for the temperature distribution of the heating reference case.

5. COOLSORP

The experimental sorbent characterization work on the COOLSORP facility was continued over the last year. Additional experiments were made to measure the sorption isotherms of helium, hydrogen, deuterium and nitrogen on the same activated carbon material SC2 (ITER reference material). The investigated temperature range covers both sub- and supercritical temperatures from 4.2 K up to 77.35 K. The new results complete former adsorption measurements on the same material [6, 7].

Following that, the COOLSORP facility was modified for high temperature measurements. Therefore the sample recipient was housed in an air circulation oven. The temperature of the oven can be chosen in the range between 50 °C and 650 °C with an accuracy of 1 K. The sample recipient is connected to COOLSORP by means of a gas transfer line.

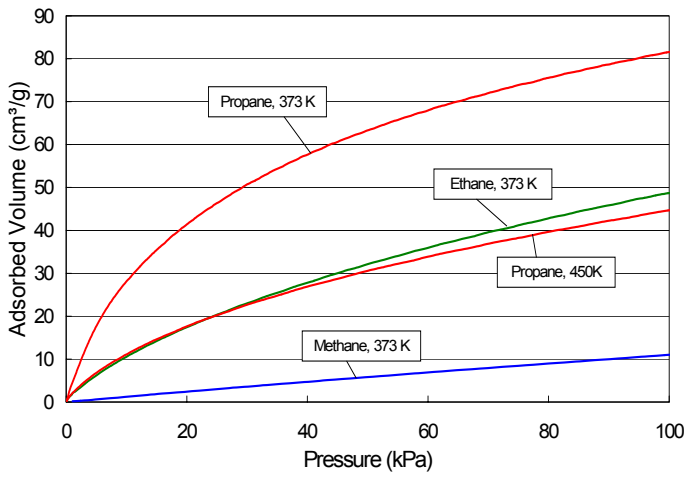

Fig. 8: Comparison of sorption isotherms of hydrocarbons under typical reactivation temperature conditions.

In this part of experimental work the adsorption of higher hydrocarbons and of ammonia was investigated [8]. Adsorption isotherms of methane, ethane and propane were measured at temperatures of 50 °C, 80 °C, 100 °C and 177 °C. The highest temperature corresponds to the highest regeneration temperature of the cryosorption panels in the planned ITER torus pump. Fig. 8 compares the results at a temperature of 100 °C. The curves show a clear dependence on the size of the adsorptive molecules. Only the adsorption amount of methane is linearly dependent on the pressure. The ethane and propane molecules are bonded much stronger to the carbon surface, which is indicated by the higher adsorption amounts and the curvatures of these two graphs. In summary, methane can completely desorb at 100 °C, however for ethane and propane it is only possible at very low pressures.

In the next step of the experimental programme measurements in the pressure range from10^{-4} to 10^{-6} mbar with the static volumetric method are planned. Helium and hydrogen are foreseen as adsorptives. The resulting adsorbed amounts are needed as design data for calculation of the pumping speed of the ITER torus and NBI pump.

6. Conclusion and Outlook

The ITER torus exhaust cryopump testing has made excellent progress. Besides the generic tests concerning the vacuum performance of the cryopump, which will be continued with the online monitoring of the composition changes of the gas mixture when being pumped, TIMO was in this reporting period increasingly used as test bed to provide design and performance data for other but closely interrelated fields. In this context, heat load and regeneration data which are essential for the ITER cryoplant design have been measured [9]. In parallel tasks, TIMO was and will further be used to generate key data in the field of safety (Task TW2-TSS-SEA5.5) or water-leak detection (Task TW0-T450). Furthermore, TIMO has also been shown to produce essential design data for the NBI cryopump system (Task TW3-TTFF-VP33). A general validation of the endurance of the cryosorption panel set-up will be performed within automatic multi-cycle tests. The small scale COOLSORP tests are a good complement to the large scale tests on TIMO, and will be continued.

The investigation of microwaves could confirm the physical feasibility, but will not be continued due to major challenges needed to be solved when implanting microwave heating in the torus cryopump design.

Staff:

A. Antipenkov
Chr. Day
A. Edinger
H. Haas
V. Hauer
H. Jensen
A. Mack
P. Pfeil
R. Simon
H. Stump
J. Weinhold
D. Zimmerlin

Literature:

[1] H. Haas, Chr. Day, A. Mack, D. Murdoch, Performance tests of the ITER model pump, Fusion Engineering and Design 69 (2003) 1-4, 91-95.

[2] Chr. Day, The use of a high-resolution quadrupole mass spectrometer system for selective detection of helium and deuterium, Vacuum 51 (1998) 1, 21-30.

[3] H. Haas, Chr. Day, A. Mack, Report on experimental plan and the tests for pumping at panel temperatures between 5 and 40 K, 100 K regeneration tests with matrix of different gas mixtures and gas loads; Internal Report FE.5130.0046.0012/I, Forschungszentrum Karlsruhe, August 2003.

[4] A. Möbius, A. Mack, Chr. Day, G. Dammertz, R. Wacker, Regeneration of cryosorbing exhaust gas panels by means of gyrotron radiation, Proc. 27th Int. Conf. On Infrared and Millimeter Waves, San Diego, US, Sept. 2002, pp. 213-214.

[5] Chr. Day, A. Möbius, Assessment of the application of microwaves for the regeneration of ITER cryosorption pumps, Internal Report FE5130.0046.0012/K, Forschungszentrum Karlsruhe, August 2003.

[6] V. Hauer, Chr. Day: Cryosorbent characterization of activated charcoal in the COOLSORP Facility, Report FZKA 6745, Forschungszentrum Karlsruhe, Sept. 2002

[7] Chr. Day, V. Hauer, The low temperature sorption behaviour of cryosorbent materials, in: C.H. Lee (ed.), Proc. of the 3rd Pacific Basin Conf. On Adsorption Science and Technology, World Scientific, Singapore, 2003, pp. 569-573.

[8] Chr. Day, A novel sorbent material test device at variable cryogenic temperatures, Proc. 2003 International Cryogenic Materials Conference, Anchorage, Alaska, Sept. 2003.

[9] R. Haange, V. Kalinine, N. Shatil, F. Millet, L. Guillemet, M. Wykes, Chr. Day, A. Mack, Cryogenic subsystem to provide for nominal operation and fast regeneration of the ITER primary Cryosorption vacuum pumps, Proc. 2003 International Cryogenic Materials Conference, Anchorage, Alaska, Sept. 2003.

EFDA 03/1095
Design of an ITER-sized Mechanical Pump Train

The aim of this task is a detailed design of an ITER relevant, dry mechanical pump train as forepumping system for the cryopump systems of ITER [1]. The tritium compatibility shall be realised with a ferrofluidic seal system, based on the results achieved in the R&D Task VP12, which is based on a modified roots blower. The design shall include other (dry) pump concepts for the pressure range not covered by roots blowers.

The ITER pump train was optimised for a torus cryopump regeneration in 1998 and uses 4200 m^3/h and two 1200 m^3/h Roots pumps backed by two 180 m^3/h piston pumps. The backing piston pumps have been manufactured by Toyo Engineering Corp. by an order of JAERI in 1992. From that time these pumps were never manufactured again. Moreover, the overall concept was reconsidered now, because, in comparison with 1998 ITER design:

1. the cryopump volume has changed from 2.25 to 7.5 m^3
2. the fuelling rate is reduced from 200 to 120 Pa·m^3/s
3. the pipeline routing is changed
4. the cryopump regeneration pattern is different – the pump down time is increased from 75 to 150 s.

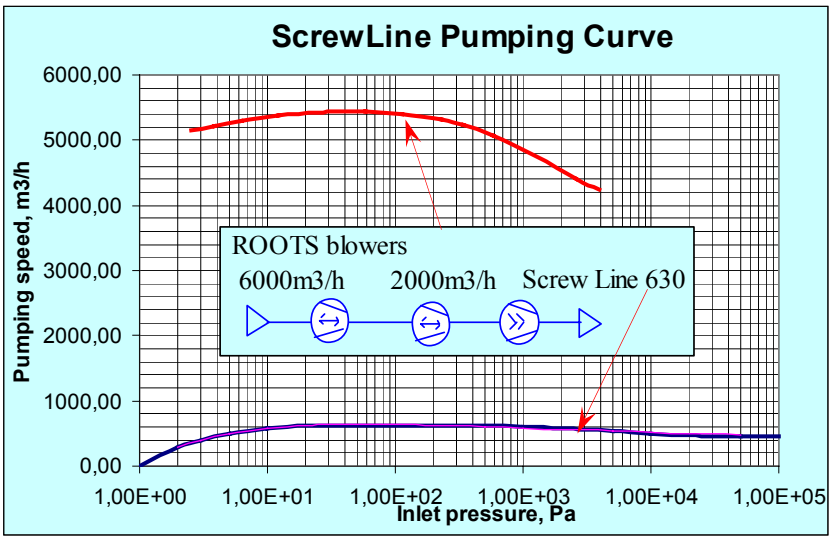

Fig. 1: Calculated pumping curve for Roots pumps of Pfeiffer and a screw pump of Leybold Vacuum

Forepumps which fulfil the ITER requirements under the aspect of pumping speed and compression ratio are commercially available, for example Roots pumps, screw pumps (see Figure 1) and different piston pumps. However, none of them are applicable for tritium. The UK Company Roots Systems develops and produces the special Roots compressors of a comparable size. It is attractive to use the experience of this company with the ferrofluidic seals and now with a full metal Roots pump, but they are not certified as a vacuum company.

Instead of the Toyo piston pump a screw pump could be used (e.g. slightly modified ScrewLine-630 of Leybold Vacuum). This pump has cantilevered rotors and uses the shaft seals from the high pressure side only, the outlet pressure does not vary and maybe the labyrinth seal could be allowed even for tritium operation, if an implementation of a ferrofluidic seal would meet problems there.

For the first stages pumps there is no alternative to the ferrofluidic seal, because they are working under variable inlet pressure (within 150 s between the switches of the regenerated cryopump the pressure varies from 2 kPa to 10 Pa) and it will be a continuous gas exchange between the process gas and oil filled volumes, thus the shaft seal has to be tight. One

should note, that the seal, which is under testing by Roots Systems Inc. now, was invented and applied as the easiest solution. It is cheap, refillable, but by the appliance of the magnetic fluid directly to the shaft it is impossible to control the distribution of the liquid among the teeth. In order to achieve the better distribution and simplify the assembling the gap between the teeth and the shaft (100 μ) is bigger than optimally needed (50 μ), and the seal is overfilled. About 2 cc liquid is usually filled into each seal, while the standard seal needs about 0.05 cc of the liquid per seal. The overfilling leads to the increase in tritium inventory, although still negligible (the uptake was measured in TLK as 500 Bq/cc per day, thus the conservative estimate gives 0,0001 Ci/year in the roughing system) and the hazard of the ingress either to the process gas in case of the pressure control failure in the oil filled volumes, or to the lubricating oil in case of the pressure rise accident in the roughing line (in some elements of the plasma exhaust processing system the pressure is 4-5 bar). As well, the oil evaporation from the open surface should be taken into account. The magnetic liquid will cover all open surfaces of the pole piece, and the oil vapour flow from the surface can be two orders of magnitude higher, than it is in the standard option. It remains nevertheless rather low: In the standard application the oil leak from the surface of four 50 μ slots can be estimated about $1.6 \cdot 10^{-10}$ Pa·m^3/s. Therefore the seal needs further development.

The calculated pumping curve of a train consisting of two Roots pumps of 6000 and 2000 m^3/h and the screw pipe of 630 m^3/h is shown in Figure 2. The scroll (Normetex) pump is not out of a consideration so far, although for the required pumping speed (even above 200 m^3/h) they are very big, and their reliability was not confirmed during exploitation under tritium at JET.Staff:

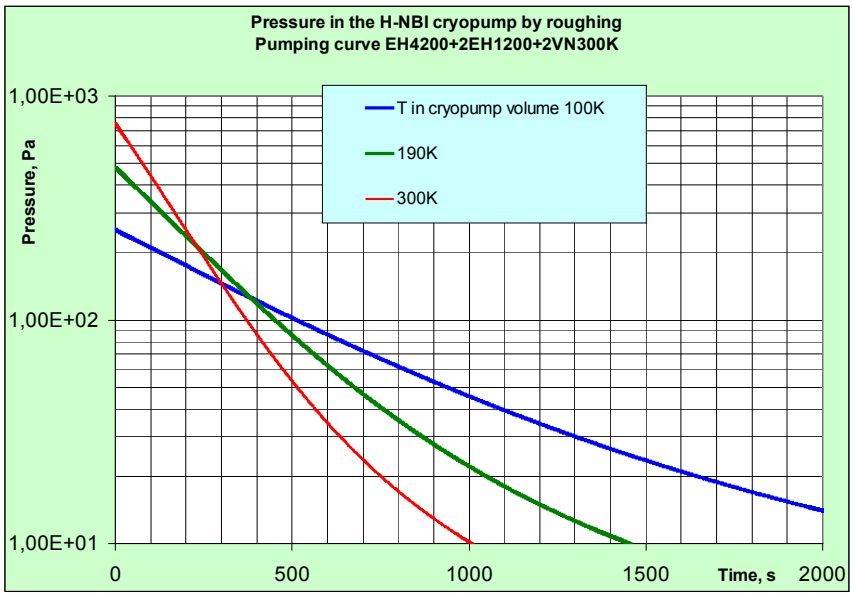

Fig. 2: Pump down time of one ITER NBI by regeneration for different gas temperatures in the vessel (the temperature in the roughing line is 300K).

A. Antipenkov
A. Mack
I. Meyer

Literature:

[1] A. Mack, A. Antipenkov, J.-C. Boissin, Chr. Day, H. Haas, D. Murdoch, M. Wykes, UHV and forevacuum pumping issues, for the fusion reactor ITER, ALCATEL Conference Imagine the new Vacuum Frontier, Annecy, France, January 2003.

TW1-TTF/VP 12
Performance Evaluation of Roots Blower with Ferrofluidic Seal System

The roughing pump sets in ITER are used for the initial pump-down of the torus, pumping of desorbed gases during torus cryopump regeneration, pumping of the neutral beam injectors during regeneration and pumping of the torus during conditioning [1]. The market for commercially available oil-free pumps has been investigated under the aspect of pumping requirements.

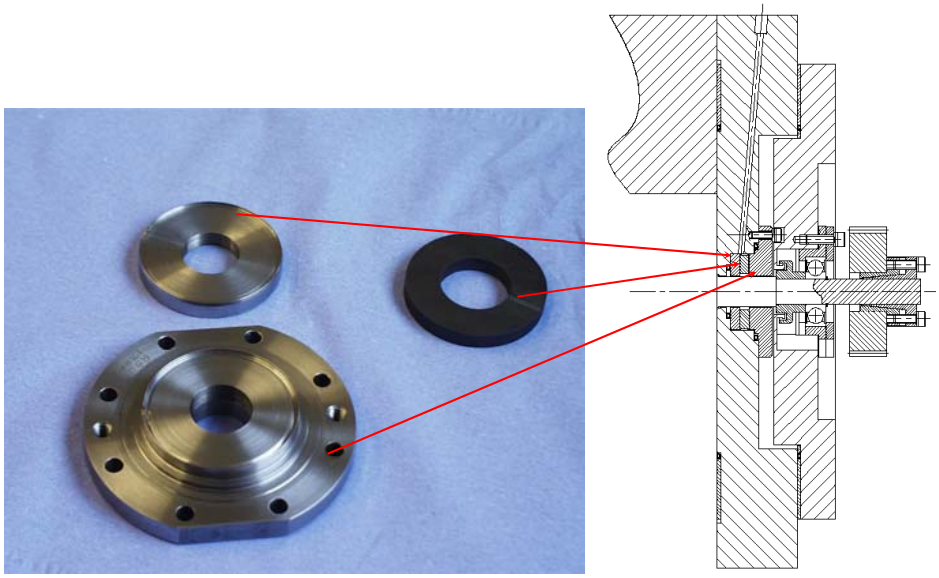

Fig. 1: Ferrofluidic seal modification.

In cooperation with industrial companies concepts for a tritium compatible operation were developed. The modification of a catalogue pump should foresee a replacement of a conventional shaft seal, which allows conventionally 10^{-3} (in the best case 10^{-5}) mbar·l/s He leak, while for the tritium handling 10^{-8} mbar·l/s is required. Such a small leak rate in the today technology can only be achieved by using a ferrofluidic seal (the space in a catalogue pump typically allows for such a modification); for all flange connections metallic seals have to be used instead of elastomer O-rings. Technical solutions involve the use of Helicoflex® seals; the housing of the pump has to be either made of stainless steel or aluminium alloy or coated with nickel or aluminium (such a coating deems to be quite feasible); between the motor and the pump a magnetic coupling has to be implemented (this coupling is a conventional one and should cause no problem); the oil filled volumes from both drive and gear sides should be equipped with an atmosphere control, because in a conventional pump they are connected through a labyrinth seal to the process gas side, while the ferrofluidic seal is leak tight and the pressure there could unexpectedly rise with temperature, as well as tritium monitoring is required. The task to implement all these modifications to a catalogue pump is rather challenging, and an option of making a special development for this purpose pump should still be considered. Such a pump has been ordered in UK Company Roots Systems in 2000 as a pilot one, aimed to test the ferrofluidic seal but not to optimise the pumping performance. The pump housing was milled of a stainless steel block; the flanges were designed to provide easier access to the seals. The design of the seals was few times modified and till June 2003 could not show positive results. The last modification (see Figure 1) seems to be successful. Now the pump has demonstrated an external leak tightness better than 10^{-9} mbar·l/s. The provisional tests of the pump showed that the seals worked excellent (see Figures 2 and 3) and now the pump is being reassembled and will soon be

ready for the final testing and delivery to FZK for long term testing in open and closed loops with air, helium and, eventually, with tritium in a glove box in the TLK.

Fig. 2: Pilot pump under leak testing.

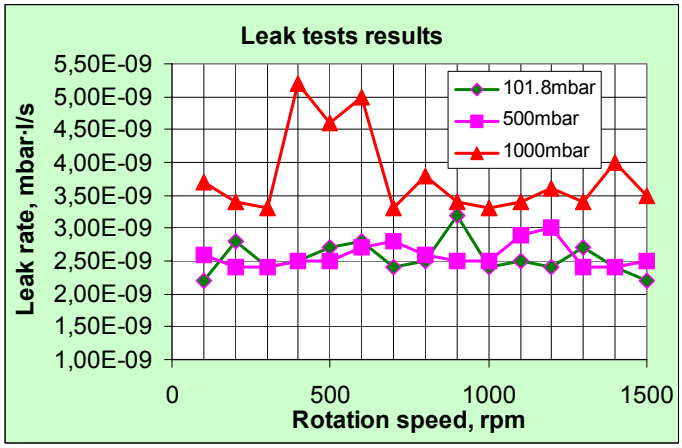

Fig 3: Provisional leak test results with modified ferrofluidic seal.

Staff:

A. Antipenkov
R. Laesser
A. Mack
R. Simon

Literature:

[1] D. Murdoch, N. Bekris, J.C. Boissin, C. Day, J. Gilroy, M. Glugla, R. Lässer, A. Mack, EU contribution to ITER fuel cycle design and R&D, Fusion Engineering and Design 69 (2003) 45-49.

TW3-TTFF/VP 33
Assessment of the ITER NBI Pumping Scenario

In ITER operation, heating and current drive (H&CD) systems provide essential functions, ranging from pre-ionization and assisted current start-up, bulk central heating, and on- and off-axis current drive. The Neutral Beam H&CD system consists of two or three injectors. Each injector will deliver a deuterium beam of 16.7 MW at 1 MeV (total 33 MW), and will be able to operate for long pulses (up to 3600 s). In addition to the H&CD NB there is a diagnostic injector, which serves for the plasma diagnostics and delivers a pulsed deuterium beam of 100 keV atoms perpendicular to the machine axis.

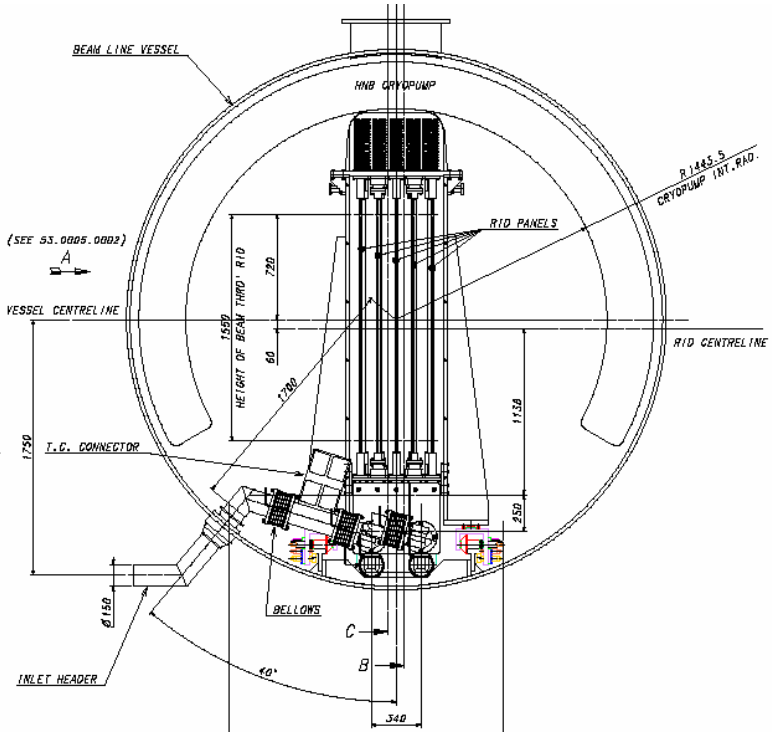

Fig. 1: Cross section of a neutral beam injector. 250° cylindrical cryopanels can be seen between the injector elements and the vessel.

The peculiarities of the NBI geometry is that in two different sections of the injector quite contradictory conditions have to be maintained: a) the neutraliser section (see Figure 1). Here the beam of negative ions has to pass through the neutralising gas cloud, where the gas density should be maintained on an optimal level (ca. 0.25-0.3 Pa inside the neutraliser). The calculations of the gas flow along the neutraliser channels and towards the cryopanels show that one can expect about 0.03 Pa in the surrounding space – the flow is in the transition range and more precise calculations cannot be provided. About 90% of all the gas supplied to the injector comes to the neutraliser and has to be pumped in this section. b) residual ions dump (RID) and calorimeter. The pressure here has to be as low as possible; the cryopump in this section collects the gas coming from the neutraliser and the gas produced by dumping of the ions. It means that the pumping speed has to be as high as possible, but the capacity of the pump should be calculated for about 10% of the total gas supply. The membrane installed between both sections baffles the gas in the neutraliser area from the ion dump area. As the gas density in both areas is maintained dynamically, it is important to calibrate the cryopump in order to optimise its design to better suit different modes of the future neutral beam injector. The TIMO facility offers a very good opportunity for this.

Within this task the different scenarios and options of the NB cryopump have been simulated with the help of the TIMO facility. Apart of 4.5 K operation, increased panel temperatures have been tested. The higher temperatures promise much cheaper helium supply while the hydrogen pumping speed is practically not affected as long as the sorbent in all points remains below ca. 30 K. The NBI cryopump is not designed to pump helium and therefore a sorbent temperature below 15 K is not needed. If the NBI cryopump assists the main torus pump for the dwell pumping, then either the 4.5 K helium should be supplied or the residual helium will not be pumped through the NBI ports, which may not create any problem,

because the outgasing from the walls is dominantly hydrogen and partly water and hydrocarbons.

It was also recommended by FZK to have the charcoal sorbent coating on one surface of the cryopanels only. Then the surface of the cryopanels, looking to the hot structure, can be polished and will condense the water-likes, while the back charcoal surface will be used practically for protium and deuterium. To simulate this on TIMO, the distribution of the gas loads between inner and outer surfaces has been calculated using Monte-Carlo code (see Figure 2), and the corresponding rating gas load in TIMO was calculated as the doubled ITER NBI gas load multiplied by the factor of reduced load to the outer surface (see Table 1).

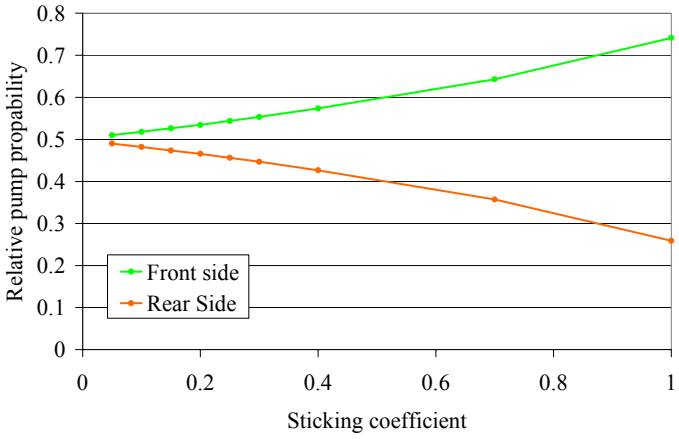

Fig. 2: Gas absorption by the front and back sides of a cryopanel.

Table 1: Gas load summary for the TIMO tests (single-side coating simulation).

NBI:		**H&CD**		**Diagnostic**	
Chamber:		Source + Neutraliser	RID + Calorimeter	Source + Neutraliser	RID + Calorimeter
Total cryopanel coated surface m^2		40	40	40	14
ITER gas load, sccm:	H_2	18,400	1,700	9,000	560
	D_2	9,200	850	7,300	560
ITER specific gas load, $sccm/m^2$:	H_2	920	85	450	80
	D_2	460	42.5	375	80
Required TIMO gas load, sccm:	H_2	**11040**	**1020**	**5400**	**800**
	D_2	5520	510	4500	800
Required maximal ITER sorbent capacity, $Pa \cdot m^3$	H_2	267300	24300	129600	8100
	D_2	133700	12450	64800	4050
Required ITER pumping speed, m^3/s	H_2	1100	3000	1600	1000
	D_2	550	1500	800	500
Required ITER specific pumping speed, $l/s \cdot cm^2$	H_2	2.75	7.5	4.0	2.5
	D_2	1.4	3.8	2.0	1.3

The results of the tests at 15 K, 20 K and 25 K are shown in Figures 3-5.

The maximum throughput available in the TIMO metering system is 10000 sccm. The maximum allowed hydrogen inventory in TIMO by reason of the safety regulation is 90000 sccm*min this corresponds to 91170 mbar·l. For instance in the tests with the maximum loads, i.e. single side modelling, with the gas load of 10000 sccm the maximum allowable pulse in TIMO is 540 s.

With this gas load the required pumping speed was fully achieved. For higher gas loads further tests in the future ITER NBI-test bed are needed.

Staff:

A. Antipenkov
Chr. Day
H. Haas
V. Hauer
A. Mack
R. Simon
J. Weinhold
D. Zimmerlin

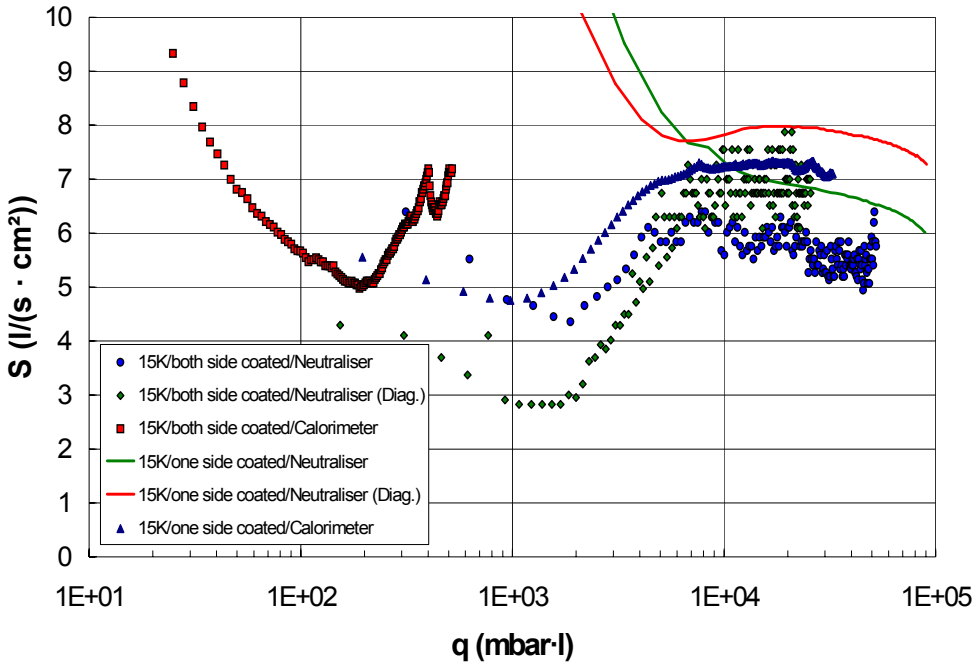

Fig. 3: NBI simulation test at 15 K.

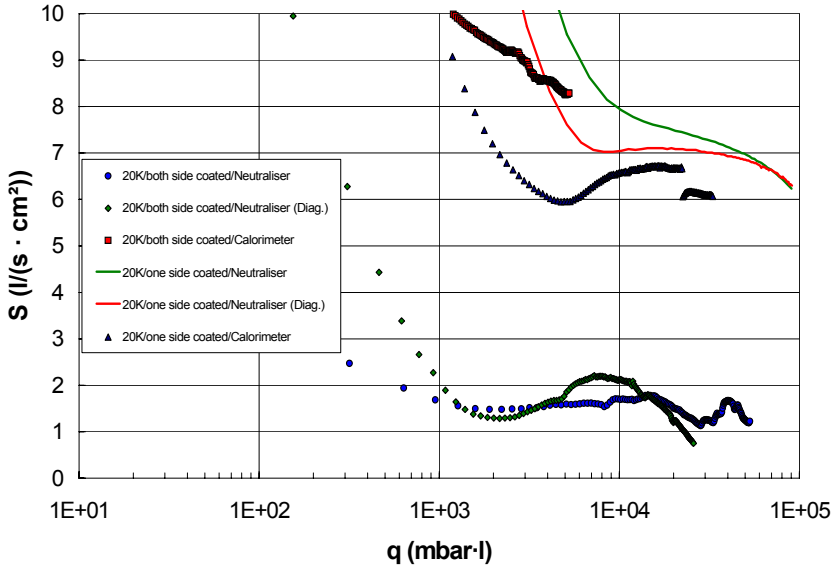

Fig. 4: NBI simulation test at 20 K.

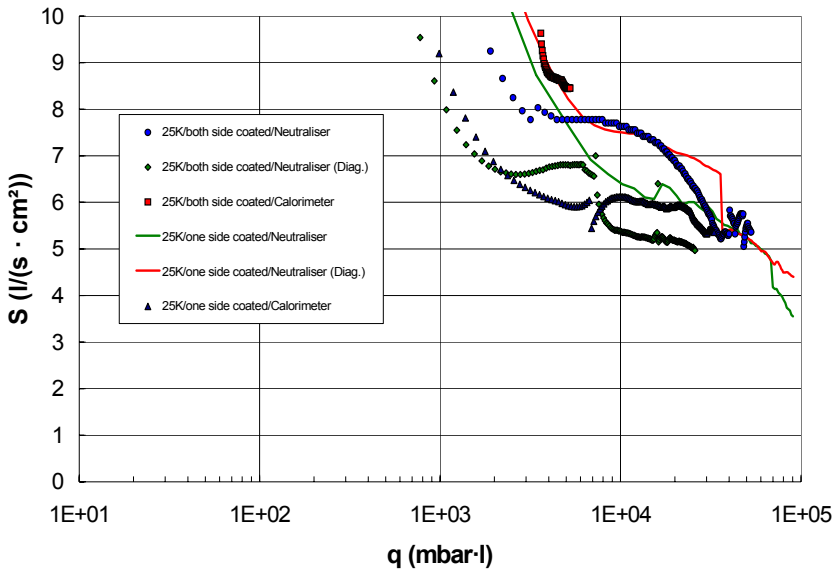

Fig. 5: NBI simulation test at 25 K.

TW0-T 450/01
Detection and Localisation of Leaks from Cooling Circuits

The object of this work is to investigate a proposed method of locating leaks in the ITER water cooling circuits. This works follows on from the initial investigations by JRC Ispra where they proposed using specific tracer materials and then looking for these tracers in the exhaust gases from the torus. The method uses a gas chromatograph/mass spectrometer (GC/MS) combination to detect the very small amounts of tracer that would be in the exhaust gases in the event of a leak. In case of a leak which prevents operation of ITER, leak localisation will start after ITER has been shut down for repair work. At this stage tracers will be injected into the various water circuits and their presence in the exhaust gases from the ITER cryopumps searched for by gas chromatography/mass spectrometry (GC/MS) techniques. One of the prime features of this technique is that the cryopumps will be used as a first stage of separation of the tracer material from the other gases in the torus.

Initial work will be in the selection of a suitable range of potential tracer materials that are readily detectable and identifiable and will not damage or poison the cryopump or any part of the tritium plant, particularly the catalyst systems. About 10 suitable tracer materials are required to allow unique identification of a leak in any of the 7 ITER water cooling circuits. Material containing halogens have already been eliminated and in general the lighter hydrocarbons will be preferred. Tracer materials will also have to be soluble in water to at least 0.1%.

After bench commissioning of the GC/MS system, this will be transferred to the TIMO facility at FZK to simulate the ITER pumping system. The GC/MS system will examine the exhaust gases after full regeneration of TIMO to look for the small quantities of water with tracers that will be introduced into the high vacuum side of TIMO. One of the main features to be investigated are the temperatures to which the cryopanels will have to be raised in order to release water and the tracers. The pressure of the gases in TIMO after regeneration is quite low, about 15 mbar. As the GC/MS system is designed to sample gases at atmospheric pressure, a small vacuum pump will be used as a compressor to feed the GC/MS. The operational procedures and conditions for the process are to be determined.

Staff:

C. J. Caldwell-Nichols

TW1-TTF/VP 13
Compatibility of Leak Localisation Tracers with Cryopanels

For ITER, a powerful and sensitive leak detection system is of utmost importance. Consequently, a multi-stage approach has been developed to meet the different leak detection requirements. One of the various strategies involved is for locating a leak in the cooling water circuits which is considered to be the most likely type of a leak into the vacuum vessel. Leak localisation will only be performed after a water leak has been noticed by poor plasma performance and confirmed.

A concept was proposed to add tracer substances at low concentrations which would be released in the gaseous phase in the event of a leak. These tracers would be pumped by the cryopumps and released during regeneration. They would then be detected by the global leak detection system located in the vacuum pump room which is connected to the torus roughing line and monitors the gases exhausted from the cryopumps. Due to the chemical species, the tracer substance will be released not after partial regeneration but after the less frequently performed regenerations at ambient temperature or high temperature (450-470 K). The use of the cryopump would ensure a high sensitivity even for very small leaks due to their accumulation effect over the pumping operational time in between the regenerations. To optimise the resolution further, another feature of the cryopump system can be exploited. To lower the proportion of hydrogen isotopes in the exhaust gas mixture to be analysed, a pump down phase could be inserted between the partial regeneration and the high temperature regeneration step, thus achieving the gas to be analysed for tracers being practically hydrogen free and by that leading to easier separation of the tracer.

Any substance to be used as a tracer must be investigated for compatibility with the cryosorption pumping concept. Different tracers may be added to the different sub-loops so that one becomes able to pinpoint the leak down to the component level. Therefore, several tracers have to be identified. In this reporting period, a meeting has taken place devoted to this issue, where it was decided to use lighter hydrocarbons in the range C1 to C3. In addition, alcohols or other organics would also be a candidate.

For detailed investigation of the release behaviour and the influence on overall pumping speed, tests on TIMO will be performed. In preparation of this, a mass spectrometer-gas chromatograph device has been procured and set into operation, which will now be integrated in the TIMO test bed (cf task TW0-T450). The gaseous tracer candidates will be introduced into the facility as fractions of the test gas mixtures being pumped. The substances which are in the liquid state at ambient conditions will be processed via a bubble column device.

Staff:

Chr. Caldwell-Nichols
Chr. Day
H. Haas

TW2-TTFD/VP 23
Localisation of In-vessel Water Leaks

Under task TWO-T450/01 work is underway to develop a method to identify individual cooling water circuits that may be leaking into the ITER vacuum vessel by detecting specific tracer materials placed in the water circuits. This method will not, however, identify where the leak is inside the vessel. Localisation of the leak inside the vessel is highly desirable in order to minimise the number of components that have to be replaced to be sure that the leak has been eliminated. An extension of the technique used for the external identification of leaking circuits is considered.

The pressure inside the vacuum vessel required for leak localisation has been established as an important parameter. A leaking fluid entering the vessel will form a plume originating at the leak site. The motion of the resulting gas molecules is determined by several factors, one of these being diffusion. Diffusion is more rapid at a lower total pressure, this means that the concentration profile of any leaking gas reduces with reducing pressure as the gas molecules move more rapidly away form the leak site. As the ability of any method to detect the leaking gas is proportional to the local concentration, then the only option is to have the ITER vacuum vessel close to atmospheric pressure during internal leak localisation, most probable in nitrogen. This is actually a benefit for the operation of the remote arm that will be required. Other effects are convection or forced gas currents which will tend to disperse the plume and make detection more difficult.

However, this brings into question which gas should be used for leak localisation and the method to be used for collecting it. Using a tracer in water is no longer appropriate as there is an immediate penalty for the sensitivity in the dilution necessary. This leaves detecting the water that is actually leaking or, if the water circuits are drained, using a gas such as neon or argon. This now becomes a conventional leak detection problem.

The task and the entire problem is now pending a review by ITER.

A report against Deliverable 1 of this task has been sent to EFDA Garching in July 2003.

Staff:

Ch. Caldwell-Nichols

GB7-T 228.1
Cryo-pumping for ITER: Considerations on the Possible Formation of Higher Hydrocarbons by Tritium Induced Radiochemical Reactions

The existing experience in the radiogenic synthesis of higher hydrocarbons in mixtures of tritium with other gases at the Tritium Laboratory Karlsruhe has been compiled and literature data included into a study. An attempt was made to assess the contribution and consequences of radiochemical reactions that eventually may lead, both in the gas phase and in the cryo-sorbed phase, to the formation of higher hydrocarbons and therefore to a progressive deposition of carbon / tritium on the adsorption sites. Ultimately, these reactions may have an impact on the tritium inventory in the ITER cryopumps and even affect its pumping characteristics.

The primary pumping system for ITER includes two major subsystems, i.e. the torus roughing system and the high vacuum system, which is characterized by a high throughput and a low tritium inventory. The high vacuum system, located in the divertor port ducts, comprising several cryopumps is operated in a cyclic batch regeneration mode. They are predominantly used for the evacuation of the torus exhaust during plasma operations. The torus exhaust gas is primarily composed of a hydrogen isotope mixture containing helium as well as other impurity gases such as nitrogen, neon and argon. The high vacuum system also serves for the evacuation during several other operational phases of the machine including pumping between plasma discharges, wall conditioning, bake-out as well and leak testing. Within the frame of the above mentioned operations, additional impurity gases such as water, carbon oxides and hydrocarbons (mostly methane together with smaller partial pressures of higher hydrocarbons) are generated via plasma / wall interactions or liberated during the course of first wall conditioning. Chemical composition and concentration of these impurity streams are highly dependant upon the selected operational parameters and the previous exposure history of the first wall.

While the technology aspects related to the cryosorption of low molecular weight species like hydrogen isotopes or helium are well established, there are still many open questions concerning the impact and radiochemical behavior of tritium. These include

i) the conceivable deposition of active particles (such as radicals like C, C_2, C_3, CQ, CQ_2, CQ_3, Q = H, D, T) transported by neutral gas into the pumping duct and even the pump itself during the pumping process

ii) radicals, such as methyl radicals, are known to have rather low sticking coefficients, i.e. 10^{-3} to 10^{-5} - as a consequence they may penetrate up to the pumping system and lead there to the formation of soft C:H films

iii) the possible role of radiochemical reactions initiated by the beta-decay of tritium in the adsorbed phase and

iv) the effect of the tritium decay heat on the sorption capacity, pumping speed and de-sorption characteristics of cryopumps.

Main products from recoil and beta radiolysis processes taking place amongst typical reactive plasma exhaust impurities, i.e. molecular hydrogen isotopes, carbon oxides, isotopically substituted water, and isotopically substituted hydrocarbons, are predominantly tritiated molecular hydrogen, low molecular weight poly-tritiated hydrocarbons, tritiated water, carbon dioxide and to a much lesser extent tritium-containing high molecular weight hydrocarbons and possibly some polymeric substances. Significant yields of higher molecular weight hydrocarbons and condensed polymeric products are only expected from tritium / hydrocarbon mixtures containing a high molar fraction of hydrocarbons. Such conditions do, however, not prevail in the ITER exhaust gas, i.e. DT >> CD_2T_2.

Experimentally it was shown that at tritium / methane ratios exceeding 16 ethane or higher hydrocarbons do not build-up even after a reaction time of two months.

The accumulation of tritiated polymers in the cryosorption panels of cryopumps are considered deleterious because of the associated persistent tritium inventory and progressive loss of pumping capacity. In this context the possible formation of para-formaldehyde (a polymeric form of formaldehyde that decomposes thermally at 413 to 453 K to yield gaseous formaldehyde), reported to be a product even at liquid nitrogen temperature from the reaction of 1:1 and 1:2 mixtures of molecular tritium with carbon monoxide, needs to be examined. From work at TLK it appears that this reaction is not favored provided the partial pressure of molecular tritium is in large excess to that of carbon monoxide. This is actually the case for the plasma exhaust gas of a fusion machine.

At cryogenic temperatures and the associated increase in density (liquid or solid phase) the primary processes are practically unaffected but the mobility of free electrons and of reactive intermediates is reduced, radical recombination reactions becoming the preferred reaction route. At the same time the yield of excited neutral molecules is augmented by the recombination of free electrons with ions and therefore a decomposition of neutral excited molecules tends to predominate over ionic reactions. Radiation induced reactions and reactions following tritium decay are basically slow at cryogenic temperatures. As a result of this the formation of higher molecular weight hydrocarbons is unlikely.

The cryopanels can be freed from low molecular weight hydrocarbons ($< C_8$) by an evacuation at <450 K. To achieve periodically a thorough regeneration of baffles and cryo-sorption panels a bake-out option at temperatures as elevated as technically acceptable should be contemplated in the design.

Staff:

U. Berndt
M. Glugla
R Laesser
R.-D. Penzhorn

GB7-T 332b.1
Influence of Higher Noble Gas Loads on the Fuel Cycle Clean-up Process

The Tokamak Exhaust Processing (TEP) system within the Tritium Plant of ITER need to be designed such that tritium is recovered from all exhaust gases produced during different modes and operational conditions of the vacuum vessel. Since tritiated waste gases will certainly also appear from operation of the different systems within the Tritium Plant itself quite a variety of gas compositions at different flow rates and their transients need to be considered in the development of a suitable physicochemical process for TEP.

The current reference process for the TEP system of ITER is called CAPER and comprises three different, consecutive steps to remove molecular hydrogen isotopes ('impurity separation', step 1), to process tritiated impurities ('impurity processing' step 2) and to provide a final clean-up ('recovery of residual tritium' step 3), while recovering tritium - along of course with the other gaseous hydrogen isotopes - at very high purity in all three steps for direct transfer into the cryogenic Isotope Separation System (ISS) of ITER.

The decontamination factor required for the TEP system is only defined for a short pulse of the deuterium / tritium burn phase of ITER and is specified in the 'Design Requirements and Guidelines (DRG) Level 2' document to be 10^8. In view of the fact that this decontamination factor is based on the ratio of tritium-inlet and outlet flow rates for a particular mode and phase the required detritiation need to be translated into a certain tritium outlet concentration for other modes and operational conditions of the tokamak or when characterizing the efficiency of the process for tritiated gases from other sources. Taking the gas compositions and flow rates detailed in the DRG for the short pulse of the deuterium / tritium burn phase of ITER into consideration a tritium concentration of $\leq 10^{-4}$ gm^{-3} (equivalent to ≤ 1 Cim^{-3} or 0.4 ppm) is required downstream of TEP, as illustrated in Fig. 1 for the 3 stages of CAPER. However, before the waste gas is sent to stack it is processed through the Vent Detritiation Systems (VDS) for final decontamination, and credit can be taken from the performance of the VDS when calculating the tritium effluents for ITER under normal operational conditions.

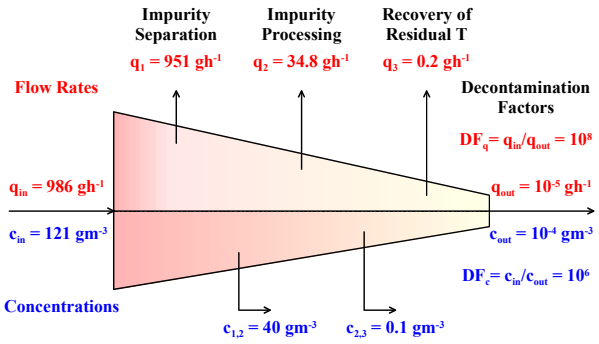

Fig. 1: Conversion of the tritium flow rates based decontamination factor required for ITER during a short burn pulse into a decontamination factor based on tritium concentrations.

During the burn phases of ITER different inert gases such as helium, nitrogen, neon or argon may be fed into the divertor region of the vacuum vessel to eventually reduce the heat loads to the plasma facing materials in this area. Under these operational conditions a maximum total flow rate of 10 Pam^{3}s^{-1} would need to be processed by TEP in addition to the off-gases from regular operation of the tokamak. It is therefore important to experimentally investigate the performance of the CAPER process employing deuterium / tritium mixtures if the above mentioned noble gases are present in the feed gas.

Transmutation of the gases introduced into the divertor region will potentially change their composition, and while nitrogen can in principal be converted into carbon-14 the neutron capture by argon-40 to argon-41 is considered to be significant. However, the experiments have been limited to tritium as the only radioactive species, and in view of the chemical processing argon-41 is assumed to behave like natural argon.

The CAPER facility, a versatile semi-technical tritium facility operated at the Tritium Laboratory Karlsruhe (TLK) for experimental investigations of tokamak exhaust processing and for the recovery of tritium from various waste gases, has been described in different

publications and in detail in EFDA reports. The performance of the first stage permeator of CAPER was tested under operational conditions expected for the front-end permeators of ITER in case of a noble gas cooled divertor by measurements of so-called break-through curves. The permeator is operated at 400°C and of multi-tube design comprising a total of 53 finger type palladium / silver tubes, each with a length of 530 mm and a wall thickness of 0.1 mm, leading to about 0.22 m^2 effective membrane area. Each break-through experiment requires about one full day of CAPER facility operation, since the bleed gases of the permeator need to be processed afterwards to also recover its tritium for reuse in the next test. In more than 50 break-trough experiments, each with about 20 l DT, at least 120 g tritium were mixed with different gases, compounds like tritiated methane and tritiated water were synthesized and the bleed gases of the permeator each time processed within the CAPER facility. In order to assure generic type results from the performance tests of the permeator the flow rates and pressures achieved in the system need to be decoupled from the capabilities of any feed or permeate pump and gas supply. For an independent management of the parameters feed flow rate, feed pressure, permeate pressure and gas composition a number of different control loops are required and have been employed.

The influence of the feed pressure, the permeate pressure and the gas composition on the performance of the first stage permeator of the CAPER facility at TLK was investigated in a systematic study. Along the course of the experiments the hydrogen isotopes involved have been recycled and thereby unavoidably went through a change in isotopic composition. However, most of the experiments have been carried out at tritium concentrations above 50%. Due to the exchange reaction between deuterated methane (CD_4) or deuterated water (D_2O) and tritium when passing such gas mixtures over an isotope exchange reactor the deuterium concentration increases on the expense of the tritium content, since all hydrogen isotopes are eventually recovered by the CAPER process.

Examples of the results are presented in Figs. 2, 3 and 4. All break-through curves have been derived by measuring the bleed flow rates as a function of step wisely increasing feed flow rates at constant feed pressures, constant permeate pressures and with a given, stable gas composition. Depending upon the actual feed pressure and permeate pressure a partial pressure equilibrium is reached at the outlet of the permeator between the bleed side and permeate side for all three hydrogen isotopes at lower feed flow rates. Consequently in this range the bleed flow rate is proportional to the feed flow rate. The partial pressure of hydrogen isotopes in the bleed is constant and the same as their partial pressures at the permeate side. At feed flow rates above the capacity limit of the permeator the bleed flow rate increases progressively, referred to as break-through of hydrogen isotopes at the permeator bleed side.

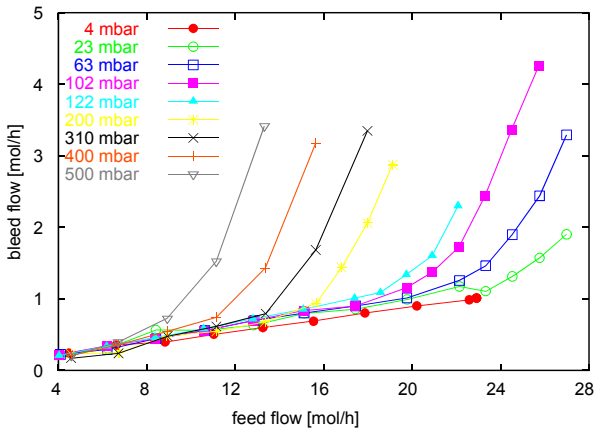

Fig. 2: Influence of the permeate pressure on the bleed flow rate as a function of the feed flow rate for higher permeate pressures.

Fig. 2 shows the influence of the permeate pressure on the bleed flow rate as a function of the feed flow rate for higher permeate pressures. The feed pressure was 140 kPa, and 6% helium was added to the hydrogen isotope mixture. The results in Figs. 3 and 4 have been obtained at a constant feed pressure of 100 kPa and a constant permeate pressure of 30 kPa. As expected break-through occurs at lower feed flow rates for higher impurity concentrations. However, the first stage permeator battery of ITER will be designed in accordance to these results with a sufficiently large permeation area to allow operation below break-through. The concentration of tritium in the gases to be processed in the second and

third stage of the CAPER process will therefore be such that the design decontamination factor can be achieved.

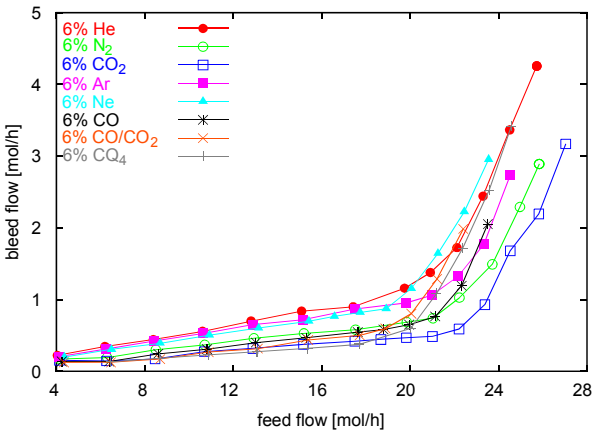

Fig. 3: Bleed flow rate as a function of the feed flow rate for deuterium/ tritium mixed with 6% of different noble gases or impurities.

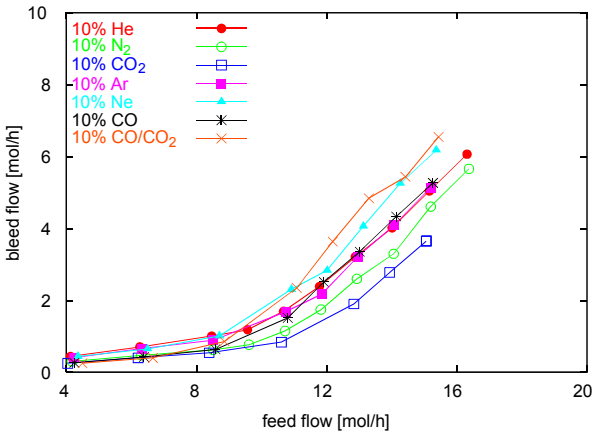

Fig. 4: Bleed flow rate as a function of the feed flow rate for deuterium/ tritium mixed with 10% of different noble gases or impurities.

Staff:

B. Bornschein
M. Glugla
K. Guenther
T.L. Le
K.H. Simon

TW3-TTFD/TR 31
Improvements to the Mechanical Design of the PERMCAT Component

Final clean-up within the three stage CAPER process for decontamination and recovery of tritium from tokamak exhaust streams and different tritiated gases appearing in the Tritium Plant of ITER is based on countercurrent isotopic swamping in a so called PERMCAT, which combines heterogeneously catalyzed isotopic exchange reactions with hydrogen permeation through palladium / silver membranes. Experiments with single-tube and multi-tube membrane PERMCAT's have shown decontamination factors of 10^4 to 10^5 if fed with gases containing tritiated methane, tritiated water or tritiated molecular hydrogen isotopes mixed with e.g. helium, nitrogen or carbon oxides. The technique is highly effective and meanwhile not only employed for systematic experiments along with the characterization of the CAPER process, but also to process tritiated waste gases from a variety of other sources in the TLK. The principle of the PERMCAT is illustrated in Fig. 1.

Palladium / silver tubes undergo a significant dilatation upon uptake of hydrogen isotopes. Therefore industrially available palladium / silver membrane permeators are either of spiral pipe geometry or employ finger type tubes dangling into a manifold. Since distances perpendicular to the direction of the counter current flows in the PERMCAT should be small to maximize exchange flow rates across the palladium / silver membrane a finger type design was chosen for the PERMCAT reactor. This has eventually led to an arrangement of three coaxial tubes, as outlined in detail for a single tube PERMCAT in Fig. 2.

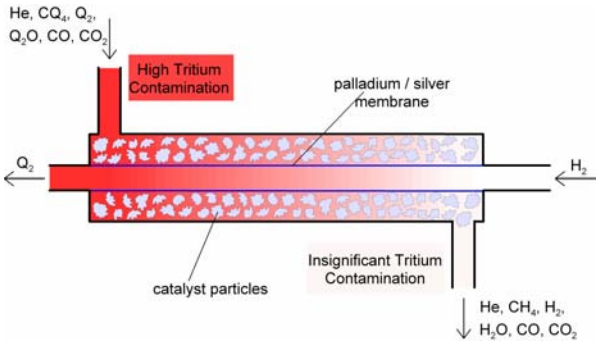

Fig. 1: Principle of the PERMCAT for counter current isotopic swamping.

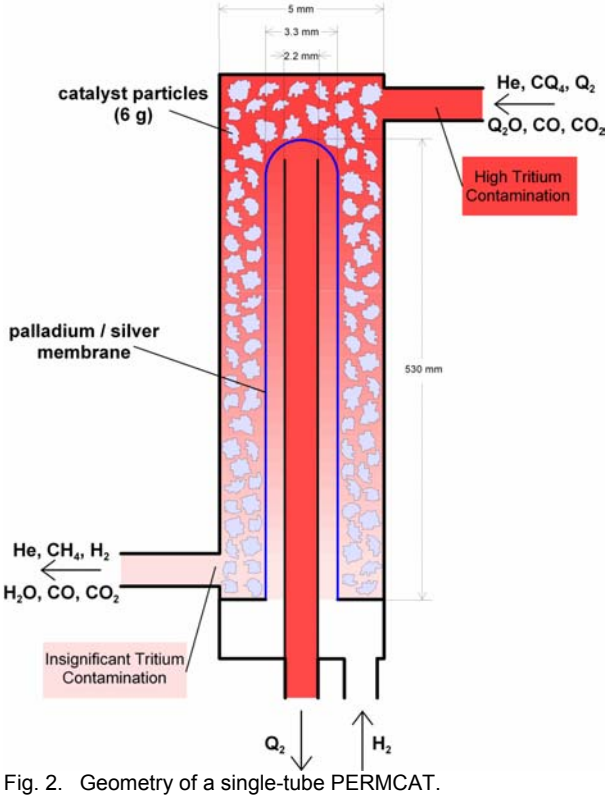

Fig. 2. Geometry of a single-tube PERMCAT.

Among other parameters the throughput of a PERMCAT is dependent upon the effective palladium / silver membrane area, and besides increasing the length of the tubes the only way to enlarge the flow rates is to assemble a number of coaxially arranged tubes together in a manifold. This was realized in PERMCAT's for the CAPER facility at TLK (6 parallel tubes, 530 mm length) and for a unit installed at the Active Gas Handling System (AGHS) of JET (21 parallel tubes, 900 mm length). However, the geometry is rather complex and is intended to be improved for ITER.

To simplify the geometry as shown in Fig. 2 and to realize a layout as illustrated in Fig. 1 a rolled bellows design for the palladium / silver tubes is under development. As for the finger type tubes bellows can also cope with the considerable dilatation of palladium / silver upon uptake of hydrogen isotopes.

In order to determine the process parameters to fabricate corrugated thin wall palladium / silver tubes with crack free convolutions and without axial cracks a number of tube samples have been annealed at different temperatures and times to produce a ductile material and to achieve a grain size distribution suitable for the corrugator tool. A picture of recently produced palladium / silver bellows tubes is shown in Fig. 3.

In a next step the hydrogen isotope permeability of the bellows type palladium /silver tubes will be measured after successful leak testing, and then PERMCAT units with a simplified geometry will be manufactured for tritium tests.

Fig. 3: Palladium /silver tube bellows for the production of advanced PERMCAT's.

Staff:

M. Glugla
S. Welte

TW1-TTF/TEP 13A
Self-Assay, Fast Delivery Tritium Storage Bed

According to the specifications in the ITER Design and Guidelines Level 1, the feed flow rate of tritium will be 120 g tritium per 450 s shot, and about 25 shots are foreseen per day. Therefore, large amounts of tritium have to be processed and stored in a safe and efficient manner. For that purpose about 20 storage metal hydride beds are foreseen in the Storage and Delivery System (SDS) of ITER to supply T_2 and the required DT mixtures to the vessel. Each storage bed will have a nominal capacity of 100 g tritium (16.67 mol) and need to be designed for a hydrogen supply rate of up to 200 Pam^3s^{-1}. Moreover, the beds have to be equipped with special features to allow in-situ accountancy using calorimetry. In such beds tritium is stored as a metal tritide and U and ZrCo are appointed as the sole candidate materials for such purpose.

To test such a bed under ITER relevant conditions a 1:1 ZrCo prototype storage getter bed was designed, manufactured and installed in the Tritium Laboratory of Karlsruhe (TLK). A detailed description of the many steps required for the production of the bed and the various parts of the primary and secondary containments are given in a corresponding report.

The primary containment of the bed is divided in 46 compartments where the getter material has to be confined. Cu fins are installed in the primary containment to conduct the power generated in the thermocoax heaters to the metal powder located between the Cu fins in the primary containment.

In each of the 46 compartments between the Cu-fins approximately 44.5 g of the ZrCo powder were introduced. Only the first compartment next to the CF flange and the very last compartment on the other end are not filled with ZrCo powder, i.e. in fine 44 compartments were filled with ZrCo powder. Two different meshs of ZrCo powder were used; one was a coarse powder of a mesh between 0.2 and 0.7 mm as obtained by the supplier. The second type was very fine powder (<0.2 mm) and it was produced by operating loading/de-loading cycles on the pieces which were larger than 0.7 mm. To reduce oxidation the 44 compartments were filled in a special argon box. The total amount of ZrCo added by this way to the bed is 1.91 kg.

After the filling the interior of the bed was inspected using an endoscope. This inspection revealed that the very fine powder can find its way down to the lowest locations leaving some compartments partially filled with getter material.

The four thermocoax heaters were vacuum brazed into the grooves and the commercial ceramic-metal transition pieces for the electrical connections were brazed to the thermocoax heaters. The electrical connections between the 8 electrical Cu-feedthroughs welded into the CF flange and the ceramic metal transition pieces were made by means of a Cu-wire around which special ceramic pieces were placed to avoid any possibility of electrical contact with other equipment (see Fig. 1) .

Fig. 1: CF-150 flange and various welded items such as feedthroughs for high electrical currents and for thermocouples.

Three thermocouples were mounted at different distances from the inner surface of the CF-150 flange on the outer surface of the primary stainless steel containment to measure and control the external heaters.

In a similar way with respect to the distances from the inner surface of the CF-150 three further thermocouples were mounted in the prefabricated long holes especially drilled into the central Cu-cylinder to measure and control the inner thermocoax heaters. The location of the three thermocouples are: one is just 5 cm away from the very far end, the other one is in the middle and the third one is located just 5 cm away from the other end of the primary containment which is next to the CF-flange.

A special Pt100 resistor was also included to the bed which measures the temperature distribution over the whole length of the bed and gives therefore a better averaged reading than the thermocouples with their indication of local temperatures.

Due to the presence of the many electrical connections, thermocouples and tubes, the installation of rigid radiation shields was too difficult. Two types of radiation shields were installed, one very near to the flat surface of the primary containment to achieve a first reduction of temperature and the other one more in the middle between the CF-150 flange and the primary containment. The radiation shields in the middle together with the cylindrical radiation shields form an optical tight radiation shield around the primary containment and will reduce the heat load on the outer containment.

Fig. 2: Equipment used for the pressure tests of the various volumes inside the hydrogen storage bed.

The pressure tests were performed with the equipment shown in Fig. 2. The storage bed was positioned on the table and connected with the gas bottle and the calibrated and certificated pressure gauges via a long tube. Argon was used as test gas.

Four different volumes were tested:

- U-shaped volume,
- Coaxial tube,
- Primary containment,
- Outer containment.

The test conditions were: 21 bar(g) of Ar at room temperature. With these test conditions the storage bed can be used up to temperatures of 550°C and up to pressures of 16 bar(g).

In each of the volumes no pressure decrease and no damage was observed within the test time of 15 minutes. Therefore, the hydrogen storage bed passed the pressure tests.

Leak tests were performed during various stages of the construction of the storage bed. At the end a final leak tests performed after the pressure tests was also successful for all four volumes mentioned above.

The tests were performed with a leak detector of the type HTL150 of the company Balzers. Helium was added by spraying to the outer surfaces.

Presently the ZrCo storage bed has been installed in the non active area of the TLK and is ready to be tested.

Staff:

N. Bekris
R. Lässer
R. Wagner

TW1-TTF/TR 13
Extended Lifetime Tests of Specified Tritium Plant Components

Several components from a redundant experimental rig for laser Raman studies and developing an Omegatron mass spectrometer with tritium and other gases have been put through post-service examination to provide information on projected lifetimes of similar components planned for the ITER tritium plant. The components are a catalyst bed, permeator and a small getter bed. The components tested had been dormant for over 10 years without being fully detritiated and stored with an indeterminate state of the gases in the system. Under these conditions nearly half of the tritium will have decayed and various radiochemical reactions would have taken place.

These components were examined for performance in the CAPER facility by exposing them to hydrogen gas mixtures suitable for the process and component. The resulting gases were analysed by gas chromatography.

The catalyst bed is still active after this time despite the carbon compounds present. Considerable regeneration took place though it is not clear if the original performance has been restored. The original thermocoax heater had failed, this is a cause for concern as other components in TLK have had similar failures.

The getter bed is in good condition but again data on the original theoretical and measured performance is not available. Deactivation work performed on another ZrCo getter bed suggest that tritium can be firmly trapped inside ZrCo and the possibility will be investigated whether this getter bed contains further tritium by calorimetry.

The permeator performed well and the indications are that it is leak tight. This will be confirmed by standard leak checking procedures and the permeator will be considered for another application if it is leak tight. Exposure of the permeate side of the permeator tube to the atmosphere of the PETRA glove box, which is nitrogen with less than 1% oxygen and about 10 ppm water vapour, led to a release of about 5 GBq of tritium. This is assumed to have come from both the surface and the bulk of the palladium-silver permeator as this has a high permeation factor at room temperature and is also an active catalyst even with small amount of oxygen. This confirmed the conclusion that the permeator is still in good condition.

A report has been delivered to EFDA Garching covering the experimental work on the redundant components. A final report, due in March 2004, will cover work on the analysis of the performance and failure modes of catalyst beds and permeators of the PETRA facility at TLK as well as an analysis of the performance over several years of use of critical components at TLK similar to those planned for the ITER tritium plant.

Staff:

C. J. Caldwell-Nichols
U. Berndt
B. Bornschein
E. Fanghänel
K. Günther
B. Kloppe
T. L. Le
K.-H. Simon

TW1-TTF/TR 16
Tritium Extraction and Helium Purification

The tritium extraction from the ITER Helium Cooled Pebble Bed (HCPB) Test Blanket Module (TBM) purge gas is proposed to be performed in a two steps process: trapping water in a cryogenic Cold Trap (CT), and adsorption of hydrogen isotopes (H_2, HT, T_2) as well as impurities (N_2, O_2) in a Cryogenic Molecular Sieve Bed (CMSB) at 77 K.

The cryogenic molecular sieve bed was designed in 2001 and then constructed in the workshop of Forschungszentrum in 2002-2003. Construction of the CMSB was delayed due to the technological difficulties during brazing of the helical tube around the molecular sieve container. The CMSB was installed in the test facility CLOE at the Tritium Laboratory to perform parametric studies with relevant purge gas composition as predicted by ITER-FEAT design for TBM.

The CMSB was designed to operate at 1.0-1.5 bar pressure and a helium flow rate of 2 m^3h^{-1} (1/6 of the ITER-TBM purge gas). A cylindrical container filled with 20 kg of MS-5A is completely submerged in a liquid-nitrogen bath in a vacuum insulated vessel, Fig.1. The process gas (He with 0.1% H_2) enters the liquid-nitrogen container at the top flange and is pre-cooled while passing through the liquid nitrogen bath in a helical tube wounded around the molecular sieve container. In the upward flow, the molecular sieve adsorbs the hydrogen isotopes from the helium. The regeneration of the CMSB is performed by heating to 600K by means of three electrical heaters installed inside the adsorption bed. In order to maintain a steady temperature profile in the bed the nitrogen heated up to 600K is passed through the helical coil welded to the surface of the inner container.

The test program has been started in the test rig CLOE in order to investigate different operation modes of the CMSB i.e. activation of MS-5A at 600K, operation of CMSB at liquid-nitrogen temperature, adsorption tests at 77K and desorption at 600K.

The results from initial tests identified changes in the test rig. A close loop for the process gas with a gas mixer must be designed and constructed in order to decrease consumption of helium and premixed gases. The cryogenic supply requires minor changes to avoid high pressure excursion in the liquid-nitrogen bath. The analytical system must be improved in order to allow a constant monitoring of hydrogen concentration in the inlet and outlet stream of the CMSB during adsorption/desorption runs.

Staff:

S. Beloglazov
E. Hutter

TW2-TTFD/TR 24
Determination Ex-situ of Tritium Content in Plasma Facing Components

The erosion of the carbon first wall material (FWM) of fusion machines by D-T plasmas leads to a co-deposition of hydrogenated carbon films in the colder part of the machine. This immobilises substantial tritium amounts in thin layers which are inaccessible to further erosion. The formation of such co-deposited tritiated layers constitutes a major issue for ITER as it increases the trapped tritium inventory inside the machine.

Moreover, tritium depth profiles obtained recently for JET divertor tiles by the coring/full combustion technique revealed that a surprisingly large fraction (> 61%) of the retained tritium had diffused deep into the bulk of the tile, most probably between the fibres of Carbon Fibre Composite (CFC). As the tritium inventory in FWM of fusion machines constitutes an important safety issue, accurate determination of tritium in these materials is of high importance.

A variety of techniques have been tested for the in-situ removal of tritium from plasma facing components, i.e. glow discharge, air ventilation, thermal release under vacuum and more recently the use of Nd:YAG lasers. Nevertheless, the experimental techniques investigated until now have been limited not only by the conditions permissible inside the torus but also by the fact that they are treating only the plasma exposed surface of the tile.

When dealing with the tiles removed from the reactor more severe heat treatment are acceptable, because no precautions concerning the structural parts of the machine need to be taken.

During preliminary tests detritiation of small disk carbon specimens investigated at the Tritium Laboratory Karlsruhe (TLK) have shown that tritium release from co-deposited layers is very rapid when temperatures rise above 350°C. In a new series of experiments at Princeton Plasma Physics Laboratory (PPPL), complete CFC and graphite tiles retrieved from TFTR were heated under air at temperatures up to 500°C for one hour not only to improve the detritiation factor but also to assess the technique in full scale.

The available tiles for the present tritium analysis at TLK were:

I. Two 4D CFC tiles (KC11 and KC18). Tile KC11 had been baked.

II. Two graphite tiles (KC19 and KC20). Tile KC19 had been baked.

The four tiles were exposed to D-D and D-T plasmas in the bay K of the inner limiter at TFTR. The 4D CFC tiles were woven with yarns oriented in four directions giving to the whole structure a tetrahedral shape.

The tritium off-gassing activity was measured three times for each baked tile at 5 different locations on the tiles prior and after the bake using an ion chamber.

The tiles' physical parameters and the released activity observed during treatment are reported on table 1.

To assess the efficiency of the detritiation method used at PPPL after the thermal treatment, the 4 tiles were sent to TLK where several cylinders were drilled out and their tritium content measured using the coring/full combustion technique. Fig. 1 and Fig. 2 are comparing the obtained tritium depth profiles for the baked tiles with the corresponding tritium profiles obtained for the unbaked tiles.

Table 1: Tritium released activity during the bake out of KC11 (CFC) and KC20 (graphite).

Tile	Tile's area (cm^2)	Mass (g)	Middle of the tile ($\mu Ci\ cm^{-2}$)	Rest of the tile ($\mu Ci\ cm^{-2}$)	Average activity ($\mu Ci\ cm^{-2}$)	Mass loss (g)	Released activity (Ci)	(GBq)
KC11(b.b)	104.33	780.08	77.1	255.1	219.5			
a.b.		779.81	19.5	12.7	14.1	0.27	0.648	24.0
KC20 (b.b.)	165.33	939.74	66.6	88.9	84.5			
a.b.		939.18	03.4	03.2	03.3	0.56	0.808	29.9

b.b. = before bake out
a.b. = after bake

The behaviour of graphite and CFC tiles during the thermal heating is quite remarkable. While after the bake out the surface tritium activity of the all tiles (CFC or graphite) strongly decreases by up to 3 orders of magnitude (in average), the bulk tritium activities for all tiles, CFC and graphite, behaves differently.

Indeed, CFC tiles exhibits almost the same bulk tritium concentration of about $2x10^{13}$ tritons per cm^{-3} before and after the bake out. This indicates that the tritium trapped in the bulk of the tiles is hardly affected by the thermal treatment at 500°C.

On the other hand, graphite tiles seems to release the trapped tritium more efficiently than the CFC does at the same temperature. Nevertheless, we have also to take into account that the graphite tiles, in comparison to CFC, allows a large amount of tritium to be trapped into the bulk (compare bulk activities for Fig.1 and 2 for both type of tiles).

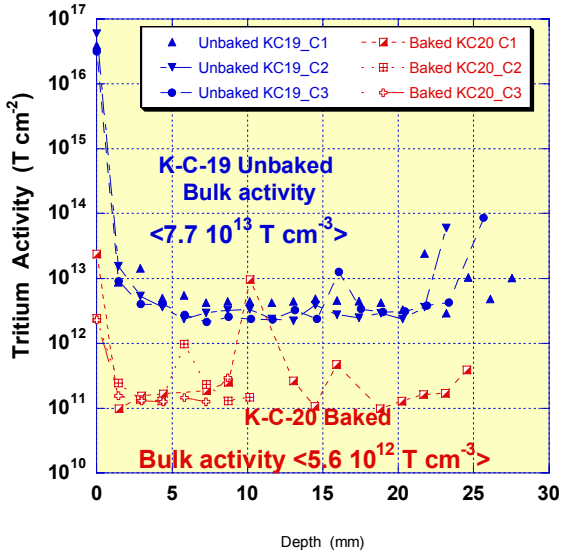

Fig. 1: Tritium depth profile comparison for the graphite tiles KC19 (unbaked) and KC20 (baked) retrieved from the K bay of TFTR.

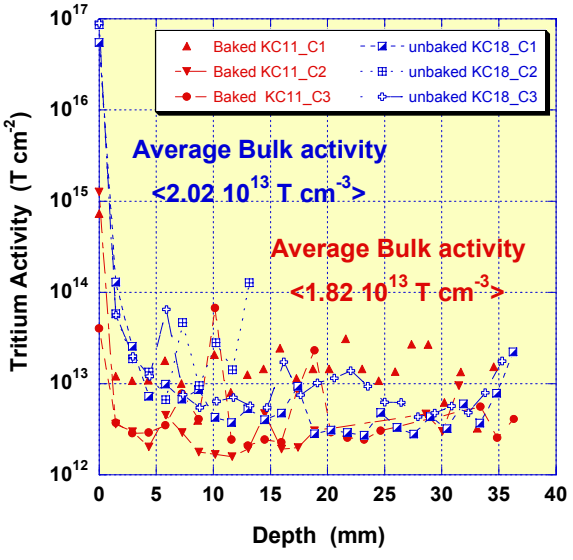

Fig. 2: Tritium depth profile comparison for the CFC tiles KC18 (unbaked) and KC11 (baked) retrieved from the K bay of TFTR.

This study led to the following conclusions. First, both type of tiles trap almost the same amount of tritium on their surface but with graphite allowing a larger amount of tritium to be

trapped into the bulk of the tile. As both materials have the same order of porosity, the transgranular diffusion seems to be the main mechanism to explain this behaviour. Second, if diffusion between the multi-directional CFC layers do not allow a higher tritium amount to be trapped in the bulk of the tiles the use of a high level of CFC weaves will keep the tritium retention by the bulk of the tiles at very low levels allowing, therefore the development of a detritiation technique to treat only the tiles' surface in-situ. Such a method may be sufficient to reduce significantly the trapped tritium inventory inside the vacuum vessel of a fusion machine.

Staff:

N. Bekris
U. Berndt
A. Erbe
W. Hellriegel

Safety Analysis and Environmental Impact

TW3-TSS-SEA 4.2
In-depth Analysis of Selected ITER Accident Sequences

Insulation Properties Impact to Unmitigated Quench Calculation of TF Coil (Parameter Study of Report EFDA 01/591)

An unmitigated quench is a severe accident of a superconducting coil where the full current is driven through the partly normal conducting cables until overheating destroys the cable and/or its insulation. An analysis of this kind of accidents for the toroidal field (TF) coils of ITER was performed with the MAGS code of Forschungszentrum Karlsruhe (FZK). The results were reported in the report EFDA01/591. A similar analysis was performed with the MAGARC code from Idaho National Engineering and Environmental Laboratory (INEEL).

Main differences between the two calculations are the assumptions for the insulation failure behaviour. While in MAGARC the insulation fails at 1173 K conductor temperature (earlier version at 973 K), in MAGS the insulation fails as itself reaches 950 K or when the neighbouring conductor reaches 2000 K. The latter value implies failure of the insulation as the jacket is melting and is even somewhat above the steel melting temperature of around 1800 K. In the MAGS analysis in fact only this second criterion was hit.

For an easier comparison of results of both codes, the MAGS analysis should be repeated with a lower insulation failure criterion closer to the MAGARC value.

Another question arose during the recalculation of TFMC experiments performed in 2001 at the TOSKA facility at Forschungszentrum Karlsruhe. It turned out that the insulation thermal conductivity as recommended by ITER had to be reduced significantly (at least below 15 K) to match the experimental results. These results were presented and discussed at the CHATS 2002 meeting at FZK. There, it was agreed that measurements to the impact of the sandwich structure on basic material properties like the thermal conductivity should be performed.

This initiated us to check the impact of insulation characteristics by repeating the TF unmitigated quench analysis. Two cases with different insulation properties were selected for a recalculation with MAGS according to the two items above:

Case 1: the thermal conductivity of the insulation is divided by a factor of 8 below 300 K as it was required in the TFMC recalculation mentioned above. The insulation failure behaviour at high temperatures remains unchanged.

Case 2: the original low temperature thermal conductivity of the insulation is used. But now the insulation fails when the neighbouring conductor reaches 1000 K.

For case 1, the drastic reduction of the low temperature thermal conductivity of the insulation to values consistent with TFMC recalculation results gives almost identical results as the reference case with only a slight slowing down of the accident propagation. This indicates that low temperature insulation properties are less decisive in this unmitigated quench case. This gives confidence to the results of other previous MAGS quench accident analyses.

For case 2 the reduction of the conductor temperature limit that causes failure of neighbouring insulation from 2000 K to 1000 K reduces the heat energy deposited in the TF coil from about 6 GJ to about 2 GJ. The accident develops less dangerous because the radial plates set in earlier as cold heat reservoir and low resistance current path. This keeps the maximum temperatures below the copper melting temperature and no conductor melting occurs.

The 1000 K were just a numerical value for the parameter study. Experiments are running at FZK to determine the effective insulation failure temperature that is to be included in MAGS.

Description of a scenario for an out-of-coil arc and derivation of requirements for an associated arc model.

Electric arcs at the busbars of the ITER toroidal field (TF) coil system are a relevant safety issue as the energy stored in the TF system is considerable and a busbar arc might move towards the cryostat wall and penetrate it by melting a hole. An existing description is partly very coarse and quantitative statements are based on energy balances and estimates. But also the transient behaviour of a busbar arc might be decisive for damage of safety relevant parts. The investigation of such effects requires a numerical model for high current arcs.

It was tried to apply an existing numerical busbar arc model by Titkov. This model starts from fundamental equations and works in principle. However, due to uncertain but sensitive input parameters and model assumptions, the accuracy for an application to an ITER TF busbar arc turned out to be poor.

A new effort is to develop a busbar arc model from a more phenomenological basis. The first two important stages of the development are:

- work out probable scenarios for busbar arcs
- small experiments that will reproduce this scenario in small scale to support modelling

The first part is the objective of this subtask, the second part is treated in task TW3-TSS-SEA 5.4 "Busbar Arcs Behaviour and Consequences".

Starting e.g. from a TF unmitigated quench scenario, a busbar arc is ignited in the coil joint box where the connections to the coil and between the coil (double) pancakes are made. The arc is expected to burn along the busbar towards the cryostat wall. As the TF busbar is always close to metal structures and the busbars only run parallel for short parts, most of the time the arc burns between one busbar and surrounding structure parts.

The most important arc parameters with regard to safety and later modelling are the arc power and propagation velocity. For the arc power, the arc length is crucial. For the arc velocity, besides the arc power, the mechanism of destruction plays an important role. The following three mechanisms cover a wide range of possible options:

1. Only the busbar insulation melts when the arc passes. The arc is fast and will not stay long enough at a location to cause much damage. For the following estimations, insulation melting is assumed to cover the half busbar diameter.

2. The whole cross section of the busbar must melt away or burn down before the arc can move. This brings more heat power into structure parts and cause partly melting.

3. The most damage to structures would be expected by a mechanism of evaporation at the busbar cross section combined with melting of structures. This might be possible as the busbar arc spot is fixed but the structure part spot is free to move over not insulated steel surfaces.

To get some idea of arc propagation velocities along a busbar, estimating calculations based on melting energies and cable and structure cross sections are made. The arc voltage is calculated from the arc length after a steelmaking formula for DC high current arcs: U = 20 V + 8 V/cm x length in cm. The arc length is estimated from ITER technical drawings.

The power of a 10 cm long arc at the TF operating current of 68 kA using the formula above is 6.8 MW. For the calculation it is assumed that half of the power is available at each arc spot.

The calculated melt down velocity of the half circumference of the 8.2 mm thick busbar insulation is about 0.5 m/s at a power of 3.4 MW. The melt down velocity for the 870 mm^2 copper cable with 420 mm^2 steel jacket and half of the insulation is about 0.2 m/s at 3.4 MW.

The expected propagation velocity is between 0.2-0.5 m/s and the time required for the arc to burn from the joint box down to the TF double feeders would be between 10-25 s.

If one assumes insulation melting and full cross section vaporization, the arc velocity reduces to about 0.03-0.04 m/s = 3-4 cm/s. In this case for equal power at both electrode spots, a maximum of about 90 MJ/m could be available at the casing arc spot.

But one could also imagine arc propagation along a small line of insulation destruction (of e.g. 10 mm width), which could allow for an arc velocity of 4-5 m/s.

This difference of two orders of magnitude indicates that the mechanisms of arc propagation play an important role and have to be identified, e.g. from experiments.

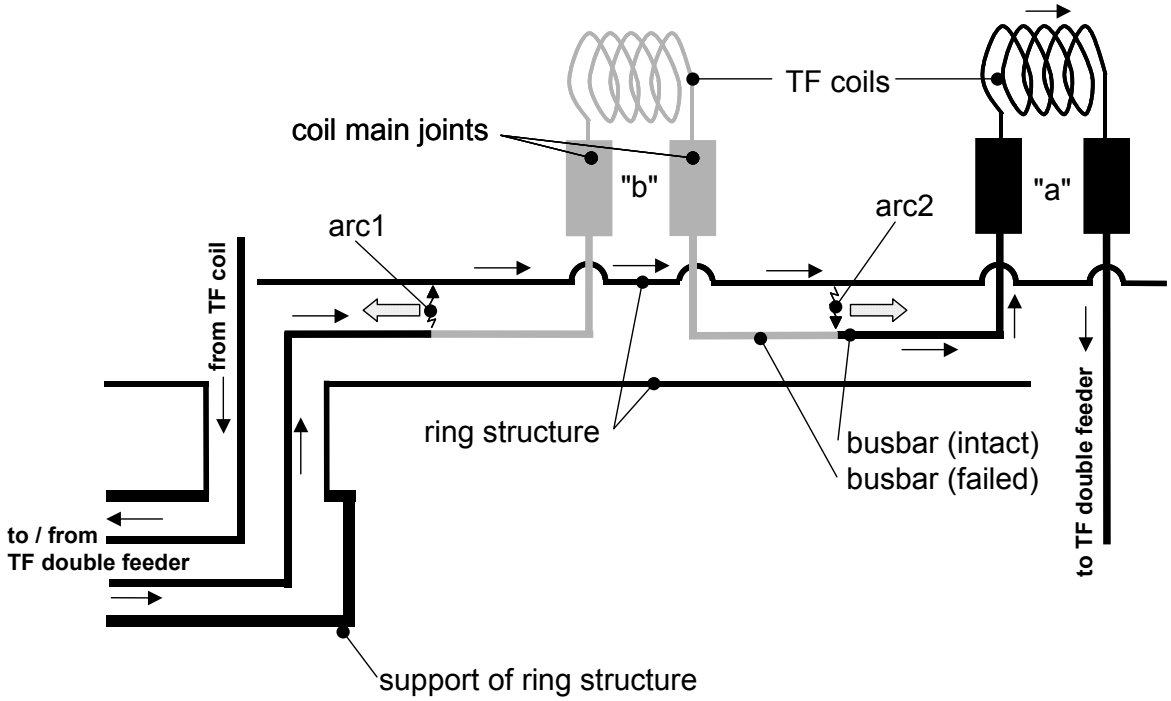

Fig. 1: Schematic representation of the arc circuit and path inside the ring structure below the TF coils. Two arcs propagate along he busbars away from the damaged coil. Structure parts between the two arcs in series close the TF circuit. There are two different position for a TF coil to be arranged on the ring labeled "a" and "b". Thin arrows indicate current direction. Wide arrows indicate arc propagation direction. Grey parts are already damaged and do not carry current any more. From the supports of the ring structure, the busbar is guided in a double feeder to and through the cryostat wall (see Fig. 2).

The path of the arc from the TF coil joints along the busbar trough the support structure down to the double feeder is shown in figure 1. Figure 2 shows the further arc path along the double feeder out of the cryostat. The double feeder carries two busbars in parallel inside a quite robust double walled steel tube. The inner and outer mid joints are also located inside the double walled part of the double feeder. The feeder is still double walled where it penetrates the cryostat wall. An energy analysis shows that even under very extreme conditions, a threatening of the outer double feeder tube wall remains unrealistic.

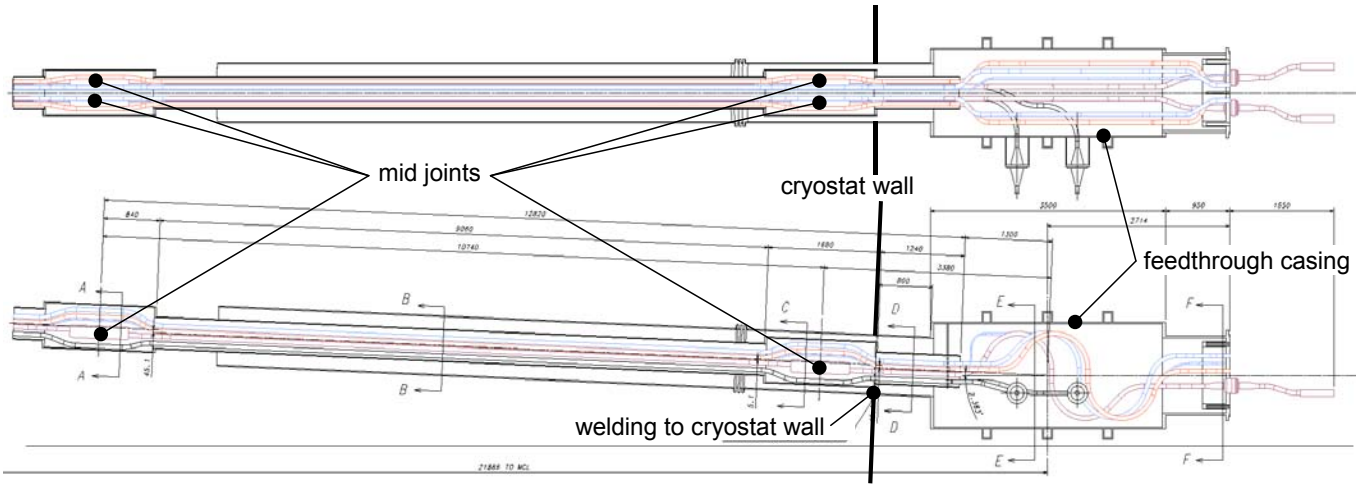

Fig. 2: Top and side view of one out of nine ITER TF double feeders with feedthrough casing. The welding location to the cryostat wall is indicated.

However, at the mid joints locations inside the double feeder the arc is slowed down and can cause more damage. If half of the mid joint insulation is melted away down, the arc is expected to pass the mid joint in about 2 s, destroying 6% of the inner tube. With full cross section melting being the dominant effect, the arc is burning at the mid joint for about 20 s. During this time, 33% of the inner tube including the separation plate between the two parallel busbars could be destroyed. Under these conditions, a change of the arc to the parallel busbar is quite probable, but it happens not necessarily. In a conservative view, one has to assume that quench is initiated and the arc leaves the joint region towards the cryostat wall.

With pure vaporization of the mid joint material, a 10 MW arc would burn about 140 s at the mid joint. Its energy could melt more than two times the complete inner tube. Consequently, the arc would burn to the outer tube for some time. The increase of arc length and consequently of arc power would reduce the burning time at the mid joint to about 90 s. In this case the question is whether the arc prefers one burning direction and destroys also parts of the outer tube or it destroys first what is next to it. The latter could mean a jump from one busbar to the other. But this mixed behaviour of vaporization and melting seems not very probable, especially as the compact copper mass in the mid joint is expected to go away preferably by melting.

But even if the outer tube will get some considerable damage at mid joint positions, this would not cause a vacuum leak. The outermost mid joint end is located still 35 cm inside from the welding seam of the outer feeder tube to the cryostat wall.

A penetration of the vacuum barrier is most likely at the feedthrough casing where long and powerful arcs seem possible. The casings are located outside the cryostat, but they are part of the vacuum barrier. The double feeder outer tube provides a direct connection to the cryostat. The casing wall thickness is 4 cm (2 cm thermal shield + 2 cm casing).

The conductor has a S-shape in the feedthrough casings with a variable wall distance between 0.5 m and 1 m. If magnetic forces prescribe a certain direction, up to 1.5 m are possible and long and powerful arcs cannot be excluded. An estimating calculation with an arc length of 1 m gives the following results:

With only busbar insulation melting assumed, a hole in the casing of about 1.7 m^2 would be possible. If the whole busbar cross section is molten down, 4.2 m^2 are calculated. However, this would require a 1 m long arc during the whole time and a concentration of the energy to molten areas. This represents a very pessimistic case as bending by magnetic forces and

the presence of the second busbar next to the first without any protective steel plate provide a large variety of less dangerous developments. Note that the real vacuum hole cross section of 0.45 m^2 is much smaller. This is because the connection to the inner cryostat is limited by the outer tube diameter of the double walled double feeder.

The above considerations give a rough overview to the possibilities of a busbar arc accident development. For a more precise investigation, a busbar arc model has to be developed.

The considerations above allow already conclusions for some requirements for a numerical out of coil busbar arc model. For safety considerations, the most important quantity is the power of the arc. As material and pressure conditions are more or less known, one decisive, remaining parameter for arc power determination is the arc length. Without further knowledge, one would assume that it is given by the geometrical conditions. But significant variations in arc column length are possible e.g. by arc splitting, arc column or conductor bending by magnetic forces or by convection (e.g. by leaking out of a helium tube that was damaged by the arc). It seems quite complicated to model these effects with some reliability and much effort on a detailed model of the structure parts and conditions inside the cryostat would be required. But as the prediction of arc behaviour from some known conditions is still quite difficult, the accuracy is expected to depend more on the arc model physics than on the structure parts model. So the effort for generating a detailed structure representation seems not justified at the present time.

Table 1: Estimated time schedule for a busbar arc accident development.

	insulation melting only (half diameter)	full cross section + half insulation melting	full cross section vaporization
unmitigated quench	0s	0s	0s
busbar arc ignition	80s	80s	80s
arc reaches inner mid joint	90s	105s	230s
arc enters double feeder	92s	125s	330s
arc enters feedthrough box	110s	200s	590s
arc burning time from ignition until vacuum wall is reached	30s	120s	510s

Besides the arc power, the time of impact of the power plays a role and an arc model should calculate the arc propagation velocity as a second main result. The speed of arc propagation depends on arc power as well as on the extent of insulation and/or busbar destruction and on the dominant mechanism of destruction that may be melting or evaporation. Table 1 summarizes the accident transient development in dependence of the arc burning mechanism. It is disregarded for simplification that it is not inevitable to have the same mechanism at all arc locations. The ignition time was taken from an earlier MAGS calculation of an unmitigated quench scenario for a TF coil. Taking this results, a busbar arc will be ignited probably about 80 s after the start of the quench inside the coil winding pack.

The obviously strong dependence on the assumed propagation mechanism indicates the need for clearing of these questions.

The discussed scenario with more or less estimating calculation examples gives some hint how a busbar arc accident may develop and represents a useful basis for a future MAGS busbar arc model. But the variety of possible arc powers and propagation mechanisms and their consequences for the accident transient behaviour and the damage to structures is very widespread. The results depend strongly on the destruction mechanism, which needs to be specified from experiments like proposed in task TW3-TSS-SEA 5.4.

A general result valid for all three arc variants is the maximum leak size of 0.45 m^2. Probably not more than two or three of these leaks can occur before the TF energy is exhausted by quenching and arcing. This is already a quite reliable estimation of the order of magnitude of the maximum possible vacuum leak that may caused by arcing in the ITER TF circuit.

Staff:

V. Pasler

Literature:

[1] V. Pasler: Report on insulation properties impact to unmitigated quench calculation of a TF coil (parameter study of report EFDA01/591), April2003.

[2] V. Pasler: Description of a scenario for an out-of-coil arc and derivation of requirements for an associated arc model, June 2003.

TW2-TSS-SEA 5.2
Dust Explosion Experiments

TW3-TSS-SEA 5.2
Dust Explosion Experiments – Tungsten

Objectives

One of the ITER safety problems is the explosion hazard of the dusts produced and accumulated during ITER operation inside its vacuum vessel. The dusts under concern are carbon, tungsten, and beryllium dusts. Currently there are no reliable data on the ITER-relevant dust properties characterizing their explosion severity. An important issue is the content of hydrogen in the dusts that could not be evaluated from the data of the existing Tokamaks. So no reliable extrapolation using other dust data are possible now.

The main objective is to provide experimental data towards clear criteria on the maximum permissible amounts of dusts in ITER vacuum vessel. The objectives of the dust explosion studies include measurements of the explosion indices of the ITER-relevant dusts, evaluation of the effect of absorbed hydrogen; construction the facilities to study mechanisms of dust explosion.

The objective of the first series of tests was to study the standard explosive characteristics of pure graphite dusts in air (Task TW2-TSS-SEA 5.2). The standard method using a 20-l-sphere was chosen for these tests. The main advantage of this method is that the explosion parameters of the ITER-relevant dusts can be compared with those of other industrial dusts and can be classified accordingly. In addition, important dust explosion parameters, such as minimum explosion concentration, maximum explosion pressure and minimum ignition energy can be evaluated with this method. The effect of the dust particle size on the explosion parameters can be also investigated.

The objectives of the next step (Task TW3-TSS-SEA 5.2) include measurements of the explosion indices of tungsten dust and tungsten/carbon dust mixtures, development of the diagnostic techniques to measure spatial dust density distribution, and construction of facilities to study mechanisms of dust explosions.

Status

During the year 2002 the experimental facility –consisting of the 20-l-sphere apparatus and related subsystems - was designed and constructed to study explosion properties of dusts (see Fig. 1). Series of tests were carried out with graphite dusts of characteristic particle size ranging from 4 to 40 μm. The tests have shown that graphite dust is able to explode in a wide range of concentrations. The explosion indices of the tested dusts were measured; the indices include the maximum overpressure during the dust/air cloud explosion, the maximum rate of pressure rise, the lowest concentration explosion limits, and evaluation of the minimum ignition energy. The important effect of particle size was studied in details.

Fig. 1: 20-liter-sphere facility.

The tests with tungsten dust and tungsten/carbon dust mixture have been started and are in progress. The dusts with 12 and 1 μm characteristic particle size are tested.

A tool to measure the laminar flame velocity of graphite dust/air mixtures – a dust Bunsen burner – is under construction and testing.

A unit to measure the dust density distribution is designed, fabricated, and being tested. The measuring probe is a pair of photodiode-photosensor coupled by glass fiber with a gap. The gap is located in the dust-filled area. The local dust concentration is measured by light beam intensity attenuation while passing through the dusted gap. The probe scans the dusted area to measure the spatial distribution of dust density.

Results

The explosion characteristics of graphite dusts were measured using the 20 l sphere facility. The dependences of the explosion indices on dust concentration and dust particle size were studied. For all the tested graphite dusts their maximum explosion overpressures rise with dust concentration from lower explosion limits on, reach maximum of about 7 bar at 250 g/cm^3 (which is about two times above the stoichiometric concentration for the reaction $C+O_2=CO_2$), and then decreases only slightly. The pressure rise rates also increase first with dust concentration and reach the maximum at about 250 g/cm^3. Further behavior differs for the finest and coarser dusts. After reaching its maximum, it noticeably decreases with concentration in case of 4 μm dust, while for coarser dusts it remains almost the same. The effect of dust particle size on the explosion behavior was studied. The maximum overpressure Pmax and maximum rate of pressure rise (dP/dt)max measured over the whole tested range of dust concentration versus the dust particle size are shown in Figs. 2 and 3, respectively. One can see that Pmax does almost not depend on particle size. The highest Pmax value – 6.6 bar – was observed for 4 μm dust. It decreases with dust particle size to 6 bar for 40 μm dust, which is almost in the range of measurement accuracy. However, (dP/dt)max strongly depends on the dust particle size. Maximum value of (dP/dt)max – 250 bar/s – features the finest dust; this one is the most dangerous dust. With particle size it decreases down to 80 bar/s for 40 μm dust.

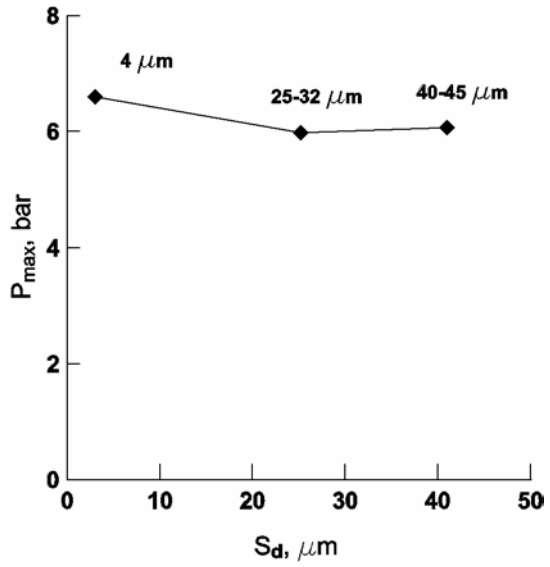

Fig. 2: Maximum overpressure of graphite dusts versus dust particle size.

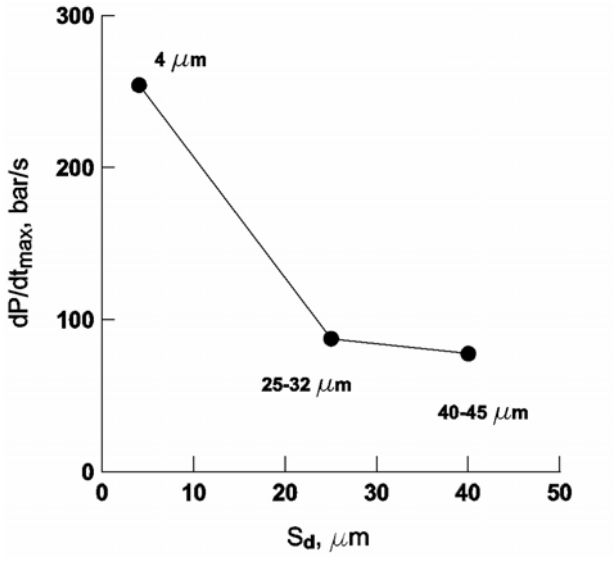

Fig. 3: Maximum rate of pressure rise of graphite dust versus dust particle size.

Lower explosion limits of the graphite dusts were measured (see Fig. 4). The finest dust has the lowest concentration explosion limit– 70 g/m^3. The lower explosion limit strongly depends on the dust size in the tested range: for 40 μm dust it is almost two times higher than for 4 μm dust.

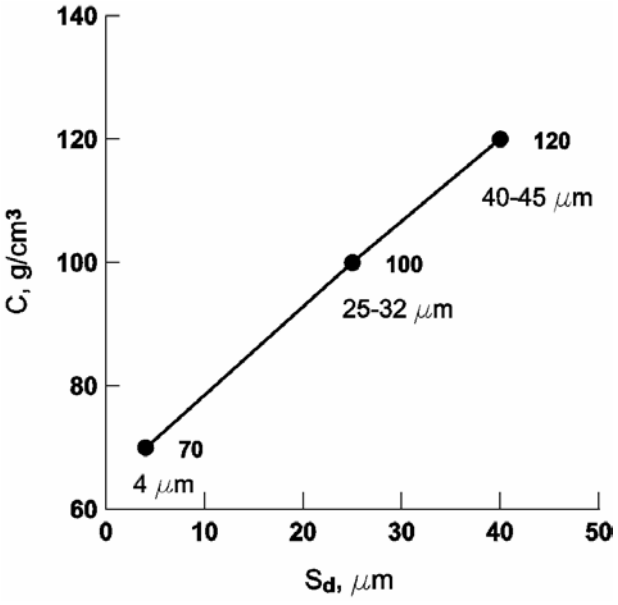

Fig. 4: Lower explosive concentration of graphite dusts versus dust particle size.

The explosibility of graphite dusts was tested as function of ignition energy. Three types of igniters were used: 1, 2, and 10 kJ. The finest dust appears to be explodable at 2 kJ in the concentration range from 125 to 500 g/cm^3 and does not explode at 1 kJ ignition energy. The coarser dust did not explode at 2 kJ.

Dusts tested were ranked as St1 class (the mildest class). Dust particle size was shown to be very important for explosion properties. The finest dust appeared to have lowest minimum explosion concentration (70 g/m^3) and the lowest minimum ignition energy (1 kJ).

The maximum overpressures and rates of pressure rise were measured for 1 μm tungsten dust in the concentration range from 300 to 7500 g/m^3. The lowest concentration explosion limit for 1 μm dust was measured to be 400 g/m^3.

Outlook

The explosion indices, lowest concentration explosion limits, and effect of ignition energy for the tungsten dusts of 1 and 5 μm particle size will be measured in the frame of Task TW3-TSS-SEA 5.2. The explosion characteristics of 1 μm tungsten and 4 μm dust mixtures will be studied. A Bunsen burner facility will be used to measure the laminar velocity of graphite dusts.

A dust combustion tube will be designed and fabricated to study the mechanisms of flame propagation in air/dust mixtures.

At the next phase the effect of absorbed hydrogen on the dust explosion characteristics will be studied. Mixtures of metal dusts (W, Al or Mg to simulate Be) with graphite containing absorbed hydrogen will be prepared, characterized and investigated with respect to the explosion characteristics.

Staff:

A. Denkevits
S. Dorofeev
B. Kaup
V. Krieger
W. Rapp
R. Vollmer

Literature

[1] A. Denkevits, S. Dorofeev. Dust Explosion Experiments: Measurements of Explosion Indices of Graphite Dusts. Report No. FZKA 6872, Forschungszentrum Karlsruhe, April 2003.

TW3-TSS-SEA 5.4
Busbar Arcs Behaviour and Consequences

Small Experiments on Busbar Arcs: Description of Experimental Setup and Planned Experiments

The ITER magnets are operated at currents in the range of tens of kilo amperes. If the circuit is interrupted, the high inductivity of the coils forces the current to bridge the gap by a powerful arc that may cause further damage to safety relevant parts. Special attention must be given to the locations where the superconducting power supply cables (busbars) pass through the vacuum barrier. Arcs in the region of the busbar might become a threat for the cryostat wall, when the TF coil shutdown system fails. A busbar arc model would be desirable to investigate these accident scenarios. The development of an out of coil arc model introduced many problems, as the mechanisms of arc propagation and behaviour are widely unclear. It turned out that the knowledge of busbar arc behaviour in very fundamental questions as propagation mechanism, destruction mechanism or splitting behaviour is still very poor. As a first step to a numerical busbar arc model, small model experiments will be performed. In the following paragraphs the objectives of the experiments and the foreseen experimental device are described.

Several important mechanisms and effects of an arc burning between an insulated busbar and a metal wall are to be investigated in small scale. Objectives of the experiments will be:

a) Investigate arc length and stability under different voltage and current conditions to get an idea of handling the apparatus and the available range of current and voltage.

b) Measure the arc propagation velocity and observe the mechanism of damage:

   - Is only insulation burned down or also a significant metal cross section?
   - Is the material only melted or is there significant evaporation?
   - Will melting propagate faster than insulation destruction?

c) Compare arc velocity from insulation destruction to the propagation velocity from full cross section destruction. It is expected than one could switch between the two mechanisms by a suitable arrangement of the current loop.

d) Behaviour of an arc when the wall distance varies along its path. To simulate the varying wall distance, a special rail can be fixed on the base plate.

e) Are there combined material (steel/copper) effects, e.g. spilling out of molten copper from the still intact steel jacket? Here a special coaxial conductor with a copper core and a steel cover is required.

f) Check for orientation effects (horizontal/vertical busbar, half tube as in double feeder).

g) Is there a tendency of arc splitting, if the arc length is growing and alternative, shorter gaps exist and/or a gas jet hits the arc column?

h) Investigate arc burning between two insulated conductors.

The experiments will take place in an argon protective gas chamber with insulated copper/steel model conductors in a current range below 200 A.

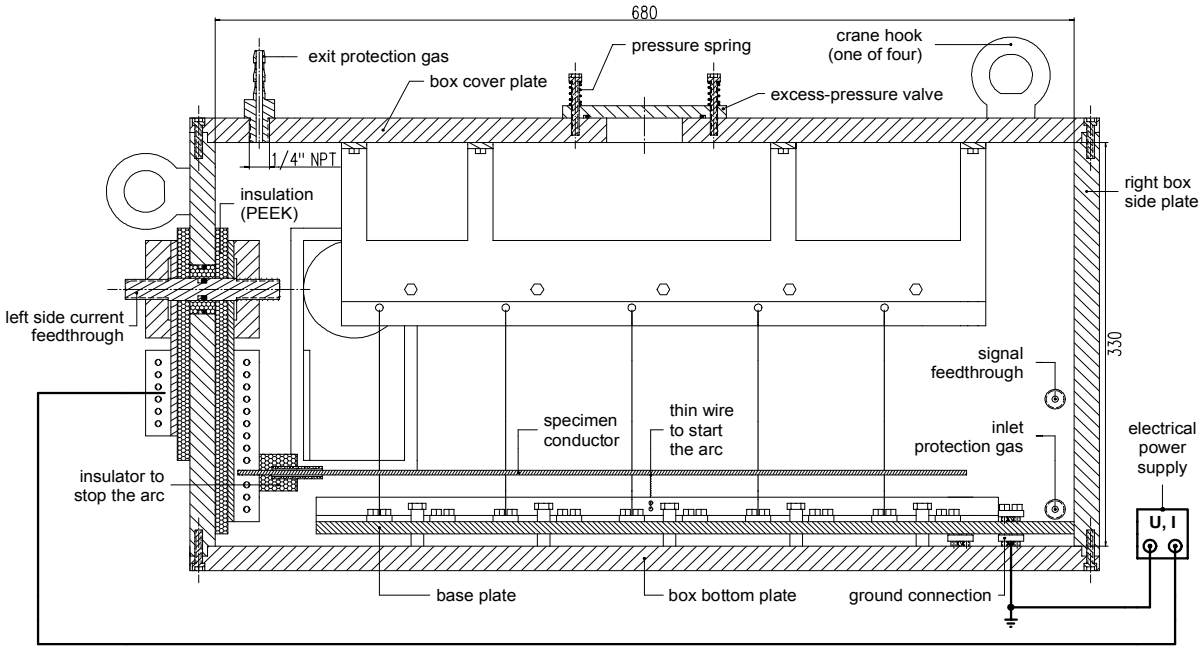

Fig. 1: Arc chamber, Longitudinal Cross Section and Electrical Circuit.

Arc burning under atmospheric conditions is very unstable due to the reaction of electrode materials with air oxygen. As no oxygen is present inside the ITER cryostat, the experiments should be consequently performed under protective gas conditions. This requires a closed arc chamber with appropriate feedthroughs and possibilities of observation. The arc chamber shown in Figs. 1 and 2 is filled with argon for the experiments. The chamber box is made from 5 aluminium plates. The front side is intended as an observation side and made from a plexiglass plate. The aluminium plates have boreholes for electrical current feedthroughs, protective gas inlet and outlet, further holes are for an excess pressure valve and for signal conductor feedthrough. Inside the experimental area a suspension gear for one or two specimen conductors and a grounded steel base plate are installed. The base plate has fastenings for circular work of fiberglass to fix the specimen conductor in position. In upward direction, the suspension gear is the fastening for the circular work of fiberglass. These installations will enable arc burning between the model busbar cable and the steel rail on the base plate as well as between two model conductors. Also a certain variation of the current loop is possible to check the influence of "railgun" forces. To examine the impact of gravity, the experiments can be made also in vertical position by placing the box with the right box side plate down on the experiment table.

The presently foreseen power supply for the experiments is a welding apparatus from our workshop. It is able to supply a direct current of 150 A, the idle voltage is 45 V. After first experiments, the requirements for ordering a more powerful power supply will be fixed.

Before starting an experiment, the arc chamber area will be evacuated by a vacuum pump and then will be filled with argon protective gas. As the plexiglass cover would not stand the pressure difference, another aluminium plate is fixed on the box front side temporarily during the evacuation and argon flushing process. When the argon pressure is in atmospheric range, the cover plate can be removed and the experiment is started. The arc will be ignited by a thin wire that evaporates and provides the initial ionic channel for the arc current to avoid high voltages at arc ignition. The quantities that are to be observed are mainly the arc propagation speed and the arc voltage and current. In addition, an optical observation is desirable to check for qualitative effects like arc splitting. For this purpose a high-speed camera will be used.

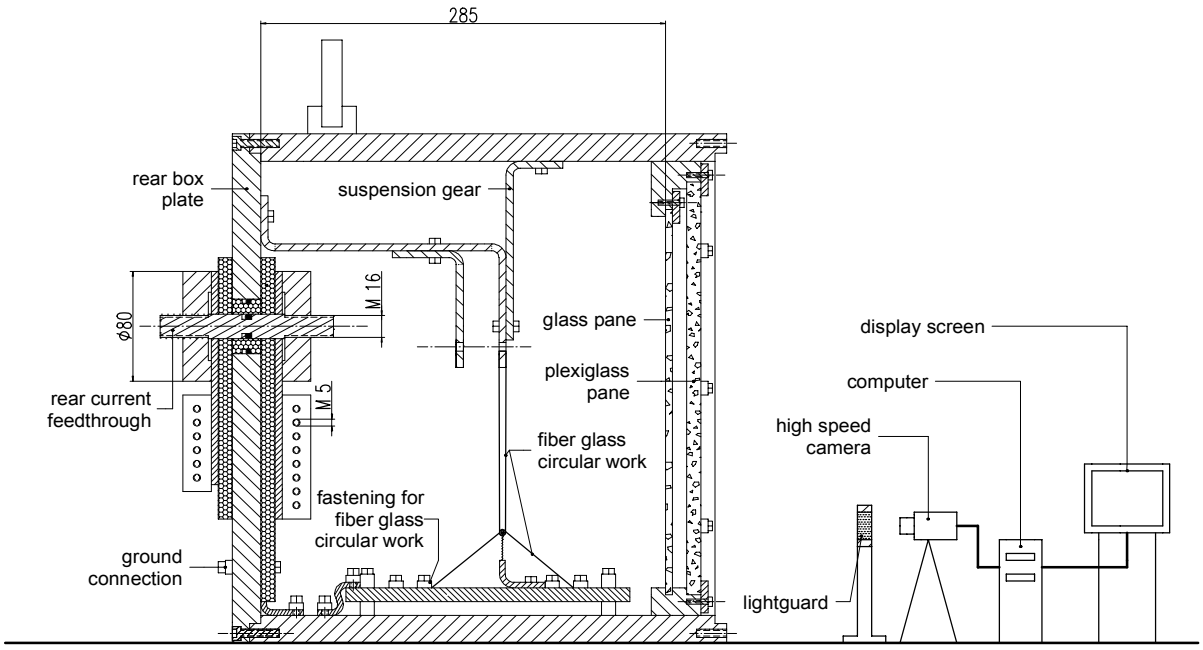

Fig. 2: Arc chamber, Cross Section and Assembly for Optical Observation.

The experimental conditions will be chosen "similar" to ITER conditions, with the choice of downscaled quantities of course being somewhat ambiguous. A first quite plausible choice of scaling is to use the same current density in the copper parts for the model conductor like in full scale. For first tests, the model busbar conductor in the experiments will be an insulated copper or steel wire of 1 to 4 mm thickness. For special measurements, a 4 mm thick copper wire inside a thin stainless steel tube surrounded by an insulator will be used. The insulation layer is a circular work of fiberglass with Araldite epoxy resin. The 4 mm model conductor will have to be operated at 925 A to meet the current density of the cable space of a full scale ITER TF busbar at 64 kA. A current of 150 A (present limit of the power supply) corresponds to 10 kA for the full-scale conductor. To achieve the equivalent current density of full-scale 64 kA with 150 A, the model conductor diameter would be only 1.6 mm/1.85 mm (without/with jacket).

The experiments are to be continued in the future as supporting and validation experiments for a busbar arc model that is to be developed in parallel.

Staff:

V. Pasler
G. Schmitz

Literature:

[1] G. Schmitz: Small experiments on busbar arcs: description of experimental setup and planned experiments (Rev. 1), July 2003.

TW3-TSS-SEA 5.5
Validation of EU Safety Computer Codes and Models

The EVITA condensation experiments at CEA in Cardarache (France) are part of a long-term validation program for several safety codes, which are intended to be prepared for a usage in the licensing procedure for ITER. EVITA is a 0.22 m3 stainless steel vessel that can be evacuated. A reservoir with an inlet system for steam and water injection and a nitrogen cooled cryogenic condensation plate are available for condensation experiments.

For the EVITA experiments with steam injection of the complementary cryogenic test matrix performed in spring 2003, pre-test calculations with an updated condensation model in the MAGS module CRYOSTAT have been performed. In the new experiments, several changes have been made on the EVITA facility to improve the ice formation on the cryogenic plate and the heat removal by the nitrogen circuit.

The calculated course of the condensation process and the stability of time step iteration depend significantly on the transient behaviour of data, for which from the experimental side only averaged values are available. Especially the state of steam upstream the injector and its flow rate and the heat removal by the nitrogen circuit are sensitive quantities. To generate realistic time dependent boundary conditions, the total injector pipe system, including valves and heating, have been simulated in the calculations and a new method to simulate the heat removal by the nitrogen circuit is involved into the CRYOSTAT module.

A time dependent steam flow rate is generated by modelling the complete injector pipe system, including valves and heating. In the pre-test calculations it is assumed, that the injector pipe heating ensures, that during drainage and injection no wet stream at the injector inlet exists. In previous experiments only the steam temperature but no pressure data were available to check for possible saturation conditions. By variation of the nozzle streaming cross-section area, the calculated average flow rate is compared with the determined average value of the experiment.

The injected steam power depends on the steam status in front of the injector and leads to a change of condition in the vacuum vessel (vv), influencing decisively the condensation rate.

For the heat removal by the nitrogen circuit only an estimation of the average removed power during steam injection is possible from experimental data. For the dynamics of ice formation, re-melting of ice layers, draining down rate of liquid condensate etc., a time dependent heat removal is necessary, having also a strong influence on the condensation process.

A value for a heat transfer coefficient (htc) [W/(m^{2}K)] for a virtual cryogenic plate mesh and the N2-circuit is assumed. At each time step the heat transfer is calculated with the temperature difference between this mesh and the nitrogen. The htc can be adapted by comparing the calculated total removed power with the estimated experimental total power.

Re-evaporation of draining down liquid condensate has not been taken into account. For this, all of the experimental data (especially: injection time, injected steam power and removed heat by the nitrogen) must be known exactly. From earlier experiments is known that re-evaporation has a considerable effect on the results.

The recalculation of the experiment 5.1 is an example for a typical cryogenic condensation calculation with MAGS module CRYOSTAT. Its development is described in the following:

0 – 50 s: drainage of the injector pipe system.

50 – 340 s: the ice layer grows on the cryogenic plate surfaces. The vv-pressure [mbar] is rather constant at a very low level at the beginning (Fig. 1). There is a complete

condensation of the injected steam. The condensate surface temperature increases with time and reaches the ice point temperature after 340 s (Fig. 2). The active top layer of the condensate becomes liquid (Fig. 4).

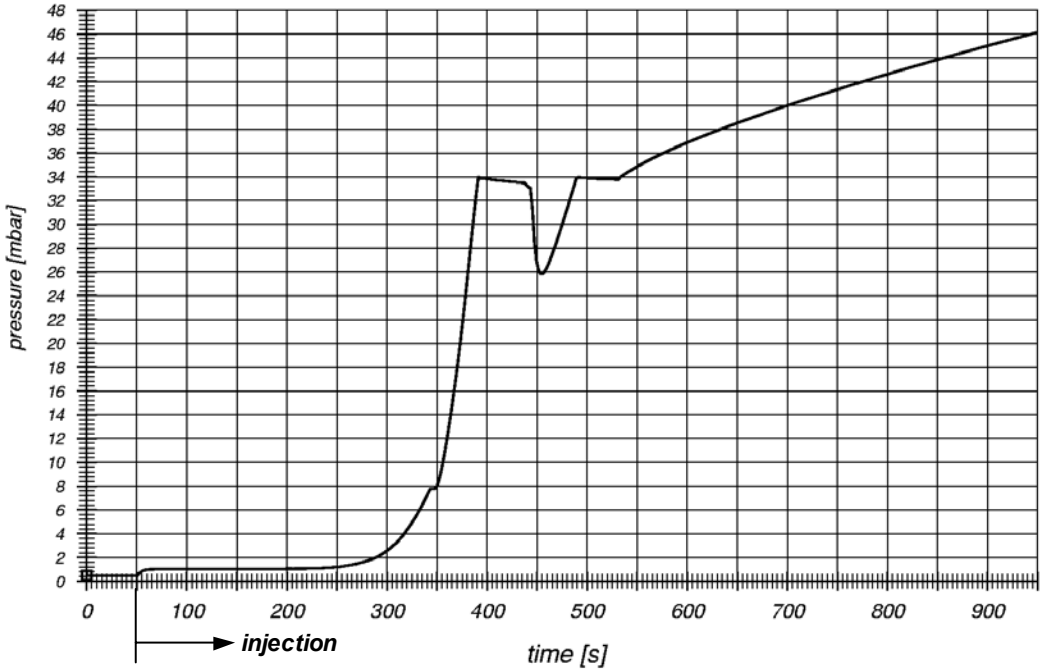

Fig. 1 Pressure history in vv-volume.

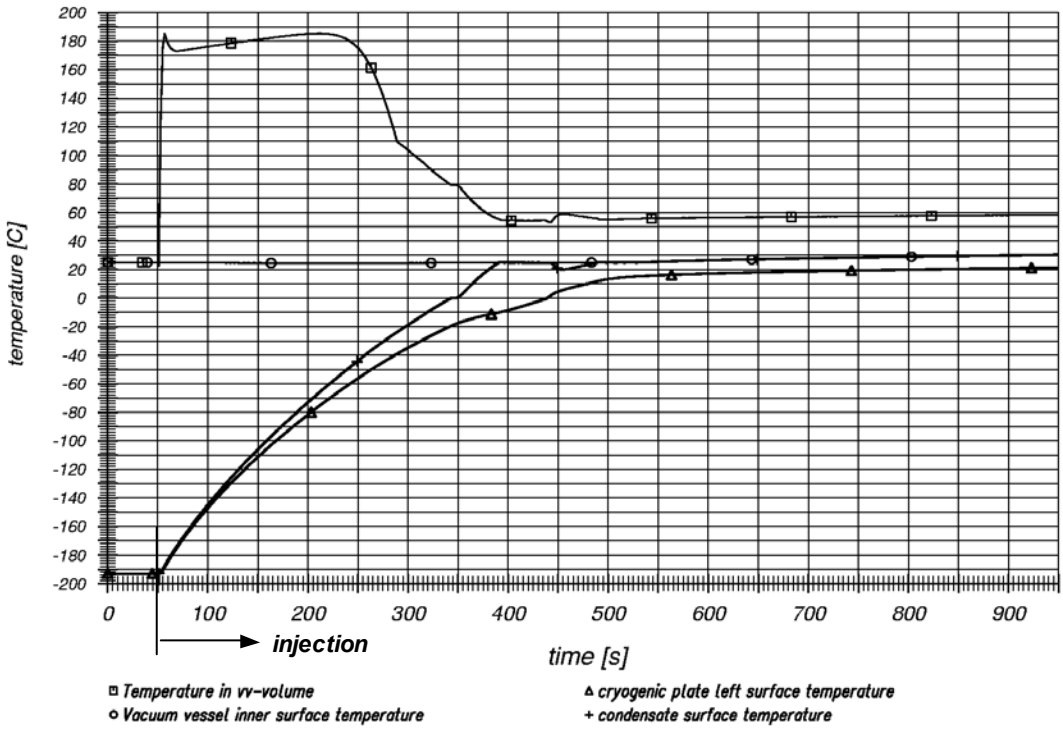

Fig. 2: Temperature in vv-volume, on vv-surface and cryogenic plate surfaces

340 – 350 s: both, the liquid and the underlying solid layer thickness are increasing. The maximum thickness of ice is 2.3 mm (Fig. 4). The condensate surface temperature is remaining at the ice point temperature (Fig. 2).

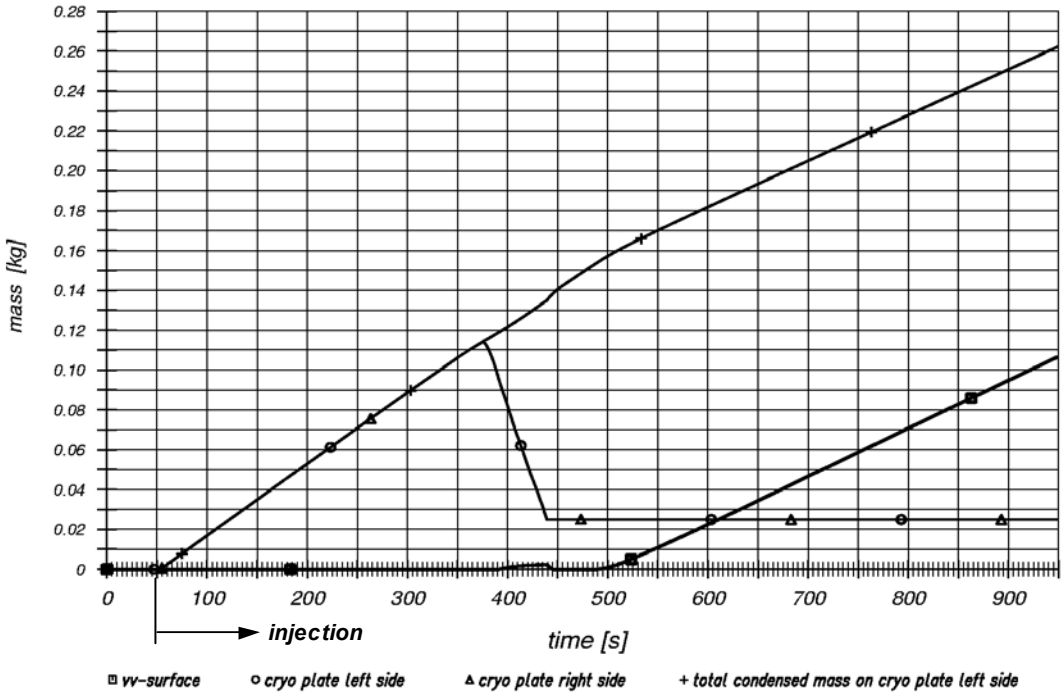

Fig. 3: Condensate mass.

350 – 385 s: the liquid layer grows up to the maximum average film thickness of 0.5 mm. Additional liquid condensate is assumed to drain down. The continued increasing curve in Fig. 3 shows the total condensed mass at each side of the cryogenic plate, including the drained down portion. The re-melting of the ice layers starts at 350 s (Fig. 4). The condensate surface reaches the temperature of the vv-surface (25°C) at 385 s (Fig. 2). This means that now also the vv-surface of 1.83 m^2 (cryo plate: 0.1 m^2) starts to play a role as an additional surface for condensation.

385 – 440 s: total re-melting of the ice layers within this period (Fig. 4). Afterwards only a liquid layer exists.

500 – 950 s: further condensation on both sides of the cryo plate and on the vv-surface. The total condensed mass on each side of the cryo plate is about 260 g. On the vv-surface 107 g (Fig. 3) of water form a liquid film of about 0.1 mm thickness at the end of injection. The high condensation rates lead to a very low increase of the vv-pressure to less than 0.05 bar (Fig. 1). The temperatures of the vv-surface, the vv condensate surface and the condensate surface temperature on the cryo plate are nearly the same. One can see only a small increase of all these temperatures by the continuing condensation process (Fig. 2).

Compared to earlier calculations, the implementation of a method to determine the time dependent heat removal by the nitrogen circuit into the condensation model led to an improvement of the results concerning the sequence of the condensation process and to a better time step integration stability. Of the same significance is the detailed determination of the steam status upstream the injector. The pressure (not measured) and temperature (thermometer TCV31) for the calculation of a time dependent flow rate (experimental data:

average flow rate during injection) are available by including the injector pipe system into the simulation. But it would be preferable to have these boundary conditions given from transient experimental data at the inlet and also to have some more data e.g. of heating power, drainage flow rate, etc..

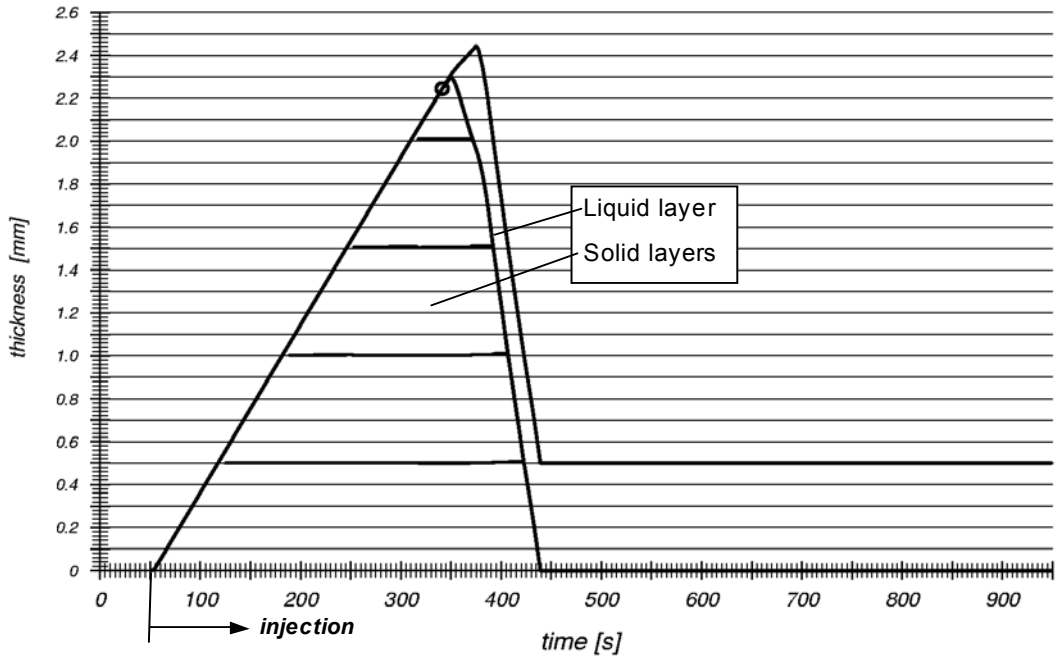

Fig. 4: Layer thickness on cryogenic plate (left side)

The MAGS condensation model calculates the condensation rate on cryogenic surfaces at ideal conditions. In our model, all of the injected steam mass is condensing on the cryogenic surfaces and the pressure remains nearly constant for some time (cryopump effect). In contrast, previous experimental data of EVITA in general showed a continuous increase of the pressure. We suppose that the following special boundary conditions of the EVITA device are responsible for this discrepancy of results:

- Spatial variation of vv-volume temperature. The EVITA thermocouple mesh points show quite varying local temperatures. Our model uses only one vessel temperature.

- The influence of internal vv-structures on the condensation process cannot be simulated. There are numerous parts as deflector plate, copper plate below the cryogenic plate, N2-pipes inside vv etc., where the re-evaporation of draining down condensate is possible.

- No consideration of the impact of the steam jet, depending on the nozzle direction, which has a great importance.

For a better agreement between calculation and experiment either the boundary conditions of the experiment must be controlled carefully or their transient behaviour must be quantified to allow a modelling of all relevant effects.

MAGS will accompany the future course of the EVITA series. Next experiments will have a noncondensable gas fraction of nitrogen.

Staff:

G. Bönisch
V. Pasler

Literature:

[1] G. Bönisch: Report on Pre-test Calculations for the Complementary Cryogenic EVITA-Experiments with Steam Injection, July 2003.

TW2-TSS-SEA 5.5A
Safety Related Experiments to Investigate Air Inbreak Events in Cryopumps

Fusion reactor design includes cryopumps for evacuation of hydrogenic gas mixtures from the torus and neutral beam systems. The hydrogen inventory of the pumps themselves is limited such that under assumption of an air inbreak into these systems and assuming an explosion, the maximum explosion end pressure (deflagration case) will be 2 bar inside the pumps, and thus not be harmful to their mechanical design. However, the ITER vacuum vessel is not designed to such pressure levels. This is why a task has been launched to investigate such a scenario in detail.

The reference accident postulates an air inbreak into the vacuum vessel (at a pressure increase rate of about 2.7 mbar/s), which floods the connected cryopumps and initiates there a complete hydrogen release because of the pressure increase causing heat transfer. Due to thermal convection between the vacuum vessel and the pump interior, this hydrogen is then assumed to be rapidly transported into the main vessel. In order to model the formation of hydrogen/air-mixtures more accurately as done in past accident analyses, which were assuming instantaneous release of all hydrogen stored in the cryopumps at time zero of an accident, now the transient release shall be considered. However, an accurate modelling requires experimental release data, which shall be determined within this task which exploits the test facility of the ITER torus model cryopump TIMO.

The release of hydrogen during normal regeneration conditions is well-known (see Task TW1-TTF/VP 11). The experimental goal was therefore to measure the hydrogen release under rapid gas ingress conditions on TIMO. For safety reasons, pure nitrogen was used in all cases as model gas for air. Due to the fact that the available gas dosage system is not able to manage the required high gas flows, a new experimental concept was used to simulate an off-normal operation. Thus, the TIMO test vessel was filled with gas at a certain pressure (200, 500, 1000 mbar) with the pump main valve being closed, see Fig. 1.

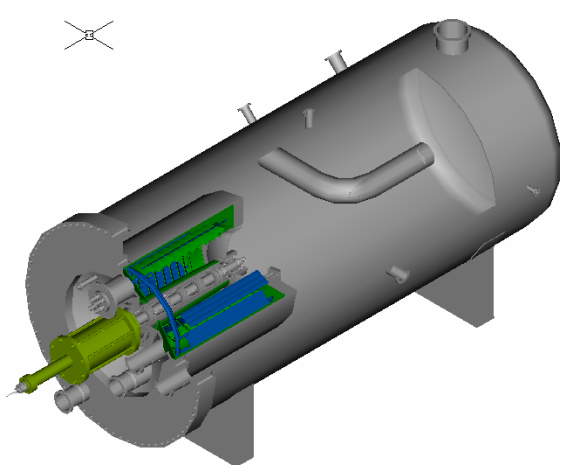

Fig. 1: Set-up of the TIMO test vessel with installed pump.

Then, the valve was opened so that the gas could rapidly expand into the cold pump. The achieved pressure increase rates were even one order of magnitude higher than according to the ITER reference scenario. All tests were performed at warm and cold conditions. The comparison of the pressure evolutions measured at these two conditions yields the pump capacity of the flooded but still cold pump for nitrogen. The cold tests were again performed twice, with and without pumped gas load. The pressures and temperatures during expansion were measured, so that by direct comparison of the two load cases, the transient hydrogen release curve could be derived.

A typical result is shown in Figure 2, which illustrates that the pressure increase rate inside the non-loaded and the loaded pump are very comparable except of the fact that the latter curve is higher by the amount of the released hydrogen. The difference between the two pressure curves corresponds directly to the amount of pumped hydrogen gas.

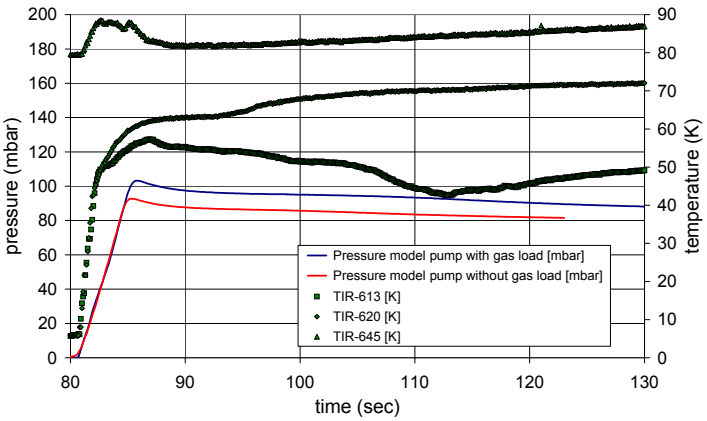

Fig. 2: Measured gas inbreak curves for two cases, with and without gas load.

Parallel simulation work performed in the meantime within other tasks in the safety field showed that the first second of hydrogen release determines the explosion hazard. Therefore, these tests in TIMO will be continued with the aim to replicate closer the ITER reference accident and to achieve a higher experimental resolution.

Staff:

Chr. Day
H. Haas
A. Mack
J. Weinhold
D. Zimmerlin

TW2-TSS-SEP 2
TW3-TSS-SEP 2
Doses to the Public

Objectives:

Volume IV “Normal Operation” of the ITER Generic Site Safety Report (GSSR) provides an assessment of the potential airborne and waterborne effluents and emissions from ITER. Volume VII “Analysis of Reference Events” and Volume VIII “Ultimate Safety Margins” include documentation of radioactive environmental source terms for the analysed representative accident sequences. Doses to the public due to these source terms are not given.

The objective of this task is to calculate in a consistent way these doses for realistic meteorological and siting conditions. Main computer codes to be used: UFOTRI, COSYMA, and NORMTRI.

Work performed

One of the important questions related to potential countermeasures was to define potential evacuation areas in case of a kerosene fire assuming the release of large amounts of activation products and tritium. Source terms provided by the PPCS study were used, however, scaled to the amount assumed to be released in such an event. Only one type of dose has been used for the calculations, defining the intervention level for evacuation.

Two different release scenarios, one representing a worst case scenario, the other average release conditions, were applied. The first scenario (category F) is dominating a release at ground level whereas set two (category D) represents average weather without rain. As the amount of energy released is unclear, three scenarios were investigated (1 MW, 10 MW and 100 MW). Tritium and activation products were treated separately. For tritium, a source term of 1kg of HTO was assumed and for activation products 100 kg. In addition, parametric studies were performed for the activation products with a source term ranging from 0.1 kg up to 100 kg. In this case, only the worst case weather was assumed.

The largest area of evacuation was calculated without any fire. In case of fire, heat is produced and this initiates plume rise. Plume rise reduces the concentration in the near range and thus the doses close to the plant. In case of a large fire of 100 MW, the doses in the near range were reduced by more than a factor of 10, compared to those with worst case weather (category F).

The calculations were completed, documented and results send to the EFDA-Team in Garching.

In a second task, support has been provided in licensing ITER for the Spanish site Vandellos. The aim of this work was to compare the methodology and the results of the local regulatory framework with international accepted methods and models which are used in the frame of ITER. In particular comparison calculations for the unit release of tritium and activation products were performed. For this purpose, local meteorological data, provided by CIEMAT, Spain, has been converted into the appropriate hourly values required by the simulation programs and used for the assessments. Other parameters were adapted to the Spanish regulatory requirements as far as possible.

The doses obtained with the Spanish models are similar to those calculated with UFOTRI and NORMTRI. For the accidental case the 95% percentile is lower by about a factor of 2 to 5 which is similar for routine releases. Only in case of the early dose, results obtained with

COSYMA are partly higher. It is remarkable that the Spanish results are identical for HT and HTO releases. This indicates, that independent of the speciation, always HTO is used.

The calculations were completed, documented and results send to the Spanish support team.

Ongoing work

Following the calculations performed in the former working period, a new task was defined to refine the estimation of potential measures to the public (TW2-TSS/SEP2). Potential source term from future fusion power plants consists of mainly activated dust (AP), activated corrosion products (ACP) and tritium in form of HTO. Main safety targets for potential accidental releases to be compared with are European intervention levels for early (evacuation, sheltering) and late (relocation, food banning) emergency actions and the regulations for European fission power plants. As the composition of realistic source terms is still open, a methodology should be developed to estimate the highest potential release which does not exceed the intervention levels. To this purpose, starting with the source terms as defined for the Power Plant Conceptual Study (PPCS) the contribution of each source term fraction to a particular dose target will be calculated. Performing this for unit releases, an equation will be derived which will allow further scaling of all three fractions that the intervention level is not exceeded. This methodology has to be developed in compliance with the European Utility Requirements.

As the number of calculations is large and the amount of data being processed and provided will be huge, and, as there is a certain possibility that the composition of a source term may change with time, a specific software tool is under development to allow an easy application for a particular case. This tool allows to

- load a particular scenario,
- load, modify or create a source term,
- and estimate the exhaust of the release targets for evacuation, sheltering, relocation and food banning.

The data base of such a tool would contain nuclide specific doses and concentrations in food for the various release conditions. Each data set for one release condition would include information for all the four release targets. Only when a new release condition has to be investigated, additional calculations with UFOTRI and COSIMA would be necessary.

As basis for the tool, Microsoft EXCEL is foreseen. This allows an easy application as this software is widely distributed and a standard spreadsheet. Specific input forms will guide the user through the application function. The development of the first version of the tool is scheduled for the end of the year 2003.

Staff:

W. Raskob
I. Hasemann
J. Ehrhardt

Power Plant
Conceptual Study

TRP-PPCS 1
Reactor Models A-D

TRP-PPCS-1, 2, 12, 13
Neutronic Analyses for Near Term and Advanced PPCS Reactor Models

Comprehensive neutronic design analyses have been performed for both the near term and the advanced power plant models considered in the PPCS study. Main issues have been the assessment of the tritium breeding capability, the evaluation of the nuclear power generation and its spatial distribution, and the assessment and optimisation of the shielding performance. The analyses were based on three-dimensional Monte Carlo calculations with the MCNP code using suitable torus sector models developed for the different PPCS power plant variants. The analyses were conducted and concluded during the previous reporting period [1]. A detailed documentation report has been prepared during the current reporting period [2]. The main results are as follows.

Tritium self-sufficiency, including a sufficient high uncertainty margin, can be provided for the PPCS models employing the HCPB, DCLL and SCLL blanket concepts, respectively. As for the PPCS model based on the water cooled lithium-lead (WCLL) blanket, the uncertainty margin of the current design is too low to compensate for TBR-losses due to blanket ports not accounted for in the TBR-calculation. With regard to the nuclear power generation, the HCPB blanket was shown to provide the highest energy multiplication. This is mainly due to the high neutron multiplication because of the high mass inventory of the Beryllium neutron multiplier. The SCLL blanket concept, on the other hand, shows the lowest energy multiplication due to the use of SiC as structural material. The shielding performance of the blanket concepts was assessed for the inboard mid-plane of the PPCS power plants where shielding is most crucial. A total thickness of about 100 cm is required for the inboard blanket/shielding system to ensure the operation of the super-conducting TF-coils over the full anticipated plant lifetime of 40 full power years. A simple shield composition based on steel and water is sufficient for the WCLL and DCLL blanket concepts. A more efficient shielding material such as tungsten carbide (WC) is required for the SCLL blanket showing an inherent low shield efficiency. WC was also shown to provide sufficient shielding for the HCPB blanket where the use of water is to be avoided to prevent any possible chemical reaction with the hot Beryllium. WC, in principle, can be applied with all blanket concepts considered in the PPCS study. When cooled by helium gas, the use of any hydrogenous material thus can be avoided for the power plant models employing the HCPB, DCLL and SCLL blanket concepts.

Staff:

Y.Chen
U.Fischer
P. Pereslavtsev
F. Wasastjerna, (VTT Processes, Finland)

Literature:

[1] U. Fischer et al, TRP-PPCS-1, 2, 12, 13 : Neutronic Analyses for Near Term and Advanced PPCS Reactor Models, in: W. Bahm (Comp.): Annual Report of the Association FZK-Euratom October 2001 – September 2002, Forschungszentrum Karlsruhe , Report FZKA-6820 (2003), 219-225.

[2] Y. Chen, U. Fischer, Y. Chen, P. Pereslavtsev, F. Wasastjerna, The EU Power Plant Conceptual Study - Neutronic design analyses for near term and advanced reactor models, Forschungszentrum Karlsruhe, Report FZKA-6763 (April 2003)

[3] Y. Chen, U. Fischer, P. Pereslavtsev, Neutronic Design Issues of the WCLL and HCPB Power Plant Models, Fus. Eng. Design 69, 655-661, 2003.

[4] U. Fischer, Y. Chen, P. Pereslavtsev, F. Wasastjerna, The EU Power Plant Conceptual Study: Neutronic design analyses for near term and advanced reactor models. Jahrestagung Kerntechnik 2003, Berlin, 20.-22. Mai 2003 Bonn : INFORUM GmbH, 2003 405-408.

TRP-PPCS 12
Model C (Dual Coolant Blanket)

TRP-PPCS 12 D7
MHD Related Issues

The dual coolant concept of a fusion blanket is based in the idea to use the breeding material, PbLi, to remove a considerable fraction of the nuclear fusion heat by convective flux of this liquid metal. In order to achieve high velocities required for heat removal, the electrically conducting structural material is electrically insulated from the liquid metal by inserts made from ceramic composites. These inserts reduce the electric currents induced inside the moving fluid and minimize the Lorentz forces acting on the fluid while it is moving through the magnetic field which confines the fusion plasma. Moreover, the inserts also act as a thermal barrier between fluid and wall, which allows to operate the blanket at acceptable wall temperatures while the fluid temperature can be higher for achieving best thermodynamic conversion efficiency.

The analysis of the flow in the blanket has been performed in 2002 and has been already described in the previous annual report. Most of the ducts in the Dual Coolant Blanket are straight rectangular ducts for which pressure drop correlations are known. As a result of the analysis the pressure drop in the blanket itself is small if all walls are covered by an electric insulation of 5mm thickness. The pressure drop for the blanket reaches values of about Dp=2.5x10-3MPa for a poloidal length of 2m. This pressure drop is really small and negligible compared with the pressure drop in the elements connecting the blanket with the rear coaxial pipes which feed and drain the blanket. Three-dimensional effects at the strong contractions and expansions will cause the major fraction of pressure drop in the Dual Coolant Blanket. These crucial elements can not be analyzed by standard correlations. Estimates for the current design of the outboard blanket yield Dp= Dp3d=0.84MPa and Dp= Dp3d=1.68MPa for the inboard blanket. These values can be reduced further by using larger dimensions of access tubes.

Results have been published by Norajitra et al. (2003). More details about the analysis are described in a technical report FZKA 6802, which appeared in April 2003.

Future work should focus on the possibility of electrical flow-coupling among neighboring flow sub regions in the blanket and in the coaxial tubes at the back of the blanket module, since the inserts are not perfectly insulating.

Staff:

L. Bühler

Literature:

[1] Norajitra, Bühler, Fischer, Gordeev, Malang, Reimann: 2003, Dual coolant liquid metal breeder blanket, Fusion Engineering and Design, 69, (1-4), pp.669-673.

[2] Bühler, Norajitra: 2003, Magnetohydrodynamic flow in the dual coolant blanket, technical report Forschungszentrum Karlsruhe, FZKA 6802.

TRP-PPCS 12 D8
Assessment of Integration of Divertor System to the Power Conversion System

This subtask was completed in Nov. 2002 [1]. The results were integrated into the system integration subtask TRP-PPCS 12 D9.

Conclusions

Application of a helium-cooled divertor together with the dual-coolant blanket concept is considered favourable for achieving a high thermal efficiency of the power plant due to its relatively high coolant outlet temperature.

A new FZK He-cooled modular divertor concept with integrated pin arrays (HEMP) is introduced. Its main features and function are described in detail. The result of the thermohydraulic analysis shows that the HEMP divertor concept has the potential of resisting a heat flow density of at least 10-15 MW/m2 at a reachable heat transfer coefficient of approx. 60 kW/m²K and a reasonable pumping power.

Integration of this divertor concept into the power conversion system using a closed Brayton gas turbine system with three-stage compression leads to a net efficiency of the blanket/divertor cycle of about 43%.

Staff:

R. Kruessmann
S. Malang
P. Norajitra
G. Reimann

Literature:

[1] P. Norajitra, R. Kruessmann, S. Malang, G. Reimann, Assessment of the integration of a He-cooled divertor system in the power conversion system fort he dual-coolant blanket concept. FZKA report 6771, December 2002

TRP-PPCS 12 D9
Mechanical Analysis, Design Integration and Draft Final Report

This task was completed in May 2003 [1].

Introduction

As a strategy of the EU PPCS, four different power plant models are investigated: model A based on the water-cooled lead-lithium (WCLL), model B based on the helium-cooled ceramic pebble breeder (HCPB), model C based on the dual-coolant (DC), and model D based on the self-cooled lead-lithium (SCLL) blanket concept. The model C [1] is a compromise between the “near-term” models A and B with their limited attractiveness and the “very advanced” model D which is characterized by very attractive features, but considerable development risks. The PPCS is concerned with an assessment of a standardized commercial power plant with a unit size of 1500 MWe.

The conceptual design of model C

A. Physics of the Reactors and Design Requirements

The models C and D are based on advanced physical assumptions characterized by: a) high β and high confinement, with realistic plasma pressure gradients, b) MHD stabilization by strong plasma shaping, c) high bootstrap current fraction, d) low divertor power loads and low Z_{eff}, no ELMs are foreseen in reactor operation. The analysis with the PROCESS code shows that, indeed, the above assumptions lead to a high Q, reduced size reactor, high bootstrap current fraction, and reduced plasma current when compared to models A and B, with nuclear loads limited to < 2.5 MW/m². Also, the heat load to the divertor could be reduced to 5 MW/m² (model D). In all cases, the net power plant output to the grid is 1500 MWe and the D-T fuel mix is 50-50.

The following overall design requirements and criteria are concerned: a) easy replacement of blanket and divertor modules, b) sufficient shielding of VV (for reweldability reason) and magnets to make them to life-time components, c) low volumetric fraction of steel to enhance the breeding ratio (TBR>1), d) the use of oxide dispersion-strengthened (ODS) steel limited to the plasma-facing zone of the first wall with highest temperature, e) sufficient high coolant inlet temperature to avoid material embrittlement (DBTT) under irradiation, and sufficient high coolant outlet temperature to allow the use of a BRAYTON cycle power conversion system f) as a small tritium permeation loss as possible, purification and tritium extraction systems for liquid-metal have to be foreseen.

B. Brief design descriptions of the blanket and divertor

Blanket: The DC concept, which is based on the study in [2] and the ARIES-ST study [3], is characterized by the use of self-cooled breeding zones with liquid-metal Pb-17Li serving as breeder and coolant at the same time, the use of a helium-cooled reduced-activation ferritic/ martensitic (RAFM) steel structure like EUROFER, and the use of SiC_f/SiC flow channel inserts (FCIs) serving as electrical and thermal insulators. The plasma-facing surface of the first wall is plated with a small

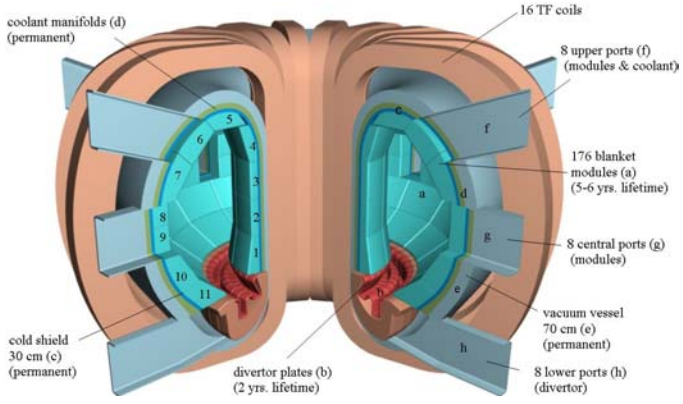

Fig. 1: Fusion reactor with DC blanket modules (model C).

layer of ODS. Instead of the “banana segments” adopted in earlier studies [4, 5], the blanket segmentation now consists of “large modules” [6], which helps to reduce thermal stresses and to cope better with the forces caused by disruptions, and the maintenance is facilitated thereby. A total of 11 modules, five of them at the inboard and six at the outboard (Fig. 1), form a 7.5° segment of the torus. They are large, stiff boxes with a helium-cooled grid structure inside forming flow channels for the Pb-17Li (Fig. 2). The modules are divided into a lifetime part (cold shield, coolant manifold, and vacuum vessel) and a breeding and hot shield part which will be exchanged at 6-years’ intervals. For cooling the entire blanket structure, high-pressure (8 MPa) helium gas is used. Two separate He systems provide for a redundancy of decay heat removal. Counter-flow manifolds ensure a uniform temperature distribution to minimize thermal stresses. The inlet temperature of the helium amounts to 300 °C, the outlet temperature to 480 °C. Besides, the liquid-metal breeder Pb-17Li also serves as a coolant. It enters the modules at 460 °C and leaves them at 700 °C, a value that is maximized for efficiency reasons. Primary coolant loop and manifold are provided with concentric tubes with the “hot outlet coolants” being in the inner tube (for Pb-17Li coolant in particular, this tube is thermally insulated with SiC_f/SiC inserts), and the “cold inlet coolants” flowing through the annular channels.

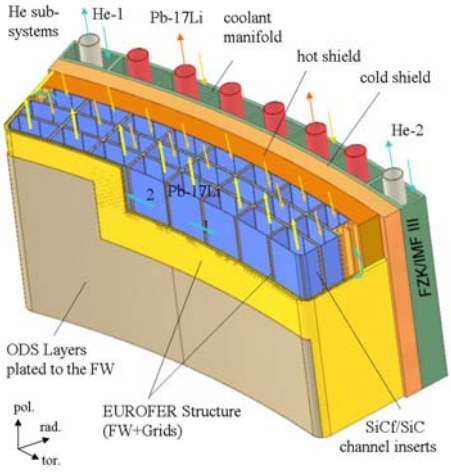

Fig. 2: DC equatorial outboard blanket module (radxtorxpol: 1.5x3.0x1.6 m3).

Divertor: About 15% of the heat energy are released into the divertor which serves at the same time as a trap for plasma impurities. A high heat flux of at least 10 MW/m² is assumed to hit the divertor target plates. For the divertor cooling, helium gas is preferred because it offers a good compatibility with other materials in view of security, and, therefore, ensures a good integration of the divertor into the power conversion system. High helium outlet temperature is, therefore, favorable for increasing the thermal efficiency. A modular design and small temperature gradients are advisable to reduce thermal stresses. The main design criteria are: a) Divertor operating temperature window has to be kept at the lower boundary higher than the ductile-brittle transition temperature (DBTT), and b) at the upper boundary lower than the re-crystallisation limit of the structural components made of refractory alloys under irradiation, c) achieving high heat transfer coefficients while the coolant mass flow rate and therefore, the pressure loss as well as the pumping power are as low as possible. The proposed design of a He-cooled modular divertor with integrated pin array (HEMP) consists of target plates divided into small modules. Underneath each tile of tungsten used as thermal shield, a finger-like heat transfer module (thimble) is brazed on. A pin array as flow promoter is integrated at the bottom of the thimble to enhance the cooling surface. Helium at 10 MPa and 600 °C enters the pin array at high velocity to cool the target plates and is heated up to about 700 °C.

Main neutronic and thermohydraulic data, as well as the power balance of the DC blanket concept are summarized in Tab. 1.

C. Neutronic analysis and shielding efficiency

The neutron wall loading distribution was calculated with the MCNP code. More than 90% of the fusion neutron power were loaded on the blanket modules, while the remainder flows through the divertor opening. Concerning the volumetric heating, a major fraction of ≅ 80% of the volumetric heat power is generated in the blanket segments, including the first wall. With the DC reference design, ≈ 4% are generated in the water-cooled low- (LT) -temperature shield. This power may not be utilized for electricity production and, therefore, must be

minimized, e.g. by enhancing the shielding capacity of the high temperature shield. Regarding the shielding efficiency, there are two essential requirements that must be fulfilled: a) re-weldability of lifetime components made of steel, and, b) sufficient protection of the superconducting toroidal field (TF) coils. Based on existing data, the current assumption is that re-welding of stainless steel should be successful at helium concentrations below 1 appm. Calculations to estimate the helium production in EUROFER steel show that even after a lifetime cycle of 40 years, re-weldability is achieved. So, the LT shield can be designed as a lifetime component, if welded joints are placed on its rear. The TF coil on the other hand is protected from the penetrating radiation by the blanket, the shield, and the vacuum vessel. An efficient neutron moderator (water or a hydride) is required to this end combined with a good neutron absorber (steel, tungsten, etc.). The radiation loads of the TF coils were calculated for the inboard mid-plane, where the shielding requirements are highest due to the minimum space available between the plasma and the TF coil. It is noted that the design limits can be met with the DC reference design.

Table 1: Main data of the DC Blanket Concept

	Blanket	Divertor
Average neutron wall load [MW/m2]	2.27	1.7
Max. neutron wall load [MW/m2]	3.0	
Max. surface heat load [MW/m2]	0.59	10
Alpha-particle surface power [MW]	546	136
Neutron power [MW]	2445	283
Energy multiplication	1.17	1.17
Thermal power [MW]	3408	583
Surface area [m2]	1077	69.3 (target)
Helium coolant:		
- inlet temperature [°C]	300	700 (target)
- outlet temperature [°C]	480	800 (target)
- pressure [MPa]	8	10 (target)
- mass flow rate [kg/s]	1528	473 (bulk) 477 (target)
- pumping power, η = 0.8 [MW]	30	3.4
Pb-17Li coolant:		
- inlet temperature [°C]	480	
- outlet temperature [°C]	700	
- mass flow rate [kg/s]	46053	
Secondary helium loop:		
- inlet temperature [°C]	285	
- outlet temperature [°C]	700	
- pressure [MPa]	15	
Thermal efficiency (power conv. system)	0.44	
Net efficiency (blanket/divertor cycle)	0.43	

D. Thermohydraulic, thermomechanic and MHD analyses

The layout of the blanket and the divertor requires iterative calculations between system code analysis and blanket layout concerning neutronic, thermohydraulic, thermomechanical, MHD, and velocity field calculations to determine a set of reactor parameters. For the ODS on the first wall, the maximum temperature should stay below 650 °C due to creep rupture, while the interface temperature of the EUROFER structure to Pb-17Li should be below 500 °C due to corrosion. For thermomechanical calculations material data of T91 were used as a substitution for ODS. The results show that the requirements can be fulfilled.

Also for the divertor, an assessment of temperatures and stresses was undertaken. Structural design criteria as required by the ITER structural design code are met, i.e. mechanical stresses do not exceed design limits under any operation condition. From these values, it is expected that fatigue of some anticipated 100-1000 cycles of reactor shut-down with cooling down from operation conditions to RT could be permissible. In a first thermohydraulic assessment of the divertor, a heat transfer coefficient of approx. 60 kW/m²K was determined with a corresponding pumping power of about 5.5% related to the heat removal. The pressure drop in the Pb-17Li-channels of the blanket due to magnetic/electrical resistance itself is small, if all walls are covered by an electric insulation in form of SiC_f/SiC inserts with 5 mm thickness. The fraction of the pumping power for the liquid-metal coolant is relatively low.

E. Power conversion system

For safety reasons (chemical reaction between water and liquid-metal) and a high thermal efficiency to be attained, a Brayton cycle (closed-cycle helium gas turbine) is considered as the reference concept. By this means, tritium permeation losses to the environment can be minimized. Four parallel Brayton cycles are used [1] leading to a thermal net efficiency of about 43%.

F. Tritium recovery and purification systems for Pb-17Li and He cooling loops

The requirements on the tritium removal and recovery system are to keep the tritium inventory low in the total blanket system and to limit the tritium losses to the environment to an acceptable value. Mainly the tritium which permeates through the walls of the heat rejection heat exchanger and intercoolers into the water is to be considered. These losses might be easily restricted to acceptable values due to the low temperatures (maximum helium temperature ≈ 300 °C, water temperature ≈ 30 °C) in these components.

Several methods were proposed and assessed for tritium removal from Pb-17Li. Further, during the breeding process, also helium is produced. Due to its low solubility in Pb-17Li, bubbles will be formed. It might be straightforward to combine the helium bubble removal with the tritium removal system discussed, since some of the methods might be also efficient for helium bubble removal. Finally, liquid-metal purification systems are also required in general to control the oxygen content of the system and remove corrosion products. For irradiated Pb-17Li, additional removal of heavy metal isotopes (Po, Hg, Ti) will be necessary.

Several helium loops cool the different systems of the plant. Helium gas has to be cleaned regularly so as to remove gaseous and radioactive impurities (especially tritium). The coolant purification system will also serve as a means for pressure control.

G. Balance of plant and fusion power plant layout

This section deals with additional components to make up an entire operational and functioning plant for generating electric power. The following main systems were considered: a) Primary heat transport system, b) Power conversion cycle, c) Service water system: for cooling auxiliary systems, d) Component cooling water system: provides cooling water to selected auxiliary components. The component cooling water system acts as an intermediate barrier between the circulating water system and potentially radioactive cooling loads to reduce the possibility of radioactive leakage to the environment, e) Circulating water system: The circulating water system provides for a continuous supply of cooling water to the heat rejection heat exchanger, the intercoolers, the component cooling water heat exchanger, and the service water system, f) Water treatment plant, g) Compressed-air system, h) Fire protection, i) Electrical power, j) HVAC Systems: The HVAC system provides for the ventilation and air conditioning of different plant buildings.

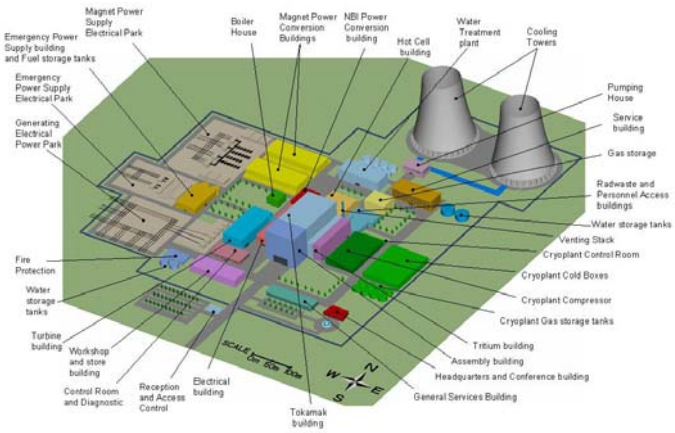

Fig. 3: Fusion power plant, general layout.

The whole site for the power plant (Fig. 3) further consists of several buildings to house the reactor, auxiliary systems, the power supply and the turbines, but also workshops and offices. The design of the tokamak building (Fig. 4) and the hot cell building is further evaluated, based on the design for the ITER site.

Conclusions

The technologies as well as the plasma physics models employed for model C are larger extrapolations between those existing of the “near-term” models A and B with their limited attractiveness and those of the “very advanced” model D with its very attractive features, but considerable development risks. The model C is based on a self-cooled lead-lithium breeding zone and a helium-cooled structure made of reduced-activation ferritic steel EUROFER, as well as a helium-cooled divertor. Flow channel inserts made of SiC_f/SiC composite in the lead-lithium channels serve as thermal and electrical insulators in order to minimize magneto-hydrodynamic (MHD) pressure loss and to obtain high coolant exit temperatures and, thus, high efficiency of the power conversion system, for which the BRAYTON cycle (closed-cycle helium gas turbine) is used. The modular designs of the DC and the He-cooled divertor are addressed. This study is concerned with an assessment of the self-cooled liquid-metal breeder blanket for a standardized commercial power plant with a typical unit size of 1500 MWe. The overall results of this study lead to the conclusion that the plant model C has a high potential to meet the goal of fusion research to develop an economically and environmentally attractive energy source.

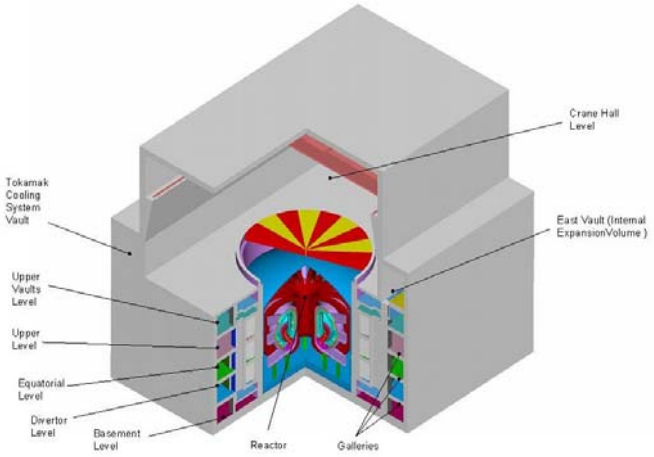

Fig. 4: Tokamak building, general view.

Staff:

L. Bühler
E. Diegele
U. Fischer
S. Gordeev
E. Hutter
R. Kruessmann
S. Malang
P. Norajitra
G. Reimann
J. Reimann

Literature:

[1] P. Norajitra, L. Bühler, A. Buenaventura, E. Diegele, U. Fischer, S. Gordeev, E. Hutter, R. Kruessmann, S. Malang, A. Orden, G. Reimann, J. Reimann, G. Vieider, D. Ward, and F. Wasastjerna, “Conceptual Design of the dual-coolant blanket within the framework of the EU power plant conceptual study (TW2-TRP-PPCS12), Final report,” FZKA 6780, May 2003.

[2] M.S. Tillack and S. Malang, “High-performance PbLi Blanket,” Proc. of the 17th IEEE/NPSS Symposium on Fusion Energy, San Diego, California, (1997) 1000-1004.

[3] D.K. Sze, M. Tillack, and L. El-Guebaly, “Blanket system selection for the ARIES-ST,” Fusion Engineering and Design 48 (2000) 371-378.

[4] P. Norajitra, L. Bühler, U. Fischer, K. Klefeldt, S. Malang, G. Reimann, H. Schnauder, L. Giancarli, H. Golfier, Y. Poitevin, and J.F. Salavy, “The EU advanced lead lithium blanket concept using SiCf/SiC flow channel inserts as electrical and thermal insulators,” Fusion Engineering and Design, 58-59 (2001), 629-634.

[5] P. Norajitra, L. Bühler, U. Fischer, S. Malang, G. Reimann, and H. Schnauder, “The EU advanced dual coolant blanket concept,” Fusion Engineering and Design, 61-62 (2002), 449-453.

[6] P. Norajitra, L. Bühler, U. Fischer, S. Gordeev, S. Malang, and G. Reimann, “Conceptual design of the dual-coolant blanket in the frame of the EU power plant conceptual study,” submitted for publication.

TRP-PPCS 13
Model D (Self-Cooled Lithium Lead Blanket)

TRP-PPCS 13 D5
MHD Related Issues

SiC/SiC composite materials offer a variety of advantages for advanced Self-Cooled Lithium Lead (SCLL) blanket concepts (Giancarli et al: 2002). The use of SiC for the walls of liquid metal filled channels helps to minimize electric currents, the magnetohydrodynamic interaction with the fluid and pressure drop. The present subtask focuses on the estimation of the MHD pressure drop within the blanket.

Most results have been obtained during the year 2002 and have been reported already in the previous annual report. The calculations show that the circular type of geometry foreseen for the improved design has better MHD performance. The pressure gradient in the annular ducts made by insulating walls is about $4p$=0.0567MPa /m at velocities as foreseen in the annular gap $v0$ =1.5-4.5 m /s . The pressure drop in the central duct is negligible in comparison with the pressure drop in the annular region. The total pressure drop is mainly created in the annular gap. Its values seem to be on acceptable magnitude. Over the total length L=7.8m of the outboard blanket the pressure drops by Δp=0.44MPa. These results have been obtained assuming a uniform magnetic field of 4 T for the outboard blanket. The top blanket is positioned in a region where the magnetic field is roughly estimated to B=6T while at the inboard blanket we have B=8T. If the geometry for the top and the inboard blanket is the same we can estimate the pressure drop there by using the linear dependence of the MHD pressure drop on the magnetic field for a reasonable extrapolation. This yields pressure gradients $4p$ =0.085MPa /m and $4p$ =0.11MPa /m and pressure drops Δp=0.19MPa and Δp=0.85MPa for the top and for the inboard blanket, respectively.

It is found that the core velocity profiles along the first wall are non-uniform. This "periodic" velocity distribution may have a negative influence on heat transfer.

The task has been performed in collaboration with L. Giancarli (CEA). Some results have been published by Giancarli et al. 2003. Details of the analysis can be found in a technical report by Bühler & Giancarli, which appeared December 2002.

Further analysis should focus on the evaluation of three-dimensional effects at the ends of the blanket and at connections of the blanket with rear piping system which supplies the liquid metal to the blanket.

Staff:

L. Bühler

Literature:

[1] L. Giancarli, H. Golfier, S. Nishio, R. Raffray, C. Wong, R. Yamada: 2002, Progress in blanket designs using SiCf /SiC composites*, Fusion Engineering and Design,* 61-62, pp.307-318.

[2] L. Giancarli, L. Bühler, U. Fischer, R. Enderle, D. Maisonnier, C. Pascal, P. Pereslavtsev, Y. Poitevin, A. Portone, P. Sardain *et al.: 2003,* In-vessel component designs for a self-cooled lithium–lead fusion reactor, *Fusion Engineering and Design,* 69*,* (1-4), September 2003, pp. 763-768

[3] Bühler, L. and Giancarli, L.: 2002, Magnetohydrodynamic flow in the European SCLL blanket, *Forschungszentrum Karlsruhe,*Technical report, FZKA 6778

TRP-PPCS 15
Environmental Assessment

TRP-PPCS 15 D6
Doses to the Public

Objective

The main objective of this task is to estimate the cost of the “externalities” for models A and B which will be used as input during the economic assessment. In particular, it is necessary to calculate in a consistent way the doses to the public for realistic meteorological and siting conditions. Results of the assessments will help to evaluate the potential impact to the public with respect to early and late countermeasure actions. These calculations will be a continuation of the assessments performed in the SEAFP and ITER-SEP2 studies and will provide a consistent data set on the doses to the public from a power reactor.

Work performed

Two different types of source terms were provided. The first set contained release information which was uniformly distributed over three different time periods, 1h, 24 hours and 168 hours. In the second set, various time functions for the releases was assumed. Probabilistic calculation with a representative meteorological year, also used in former ITER studies, were performed. Source terms defined for the two conceptual plants A and B were used. The different materials released were treated separately. The source terms were defined for HTO, activation products from the first wall, from divertor, and ACP. Endpoint of the calculations was the comparison with the evacuation criteria at 1 km distance.

When probabilistic calculations are evaluated, the 95%-fractile is often used in regulatory guidelines to define a criterion for licensing nuclear installations. Assuming a release duration of one hour, these percentile dose values from all source terms, except from the First Wall and also Divertor of Plant Model B, are far from any potential evacuation criteria of 50 or 100 mSv at one kilometre distance which is assumed the plant boundary. In particular the First Wall source term of Model B exceeds the 50 mSv when looking at the maximum dose value. Extending the release duration to 24 or even 168 hours, the maximum doses are far below any intervention criteria for evacuation.

Besides the assessment of the individual source terms, it might be interesting to look at the contribution of each source term fraction to the total dose. This was possible to investigate for four source terms with a duration of 24 hours. These source terms comprises wither tritium and activated dust of tritium and activated corrosion products. In case of the first composition, the contribution of both fractions were similar, whereas the source term with activation corrosion products and tritium was dominated by the tritium fraction.

Staff:

W. Raskob
I. Hasemann
J. Ehrhardt

Literature:

[1] W. Raskob and I. Hasemann, Dose calculations for the Power Plant Conceptual Study (PPCS), Forschungszentrum Karlsruhe, internal report IKET, August 2003

TW3-TRP-001
PPCS He-cooled Divertor Concepts

TW3-TRP-001 D2
PPCS: He-cooled Modular Divertor Concept with Integrated Pin Array (HEMP)

Introduction

The divertor is an integral part of a fusion power plant and one of the high-heat-flux components (HHFC). Its main purpose is to remove the fusion reaction ash (α-particles), unburned fuel, and eroded particles from the reactor. About 15% of the total thermal power gained from the fusion reaction have to be mastered by the divertor, which results in high heat loads of up to 15 MW/m² on the divertor surface. Sufficient cooling of the divertor is not only necessary to prevent overheating and, thus, a failure of this unit. This energy fraction plays also a role in the total balance of the power station and, therefore, has to be used in an economically efficient manner, i.e. it has to be included in the power generation cycle.

The high heat load requires a careful and sophisticated divertor design, including manufacturing technology and materials processing techniques. In particular, this applies to the choice of the protective W-based layer material and the structure material on the basis of low-activating ferritic-martensitic steel or, alternatively, tungsten and/or Ni-based alloys. The conceptual design, materials and fabrication issues as well as analyses and experiments with respect to thermohydraulic and thermomechanical problems are closely linked to each other. An iterative design approach is therefore considered to be necessary.

For safety reasons, water should be avoided as a coolant according to the blanket concepts pursued by Forschungszentrum Karlsruhe (FZK). Therefore, a He-cooled modular divertor concept with integrated heat transfer promoters is developed.

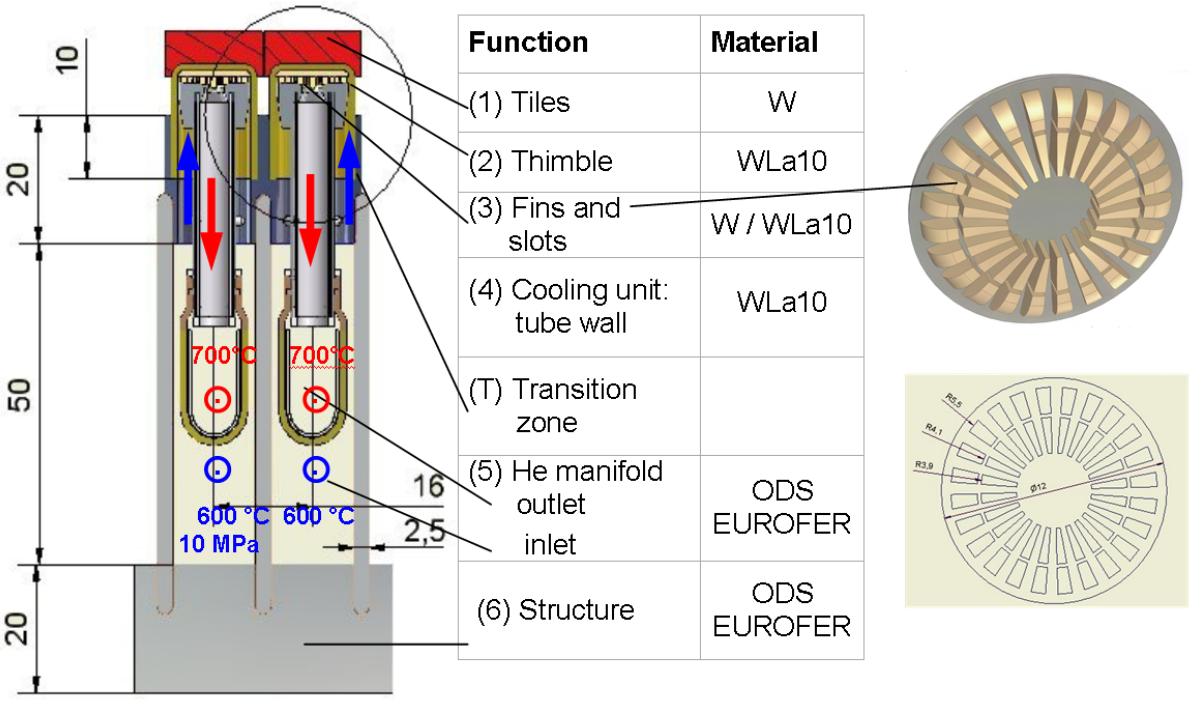

Fig. 1: The FZK modular divertor concept with integrated fin array.

The target plates of HEMP are equipped with W as a thermal shield and are sub-divided into small modules to reduce thermal stresses. One of such modules is illustrated schematically in Fig. 1. The Figure (left) shows the radial-toroidal cross-section of the divertor modules with

all dimensions of interest. The following numbers in brackets refer to this Figure. Details of the thimble are shown on the right hand side. The HEMP concept employs small tiles made of tungsten (1) brazed to a finger-like (2) (or thimble-like) structure made of W-alloy, preferably WL10. These fingers have a width of 16 mm, a wall thickness of 1 mm and are inserted into a front plate (6a) made of ODS steel. This plate is connected to a back plate (6b) by parallel walls (ODS steel). Helium with a pressure of 10 MPa and an inlet temperature of 600 °C flows upwards to the fins (3) at the outer wall and is then passed via an inner tube wall (4) downwards to the He manifolds (5). The tiles are of quadratic shape with a mean area of about 16 x 16 mm^2 and 5 mm thick. In order to improve heat transfer to the coolant at the top of the finger, a plate is inserted at the bottom of the thimble with a fin array (3).

Status of work

Design

In comparison to our earlier publications [1, 2], the design has now been optimised. The helium is now routed upwards through an annular gap which contains less inserts (spacers, etc.) and enters the fin array through a plate with special openings to reduce pressure loss and optimise the flow path, so that the edges of the tile are cooled more effectively. The outlet manifolds are now constructed with a double wall in order to avoid the recuperator effect. Additionally, they are rounded to reduce pressure losses.

Instead of the fin array, also other geometries could be envisaged. A concept consisting circular pins is also under investigation. The existing fins could be formed as straight slots or curved slots.

Material issues

A crucial point in divertor development is the materials issues. It is common to all cooling concepts suggested that such small modular structures are very difficult to manufacture. Apart from the technical requirements resulting from manufacturing, the materials used must also meet thermal and neutronic requirements. Furthermore, their tritium retention should be low. The necessity to withstand high heat loads requires the use of materials with appropriate thermal characteristics (heat conductivity, heat capacity, melting point, etc.). However, they also have to withstand high neutron loads and heat loads at temperatures and pressures favourable for power generation, i.e. a sufficient thermal strength under irradiation is requested. Hence, their neutronic characteristics should be superior [3].

Therefore, the choice of materials is limited. For the target plates, an armour material is necessary. The only promising material in question is tungsten, although it is very brittle in comparison to steel [3].

Tungsten has a high melting point and a high conductivity. However, it has the disadvantage of its operation temperature range being limited at the lower boundary by the ductile-brittle transition temperature (DBTT), below which it loses its ductility. At the upper boundary, the temperature window is limited by the recrystallisation temperature (RCT), above which tungsten loses its strength [4]. The operation temperature must lie within these two boundaries. A careful design of the divertor components made of tungsten is therefore necessary.

For the components between the target plate and the structure, a material has to be found which combines the good sputtering resistance and thermal characteristics of tungsten with a higher ductility and increased mechanical strength. An alloy of tungsten could be envisaged, like WL10. For this material and many others too, however, data with respect to their behaviour under irradiation are still incomplete. At present, preliminary DBTT and RCT

values of approx. 600 °C and approx. 1300 °C, respectively, are recommended by material experts for irradiated WL10.

For the structure material of the cassette a reduced-activation ferritic-martensitic (RAFM) steel would be the material of choice. However, transition materials and/or a design solution for the transition pieces to the tungsten target plates or tungsten alloy components must be found, since the thermal coefficients of expansion of these two materials are very different. Moreover, the temperature windows of the tile and thimble materials and the structure material should overlap.

All materials have to be available on the market and except for the material for the target plates, they must exhibit good mechanical properties, i.e. mechanical and thermal strength, to withstand the severe operation conditions and the large forces in case of disruptions.

The divertor cooling concepts also have to be optimised in terms of fabrication. It must be possible to manufacture them in a mass production process (for the state of the art HEMP divertor concept, about 300,000 modules will be necessary for one reactor every two years). Different production methods for tungsten components are currently under development, namely Electrical discharge machining (EDM), Electro-chemical machining (ECM) and Powder injection moulding (PIM). To reduce the number of necessary tiles, it is planned to increase the size of the finger unit and to investigate quadratic and hexagonal shapes of the tiles.

At the moment, a design can therefore only be based on an “intelligent” extrapolation of known material parameters. More research has to be done to develop new, suitable materials and manufacturing technologies.

Thermohydraulic layout

A first estimation of the heat transfer coefficient and the pumping power within the fin array was made using the standard correlations from the VDI Wärmeatlas [5] for tube bank heat exchangers. These correlations are not exactly suitable, but they give an idea of the range of the values. The pressure loss in the manifolds was assessed by correlations taken from [6].

The target plate will be divided into three parts. The coolant is routed into the three regions in series. The fingers in each region are cooled in parallel to minimise pressure losses.

For reasons of materials choice, it was decided to enter the plates with a coolant temperature of 600 °C and to allow for a maximum temperature rise of 100 K during the whole target cooling and a total temperature rise of 200 K per cassette.

For the calculation the normalised heat flux profile of the vertical target plates as assumed by Kleefeld [7] was used. The integration of the surfaces under this curve was performed by means of the program Origin 6.1G. Thus, estimations were obtained for the heat flux and the temperature rise of the coolant on each part of the target plate. For a conservative assessment, the calculation was performed for a finger of region II assumed to be loaded with 10 MW/m², where the peak heat flux was expected to occur at an elevated helium inlet temperature.

It was finally found that a heat transfer coefficient of larger than 65 kW/m²K is possible at a pumping power of less than 10% of the thermal energy gain.

At the moment, calculations with commercial fluid dynamics programs (CFD) are in progress. First results show that the correlations from [5] are too optimistic in h.t.c. and pressure loss.

Experiments

Experiments were carried out by our partners from EFREMOV Institute in St. Petersburg, Russia, so far only to measure values for the pressure loss. The measured values were considerably lower than the calculated ones.

In the next months, a new facility will be built, which is supposed to be an improved version of the existing one with a higher accuracy. The new facility will also allow for the execution of heat transfer tests.

In addition, a large helium loop is planned to be constructed at the EFREMOV Institute in St. Petersburg, Russia. An electronic beam facility is available there, which allows for the simulation of a high heat load of at least 10 MW/m². Planning and specification of the experiment programmes are under way. A technological study of a high-temperature or hot helium pump as an alternative to the conventional cold pump was carried out by EFREMOV. The loop is scheduled to be in operation by the end of 2004 and to deliver first test results in 2005.

Conclusions and outlook

The improved design of the FZK divertor concept was described. It meets a large variety of requirements imposed by the vessel, plasma physics, safety, and materials issues, etc. It must be emphasized in particular that in comparison to the preceding designs, the choice of materials was revised. The earlier envisaged TZM was rejected because it is no low-activation material and has been replaced by a tungsten alloy (WL10) as thimble material and by ODS EUROFER as structure material. Materials data were collected and fabrication routes were discussed. Furthermore, thermohydraulic estimations as well as first experimental results were presented.

The design will be further investigated. In particular, the details of the manifolds and the cassette body will be studied. Materials development will be continued, tests with different fabrication methods will be performed. Thermohydraulic performance will be assessed by means of different commercial CFD tools which will be compared mutual by means of benchmark tests. The objective is to optimize heat transfer, while keeping the pumping power at considerably less than 10% of the thermal energy gain. Thermomechanical calculations are also under way. First results of heat transfer experiments are expected to be obtained at the end of 2003. Additionally, developments of manufacturing technologies - EDM, ECM and PIM - for divertor components made of tungsten or tungsten alloys will be continued.

Staff:

L. Boccaccini
T. Chehtov
S. Gordeev
O. Jacobi
J. Konys
W. Krauss
R. Kruessmann
R. Lindau
A. Möslang
P. Norajitra
C. Petersen
G. Reimann
M. Rieth
R. Ruprecht
R. Sunyk

Literature:

[1] P. Norajitra, L. Bühler, A. Buenaventura, E. Diegele, U. Fischer, S. Gordeev, E. Hutter, R. Kruessmann, S. Malang, A. Orden, G. Reimann, J. Reimann, G. Vieider, D. Ward, F. Wasastjerna: Conceptual Design of the Dual-Coolant Blanket within the Framework of the EU Power Plant Conceptual Study (TW2-TRP-PPCS12), Final Report, FZKA 6780 (May 2003)

[2] P. Norajitra, R. Kruessmann, S. Malang, G. Reimann, Assessment of integration of a He-cooled divertor system in the power conversion system for the dual-coolant blanket concept. FZKA 6771 (2002)

[3] K. Ehrlich, M. Gasparotto, L. Giancarli, G. Le Marois, S. Malang, B. van der Schaaf, European Material Assessment Meeting. Karlsruhe, 5-8 June 2001. EFDA Report, EFDA – T – RE – 2.0 (2001)

[4] A. Möslang, Personal communication, FZK, June 2003

[5] VDI – Wärmeatlas, 3rd issue 1977, Sheet Ge1 and Ld1.

[6] W. Kalide, Einführung in die Technische Strömungslehre. 7th edition, Hanser, München 1990, pp. 52 – 72

[7] K. Kleefeldt, S. Gordeev, Performance limits of a helium-cooled divertor (Unconventional Design), FZKA 6401, 2000

TW3-TRP-001 D4
Task Co-ordination

The objective of this sub-task was the co-ordination of the task work in TW3-TRP-001, in which two concepts for the He cooled divertor (target max. heat flux >10MW/m^2) are under investigation, namely HETS (High Efficiency Thermal Shield) concept in ENEA and the HEMP (Helium Cooled Modular Divertor with Integrated Pin array) concept in FZK. Both concepts share a modular architecture of the High Flux Plate in order to reduce the thermal stress, a thermo-hydraulics lay-out based on a parallel He flow in the module arrangement and almost the same materials (e.g. use of W and W-alloy for the manufacturing of the high heat flux elements). Heat transfer promoters are used to achieve the high heat transfer coefficient (>30 kW/m^{2}K) required in these concepts to remove within acceptable temperature the locally high plasma heat flux. Two different concepts for this promoter distinguish basically the two proposals, the HETS use an heat transfer mechanism based on jet impingement and radial flow in small channels at high velocity, while the HEMP concept adopts a pin array (or alternatively a slot array) structure concept, to increase both Helium velocity and heat transfer surface (see Fig. 1).

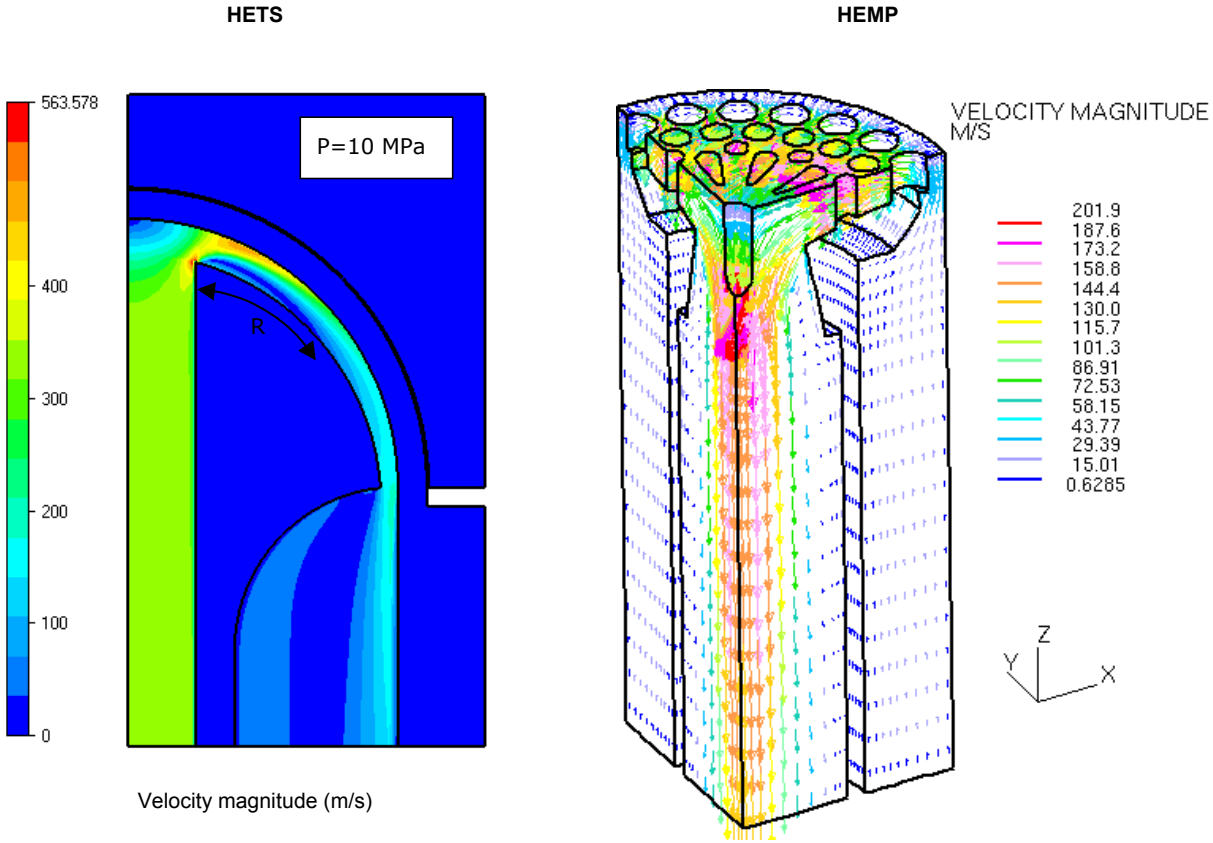

Fig. 1: Heat Transfer Promoter for the HETS and HEMP concept.

Expected results of this task will be: the definition of a preliminary conceptual design of a divertor based on these concepts, the evaluation and comparison of the two proposed heat transfer mechanisms and the definition of the critical issues and needs for a future R&D Programme.

Staff:

L.V. Boccaccini

Physics Integration

HGF Strategy Fond "Advanced ECRH"

Magnetohydrodynamic (MHD) instabilities are one of the main reasons for the limited confinement of plasmas. The stability is to a large extent determined by the distribution of plasma currents and driving localized currents in a plasma is a very important tool to suppress current-driven instabilities and thus to optimize the performance of tokamaks. The suppression of plasma pressure limiting MHD instabilities (so called 'Neoclassical Tearing Modes') has been demonstrated successfully by localized electron cyclotron current drive (ECCD) at ASDEX-Upgrade.

The absorption of RF-waves is dependent on the resonance condition (the RF-frequency has to be equal to the cyclotron frequency). Thus, the driving currents can be counteracted by an external current drive at the same localization either by changing the injection angle or the RF-frequency.

For plasma stabilization, multi-frequency tunable 1 MW long-pulse gyrotron (with a pulse length of 10s) are highly needed by ASDEX-Upgrade at IPP Garching for advanced ECRH and ECCD experiments [1]. Four gyrotrons will be or were already ordered by IPP Greifswald, two of them operating as two frequency gyrotrons at 105 GHz and 140 GHz , two of them will be multi-frequency gyrotrons operating at different frequencies between 105 GHz and 140 GHz. The $TE_{22,8}$ mode was chosen as cavity mode at 140 GHz [2,3]. The frequency of 105 GHz corresponds to the $TE_{17,6}$ mode. These gyrotrons are being developed at Gycom / IAP in Russia.

To compare with results from the "Institute for Applied Physics (IAP)" in Nizhny Novgorod, the $TE_{22,6}$ gyrotron existing at FZK has been modified to operate in the $TE_{22,8}$ mode. This gyrotron had been used for very successful experiments concerning fast step-tunability for which tuning at the MW power level within 1 s was proven. Electron gun, beam tunnel, collector and the superconducting magnet system of the $TE_{22,6}$ gyrotron are used in the new experiment, the resonator, quasi-optical mode converter and window will be changed for optimized operation at different frequencies.

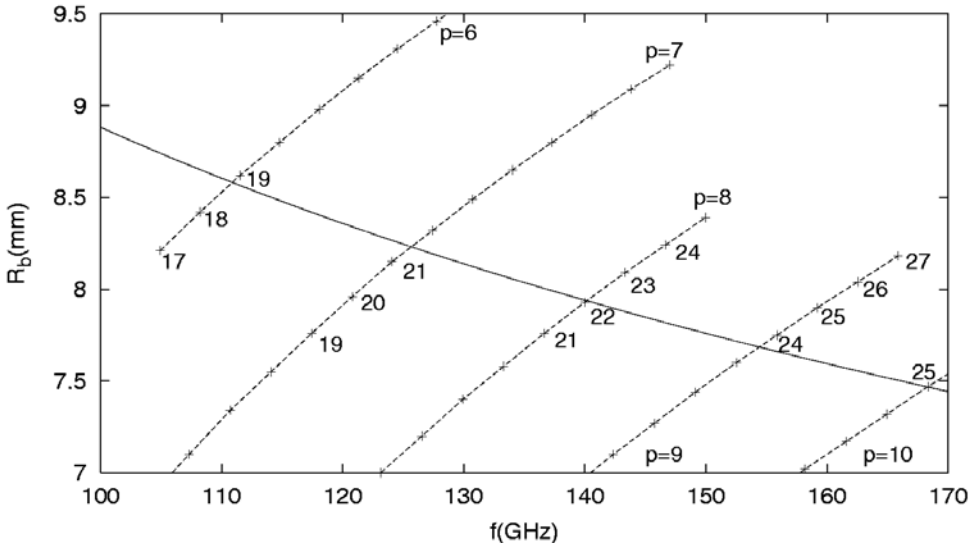

Fig. 1: Beam radius for different output frequencies ($_{TEm,p}$-modes). Shown is also the electron beam radius for diode-gun operation.

The resonator with uptaper has been redesigned and was manufactured. It was optimized for a series of modes from $TE_{17,6}$ to $TE_{23,8}$ (Fig. 1). Some additional modes from $TE_{24,8}$ to $TE_{25,10}$ can also be excited. However, multi-frequency gyrotrons have to be equipped with a matched window in order to avoid reflections, that is either a Brewster angle window or a

tunable double-disk window, both from synthetic diamond and with a broadband quasi-optical mode converter system.

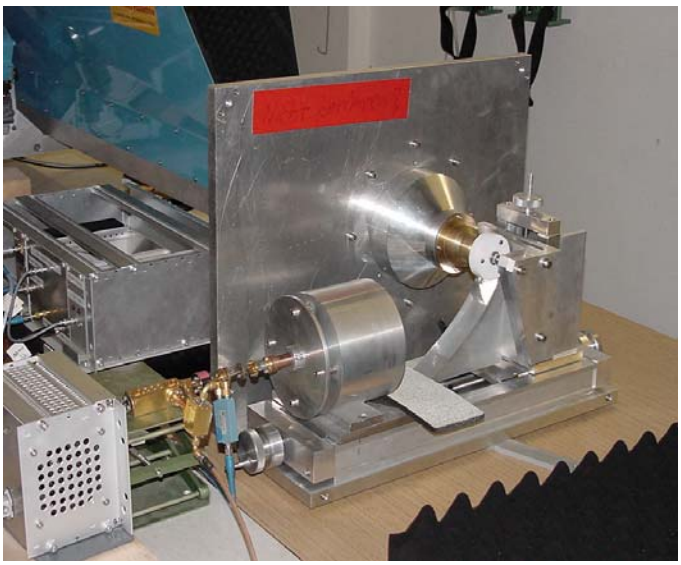

Fig. 2: Mode generator for different gyrotron modes.

The quasi-optical mode converter of the gyrotron consists of a dimpled-wall antenna and a beam-forming mirror system optimized for nine modes from $TE_{17,6}$ to $TE_{23,8}$ [6,7]. The first mirror is a large quasi-elliptical one, the second and third are phase correcting mirrors with a non-quadratic shape of the surface. These two mirrors were optimized for broadband operation in the designed modes. Two sets of quasi-optical output systems have been machined at different companies for evaluation of manufacturing precision.

To test this converter output system outside the gyrotron, a new quasi-optical mode generator for low power tests has been developed and fabricated [4,5]. A Gaussian-like beam is coupled via two cylindrical lenses and a quasi-parabolic caustic mirror into a perforated gyrotron-like coaxial resonator (Fig. 2). The caustic mirror is shaped in a way, so that all waves are tangent to the so-called caustic of the mode. As the eigenvalues of an overmoded resonator are very close to each other, an inner rod is used to improve the mode selection (coaxial resonator). Since all modes of interest for such a gyrotron have a similar structure, with their caustic radius being approximately half the cavity radius, only one set of resonator and lenses is required. Only a minor readjustment of the quasi-optical components is needed for excitation of different modes.

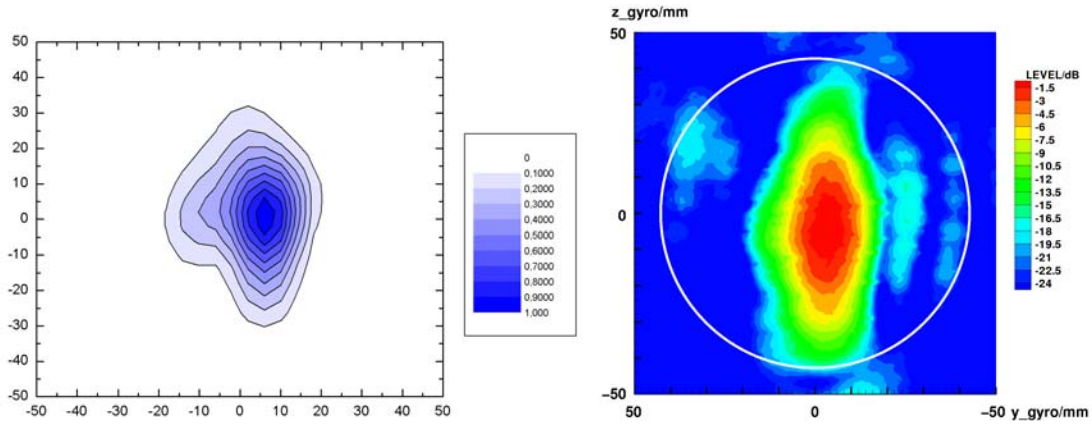

Fig. 3: Calculated (left) and measured (right) field pattern of the $TE_{22,8}$-mode at the window position.

For the $TE_{22,8}$ mode, Fig. 3 shows the field distribution of the Gaussian output mode at the position of the Brewster window (the waist of the Gaussian beam was designed to be situated at the position of the window flange where the beam profile is circular). The measured field distribution showed very good agreement with the calculated one. The two sets of quasi-optical output systems showed practically the same results. Thus one set can be used to continue the low power measurements for the other modes while the other set is used for being installed inside the gyrotron.

Efficient operation for the large number of operating modes at different frequencies is possible by using a broadband diamond Brewster window fabricated by chemical vapor deposition (CVD) [11]. Due to the large Brewster angle, the diameter of the disk has also to be rather large in order to have sufficient aperture for the RF beam. These disks with diameters of more than 106 mm are under development at Element Six (formerly DeBeers). One disk with a thickness of 1.923 mm and a diameter of 120 mm has already been delivered. It showed a homogeneous distribution of the loss tangent in an elliptic area, which can be used for the elliptic shape of a Brewster window. The measured values of the complete disk are between $2 \cdot 10^{-5}$ and $8 \cdot 10^{-5}$. The average of the loss tangent is 3.6×10^{-5}. Due to the elliptical shape of the Brewster window only the best area of the disk will be used. A 140 mm diameter disk for a full-size diamond Brewster angle window has been ordered and will be delivered in near future.

Up to now the gyrotron has been fully mounted with the new resonator, quasi-optical mode converter and a quartz glass Brewster window. The gyrotron is now in process of conditioning. High power tests are expected in the next time.

Staff:

A. Arnold (Uni Karlsruhe)
E. Borie
H. Budig
G. Dammertz
R. Heidinger (IMF I)
S. Illy
M.V. Kartikeyan (AvH Fellow)
K. Koppenburg
B. Piosczyk
M. Thumm
X. Yang

Literature:

[1] F. Leuterer, K. Kirov, F. Monaco, M. Münich, H. Schütz, F. Ryter, D. Wagner, R. Wilhelm, H. Zohm, T. Franke, K. Voigt, M. Thumm, R. Heidinger, G. Dammertz, K. Koppenburg, W. Kasparek, G. Gantenbein, H. Hailer, G.A. Müller, A. Bogdashov, G. Denisov, V. Kurbatov, A. Kuftin, A. Litvak, S. Malygin, E. Tai, V. Zapevalov: "Plans for a new ECRH system at ASDEX-Upgrade", 22nd Symp. on Fusion Technology (SOFT), Helsinki, SF, September 9-13, 2002, C17.

[2] E. Borie, G. Dammertz, O. Drumm, S. Illy, M. V. Kartikeyan, K. Koppenburg, B. Piosczyk, M. Thumm, D. Wagner, X. Yang: "Possibilities for multifrequency operation of a gyrotron at FZK", IEEE Trans. on Plasma Science, 2002, pp. 828-835.

[3] K. Koppenburg, A. Arnold, E. Borie, G. Dammertz, O. Drumm, M.V. Kartikeyan, B. Piosczyk, M. Thumm, X. Yang: "Design of a multifrequency high power gyrotron at FZK", Proc. 27th Int. Conf. on Infrared and Millimeter Waves, San Diego, USA, 2002, pp. 153-154.

[4] A. Arnold, G. Dammertz, D. Wagner, M. Thumm: "Measurements on a mode generator for cold tests of step-tunable gyrotrons", Proc. 27th Int. Conf. on Infrared and Millimeter Waves, San Diego, USA, 2002, pp. 289-290.

[5] D. Wagner, M. Thumm, A. Arnold: "Mode generator for the cold test of step-tunable gyrotrons", Proc. 27th Int. Conf. on Infrared and Millimeter Waves, San Diego, USA, 2002, pp. 303-304.

[6] O. Drumm, O., G. Dammertz, M. Thumm: "Design methods for mirrors in a quasi-optical mode converter for a frequency step-tunable gyrotron", Proc. 27th Int. Conf. on Infrared and Millimeter Waves, San Diego, USA, 2002, pp. 191-192.

[7] O. Drumm: "Numerical optimization of quasi-optical mode converter for frequency step-tunable gyrotron", Dissertation, Universität Karlsruhe, FZKA 6754, 2002.

[8] K. Koppenburg, A. Arnold, E. Borie, G. Dammertz, O. Drumm, M.V. Kartikeyan, B. Piosczyk, M. Thumm, X. Yang: “Recent results of the multifrequency high power gyrotron development at FZK”, Proc. 28th Int. Conf. on Infrared and Millimeter Waves, Otsu, Japan, 2003, pp.125-126.

[9] A. Arnold, G. Dammertz, D. Wagner, M. Thumm: “Low power measurements on a mode converter system of step-tunable gyrotrons”, Proc. 28th Int. Conf. on Infrared and Millimeter Waves, Otsu, Japan, 2003, pp. 415-416.

[10] Yang, X, O. Drumm, A. Arnold, E. Borie, G. Dammertz, K. Koppenburg, B. Piosczyk, D. Wagner, M. Thumm: “Design of a quasi optical mode converter for a frequency step tunable gyrotron”, Proc. 28th Int. Conf. on Infrared and Millimeter Waves, Otsu, Japan, 2003, 353-354

[11] M. Thumm, G. Dammertz, I. Danilov, R. Heidinger, A. Meier: “Low and high power experiments on CVD-diamond windows for ECRH”, 6th ECH Transmission Line Workshop, General Atomics, San Diego, CA, September 19-20, 2002.

Microwave Heating for Wendelstein 7-X

Introduction

Electron Cyclotron Resonance Heating (ECRH) has an inherent capability for plasma start up, localized heating and current drive and is of particular importance for stellarators. ECRH is thus foreseen as a basic heating system in the first operation stage of W7-X with 10 MW heating power in continuous wave (CW) operation [1]. The complete ECRH-system for W7-X will be provided by FZK, which has established the 'Projekt Mikrowellenheizung für W7-X' (PMW) in 1998 to run the project. The responsibility covers the design, development, construction, installation and integrated tests of all components required for stationary plasma heating on site at IPP Greifswald. PMW coordinates the contributions from IPF Stuttgart, which is responsible for the microwave transmission system and part of the HV-system, and from the team at IPP Greifswald, which is responsible for the integration of all subsystems on site. In particular a European collaboration has been established between the Forschungszentrum Karlsruhe, Centre de Reserche de Physique des Plasmas (CRPP) Lausanne, Institut für Plasmaforschung (IPF) of the University Stuttgart, Commissariat à l´Energie Atomique (CEA) in Cadarache and Thales Electon Devices (TED) in Vélizy, to develop and build a prototype gyrotron for W7-X, with an output power of 1 MW for CW operation at 140 GHz.

Development of the Prototype Gyrotron

The major problems of the high power, high frequency gyrotrons are given by the Ohmic heating of the cavity surface, by the dielectric losses in the output window, by the power capability of the collector and by the amount of stray radiation absorbed inside the gyrotron. The technical limit of the power density on the resonator surface is assumed to be 2 kW/cm² for CW operation. For this reason high power gyrotrons are operated in high order volume modes with a large cavity.

A major breakthrough for a CW compatible source is the use of a diamond window fabricated by chemical vapor deposition (CVD), which allows the design and the operation of a CW tube at the 1 MW power level [2-6]. The single-stage depressed collector brings the overall efficiency of the gyrotron in the 50% range and at the same time significantly reduces the thermal loading on the collector.

A contract between European Institutes (CRPP Lausanne, IPP Garching / Greifswald, IPF Stuttgart and FZK Karlsruhe) and Thales Electron Devices (TED), Vélizy, had been settled to develop continuously operated gyrotrons at an output power of 1 MW. A pre-prototype gyrotron “Maquette” had been tested successfully at the Forschungszentrum Karlsruhe. The pulse-length limitations were mainly due to a pressure increase inside the tube. Modulation experiments with the “Maquette” in short-pulse operation showed frequency modulation capabilities up to 50 kHz with cathode voltage modulation (constant depression voltage) and 1.5 kHz with depression voltage modulation [7].

The prototype gyrotron had been built with some improvements concerning the water cooling of the mirror box and had also been tested successfully. An output power of 970 kW could be achieved for a pulse length of 11.7s with an efficiency of 44%. The specified output power of 900 kW for a Gaussian beam (directed power) could be obtained during 55s at a total output power of 922 kW. The long-pulse results are given in Table 1 [4].

Table 1: Results and pulse-length limitation at different output powers.

Pulse length	Power (kW)	Current (A)	Efficiency	Energy (kJ)	limitation
3^{m}	890	41	0.41	160	power supply
$15^{m}37^{s}$	537	24	0.42	505	pressure
$21^{m}40^{s}$	257	26		350	pressure

At reduced output power, the pulse lengths were limited by the pressure increase inside the gyrotron, though the stray radiation inside the mirror box is very low. Table 2 shows a power balance for two pulses: for the 890 kW/180s and for the 922 kW / 55s pulse mentioned above. Within the measurement tolerances, the relative power losses (related to the generated output power) are the same for the two pulses.

The internal stray radiation was measured to be only 1.2 to 1.3 % of the generated power, the total stray radiation (sum of external and internal stray radiation) is only about 3%. Though the theoretical amount of stray radiation is calculated to be only 2.1 %, it is assumed that – due to fabrication tolerances - the experimental level of stray radiation cannot be reduced further.

Table 2: Power balance for the prototype gyrotron.

	922 kW; 55 s		**892 kW; 180 s**	
	efficiency (SDC)	42.2%	efficiency (SDC)	40.9%
	Power / kW	Power / %	Power / kW	Power / %
Generated Power	**972 ± 48**	100	**941 ± 47**	100
Ohmic losses	37 ± 5	3.8	37 ± 5	4.0
Internal Stray Radiation	13 ± 4	1.3	12 ± 4	1.2
Window Losses	0.4	0.04	0.4	0.04
Output Power	**922 ± 46**	95.2	**892 ± 45**	95.0
External Stray Radiaton	16 ± 4	1.7	16 ± 4	1.6
Directed Power	**907 ± 45**	93.5	**876 ± 44**	93.3

Two problems have to be solved: The limitation in output power and the limitation in pulse length (30 minutes). Figure 1 shows the output power as function of the beam current. The output power agrees very well with the theoretical value (dashed line) at low beam currents, however the experimental output power starts saturating with increasing beam current, whereas the theoretical output power does not. As this effect was not observed with the pre-prototype tube (for this tube 1.15 MW had been achieved in short pulse operation), the effect is very unlikely caused by spurious mode oscillations and/or misalignment between gyrotron and magnetic field. This effect is assumed to be caused by an azimuthally inhomogeneous emission of the electrons from the cathode surface. Indeed, a visual inspection showed inhomoge-neities on the emitter ring surface.

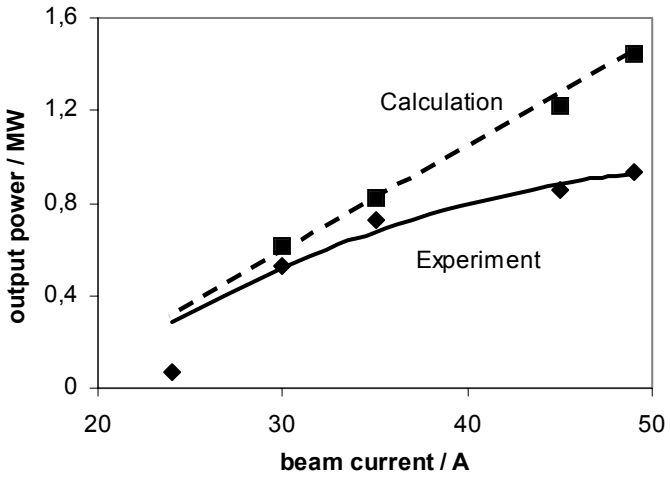

Fig. 1: Output power versus beam current.

The second problem is related to the limitation of the pulse length even at reduced output power. An infrared measurement of the internal ion getter pumps (through the diamond window) immediately after a long pulse of 15 minutes indicated a strong temperature increase of some parts of the pumps up to 250°C. It is, however, assumed that the temperature increase of the interior parts is measured through the pumping grid, and this temperature increase is even much higher.

Despite these two problems, it was decided not to enter the next development phase, but to stop the contract and to solve these problems during the fabrication of the series tubes.

The prototype tube was sent back to the manufacturer for visual inspection. No severe damage was observed. The tube was reassembled with two improvements: a new emitter ring with a better homogeneity of emission and an improved cooling for the ion getter pumps.

The pre-prototype tube “Maquette” and the superconducting magnetic system of Oxford Instr. was delivered to IPP. The magnetic axis of the system was measured with respect to the geometrical axis of the gyrotron. Despite the transport of the system to IPP Greifswald by truck, no deviation was found to the previous alignment. Within the tolerances, an axis deviation of about 0.2 mrad and a shift of less than 0.3 mm was found.

A shielding tube has been developed to avoid RF radiation inside the gyrotron hall at IPP. This tube is placed between the gyrotron window and the concrete wall of the gyrotron hall and will be tested during the experiment with the pre-prototype tube now installed at IPP Greifswald.

Series Gyrotrons

The call for tender for series gyrotrons and for the superconducting magnetic system (SCM) was sent to the companies. Meanwhile, seven gyrotrons have been ordered. Including the pre-prototype tube, prototype tube and the IPP tube manufactured by CPI, ten gyrotrons will be operated at Wendelstein 7-X. To be able to operate these gyrotrons, eight more superconducting magnetic systems are necessary and have been ordered at Cryomagnetics, Oak Ridge, USA.

Transmission line

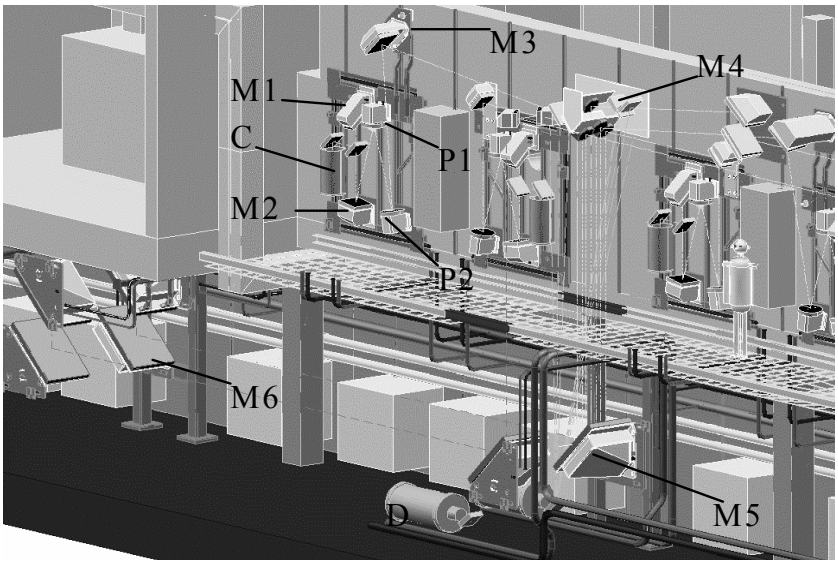

Fig. 2: Schematic view of the under-ground duct and the transmission system. On top one can see three matching and polarizer mirror assemblies (M1, M2, P1, P2, M3) with calorime-tric loads (C) and the plane mirror array (M4) injecting the individual beams into the MBWG system (M5, M6,....). At the bottom, two dummy loads (D) are installed.

The transmission line consists of single-beam waveguide (SBWG) and multi-beam waveguide (MBWG) elements [8,9]. For each gyrotron, a matching assembly of five single-beam mirrors is used. Two of these mirrors match the gyro-tron output to a Gaussian beam with the correct beam parame-ters, two others are used to set the appropriate polarization needed for optimum absorption of the radiation in the plas-ma. A fifth mirror directs the beam to a plane mirror array, which is situated at the input plane of a multi-beam wave guide (Fig. 2). This MBWG is designed to transmit up to seven beams (five 140 GHz beams, one 70 GHz beam plus an additional spare channel) from the gyrotron area (input plane) to the stellarator hall (output plane). It consists of four focusing mirrors with optimized surfaces in a confocal arrange-ment in square configuration to get low mode conversion. Additional plane mirrors are installed to fit the transmission lines into the building. At the output plane of the MBWG, a mirror array separates the beams again and distributes them via vacuum barrier windows to individually movable antennas in the torus. To transmit the power of all gyrotrons, two symmetrically arranged MBWGs are used.

The supporting structures for the SBWG-mirrors and for the MBWG-mirrors are installed inside the beam duct (Fig. 3, Fig.4). The SBWG mirrors (M1,M2) are in fabrication, the mirrors M3 and special mirrors, like switching mirrors, which are required for launching the microwave power to different locations in the W7-X plasma or for testing the complete trans-mission path, are designed or under construction. The MBWG mirrors have been manufactur-ed and are installed (Fig. 4).

Fig. 3: Matching optics and polarizers for one gyrotron.

The surfaces of the individual mirrors M1 and M2 depend on the specific distribution of the output radiation of the gyrotrons. Therefore, these mirrors have been manufactur-ed partly, leaving the possibility to optimize the final surface to the special gyrotron. For the Maquette gyrotron the field distribution was analyzed, from the phase reconstruction the beam parameters were defined and the surface profile of mirrors M1 and M2 were determined. M1 includes a waveguide coupler, embedded in the Cu layer, to measure the output power of the gyrotron and a grating structure to couple a diagnostic beam to the transmission line. The surfaces will be machined, they are near to completion and installation.

Fig. 4: View of the beam duct with MBWG mirrors and RF loads.

A short-pulse calorimeter will be installed in order to detect the output power of each gyrotron. Some problems with the manufacturing of the ceramic cylinders were found during the fabrication. Nevertheless, one calorimeter has been fabricated and will be installed at IPP Greifswald for measurements with the Maquette.

HV-systems

Experimental results from the first test phase of the HV-power supply (65 kV, 50 A) from Thales / Siemens have been the reason for design improvements concerning transient behavior and ripple of the output voltage. The improved device is now under test.

A first test of this supply in conjunction with the „Maquette“ gyrotron will be done in combination with a pre-prototype version of a fast crowbar for gyrotron protection and a pre-prototype version of a regulator-modulator for the acceleration voltage control (energy recovery with single-stage depressed collector). The design of the prototype version is

almost completed and under assembly. Tests of the new system for gyrotron power control and protection are expected until the end of this year. Planning and ordering of parts for the serial production have been started.

The concept of a safety system for personal HV protection has been developed. The installation is under commission.

In-vessel components

Different possibilities for movable launcher mirrors were investigated. The problem is that the mechanics for the movement and the connections for cooling water have to be integrated in very small place. The most reliable solution seems to be a push-pull rod in which the water cooling is integrated. The design and fabrication of a prototype launcher is under way. The design of the out-vessel motor drive has been started. The system will be tested in the RF test chamber which is used for testing all microwave-sensitive components before installing those into the plasma vessel. The design of the stray radiation antenna to launch the RF into the chamber has been finished.

A call for tender for the torus windows with CVD diamond disks has been started.

Detailed FE-calculations for the heat- and stress-loading of the ports were performed. Despite a heat shield, stresses at welded joints are severe. A better heat shield will be developed.

Fig. 5: Gyrotron water cooling modules.

Auxiliary systems

The water cooling for all the gyrotrons from Thales (according to the specifications for the cooling system by Thales) are installed. The cooling system for the CPI gyrotron is in fabrication.

As the pre-prototype gyrotron “Maquette” is installed at IPP, this tube has already been connected to the cooling circuits. The tests at nominal flow rates met the specified parameters. The connection between cooling modules and gyrotrons for the other ones is almost completed

The installation of the automatic liquid nitrogen supply with 600 l/h capacity for the superconducting magnets has been finished. The same applies for the gaseous Helium recovery with 16 Nm^3/h capacity.

The oil supply for the insulation and cooling of the gyrotron cathodes are in fabrication. The oil tanks of the gyrotrons are ready.

For all these installations, the controlling system and the visualization was designed and installed. Further, the low voltage installations and the installation for the optical and electrical signal transmission are in progress.

Staff:

IHM / FZK	IPF (University of Stuttgart)	IPP (Greifswald/Garching)
DI A. Arnold (Uni KA)	H. Babilon	H. Braune
E. Borie	P. Brand	V. Erckmann (PMW)
G. Dammertz	G. Gantenbein	H. Hofner
A. Götz	M. Grünert	F. Hollmann
P. Grundel	H. Hailer	L. Jonitz
R. Heidinger (IMF I)	W. Kasparek	H. Laqua
S. Illy	M. Krämer	G. Michel
H. Kunkel	R. Munk	F. Noke
K. Koppenburg	G. Müller	F. Purps
M. Kuntze (till 31.8.03)	P. Salzmann	T. Schulz
W. Leonhardt	H. Schlüter	M. Weißgerber
R. Lukits	K. Schwörer	
D. Mellein	R. Wacker	
G. Neffe		
B. Piosczyk		
M. Schmid		
W. Spiess		
J. Szczesny		
M. Thumm		

Literature:

[1] V. Erckmann et al.; “ECRH and ECCD with high power gyrotrons at the Stellarator W7-As and W7-X”, IEEE Trans. Plasma Sci., vol. 26, pp. 393-401, June 1998

[2] S. Alberti et al., “European High Power CW Gyrotron Development for ECRH systems”, Fusion Engineering and Design 53 (2001) 387-397

[3] G. Dammertz et al., “Development of a 140 GHz, 1 MW, Continuous Wave Gyrotron for the W7-X Stellarator”, IEEE Trans. Plasma Sci., vol. 30, pp. 808-818, June 2002

[4] G. Dammertz et al., “Prototype of a 1 MW, CW Gyrotron at 140 GHz for Wendelstein 7-X”, Proc. of the 28th Int. Conf. on Infrared and Millimeter Waves, Otsu, Japan, Sept. 2003, pp. 121-122

[5] M. Thumm, “Progress in Gyrotron Development”, 22nd Symposium on Fusion Technology (SOFT), Helsinki, SF, Sept. 2002, p.173

[6] G. Dammertz et al., “Progress in the Development of a 1-MW, CW Gyrotron at 140 GHz for Fusion Plasma Heating”, Proc. of 4th IEEE Int. Vacuum Electronics Conf., Seoul, Korea, 2003, pp. 34-35

[7] G. Dammertz et al.,”Power Capabilities of the 140 GHz/1 MW gyrotron for the stellarator Wendelstein 7-X”, Fusion Engineering and Design 66-68 (2003) 497-502

[8] W. Kasparek et al., “The transmission system for ECRH on the stellarator W7-X: design issues and tests of prototype components”; Int. Workshop on Strong Microwaves in Plasmas; Russia, August 2002;

[9] W. Kasparek et al., “Status of the 140 GHz / 10 MW CW Transmission System for ECRH on the Stellarator W7-X”, Proc. of the 28th Int. Conf. on Infrared and Millimeter Waves, Otsu, Japan, 2003, pp. 367-368

Tritium Inventory Control

TW3-TI-VP 31
High Temperature Regeneration Tests of the ITER Model Torus Cryopump

Objectives

After demonstration in principle of the suitability of the ITER pump concept by extensive test series in the TIMO test facility at FZK, now the influence of the ITER plasma exhaust gas impurities on the pump performance should be clarified. It was demonstrated in former tests in TITAN that the impurities may have a negative effect on pumping speed when accumulated over many subsequent pumping cycles with only partial regeneration in between. Consequently, it must be checked which are the necessary procedures to reduce this influence on the pump performance and whether the ITER requirements can still be met. Also the temperature levels needed in order to release the accumulated impurities have to be identified.

Test programme

Two different classes of impurities have to be treated separately: On one hand the air-like impurities, which are released below ambient temperature, on the other hand the water-like impurities, which need higher regeneration temperatures. Both classes of impurities will be studied within this task. The experiments fully exploit the new capabilities of TIMO upgrade [1], such as the new heating device, the high resolution quadrupole mass spectrometer for on-line gas analysis and the buffer tank in the TIMO exhaust line for gas species specific mass balance purposes (compare Task TW1-TTF/VP11).

For the regeneration/reactivation tests, different combinations of panel system temperatures (between 80 and 450 K) and shield system temperatures will be investigated. Each test includes a pump test sequence and a regeneration/reactivation sequence under ITER relevant operation conditions.

The tests of the air-likes start with the reference D_2-Base gas mixture (96.2% of D_2, 1.4% CO; 1.2% CH_4, 0.7% CO_2, 0.5% O_2). Further air-like impurities such as nitrogen, argon and neon will also be tested as added shares to the D_2-Base mixture. Any gas mixture can be produced from the pure gases in our gas mixing facility GASMIX, so that the experimental programme can be planned very flexibly. The accumulation of the impurity fractions over a number of cycles can, thus, be simulated directly within multi-cycle tests, or by pumping a modified gas mixture with a correspondingly higher percentage of the impurity gas.

In the second experimental stage, the influence of water will be investigated. The water will be introduced into the system via a bubble column, adopting the technique which was developed for TITAN [2].

Staff:

Chr. Day
A, Edinger
H. Haas
H. Jensen
A. Mack
J. Weinhold
D. Zimmerlin

Literature:

[1] H. Haas, Chr. Day, A. Mack, Report on experimental plan and the tests for pumping at panel temperatures between 5 and 40 K, 100 K regeneration tests with matrix of different gas mixtures and gas loads; Internal Report, Forschungszentrum Karlsruhe, August 2003.

[2] Chr. Day, B. Kammerer, A. Mack, The influence of water on the performance of ITER cryosorption vacuum pumps, Fusion Engineering and Design 51-52 (2000) 229-235.

European ITER Site Study

EFDA 01/641
European ITER Site Study-2 Cadarache 2002

EFDA 02/693
European ITER Site Study Vandellós 2002

The European ITER Site Study (EISS) is not only dealing with the proposed ITER sites in Cadarache, France and in Vandellós, Catalonia (Spain) during the CTA, but is also in charge as far as general questions are concerned in view of potential ITER sites outside of Europe. EISS was started by the end of the year 2000 and was initially organized through a European ITER Site Study Group (EISSG). To effectively manage the activities of the associations a project board for EISS was established in the year 2002.

Four members of the EISS project board - one of them from the Tritium Laboratory Karlsruhe (TLK) - have been appointed to constitute the European delegation for the Joint Assessment of Specific Sites (JASS) ad-hoc group, which had its first meeting in Clarington, Canada from the 12th to 15th September 2002 for a technical and socio-economical assessment of this proposed ITER Site. Three further distinct assessment meetings took place in Rokkasho, Japan from the 2nd to 5th October 2002, Cadarache, France from the 3rd to 6th December 2002, and Vandellós, Spain from the 11th to 14th December 2002. During the meetings respective 'Findings Reports' have been prepared on the basis of detailed input documents, based in turn on in depth studies, and on visits of the surroundings of the proposed site and meetings with representatives of the local authorities. Although it was concluded by JASS in their final report that all four sites responded to the ITER requirements and assumptions as outlined in the EDA Final Design Report, certain weaknesses and strengths of the different sites have been identified. To some extent larger differences have been recognized in the areas of transportation, financial support, workforce and socio economics. However, JASS concluded that ITER may be favorably sited on any of the settings offered by the four countries.

To directly support the safety considerations and the licensing process for the European ITER sites in Cadarache and in Vandellós the TLK continued to provide input information and reports for different tasks with emphasis on tritium tracking and accountancy and on licensing experience. For the latter a summary was produced for three experimental tritium facilities, namely the TLK, Germany, the Tokamak Fusion Test Reactor (TFTR), USA and the Joint European Torus (JET), UK. The compilation included published or official literature outlining the reasons each site required tritium, the restrictions on the amount and the use of tritium, and the approvals that had to be obtained from the relevant authorities.

Staff:

C. Caldwell-Nichols
L. Doerr
M. Glugla
R. Laesser

JET Technology

JW0-FT-1.1
Removal of Tritium-contaminated Flakes/Dust from the Sub-divertor Region of JET

From May to November 1997 JET was operated using mixed deuterium-tritium (D-T) plasmas with the divertor geometry MKIIA in a campaign known as 'Deuterium Tritium Experiment' (DTE1). During the DTE1 campaign the torus was fuelled with a total of 35 g of tritium, mostly by gas puffing and the amount recovered from the vessel was reprocessed and accurately measured in the Active Gas Handling System (AGHS). The AGHS measurements showed that the tritium inventory retained in the vessel was about 40% of the amount fed into machine.

After the DTE1 campaign a part (150 g) of the flakes accumulated in the inner divertor leg were collected. These flaks appeared to hold the majority of the tritium retained inside the JET vacuum vessel.

Approximately 1 g of these flakes were sent to the Tritium Laboratory Karlsruhe (TLK) to investigate their tritium thermal release behaviour, to assess the tritium content by calorimetry and to measure their BET surface.

Tritium thermal release from JET flakes collected after the DTE1 campaign was investigated by Thermal Differential Analysis (TDA). As it is evident from Fig. 1, a significant liberation of tritium starts only at temperatures above 300°C. Remarkably, even when a small specimen of flakes is heated progressively from ambient temperature up to 800°C at a rate of approx. 4 °Cmin^{-1} for a total time of nearly three hours, only 89% of the total tritium inventory is released. This conclusion was reached after carrying out a subsequent experiment where the previously baked-out specimen was fully combusted under air at 900 °C.

An analogous tritium release study with carbon dust specimens collected from TFTR is in line with the observations made with JET flakes, i.e. the maximum tritium (and deuterium) liberation rates have been found at 780 °C when the dust is subjected to a linear heating ramp of 10 °Cmin^{-1}. A comparison of tritium release rates from JET flakes and TFTR flakes showed similar thermal release behaviour in spite of rather different sample origin and different initial tritium concentration. This is an indication that the co-deposited material from both machines is chemically analogous.

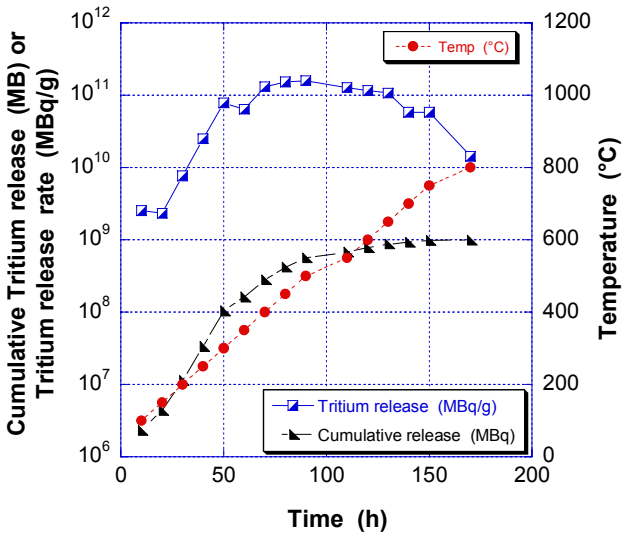

Fig. 1: Thermal release of tritium from a flake (weight 0.9 mg) retrieved from JET after the DTE1 campaign. The specimen was subjected to a linear heating ramp of 5 °Cmin^{-1}.

One conclusion from these results is that hydrogen isotopes are tenaciously held in flakes and dust from JET and TFTR, being released only when heated to very high temperatures for an extended period of time. Debris from JET and TFTR show essentially no differences in their thermal stability.

An important observation concerning the tritium content of flakes and dust retrieved from JET is that JET flakes have more than one order of magnitude higher activity than that collected from TFTR. There are two major reasons for this difference. First, the flake composition reflects the entire history of the deposit, so that the ratio of D/T depends on the ratio of D fuelling to T fuelling of the tokamak, and about one order of magnitude more tritium was used

in JET than in TFTR. Second, the ratio of carbon to total hydrogen isotope content of deposits depends on their location and temperature history. TFTR is a limiter machine, and all deposits are subject to bombardment by energetic particles from the plasma which limits the H/C ratio. Furthermore, the TFTR flakes are mostly from the sides of limiters that may reach high temperatures (>1000 °C) during plasma discharges (the H/C ratio is reduced when temperature exceeds 300 °C). Similarly, low H/C ratios are found in all deposits in the main chamber of JET. However, in JET the majority of the flakes are located in areas shadowed from all energetic particles, and the temperature is controlled by proximity to the water-cooled divertor structures. In both cases, a large initial retention of tritium during plasma operation (40% and 90% respectively) as well as a large long-term tritium retention (17% and 51% respectively) were observed.

BET surface areas of 675 m^2g^{-1} have been reported for flakes collected from the vacuum vessel of JET after the DTE1 campaign. This value is surprisingly high and should be verified by additional measurements, especially as previously measurements for a large size fraction of flakes after the Preliminary Tritium Experiment at JET (PTE) have shown a specific BET surface area of (4 ± 2) m^2g^{-1}. The latter is in line with results from TLK on PTE JET flakes (sample 3-4) haing a mass of 156 mg and giving a BET surface 7.2 m^2g^{-1}.

The three measurements performed on three samples from the 930 mg of the DTE1 flakes sent to the TLK (384 mg, 631 mg and 758 mg respectively) showed an average BET surface of (4.5 ± 0.6) m^2g^{-1}.

Staff:

N. Bekris
D. Adami
U. Besserer
L. Doerr
F. Kramer

JW1-FT-1.6
Surface and Depth Profiling of Tritium in Selected JET Tiles

Tritium [and deuterium] co-deposition with carbon in the colder remote areas of the JET vessel demobilises a substantial amount of the fuel and increases the tritium inventory of the machine. A well defined chemical composition of these co-deposits is still not available. They are reported in the literature as a carbonaceous amorphous C:Q layer (Q=H, D, or T) and incorrectly sometimes as “diamond-like films”.

In a former experimental investigation an elementary analysis of such co-deposited layers found on the JET divertor tiles, gave a D/C ratio of about 0.75. Such a high ratio can only be explained if the layers are composed of short chain aliphatic carbons not completely saturated with deuterium, i.e. carbon chains having a sp^2 hybridisation such as $C_2D_xH_y$ (x+y=4).

Previous thermo-desorption measurements on small disk specimens retrieved from the plasma exposed surface of a JET tile, had shown that under a stream of He containing 0.1% H2, tritium is released only at temperatures above 400°C, while, after heating at 1100°C full combustion measurements confirmed that there is no more tritium remaining in the sample.

To determine the chemical composition of the gaseous species released during a thermal treatment, several plasma exposed and bulk samples retrieved from some divertor tiles of JET were heated under the same experimental conditions mentioned above.

For the preparation of the samples a hollow drill was used. The cylinders obtained had a diameter of approx. 7.6 mm and a height corresponding to the thickness of the tile. From the cylindrical specimens, disks with a thickness of 1 mm were cut employing a diamond-grinding disk. Starting from the plasma exposed side of the tile the disks were numbered beginning with A1 up to AN.

The tritium release kinetics from 6 plasma exposed and bulk specimens obtained from the MKIIA CFC inner divertor tile 1IN3S1 (samples 8, 9 and 10) and from the outer divertor tile 1BN7 were examined.

The experimental set-up comprises a purge gas supply and control, a high temperature stainless steel chamber containing the sample, a reduction bed containing granulated zinc operated at approx. 390°C and an ionisation chamber for the detection of tritium. The sample chamber is heated from the outside with a controllable tubular furnace. The zinc bed converts tritiated water to molecular gaseous tritium (HT, DT, and traces of T2). The tubing downstream of the ionisation chamber is trace-heated to about 300°C. This heating minimises memory effects caused by tritiated water. The whole system is contained in a glove box except for the pure gas supply and control and a quadrupole mass spectrometer used for the analysis of the released gaseous species.

In normal operation, the sample temperature is initially increased linearly with time up to an end temperature of max. 1100°C. This temperature was then kept constant for a pre-determined time for the isothermal part of the experiment.

Applying mass spectrometry to the thermal desorption set-up allows many accurate measurements to very low partial pressures down to 10-9 Pa to be made and large spectra of gas compositions released during the thermal treatment of the sample were obtained.

Table 1: Tritium fractions liberated from the A_1 specimens of cylinders 8, 9 and 10 of tile $IN3_{S1}$ at various heating rates.

Cylinder/ specimen	Heating range in °C (heating ramp: 7°Cmin^{-1})	Fraction released (%)	Tritium released (MBqg^{-1})
$8A_1$	20 – 500	77.4	531
	20 – 1100	18.9	130
	20 – 1100	3.7	25
$9A_1$	20 – 550	89.0	848
	550 – 1100	11.0	105
$10A_1$	20 – 600	94.6	1000
	600 – 1100	5.4	57

As it is shown in table 1, during the isothermal part of the experiment, raising the final temperature from 500°C to 550°C and 600°C for the samples $8A_1$, $9A_1$ and $10A_1$ respectively, the tritium released fraction rises from 77.4% to 94.6% (see also Fig. 1).

The tritium release after a thermal treatment at 1100°C under helium containing 0.1% hydrogen shows that the highest tritium release rate is observed at about 850°C. Moreover, the combustion of carbon samples retrieved from the JET graphite tile 004/2-20 and formerly heated at 1100°C revealed that after such a thermal treatment the samples are tritium free.

The gaseous species released during the thermal treatment of such samples heated up to 1000°C are illustrated in Fig. 2.

Taking into account the fact that the masses 2 and 4 are mainly associated with the purge gas (He/H_2), only masses 16 (CH_4), 17 (CH_3D) and 18 (H_2O) are related to the samples, corresponding to methane and water. Unfortunately, all water isotopic species (mass 18 to 20) are related to the contamination of the pipes, as the Zn-bed reduces the water (if any) released by the sample, to molecular hydrogen. Very small amounts of tritiated water was also detected (mass 20).

From the present study it appears that the gas-solid reactions taking place during the thermal treatment of a carbon sample is quite complicated involving various tritiated species and other gaseous species, such as small chain hydrocarbons.

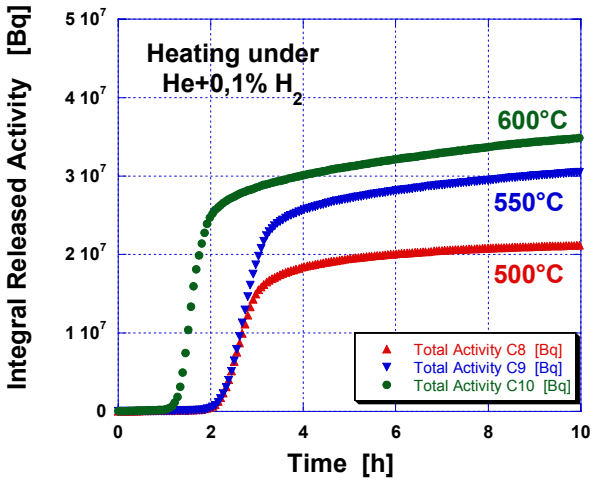

Fig. 1: Tritium released by three A_1 discs, retrieved from the $1IN3_{s1}$ JET divertor tile during a thermal treatment at various temperatures.

It is also evidenced that the co-deposited tritium is strongly bound and therefore it is necessary to heat the samples at very high temperatures (above 1000°C) to release all the contained tritium.

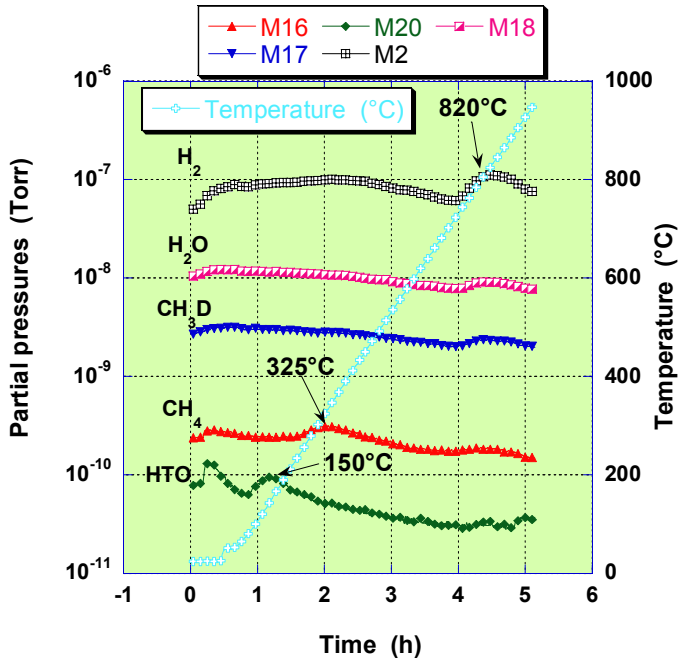

Fig. 2: Detected compounds by mass spectrometry after heating of the 1BN7 C16 A_1 sample under He containing 0.1% H_2.

Staff:

N. Bekris
U. Berndt
E. Damm
A. Erbe

JW0-FT-2.1
Water Detritiation

Introduction

A Combined Electrolysis Catalytic Exchange facility (CECE) employing a Liquid Phase Catalytic Exchange (LPCE) column for water detritiation is currently being developed at the Tritium Laboratory Karlsruhe (TLK). The so-called TRENTA water detritiation facility is needed for process performance studies to support the design of the Water Detritiation System (WDS) for JET and finally for a system at ITER.

Due to its complexity the TRENTA facility was conceived to be developed in a staged approach:

TRENTA 1 - a laboratory sized test installation employing only a LPCE column. The selection of the most suitable hydrophobic catalyst-packing combination for the LPCE column and characterisation of the separation performances under different working conditions were the first important goals. TRENTA 1 was used to compare the separation performances of various catalyst/packing mixtures by determining the deuterium transfer parameters.

TRENTA 2 - a CECE facility employing a LPCE column and solid polymer electrolysers. This facility was installed in the controlled area of TLK, and therefore was used to investigate separation performances at tritium transfer at concentrations of up to 100 $\mu Cikg^{-1}$ tritium activity in the water.

TRENTA 3 - The design and commissioning of this semi-technical scale facility at TLK to investigate the possible tritium decontamination factor with a LPCE column of 8 m length is ongoing. The facility was designed to fulfil the requirements for parametric studies of the LPCE process when the tritium contained in the liquid phase and in the gaseous phase is processed in a closed loop. An additional system devoted to oxygen purification i.e. to remove the tritium from vapour phase accompanying the oxygen stream is included as well. In these experiments the tritium activity in the water will be up to 1 $Cikg^{-1}$. The experimental results and corresponding mathematical model will be employed to design the water detritiation facility for JET.

TRENTA 4 - a complete system for tritium recovery from tritiated water at TLK. This facility will consist of the CECE, the existing Isotope Separation System at TLK - based on displacement gas chromatography (ISS-GC), and a new Cryogenic Distillation (CD) system that will enrich tritium from the activity of ~1 $CiNm^{-3}$, at the outlet of CECE to up to ~1% as required for the input feed to ISS-GC.

CECE experimental facility TRENTA at TLK

The new catalytic isotope exchange facility TRENTA, shown schematically in Figure 1 was installed in the active area of TLK in order to investigate tritium transfer from water to gas using tritiated water at a tritium activity in the range 1 $\mu Cikg^{-1}$ - 100 $\mu Cikg^{-1}$. For visual examination this facility initially employs glass columns with an active zone of about 2 m height.

There are two major topics for which the CECE facility at TLK is used for investigation:

1. *Establish the influence of deuterium transport on tritium transport when the two processes take place simultaneously*.

2. *Determine the concentration profiles along the column.* The exchange column is designed with several extraction points for both liquid and gas phases. Deuterium and

tritium distribution along the column will provide information about possible differences in the HETP along the column and also the differences in the mass transfer coefficients. The measured values of the concentrations will also be used for comparison with the predicted values from the model. In this way, the mathematical model for describing the transfer will be validated and improved.

In normal operation tritiated water is fed into the electrolyser. Deuterium and tritium enriched hydrogen coming from the electrolyser is then introduced as gaseous feed into the catalytic isotopic exchange column. The column is fed with demineralised natural water at the top, where also condensed vapours are recovered from gas phase and returned into the column. Tritium and deuterium depleted hydrogen from the top of the column is sent to stack. In the presented configuration the facility will be used for investigating the decontamination factor for tritium, and since no cryogenic distillation is currently available, no tritium recovery is possible. As a result of the experiment, a smaller amount of tritiated water at higher tritium activity will be produced.

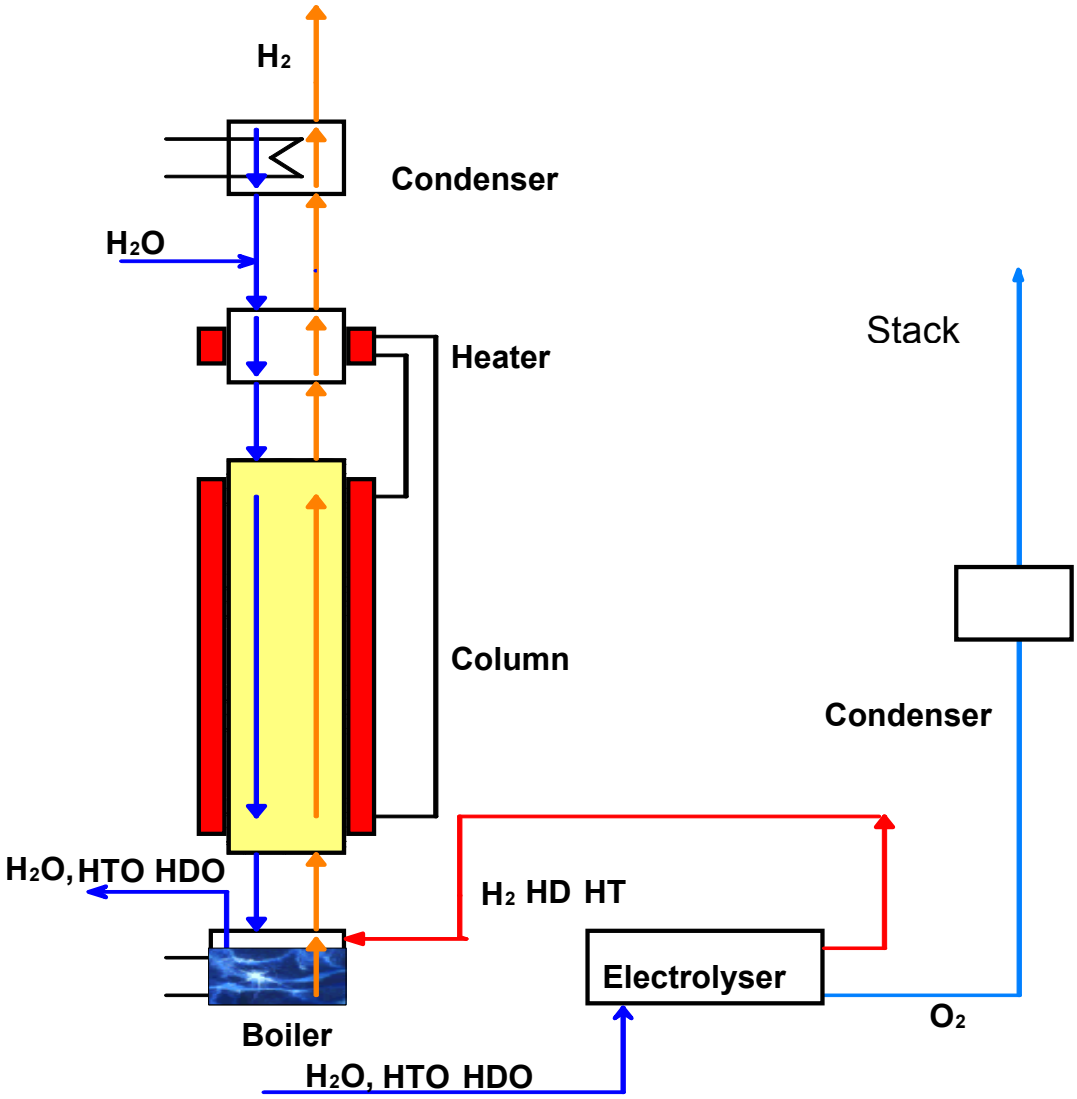

Fig. 1: Scheme of the catalytic isotope exchange facility TRENTA.

A hydrogen-explosion proof design was applied to the WDS because the electrolysers produce approximately 2 m^3h^{-1} (STP) of hydrogen which is continuously discharged from the top of the LPCE column to stack. The ventilation system of the laboratories assures an air flow rate of 58,000 m^3h^{-1} (STP). Two hydrogen sensors with visual and audio alarm were installed at the top of the WDS facility and at the highest point in the laboratory (just over the WDS facility).

Similarly to the ITER design for the Water Detritiation System, at TLK an electrolyser with a solid polymer electrolyte has been chosen.Two solid polymer electrolysers of 1 m^3h^{-1} (STP) hydrogen production with a hydrogen purity of 99.99%. have been installed and tested.

Analytic instrumentation and measurements

The analytic instrumentation for the TRENTA facility are FT-IR spectrometry for measuring the deuterium content and LSC for measuring the tritium content in aqueous flows. In the gas phase, the tritium content is measured by converting gaseous samples to water followed by LSC measurement and for the deuterium content an Omegatron mass spectrometer has been chosen.

The advantage of the Omegatron is that it can distinguish ions with very close masses, like D_2 and He or HT and D_2, as the resolution is inversely proportional to the ion mass. The Omegatron at TLK has proved to be a very useful device in qualitative analysis of tritiated gas mixtures. However, quantitative measurements on known gas mixtures have revealed several anomalies; therefore a calibration procedure had to be developed. Pure H_2, D_2, N_2 and He and the compositions of several mixtures were investigated using the Omegatron and Quadrupole mass spectrometers. Different mixtures prepared by the partial pressure method, chemical equilibrated, have been intensively analysed with respect to the parameter settings of the Omegatron.

Two effects were found to influence the quantitative measurements and therefore have been investigated:

a) An important level of ion-molecule reactions products in the Omegatron was found. Ions like H_3^+,D_3^+, D_2H^+ were found and their contribution to the total signal was considered. For the special case of H_3^+, at low values of deuterium content (1000 ppm to 5%at.) the peaks of HD^+ and H_3^+ can not be clearly resolved. The square dependence on partial pressure of the H_3^+ signal as proved in Quadrupole mass spectrometers was not found in the pressure range around 10^{-7} mbar, at which the Omegatron is operated. Hence a different procedure of subtracting the contribution of H_3^+ from the total signal of mass 3 was implemented.

b) The response of the Exkoll type Bayard Alpert (ionisation) gauge used in the Omegatron is gas dependent and it was necessary to be calibrated against an absolute gauge for various gases.

Considering the necessity of simultaneous withdrawing samples along the column, a method of transferring the gas samples into the Omegatron glove box was realised.

Tests of TRENTA

The first tests on the solid polymer electrolyser had in view to test the electrolyser functioning, to establish the enrichment factor for deuterium and to determine the time necessary until steady state is reached. Approximately 100 hours were necessary until steady state was reached. The corresponding steady state value for the deuterium enrichment factor was between 2.3 and 2.6.

Different components of the CECE facility were tested separately to determine the performances of different packings (4 types) investigated in the LPCE column and catalyst materials (3 types) investigated in the VPCE column. The tests had as goal to determine the optimum catalyst/packing ratio for a higher decontamination factor.

With aid of mass transfer coefficients determined for packings and catalyst, the numerical model allows to compute the optimum ratio packing/catalyst. Two types of packing-catalyst mixtures were used to fill in the LPCE column in the respective determined ratios and were initially investigated at deuterium transfer. A column of 90 cm length with an active length of 70 cm and diameter of 55 cm was used for these experiments. The separation performances have been measured at 60°C. In Table 1 the experimental data are presented, type I uses the DX Sulzer packing, type II uses the DX* Sulzer packing. The decontamination factor was computed as the ratio between the deuterium concentration in water at the top to the deuterium concentration in water at the bottom of the column. The catalysts used have also a slightly difference in the composition and dimensions.

Table 1: Separation performances of two types of packings.

Column	Molar ratio G/L	Deuterium concentrations at the bottom (%)		Deuterium concentrations at the top (%)		Decontamination factor
		Liquid (HDO)	Gas (HD)	Vapours (HDO)	Gas (HD)	
Type I	2.7	2.97	0.75	0.43	0.28	2.68
Type II	2.7	3.64	0.79	0.51	0.21	3.76

Conclusions

A broad series of tests on various packings and catalysts have been made in order to increase the LPCE column performance. Tests will continue with tritium with activity up to 1 $Cikg^{-1}$ and to investigate simultaneous tritium and deuterium transfer.

The design and commissioning of TRENTA 3 semi-technical scale facility at TLK to investigate the achievable tritium decontamination factor along a LPCE column of 8 m length are ongoing. The LPCE column is designed with extracting points for gas and liquid samples and will allow validating and improving the mathematical model for a large-scale WDS design.

Staff:

I. Cristescu
Ioana-R. Cristescu
M. Glugla
L. Dörr
S. Welte
Ch. Caldwell-Nichols
P. Schäfer
G. Hellriegel

JW1-FT-6.1
Impact of Tritium on the Performance of a Prototype Cryosorption Pumping Panel

1. Objectives

This task is an essential complement to the parallel assessment of the pump performance of the ITER torus model cryopump (Task TW1-TTF/VP11), where the tritium fractions have been replaced by deuterium. The central objective of this task, which will be performed within the Task Force Fusion Technology at JET [1], is to study the interaction of tritium and tritiated gas mixtures with the panel, in terms of pumping performance, desorption characteristics and structural influences. The existing knowledge in this field is limited to qualitative results gained in other fusion devices and only one small scale phenomenological experiment. Together with the existing data for protium and deuterium, a sound assessment of any isotopic effect is aimed at. The understanding of the pumping mechanism of tritiated gases, which is expected from this experiment, is needed to develop advanced regeneration procedures for cryosorption panels. This experiment is a benchmark test which would reveal any showstoppers to the ITER cryopumping concept arising from tritium interaction, which is the only field not having been fully covered yet.

Fig 1: Manufacturing steps for the cryopanels: (1) blank panel, (2) attachment of resistance heaters, (3) copper coating, (4) charcoal bonding, (5) equipment of cryotemperature sensors, (6) thermal cycling in liquid nitrogen for quality control.

2. Completion of the manufacturing of the test assembly

Within this task, a Prototype Cryosorption Pump (PCP) was designed, manufactured and installed into an existing cryogenic forevacuum (CF) module of the Active Gas Handling System (AGHS) at JET. With respect to the outer dimensions, the PCP is a complete copy of the existing ACP pump, which will be re-installed in the CF module after completion of the

task. However, the interior parts are designed completely different to provide for a cryosorption pumping effect, whereas the ACP is working on cryocondensation at lower temperatures. The total manufacturing process was shared among two main parties. FZK took over the responsibility for the cryopanel arrangement itself, including all sensors (temperature and pressure), cabling and internal wiring, as shown in Figure 1. The panel set-up exactly meets the ITER design requirements and the test results are, therefore, fully representative. The manufacturing of the PCP interior parts and the outer vessel, especially the welding work, was given to an external vacuum company, see Figure 2. The acceptance tests at the company´s premises were performed by JET approved Third Party inspectors at early April; the PCP itself arrived at JET just before Easter holiday. Figure 3 shows the completed PCP. The whole manufacturing process was accompanied with detailed welding and quality plans to ensure compliance with JET requirements.

3. Installation at JET

During the May-August intervention period, the CF module was prepared for opening by extensive purging with deuterium and air to achieve sufficiently low tritium contamination, as both primary and secondary containment have to be breached for the installation of the PCP. Followed by Argon blanketing of all process volumes inside the module and using plastic isolation containments, the ACP was removed and bagged off and the PCP fitted into the open space. In the next step, it was completely connected (sensors, piping) and successfully leak-tested. The internal pipework had to be adapted, which was prepared prior to the installation procedure, such that the incoming gas can be taken from two sources. This is to reflect the two-stage strategy foreseen for testing the pump. In the first stage, the PCP will be operated within the JET trace tritium campaign (TTE) directly on the main torus volume. In the second stage, PCP parametric tests will be performed in which the gas is supplied at pre-defined composition from an external reservoir. This latter campaign is most relevant to

Fig. 2: Complete view and manufacturing details (internal and external feedthroughs for heaters and temperature sensors) of the PCP interior system.

obtain the underlying data needed to design the regeneration and pumping parameters for tritium operation of the ITER torus cryopump, as described in detail in [2].

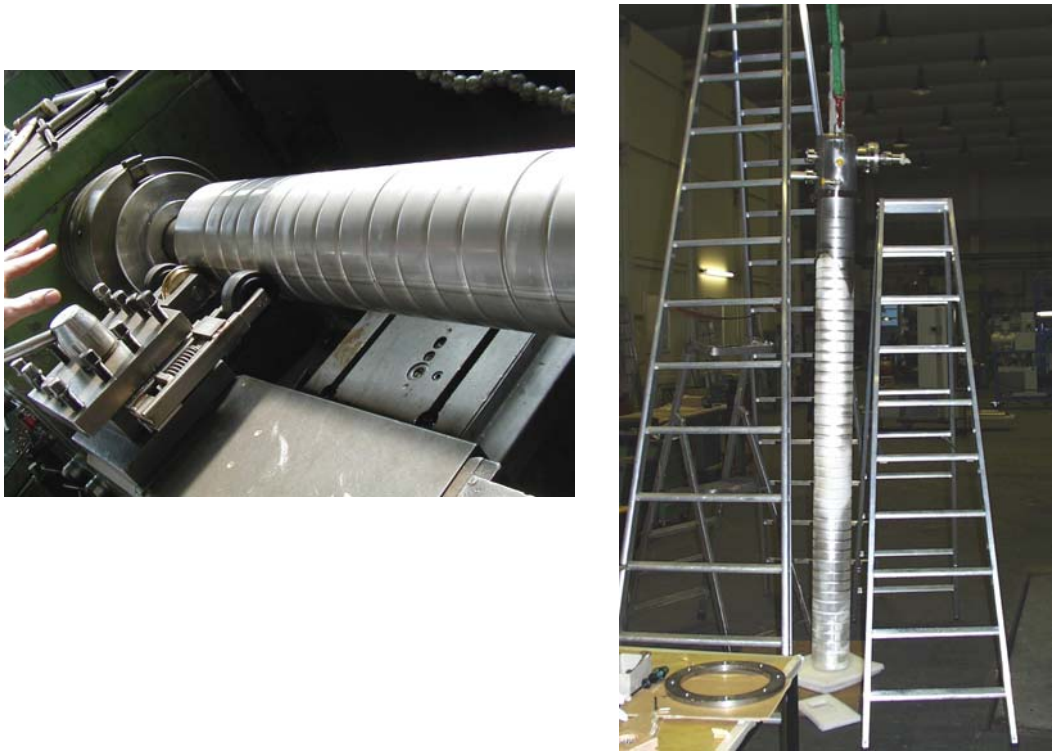

Fig. 3: Stiffening corrugation work at the lower container and fully assembled PCP, as shipped to JET.

The second test campaign asks for a control device to arrange for a pre-defined gas flow from a 100 l reservoir into the pump. Originally it was agreed to use a pneumatically controlled small diameter valve, especially upgraded to application in AGHS by means of a special bellow. The idea was to use this valve as a flow control valve in a feedback control loop – adjusted by the pneumatic pressure level. However, it had to be calibrated for outside vacuum conditions before the installation in module 5. For this purpose, such a valve was shipped to FZK and investigated with respect to its flow and control characteristics. Unfortunately, it turned out that this valve has virtually no control behaviour. Moreover, the flow rate of the opened valve was by a factor of 10 too high. To be able to operate with appropriate flow rate and still use the existing JET-approved valve (then at fully opened condition), it was agreed to operate it together with a fixed orifice at choked flow. The latter shall be designed such that the resulting flow rate becomes of ITER-relevant magnitude, i.e. about 10 (mbar·l)/s. However, at choked flow, the flow rate is proportional to the forepressure, which therefore must also be set to a pre-defined value. Due to the valve characteristics, the flow rate will become smaller with increasing dosage time because of the pressure decrease in the reservoir vessel. To minimize this effect, the forepressure should be chosen to be high. On the other hand, tests with high tritium content shall be performed, thus asking for moderate inventories in the vessel. As a compromise, it was agreed to limit the maximum tritium inventory in the reservoir to 5 g (approximately 200 mbar filling pressure with pure tritium at ambient temperature). The valve was tested in combination with different orifices to define the most suitable diameter. The optimised combination included a 0.35 mm diameter orifice and a 10 micron filter, see Figure 4, which was then shipped back to JET and installed during PCP installation.

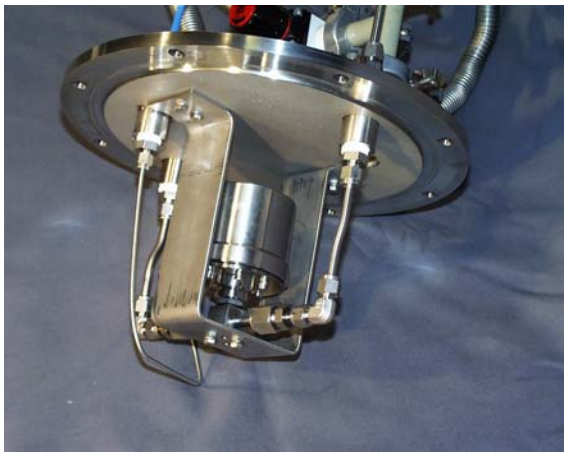

Fig. 4: Calibrated JET-approved (valve+orifice) device for flow control.

To replicate ITER-relevant cryogenic sorption conditions, it was agreed to install an upgraded cryosupply system for the PCP, which was designed to provide higher flow rates of liquid helium at the ITER relevant temperature of 4.2-4.5 K; the existing system supplies helium under reduced pressure at boiling temperatures between 3.4 and 3.8 K, thus leading to condensation of the hydrogen isotopes, which is not ITER–relevant. Due to time conflicts with the recommissioning of the overall AGHS cryogenic plant, which has to supply in parallel several CF modules under TTE, the installation of the upgraded PCP cryosupply system could not be completed within the time plan. In addition, some electrical and data acquisition and storage issues also still have to be completed.

For this reason will the PCP not be operated directly from the beginning of the TTE. It is planned to integrate the PCP still within TTE, but only in connection with the existing cryosupply. Emphasis of this task will therefore be laid on the separate parametric test campaign after TTE. It is planned to conduct this test programme relatively close to the end of TTE, preferably to finish it still this year. A time slot in the Beryllium Handling Facility at JET for dismantling and cutting the pump interior parts has already been allocated for mid 2004.

Staff:

Chr. Day
H. Jensen
P. Pfeil
R. Simon
D. Zimmerlin

Literature.

[1] R. Lässer, N. Bekris, A.C. Bell, C. Caldwell-Nichols, I. Cristescu, S. Ciattaglia, P. Coad, Chr. Day, M. Glugla, J. Likonen, D.K. Murdoch, S. Rosanvallon, F. Scaffidi-Argentina, Tritium related studies at the JET facilities, Fusion Engineering and Design 69 (2003) 1-4, 75-80.

[2] Chr. Day, D. Brennan, H.S. Jensen, A. Mack, A large scale cryopanel test arrangement for tritium pumping, Fusion Engineering and Design 69 (2003) 1-4, 97-102.

JW2-FT-2.8
Detritiation and Deactivation of Tritium Storage Beds

Following on from the experiments made during 2002 on the PETRA ZrCo getter bed, further work was performed to determine why the tritium activity measured during the oxidation of the getter bed disappeared during the later stages of the experiment. The gas chromatograph used for the measurement cannot detect water and as the hydrocarbons and tritium disappeared in an oxygen atmosphere, the production of water was strongly suspected.

A small molecular sieve bed was manufactured which was placed into the gas circuit of the oxidising loop. This was then removed and measured in a calorimeter where 7.7 TBq (210 Ci) of tritium was found. This meant that the tritium and tritiated hydrocarbons had been oxidised, but more importantly the ZrCo getter material had retained a lot more tritium than had previously been thought despite being repeatedly isotopically swamped before the oxidation process. This will have implications for not only the disposal of ITER getter beds but also their operation if ZrCo is chosen as the getter material. However it is clear that oxidation is a very effective method of deactivation.

The bed has been subject to further deactivation processes by isotopic swamping of the bed and the vacuum interspace and finally pumped out to high vacuum whilst at high temperature to remove as much as possible of the remaining tritium that can be readily removed.

This task is finished and the final report has been accepted by the Fusion Technology Task Force at EFDA-JET.

Staff:

Ch. Caldwell-Nichols

JW2-FT-2.9
Tritium Removal from JET Tiles

The accumulation of tritium on the surface and in the bulk of the divertor carbon target of the International Thermonuclear Experimental Reactor (ITER) is a very important issue not only from the point of view of fuelling but also for radiological and safety reasons. Therefore detritiation of these specific divertor components and more generally of Plasma Facing Components (PFC's) of tritium burning machines will play an increasingly important role in the future development of fusion. For graphite tiles it is important to develop a technology for their detritiation for waste conditioning and disposal. For practical and economic reasons procedures should aim at producing tiles conditioned to the point that they fall into the category of low level waste (LLW), in UK this is presently specified to be less than 12 $MBqkg^{-1}$.

The detritiation concept TIDE (Tritium Decontamination Facility) presently in operation at TLK basically exploits very rapid heating of carbon tile surfaces using the Radio-Frequency (RF) induction heating. The high frequency power is supplied by a 5 kW industrial generator with an operating frequency of 200 kHz. Fig. 1 shows the experimental set-up in TLK. The tiles are enclosed and heat-treated in a specially designed outer containment made from stainless steal. During the preliminary test this containment reached temperatures as high as 120°C while the tile's temperature was about 800°C. To avoid excessive heating of this containment the power generator is shut down when the temperature of the stainless steel containment reaches 160°C, measured by a thermocouple attached to the containment. In the unlikely event of a pressure excursion inside of the stainless steel containment a pressure relief valve adjusted to the pressure of 1.5 bar absolute is fitted and vents the excess pressure into the glove box.

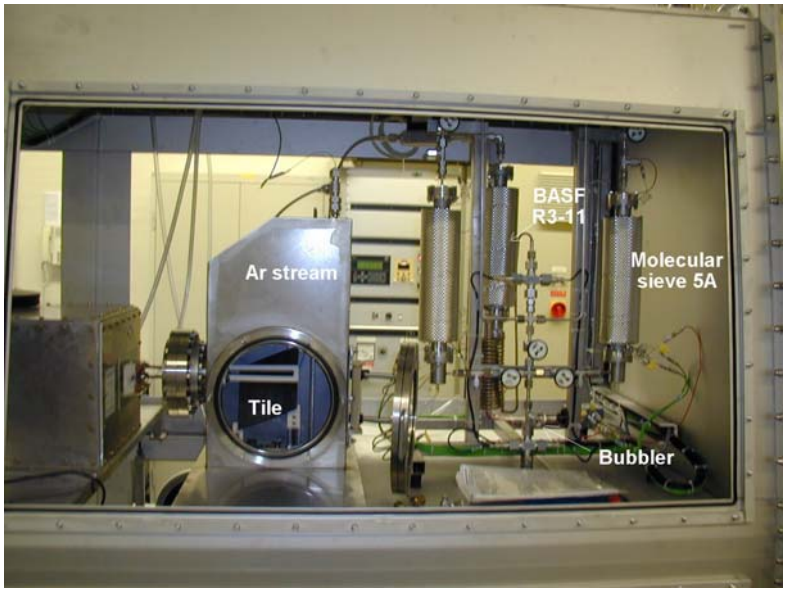

Fig. 1: The TIDE facility as it is in the TLK.

An accurate method to measure the tritium content of plasma facing components (graphite, or CFC tiles) before and after detritiation, is calorimetry. With this non-destructive technique very low detection limits can be achieved for the measurement of total tritium in the sample regardless of its chemical form. The calorimetric technique measures the heat resulting from beta decay of tritium and is completely independent of the chemical form in which the tritium is present. The energy of the beta particles of tritium is fully absorbed by the measuring vessel of the calorimeter. Any exothermic or endothermic reactions taking place inside of the vessel containing the sample, i.e. oxidation, adsorption or de-sorption processes, will have a bearing on the results and need to be taken into account, especially when low tritium inventories are being analysed. At very low tritium inventories thermal equilibrium is attained in the calorimeter only after more than 100 hours.

A prototype precision Inertial Guidance Vacuum Calorimeter (IGC-V) delivered during April/Mai 2003 with a total sample volume of 20 l is presently in operation at TLK. The calorimeter was manufactured by AS Scientific Products Ltd., England. Temperature

stabilisation takes place by an inertial feedback control providing a temperature stability to ± 1x10^{-7}K. The detection limit of the instrument given by the manufacturer is about 5 μW (equivalent to about 5.5 GBq or ≈ 0.15 Ci).

Prior to their detritiation, two JET divertor tiles (1IN3 and 1BN4) were introduced into the new IGC-V and their tritium activity was assessed between two baseline measurements. As it is illustrated in Fig. 2, after 150 hours of measurement time the total tritium content for both tiles was evaluated to be about 4 Ci.

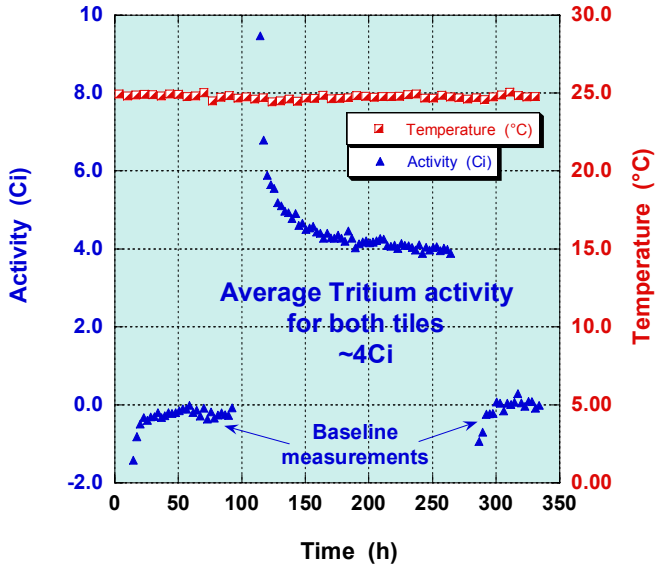

Fig. 2: Total tritium content for two complete JET divertor tiles; 1IN3 and 1BN4.

In order to fit into the containment of the TIDE Radio-Frequency (RF) detritiation process, the two tiles are each cut in two before thermally treated by RF. Tritium concentration profiles in JET tiles before detritiation were already determined and after the RF treatment cylindrical specimens will be drilled obtained using a hollow drill and disks will be cut from the obtained cylinders. The tritium measurement will be performed as usual by full combustion together with liquid scintillation counting. In this way reliable surface and depth profiles of tritium can be obtained. This data will allow us to evaluate the efficiency of the RF detritiation process.

Staff:

N. Bekris
U. Berndt
U. Besserer
H. Dittrich
L. Doerr

JW2-FT-5.5
Activation and Shutdown Dose Rate Calculations for JET

In the frame of the European Fusion Programme, FZK has developed the rigorous 2-step (R2S) system for the calculation of shutdown dose rate distributions in full three-dimensional geometry [1]. The system is based on the use of the Monte Carlo code MCNP [2] for the transport calculations (neutron and decay gammas) and the FISPACT [3] inventory code for the activation calculations with a suitable coupling scheme for the automated routing of decay gamma source distributions and neutron flux spectra. The decay gamma source distribution is sampled in a source routine linked to MCNP. This enables to conduct shut-down dose rate analyses for large and complex devices such as ITER or JET.

The R2S system had been previously applied to shut down dose rate analyses of the ITER mid-plane maintenance port [4]. Validation was achieved against the results of an irradiation experiment on a ITER shield mock-up [5]. The objective of JET FT Task JW2-5.5 was to apply the R2S system to the JET machine to demonstrate its applicability and suitability for shutdown dose rate calculations of an existing experimental fusion device [6]. As part of Task JW2-5.5, comparison calculations were performed by ENEA Frascati [7] using another approach for 3D shut-down dose rate calculations, the so-called direct 1-step (D1S) method. According to the task specifications, shut down dose rates were to be calculated and compared for five detector locations using the MCNP model of JET octant 5 provided by UKAEA Culham.

A two step approach was followed at FZK to obtain a sufficient accuracy for the dose rates calculated by the R2S system. In the first step the dose rates were calculated with no changes applied to the geometry model so as to identify the material cells which contribute significantly to the shutdown dose rate. In the second step these material cells were segmented in radial, poloidal and toroidal direction to provide a better spatial resolution of the neutron flux and, in effect, the decay gamma source distribution. The number of material cells increased in this way from 383 to 1030. The neutron flux spectra were then calculated for all material cells in 11 separate Monte Carlo runs with weight windows optimised for the different scoring regions. These calculations were performed on the HPC Linux cluster with MCNP running in the parallel mode under PVM (Parallel Virtual Machine). FISPACT inventory calculations and MCNP transport calculations of the decay gamma radiation were finally performed for the refined models assuming a representative JET irradiation history with a total neutron production of $2.4 \cdot 1019$ and decay times between 1 hour and 1 year. The decay photon spectra were calculated at the specified five detector locations by applying the MCNP track length estimator. The resulting dose rates were obtained by making use of the ANSI/ANS-6.1.1-1977 photon flux-to-dose rate conversion factors.

The shutdown dose rates calculated for the five detector positions are displayed in Figure 1 as function of the decay time after the last plasma shot. At positions D1, D2 and D4 inside the JET machine, the shutdown dose rates are mainly fed by decay gammas from the poloidal limiters and the vacuum vessel made of Inconel. This applies also to the dose rate for position D3 on the wall opposite the main horizontal wall with a direct view to the vacuum chamber. Main contributor to the shut-down dose rate at short decay times (few hours) is 56Mn generated through the 56Fe (n,p) 56Mn reaction. 57Ni , generated through the 58Ni(n,2n) 57Ni reaction becomes dominant afterwards, while 58Co, produced through the 58Ni (n,p) 58Co reaction dominates the shut-down dose rate for decay times larger than a few days.

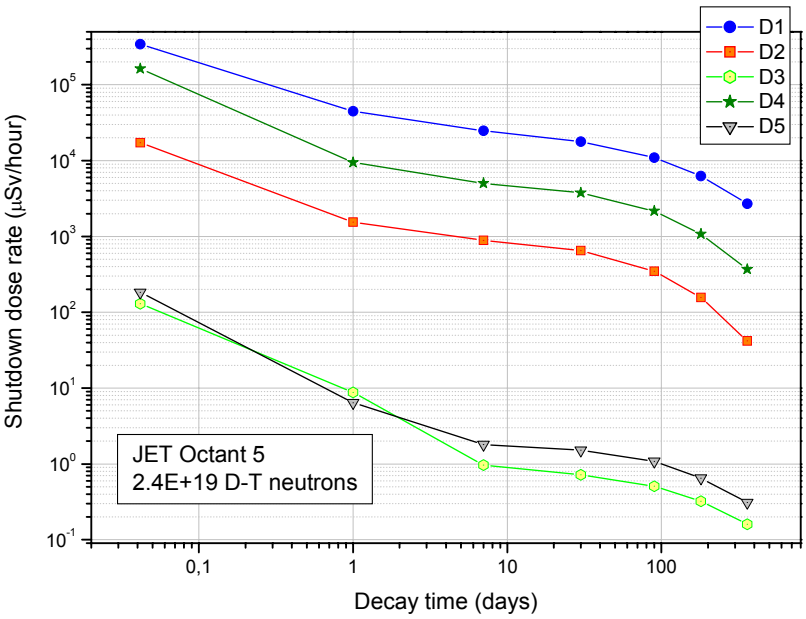

Fig. 1: JET shutdown dose rates calculated by the R2S procedure for the five detector positions as function of the decay time after the last shot.

Comparison calculations were performed by ENEA Frascati using the direct 1-step (D1S) method where it assumed that a radioactive nuclide generated during irradiation spontaneously emits the associated decay gammas. Neutron and decay gamma transport then can be treated in one single Monte Carlo calculation run. A modified version of the MCNP code is required to this end with special cross-section data to describe the generation of the radioactive nuclides along with the associated decay photon spectra. As no activation calculation is performed, nuclide specific time-dependent adjustment factors have to be applied to account for the proper decay rate of the considered radioactive nuclide.

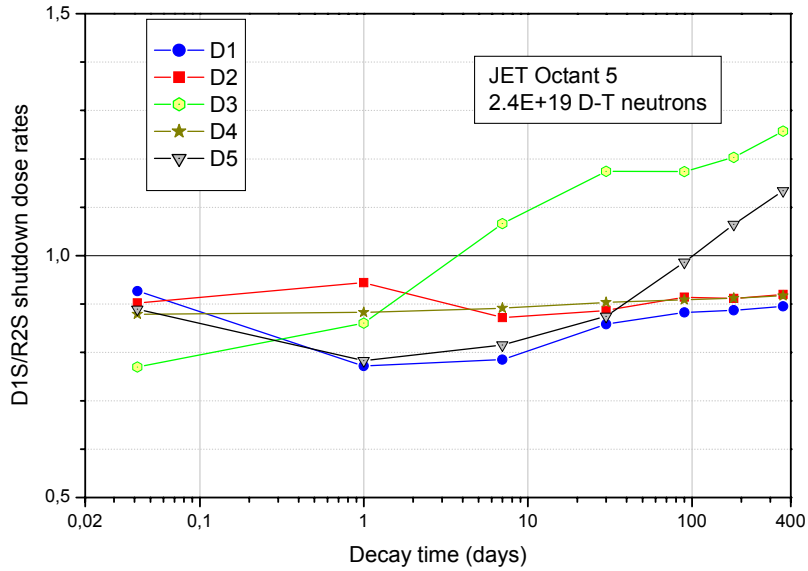

Fig. 2: Ratio D1S/R2S of the shutdown dose rates calculated by the D1S (ENEA) and R2S procedures (FZK) for the five detector positions as function of the decay time.

Figure 2 displays the ratio D1S/R2S of shut-down dose rates calculated by the D1S and R2S methods for the five detector positions in JET octant 5. Depending on the considered decay times and the detectors considered, the R2S and D1S calculation results agree within ± 25 %. This agreement is considered satisfactory taking into account the very different computational approaches. A comparison of D1S and R2S results to dose rate measurements available from the JET D-T campaign is thus required to evaluate the prediction capabilities of the two approaches for JET shut-down dose rate calculations. This comparison is the subject of the running follow-up task JW3- FT-5.8.

Staff:

Y. Chen
U. Fischer
P. Pereslavtsev

Literature:

[1] Y. Chen, U. Fischer, H. Tsige-Tamirat, Rigorous MCNP Based Shutdown Dose Rate Calculations, Forschungszentrum Karlsruhe, Internal Report, Januar 2001

[2] J.F. Briesmeister (ed.), MCNP - A General Monte Carlo N-Particle Transport Code, Version 4C, Los Alamos National Laboratory, Report LA-13709-M, April 2000.

[3] R. A. Forrest, J-Ch. Sublet, “FISPACT-99: User manual”, Report UKAEA FUS 407, December 1998

[4] Y. Chen, U. Fischer, ITER-FEAT Shutdown Dose Rate Analysis by Rigorous Method, Forschungszentrum Karlsruhe, Internal Report, September 2001

[5] Y. Chen, U. Fischer, Rigorous MCNP Based Shutdown Dose rate Calculations: Computational Scheme, Verification Calculations and Application to ITER, Fus. Eng. Design 63-64 (2002), 107-114.

[6] U. Fischer, P. Pereslavtsev, Activation and Shutdown Dose Rate Calculations for JET, Forschungszentrum Karlsruhe, Internal Report, May 2003

[7] P. Batistoni, L. Petrizzi, Activation and Shutdown Dose Rate Calculations for JET, ENEA Frascati, Report FUS-TN-JET-R-001, May 2003

JW3-FT-2.13
Studies about the Performances and Required Improvements to Use a Solid Polymer Electrolyser in a CECE Process for Water Detritiation

The most suitable process for water detritiation and tritium recovery is the well known CECE process, a combination of electrolysis and catalytic exchange of hydrogen isotopes e.g. in a Liquid Phase Catalytic Exchange (LPCE) column for tritium recovery from hydrogen, followed by a cryogenic distillation system for final tritium enrichment.

Before a full scale water detritiation plant for JET and ITER can be designed, laboratory experiments to investigate the separation performances of different catalysts/packing mixtures and the electrolysis unit have to be carried out.

The so-called TRENTA water detritiation facility from TLK is needed for process performance studies to support the design of the WDS system for JET and finally for ITER. The TRENTA facility was conceived to be developed in staged approach allowing performance tests of key components in the water detritiation process.

Similarly to the ITER design for the Water Detritiation System, in the experimental facility of TLK with the aim to support the WDS design for JET an electrolyser based on solid polymer electrolyte has been chosen. This type was preferred instead of the classical one using KOH electrolyte due to the following main advantages:

- it avoids the K^+ ions transportation into the packing and catalyst material that fills the catalytic exchange column;
- it has a lower inventory of tritiated water;.
- no request to detritiate the waste electrolyte;

In the present report the correlation between the water hold-up of the electrolysis unit and the enrichment factor for an electrolyser based on solid polymer electrolyte have been investigated in detail with respect to deuterium.

In order to extend the investigation related to the tritium enrichment factor, which at the time being may be only theoretically evaluated, the necessary improvements for a solid polymer electrolyser to achieve tritium compatibility have been identified.

A list of the main components that have to be improved and also an appropriate configuration of the electrolyser based on the particular requirements for the combination with the LPCE and further with the Cryogenic Distillation is presented as well.

Beside the activity to select the most suitable hydrophobic catalyst-packing combination for the LPCE column and to determine the separation performances under different working conditions the detailed investigation of the behaviour of the solid polymer membrane under tritiated water exposure and the tritium inventory in the electrolysis process is a very important issue.

In order to evaluate the life time under tritiated water exposure of a solid polymer membrane two methods are under development:

- To compare the mechanical properties as tensile strength and elongation for a solid polymer membrane before and after exposure to highly tritiated water: 500 $Cikg^{-1}$ and 5 000 $Cikg^{-1}$;

– To investigate the behavior of a small electrolyser cell based on a solid polymer membrane during a long time functioning with tritiated water with tritium activity increasing in several steps from 1 Cikg^{-1} to 100 Cikg^{-1}.

Fig. 1: Experomental rig for endurance testing of a small electrolyser cell.

Staff:

I. Cristescu
R. Wagner
S. Welte

JW3-FT-5.6
CAD Interface for MCNP

The overall objective is to develop an interface between a Computer Aided Design (CAD) system and a Monte Carlo (MC) particle transport code in order to access the geometric and topological data of manifold solids in CAD systems and construct from it a geometry representation appropriate for MC particle transport. The near-term goal of task JW3-FT-5.6 is to enable the automated processing of CAD generated data and their conversion into surface data as required by the MCNP Monte Carlo code. A full MCNP geometry model is then constructed in the traditional way by defining the geometry cells through Boolean operations on the automatically generated surface data. The long-term goal, however, is to develop the MCNP geometry model completely by a CAD system such as CATIA and then covert it automatically to an MCNP input deck.

The geometry needed for the MC particle transport simulation is a decomposition of the problem space into a finite collection of disjoint regions whose union is the problem space. It is usually represented as a Boolean form of primitive solids or algebraic half-spaces. In CAD systems, a shape of a rigid solid object (manifold solids) is described as a compact and regular point set in 3D-space either by defining its oriented boundary (boundary representation, B-rep) or by Boolean forms using regular half-spaces (constructive solid geometry, CSG).

The goal of constructing a geometry model for MCNP by using the geometric and topological data of B-rep solids requires to access to the CAD data and convert them into a representation appropriate for MCNP. While the first step is merely technical, the second step requires a suitable conversion algorithm. The development of such an algorithm has been a major task in the past.

The conversion algorithm can be roughly described by the following steps:

- Traverse the data structure of a solid and extract the boundary supports. These are the surfaces defining the boundary.

- Perform a sign constant decomposition of the solid by the boundary supports. This means to construct basic semi-algebraic sets.

- Determine if the constructed semi-algebraic sets represent the solid. If this is not the case enlarge the boundary support set until equality is achieved.

The theoretical feasibility of the algorithm was shown by methods of semi-algebraic geometry [1].

The interface programme which has been developed for the (automated) conversion of the CAD data into the semi-algebraic surface representation of MCNP is based on a software design integrating a CAD kernel, which is C++ class library, a C++ graphical user interface (GUI) application framework and the conversion algorithm. The CAD kernel provides core data, structures and algorithms. The design approach is based on object oriented design patterns. The so-called Model-View-Controller (MVC) pattern enables to divide the interface into mainly three components. The model contains the core functionality and data, views display information to the user, and the controller handles user operations.

The following list summarizes the implementation details:

- A framework-like library in front of the CAD kernel realizes MVC.

- Core data structures are supplied by the CAD kernel.

- The interface application integrates this library with the GUI frame work.
- Implementation of conversion algorithm specific data structures.
- Basic user operations with undo-redo support; creation, selection, modification, projection, zooming, panning etc.
- File exchange interface for standard files STEP, IGES, and native file formats.
- Externally the MCNP output is represented as a file exchange interface.

Most parts of the software have been implemented and are partially functional in a test version. Integration, testing, and debugging are major current activities in the frame of the running task JW3-FT-5.6.

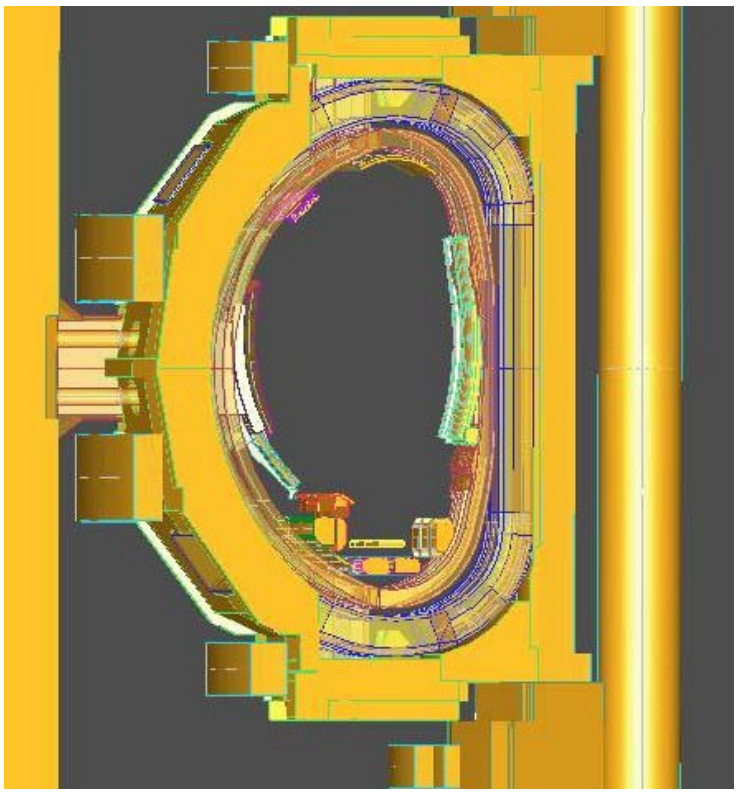

Fig. 1: JET octant 3 model visualised by the interface programme

CAD files of JET octant 3 generated by CATIA V5 in STEP format AP-214 at UKAEA Culham were used for first tests of the interface programme. The analysis of the four test files including parts of the outer vessel, coils, tiles and dump plates showed that most parts of the CAD model meet the requirements for the use with the interface and subsequent MCNP calculations. In a second step, a complete set of 31 STEP files describing the full JET octant 3 was provided by UKAEA Culham. Fig.1 displays a 3D view of the model as visualized by the interface programme. The analysis of the STEPS data files by the interface programme showed that another iteration step is required to remove non analytic surfaces and curves in some of the models and reduce the complexity of the geometry.

Staff:

U. Fischer
H. Tsige-Tamirat

Literature:

[1] H. Tsige-Tamirat, On the use of CAD geometry for Monte Carlo particle transport, Proc. of the Monte Carlo 2000 conference, Lisbon 23-26 October 2000, p. 511

JW3-FT-5.8
Validation of Shutdown Dose Rate Calculations for JET

The objective of Task JW3-FT-5.8 is to validate the system of codes, data and interfaces for the automated calculation of 3D shut-down dose rate calculations through the comparison with experimental results obtained at JET.

By making use of the R2S code system, developed in the frame of Task JW2-FT-5.5 for automated shut-down dose rate calculations of JET [1], and a suitable JET MCNP model, full 3D shut-down dose rate calculations are performed for several locations inside the vessel and the torus hall where radiation dose measurements are available from the DTE1 experimental D-T campaign conducted at JET in 1997. Similarly, the D1S code system [2] is used by ENEA Frascati for comparison calculations. The results of R2S and D1S shutdown dose rate calculations are to be checked against the available dose measurements in a blind comparison.

The information and data required to perform the shut-down dose rate calculations for Task JW3-FT-5.8 were provided by UKAEA Culham including the MCNP model of JET for the DTE1 campaign, specifications of the dose measurements and the associated irradiation data.

In several steps, the JET DTE1 model was updated at FZK to comply with the requirements for the calculations with the R2S code system. In a preparatory step, preliminary shutdown dose rate calculations were performed using the irradiation history, the neutron spectra and decay gamma source intensities as available from the calculations performed previously for Task JW2-FT-5.5 [1]. Dedicated importance sample techniques were applied to obtain the dose rates at the new detector positions as specified by UKAEA. The results of these calculations enabled to identify the decay gamma source cells contributing significantly to the shut-down dose at the specified positions. In the next step, a fine spatial segmentation was applied to these geometry cells. This is required with the R2S-approach to achieve a sufficiently high accuracy when calculating the neutron flux and decay gamma source distribution. Thus about 800 new geometry cells were generated, increasing the total number of geometry cells of the DTE1 MCNP model to about 1800.

Tab. 1: Main computation features of MCNP neutron transport calculation for neutron flux distribution.

	Detector 1	Detector 2	Detector 3	Detector 4
DT – plasma				
Number of source neutron histories [10^6]	200	500	200	200
CPU time [hours]	270	700	570	500
Statistical error	< 0.01 %	< 1%	< 0.1 %	< 0.1%
DD – plasma				
Number of source neutron histories [10^6]	200	500	200	200
CPU time [hours]	200	600	500	400
Statistical error	< 0.01 %	< 1%	< 0.1 %	< 0.1%

MCNP transport calculations were then performed to obtain the neutron flux distribution for the refined geometry model. Separate MCNP runs were performed for each of the four detectors by optimising the weight window set for each run. In this way the highest statistical accuracy at the lowest computation effort was achieved. Since JET was operated with a D-D plasma prior to the D-T campaign, the activation of the machine and thus the shut-down dose could be affected. Therefore, separate neutron transport calculations were performed with a D-D and a D-T plasma source to take into account the different sources in the

following activation calculation. Table 1 summarises the main features of the Monte Carlo runs of neutron transport calculations.

Staff:

U. Fischer
P. Pereslavtsev

Literature:

[1] U. Fischer, P. Pereslavtsev, “Activation and Shutdown Dose Rate Calculations for JET”, Forschungszentrum Karlsruhe, Interner Bericht, May 2003

[2] P. Batistoni, L. Petrizzi, “Activation and Shutdown Dose Rate Calculations for JET”, ENEA Frascati, Report FUS-TN-JET-R-001, May 2003

JW3-FT-5.14
Simulation of Tritium Spreading in Controlled Areas after a Tritium Release

The knowledge on tritium distribution in the confinement area, and the tritium removal rate is useful to determine the removal time for existing ventilation conditions in a tritium handling room for the case of a tritium leak or in the process of design suitable detritiation systems and effective monitor locations in a facility. At the Tritium Process Laboratory (TPL) at Japan Atomic Energy Research Institute (JAERI), a 12 m^3 airtight vessel called Caisson was installed to collect systematic data related to tritium behaviour in a ventilated area. The main goal of the present task is to develop a model to simulate tritium behaviour after an accidental tritium release in a confined area, the model is currently under validation using the existing experimental data from TPL.

Description of the experimental set-up – CATS at TPL

The licensed maximum tritium release amount in the Caisson is 38 GBq (1 Ci) per each experiment. The connection between the Caisson and the ventilation system is realised through a supply duct and an exhaust duct. In each experiment, tritium was diluted with nitrogen and filled in a small stainless steel container, that can be connected with two different locations within the Caisson, one in a corner and the other in the centre. Tritium from the container was remotely released by purging the small container with nitrogen for a short time (~60s). Seven ionisation chambers, designated TM0-TM6 were installed in Caisson for tritium concentration monitoring.

Model to simulate tritium spreading in controlled areas

Since the ventilation system should assure a rapid tritium removal in case of a leak, the air velocity in the ventilated rooms for tritium handling is usually turbulent. Presently several models are available to describe the turbulence flow field. The most widely used, due to its combined relative simplicity and good accuracy is the K-ε model and is used in the problem of tritium spreading in controlled areas as well.

Tritium diffusion from the leak source inside the Caisson is characterized by the mass diffusion equation. The temperature usually plays no role in the problem of tritium release in a room.

The boundary and initial conditions describing the condition of the Caisson are: temperature - 300 K, pressure 0.9497 bars, inlet duct: air velocity of equals 3.8 ms^{-1}, corresponding to a ventilation flow rate of 50 m^3h^{-1}, with uniformly distributed velocity in the cross section of the inlet duct. For the outlet duct, boundary condition of the type specified pressure and equal with 0.9497 bar was considered. Conditions on the wall of the Caisson: rigid, impenetrable walls. In the first experiments made at TPL, the amount of water in the initial tritium release was negligible, and therefore no adsorption - desorption phenomena on the walls need to be taken into account.

For solving the equations of motion in the above boundary conditions, GASFLOW software was used.

Results and discussions

From the two locations of tritium release that were experimentally investigated at TPL, the tritium release location on the corner was until now considered.

In Figure 1 the time histories of tritium concentration at locations corresponding to three monitors TM1, TM4, TM6 form the Caisson calculated from GASFLOW are presented. For

comparison purposes, see Figure 2, where the initial tritium behaviour, experimental results and calculated results with FLOW-3D, performed at TPL Japan are presented.

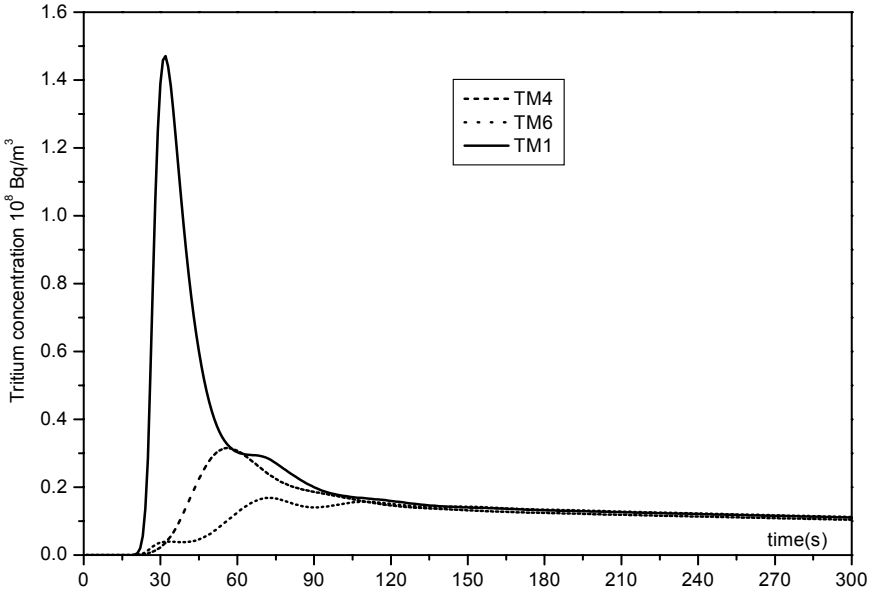

Fig. 1: Initial tritium behaviour in ventilated Caisson as computed with GASFLOW.

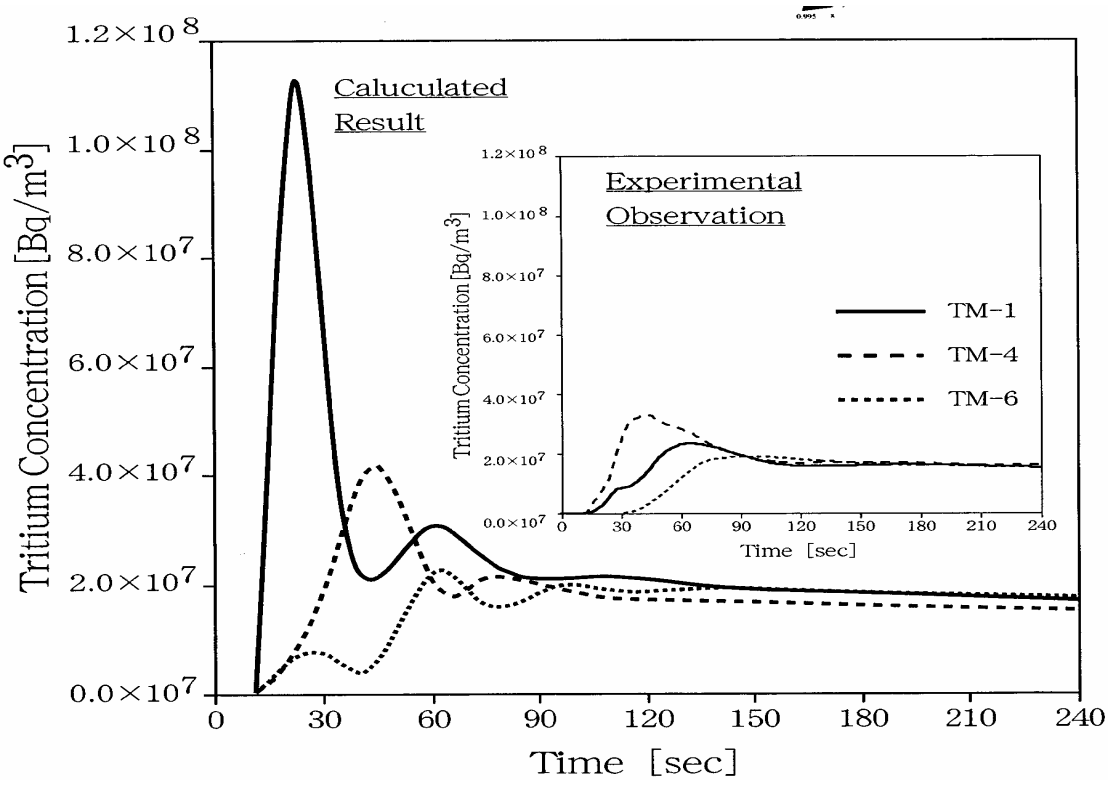

Fig. 2: Initial tritium behaviour in ventilated Caisson as computed with FLOW3D at TPL and experimental results.

As it can be seen from Figures 1 and 2 the computed results with GASFLOW reproduce with a good accuracy the experimental values from the locations of the monitors TM4 and TM6, somehow better then the computations with FLOW-3D which were performed at TPL.

However for monitor TM1, situated under the ceiling, just above the tritium release point and close to the back wall, the computed tritium concentration with both GASFLOW and FLOW 3D, in the first moments after the release is much higher then the recorded value.

This behaviour describes a rapid tritium movement near the wall up to the ceiling, quickly carried by the nitrogen stream, which was not observed in the experiments. This difference needs further investigation.

Fluid velocity and velocity field in the Caisson

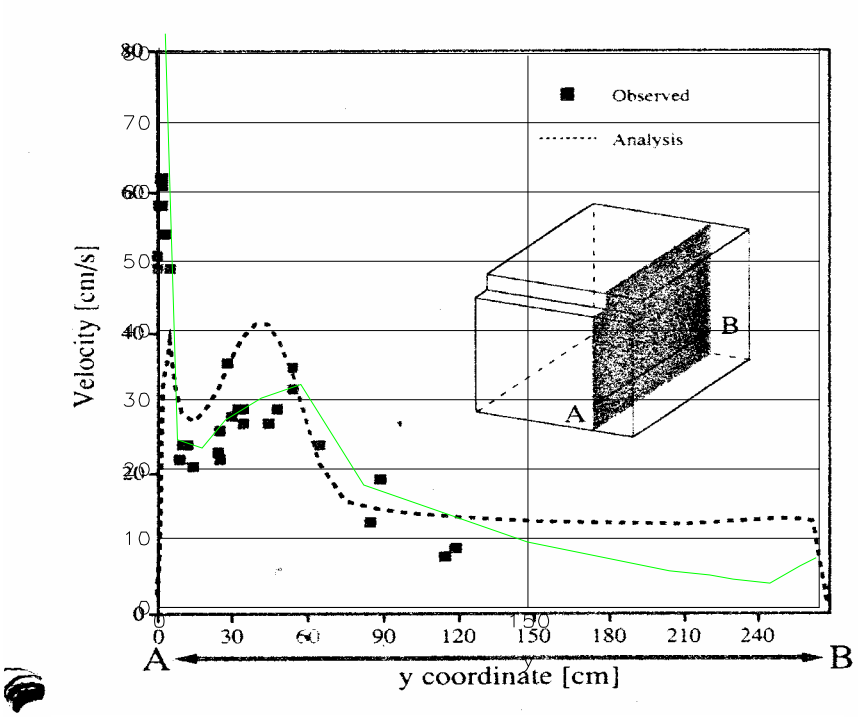

Fig. 3: Typical velocity distribution along y-direction

As already pointed out, the release is the key for the initial tritium behaviour. In the investigated case when tritium was released in the corner (near the wall), tritium is quickly carried by the strong flow near the wall. In Figure 3 typical velocity distributions along the y axis are plotted. In the plot where all results are located on the sections presented in the small attached drawing, the dotted lines represent the computed values from results of the simulation made with FLOW3D at TPL, the solid squares represent experimenttal data, and the green line, the computed velocity results of GASFLOW. As it can be seen, there is a very good agreement between the computed and the measured values.

Future work

There are other experiments carried out at TPL that will be theoretically investigated. These experiments involve different locations for the tritium release point as well as consideration of water vapour in the tritium release. In this later case, the boundary conditions for the Caisson walls need to be modified to account for adsorption - desorption phenomena on the walls. A refined meshing of the Caisson geometry will be made.

Staff:

Ioana.-R. Cristescu
J. Travis (IKET)

Literature:

[1] Y.Iwai et al - Simulation study of intentional tritium release experiments in the caisson assembly for tritium safety at TPL/JAERI., Fus. Eng. & Design 54, 523 (2001)

EFDA 02/1019
Detailed Design of a Water Detritiation System for JET

Development of a Water Detritiation System (WDS), i.e. configuration, design and performance testing of critical components is essential for both JET and ITER. For JET a WDS is needed to process tritiated water which was accumulated from operation and also the tritiated water which will be generated during decommissioning. For ITER, the WDS is one of the key systems to control the tritium content in the effluent streams, to recover as much tritium as possible and consequently to minimize the impact to the environment.

For water detritiation the Combined Electrolysis Catalytic Exchange (CECE) process has been chosen. To reduce the cost and the necessary time to build the facility it has to be incorporated in the existing Active Gas Handling System (AGHS) of JET as much as possible. The proposed Water Detritiation System for JET is schematically shown in Fig. 1. The main components of the WDS facility are the electrolysis unit, a liquid phase catalytic exchange (LPCE) column including the boiler and the condenser and a permeator for connecting the WDS with a cryogenic distillation unit which is not part of the WDS.

Tritiated water is fed at a certain location into the LPCE column, the feeding point depending on the tritium content in the tritiated water. At the top of the LPCE column natural water is added. The enriched tritiated water is collected in the column boiler from where is sent to the electrolysis unit. The electrolyser converts the water into tritium and deuterium enriched molecular hydrogen. This mixture is sent to the permeator (F) for chemical purification, and the purified permeate is fed into the cryogenic distillation (CD) system. From the top of the CD system, depleted hydrogen is combined with the bleed from the permeator and fed into the boiler of the LPCE column. In the boiler, tritiated and deuteriated hydrogen is saturated with water vapors and then flows upwards in counter-current to the water in the LPCE column. Tritium depleted hydrogen is released at the top of the LPCE column to the stack. From the bottom of the CD system, the tritium-enriched product is transferred to the Gas Chromatography (GC) isotope separation system of the AGHS for final recovery of tritium.

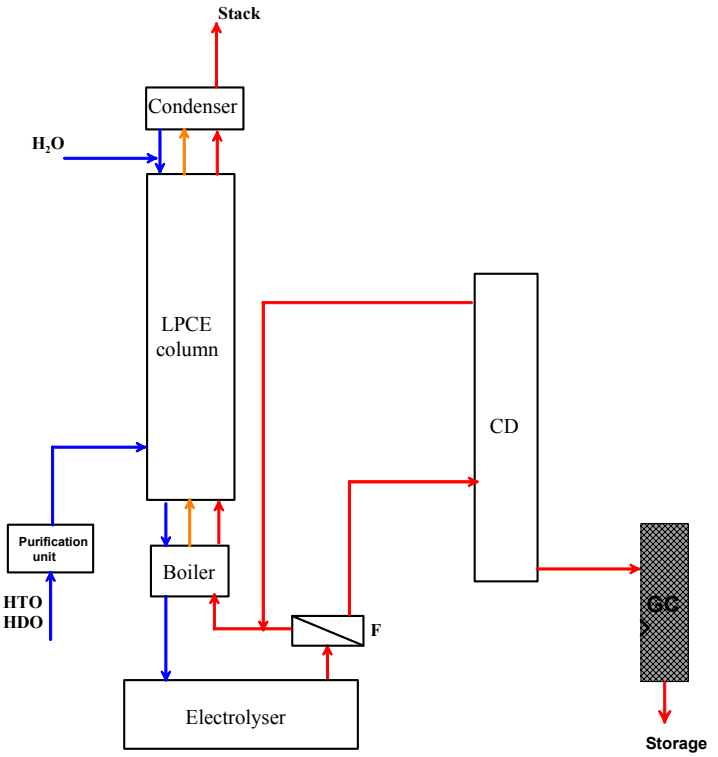

Fig. 1: Water Detritiation System for JET.

The main requirements to design a WDS for JET are: the WDS capacity of 10 t/year, the average tritium activity in the input water of 2.22 E10 $Bqkg^{-1}$ (0.6 $Cikg^{-1}$), and a decontamination factor along the LPCE column expressed as the ratio between the tritium content in the feeding water and the tritium content in the exhaust gas at the top of the column: 10^4.

Solving the system of mass balance equations on each sub-system from figure 1 gives the information related to mass flows and composition for each mass stream between the

various components of the WDS system and also for the interfaces to CD system and release to stack. With this information a process flow diagram based on the connections as described in figure 1 can be completed. In order to evaluate different options for WDS, especially regarding the cryogenic power available for the CD column and the hold-up of the electrolyser, a program was written and was used to analyse several options for WDS design, evaluated with respect to:

- Ratio between hydrogen gas, feed in at the bottom of the LPCE column and fresh water feed in at the top of the LPCE column (λ).

- Cryogenic power available for cryogenic distillation.

Related to the cryogenic distillation system for tritium enrichment, the refrigeration facility from JET AGHS is considered to be the cooling unit. Two possible combinations have been evaluated:

I. CECE system in combination with a new single cryogenic distillation column having the cooling capacity for the condenser of up to 100 W

II. CECE system in combination with the existing AGHS cryodistillation unit

I. CECE - new CD column

In table 1 the column length as function of λ are presented for two values of the reflux ratio in the CD column.

Table 1: LPCE column length for the system CECE-new CD

CD reflux ratio (*r*)	**5**	**10**
2	4,2 m	4,2 m
3	7,5 m	7,5 m
4	16 m	16 m

In Table 2 the tritium inventory in the electrolyser is presented for both Solid Polymer Membrane type of electrolyser and KOH type of electrolyser for the input data from above.

Table 2: Tritium inventory in the electrolyser unit for the CECE - new CD connection.

CD reflux ratio (*r*) λ	**SPM electrolyser**		**KOH electrolyser**	
	5	**10**	**5**	**10**
2	1.77 TBq (49 Ci)	3.59 TBq (97 Ci)	7.25 TBq (196 Ci)	14.3 TBq (3120 Ci)
3	2.37 TBq (64 CI)	4.77 TBq (129 Ci)	9.47 TBq (256 Ci)	19.4 TBq (561 Ci)
4	2.70 TBq (73 Ci)	5.40 TBq (146 Ci)	10.80 TBq (292 Ci)	21.6 TBq (584 Ci)

II. CECE system in combination with the existing AGHS cryodistillation unit

Considering all the additional costs related to design, manufacturing and commissioning of a new CD column at AGHS, the possibility and implications of using the existing CD system from AGHS JET was analyzed. The study is based on the assumption that during decommissioning the existing CD from AGHS will no longer be used for operation of the machine. For the combination CECE existing CD from AGHS, the available cryogenic power in column CD1 is only 10 W, therefore the maximum flowrate that can be fed in the CD is only 6 $molh^{-1}$ for the maximum reflux ratio of eight. In table 3 the length of the LPCE column and the tritium inventory in a SPM and KOH electrolyser are presented.

Table 3: LPCE column length and tritium inventory.

λ	**LPCE column length (m)**	**Tritium inventory in the SPM electrolyser**	**Tritium inventory in the KOH electrolyser**
2	5	28.9 TBq (780 Ci)	115.44 TBq (3120 Ci)
3	8	38.22 TBq (1033 Ci)	152.88 TBq (4132 Ci)
4	17	43.9 TBq (1170 Ci)	173.16 TBq (4680 Ci)

As it can be seen from table 3 and table 1 related to the length of the LPCE column the differences between the two solutions, CECE in combination with a new single CD column and respectively with the existing CD system from AGHS are minor. The only major difference is related to the tritium inventory in the electrolyser which in the later case is by almost one order of magnitude higher.

Conclusions

The Process Flow Diagram for Water Detritiation System at JET corresponding to the combination CECE-new CD and corresponding to the combination CECE- existing CD from AGHS have been made and presented in a report. The WDS for JET as described in PFD is composed from the systems:

- Front –end system, were tritiated water is purified and prepared to the desired feeding concentration in order to be fed into the LPCE column,
- LPCE column
- Electrolysis unit
- Tritium bearing oxygen stream unit, consisting of a stripping column for tritiated water coming from different subsystems.
- Hydrogen gas exhaust system, with the role to discharge in a safety mode the tritium and deuterium depleted hydrogen from the top of the LPCE column into the environment.

As three grams of tritium still remained in the machine and may be recovered during decommissioning, possible as HTO, the corresponding maximum total inventory is 30000 Ci. Considering that a minimum value of ten tons of water will be generated during decommissioning, the maximum tritium activity in tritiated water will be 2.4 $Cikg^{-1}$. From an assessment related to the cost for various operating modes, referring to λ, it is recommend

that the value of λ=3 should be chosen in the design of the CECE. This will also give higher flexibility to process feeding tritiated water with tritium activity in a wider range.

From the already presented implications related to the WDS cost (LPCE column length) it is obvious that there is no difference between the two combinations CECE-CD. It is also obvious that if the existing CD system from AGHS is used all the cost related to design, manufacture, install and commission the new CD system are avoided.

Staff:

I. Cristescu
I.R. Cristescu
M. Glugla
S. Welte

Heating Systems Technology Project

EFDA 03/1048
The First ITER NB Injector and the ITER NB Test Facility: Design

Background and Objectives

The design of the Neutral Beam (NB) system to be used in ITER and the results of the relevant R&D are described in the documents which were produced at the end of ITER-EDA (July 2001). FZK is now reviewing the design of the cryopump for the ITER NB Injector. Starting from the final report of the task TW1-TTF/D465-3, dated February 2002, FZK is working further on the technical assessment of the cryopumps [1].

The key NB design parameters and required pressures by given gas flows are summarized in table 1.

Table 1: Design parameters.

Power delivered to the plasma per injector	16.5 MW
Beam energy	1 MeV
Ion species	D^-
Accelerated ion current	40 A
Average accelerated ion current density	200 A/m^2
Current density uniformity over the extraction area	+-10 %
Source filling pressure	0.3 Pa
Hydrogen source gas flow (max. flow)	1.73 $Pa \cdot m^3/s$
Hydrogen gas flow from neutralizer	31.6 $Pa \cdot m^3/s$
Hydrogen gas flow to Residual Ion Dump (RID)	3 $Pa \cdot m^3/s$
required pressure in chamber 1 (neutralizer)	0.03 Pa
required pressure in chamber 2 (RID, calorimeter)	0.001 Pa
Pulse lengths	<= 3600 sec.

Design Concepts

The cryopump has a cylindrical shape and is split up into six submodules. In each of these, there are 28 cryopanels installed, 14 of them are serially connected. The distribution of the cryosupply starts at the inlet on the top of the cryopump and is then split up in two portions for each side of the cryopump. Each of these sides has a parallel connection of six halves of the submodules, see Fig. 1.

Cooling Principles

The technical design foresees a cooling of the cryopanels by a forced flow of SCHe of about 4.7 K and 4 bar inlet pressure to the cryopanel system. The backside of the panels facing the outer electropolished radiation shield is coated with charcoal. To reduce the heat load onto the cryopanels, their front side which is facing the blackened baffle is electropolished. The radiation shield consists of a closed radiation wall to the vessel and a chevron baffle facing the inner NBI vessel. Front endings and bottom openings are passively cooled by closed electropolished plates, but this could be changed to chevron baffles to increase the pumping speed. The shielding is cooled by a forced flow of SCHe at 80 K and a pressure of about 18 bars.

Pump Performance

The assessment of the pump performance is based on the actual pump design without any changes and assuming one side coated panels facing the coated side towards the outer electropolished 80 K shielding. The pump capacities of this design are for both chambers high enough to handle the gas load occurring during a pulse length of 3600 sec without any problems. The pressure needed in chamber 1 at the neutralizer can be reached without any problems even if the gas load there is high. In chamber 2 where the residual ion dump and the calorimeter are situated the pressure reached by the cryopumps is about 0.0021 Pa which is about the double of the required pressure.

Heat loads

For the cryopump design a calculation of the heat loads has been performed based on the highest gas load, i.e. for protium operation. For the Heating NBI system a heat load onto the 80 K shielding of 10.9 kW in steady state modus and a heat load of 12.3 kW in operation

mode was determined. For the cryopanels during steady state modus a resulting heat load of 35.4 W was calculated, which increases during operation to 145.7 W due to the amount of the pumped gas.

For the cooldown procedure the weights and associated energies have been determined. The 4.7 K cryopanels have an overall mass of 960 kg, requiring the amount of 78 MJ of heat to be removed for cool-down, of which 7.7 MJ are the part for each regeneration step from 90 K to 4.7 K. The shielding has a total mass of 4.6 tons with a part of 3 tons for the copper chevrons of the baffle. The shielding has to be cooled down from 300 K to 80 K and this corresponds to a heat of 340 MJ.

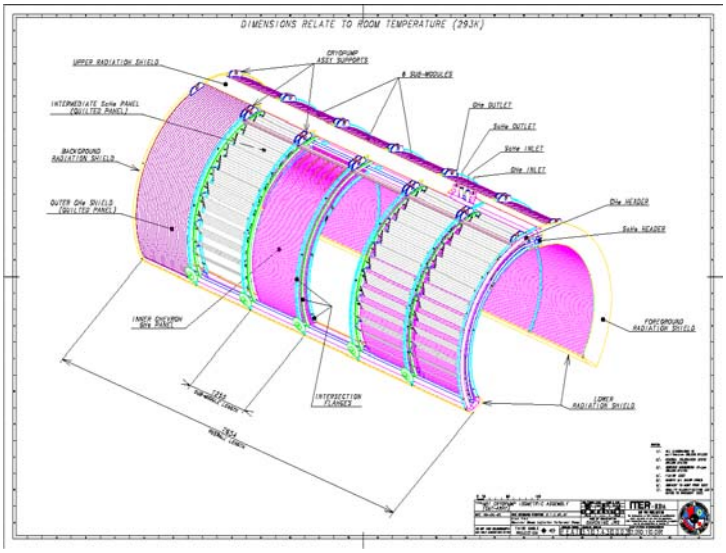

Fig. 1: NBI cryopump concept.

Hydrogen Safety

In case of hydrogen safety an air leak scenario has been considered to estimate the possibilities of an ignition of the air/hydrogen mixture in the ITER NBI vessel. It is shown that even the amount of hydrogen after 7200 sec pumping time is not enough to fulfil the necessary pressure for ignition during the flow of air through a leak into the ITER NBI vessel.

Further Activities

FZK will continue with the pressure drop calculations of the pipe routing of the ITER NBI cryopump to determine exactly the necessary cryogenic mass flows for the cooling of the cryopanels and the shielding. Furthermore, the safety assessments will be widened to include further scenarios of safety problems and the pump design will be partly revised to improve the pumping speed.

The mechanical forepumps needed as backing pumps for the cryopump system under the different operation modes will also be specified and designed.

Staff:

A. Antipenkov
Chr. Day
M. Dremel
A. Mack
R. Simon

Literature:

[1] M. Wykes, A. Mack, Chr. Day, D. Murdoch, R. Tivey, Hydrogenic inventory minimisation for the ITER torus and neutral beamline cryopumps, IEA Workshop on in-vessel tritium inventory, Abingdon, UK, March 2003.

TW3-THHN-NB-RFS
Cryopumps for the NBI-Testbed at IPP Garching

Background and Objectives

IPP Garching is being charged to develop a powerful negative ion source for the ITER Neutral Beam Injection System. It is planned to use the existing NBI-testbed L6 at IPP for this development work. However, with respect to pulse length, an upgrading of vacuum pumping is required. It has therefore been decided to replace the existing small capacity titanium sublimation pumps by a cryopump system to be connected with the ASDEX upgrade cryosupply. FZK is responsible for this upgrade.

The scope of the work is the development and manufacturing of a system of two cryopumps including the required cryo-, valve and intermediate storage systems for connection with the existing ASDEX cryoplant according to the technical specifications given in table 1.

Table 1: Technical Specifications for the cryopumps.

Gas load	≤ 3 Pa m^3 / s (H_2)
Pumping speed	≥ 700 m^3 / s (H_2)
Pulse length of gas load	3600 s
Pumping capacity	10^5 Pa·m^3
Operating pressure	Several 10^{-5} mbar
Max. leak rate (per pump)	1 x 10^{-7} Pa·m^3/s
Cryogenic media	Liquid helium at 4.45 K , 1.25 bar Liquid nitrogen at 80 K, 1.3 bar
Dimensions	ca. 4400 x 1500 x 260 mm (h x w x l)

Development work for the cryo-pumps

The hydraulic design of the cryopumps, including pressure drop calculations of the total pipework for the 5 K panel system cooled by a forced flow of liquid Helium at 4.5 K was carried out. The calculations for the radiation shielding cooled with liquid nitrogen to about 80 K has been done and the design of the shielding was finalised. This was necessary for the determination of the needed cryosupply system consisting of the liquid helium cryostat, the valve box and the transfer lines for the cryogenic liquids and offgas systems.

Thus the thermodynamic and vacuum technological design of the cryopumps to achieve the necessary cryogenic requirements to fulfil the pumping demands has been developed.

Design of the cryopumps

The mounting place of the two identical cryopumps is given by the present place of the titanium sublimation pumps in the NBI testbed. Thus the cryopumps are rectangular shaped with a height of 4.4 m. The backside will be radiation shielded by a closed wall in quilted design cooled with liquid nitrogen. The frontside will be a blackened chevron-baffle with a transmission for gas of about 22% and an optical transmission with less than 0.1% to minimize the optical radiation onto the 5 K cryopanels.

There are 27 of the 5 K cryopanels with a surface area of 0.44 m^2 each installed in one cryopump and all of them are serially connected. The overall pumping surface is given then with 11.88 m^2 and is going to fulfil the required pumping capacity sufficiently. The cryopanels are coated with charcoal on both sides and for the regeneration of the cryopanels each cryopanel is equipped with electrical heaters.

The cooling of the cryopanels will be realized with a forced flow of liquid helium at saturation conditions. In this case there will result a two phase flow to cool down the cryopanels by vaporization of liquid helium. The vapour part of the helium flow in the cryopanel system has been minimized and the design has been optimized with regard to pressure drop and heat load during all operation conditions of the cryopumps.

Status of Manufacturing

Since the beginning of the design conceptuation in January 2003, the call for tenders for all components has been realized. The cryopump subcomponents have all been ordered. Some of the cryogenic subcomponents, especially the main contract for cryostat and valve box, are still in the tendering procedure.

Each cryopump comprises mainly 3 parts, the cryopanel system, the chevron baffle system and the backwall. The 5 K cryopanels are under manufacturing and the electrical heaters are already manufactured. All welding and pressure tests for the cryopanels and the fixation of the electrical heaters have already been carried out. The chevron baffle consists of 145 brazed chevrons which are all blackened by plasma spray coating with Al_2O_3/TiO_2. For these items, the brazing tests are carried out and the optical emission properties of different mixtures of the coating material are determined to optimise the blackening of the chevron baffle.

Further Activities

FZK is continuing to control the manufacturing of the cryopumps and establish the overall pump design with the Main Assembly Contractor of the pumps. The integration of the cryosupply in the experimental hall at IPP Garching is another main aspect of the work which has to be carried out in the first half of 2004. The cryopumps shall be delivered to IPP in summer 2004 to integrate the cryosupply with the cryopumps in the summer break of ASDEX UPGRADE. Until now FZK work is in time with the given schedule for the project.

Staff:

Chr. Day
M. Dremel
H. Haas
H. Jensen
A. Mack
P. Pfeil
R. Simon
H. Stump
J. Weinhold
D. Zimmerlin

Underlying Technology

Underlying Technology

Operation and Upgrade of the Fusion Materials Laboratory

The Fusion Materials Laboratory provides the infrastructure for the performance of tasks defined in the EFDA workprogramme related to the characterisation of irradiated and non-irradiated materials. Methods such as optical and electron microscopy, He-pycnometry and Hg-porosimetry, crush-, micro-hardness- and charpy tests as well as long time annealing tests are applied.

The PIE of the HFR Phase IB Irradiation Programme was completed. Different OPTIFER and F82H mod materials had been irradiated up to 2.4 dpa at 250 - 450 °C. The Charpy impact and tensile testing specimens under investigation represented different heat treatment procedures and welding techniques.

Results of the measurements and consecutive analysis are reported in this report in the relevant chapters.

The aim of the investigations was to study the irradiation effects on the mechanical and structural properties of these materials. For this reason the broken samples were also investigated by light optical, scanning electron and transmission electron microscopy.

In the Fusion Ceramics Lab (Fig. 1) the investigation of blanket materials was continued with the completion of the PIE of EXOTIC-8 material. Both irradiated lithium orthosilicate and beryllium pebbles were tested in terms of tritium and helium release and irradiation-induced changes of porosity and deformation hardness of the structure. Different batches of unirradiated lithium orthosilicate material were characterised with respect to the influence of parameters of the fabrication process on the mechanical and structural properties.

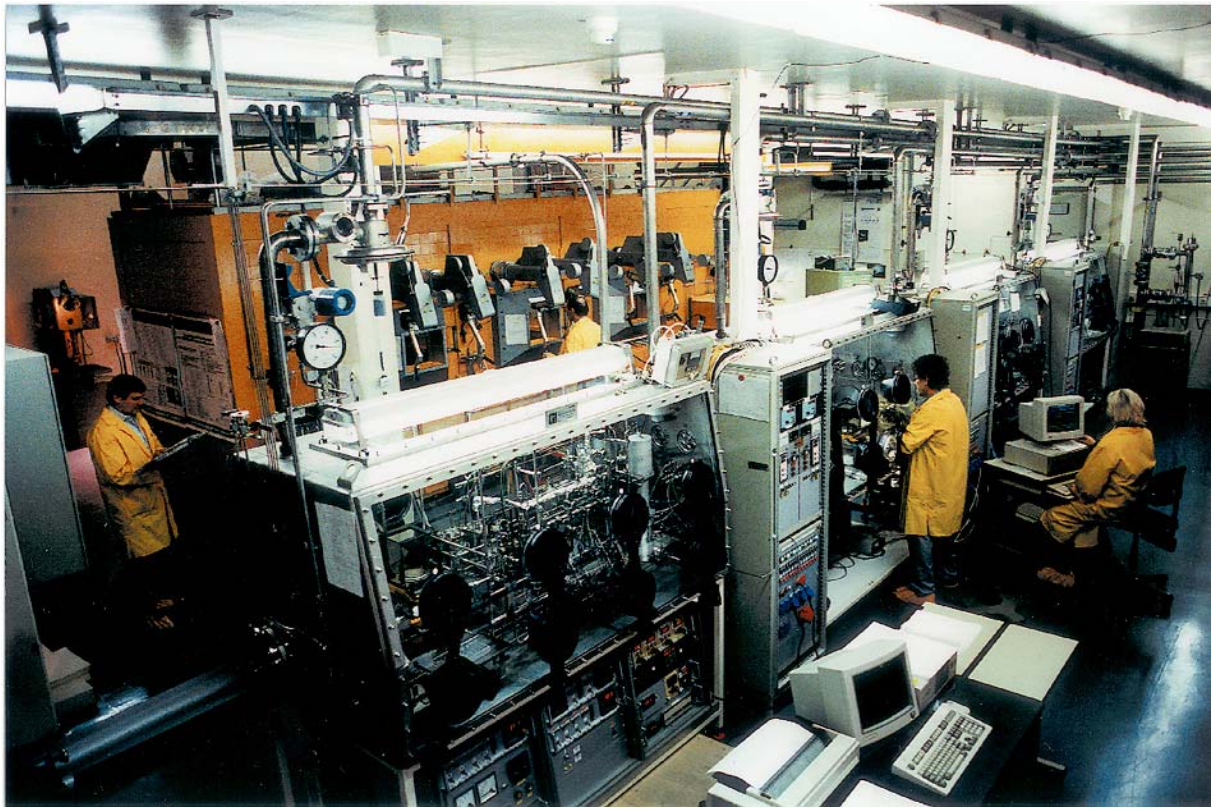

Fig. 1: Fusion Ceramics Laboratory.

Further samples from ASDEX, JET and TFTR carbon tiles were prepared for the investigation of tritium retention in these materials. In the TLK these samples were analysed.

In collaboration with the Hydrogen Isotope Research Center, Japan the distribution of tritium retained in carbon tiles was for the first time measured non-destructively by analysing both the bremsstrahlung of the decay electron in graphite and the excitation of argon gas atoms above the carbon surface.

For the PIE the following equipment was used:

- Charpy and tensile testing devices
- Light optical, scanning electron and transmission electron microscopes, electron microprobe analysis
- Desorption device with high temperature furnace for tritium and helium release measurements
- He-pycnometer and Hg-porosimeter
- Sphere crush and creep testing apparatus

Results of the measurements and consecutive analysis are reported in the respective chapters of this report.

In the frame of our upgrading programme, two new lead-shielded cells for materials testing and optical microscopy are under construction (Fig. 2).

Fig. 2: New Materials Testing Cell under Construction.

Staff:

Barie, P.
Damm, E.
Erbe, A.
Gilpert, M.
Holzer, M.
Jackisch, H.
Lautensack, S.
Lauterbach, P.
Ludat, J.
Mangei, G.
Mitschke, H.
Nägele, W.
Reichmann, D.
Ries, H.
Rolli, R.
Romer, O.
Rösch, G.
Schmidt, R.
Steinle, H.
Veit, A.

Operation and Improvements of the Tritium Laboratory Karlsruhe (TLK)

With its closed tritium cycle and the license to handle 40 g of tritium, the Tritium Laboratory Karlsruhe (TLK) is a unique facility. In general TLK has many similarities with the Tritium Plant of a fusion reactor like ITER, since it comprises a storage system, a plasma exhaust processing system for the recovery of tritium and an isotope separation system. The operation of the TLK is in itself an essential contribution to the fusion R&D work with tritium. The experience gained has for example been utilized for European ITER site studies and licensing considerations.

An experimental area of around 1000 m^2 and a total glove box volume of about 125 m^3 is available for experiments and support facilities at TLK. All molecular sieve beds from the tritium retention systems of each separate glove box system as well as the molecular sieve beds from the TLK central tritium retention system need to be periodically regenerated. More then 200 l of tritiated water has been collected. Since currently experimental work is going on to process this tritiated water such that its tritium is recovered it does not need to be disposed off as waste.

To support the research program a glove box for the characterization of flakes has been commissioned and a new glove box including its local tritium retention system for the testing of an ITER getter bed has been installed. After more than 10 years of operation some components and even complete test set-ups have reached their end of life, failed or are no longer required within the ongoing experimental program. The hardware of the infrastructure process control system was out of date and therefore a replacement was started to ensure safe operation of the TLK. The migration of the visualization and operating software of the infrastructure process control system has already been finished. The laboratory chiller system (two units with 600 kW cooling power each) has been replaced completely and a helium return line for a refrigerator has been installed. Intensive efforts were devoted to licensing matters and documentation during the past period.

The wide-ranging experimental program carried out especially with the CAPER facility has involved round the clock operation of the TLK, with frequent transfers of tritium and tritiated hydrogen isotopes between the CAPER facility and the TLK infrastructure, i.e. the Tritium Transfer System (TTS), the Tritium Storage System (TLG) and the Isotope Separation System (ISS). More then 70 separation runs with the ISS have been carried out to separate tritium and deuterium for reuse in experiments. Tritium accountancy was carried out by calorimetric measurements. The integral operation of the CAPER facility with the infrastructure of the TLK provides essential information of tritium tracking and control and is a good example for accuracy limitations of accountancy procedures.

Staff:

H-D. Adami
U. Besserer
L. Dörr
H. Dittrich
M. Göckel
G. Hellriegel
W. Hellriegel
B. Kloppe
F. Kramer
S. Krieger
K. Nolte
E. Porter
P. Schäfer
P. Schuster

Test of the TFMC during Test Phase II in the TOSKA Facility

After the preparation of the facility the test phase II (TFMC tested together with the LCT coil) was performed in TOSKA in 2002. The diagram shows the very successful test course starting with the cool down in August and ending with the warm up in December, 2003.

During the test phase II several short breaks have been made to optimize the control of the 20 kA Bruker power supply. During these tests it has been decided to replace the digital controller with an analog controller (Bruker is still working on the optimization of the digital controller).
However, despite these minor problems the TOSKA facility was operated very reliable with an availability of 98%.

Preparation for the test of the High-Tc current lead test

The following hard- and software upgrades have been performed in order to prepare the TOSKA facility for the testing of the High-Tc current lead:

- The cryogenic system is being adapted to meet the needs during the test of the High-Tc current lead and the BBIII experiments.
- The PLC programming of the interlocks is being implemented currently.
- Adaptation of the DAS and control system as needed for the High-Tc current lead test
- The demineralised water circuit has been renewed
- A prolongation of the Al-bus bar system has been installed to allow a horizontal feeding of current into the new High-Tc current lead
- The high Tc current lead is being manufactured presently
- Busbar III has been equipped with numerous sensors (voltage taps, temperature sensors, Hall probes) to meet the needs of the current distribution measurement experiment.

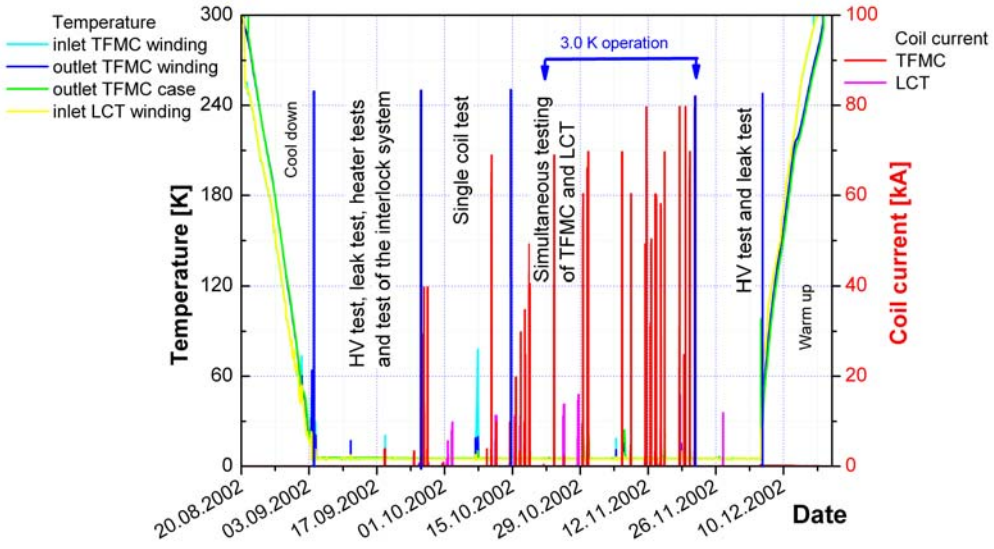

Overview of test phase II (TFMC test together with LCT coil)

Further improvements of the TOSKA facility

New centrifugal He pump

After the new centrifugal pump has been found to have a to high heat load during the year 2002 several tests have been made to identify the origin of these problems together with the supplier of the pump. Modifications of the internal construction have been developed and integrated in the pump. The pump will be retested at the end of 2003.

20 kA power supply:

The changed digital controller for the 20 kA power supply was retested together with the manufacturer Bruker. Further improvements are underway.

Staff:

M.S. Darweschsad
G. Dittrich
P. Duelli
W. Fietz
S. Fink
U. Fuhrmann
R. Heger
R. Heller
W. Herz
A. Kienzler
H. Kiesel
O. Langhans
V. Leibbrand
A. Lingor
V. Marchese
I. Meyer
J. Müller
G. Nöther
A. Nyilas
M. Röhrling
V. Schulmeister
E. Specht
M. Süßer
A. Ulbricht
K. Weiss
F. Wüchner
G. Zahn
V. Zwecker

Appendix I: FZK Departments Contributing to the Fusion Programme

FZK Department	FZK Institut/Abteilung	Director	Ext.
Institute for Materials Research	Institut für Materialforschung (IMF)	I. Prof. Dr. K.-H. Zum Gahr	3897
		II. Prof. Dr. O. Kraft	4815
		III. Prof. Dr. H. Haußelt	2518
Institute for Pulsed Power and Microwave Technology	Institut für Hochleistungsimpuls- und Mikrowellentechnik (IHM)	Prof. Dr. M. Thumm	2440
Institute for Nuclear and Energy Technology	Institut für Kern- und Energietechnik (IKET)	Prof. Dr. T. Schulenberg	3450
Institute for Reactor Safety	Institut für Reaktorsicherheit (IRS)	Prof. Dr. D. Cacuci	2550
Institute for Technical Physics	Institut für Technische Physik (ITP)	Prof. Dr. P. Komarek	3500
Institute for Micro Process Engineering	Institut für Mikroverfahrenstechnik (IMVT)	Dr. K. Schubert	3114
- Tritium Laboratory Karlsruhe	- Tritiumlabor Karlsruhe (TLK)	Dr. M. Glugla	3226
Institute for Data Processing and Electronics	Institut für Prozessdatenverarbeitung und Elektronik (IPE)	Prof. Dr. H. Gemmeke	5635

Contributing:

Institute for Nuclear and Particle Physics, Technical University Dresden	Institut für Kern- und Teilchenphysik Technischen Universität Dresden	Prof. Dr. H. Freiesleben	+49 351/4635461
Max-Planck-Institute for Plasma Physics Berlin	Max-Planck-Institut für Plasmaphysik Berlin	Prof. Dr. G. Fussmann	+49 30/20366130
Institute for Applied Physics University Frankfurt	Institut für Angewandte Physik J.W. Goethe-Universität Frankfurt	Prof. Dr. H. Klein	+49 69/7982 3489

Appendix II: Fusion Programme Management Staff

Head of the Research Unit	Dr. G. Janeschitz	ext. 5460 e-mail: guenter.janeschitz@fusion.fzk.de
Secretariat:	Mrs. M. Winkelmann	ext. 5461 e-mail: miriam.winkelmann@fusion.fzk.de
	Mrs. I. Sickinger	ext. 5466 e-mail: ingeborg.sickinger@fusion.fzk.de
Program Budget, Administration, Reports, EU-Affairs	BW. G. Kast	ext. 5462 e-mail: guenter.kast@fusion.fzk.de
	Mrs. V. Lallemand	ext. 6461 e-mail: vera.lallemand@fusion.fzk.de
	Mrs. I. Pleli	ext. 6461 e-mail: ingrid.pleli@fusion.fzk.de
Blanket Development, Neutron Source, Reactor Studies, Plasma Heating Technology, Public Relations	DI. W. Bahm	ext. 5465 e-mail: werner.bahm@fusion.fzk.de
Tritium Technology, Structural Materials, Irradiations, Superconducting Magnets	DI. S. Gross	ext. 5468 e-mail: sigurd.gross@fusion.fzk.de

Address:	**Forschungszentrum Karlsruhe GmbH** **Nuclear Fusion Programme Management** **Post Office Box 3640, D - 76021 Karlsruhe / Germany**
Telephone No:	**07247-82- Extensions .....**
Telefax No:	**07247-82-5467**
world wide web:	**http://www.fzk.de/fusion**

Appendix III: Glossary

AC	Alternating Current
ACP	Actived Corrosion Products
ADC	Analog Digital Converter
AGHS	Active Gas Handling System
AMSC	American Superconductor Corp.
ANFIBE	Analysis of Fusion Irradiated Beryllium
AP	Activated Particles
ASER	Actively Stabilized External Resonator
CAD	Computer Aided Design
CCD	Charge Coupled Device
CD	Current Drive
CD	Cryogenic Distillation
CDE	Conceptual Design Evaluation
CEA	Commissariat à l'Energy Atomique
CECE	Combined Electrolysis and Catalytic Exchange
CF	Con Flat
CF	Cryogenic Forevacuum
CFC	Carbon Fibre Composite
CFD	Computational Fluid Dynamics
CICC	Cable in Conduit Conductor
CL	Current Lead
CMSB	Cryogenic Molecular Sieve Bed
COOLSORP	Measurement of Sorption Isotherms at Cryogenic Temperatures
CRPP-EPFL	Centre de Recherches en Physique des Plasmas Ecole Polytechnique Fédérale de Lausanne
CS	Central Solenoïd
CT	Cold Trap
CVD	Chemical Vapor Deposition
CW	Continuous Wave
DAQ	Data Acquisition System
DAS	Data Acquisition System
DBTT	Ductile Brittle Transition Temperature
DC	Direct Current
DCLL	Dual Coolant Lithium-Lead
DEMO	Demonstration Power Station
DRG	Design Requirements and Guidelines

DT	Deuterium Tritium
DTE1	Deuterium Tritium Experiment 1 at JET
DTL	Drift Tube Linear, accelerator structure
EAF	European Activation File
EASY	European Activation System
EB	Electron Beam
EC(R)H	Electron Cyclotron (Resonance) Heating
ECCD	Electron Cyclotron Current Drive
ECM	Electro-chemical Machining
EDA	Engineering Design Activity
EDM	Electro Discharge Method
EDX	Energy Dispersive X-Ray
EFDA	European Fusion Development Agreement
EFF	European Fusion File
EFTEM	Energy Filtered Transmission Electron Microscopy
EISS	European ITER Site Study
EISSG	European ITER Site Study Group
ELM	Edge Localized Mode
ENEA	Italian National Agency for New Technologies, Energy and the Environment
ESIS	European Structural Integrity Society
ESRF Grenoble	European Synchrotron Radiation Facility
EVITA	Experimental Vacuum Ingress Test Apparatus
FCGR	Fatigue Crack Growth Rate
FE	Finite Element
FEAT	Fusion Energy Advanced Tokamak
FEM	Finite Element Method
FM	Ferritic-martensitic
FMI	Fractographic and Microstructural Investigations
FNG	Frascati Neutron Generator
FT – IR	Fourier Transform – Infra Red
FW	First Wall
FWM	First Wall Material
GC	Gas Chromatograph
H & CD	Heating & Current Drive
HAADF	High Angle Annular Dark Field Detector
HCLL	Helium Cooled Lithium-Lead
HCPB	Helium Cooled Pebble Bed

HECOP	Heat Conduction of Pebble Bed
HEMP	Helium Cooled Modular Divertor Concept with Pin Array
HETP	High Equivalent to a Theoretical Plate
HETS	High Efficiency Thermal Shield
HFR	High Flux Reactor at Petten
HFTM	High Flux Test Module
HHFC	High Heat Flux Components
HIDOBE	High Dose Beryllium Irradiation
HIP	Hot Isostatic Pressing
HTM	High Flux Test Module
HTS	High Temperature Superconducting
HTSCLM	HTS Current Lead Module
HV	High Voltage
HVAC	Heating, Ventilation, Air Conditioning
IAEA	International Atomic Energy Agency
IEAF	Intermediate Energy Activation File
IFMIF	International Fusion Materials Irradiation Facility
IPF	Institut für Plasmaforschung der Universität Stuttgart
IPP	Max-Planck-Institut für Plasmaphysik
ISS	Isotope Separation System
ISTC	International Science and Technology Center
ITER	International Thermonuclear Experimental Reactor
ITHEX	Teststrecke für thermohydraulische Experimente zur IFMIF-Hochflusszelle
JAERI	Japan Atomic Energy Research Institute
JASS	Joint Assessment of Specific Sites
JET	Joint European Torus
JETT	J Evaluation on Tensile Test
KONUS	Kombinierte Nullgrad-Struktur
LCF	Low Cycle Fatigue
LCT	Large Coil Task
LEBT	Low Energy Beam Transport
LLL USA	Lawrence Livermore National Laboratory
LLRM	Linear-Low-Reynolds-Model
LLW	Low Level Waste
LN2	Liquid Nitrogen
LPCE	Liquid Phase Catalytic Exchange
LSC	Liquid Scintillation Counting

LT	Low Temperature
MAGS	Magnet Safety (software module)
MBWG	Multi Beam Wave Guide
MCNP	Monte Carlo Neutron Particle
MD	Molecular Dynamics
MEBT	Medium Energy Beam Transport
MEKKA	Magneto-hydrodynamic Experiments in Sodium and Potassium Karlsruhe
MFTM	Medium Flux Test Module
MHD	Magneto Hydrodynamics
MS	Mass Spectrometry
NB	Neutral Beam
NBI	Neutral Beam Injection
NRT	Norgett Robinson Torrens
ODS	Oxide Dispersion Strengthened
ORNL	Oak Ridge National Laboratory
PBA	Pebble Bed Assembly
PCP	Prototype Cryosorption Pump
PERMCAT	Permeator Catalyst
PFC	Plasma Facing Components
PHHT	Post HIP Heat Treatment
PICOLO	Pb-Li Corrosion Loop
PIE	Post Irradiation Examination
PIM	Power Injection Molding
PKA	Primary Knocked on Atom
PLC	Programmable Logical Controller
PMW	Projekt Mikrowellenheizung
POLO	Poloïdal Coil
PPCS	Power Plant Conceptual Study
PPPL	Princeton Plasma Physics Laboratory
PTE	Preliminary Tritium Experiment
PVM	Parallel Virtual Machine
PWHT	Post Welt Heat Treatment
RAFM	Reduced Activation Ferritic Martensitic
RCT	Recrystallisation Temperature
REP	Rotating Electrode Process
RF	Radio Frequency
RFQ	Radio Frequency Quadrupol, accelerator structure

RID	Residual Ions Dump
RT	Room Temperature
SAD	Secondary Angular Distributions
SANS	Small Angle Neutron Scattering
SBWG	Single Beam Ware Guide
SC	Superconducting
SCHe	Supercritical Helium
SCLL	SiC Lithium Lead
SDS	Storage and Delivery System
SEAFP	Safety and Environmental Assessment of Fusion Power
SEM	Scanning Electron Microscope
SOL	Scrape-off Layer
SPICE	Sample Holder for Irradiation of Miniaturised Steel Specimens Simultaneously at Different Temperatures
SPM	Solid Polymer Membrane
STP	Standard Temperature Pressure
TBM	Test Blanket Module
TCS	Current Sharing Temperature
TDA	Thermal Differential Analysis
TED	Thales Electron Devices, Velizy
TEM	Transmission Electron Microscope
TEP	Tokamak Exhaust Processing
TF	Toroïdal Field
TFMC	Toroïdal Field Model Coil
TFTR	Tokamak Fusion Test Reactor
THELMA	Thermo-Hydraulic Electro-Magnetic Analysis
TIDE	Tritium Decontamination Facility
TIG	Tungsten Inert Gas
TIMO	Test Facility for ITER Model Pump
TITAN	Tieftemperaturadsorption
TLG	Tritium Storage System
TLK	Tritium Laboratory Karlsruhe
TOF	Time of Flight
TOSKA	Torusspulen Testanordnung Karlsruhe
TPL	Tritium Process Laboratory
TTE	Trace Tritium Experiment
TTS	Tritium Transfer System
TUD	Technische Universität Dresden

UCT	Uniaxial Compression Test
UKAEA	United Kingdom Atomic Energy Authority
USE	Upper Shelf Energy
VDS	Vent Detritiation System
VPCE	Vapour Phase Catalytic Exchange
VTA	Vertical Test Assemblies
WCLL	Water Cooled Lithium-lead Blanket
WDS	Water Detritiation System